

Manjaree Pandit
Laxmi Srivastava
Ravipudi Venkata Rao
Jagdish Chand Bansal *Editors*

Intelligent Computing Applications for Sustainable Real-World Systems

Intelligent Computing Techniques and
their Applications



 Springer

The Springer logo features a stylized chess knight (horse) facing left, positioned above the word 'Springer'.

Proceedings in Adaptation, Learning and Optimization

Volume 13

Series Editors

Meng-Hiot Lim, Nanyang Technological University, Singapore, Singapore

Yew Soon Ong, Nanyang Technological University, Singapore, Singapore

The role of adaptation, learning and optimization are becoming increasingly essential and intertwined. The capability of a system to adapt either through modification of its physiological structure or via some revalidation process of internal mechanisms that directly dictate the response or behavior is crucial in many real world applications. Optimization lies at the heart of most machine learning approaches while learning and optimization are two primary means to effect adaptation in various forms. They usually involve computational processes incorporated within the system that trigger parametric updating and knowledge or model enhancement, giving rise to progressive improvement. This book series serves as a channel to consolidate work related to topics linked to adaptation, learning and optimization in systems and structures. Topics covered under this series include:

- complex adaptive systems including evolutionary computation, memetic computing, swarm intelligence, neural networks, fuzzy systems, tabu search, simulated annealing, etc.
- machine learning, data mining & mathematical programming
- hybridization of techniques that span across artificial intelligence and computational intelligence for synergistic alliance of strategies for problem-solving.
- aspects of adaptation in robotics
- agent-based computing
- autonomic/pervasive computing
- dynamic optimization/learning in noisy and uncertain environment
- systemic alliance of stochastic and conventional search techniques
- all aspects of adaptations in man-machine systems.

This book series bridges the dichotomy of modern and conventional mathematical and heuristic/meta-heuristics approaches to bring about effective adaptation, learning and optimization. It propels the maxim that the old and the new can come together and be combined synergistically to scale new heights in problem-solving. To reach such a level, numerous research issues will emerge and researchers will find the book series a convenient medium to track the progresses made.

** Indexing: The books of this series are submitted to ISI Proceedings, DBLP, Google Scholar and Springerlink **

More information about this series at <http://www.springer.com/series/13543>

Manjaree Pandit · Laxmi Srivastava ·
Ravipudi Venkata Rao · Jagdish Chand Bansal
Editors

Intelligent Computing Applications for Sustainable Real-World Systems

Intelligent Computing Techniques
and their Applications

 Springer

Editors

Manjaree Pandit
Department of Electrical Engineering
Madhav Institute of Technology and Science
Gwalior, India

Laxmi Srivastava
Department of Electrical Engineering
Madhav Institute of Technology and Science
Gwalior, India

Ravipudi Venkata Rao
Mechanical Engineering Dept, A-2 Quarter
S.V. National Institute of Technology
Surat, Gujarat, India

Jagdish Chand Bansal
Department of Mathematics
South Asian University
New Delhi, Delhi, India

ISSN 2363-6084 ISSN 2363-6092 (electronic)
Proceedings in Adaptation, Learning and Optimization
ISBN 978-3-030-44757-1 ISBN 978-3-030-44758-8 (eBook)
<https://doi.org/10.1007/978-3-030-44758-8>

© Springer Nature Switzerland AG 2020

This work is subject to copyright. All rights are reserved by the Publisher, whether the whole or part of the material is concerned, specifically the rights of translation, reprinting, reuse of illustrations, recitation, broadcasting, reproduction on microfilms or in any other physical way, and transmission or information storage and retrieval, electronic adaptation, computer software, or by similar or dissimilar methodology now known or hereafter developed.

The use of general descriptive names, registered names, trademarks, service marks, etc. in this publication does not imply, even in the absence of a specific statement, that such names are exempt from the relevant protective laws and regulations and therefore free for general use.

The publisher, the authors and the editors are safe to assume that the advice and information in this book are believed to be true and accurate at the date of publication. Neither the publisher nor the authors or the editors give a warranty, expressed or implied, with respect to the material contained herein or for any errors or omissions that may have been made. The publisher remains neutral with regard to jurisdictional claims in published maps and institutional affiliations.

This Springer imprint is published by the registered company Springer Nature Switzerland AG
The registered company address is: Gewerbestrasse 11, 6330 Cham, Switzerland

Preface

The concept of sustainability is central to all developments. The term becomes more relevant by each passing day as the very existence of life on this planet is endangered due to the continuous and mindless exploitation of nature and natural resources due to population explosion, economic growth, infrastructure development, lifestyle changes and many other such factors. Nature, defined by its abundance, is a miraculous entity; it nurtures and blesses our lives in a million ways; nature keeps rejuvenating, replenishing, recycling and renewing itself constantly, at a steady pace. However, alarm bells are ringing now in every corner of the globe as the latest figures reveal a very grim picture, showing a huge gap between the rate of resource depletion and rate of recycling.

The professionals of engineering, management, science and technology fraternity need to redefine their role at this crucial point in the history of humanity, where the saying, “the last straw breaks the camel’s back” seems to fit so well. The signs are already visible everywhere, be it heavy smog in winter, frequent floods and cyclones, erratic climate pattern, unmanageable burgeoning piles of waste, polluted air, water, earth; even the stars are losing their sheen. Nature is crying out for help! We urgently need to answer that call to help ourselves and to the future generations.

However, sustainability is a rather controversial issue; some would argue that development comes at the cost of sacrificing resources or else the human race will regress to the dark ages. I would say that striking a balance between development and sustainability is perhaps the biggest challenge before mankind. Accepting this challenge is our only hope, else we are doomed for sure; the only question is when and how.

The idea behind the conference is to bring together engineers, scientists, researchers, academicians, sociologists, planners and all those who can make a difference by introducing new policies, models, techniques and ideas that may help in creating a better tomorrow.

This interdisciplinary International Conference on “Sustainable and Innovative Solutions for Current Challenges in Engineering & Technology”, ICSISCET 2019, was planned about two years ago, but it got a final form after receiving the sanction from the All India Council of Technical Education, New Delhi (AICTE). The idea

was to encompass and link all domains of engineering and technology with sustainable development. Overall, there were ten tracks; broadly based on exploring sustainability in infrastructure, manufacturing practices and design, power and energy systems, and computing and information technology. Tracks were also planned on the latest developments in computational intelligence and machine learning, embedded systems and VLSI design and advances in electronics and communication technology; two tracks on societal implications of technology and multidisciplinary research and practices.

The conference received 148 papers through the “easy chair conference management system”. The papers were checked for plagiarism using the standard Turnitin software before sending the papers for review. After a rigorous review (each paper was reviewed by minimum two reviewers), 88 papers were accepted and presented in 16 separate sessions. There was one Skype session. Five sessions were run in parallel on 2nd November afternoon, 3rd November morning and afternoon. Each session was chaired by one internal and one external expert. Also, spread over these two days, ten expert lectures were arranged which were delivered before the paper presentations in each session. Overall, 24 experts from diverse fields of engineering, technology and science had participated in the conference.

The session chairs and supporting teams had been provided with the review comments and soft copies of all camera-ready papers assigned to their respective sessions, in advance.

In keeping with the conference theme of “sustainability”, the organizing chairs had tried to avoid the use of paper as far as possible; all communications, review process, data management, registration, most of the session documentation, etc. had been done electronically, to the extent that we had given e-certificates to all participants, session chairs and experts, as a best practice and also as a small initiative towards the commitment of the institute to sustainability.

Organization

Advisory Committee Members

Daizhong Su	Nottingham Trent University Burton Street, Nottingham, UK
Joze Balic	University of Maribor, Smetanova, Slovenia
J. Paulo Davim	University of Aveiro, Portugal
Felix T. S. Chan	The Hong Kong Polytechnic University, Hong Kong
Ajith Abraham	Machine Intelligence Research Labs, Washington, USA
P. N. Suganthan	Nanyang Technological University, Singapore
Duc T. Pham	University of Birmingham, Birmingham, UK
S. G. Deshmukh	Director, IIITM, Gwalior, India
Andrew Kusiak	University of Iowa, Iowa City, USA
D. P. Kothari	Former Director I/c, IIT, Delhi, India
Ali Cemal Benim	Duesseldorf University of Applied Sciences, Germany
S. N. Singh (Vice Chancellor)	MMM University, Gorakhpur, India
B. K. Panigrahi	IIT Delhi, India
G. A. Vijayalaxmi Pai	PSG College of Technology, Coimbatore, Tamil Nadu, India
Aparajita Ojha	PDPM IIITDM Jabalpur, India
Shekhar Verma	IIIT Allahabad, India
Vikas Rastogi	Delhi Technological University (DTU), Delhi
C. Patvardhan	Dayalbagh Educational Institute, Dayalbagh, Agra
Kapil Sharma	Delhi Technological University (DTU), Delhi
D. K. Chaturvedi	Dayalbagh Educational Institute (DEI), Agra, India
Lillie Dewan	NIT, Kurukshetra, India

Sumam Mary Idicula	Cochin University of Science and Technology, Cochin, India
Surender Reddy Salkuti	Woosong University, Republic of Korea, South Korea
Amit Shrivastava	Delhi Technological University (DTU), Delhi
A. K. Saxena	Dayalbagh Educational Institute, Dayalbagh, Agra
S. C. Choube	UIT, RGPV, Bhopal, India
Sandeep Gandhi	Tata Projects Ltd., India
(General Manager (QS))	
R. K. Mishra	IIT, BHU, Varanasi, India
Ashutosh Chincholikar	Smart Controls India Ltd (Member Zeppelin Group), India
K. V. Arya	ABV-IIITM, Gwalior, India
Rajesh Kumar	Malaviya National Institute of Technology, Jaipur, India
Aditya Trivedi	ABV-IIITM, Gwalior, India
H. M. Suryawanshi	VNIT, Nagpur, India
P. K. Singh	ABV-IIITM, Gwalior, India
Manohar Singh	Central Power Research Institute, Bengaluru, India
M. M. Tripathi	Delhi Technological University (DTU), Delhi
Majid Jameel	Jamia Millia Islamia, New Delhi, India
Surekha Bhanot	BITS, Pilani, India
R. N. Sharma	NIT, Hamirpur, India

Programme Committee Members

Harimohan Dubey	MITS, Gwalior, India
Trapti Jain	IIT Indore, India
Jawar Singh	IIIT, Patna
Pushpendra Singh	Delhi Technological University (DTU), Delhi
Tripta Thakur	MANIT, Bhopal, India
Abhishek Asthana	Sheffield Hallam University, UK
Rolf Crook	University of Leeds, UK
A. K. Wadhvani	MITS, Gwalior, India
Rajesh Kumar	Delhi Technological University (DTU), Delhi
R. S. Thakur	MANIT, Bhopal
C. S. Malvi	MITS, Gwalior, India
Y. Kumar	MANIT, Bhopal
Sonali Agarwal	IIIT, Allahabad
Manisha Sharma	NIT, Hamirpur, India
Perminderjit Singh	Punjab Engineering College, Chandigarh, India

Kamal Raj Pardasani	MANIT Bhopal
Arvind Jain	NIT, Agartala
Debashis Chatterjee	Jadavpur University, Kolkata, India
Shailaja Kumari M.	NIT, Warangal, India
P. K. Singhal	MITS, Gwalior, India
Sanjay Tiwari	MITS, Gwalior, India
Pratesh Jayaswal	MITS, Gwalior, India
V. P. Vishwakarma	GGSIPIU, Delhi
Geetam Singh Tomar	THDC Institute of Hydropower Engineering and Technology, Tehri, Uttarakhand, India
Anmol Ratan Saxena	NIT Delhi, New Delhi, India
Himmat Singh Ahirwar	MITS, Gwalior, India
Adikanda Parida	Regional Institute of Science and Technology, Nirjuli, Arunachal Pradesh, India
Sulochana Wadhvani	MITS, Gwalior, India
Rekha Gupta	MITS, Gwalior, India
D. K. Saini	University of Petroleum and Energy Studies, Dehradun, India
R. Kansal	MITS, Gwalior, India
N. S. Raghava	Delhi Technological University (DTU), Delhi
S. K. Jain	MITS, Gwalior, India
Akhilesh Tiwari	MITS, Gwalior, India
M. K. Trivedi	MITS, Gwalior, India
Nitin Mallik	The NorthCap University, Gurgaon, India

Acknowledgement

The organizing chairs of the International Conference on “*Sustainable and Innovative Solutions for Current Challenges in Engineering & Technology*” gratefully acknowledge financial support from the **All India Council for Technical Education (AICTE)**, New Delhi, India (Sanction order no. No. 67-6/RIFD/GOC/Policy-1/ 2017-18 dated 22.04.2019) and Technical Education Quality Improvement Programme (TEQIP), Phase III (a Government of India Project assisted by the World Bank).

The organizers also acknowledge support from the **Delhi Technological University (DTU), Delhi**, India, under twinning arrangement in TEQIP-III.

The **conference patron Prof. K. K. Aggarwal, Chairman NBA**, was the guiding force behind the conference, and he also kindly accepted to deliver the keynote address, for which the organizers are eternally indebted.

Dr. S. N. Singh, Vice Chancellor, Madan Mohan Malaviya University of Technology, Gorakhpur, India, deserves a special mention for accepting the offer to deliver the **Plenary Talk**.

The organizers are grateful for the constant inputs and support from our conference chairs **Prof. R. V. Rao of NIT, Surat**, **Dr. J. C. Bansal of South Asian University, New Delhi**, and **Dr. Mukhtiar Singh of DTU, Delhi**. Without their support the conference could not have been conducted at this scale.

Dr. M. H. Lim of **Nanyang Technological University, Singapore**, deserves special thanks for helping the organizers in publishing the proceedings.

The organizing team is grateful to **Shri Prashant Mehta, Former Director General of the Academy of Administration**, Bhopal, for sparing time to inaugurate the conference.

Sincere thanks to Alumnus and Secretary of **The Scindia Engineering College Society, Gwalior**, **Er. Ramesh Agrawal**, who has been a constant source of support. The conference could not have been possible without the support of the Director, MITS, **Dr. R.K. Pandit**.

Thanks are also due to all the **esteemed reviewers** for their time and significant contribution in maintaining the quality of the papers.

The contribution of **internal and external experts as session chairs** and the **session support teams** during the two days was most important for the effective conduction of the conference. They accepted the invitation and played a key role in conference conduction by giving valuable comments for improving the quality of the paper, post-conference, before publication. The organizers are grateful for their support and efforts in conference conduction.

We thank the experts who have taken time from their busy schedules for delivering expert sessions during the conference.

The hard work and efforts of the Conference Core Team are sincerely acknowledged. The members have worked relentlessly and have left no stone unturned to make the conference a reality.

Thanks are also due to media persons, guests, authors and all those who have directly or indirectly contributed in organizing and conducting this conference.

Contents

Improvement in Side Lobe Reduction in FIR Filter Design Using Proposed Hybrid Blackman Window	1
Poonam Parmar, Rahul Dubey, and Karuna Markam	
Low Frequency Stochastic Electromagnetic Field Observed in the Ionosphere Possibly Associated with an Earthquake Activity	12
Shourabh Bhattacharya	
A Review on Role of Solar Drying Technology in Sustainable Development	18
Pushpendra Singh and M. K. Gaur	
Role of Advance Solar Desalination Technique for Sustainable Development	28
Vikas Kumar Thakur, M. K. Gaur, and M. K. Sagar	
Effect of Reinforced Nano-Composites on AMC Solidification Curve	39
Siddhartha Kostil and Chandra S. Malvi	
An Efficient Performance of Enhanced Bellman-Ford Algorithm in Wireless Sensor Network Using K-Medoid Clustering	52
Garima Sharma, Praveen Kumar, and Laxmi Shrivastava	
Wavelet Based Compression of Acne Face Images with Automatic Selection and Lossless Compression of Acne Affected Region	66
Garima Nain, Ashish Gupta, and Rekha Gupta	
Absolute Ionization Cross Sections of Hydrogen Chloride Gaseous Molecule by Electron Impact	77
Ravinder Sharma and Satya Prakash Sharma	
A Weight Function RSA Strategy Based on Path Length and Bandwidth Demand for Static Traffic in Elastic Optical Network	88
Deepak Batham and Dharmendra Singh Yadav	

GIS and AHP Based Site Suitability Analysis for Desirable Obnoxious Facilities in Sultanpur District in India	97
Ruchin Agrawal, Amitabh Kumar Srivastava, and Anjani Kumar Nigam	
Supplementary Cementitious Material: An Elixir for Concrete	111
Abhishek Kumar Jaiswal and Manoj Kumar Trivedi	
A Two Variable Adjustable Window Function Approach to Design FIR Filter	123
Awadhesh Gupta, Juhi Afridi, Shikha Shrivastava, and Vandana Vikas Thakre	
Performance Analysis of a Twin Rotor MIMO System Using Fuzzy Logic Controller	132
Piyali Das, Pema Rinzing Bhutia, Ram Krishna Mehta, and Om Prakash Roy	
Solar Cell Efficiency Enhancement Using Embedded Surface Plasmonic Nanoparticles in Various Medium	146
Diptanu Dey, Amit Chakraborty, Anurendra Singh, and Priyanath Das	
Age Estimation and Gender Prediction Using Convolutional Neural Network	163
Bulbul Agrawal and Manish Dixit	
Pattern Based Detection and Mitigation of DoS Attacks in MANET Using SVM-PSO	176
Divya Gautam and Vrinda Tokekar	
Exploring the Optimal Path for Supply Chain System Using Queueing Models	185
Jitendra Kumar and Vikas Shinde	
Thermal Aging Analysis of Nomex Paper Solid Insulation Impregnated in Ester Insulation Oil for Possible Use in Transformer	209
Rajesh Roshan, Manisha Sharma, and Raj Kumar Jarial	
Retrieval of Content-Based Images by Fuzzified HSV and Local Textural Pattern	219
Punit Kumar Johari and R. K. Gupta	
A Novel Meta-material Based Mirco-strip Patch Antenna	230
Vikas Mahor and Madhav Singh	
A Study on Sampling-Based Parameter Estimation Techniques in Big Data Analytics Environment	237
Abdul Alim and Diwakar Shukla	

Development of Framework for Greenness Identification 249
 Chandrika Dabariya and Rajeev Kumar Singh

Wideband Crossed Dipole Antenna for Base Station Antenna 261
 Anshul Agarwal, P. K. Singhal, and V. V. Thakare

Automated Diagnosis of Optic Atrophy Using Empirical Wavelet Transform 271
 K. Sneha and T. P. Byjubai

Improvement of Pavement Soil Sub-grade Using Industrial Waste: Cement Kiln Dust & Brick Kiln Dust 282
 Vikas Shukla and M. K. Trivedi

Schedule Compression of Construction Project: A Review 292
 Manish Bharadwaj, M. K. Trivedi, and Vikas Shinde

A Hybrid Approach to Decision Support Environment: Onto-DM-DSS Model 300
 Aastha Mishra, Amit Yadav, and Preetvanti Singh

Immiscible Liquid-Liquid Flow in Coiled Tube 307
 Nazim Ali and Monisha Mridha Mandal

Numerical Analysis of Joukowski ($T = 12\%$) Airfoil by $k-\epsilon$ Turbulence Model at High Reynolds Number 320
 Ravi Jain, Mohd. Yunus Sheikh, Dharmendra Singh, and Manoj Tripathi

FDTM Modeling to Analyze Flow Circulation Inside a Lid-Driven Cavity 330
 Siddhartha Kosti

Adsorptive Removal of Cadmium Using Agro-Residue 340
 Chavi Tomar, Vinita Khandegar, and Perminder Jit Kaur

Optimization of EC Variable for Removal of Acid Violet 17 Dye 346
 Anupam Pathak, Vinita Khandegar, and Arinjay Kumar

Optimal Weight Design of a Spur Gear Train Using Rao Algorithms 351
 R. Venkata Rao and Rahul B. Pawar

Image Enhancement Techniques: An Exhaustive Review 363
 Shradha Dubey and Manish Dixit

Performance Evaluation of 30.5 kWp On-Grid Solar System Using PVsyst 376
 Ramdew Rawat, Vishal Chaudhary, Hari Mohan Dubey, and Manjaree Pandit

Wiener System Identification Using Iterative Instrumental Variable Method	389
Vikram Saini and Lillie Dewan	
Role of Computational Fluid Dynamics in Sustainable Urban Built Environment: A Review	399
Rishika Shah, R. K. Pandit, and M. K. Gaur	
A Smart Grid Technique for Dynamic Load Prediction in Nigerian Power Distribution Network	412
E. Ndidi Osegi, O. Egerton Taylor, B. Alexander Wokoma, and A. Ogacheko Idachaba	
Modeling and Control of Wind Energy System with PMSG Using Maximum Power Tracking	424
Hitesh Joshi and A. K. Swami	
Retail Market in India and Its Best Practices: A Review on Initiatives and Challenges	437
TRIPTA THAKUR and TUSHAR KUMAR	
Laminar Airflow Computational Modelling in the Human Nasal Cavity	443
Punjan Dohare and Amol P. Bhondekar	
Non-invasive Estimation of HRV Performance for Diabetes Mellitus with Cardiac Disorder on the Basis of Time-Frequency and Poincare Plot Analysis	454
Monika Saraswat, A. K. Wadhvani, and Sulochana Wadhvani	
Analysis of Dispersion Characteristics of Helical Metal Clad and Graphene Clad Circular Core Step Index Fiber	467
Raghvi Gupta, Archana Tripathi, and Amritanshu Pandey	
T-Type Multilevel Inverter Topology with Reduced Switch Count Using Different PWM Techniques	476
Monika Agrawal, Vijay Bhuria, and Shishir Dixit	
A Comprehensive Study on AC Microgrid Control Strategies at Primary Control Level	488
Bhavna Rathore, Laxmi Srivastava, Nipun Gupta, Shailendra Pratap Singh, and Rahul Sagwal	
Collaborative Filtering Techniques for Trust Prediction in Online Social Network	503
Rajeev Goyal, Arvind Kumar Upadhyay, and Sanjiv Sharma	
Improved Multi-verse Optimizer for Numerical Optimization	513
Dilip Kumar Mishra, Vikas Shinde, Kamal Wadhwa, and Sanjay Chaudhary	

Smart Grid Communication: A Survey of State-of-the-Art 524
Vimal Tiwari, Salil Madhav Dubey, Hari Mohan Dubey,
and Manjaree Pandit

**A Study on Adsorptive Removal of Malachite Green Dye from
Model Liquid Phase onto Activated Pongamia Pinnata Pod Powder:
An Eco-Friendly Bioadsorbent** 535
Anjula Gaur, Swati Goyal, and Preeti Gupta

**Comparative Analysis of Wideband Integrated Circular Slot and Dual
Band Integrated Elliptical Slot Microstrip Patch Antennae
for RF Energy Harvesting** 545
Himanshi Sharma and Laxmi Shrivastava

**Identification of Urban and Water Areas from Polarimetric SAR
Images Using Thresholding Algorithm** 555
Tanvi Agarwal and Laxmi Shrivastava

Author Index 567



Improvement in Side Lobe Reduction in FIR Filter Design Using Proposed Hybrid Blackman Window

Poonam Parmar^(✉) , Rahul Dubey^(✉) ,
and Karuna Markam^(✉) 

Electronics Department, MITS, Gwalior, MP, India
poonaml23parmar@gmail.com, rahul.dubey0686@gmail.com,
karunamarkam@gmail.com

Abstract. To obtain better quality signal, processing of signal should be done. Digital filters are most widely used to processing the signal in communication system. Windowing is a scheme to represent Finite Impulse Response (FIR) filters. This paper, proposes a flexible hybrid Blackman window to design an FIR filter. By changing variable's value window can be regulate. The hybrid Blackman window is convolution of Blackman & Blackman-Harris window in time domain and it shows better side-lobe rejection than some ordinary windows. the spectral properties of hybrid Blackman window compared with Gaussian, Hamming & Kaiser window and it can be seen that side-lobe fall off ratio of hybrid Blackman window (45.312 dB) is superior in comparison to Gaussian (13.832 dB), Hamming (5.804 dB) & Kaiser (22.162 dB) window. The Gaussian, Hamming & Kaiser window has ripple ratio -44.106 dB, -42.484 dB & -13.779 dB respectively, whereas the proposed window shows finer ripple ratio -47.225 dB.

In this paper FIR filter has designed by using proposed window with ripple ratio -146 dB which is less than FIR filter designed using Gaussian (-135 dB), Kaiser (-49 dB) & hamming (-128 dB) windows. The present paper also shows biomedical application of proposed window. The noise present in ECG signal due to power line interference omitted using proposed hybrid Blackman window.

Keywords: Window function · Spectral properties of window · Gaussian window · Hamming window · Kaiser window · FIR filter design · ECG signal noise reduction

1 Introduction

Digital filters are the element that most widely used in Digital Signal Processing. Digital filters give many of the advantage over analog filters like it is programmable filter so we can easily reconfigured digital filter by change the program only. Digital filters shows higher signal SNR over analog filters. Digital filters can be defined in two categories, Infinite impulse response filters and Finite impulse response filters, in general known as IIR and FIR respectively.

FIR filters shows linear phase response and unconditional stability and they are reliable. Because of their reliability it is possible to simply make causal FIR filters from

non-causal FIR filters. The different scheme of representing FIR filters are (a) Windowing, (b) Frequency sampling, (c) Computer added design (CAD) or optimal.

Window function provides output-values in a certain interval outside of this interval it gives zero-value. There are two desired condition for window function, the ripple ratio should be smaller and main lobe width should be narrow. In this correspondence, a new window is proposed by take combination of windows which have to be more efficient over the standard windows.

This paper proposed an adjustable window function with two variable parameters, window length and variable ‘ r ’, which can be adjusted according to need. These variables are deployed to manage the spectral properties of window. The proposed window has superior performance over several ordinary windows. By adjusting these independent parameters spectral properties can be controlled, such as the main-lobe width, the ripple ratio, peak side-lobe level and the side-lobe fall off ratio. Combinational window that shows high side-lobe fall off ratio give better far end rejection. This property reduces the aliasing problem.

2 Spectral Characteristic of Window

A general characteristic of a window in frequency domain is given in “Fig. 1”.

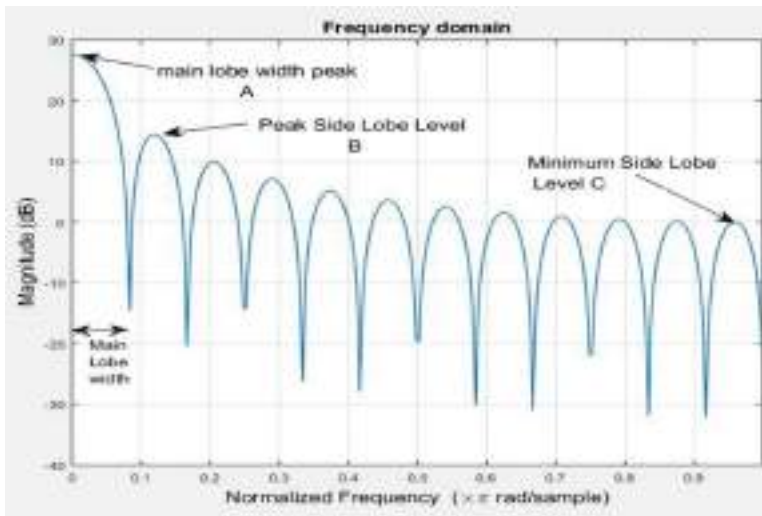


Fig. 1. A window’s characteristic representation

2.1 Ripple Ratio

Ripple ratio given as the ratio of peak side lobe amplitude and main lobe amplitude of frequency characteristic of a signal. For side-lobe rejection ripple ratio should be low.

$$RR = \frac{\text{peak sidelobe amplitude value}}{\text{mainlobe amplitude value}}$$

2.2 Side-Lobe Fall-Off Ratio

In a frequency response ratio of peak-side lobe amplitude to minimum side lobe amplitude known as the side-lobe fall-off ratio. To prevent aliasing problem it should be high. It is known as

$$SLFR = \frac{\text{peak side - lobe amplitude}}{\text{Minimum side - lobe amplitude}}$$

$$SLFR \text{ (in dB)} = S_1 - S_L$$

2.3 Side-Lobe Peak

Attenuation of side lobe should be high to result higher side lobe reduction. Attenuation has value inversely proportional to side lobe peak amplitude. Hence, peak amplitude value of side lobe should be low.

$$\text{Side-lobe peak} \propto \frac{1}{\text{attenuation}}$$

3 Proposed Hybrid Blackman Window

The hybrid Blackman window is a convolution of Blackman and Blackman-Harris windows. The Blackman window is close to optimal, only slightly worse than a Kaiser window. It was designed to have minimal leakage possible.

The Blackman window define as

$$W_1(n) = a_0 - a_1 \cos\left(\frac{2\pi n}{N-1}\right) + a_2 \cos\left(\frac{4\pi n}{N-1}\right) \quad (1)$$

Here, $a_0 = \frac{1-\alpha}{2}$, $a_1 = \frac{1}{2}$, $a_2 = \frac{\alpha}{2}$

$\alpha = 0.16$ ($a_0 = 0.42$, $a_1 = 0.5$, $a_2 = 0.08$)

The Blackman-Harris window express as:

$$w_2(n) = a_0 - a_1 \cos\left(\frac{2\pi n}{N-1}\right) + a_2 \cos\left(\frac{4\pi n}{N-1}\right) - a_3 \cos\left(\frac{6\pi n}{N-1}\right) \quad (2)$$

Here, $a_0 = 0.35875$, $a_1 = 0.48829$, $a_2 = 0.14128$, $a_3 = 0.01168$

The proposed window or hybrid Blackman window is convolution of Blackman window and Blackman-Harris window, which is:

$$w(n) = \frac{1}{b} \{w_1(n) * w_2(n)\}^r \tag{3}$$

Here, $b = 8.64$ (constant)

N = window length

r = variable parameter

‘*’ represent a convolution sign

In “(3)”, by varying the value of variable r , pattern and response in frequency domain will change. The mathematical expression of proposed window is,

$$w(n) = \begin{cases} \frac{1}{b} \{w_1(n) * w_2(n)\}^r, & \text{where } 0 \leq n \leq N \\ 0, & \text{otherwise} \end{cases} \tag{4}$$

For a good resolution, main-lobe width should be narrow and to achieve minimum power loss, peak side-lobe level should be low. To reject the far end interference side-lobe rejection ratio should be high and ripple ratio should be low. On the basis of these conditions, this paper has been shown the comparison of the proposed window with some ordinary windows [4] for window length $N = 64$ & variable $r = 0.37$.

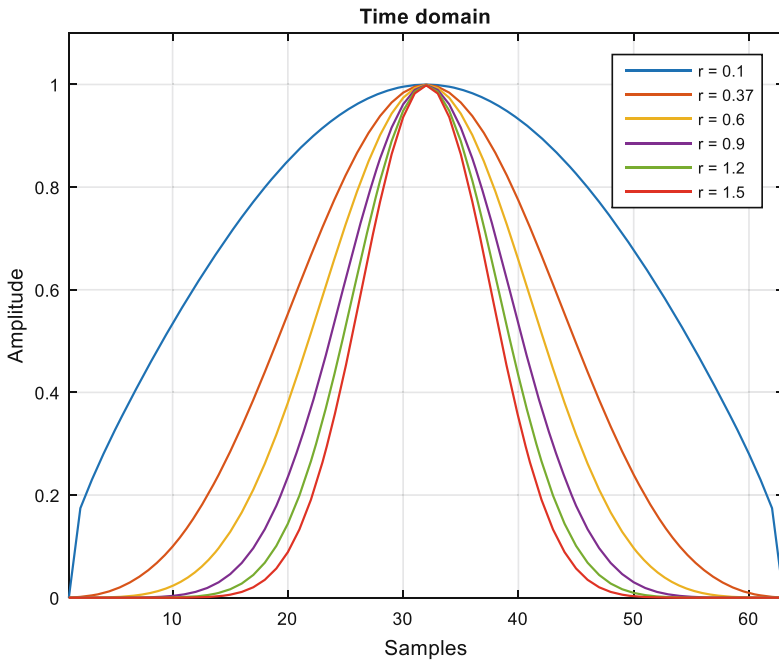


Fig. 2. Characteristic of hybrid Blackman window for different value of variable r

“Figure 2” indicates that, as the value of r decreases, the window becomes wider in time domain. Hence, window has been regulated by varying the value of variable r according to need.

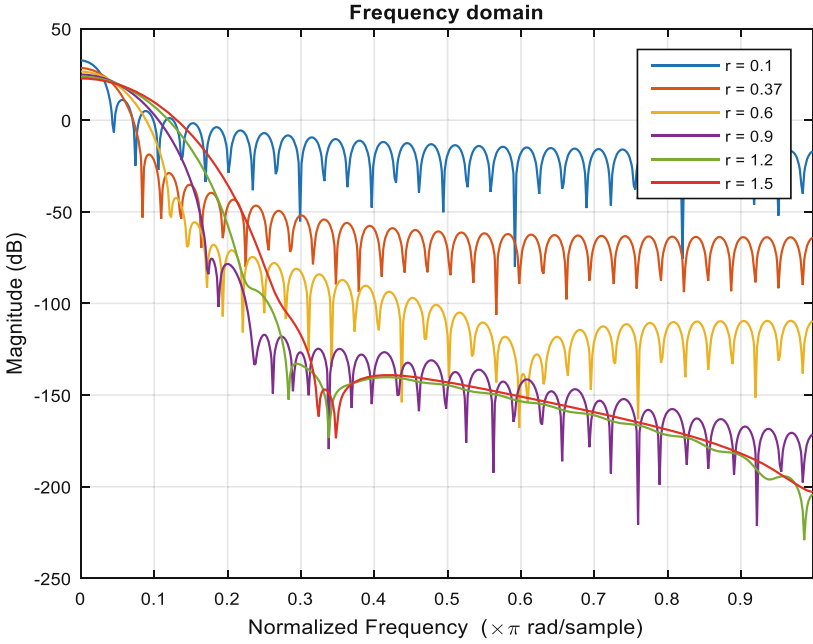


Fig. 3. Frequency response for different value of variable r

As the value of variable r increases, hybrid Blackman window will show good side-lobe reduction with increase in main-lobe width. Some results are shown for proposed window with different value of r .

“Figure 3”, represents frequency domain representation of proposed window for different value of r . As the value of r increases proposed window gives better side lobe reduction and main-lobe width also increases. It is known these two are contradictory conditions.

4 Performance Survey of Windows

The hybrid Blackman window compared with some ordinary windows which are Gaussian, hamming & Kaiser Window. “Figures 4 and 5” shows the time domain and frequency domain representations of these functions respectively.

4.1 Gaussian Window

The Gaussian window function is,

$$w(n) = e^{-\frac{1}{2} \left(\frac{n-(N-1)/2}{\sigma(N-1)/2} \right)^2} \quad (5)$$

$\sigma \leq 0.5$ & $\sigma(N-1)/2 =$ standard deviation of Gaussian function

“Figure 4” concludes that the Gaussian window has some amplitude value when the numbers of samples are zero and it is wider in comparison to proposed window.

“Figure 5” indicates the frequency domain representation for windows, where, Gaussian window has -44.106 dB ripple ratio and $(2\pi \times 0.0996)$ rad/second main-lobe width and hybrid Blackman window has $(2\pi \times 0.0832)$ rad/second main-lobe width and ripple ratio -47.225 dB. The side lobes of the Gaussian window become constant with increase in distance from zero and the lobes of hybrid Blackman window are decrease, which rejects the far end interference better.

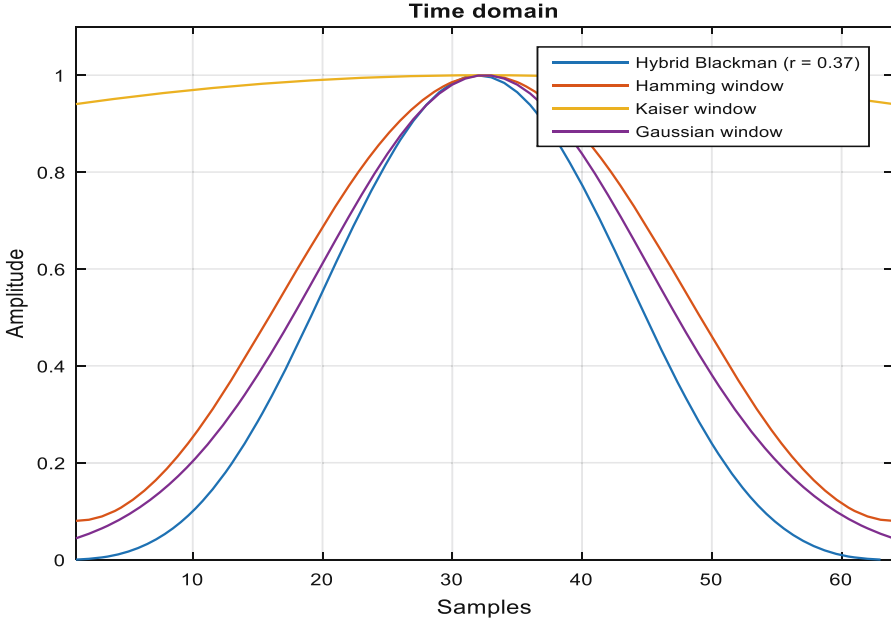


Fig. 4. Characteristics representation in time domain

4.2 Hamming Window

Hamming window is given as:

$$w(n) = 0.54 - 0.46 \cos\left(2\pi \frac{n}{N-1}\right), 0 \leq n \tag{6}$$

Hamming window has very slow side-lobe fall of rate because of discontinuity in amplitude at its end point. Proposed window shows rate of side-lobe fall better than hamming window. “Figure 4” shows that hamming window is wider than proposed window and has some amplitude value at zero samples which represents leakage. Leakage factor of hamming window is 0.03% while proposed hybrid blackman window gives 0% leakage factor and it starts with zero amplitude. On the other hand, in “Fig. 5” frequency response of the hamming window gives main lobe width

$(2\pi \times 0.0644)$ rad/s with ripple ratio -42.484 dB and the proposed hybrid window shows ripple ratio -47.225 dB with $(2\pi \times 0.0832)$ rad/s main-lobe width.

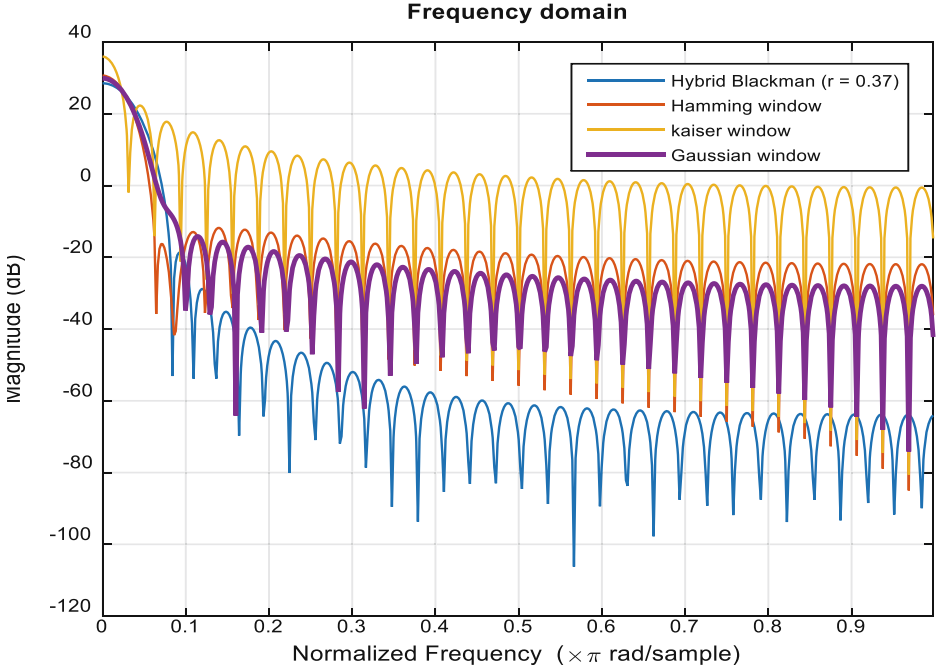


Fig. 5. Characteristic representation in frequency domain

4.3 Kaiser Window

Kaiser Window function is,

$$w(n) = \frac{I_0\left(\pi\alpha\sqrt{1 - \left(\frac{2n}{N-1} - 1\right)^2}\right)}{I_0(\pi\alpha)} \quad \text{where, } 0 \leq n \leq N \quad (7)$$

Where I_0 = Zero order Bessel function.

Kaiser window is a flexible window with an adjustable parameter α , with the variation of α , the window gets changed so the spectral characteristic of Kaiser Window can be controlled by varying the parameter α .

“Figure 4” indicates that Kaiser Window is wider in comparison of proposed window where $r = 0.37$. Hybrid Blackman window is starting with zero while Kaiser Window has some amplitude value with zero samples. The response of proposed window and Kaiser window in frequency domain gives ripple ratio -47.22 dB, -13.779 dB & main-lobe width $(2\pi \times 0.0832)$ rad/sample, $(2\pi \times 0.0312)$ rad/sample

respectively, which clearly shows that hybrid Blackman window is enough efficient over Kaiser window (Table 1).

Table 1. Comparison of spectral parameters for proposed, Gaussian, hamming and Kaiser window.

Window	Main-lobe width (rad/sample)	RR (dB)	Peak Side-lobe level (dB)	SLFR (dB)
Hybrid Blackman ($r = 0.37$)	$2\pi \times 0.0832$	-47.225	-18.732	45.312
Gaussian	$2\pi \times 0.0996$	-44.106	-14.214	13.832
Hamming	$2\pi \times 0.0644$	-42.484	-16.298	5.804
Kaiser	$2\pi \times 0.0312$	-13.779	22.317	22.162

5 Spectral Analysis of Filters

Low-pass FIR filter designed, with the help of hybrid window for $r = 0.37$ and compare that response with the low-pass FIR filter designed by using the Gaussian, hamming and Kaiser Window. From “Fig. 6”, it can be seen that ripple ratio of hybrid Blackman, Gaussian, Kaiser & hamming window are -146 dB, -135 dB, -49 dB & -128 dB respectively, while side-lobe fall off ratios are 100.5 dB, 20 dB, 43 dB & 14 dB respectively (Table 2).

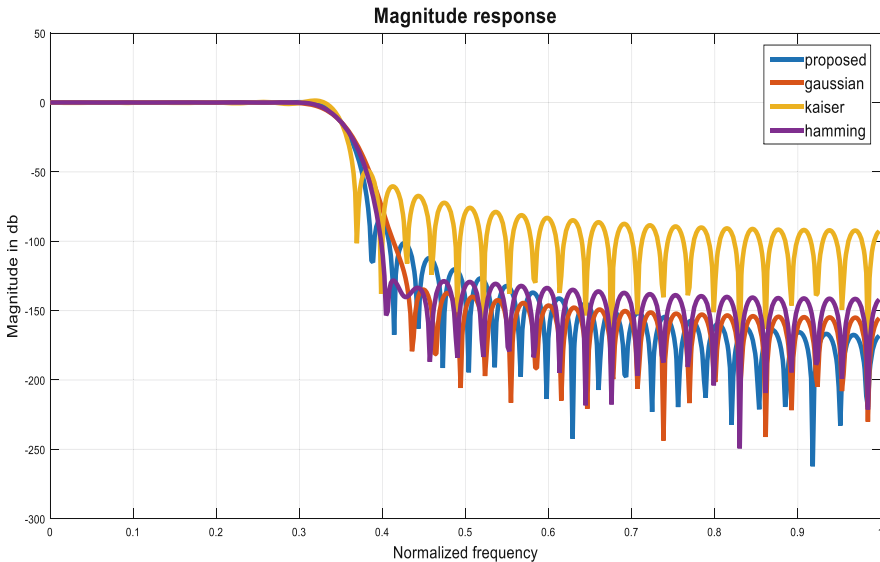


Fig. 6. Spectral analysis of FIR low pass filter for some ordinary windows & proposed window

Hence, Transition bandwidth can be reduce by reducing the value of r and FIR filter designed using hybrid Blackman window will show better side lobe reduction for higher value of r .

Table 2. Spectral parameter of Gaussian, Kaiser, Hamming & Proposed window

Window filter	Main-lobe width (rad/sample)	RR (dB)	SLFR (dB)
Gaussian	$2\pi \times 0.435$	-135	20
Kaiser	$2\pi \times 0.369$	-49	43
Hamming	$2\pi \times 0.404$	-128	14
Hybrid Blackman ($r = 0.37$)	$2\pi \times 0.424$	-146	100.5

6 Noise Reduction in ECG Signal

Proposed window can rectify the corrupted ECG signal, which is a biomedical application. While recording an ECG signal, presence of some noise can be observe in the waveform. Base line wondering, power line interference and instrumentation noise are some well-known noise present in ECG signal [11]. In this paper power line interference noise has omitted by using proposed window. Power line interference noise is produce due to loose contact of cable. It has frequency 50 Hz which depends on power supply.

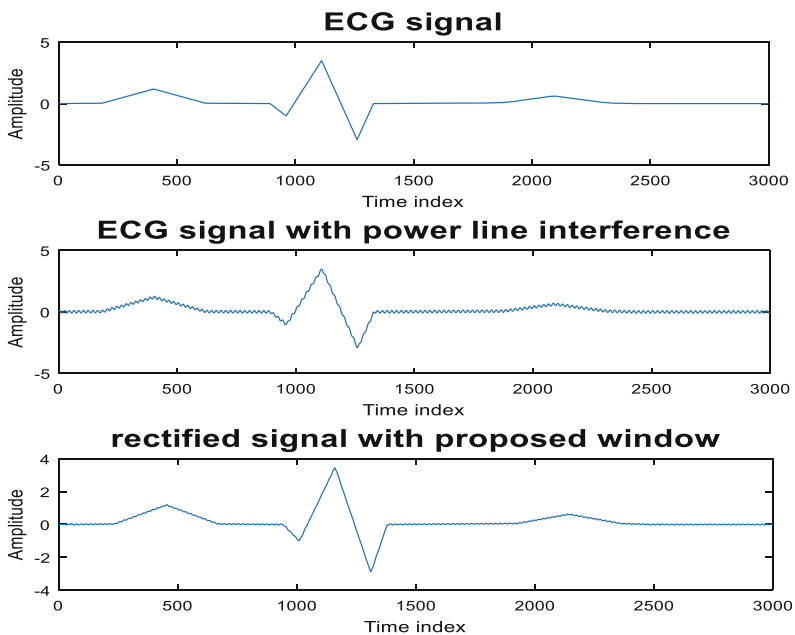


Fig. 7. Rectified ECG signal with proposed window

“Figure 7”, has been shown the de-noising of the signal with the help of proposed window and the “Fig. 8” has been shown results in power spectral density form.

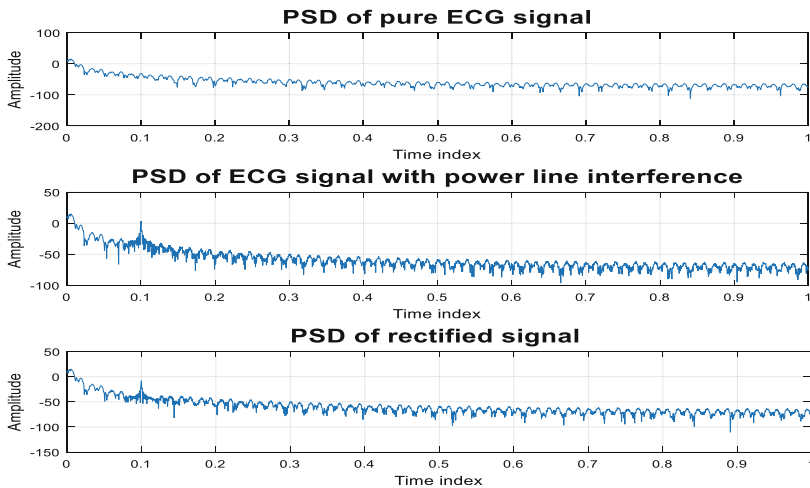


Fig. 8. Representation of power spectral density of signal

7 Conclusion

This work has been shown that the hybrid window or proposed window is more efficient than Gaussian, Hamming & Kaiser window. According to our need window can be adjusted by varying value of variable r . Convolution of Blackman & Blackman-Harris window, that shows side-lobe roll off ratio 45.312 dB and ripple ratio -47.225 dB is superior than Gaussian, hamming and Kaiser window. This paper has shown the application of the proposed hybrid Blackman window in biomedical field and FIR filter designing. The low pass FIR filter plotted by hybrid Blackman window gives -146 dB ripple ratio and side-lobe fall off ratio 100.5 dB. Electrical cardiac signal or ECG signal corrupted with power line interference rectified using proposed hybrid Blackman window.


References

1. Karmaker, T., Anower, M.S., Khan, M.A.G., Habib, M.A.: A new adjustable window function to design FIR filter and its application in noise reduction from contaminated ECG signal. In: 2017 IEEE Region 10 Humanitarian Technology Conference (R10-HTC), Dhaka, Bangladesh, December 2017
2. Kumar, V., Bangar, S., Kumar, S.N., Jit, S.: Design of effective window function for FIR filters. In: IEEE International Conference on Advances in Engineering & Technology Research (ICAETR-2014), 01–02 August 2014

3. Eleti, A.A., Zerek, A.R.: FIR digital filter design by using windows method with MATLAB. In: 14th International Conference On Sciences and Techniques of Automatic Control & Computer Engineering-STA'2013, Sousse, Tunisia, 20–22 December 2013
4. Rakshit, H., Ullah, M.A.: A comparative study on window functions for designing Efficient FIR filter. In: The 9th International Forum on Strategic Technology (IFOST), Cox's Bazar, Bangladesh, October 2014
5. Sahil, M., Rakshit, H., Ullah, H.: An adjustable window function to design an FIR filter. In: IEEE International Conference on Imaging, Vision & Pattern Recognition (icIVPR) 2017
6. Antonious, A.: Digital Signal Processing: Signal System and Filters. TataMcGraw-Hill Education, New York (2006). ISBN 0071454241
7. Khatun, M.: Implement a new window function and design FIR filters by using this new window. IJECS, **3**(3) (2014)
8. Eleti, A.A., Zerek, A.R.: FIR digital filter design by using windows method with MATLAB. In: 2013 14th International Conference on Sciences and Techniques of Automatic Control and Computer Engineering (STA), Sousse, pp. 282–287 (2013)
9. Proakis, J.G., Manolakis, D.G.: Digital Signal Processing. Prentice-Hall, Upper Saddle River (2007)
10. Kumar, V., Bangar, S., Kumar, S.N., Jit, S.: Design of effective window function for FIR filters. In: 2014 International Conference on Advances in Engineering & Technology Research Unnao (2014)
11. Gupta, A., Chaskar, U.M.: Hardware implementation and reduction of artifacts from ECG signal. In: International Conference on Information Processing (ICIP) Vishwakarma Institute of Technology, 16–19 December 2015
12. Hossin, M.A., Shil, M., Thanh, V., Son, N.T.: An adjustable window-based FIR filter and its application in audio signal de noising. In: 3rd International Conference on Robotics and Automation Engineering (2018)
13. Shil, M., Goni, T.M.O., Nath, C., Rakshit, H.: An adjustable cotangent based window function for designing an FIR filter. In: IEEE International Conference on Smart Technologies and Management for Computing, Communication, Controls, Energy and Materials (ICSTM), Veltech Dr. RR & Dr. SR University, Chennai, T.N., India, pp. 344–348, 2–4 August 2017
14. Capizzi, G., Coco, S., Sciuto, G.L., Napoli, C.: A new iterative FIR filter design approach using a Gaussian approximation. IEEE Signal Process. Lett. **25**(11), 1615–1619 (2018)



Low Frequency Stochastic Electromagnetic Field Observed in the Ionosphere Possibly Associated with an Earthquake Activity

Shourabh Bhattacharya^(✉) 

Department of Applied Science (Physics),
Madhav Institute of Technology and Science, Gwalior 474005, India
shourabhbhattacharya@gmail.com

Abstract. The atmospheric envelope surrounding the Earth also constitutes to the key ingredients of the environmental systems. In this regard, one of the key areas in the investigation in the subject of Environmental Physics is the observations that pertain to the electromagnetic signatures in the ionosphere. The irregularities in the electric and magnetic fields may have a complex effect in the ionosphere and may occur owing to geomagnetic irregularities such as storms, scintillations, earthquakes or lightning phenomena. This paper is written with an objective to discuss the stochasticities in the low frequency electromagnetic emissions that have been studied from the data of DEMETER (Detection of Electro Magnetic Emissions Transmitted from Earthquake Region) satellite, a low Earth orbiting satellite that aims to investigate ionospheric perturbations. More importantly, it is believed that persistent studies carried out in the exploration of such geophysical activities could prove to be an effective diagnostic tool for setting up early warning systems, thereby providing a novel solution to the challenge of predicting Earthquakes.

Keywords: DEMETER · Ionosphere · Low frequency

1 Introduction

The climatic investigations are merely not restricted to evaluate the nearby environmental phenomenology but also involves investigation and observations of the complex processes that extend to the upper atmosphere, more popularly known as the ionosphere. Studies related to investigation of electrically and magnetically perturbed fields associated with earthquakes have been acclaimed widely. Several studies of analyzing electric and magnetic field variations during the course of strong seismic events have been performed by the scientists on a long and short term basis. The observational part involves the initial work on Ultra Low Frequency (ULF) magnetic field anomaly by [1] during Loma Prieta earthquake and during the earthquake of in the past [2, 3] for studying the electromagnetic precursors in the ULF band before some major seismic events. On the other hand scientists have also investigated the propagation of Ultra Low Frequency (ULF)/Extremely Low Frequency (ELF)/Very Low Frequency (VLF) emissions in the ionosphere before strong seismic events performed

with the help of low altitude satellites [4, 5]. Furthermore, a number of methods owing to methodologies and observations for earthquakes related phenomena have been studied [6, 7] in recent times. In this paper, the author has discussed the example of the ULF/ELF perturbations before earthquakes that have been observed by Low Earth Orbiting Satellite DEMETER. In this paper some results of anomalous signatures are discussed that may be accountable for seismic or geomagnetic events.

2 Methodology

For the investigation of the ionospheric disturbances associated with seismic events and also to investigate about the global electromagnetic environment of the earth, DEMETER satellite as shown in Fig. 1 has been launched in 2004. It is a low earth orbiting satellite at an altitude of roughly 700 km weighing merely 130 kg. The scientific payload comprised of the following instrumentation systems viz, complex sensors for electric and magnetic field measurements, ion temperature detectors and plasma analyzer. Figure 1 depicts the DEMETER satellite orbiting around the Earth for investigation of ionospheric complex signatures. However, in this paper the data from electric and magnetic field sensors on-board DEMETER satellite have been utilised.



Fig. 1. DEMETER satellite orbiting around the Earth

3 Results and Discussion

In this section two different conditions have been presented for depicting the anomalies in the electric and magnetic field signatures observed ten days prior to a high magnitude earthquake activity in the vicinity of Scotia Sea region on 20.08.2006 ($M = 7.1$, 03:41:47 h UTC, 61.01°S , 325°E , $d = 10$ km). Ten days prior to the earthquake activity, certain stochastic electric and magnetic field patterns are observed in the epicenter region during the pass of the satellite as in Figs. 2 and 3. The anomalies are stronger in the lower frequency region around 50 Hz–100 Hz range, especially in the electric field. Since 10.08.2006 is also noted to be a geomagnetic quiet day, as shown in Fig. 4 where the values of the Geomagnetic Index $K_p \leq 3$ during the whole day, the observed anomalies could possibly be related to the earthquake of the Scotia sea which has a reasonably high magnitude.

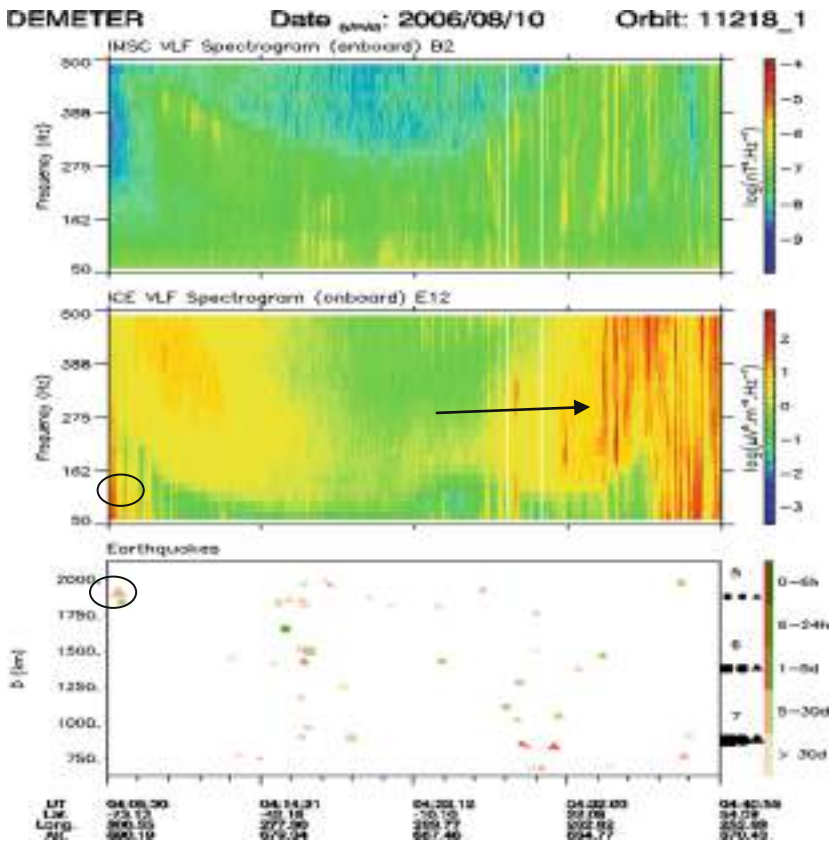


Fig. 2. Electric and magnetic field spectrogram plots on 10.08.2006 for Orbit No.11218_1

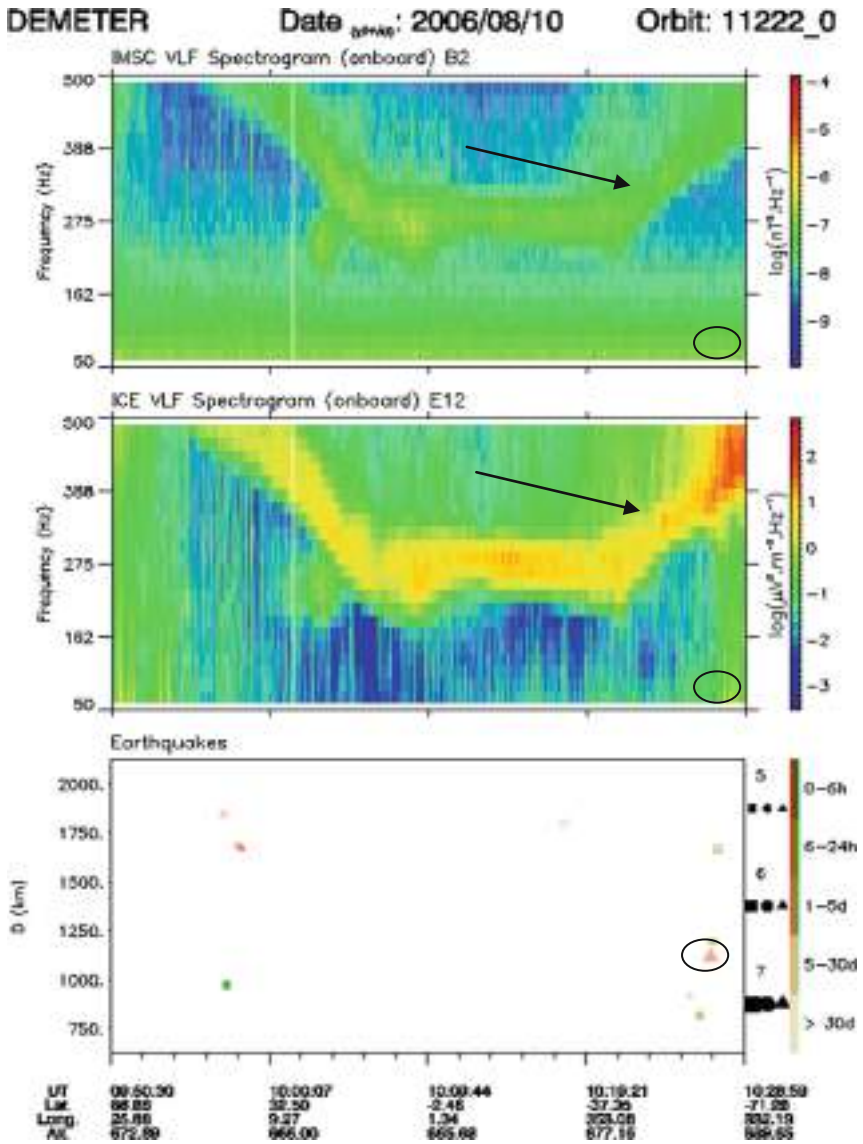


Fig. 3. Electric and magnetic field spectrogram plots on 10.08.2006 for Orbit No.11222_0

However in the same figures one may observe extreme intensifications that are also observable (depicted by arrows). This may be attributable to the high latitude stochasticity in the aurora region during the transition of the DEMETER satellite above the region in the orbits.

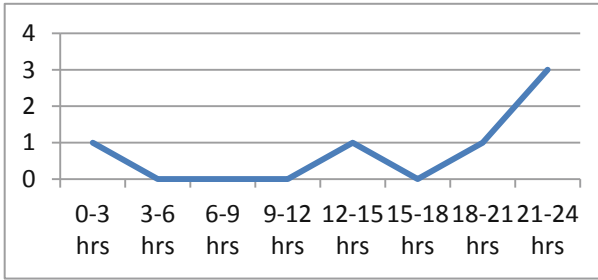


Fig. 4. Plot of Kp index on 10.08.2006 showing a quiet day

4 Conclusions

In this paper, an example of the electromagnetic phenomena possibly related to the Scotia Sea earthquake has been presented. The results are further supported by recent works that have been carried out in the field of electromagnetic anomalies and stochastic occurrences [8–10] carried out in the recent times. It is a well known fact that earthquake related anomalies have been present since more than three decades yet, a lot needs to be explored in studying the complexities in the upper atmosphere, it may be stated that the contribution of satellite technology is instrumental in analysis of climatic and atmospheric data. On a concluding note it is believed that long term consistent efforts at the academia and scientific level may constitute towards a the formation of a framework which allows amalgamation of satellite as well as ground based data to substantiate a new chapter in the field of atmospheric and environmental studies to counter the challenge of earthquake prediction with a novel solution through ground as well as satellite based studies.

Acknowledgements. The author is indebted to Director, MITS, Gwalior, for providing the necessary support and opportunity. Sincere gratitude is expressed towards the TEQIP-III Programme under AICTE for the same. The authors also wish to thank CNES/LPCE-France and its team members for providing the valuable suggestions and also to the World Data Center (WDC) website for geomagnetic index values.

References

1. Chmyrev, V.M., Isaev, N.V., Serebryakova, V.M., Sorokin, V.M., Sobolev, Y.P.: Small-scale plasma inhomogeneities and correlated ELF emissions in the ionosphere over an earthquake region. *J. Atmos. Sol.-Terr. Phys.* **59**(9), 967–974 (1997)
2. Fraser-Smith, A.C., Bernardi, A., McGill, P.R., Ladd, M.E., Helliwell, R.A., Villard Jr., O. G.: Low-frequency magnetic field measurements near the epicenter of the M_s 7.1 Loma Prieta earthquake. *Geophys. Res. Lett.* **17**, 1465–1468 (1990)
3. Hayakawa, M., Kawate, R., Molchanov, O.A., Yumoto, K.: Results of ultra-low-frequency magnetic field measurements during the Guam earthquake of 8 August 1993. *Geophys. Res. Lett.* **23**, 241–244 (1996)

4. Molchanov, O.A., Kopytenko, Y., Voronov, P.M., Kopytenko, E.A., Matiashvili, T.G., Fraser-Smith, A.C., Bernardi, A.: Results of ULF magnetic field measurements near the epicentres of the Spitak ($M_s = 6.9$) and Loma Prieta ($M_s = 7.1$) earthquakes: comparative analysis. *Geophys. Res. Lett.* **19**, 1495–1498 (1992)
5. Parrot, M.: Statistical study of ELF/VLF emissions by a low altitude satellite during seismic events. *J. Geophys. Res.* **99**(23), 339 (1994)
6. Sgrigna, V., Conti, L.: A deterministic approach to earthquake prediction. *Int. J. Geophys.* (2012). <https://doi.org/10.1155/2012/406278>
7. Bhattacharya, S.: Possible electromagnetic signatures detected during Hindu-Kush seismic activity in the ionosphere. *Int. J. Res. Anal. Rev.* 6.2.867
8. Li, M., Lu, J., Zhang, X., Shen, X.: Indications of ground-based electromagnetic observations to a possible lithosphere-atmosphere-ionosphere coupling before the 12 May 2008 Wenchuan $M_s = 8$ earthquake. *Atmosphere* **10**(7), 355 (2019)
9. Stanica, D.A., Stanica, D.: ULF preseismic anomalous signal related to Mw 8.0 offshore Chiapas earthquake Mexico on 8 September 2017. *Entropy* **21**(1), 29 (2019)
10. Snarlis, N.V.: Statistical analysis of earth's electric and magnetic field variations preceding earthquakes in Greece and Japan revisited. *Entropy* **20**, 561 (2018)



A Review on Role of Solar Drying Technology in Sustainable Development

Pushpendra Singh  and M. K. Gaur 

Department of Mechanical Engineering,
Madhav Institute of Technology and Science, Gwalior 474005, India
pushpendra852@gmail.com, gmanojkumar@rediffmail.com

Abstract. Sustainable development is basically a progress in such a manner that the present condition becomes better but not on the compromise of future generation ability to fulfill their needs. Due to growth in population, some people are still facing the problem in fulfilling their basic needs which are food, water, shelter etc. The need of food is tried to meet by utilizing solar energy via solar dryers. Solar dryer reduces the post-harvest losses and increases the storage time. Solar drying is now not limited to agricultural production and drying but it is also used in some other sectors like textile, rubber, dairy, sludge drying etc. The paper presents how the solar dryers are contributing in sustainable development.

Keywords: Solar dryers · Sustainable development · Drying techniques · Non-agricultural drying

1 Introduction

Sustainability is the effort to meet the needs of people without destroying the environment. The ecological balance needs to be maintained so as to maintain the existence of life in the Earth. The development should be in such a way that developed products should not harm the atmosphere during its use as well as when their life is over.

UN General Assembly sets 17 sustainable development goals and its associated 169 targets. Some of targets are food, poverty, health, education, women, water, energy, economy, infrastructure etc. Solar dryers are developed to reduce the scarcity of food by drying it and storing it for long duration. As the world population is increasing at the faster rate and it is not possible to produce the crop in large quantity due to limited land available for agriculture. So to meet their food requirement, the produced crop must be preserved [1]. This is done by reducing the moisture content of crop below the safe moisture limit [2].

Solar dryers are the setup for drying agricultural or non-agricultural products by utilizing the solar thermal energy. There are other means also for drying the things like mechanical dryers, electrical dryers, spray dryer etc. but amongst these solar drying is emerging as the best solution for drying as it is dependent on renewable source of energy only [3]. Solar drying is a very ancient technique for drying mostly the agricultural products under the direct sun, The open sun drying (OSD) had various

limitations like crops gets affected by pests, birds, rain, storm, dirt etc. [4, 5]. Also the quality is not of international standard so the farmers were not getting good return from their crops.

In order to overcome the limitations of the OSD, solar dryers were firstly developed by Everitt and Stanley in 1976 [6]. The solar dryers are basically of three types namely direct, indirect and hybrid dryers [7]. The dryers operate either on active or on passive mode. Under active or force convection, some external device needs to be fitted in the dryer like blower or fans. While in Passive mode, the air circulates due to density difference [8]. The classification of dryer is shown by Fig. 1. The design of basic types of solar dryer is shown by Fig. 2.

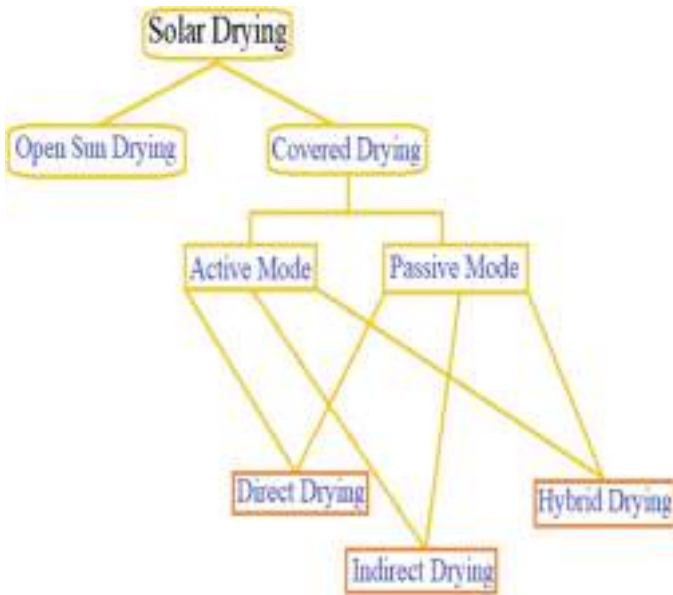


Fig. 1. Classification of solar drying

Previously the solar dryer were developed for drying agricultural products but now a days it used in industrial sectors also for drying or heating the processed material. Bhardwaj et al. dried the medicinal plant (Valeriana Jatamansi) inside the forced convection dryer [9]. Mewa et al. dried the beef inside the tunnel dryer and found better quality than conventional drying [3]. Lamrani et al. dried the wood inside the hybrid dryer and then used TRNSYS software for its performance analysis [10].

The paper presents the utilization of renewable source of energy for drying purpose. It has been described that how solar drying is the sustainable solution for drying the agricultural or non-agricultural products. The researches that made the solar drying technique more efficient and effective are also presented in the paper.

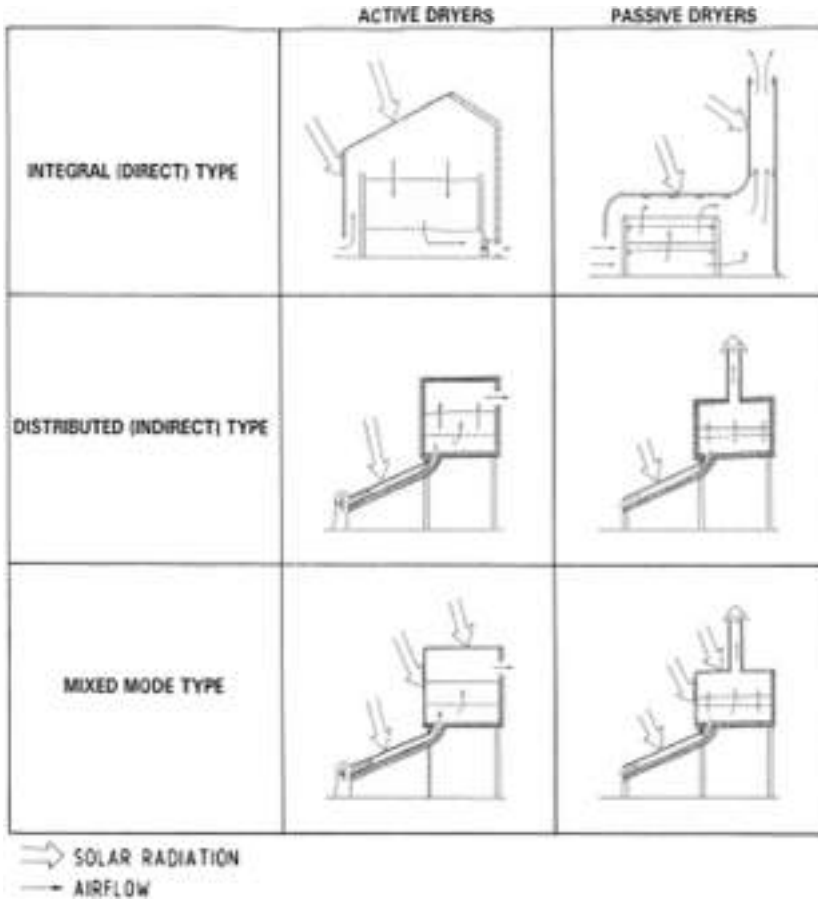


Fig. 2. Basic design of direct, indirect and mixed mode solar dryers [8]

2 Environmental Impact of Dryer

The three pillars of sustainable development are economic, environmental and social development. The product developed must be economical and of social importance along with no negative impact on environment. The solar dryers are totally operated using renewable source of energy i.e. solar energy, so it does not harm the environment in any way. Various researches had carried out in past that shows the amount of CO₂ mitigated by using different types of solar dryers. By 2020, mixed mode dryers can reduce the CO₂ emission by 23% [11]. The use of even 40% efficient solar dryer will reduce the conventional energy consumption by 27–80% [11, 12]. Some of the researches showing the CO₂ mitigated by the solar dryer are shown in Table 1.

Table 1. Researches showing impact of dryer on environment

Author (Year)	Type of solar dryer	Dryer floor area (m ²)	CO ₂ mitigated	Earned carbon credit (Rs)
Barnwal and Tiwari (2008) [13]	Hybrid greenhouse	6.5	27.5 Tonnes (for clear sky and 20 years of life span)	29,155 (for clear sky and 20 years of life span)
Shrivastava and Kumar (2017) [14]	Indirect solar dryer	–	391.52 kg/year	46,982–1,87,931
Singh and Kumar (2013) [15]	Mixed mode dryer	0.18	178–612 kg/year (when replacing with coal)	6,670–1,00,950
Prakash Om et al. (2016) [16]	Greenhouse dryer (Active)	1.5	28–38 Tonnes	9,456–50,245
	Greenhouse dryer (Passive)		28–35 Tonnes	9,470–46,680
Prakash and Kumar (2014) [17]	Modified greenhouse	1.5	38.06 Tonnes	12,561–50,245

The only device attached in standalone solar dryer having negative impact on environment is the PV panels or modules and batteries. During the utilization of PV panels, they emit certain amount of CO₂ and also they harm the environment when they are disposed as they contain toxic materials [18]. But when the CO₂ emission from solar panels is compared to other conventional sources like coal, oil and gas, it is found negligible. As by 2030, the about 140,000 MW electricity is produced through PV panels worldwide [19]. The batteries used for storing electricity are also not environment friendly, as they emit greenhouse gases when decomposed. Thus, the efforts are being made to utilize the renewable sources of energy as maximum as possible to reduce and finally eliminate the dependency on fossil based energy sources.

3 Economic Impact of Dryer

The other factor of sustainability development is the economy. The economic growth of the country is directly proportional to energy demand [20]. Demand of energy is mostly in the form of heat or electricity. Both the need is tried to be fulfilled by utilizing renewable sources. Solar dryers are also an attempt to meet thermal need. But anything developed, must be economical and affordable by all. The solar dryers are basically a one-time investment and then utilize it for no-cost. The payback time is also very less when it is compared to the life of dryer. The colour, odor and taste of the product dried inside the solar dryer is also of very good in comparison to oven drying, mechanical or

any other electric drying [1]. The cost of small scale, domestic purpose dryer is not very high but the cost of commercial dryer is high but that much cost is recovered in very less time. Table 2 shows the economic analysis of solar dryers developed by different researchers around the globe for drying different crops.

Table 2. Economic analysis of various solar dryers for drying different crops

Authors	Type of dryer	Crop dried	Life of dryer (Years)	Payback Time (Years)	Cost of dryer (Rs)
Shrivastava and Kumar [14]	Indirect solar dryer	Fenugreek	15	9 months	15,000
ELkhadraoui et al. [21]	Novel mixed mode solar greenhouse dryer	Red pepper and Sultana grape	20	1.6	90,082.64
Boonyasr et al. [22]	Semi-cylindrical shaped greenhouse dryer	Pork	10	1.15	1,18,909
Janjai et al. [23]	PV-ventilated greenhouse solar dryer	Chilly	15	3.36	2,63,737.56
Janjai et al. [24]	PV-ventilated solar greenhouse dryer	Peeled longan and banana	15	2.3	3,28,057
Janjai et al. [25]	Greenhouse solar dryer	Macadamia nuts	15	1	3,30,345
Prakash Om et al. [16]	Greenhouse solar dryer (Active mode)	Potato, capsicum, tomato	35	1.89	12,844
Prakash and Kumar [17]	Modified greenhouse	Tomato flakes	35	1.9	12,843

The major limitations reported by various researchers in their research is that solar dryers cannot used in off sunshine period. But now this limitation is also tried to overcome by using energy storage materials like rockbed, pebbles, sand, bricks, PVC sheets, PCMs etc. [9, 26, 27]. The use of these materials makes the utilization of dryer for longer duration and in off sun shine period also. The comparison of thermal efficiency and time saving due to utilization of solar dryer with other dryers is shown in Fig. 3. From figure it is clear that hybrid solar dryers gives better thermal efficiency and results in greater time saving [28].

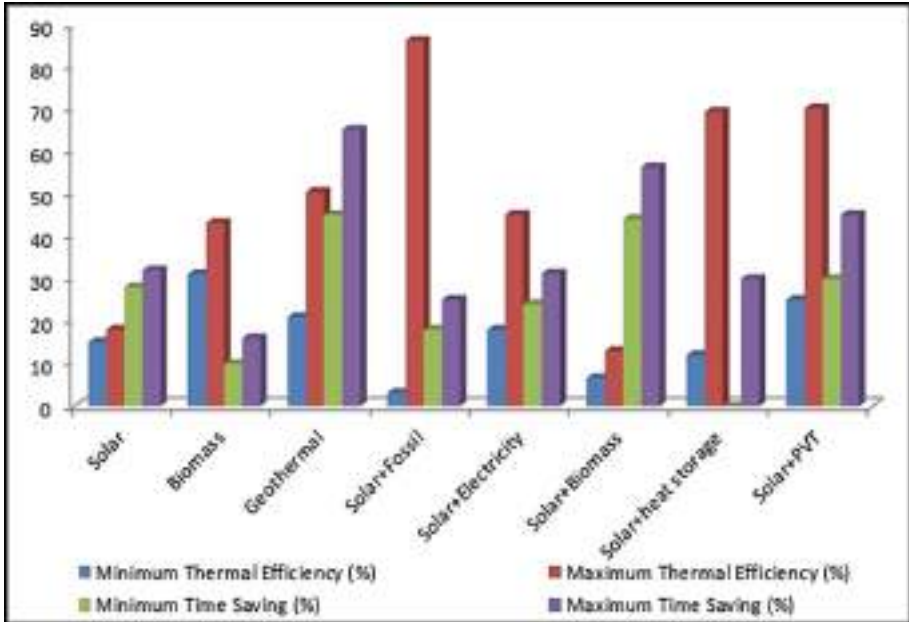


Fig. 3. Comparison of thermal efficiency and time saving of various dryer utilizing different renewable energy sources.

4 Social Impact of Dryer

Food is the basic need of human being. The increasing population creates the bigger problem of food scarcity. By 2030, the food demand will increase by 50% [6]. As uneven climate change due to global warming effects the agriculture sector also. So the food produced needs to be stored for present and future requirement. For drying crops, solar drying is emerging as the best method [29]. Solar dryers were developed basically for the drying of agricultural products. But as the time progresses, the solar dryers are also used for some other purposes. Solar drying emerges as one of the fruitful method for rural and urban areas.

4.1 Impact of Solar Dryers in Rural Areas

In rural areas, the major occupation is farming and so basic source of income is the agriculture. The farmers expect that the crops grown by them must give the better return when they sale it in the market. But due to various postharvest losses, some of the crops get wasted and the remaining one does not give that much return as they expected. As farmers in rural areas cannot afford the dryers due to very high cost, so they prefer open sun drying of crops. But the along with waste of crop in OSD, also the crop is not of international standard. So the return in crop is also not good.

All these problems are eliminated by the development of various low cost solar dryer which operates only on solar energy, so requiring no additional cost for their

operation. Solar dryers not only gives better quality product but are also better in terms of economic, environment and social point of view [30]. The farmers can easily afford it and get good quality dried crops in lesser time without any fear of dirt, pests, rain etc. The dried crops can be stored for longer duration and thus gives better return to the farmers [31].

4.2 Impact of Solar Dryers in Urban Areas

In urban area also the solar dryers play an important role in reducing the dependency of industrial sectors on other methods of drying operated by fossil based energy sources. The solar dryers are now utilized for drying various non-agricultural products like rubber, paper, cotton, sludge, timbers etc. Timbers had been dried from 68% to 11% in 8 h through solar dryers [32]. The hybrid dryer dries the rubber sheet from 34.26% to 0.34% in 48 h with better quality [33]. The silk cocoons were also dried in solar dryer and it gets dried in 16–19 h. The quality of silk obtained from solar drying was reported better than conventional electric dryer [34]. Thus, the dependency on fossil fuels is tried to reduce by using solar dryers. This will surely help in reducing the effect of global warming and creates a better environment for the people. Some of the researches done in different sectors for drying different commodities are shown in Table 3.

Table 3. Solar dryer used for drying different products other than crops

Author	Year	Sector	Purpose
Ferreira et al. [32]	2014	Steel wire industry	For drying industrial waste
Sonthikun et al. [33]	2016	Rubber drying	For drying rubber sheets
Bennamoun [35]	2012	Waste water treatment	For drying sludge
Singh [34]	2011	Silk production	For cocoon drying
Perre and Keey [36]	2014	Wood and timber industry	For drying wood
Atkins et al. [37]	2010	Milk powder industry	For making milk powder by drying milk
Bhardwaj et al. [9]	2019	Medical	For drying Valerina Jatamansi (medicinal herb)

5 Conclusions

Sustainability development is the development of present without compromising the needs of the future. The solar dryer is also fulfilling the criteria of sustainable development. The various factors like global warming, uneven climate change, rapid increase in population, scarcity of food etc. creates the need of solar dryer. It not only

eliminates the utilization of fossil fuels which are harming the environment but also helps in meeting the food requirement of the people. The use of fossil fuel for space heating contributes a lot in release of greenhouse gases and other harmful gases responsible for global warming. The solar dryer helps in reducing the CO₂ emission and thus helps in making environment clean.

The solar dryers are also socially and economically viable. The dryers are of low cost and affordable by farmers thus helping in development of agricultural sector. This improves the economy of the country. Also the dryer meets the food requirement as the dried products can be stored for longer duration. Along with this the farmers get better return in their crops by using dryers. Thus the solar dryer not only helps in improving the economy of the nation but also makes the people of that nation healthy. Thus solar dryer fulfills the all basic three requirements of sustainability developments.

References




1. Singh, P., Shrivastava, V., Kumar, A.: Recent developments in greenhouse solar drying: a review. *Renew. Sustain. Energy Rev.* **82**, 3250–3262 (2018). <https://doi.org/10.1016/j.rser.2017.10.020>
2. Eltawil, M.A., Azam, M.M., Alghannam, A.O.: Solar PV powered mixed-mode tunnel dryer for drying potato chips. *Renew. Energy* **116**, 594–605 (2018). <https://doi.org/10.1016/j.renene.2017.10.007>
3. Mewa, E.A., Okoth, M.W., Kunyanga, C.N., Rugiri, M.N.: Experimental evaluation of beef drying kinetics in a solar tunnel dryer. *Renew. Energy* (2019). <https://doi.org/10.1016/j.renene.2019.02.067>
4. Sallam, Y.I., Aly, M.H., Nassar, A.F., Mohamed, E.A.: Solar drying of whole mint plant under natural and forced convection. *J. Adv. Res.* **6**, 171–178 (2015). <https://doi.org/10.1016/j.jare.2013.12.001>
5. Zoukit, A., El, Ferouali H., Salhi, I., Doubabi, S., Abdenouri, N.: Takagi Sugeno fuzzy modeling applied to an indirect solar dryer operated in both natural and forced convection. *Renew. Energy* **133**, 849–860 (2019). <https://doi.org/10.1016/j.renene.2018.10.082>
6. Kumar, M., Sansaniwal, S.K., Khatak, P.: Progress in solar dryers for drying various commodities. *Renew. Sustain. Energy Rev.* **55**, 346–360 (2016). <https://doi.org/10.1016/j.rser.2015.10.158>
7. Shalaby, S.M., Bek, M.A., El-Sebaai, A.A.: Solar dryers with PCM as energy storage medium: a review. *Renew. Sustain. Energy Rev.* **33**, 110–116 (2014). <https://doi.org/10.1016/j.rser.2014.01.073>
8. Visavale, G.L.: Principles, Classification and Selection of Solar Dryers. National University of Singapore Press, Singapore (2012)
9. Bhardwaj, A.K., Kumar, R., Chauhan, R.: Experimental investigation of the performance of a novel solar dryer for drying medicinal plants in Western Himalayan region. *Sol. Energy* **177**, 395–407 (2019). <https://doi.org/10.1016/j.solener.2018.11.007>
10. Lamrani, B., Khouya, A., Draoui, A.: Energy and environmental analysis of an indirect hybrid solar dryer of wood using TRNSYS software. *Sol. Energy* **183**, 132–145 (2019)
11. Tripathy, P.P.: Investigation into solar drying of potato: effect of sample geometry on drying kinetics and CO₂ emissions mitigation. *J. Food Sci. Technol.* **52**, 1383–1393 (2015). <https://doi.org/10.1007/s13197-013-1170-0>

12. Arata, A., Sharma, V., Spagna, G.: Performance evaluation of solar assisted dryers for low temperature drying application-II Experimental results. *Energy Convers. Manag.* **34**, 417–426 (1993)
13. Barnwal, P., Tiwari, G.N.: Life cycle energy metrics and CO₂ credit analysis of a hybrid photovoltaic/thermal greenhouse dryer. *Int. J. Low Carbon Technol.* **3**, 203–220 (2008). <https://doi.org/10.1093/ijlct/3.3.203>
14. Shrivastava, V., Kumar, A.: Embodied energy analysis of the indirect solar drying unit. *Int. J. Ambient Energy* **38**, 280–285 (2017). <https://doi.org/10.1080/01430750.2015.1092471>
15. Singh, S., Kumar, S.: Solar drying for different test conditions: Proposed framework for estimation of specific energy consumption and CO₂ emissions mitigation. *Energy* **51**, 27–36 (2013). <https://doi.org/10.1016/j.energy.2013.01.006>
16. Prakash, O., Kumar, A., Laguri, V.: Performance of modified greenhouse dryer with thermal energy storage. *Energy Rep.* **2**, 155–162 (2016). <https://doi.org/10.1016/j.egy.2016.06.003>
17. Prakash, O., Kumar, A.: Environmental analysis and mathematical modelling for tomato flakes drying in a modified greenhouse dryer under active mode. *Int. J. Food Eng.* **10**, 1–13 (2014). <https://doi.org/10.1515/ijfe-2013-0063>
18. Kaygusuz, K.: Environmental impacts of the solar energy systems. *Energy Sources Part A Recover Util. Environ. Eff.* **31**, 1376–1386 (2009). <https://doi.org/10.1080/15567030802089664>
19. Solangi, K.H., Islam, M.R., Saidur, R., Rahim, N.A., Fayaz, H.: A review on global solar energy policy. *Renew. Sustain. Energy Rev.* **15**, 2149–2163 (2011). <https://doi.org/10.1016/j.rser.2011.01.007>
20. Kannan, N., Vakeesan, D.: Solar energy for future world. *Renew. Sustain. Energy Rev.* **62**, 1092–1105 (2016)
21. ELkhadraoui, A., Kooli, S., Hamdi, I., Farhat, A.: Experimental investigation and economic evaluation of a new mixed-mode solar greenhouse dryer for drying of red pepper and grape. *Renew Energy* (2015). <https://doi.org/10.1016/j.renene.2014.11.090>
22. Boonyasri, M., Lertsatitthanakorn, C., Wiset, L., Poomsa, N.: Performance analysis and economic evaluation of a greenhouse dryer for pork drying. *KKU Eng. J.* **38**, 433–443 (2011)
23. Janjai, S., Khamvongsa, V., Bala, B.K.: Development, design, and performance of a PV-ventilated greenhouse dryer. *Int. Energy J.* **8**, 249–258 (2007)
24. Janjai, S., Lamlert, N., Intawee, P., Mahayothee, B., Bala, B.K., Nagle, M., et al.: Experimental and simulated performance of a PV-ventilated solar greenhouse dryer for drying of peeled longan and banana. *Sol. Energy* **83**, 1550–1565 (2009). <https://doi.org/10.1016/j.solener.2009.05.003>
25. Janjai, S., Phusampao, C., Nilnont, W., Pankaew, P.: Experimental performance and modeling of a greenhouse solar dryer for drying macadamia nuts. *Int. J. Sci. Eng. Res.* **5**, 1155–1161 (2014)
26. Akmak, G., Yildiz, C.: The drying kinetics of seeded grape in solar dryer with PCM-based solar integrated collector. *Food Bioprod. Process.* **89**, 103–108 (2011). <https://doi.org/10.1016/j.fbp.2010.04.001>
27. Ayyappan, S., Mayilsamy, K., Sreenarayanan, V.V.: Performance improvement studies in a solar greenhouse drier using sensible heat storage materials. *Heat Mass Transf.* **52**, 459–467 (2015). <https://doi.org/10.1007/s00231-015-1568-5>
28. Lamidi, R.O., Jiang, L., Pathare, P.B., Wang, Y.D., Roskilly, A.P.: Recent advances in sustainable drying of agricultural produce: a review. *Appl. Energy* **233–234**, 367–385 (2019). <https://doi.org/10.1016/j.apenergy.2018.10.044>

29. Zarezade, M., Mostafaeipour, A.: Identifying the effective factors on implementing the solar dryers for Yazd province. Iran. Renew. Sustain. Energy Rev. **57**, 765–775 (2016). <https://doi.org/10.1016/j.rser.2015.12.060>
30. Mustapha, M.K., Salako, A.F., Ademola, S.K., Adefila, I.A.: Qualitative performance and economic analysis of low cost solar fish driers in Sub-Saharan Africa. J. Fish. **2** (64) 2014. <https://doi.org/10.17017/jfish.v2i1.2014.23>
31. Singh, P., Shrivastava, V.: Thermal performance assessment of greenhouse solar dryer under passive mode. Int. J. Adv. Technol. Eng. Sci. **5**, 530–538 (2017)
32. Ferreira, A.G., Gonçalves, L.M., Maia, C.B.: Solar drying of a solid waste from steel wire industry. Appl. Therm. Eng. **73**, 102–108 (2014). <https://doi.org/10.1016/j.applthermaleng.2014.07.047>
33. Sonthikun, S., Chairat, P., Fardsin, K., Kirirat, P., Kumar, A., Tekasakul, P.: Computational fluid dynamic analysis of innovative design of solar-biomass hybrid dryer: an experimental validation. Renew. Energy **92**, 185–191 (2016). <https://doi.org/10.1016/j.renene.2016.01.095>
34. Singh, P.L.: Silk cocoon drying in forced convection type solar dryer. Appl. Energy **88**, 1720–1726 (2011). <https://doi.org/10.1016/j.apenergy.2010.11.016>
35. Bennamoun, L.: Solar drying of wastewater sludge: a review. Renew. Sustain. Energy Rev. **16**, 1061–1073 (2012). <https://doi.org/10.1016/j.rser.2011.10.005>
36. Perré, P., Keey, R.B.: Drying of wood principles and practices. In: Handbook of Industrial Drying, 4th edn, pp. 797–846 (2014). <https://doi.org/10.1201/b17208>
37. Atkins, M.J., Walmsley, M.R.W., Morrison, A.S.: Integration of solar thermal for improved energy efficiency in low-temperature-pinch industrial processes. Energy **35**, 1867–1873 (2010). <https://doi.org/10.1016/j.energy.2009.06.039>



Role of Advance Solar Desalination Technique for Sustainable Development

Vikas Kumar Thakur^(✉) , M. K. Gaur , and M. K. Sagar 

Department of Mechanical Engineering, Madhav Institute of Technology and Science, Gwalior 474005, India
vikasthakurl502@gmail.com, gmanojkumar@rediffmail.com, manishsagar@gmail.com

Abstract. Researchers are constantly doing research which beneficial for our environment and society, at the same time; it is also beneficial to the economy. Environment is affected by various activities of the human being. The use of fossil fuel emits greenhouse gases, which is causing the harmful effects to the environment. Therefore more research is being done on renewable energy in the present time. This paper shows sustainability development in the field of Solar Desalination, the desalination process is divided into two parts, the first is direct solar desalination, and the second is indirect solar desalination. In direct solar desalination, sustainability is explained by solar still. Cost analysis, CO₂ emissions, and social benefits have been studied through previous paper in the field of solar still. In indirect Solar Desalination shows CO₂ emission and cost analysis of RO-system. After study some previous paper, it was observed that solar still produces 15.6 tons less carbon comparison to other direct solar distillation technology. In this paper it has been shown that the fabrication cost of double slope stills is less than that of single slope and also it was observed that the fabrication cost and distilled water cost of solar energy based indirect RO-system is 33% lower than the other RO-system. After analyzing the daily productivity it was observed that if daily yield was increases then the cost of distilled water will be reduced.

Keywords: Sustainability · Desalination · Solar still · RO-system · CO₂ emissions · Cost analysis

1 Introduction

The use of fossil fuel increases the amount of greenhouse gases in the atmosphere, which are very harmful for human and animals. Therefore, researchers engaged in developing the system which operates through renewable energy. Such devices are being produced, which have reduced built cost, minimized environmental pollution and is economical for our society. In the renewable energy sector, more work is being done on solar energy. In this paper, the sustainability of solar still and the RO-system operated with solar energy are studied, which is a great contribution in the field of sustainable renewable energy [1]. 3.7 billion People are affected by the shortage of drinking water and it will be increase in future and reach at 5.7 billion in 2050 according to a report generated by United Nations [2]. 96.45% water is available in the

form of sea water, only 2.53% fresh water is present on the earth, out of this only 0.36% of fresh water is accessible to humans, the remaining pure water is present in the form of glacier, polar ice caps and underground water [3, 4]. Fresh water requires fulfilling the basic needs of human. Along with it, agriculture, industries, research centers and construction work needs fresh water. Desalination method has been developed, such that we can convert saline and dirty water in potable water [5, 6].

Solar desalination system can be divided into two parts, one is direct solar desalination and another is indirect solar desalination system. Direct solar desalination is very simple, eco-friendly, low cost method that requires low maintenance. Solar still is one of the oldest direct solar desalination system which consists of water basin in which saline water is stored, usually constructed by wood or cement/concrete, it is covered by transparent glass or FRP sheet, their inner base is painted by black paint to absorb more radiation from sun light to achieve more distilled water. The indirect solar desalination system has PV panels or solar arrays, used to generate electricity. This electricity helps to control the energy management and operates various devices of RO (reverse osmosis) module like DC battery, inverter, pump, motor [7]. This paper is focused on CO₂ emission, cost analysis and social benefits by the help of solar direct and indirect desalination processes. In this paper, the solar still sustainability and RO-system sustainability are discussed (Fig. 1).



Fig. 1. Classification of solar desalination on the basis of direct and indirect solar energy utilization.

2 Solar Desalination Technology

2.1 Direct Solar Desalination

Solar still is the one of the efficient and oldest desalination process, which works through direct solar radiation. Initially solar radiation passes through the glass and after that incident on the saline water. This way the water gets heated through the process of evaporation and settles on the inner surface of the glass, after losing the latent heat, the process of condensation takes place and converts the saline water into distilled water, which is then collected in a container [8].

2.2 Cost and Economics of Desalination

In solar desalination process many factors are covered in the economical aspect like material cost, labor cost, quality of water, type of solar still/design/size, and maintenance cost. Through all factors, we can calculate the total cost of the setup. Many researchers are working on the cost analysis of water productivity (Table 1).

Table 1. Component and installation cost of solar still [9].

Setup components	Item cost (\$)	Contingency (%)	Cost (\$)
Land	1000	10	1100
Civil work	500	10	550
Solar still	12500	10	13750
Auxiliary system	1250	10	1375
Pretreatment system	1000	10	1100
Post treatment system	1000	10	1100
Total capital cost			18975
Total facility cost			19924
Total installed cost			25502
Other cost			10,352
Total cost			29328
			INR 20,96,658/-

*Note-1\$ = 71.49 INR in 2019 [10]

Al-Hinai et al. [9] studied the analysis of cost on a simple solar still. They supply the fresh water through 250 installed solar still, to 100 villagers. They assumed, each user consumed 10 L distilled water per day. The cost of 1000 m² land is 2000 US Dollars and total solar still setup cost is \$50/m² on the basis of daily yield and productivity which are 4.15 l/m² and 1000 l/day respectively. Cost analysis is shown in table

- i. Results are found that the 1 gallon cost of distilled water is 0.074 \$/gal which is nearly about 16.3 \$/m³. Results of this cost analysis shows, the fresh water can supply to people in remote areas at reasonable cost.
- ii. The average annual yield of the solar still is 4.15 kg/m²day.
- iii. Other cost includes various component's installing cost like, spare parts which is 10% of the total facility cost, maintenance cost is 10% of the total installed cost, construction management cost is 5% of TCC and Interest of the Setup during construction is 8% of the total facility cost are added hence total other cost becomes 10352\$.

Singh et al. [11] developed a PVT based hybrid active double slope solar still. The yield of this new setup is 1.4 times greater than the single slope PVT based hybrid active solar still, it produces 7.5 kg water in a day and is expected to have annual productivity is 1939 kg with 30% less energy payback time in three years than that of the hybrid PVT based single slope active solar still. Components cost of the solar still is shown in Table 2.

Table 2. Various component cost of solar still [11].

Component	Items	Quantity	Cost (Rs.)
Solar still	GRP body	1	8000
	4 mm Glass cover	2	400
	Mild still stand	1	900
2 Flat plate collector	Other auxiliary		240
	Al box		20,000
	Cu sheet		
PV-module	Glass to glass	1	8000
Dc water pump	Brought on stand		1000
Important auxiliary			1000
Total cost			39,580

*Note-1\$ = 71.49 INR in 2019 [10]

- a. Total cost of the solar still is Rs.39580.
- b. Singh et al. [11] made a hybrid PVT double slope active solar still whose fabrication cost is 39,580 rupees, its fabrication cost has been compared to the single slope hybrid (PVT) active solar still made by Kumar and Tiwari [12], Whose fabrication cost is 45,760 rupees. So based on the fabrication cost of both these PVT based solar stills, it is assumed that double stills are 14% cheaper than single stills and there is another example in which the cost of double slope solar still is 16.52% less than the single slope solar still. Schematic diagram is shown in Fig. 2.



Fig. 2. Hybrid active solar still, Double slope PVT hybrid active solar still [11]

- c. Yearly Productivity of the distilled water is dependent on the number of clear day in a year, in present study predicted the 3 different number of days water production, 1st take 250 clear day, second take 275 clear day and last is 300 clear day in whole year. Fresh water yield in case 1, 2 and 3 are 1616 kg, 1777 kg and 1939 kg respectively.

Tiwari and Sahota [13] developed a solar still, in which thermoelectric modules are placed on the glass of solar still and evacuated tube are integrated with solar still basin. The authors utilized the heat of the condensed vapor on the glass to perform the

experimental work. They improved the performance of the solar still and increased the productivity of distilled water at low cost and also managed the economical rate of the distilled water in comparison to other solar still.

Cost of the water per liter of the present system is 0.0138\$/l/m² this values are compared with three different solar still first is inverted absorber solar still [14], passive or conventional solar still [15] and Sun tracking Active solar still [16]. Their cost is 0.0121\$/l/m², 0.0064\$/l/m² and 0.0478\$/l/m² respectively. Passive solar still gives minimum rate of distilled water as compared to the other solar still. Present solar still gives lower price of water as compared to active solar still. Component cost is shown in Table 3.

Table 3. Component cost [13].

Components	No.	Per unit price in \$	Total price in \$
Thermoelectric module	20	6	120
Heat sink	20	3.5	70
Condensation box	1	1	20
Propeller fan	1	1	1
Evacuated tube	2	6	12
Other component			12
Total			235 \$/INR 16,800/-

*Note-1\$ = 71.49 INR in 2019 [10]

- a. Total cost of the solar setup is 235\$.
- b. Cost of the distilled water is 0.0138\$/l/m² which is lower than the sun tracking active solar still.

Table 4. Some previous work on cost and economic analysis are presented in following table [14].

Design	Principle cost (Rs)	Principle cost (\$)	Daily yield	Distilled water cost	Reference
ETC based	9,672/-	135.3	4.1 kg/m ²	0.0121 \$/l/m ²	[14]
Heat pipe	2,523/-	35.3	1.976 kg/m ²	0.0064 \$/l/m ²	[15]
Heat Pipe	40,606/-	568	4.03 kg/m ²	0.0478 \$/l/m ²	[16]
ETC based	16,800/-	235	6.186 kg/m ²	0.0138 \$/l/m ²	[14]
P.V. Module	–	–	0.8 m ³ /day	12.5 \$/m ³	[17]
P.V. Module	8006/-	112	1 m ³ /day	12 \$/m ³	[18]

*Note-1\$ = 71.49 INR in 2019 [10]

After analyzing Table 4, it is observed that if the daily productivity increases then the cost of distilled water decreases.

3 Social Benefits of Solar Still

Solar still desalination process is completely reliable. Pondering upon Conventional Solar Still, it can be easily made anywhere at low prices. To run solar still desalination no fossil fuel is required, due to which CO₂ emission is equal to negligible [19]. The use of solar still does not harm the environment. In context of the cost and economy of solar still, it does not cost much money in the making and the cost of distilled water obtained by it is very low, approximately \$3 per 3785.412 L (approximately 1.00 rs per 3 L) [20]. Therefore, it proves to be sustainable in regard to fabrication cost and economy. Solar still is very helpful for those places where people have inaccessible clean water. Especially in the villages and the remote areas where the ponds, wells and rivers are drought prone, or even if there is water available but is not fit to drink, then impure water can be cleaned with the help of solar still. Therefore, Solar Still is a boon for remote areas not only from economical but also from a social point of view.

4 Desalination and Environment

Environment is affected by emission of CO₂ and GHG which produces after burning the fossil fuel, when fossil fuel are burnt then various harmful gasses are generated like CO, CO₂, Nitrogen oxide and Sulphur oxide which are harmful for our environment. Fossil fuel is used where large amount of energy is needed for operating the various large desalination setups for more production of water, but with the use direct solar energy for fresh water production CO₂ gas emission can be reduced and positively influence the environment and climate change. Only renewable energy project can reduce the GHG emission and use of fossil fuel [21].

Yousef et al. [22] constructed three different types setup, schematic shown in Fig. 3. first is traditional or conventional solar still, in second setup pin fin placed on the basin liner and in last setup still wool fiber mixture are spread in the basin surface SWF which work as the absorber. The experimental results of second and third setup are compared with traditional solar still. Total daily yield of second and third setup of distilled water is 16 and 25% more than the traditional solar still respectively. 52.5% is the maximum energy efficiency value of the 3rd setup, in case of first and second the maximum energy efficiency is 42% and 45.5% respectively (Table 5).



Fig. 3. Solar still setup with hollow cylindrical pin fins on solar basin surface [22].

Table 5. Shows the carbon emission and mitigation through three solar still in 10 year life time and also shows carbon credit added in life time [22].

Cases	Traditional or conventional solar still	Pin fin integrated solar still	Still wool fiber mixture based solar still
Yearly yield (kg)	1190.63	1394.9	1496.5
CO ₂ mitigation in life time (ton)	12.38	14.4	15.63
CO ₂ emission over life time (kg)	371.3	502	395
Carbon credit added	179.5	208.9	226.6

*Note-1\$ = 71.49 INR in 2019 [10]

- Maximum cost is 0.0427\$ for 1L/m² water of traditional solar still, remains two solar still water cost is lower than the traditional solar still, 1L/m² water cost of second setup is 0.0416\$ and 0.0343\$ of 3rd setup. Water cost of all three solar still is lower than the market water bottle price.
- Reduction of CO₂ emission through the case 2 and 3 are 14.4 and 15.6 tons respectively.

5 Indirect Solar Desalination

This desalination process is divided into two parts, first is membrane process and another is thermal process, this chapter is focused on reverse osmosis process which is the part of the membrane desalination process. Various members of RO system like water pump, motor, filters, DC batteries, inverter for convert the DC power to AC and recycler pump are driven by electric power, power is generated through solar PV-module from solar radiation. When solar energy is used in RO-system then it produces less amount of CO₂, reducing the fossil fuel consumption which reduces the negative impact on environment and after using the solar energy in the RO-system it reduces the overall cost, water cost and fabrication cost [23].

5.1 Reverse Osmosis

In 21st century RO-system is the most efficient desalination process, and fastest growing technology of water purifier. The market size of the RO purifier is expected to be \$9.227 billion in 2022. RO process works on pressure which is generated by high pressure pump driven by electricity and mechanical power. In this process feed water enters with pressure in semipermeable membrane, membrane separates the pure water and salt from the saline or sea water. Pressure on the feed water is dependent on the quality of water, pressure vary on sea water is 55 to 70 bars and 15–30 bar for brackish water [24]. Feed water passes through various steps of filters, in first step saline water passes through pre-filter housing, here physical impurity of water is removed and then passes through carbon filter here taste of water is improved and finally reached at membrane. In second stage reduces the boron concentration from water and finally gets

fresh water for drinking and agriculture use. Commercial membranes for RO are usually nonporous thin film composites from polyamide and cellulose acetate. The membranes are configured as spiral-wound with spacers for feed and product water between the films shown in Fig. 4.

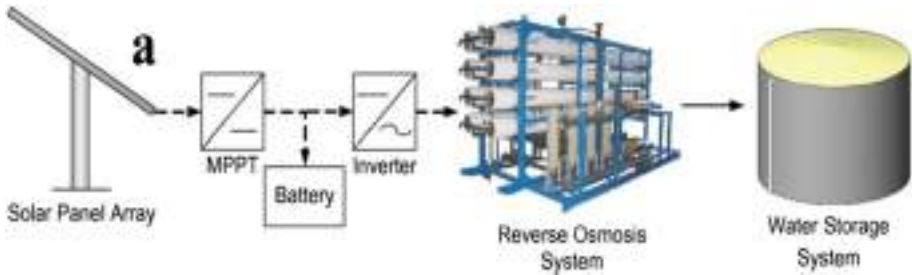


Fig. 4. Schematic diagram of PV-panel based RO system, it consist of maximum power point, DC-battery and inverter which convert DC power in AC [7].

Table 6. CO₂ emission through large water desalination projects.

Source	Water productivity	CO ₂ -emision	References
Electricity/Fossil fuel	1.2 million m ³	1900 t/day	[26]
Electricity/Fossil fuel	250000 m ³ /day	1060 t/day	[27]
Electricity/Fossil fuel		679 t/day	[28]
Solar powered	100 to 1,40,000 m ³ /day	80 t/day	[7]
Solar powered	12,000 m ³ /day	40 t/day	[29]

Table 6 shows the CO₂ emission generated by the large desalination project, whose energy source is electricity/fossil fuel and solar radiation.

Table 7. Some previous data which shows the water capacity, fossil fuel consumption and CO₂ emission during the RO-system [25].

Year	World desalination capacity (million m ³ /day)	Oil consumption (Million metric ton/day)	GHG/CO ₂ emission (Metric tons CO ₂ /day)
1990	13	0.36	39
2000	23	0.63	69
2008	52	1.42	156
2010	82	3.49	210

- a. It is shown in the Table 7 that, as the water demand is increasing, the consumption of fossil fuel is also increasing, due to which the amount of CO₂ is also increasing

rapidly in the atmosphere. If we use Solar Energy in the Ro-system then it can be reduce 27.6% carbon emission, which is equivalent to 2.1 million ton of carbon [30].

- b. Large amounts of concentrate are produced during the RO process. In water desalination plant sea water is separated in two parts fresh water and concentrated water, this high concentrated water is released in the sea, which are effect on the marine environment and aquatic life [31].

Table 8. Capacity of the daily productivity and cost of desalination water, of the RO-system on the basis of energy source it is shown in below [25].

Source of energy	Capacity of daily productivity (m ³ /day)	Water cost (\$/m ³)	Reference
Solar	1	12.05	[28]
Solar	1	3.73	[32]
Electric	10	4	[28]
Diesel generator	350	1.36	[33]
Diesel generator	500	2.57	[34]
Conventional	0.6	0.66	[35]

*Note-1\$ = 71.49 INR in 2019 [10]

Data is given in Table 8 it is analyzed that if the daily production increases then the cost of distilled water will be decrease [25].

6 Conclusions

In this paper, solar desalination technology is divided into two parts, direct and indirect solar desalination technology and shows theirs sustainability in terms of CO₂ emission, cost-economic analysis and for society benefits. Following conclusions are noted from this paper:-

- Indirect desalination technology has more complicated experimental setup than direct solar desalination technology.
- The daily productivity of indirect PVRO-system is more than the direct solar still. Through PVRO-system get 500L distilled water in a day and 7–8L through solar still.
- Solar still is one of the most efficient desalination technologies in terms of sustainability, no large amount is needed for fabrication, less amount of CO₂ emission and it is beneficial for our society. Water cost is very low as compared to other direct solar desalination, the demerit of solar still is its slow water productivity rate; it produces 7 to 8 L in a day. We can use solar still for the drought prone areas. Even if the impure water is available and then the water can be cleaned by using solar still.

- By using solar still 15.6 ton CO₂ emission is reduced in the atmosphere in comparison to other direct solar desalination technology. Through solar RO-system 27.6% CO₂ emission is reduced in comparison to other RO-system.
- Fabrication cost and distilled water cost of solar indirect RO-system is 33% lower than the other RO-system.

References

1. Li, Q., Loy-benitez, J., Nam, K., Hwangbo, S., Rashidi, J., Yoo, C.: SC, Energy (2019)
2. Nature-based Solutions, Available: The United Nations World Water Development Report (2018)
3. El-Ghonemy, A.M.K.: Water desalination systems powered by renewable energy sources. Review. Renew. Sustain. Energy Rev. **16**(3), 1537–1556 (2012)
4. Kalogirou, S.A.: Seawater desalination using renewable energy sources. Prog. Energy Combust. Sci. **31**(3), 242–281 (2005)
5. Jalihal, P., Venkatesan, R.: Advanced desalination technologies. In: Sustainable Water and Wastewater Processing. Elsevier. Amsterdam (2019)
6. Buros, O.K.: The ABCs of desalting. Int. Desalin. Assoc. Mass **2**, 1–32 (2000)
7. Ahmed, F.E., Hashaikeh, R., Hilal, N.: Solar powered desalination – Technology, energy and future outlook. Desalination **453**, 54–76 (2019)
8. Rufuss, D.D.W., Iniyan, S., Suganthi, L., Davies, P.A.: Solar stills: a comprehensive review of designs, performance and material advances. Renew. Sustain. Energy Rev. **63**, 464–496 (2016)
9. Al-Hinai, H., Al-Nassri, M.S., Jubran, B.A.: Effect of climatic, design and operational parameters on the yield of a simple solar still. Energy Convers. Manag. **43**(13), 1639–1650 (2002)
10. Online currency converter, United States dollar (USD) and Indian rupee (INR) Year 2019 Exchange Rate History: FCR. <https://freecurrencyrates.com/en/exchange-rate-history/USD-INR/2019>
11. Singh, G., Kumar, S., Tiwari, G.N.: Design, fabrication and performance evaluation of a hybrid photovoltaic thermal (PVT) double slope active solar still. Desalination **277**(1–3), 399–406 (2011)
12. Kumar, S., Tiwari, G.N.: Life cycle cost analysis of single slope hybrid (PV/T) active solar still. Appl. Energy **86**(10), 1995–2004 (2009). <https://doi.org/10.1016/j.apenergy.2009.03.005>
13. Tiwari, G.N., Sahota, L.: Review on the energy and economic efficiencies of passive and active solar distillation systems. Desalination **401**, 151–179 (2017). <https://doi.org/10.1016/j.desal.2016.08.023>
14. Shafii, M.B., Shahmohamadi, M., Faegh, M., Sadrhosseini, H.: Examination of a novel solar still equipped with evacuated tube collectors and thermoelectric modules. Desalination **382**, 21–27 (2016)
15. Abad, H.K.S., Ghiasi, M., Mamouri, S.J., Shafii, M.B.: A novel integrated solar desalination system with a pulsating heat pipe. Desalination **311**, 206–210 (2013)
16. Mosleh, H.J., Mamouri, S.J., Shafii, M.B., Sima, A.H.: A new desalination system using a combination of heat pipe, evacuated tube and parabolic through collector. Energy Convers. Manag. **99**, 141–150 (2015)

17. Ayoub, J., Alward, R.: Water requirements and remote arid areas: the need for small-scale desalination. *Desalination* **107**(2), 131–147 (1996)
18. Banat, F., Jwaied, N.: Economic evaluation of desalination by small-scale autonomous solar-powered membrane distillation units. *Desalination* **220**(1–3), 566–573 (2008)
19. Arslan, M.: Experimental investigation of still performance for different active solar still designs under closed cycle mode. *Desalination* **307**, 9–19 (2012)
20. Jani, H.K., Modi, K.V.: A review on numerous means of enhancing heat transfer rate in solar-thermal based desalination devices. *Renew. Sustain. Energy Rev.* **93**, 302–317 (2018)
21. Estahbanati, M.K., Feilizadeh, M., Jafarpur, K., Feilizadeh, M., Rahimpour, M.R.: Experimental investigation of a multi-effect active solar still: the effect of the number of stages. *Appl. Energy* **137**, 46–55 (2015)
22. Yousef, M.S., Hassan, H., Sekiguchi, H.: Energy, exergy, economic and enviroeconomic (4E) analyses of solar distillation system using different absorbing materials. *Appl. Therm. Eng.* **150**, 30–41 (2019)
23. Delgado-torres, M., Garcí, L., De Fuente, J.A., Melia, G.: Water desalination by solar-powered RO systems (2019)
24. Dashtpour, R., Al-zubaidy, S.N.: Comparisons between the submerged reverse osmosis system current schemes. **3**(4) (2012)
25. Gnaneswar, V., Nirmalakhandan, N., Deng, S.: Renewable and sustainable approaches for desalination. *Renew. Sustain. Energy Rev.* **14**(9), 2641–2654 (2010)
26. Darwish, M.A., Al-Awadhi, F.M., Darwish, A.M.: Energy and water in Kuwait Part I A sustainability view point. *Desalination* **225**(1–3), 341–355 (2008)
27. Development of an Environmental Impact Assessment and Decision Support System for Seawater Desalination Plants. CRC Press, London (2010). <https://doi.org/10.1201/b10829>
28. Ghaffour, N., Lattemann, S., Missimer, T., Choon, K., Sinha, S., Amy, G.: Renewable energy-driven innovative energy-efficient desalination technologies. *Appl. Energy* **136**, 1155–1165 (2014)
29. Fane, A.G.T.: A grand challenge for membrane desalination: more water, less carbon. *Desalination* **426**, 155–163 (2018). <https://doi.org/10.1016/j.desal.2017.11.002>
30. Salcedo, R., Antipova, E., Boer, D., Jiménez, L., Guillén-Gosálbez, G.: Multi-objective optimization of solar Rankine cycles coupled with reverse osmosis desalination considering economic and life cycle environmental concerns. *Desalination* **286**, 358–371 (2012)
31. Lattemann, S., Höpner, T.: Environmental impact and impact assessment of seawater desalination. *Desalination* **220**(1–3), 1–15 (2008)
32. Ahmad, G.E., Schmid, J.: Feasibility study of brackish water desalination in the Egyptian deserts and rural regions using PV systems. *Energy Convers. Manag.* **43**(18), 2641–2649 (2002)
33. Lamei, A., van der Zaag, P., von Münch, E.: Impact of solar energy cost on water production cost of seawater desalination plants in Egypt. *Energy Policy* **36**(5), 1748–1756 (2008)
34. Rayan, M.A., Djebedjian, B., Khaled, I.: Water supply and demand and a desalination option for Sinai, Egypt. *Desalination* **136**(1–3), 73–81 (2001)
35. Tzen, E., Morris, R.: Renewable energy sources for desalination. *Sol. Energy* **75**(5), 375–379 (2003)



Effect of Reinforced Nano-Composites on AMC Solidification Curve

Siddhartha Kosti¹  and Chandra S. Malvi² 

¹ Department of Mechanical Engineering, Rajkiya Engineering College,
Banda 210201, India

siddharth.kosti@gmail.com

² Department of Chemical Engineering, Madhav Institute of Technology
and Science, Gwalior 474005, India

Abstract. Nano-composites are the extensively used materials in the field of heat transfer and automobile because of their higher mechanical properties compared to conventional material. Present work focuses on the reinforced nano-composites effect on Aluminium matrix composites (AMC) solidification curves. Silicon carbide (SiC) and boron carbide (B₄C) as nano-composites are considered with varying percentage weight up to 30 while Aluminium as a base material is considered. A mathematical model is developed to analyse the solidification curve governs by heat conduction equation using MATLAB. 800 s of end-time is considered for solidification of the AMC. Results indicate that the present model predict solidification curves accurately. The increment in nano-composites percentage weight shows steeper solidification curves indicating a lower solidification rate due to the thermal conductivity decrement. Al-SiC shows higher steeper curves compared to Al-B₄C for all percentage weight considered due to less thermal conductivity. Difference between the melting point temperature and maximum temperature at the end of 800 s is found to be decreased with increment in the reinforcement percentage weight because of the decreased solidification rate. Both the thermal conductivity model shows the same solidification curves for all AMC compositions.

Keywords: AMC · Nano-composites · Solidification

1 Introduction

Reinforcement of the composites in aluminium matrix is called (AMC) Aluminium matrix composites. AMC is being widely used in the automobile industry for making of disk brake calipers, driveshaft and cylinder liners because of their great mechanical properties they also have applications in power electronics field. Rohatagi [1] says that metal-matrix-composites (MMC) may have good properties like thermal conductivity, wear resistance, strength, coefficient of expansion etc., compared conventional materials. Wide varieties of composites are available like SiC, Al₂O₃, B₄C, Graphite etc., which can be reinforced into the aluminium matrix to make AMC.

They utilized ANSYS to study reinforced nano-particles and flow distribution [2, 3]. Hu and Argyropoulos [4] conducted review study on mathematical modelling of solidification and melting. They reviewed different methods to study the solidification and melting process and categorized them on the basis of their merits and demerits. They also studied the effect of particle motion during the solidification and melting. Variable grid methods gives more accurate results compared to fixed grid methods [4, 5]. Thomas et al. [6] compared numerical methods results of solidification by solving two-dimensional transient heat conduction problem while Sclicudean and Abdullah [7] used stream-vorticity approach to study the heat transfer and fluid flow during solidification process. Peng et al. [8] developed a new computational method to study the solidification process in overheated slab for large and small values of Stefan number. They derived an equation which shows the relationship between the time and phase change front position.

Liu and Chao [9] studied the consequence of modified effective specific heat method in solidification problem. They validated the results of their method with the results if Stefan and Neumann problem. They also validated their results with the crystal growth problem results. Wen-bang et al. [10] mathematically derived the time step modal for solidification problem while Nikolic et al. [11] studied the interfacial heat transfer coefficient by finite difference method during rapid solidification of spherical samples. Reddy and Murthi [12] studied grey-cast iron solidification process using finite difference method. Some researchers found that reinforcement of silicon carbide enhances the mechanical properties [13–17]. Some researcher analyse the effect of graphite reinforcement into base materials [18–23]. Artificial intelligence [31] and genetic algorithm [32] is utilized to analyse the behaviour of composites.

Literature reveals that AMC is studying widely using finite element analysis commercial available FEM software but much information is not available on finite difference solution technique to study their solidification curves. Therefore present work focuses on the AMC solidification curves study using finite difference technique to solve unsteady heat conduction equation. Results from the present work are compared with experiments and found in good agreement.

2 Mathematical Formulation

2.1 Physical Domain

Physical domain of the geometry considered in shown in Fig. 1 with appropriate boundary conditions at the walls. Outward direction shows that the heat is losing to atmosphere by convection. Length (X-direction) and width (Y-direction) of the casting assembly are considered to be equal to make the casting assembly of square shape.

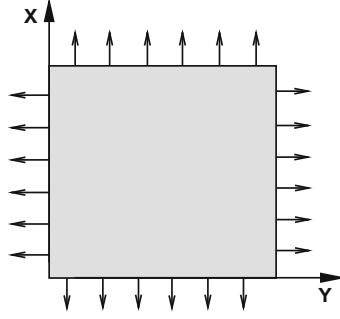


Fig. 1. Schematic of physical domain

2.2 Governing Equation and Boundary Conditions

$$\frac{\partial T}{\partial t} = \alpha \nabla^2 T \quad (1)$$

$$\vec{q} = -k \cdot \Delta T \quad (2)$$

Initial condition ($t = 0$)

Initially it is assumed that all the points of casting are at the molten metal temperature, mathematically it can be represented as,

$$T_{\text{initial}} = 720^\circ\text{C}, \text{ for all } x \text{ and } y; (0 \leq x \leq L) \& (0 \leq y \leq L)$$

Equation (1) represents the governing equation and Eq. (2) represents the convective boundary conditions. Term on the left-hand side of Eq. (1) represents the temperature variation with respect to time while terms on the right-hand side of Eq. (1) represents the temperature variation with respect to spatial directions.

Where: ∇^2 is laplacian operator, Δ is gradient, \vec{q} is heat flux, $\alpha = k/\rho C_p$ is thermal diffusivity in m^2/s , k is thermal conductivity in $\text{W}/\text{m-K}$, ρ is density in kg/m^3 , C_p is specific heat $\text{J}/\text{kg-K}$, T is temperature in (K), t is time in seconds.

2.3 Finite Difference Technique

Explicit scheme with uniform grid [24–30] is utilized to convert the Eq. (1) from partial differential form to algebraic form. In explicit scheme temporal term is discretized using forward scheme and spatial terms are discretized using second order central scheme. Equation (3) represents the explicit discretization of Eq. (1) for present problem.

$$\frac{T_{t+1,i,j} - T_{t,i,j}}{\Delta t} = \alpha \left(\frac{T_{t,i+1,j} + T_{t,i-1,j} - 2T_{t,i,j}}{(\Delta x)^2} + \frac{T_{t,i,j+1} + T_{t,i,j-1} - 2T_{t,i,j}}{(\Delta y)^2} \right) \quad (3)$$

Equation (3) can be rewritten as [26],

$$T_{t+1,i,j} = T_{t,i,j} + \alpha \Delta t \left(\frac{T_{t,i+1,j} + T_{t,i-1,j} - 2T_{t,i,j}}{(\Delta x)^2} + \frac{T_{t,i,j+1} + T_{t,i,j-1} - 2T_{t,i,j}}{(\Delta y)^2} \right) \quad (4)$$

2.4 Stability Condition

$$\alpha \times \left(\frac{\Delta t}{(\Delta x)^2} + \frac{\Delta t}{(\Delta y)^2} \right) \leq \frac{1}{2} \quad (5)$$

Above relation called as Courant-Friedrichs-Lewy condition or stability condition for two-dimensional case [26].

$$\Delta t \leq \frac{1}{2\alpha \left(\frac{1}{(\Delta x)^2} + \frac{1}{(\Delta y)^2} \right)} \quad (6)$$

A grid-size of 11×11 is adopted (explained in Sect. 2.7) to solve the present problem, due to which step-size ‘ Δx ’ and ‘ Δy ’ values get fixed and are equal to 0.1 and value of ‘ α ’ is also constant. In the algorithm right hand side value is calculated first, than the value of ‘ Δt ’ is calculated appropriately so that the value of ‘ Δt ’ is less than the calculated value to satisfy the stability condition.

2.5 Materials and Models

Boron carbide (B4C) and Silicon carbide (SiC) are considered as reinforcement materials while aluminium (Al) is considered as base material. Table 1 represents properties of these materials.

Table 1. Properties of base material and reinforced nano-composites material

Material	B4C	SiC	Al
ρ (kg/m ³)	2550	3200	2712
k (W/m-K)	42	100	205
CP (J/kg-K)	1288	1300	910

Effective thermal conductivity of AMC is calculated using [1, 26] while effective density & specific heat are calculated using [1].

2.6 Flow Chart

Flow chart of the mathematical model developed and solved is shown in Fig. 2. T_{atm} and T_C are the atmospheric temperature and temperature at the centre of assembly.

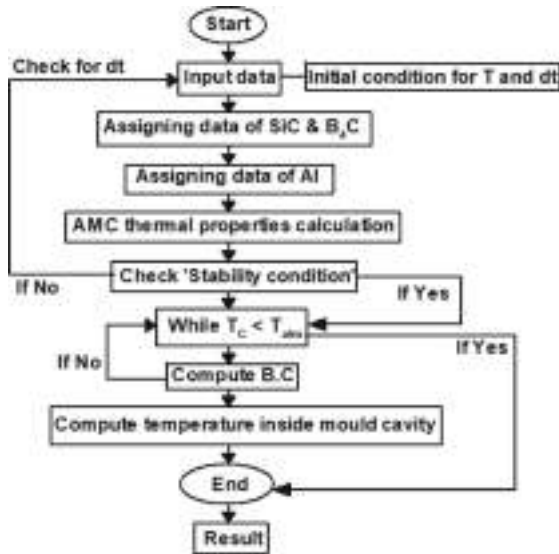


Fig. 2. Flow chart of the mathematical model

2.7 Grid Validation

Grid validation test is performed for different grid-sizes as shown in Fig. 3 and from the figure it can be observed that solidification curve is same for all grid-sizes. So 11×11 grid-size is considered [26].

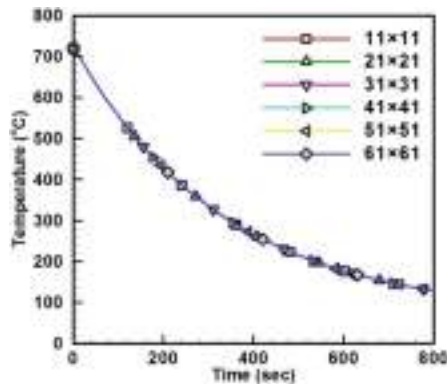


Fig. 3. Grid validation test

2.8 Experimental Validation

Ramesh et al. [15] experimental result is considered to validate the present results. It can be observed that present result initially matches well with the experimental results then it starts to deviate and shows higher solidification-curve for same period of time,

this can be because of boundary conditions and model considered in present study does not includes temperature dependent thermal properties variation and any outside effect (Fig. 4).

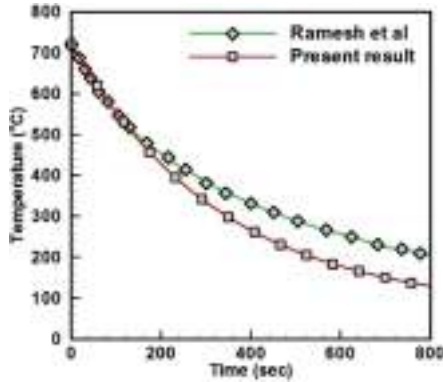


Fig. 4. Experimental validation test

2.9 Analytical Validation

Present result is validated with the analytical results of Mackowski [33] shown in Eq. 7. Figure 5 represents the comparison of the temperature contours. Analytical results are generated for square cavity of unity dimension in each direction while the present results are generated for 41×41 grid size. In both the cases non-dimensional temperature at the top boundary is considered to be unity while non-dimensional temperatures on the other three boundaries are considered to be zero. Similarity between the two contours can be observed easily.

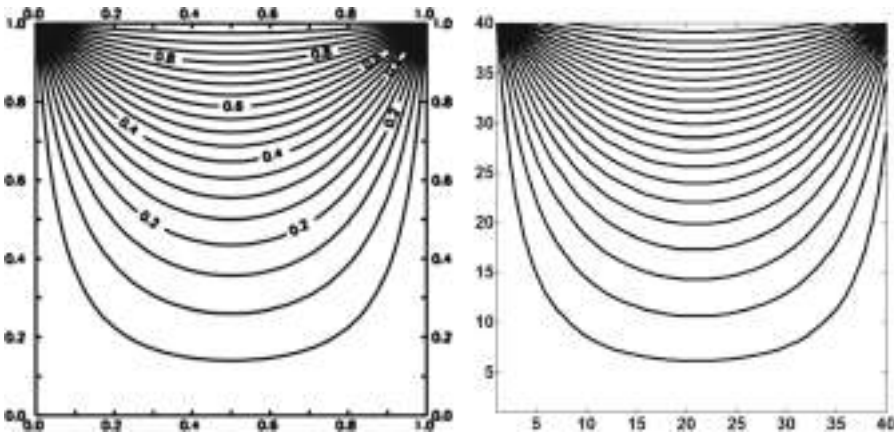


Fig. 5. Analytical validation

$$T = \frac{4}{\pi} \sum_{n=1}^{\infty} \frac{\sin[(2n-1)\pi\bar{x}] \sinh[(2n-1)\pi\bar{y}]}{(2n-1) \sinh[(2n-1)\pi\bar{y}]} \quad (7)$$

3 Result and Discussion

Effects of nano-composites (SiC and B4C) reinforcement in the Al matrix are studied in the present work by varying their percentage weight up to 30. Individual (Al-SiC and Al-B4C) and cumulative (Al-SiC-B4C) effects of reinforcement on solidification curves are studied by solving 2D heat conduction using finite difference explicit technique. Mixture rule for specific heat and density calculation of AMC is considered while thermal conductivity is calculated by Mixture rule and Maxwell model.

Tables 2, 3 and 4 show the thermal properties of the Al-SiC, Al-B4C and Al-SiC-B4C respectively for different percentage weight variation of base material and reinforcement. Tables 2 and 3 shows the individual variation of SiC and B4C, while Table 4 shows the cumulative variation of SiC and B4C. For individual variation both thermal conductivity models are considered while for cumulative variation only mixture rule is considered.

Table 2. Thermo-physical properties of Al-SiC

Percentage weight		Al-SiC			
Al	SiC	CP (J/kg-K)	ρ (kg/m ³)	k (W/m-K)	
		Mixture		Mixture	Maxwell
1.0	0.0	910.0	2712.0	205.0	205.0
0.9	0.1	949.0	2760.8	194.5	192.6
0.8	0.2	988.0	2809.6	184.0	180.7
0.7	0.3	1027.0	2858.4	173.5	169.2

Table 3. Thermo-physical properties of Al-B4C

Percentage weight		Al-B4C			
Al	B4C	CP (J/kg-K)	ρ (kg/m ³)	k (W/m-K)	
		Mixture		Mixture	Maxwell
1.0	0.0	910.0	2712.0	205.0	205.0
0.9	0.1	947.8	2695.8	188.7	183.6
0.8	0.2	985.6	2679.6	172.4	163.6
0.7	0.3	1023.4	2663.4	156.1	145.0

Table 4. Thermo-physical properties of Al-SiC-B4C

Percentage weight			Al-SiC-B4C		
Al	SiC	B4C	CP (J/kg-K)	ρ (kg/m ³)	k (W/m-K)
1.0	0.0	0.0	910.0	2712.0	205.0
0.9	0.05	0.05	948.4	2728.3	191.6
0.8	0.15	0.05	987.4	2777.1	181.1
0.7	0.25	0.05	1026.4	2825.9	170.6
0.8	0.05	0.15	986.2	2712.1	175.3
0.7	0.05	0.25	1024.0	2695.9	159.0

Figure 6(a–c) shows the variation of the thermal conductivity, density and specific heat of the AMC for varying percentage weight of the reinforcement. From the thermal conductivity figure it can be observed that AMC thermal conductivity is decreasing with increment in the percentage weight of the reinforcement. Reinforcement of B4C

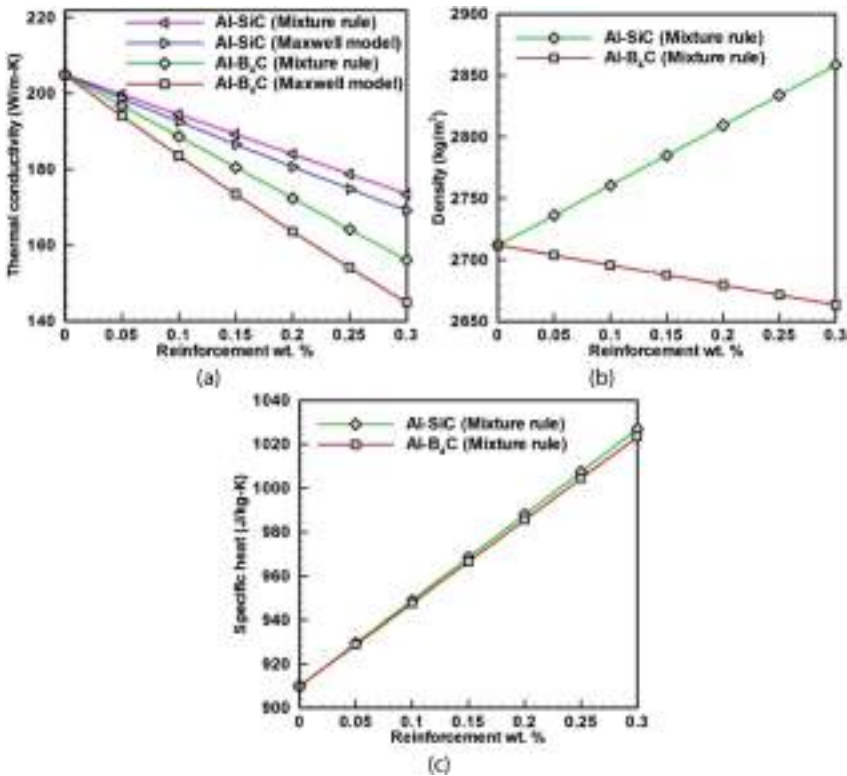


Fig. 6. AMC thermal properties vs. reinforcement percentage weight (a) Thermal conductivity (b) Density (c) Specific heat

shows high decrement in the thermal conductivity compared to SiC reinforcement. Maxwell model shows high decrement in AMC thermal conductivity compared to mixture rule and as the percentage weight is increasing deviation between the two is increasing. Reinforcement of SiC and B4C show inverse effect on the AMC density. Al-SiC density is increasing while Al-B4C density is decreasing with increment in percentage weight, this is due to the higher density of the SiC and lower density of B4C compared to Al. From the AMC specific heat figure it can be observed that AMC specific heat is increasing with percentage weight for both of the nano-composites reinforcement, this is because of the higher specific heat values of SiC and B4C compared to Al.

Figures 7 and 8 represents solidification curves for SiC and B4C reinforcement varying percentage weight into Al metal matrix. On the vertical axis temperature is plotted and on the horizontal axis time is plotted. An end time of 800 s is adopted and reinforcement percentage weight is varied up to 30 by a difference of 10. From the figures it can be noticed that with increment in the reinforcement percentage weight solidification curves are getting steeper as observed in the experimental results of Ramesh et al. [15]. Steeper solidification curves indicate particular composition have decreased solidification rate [16]. Lower cooling rates may be impute to the decreased thermal conductivity of the AMC as explained in Fig. 6. Maximum temperature at the end of the 800 s is also affected by the addition of the SiC and B4C reinforcement. For Al casting maximum temperature is 112.64 °C while for 10% weight, 20% weight and 30% weight reinforcement of SiC in the Al, maximum temperature with mixture rule are 119.96 °C, 127.70 °C, 135.90 °C and with Maxwell model are 119.96 °C, 127.78 °C, 135.98 °C. This behavior may be imputing to decreased effective thermal conductivity which is the reason for decay in solidification [16].

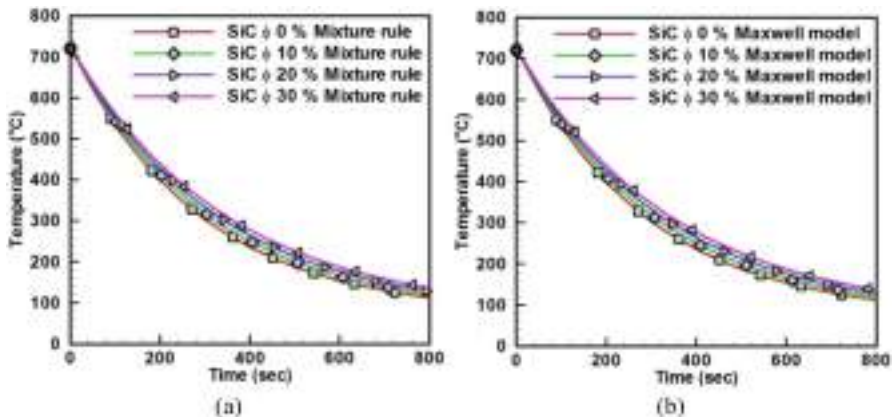


Fig. 7. Solidification curves for SiC reinforcement percentage weight (a) Mixture rule (b) Maxwell model

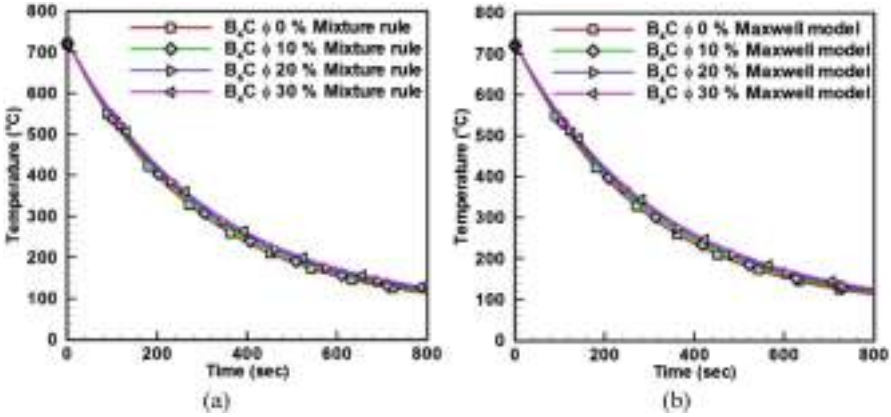


Fig. 8. Solidification curves for B4C reinforcement percentage weight (a) Mixture rule (b) Maxwell model

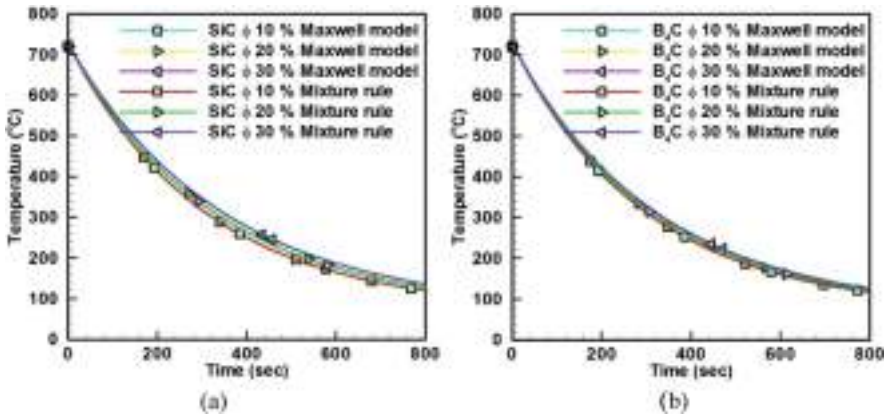


Fig. 9. Solidification curves for thermal conductivity models (a) SiC (b) B4C

Figure 9 represents the comparison of solidification curves between thermal conductivity models and percentage weight of the reinforcement. Results indicate that there is no substantial change in the solidification curve by changing the thermal conductivity models [26].

Figure 10 represents the cumulative effect of the reinforcement percentage weight. Five different run are executed as shown in Table 4. Total reinforcements percentage weight considered are 10, 20 and 30, first, B₄C percentage weight is kept constant and SiC percentage weight is varied than SiC percentage weight is kept constant and B₄C percentage weight is varied. It can be observed that steeper cooling curves are observed for higher percentage weight of SiC compared to higher percentage weight of B₄C. Increment in percentage weight makes the solidification curve steeper as explained in the earlier text.

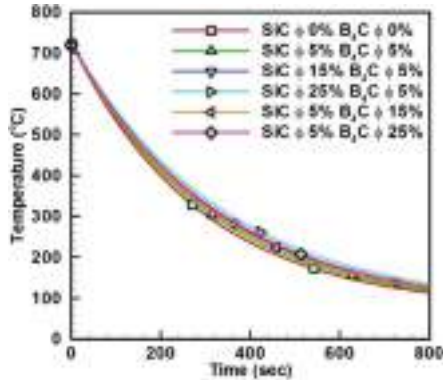


Fig. 10. Cumulative effect of SiC and B4C percentage weight on solidification curve

4 Conclusion

Solidification curves are plotted for individual and cumulative effect of SiC and B4C in the Aluminium matrix (Al) for varying percentage from 10% weight to 30% weight by a difference of 10% weight. Finite difference techniques are adopted to solve the mathematical problem using MATLAB. Results indicate that finite difference technique can predict the solidification curves accurately of AMC. With increment in the percentage weight solidification curves becomes steeper indicating lower solidification rate. Al-SiC shows higher steeper curves compared to Al-B4C metal matrix for all percentage weight considered. Both the thermal conductivity model shows same solidification curves for all AMC compositions. Difference between the melting point and maximum temperature at the end of solidification process is decreases with reinforcement percentage weight increment. Solidification curves obtained by present methods matches with experimental results.

References

1. Rohatagi, P.K.: Metal matrix composites. *Defence Sci. J.* **43**(4), 323–349 (1993)
2. Rajeshwari, P., Dey, T.K.: Finite element modelling and experimental investigation on effective thermal conductivity of AlN (Nano) particles reinforced HDPE polymer nanocomposites. *Thermochim. Acta* **638**, 103–112 (2016)
3. Zhang, D., Nastac, L.: Numerical modelling of the dispersion of ceramic nanoparticles during ultrasonic processing of aluminium-based nanocomposites. *J. Mater. Res. Technol.* **3** (4), 296–302 (2014)
4. Hu, H., Argyropoulos, S.A.: Mathematical modelling of solidification and melting: a review. *Model. Simul. Mater. Sci. Eng.* **4**, 371–396 (1996)
5. Jana, S., Ray, S., Durst, F.: A numerical method to compute solidification and melting processes. *Appl. Math. Model.* **31**, 93–119 (2007)

6. Thomas, B.G., Samarasekera, V., Brimacombe, J.K.: Comparison of numerical modeling techniques for complex two-dimensional, transient heat-conduction problems. *Metall. Trans. B* **15B**, 307–318 (1984)
7. Scuddean, M., Abdullah, Z.: On the numerical modelling of heat transfer during solidification processes. *Int. J. Numer. Methods Eng.* **25**, 445–473 (1988)
8. Peng, Q., Chaomin, Z., Hiaohong, L., Xiugan, Y.: A new computation method for solidification process in a finite initially overheated slab. *J. Thermal Sci.* **1**(4), 272–277 (1992)
9. Liu, Y.C., Chao, L.S.: Modified effective specific heat method of solidification problems. *Mater. Trans.* **47**(11), 2737–2744 (2006)
10. Wen-bang, G., Li-Liang, C., Rui-Xiang, L., Jing, H.: Derivation and application of time step model in solidification process simulation. *Chin. Foundry* **4**(3), 206–209 (2007)
11. Nikolic, Z.S., Yoshimura, M., Araki, S., Fujiwara, T.: Finite difference method for computer study of the interfacial heat transfer coefficient during rapid solidification of spherical samples on a metallic substrate. *Sci. Sinter.* **39**(2), 111–116 (2007)
12. Reddy, A.C., Murthi, V.S.R.: Finite difference analysis of grey cast-iron solidification process. In: 2nd National Conference in Computer Integrated Manufacturing, vol. 1, pp. 103–108 (2003)
13. Cetin, A., Kalkanli, A.: Numerical simulation of solidification kinetics in A356/SiC_p composites for assessment of as-cast particle distribution. *J. Mater. Process. Technol.* **209**, 4795–4801 (2009)
14. Jagadeesh, S.K., Ramesh, C.S., Mallikarjuna, J.M., Keshavamurthy, R.: Prediction of cooling curves during solidification of Al 6061–SiC_p based metal matrix composites using finite element analysis. *J. Mater. Process. Technol.* **210**, 618–623 (2010)
15. Ramesh, C.S., Jagadeesh, S.K., Keshavamurthy, R.: Solidification studies on sand cast Al 6061–SiC_p composites. *J. Alloy. Compos.* **509S**, S371–S374 (2011)
16. Lelito, J., Zak, P.L., Shirzadi, A.A., Greer, A.L., Krajewski, W.K., Suchy, J.S., Haberb, K., Schumacher, P.: Effect of SiC reinforcement particles on the grain density in a magnesium-based metal-matrix composite: modelling and experiment. *Acta Mater.* **60**, 2950–2958 (2012)
17. Rahman, M.H., Rashed, H.M.M.A.: Characterization of silicon carbide reinforced aluminium matrix composites. *Procedia Eng.* **90**, 103–109 (2014)
18. Barekar, N., Tzamtzis, S., Dhindaw, B.K., Patel, J., HariBabu, N., Fan, Z.: Processing of aluminum-graphite particulate metal matrix composites by advanced shear technology. *J. Mater. Eng. Perform.* **18**(9), 1230–1240 (2009)
19. Radhika, N., Subramanian, R., Prasat, S.V.: Tribological behaviour of aluminium/alumina/graphite hybrid metal matrix composite using Taguchi's techniques. *J. Min. Mater. Charact. Eng.* **10**(5), 427–443 (2011)
20. Weiss, D., Grassi, J., Schultz, B., Rohatagi, P.: Ablation of Hybrid Metal Matrix Composites. *American Foundry Society*, pp. 2–7 (2011)
21. Saheb, D.A.: Aluminium silicon carbide and aluminium graphite particulate composites. *ARPN J. Eng. Appl. Sci.* **6**(10), 41–46 (2011)
22. Muthazhagan, C., Babu, A.G., Bhaskar, G.B., Rajkumar, K.: Influence of graphite reinforcement on mechanical properties of aluminium-boron carbide composites. In: *Advanced Materials Research*, vol. 845, pp. 398–402 (2013)
23. Sudindra, S., Kumar, A.C.: Studies on Al6061/Al₂O₃ and graphite hybrid metal matrix composites. *Int. J. Metall. Mater. Sci. Eng.* **3**(3), 35–42 (2013)
24. Kosti, S., Grover, K.: Particle concentration effect on thermal properties of nano-fluids. *NanoTrends J. Nanotechnol. Appl.* **19**(2), 18–21 (2017)

25. Kosti, S., Pathak, P.: Genetic algorithm based finite difference simulation of solidification process for MMC's. *Mater. Today: Proc.* **5**(2), 8271–8279 (2018)
26. Kosti, S., Malvi, C.S.: Cumulative influence of nanoparticles on MMCs' time–temperature history curve. *Nanomater. Energy* **7**(1), 1–10 (2018)
27. Kosti, S., Kundu, J., Malvi, C.S.: Nanoparticle reinforcement effect on the MMC's. In: *Advances in Interdisciplinary Engineering*, pp. 459–469 (2019)
28. Kosti, S.: Nanomaterials and nanocomposites thermal and mechanical properties modelling. In: *Nanotechnology in Aerospace and Structural Mechanics*, Chap. 7, pp. 234–256, IGI Global (2019)
29. Kosti, S.: Numerical study of heat flux boundary in nanofluid-filled cavity. *Nanomater. Energy* **3**(6), 193–205 (2014)
30. Kosti, S.: Heat-flux and convective boundary influence on nano-fluids filled cavity. *Emerg. Mater. Res.* **4**(8), 1–9 (2019)
31. Shabani, M.O., Mazahery, A.: Artificial intelligence in numerical modelling of nano sized ceramic particulates reinforced metal matrix composites. *Appl. Math. Model.* **36**, 5455–5465 (2012)
32. Shabani, M.O., Mazahery, A.: Application of GA to optimize the process conditions of Al matrix nano-composites. *Compos. Part B* **45**, 185–191 (2013)
33. Mackowski, W.D.: Conduction heat transfer notes for MECH 7210, Mechanical Engineering Department Auburn University, pp. 93–98 (2004)



An Efficient Performance of Enhanced Bellman-Ford Algorithm in Wireless Sensor Network Using K-Medoid Clustering

Garima Sharma, Praveen Kumar^(✉), and Laxmi Shrivastava^(✉)

Department of Electronics and Communication Engineering,
Madhav Institute of Technology and Science, Gwalior, Madhya Pradesh, India
sharmagarima2411@gmail.com,
kumarpraveensingh90@gmail.com, lselex@mitsgwalior.in

Abstract. Wireless sensor network (WSN) is an accumulation of smart sensor nodes which has firmly restricted control, calculation ability, storage and communication facility. Wireless sensor network (WSN) is the most standard services engaged in commercial and industrial applications like military surveillance, animal monitoring, target tracking, forest fire detection and industry security. The Sensor Node (SN) automatically construct a network connected to the sink node after deploying manually. Each SN is accountable for monitoring surrounding environment and data which is delivered to the sink node in a one-hop or multihop manner. The collected data are transmitted to the remote server by sink node through satellites or internet. Hence, an energy optimization technique is used to reduce the actual power consumption of the SN in place of sink node. Here, the Bellman Ford Shortest Path Algorithm is used for efficient data transmission purposes which helps in reducing the energy consumption of sensor nodes. The Bellman-Ford algorithm is used as a shortest path algorithm in this work. In a given paper K-medoid clustering algorithm is used for cluster formation. K-medoid clustering chooses the sensor node as a cluster head (CH) which lies at the center of the cluster. Further, The MATLAB software is used for the simulation of the Bellman Ford Shortest Path Algorithm for acquiring better results. The simulated results show that the Bellman Ford Shortest Path Algorithm is better than the K-Medoid Algorithm in place of energy consumption and network lifetime.

Keywords: WSN · Source · Base station · Shortest path · Enhanced Bellman-Ford Algorithm

1 Introduction

WSN is a new technology meant for detecting as well as monitoring the phenomenon of life. The efficient design of WSN has become a leading area of research. A WSN is described as a web of smaller devices called Sensor Nodes (SN). The Sensor Nodes usually being deployed in the open & unsecured environment. capabilities for Communication, as well as the power of Battery, are two limitations for sensor node. Now a day's sensor nodes are extensively expanding due to quick technological advances in

the industries of micro-electronic form also the latest developed routing protocols that save much communication & computation of the power. The target tracking, environmental monitoring, and battlefield surveillance are the applications which use WSNs. WSN is the collection of the hundreds/thousands SN being worked through batteries of small form. They are being spread in the open environment to observe as well as accumulate data as of enclosed phenomenon. Then the remote base station obtained report messages on or after SN. Heterogeneous uses are being reliant on the WSNs like an exploration of the military field, protection on the border as well as forest fires [1] (Fig 1).

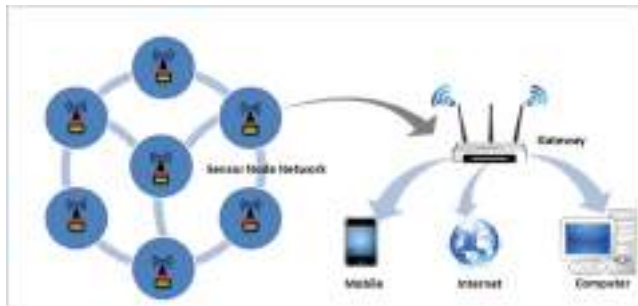


Fig. 1. WSN architecture

The task in which the data points are split into homogenous classes or clusters is called Clustering. Homogeneous means that they are similar. Items available within the same class are more similar. Thus, this process is known as Grouping.

1.1 K-Means Clustering [2]

In 1967, the simplest clustering methods i.e. K Means is first used by MacQueen which is under algorithms of unsupervised learning type. The Unsupervised Learning Algorithm is needed to resolve the clustering issue of well-known form. It works in an easy manner to organize a specified data set all the way through assertive no: of clusters.

K-Means clustering technique which is beneath partitioning ways category. In the partitioning method, database denoted by D having n no: of objects are partitioned within the set of the k form of clusters. Given k , the major task is on searching a partition of the k clusters that enhances the selected form of the criterion for partitioning. So, k -means clustering is preferred for given work. The k is the input to given algorithm & operation is to partition n no: of objects set within the k no: of clusters. In these outcomes, the intra cluster analogy is far above the ground but the inter-cluster analogy is low. Cluster analogy is evaluating the object in a cluster in terms of mean value, which is being considered as the cluster's centroid/center of the gravity. The algorithm has the following steps:

1. The k points are placed into network space which is clustered. Initial group centroids are defined by these points.

2. assign every object to the group which consists of the closest centroid.
3. After the allocation of several objects, then estimate k centroids positions.
4. Repeat Steps 2 & 3 till centroids have moved no longer (Fig. 2).

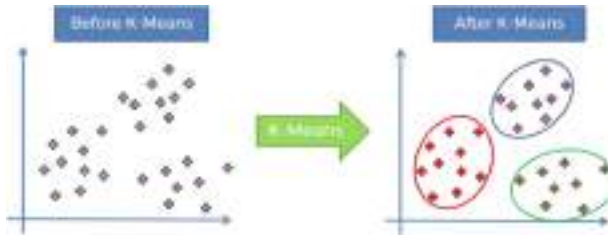


Fig. 2. K-Means clustering

1.2 K-Medoids Clustering Algorithm (KMCA)

The k-medoids algorithm is an algorithm for clustering which is linked to both algorithms i.e. k-means algorithm and the Medoid shift algorithm. Mutually these algorithms are being partitional (dataset is broken within the groups) & are used to reduce the separation among the points which is tagged in the cluster. This point is designated as a cluster center. In contrast to k-means named algorithm, k-medoids opted data points as the centers (medoids). k-medoid is being a partitioning method of the classical form of clustering in which set of data given n no: of objects are split into k clusters. It's much more vigorous to the noise & their extreme value is compared to k-means because in spite of taking some of the squared Euclidean distances it prefers to the reduced sum of the pairwise dissimilarities. A medoid (Medoids are depicted as the data set of objects whose average distinction to all objects in the cluster is the minimum.) can be determined by the object of a cluster. The average distinction of all objects in the lowest form of cluster. that is mostly situated in the center of the cluster.

In WSN, distance matrix of each sensor node is measured by the K-medoid protocol. In distance matrix, its reserve separation among every sensor form of a node with the other form of nodes which lies within the network. K-medoid chooses K CH randomly (CH) from the network. Then it also adds every form of SN to the nearest CH dependent on minimum space. It constructs K no: of clusters by glancing at the distance matrix. After the formation of the cluster, it re-elects CH which lies approximately in the center of the cluster. Cluster head sensor node has improved communication & lower form of packet delay because of the centroid node.

K-medoid Algorithm:

1. Select K initial CH at random.
2. Adds every sensor node to the primary cluster heads based on the minimum separation.
3. Creation of K clusters within a network.
4. Re-elect the central CH in clusters.

2 Shortest Path Algorithm (SPA)

In 1959, Dijkstra's developed first shortest path algorithm problem, but this path was being measured only for the single form of source. Then, in 1962 Floyd developed the several pair of shortest path Floyd Warshall's also also obtained outcome is based on the theorem by means of Warshall's in (1962). The numerous researchers include studied shortest path issue in modern years. This makes an attempt to crack several real-world queries such as traffic routing in the communication form of networks, transportation in the routing of vehicle. In the WSN, Dijkstra's algorithm is being required for repulsing in the target being tracking by allowing for different frameworks such as no: of nodes, packet delivery ratio, throughput, & the optimization of energy. Dijkstra's algorithm is employed to search out shortest paths as of a destination vertex of a single form to extra entire vertices. The CH is considered as the vertex of destination. The Dijkstra's Algorithm, Algorithm Floyd Warshall's & Bellman-Ford's Algorithm are the algorithms of the shortest path. The Dijkstra's Algorithm is apt for the routing by the transitory path in a WSN. Dijkstra's algorithm opts for directionless graphs. The consecutive shortest path algorithm is the algo of Floyd-Warshall's that is the fusion of the Floyd algorithm and Warshall's algorithm. The Floyd-Warshall's algorithm is not suitable for wireless sensor network therefore, it is not used for routing purposes. It only works with shortest paths among the different nodes in the standard form of a graph. Thus, Floyd Warshall's Shortest Path Algorithm has been altered & a novel algorithm has liable for the routing in WSN. Therefore, altered Floyd Warshall's algorithm is considered for the energy form of optimization in WSN [2].

3 Literature Survey

In this paper, a path planning technique of WSNs is proposed which is based on service priority and an altered Dijkstra algorithm is utilized for tackling this issue. For balancing left out the energy of all nodes this strategy is useful for minimizing total energy consumption. The simulation results demonstrate the method which not only enhances the network lifetime but also ameliorate network reliability performance compared to the shortest-path algorithm (SPA) [3].

An effective form of cost with the shortest path directing algoModLeach-A* dependent on heuristic finding algorithm A* in the WSNs which is presented in this paper. This integrates distance of the CH node and energy to formulate multi-hop communication with the heuristic algorithm. It also can dodge foregoing death of different CH nodes also the energy utilization load alter from CH nodes to WSN. As an outcome, this increases the lifetime of network & advancement done in data transmission quality. Programs, hence to develop the existence time of the procedure & progress character of transmission of data. The simulation outcome on the MATLAB stage demonstrates that execution of the ModLeach-A* Algorithm for its illustration, data transmission to the sink hub, a lifetime of network, network energy utilization is smarter to that of the leech-A*, Leach-C & algorithm named Leach [4].

The simulation outcome did on the MATLAB platform which illustrates the new performance of the ModLeach-A* algo for its illustration. For example, data

transmission to the sink hub, a lifetime of network, network energy utilization gives more satisfactory results as compared to these algorithms i.e. Leach-A*, Leach-C and Leach algorithm [4].

In this paper, The Distance Energy Evaluated (DEE) clustering algorithm is proposed to stabilize the energy consumption in WSN. This is basically designed for the characteristics of homogenous WSN where CH are chosen by probability. This probability is dependent on the ratio among the distance & the left out the energy of a node. Finally, DEE is achieved with more effectual messages and longer lifetime. Since this paper proposes a clustering algorithm with a stationary sensor node but there is further research needed for heterogenous sensor nodes having a prominent capacity of energy in consumption of energy also the likely existence [5].

In paper [6], The Compression Data Gathering dependent on the random path for achieving higher communication, energy consumption is proposed. This proposed form of algorithm is used to set projection nodes of an effective form via a random path, which creates each form of measurement through a single path transmission. Analogize with methods of data gathering depend on the compressive sensing, proposed ways can remarkably debase communication of the energy consumption of gathering of data, & can effectually make longer the lifetime of the network.

In the given paper, an assured Shortest Path Routing Algorithm (SPRA) is being proposed to protect against Compromised Regions (CRs) which is zone to protect a lot of compressed cluster modes (CNs). The calculation is done through geometric shortest path algorithm by naturally selecting several turning points. A complex way is introduced to elect nodes of the agent throughout turning points and their packages are being transferred among nodes of the agent. The SPRA is operated in the distributed model. This supervises experiments of series to compare this method through dynamic Greedy Perimeter Stateless Routing (GPSR), Directed Diffusion (DD) algorithms. The simulation outcomes show the SPRA, secure shortest routing path algorithm and it also enhances energy efficiency [7].

In a given paper, we offer a further algorithm for clustering routing to address the lifetime hassle which improves WSN. The routing form of algorithm which adjusts the vigor of the utilization of personal sensor through utilizing another ideal K-Medoid algorithm for choosing the various arrangements of the sensors for packet transmission in the system. The idea of search space forwarding is being focused to minimize redundant transmissions & unfit CHs. as a result of prohibiting inappropriate CHs sensors as of taking part in path searching the process, avoidable transmissions are minimized, and a lifetime of the network is maximized. The proposed routing form of algorithm illustrates their capability in the time period of conveyance of the data packets & NW lifetime contrasted in LEACH, Bee Cluster, O-LEACH [8].

4 Proposed Methodology

In the paper, [9] efficient form of energy-saving economic scheme is work on to decrease the energy utilization & also to drag out the lifetime of the network. One of the famous situations is to decrease the energy utilization for the WSNs which involves

clustering technology. The fundamental thought of this strategy is to decrease the correspondence separation of SNs by utilizing the grouping method. The ultimate goal of a given way is to minimize communication separation of the sensor nodes via using clustering methods. To obtain the absolute reaction of the cluster, this uses the K-medoids algorithm to measure medoids of optimal form among the sensor nodes.

At that point, this can select a suitable CH. By adjusting system load all among the clusters, energy proficiency can be enhanced and organize lifetime which can be archived by broadening energy. Simulation demonstrates that the proposed ALGORITHM is effective in energy utilization and NW lifetime.

The Bellman-Ford algorithm (BFA) is a graph search algorithm that searches the shortest path (SP). This elects source vertex from the different vertices in the graph. This algorithm can be utilized for both weighted as well as the unweighted graph.

The BFA is used to locate the Shortest Path in the graph. In spite of the fact that it's slower from Dijkstra's algorithm, Bellman-Ford is much accomplished of taking care of the graph that consists of negative edge weight, so it's progressively flexible. For an event with a negative cycle, BFA can establish the shortest path to the negative weight also. Spin the negative cycle unlimited no: of times to reduce the cost of the proposed path. Along with this, Bellman-Ford which can likewise recognize cycles of negative form that is a very useful characteristic.

In the proposed work, BFA is required to search the shortest path (SP) from the source station to base station (BS). When an event is sensed by the SN, then an optimal route is established. Sink node hub is accountable for gathering records of different nodes. It acts as a link among WSNs as well as with the outer nation. The SN is robust than various nodes. It consists of additional memory capacity & supplementary computational power. The source node is accountable for asset sensing and transferring sensed data to the sink node along with the communication of multi-hop. basic nodes are pre-owned to transmit packets from source to that of sink node. Communication from that of a node is normally being modeled from circular communication range being centered at the node. Every sensor nodes are of homogeneous in nature & consist of a similar form of communication range. Nodes perform the 1-hop communication with the neighboring node which is capable to interchange data. The network is the event which is triggered, that is, when the source node being sensed as an asset, it initiates the transfer the packets occasionally to sink hub. When a hub searches ability in its area which is monitored, its leftovers active asset till asset transfer in its area of monitoring. When advantage transferred to the newest site, it triggers other SN to become a novel form of the source code. When advantage is not searched, nodes further proceed to go after their schedule.

About Relaxing Edge

Let's take an edge $u \rightarrow v$ right here u is, v is tip vertex in that order. Relaxing edge relax denoted by (u,v) is to search the SP to arrive at v while allowing for edge $u \rightarrow v$

Notations that make use for specified as:

u = start vertex

v = end vertex

$u \rightarrow v$ = directed edge from the vertex u to v

$w(u, v)$ = weight of directed edge $u \rightarrow v$

$v.d$ = distance from the source vertex 0 to the vertex v

$u.d$ = distance from source vertex 0 to the vertex u $w(u, v)$ = edge weight $u \rightarrow v$

$v.pi$ = predecessor of the vertex v

So, if exist an improved path to achieve vertex v in that case, this improves distance as well as vertex v predecessor (Fig. 3).

Proposed Algorithm:

Step 1: Start

Step 2: Network Formation

Step 3: Sensor Deployment with Base Station

Step 4: K-Medoids used for cluster formation

Step 5: Elect Cluster Head of each cluster

Step 6: Data transmission performed

Step 7: Path established between source to Base Station

Step 8: Bellman-Ford Algorithm used to find the shortest path

Step 9: BELLMAN-FORD (G, w, s)

1. INITIALIZE-SINGLE-SOURCE (G, s)

2. for $i = 1$ to $|G.V|-1$

3. for every one edge $(u, v) \in G$

4. RELAX (u, v, w)

5. for all edge $(u, v) \in G.E$

6. if $v.d > u.d + w(u, v)$

7. return FALSE

8. return TRUE

Step 10: INITIALIZE-SINGLE-SOURCE (G, s)

1. for each vertex $v \in G.V$

2. $v.d = \infty$ //Initialize the distance to all vertices to infinity

3. $v.pi = NIL$

4. $s.d = 0$ //The distance from the source to itself is, of course, zero

Step 11: RELAX (u, v, w)

1. if $v.d > u.d + w(u, v)$

2. $v.d = u.d + w(u, v)$

Step 12: $v.pi = u$

Step 13: Exit

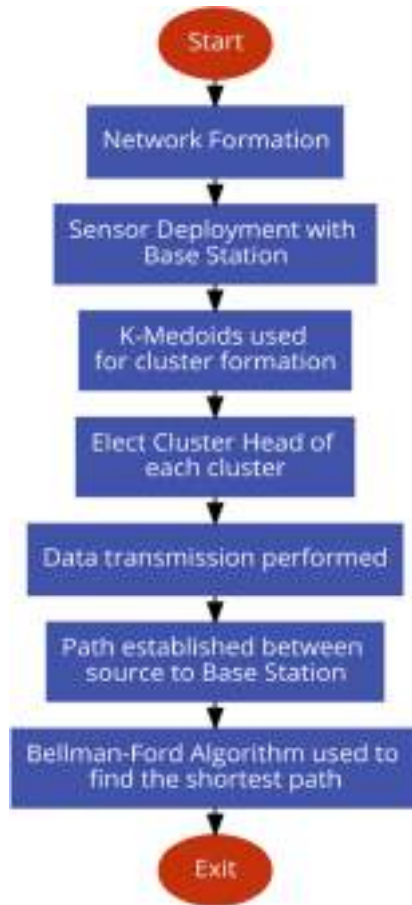


Fig. 3. Block diagram of proposed methodology

5 Simulation and Results

The simulation of the proposed work has been performed on MATLABR2018a tool. It consists of 50 nodes in the network and area is $100 \times 100 \text{ m}^2$. The table below shows the parameters used in the execution of the work (Table 1).

Table 1. Simulation parameters

Parameters	Value
Area	100 × 100 m ²
Number of nodes	50
Coordinates of BS	(50,180)
The initial energy of the node	2 J
Packet size	2000 bits
Energy for data aggregation	5 nJ/bits/signal
Energy consumption on the circuit	50 nJ/bits

In this the coordinates of Base Station is located in the middle of the scenario but it can be anywhere according to the requirement. These parameters are allocated with respect to the shortest path algorithm and used clustering technique.

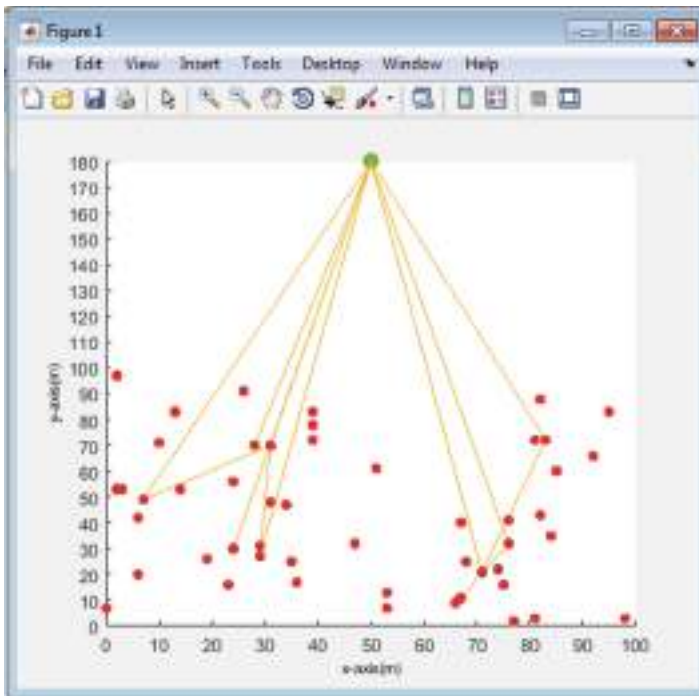


Fig. 4. Data transmission using enhanced Bellmen-Ford Algorithm

Figure 4 shows the proposed structure of the BFA scenario. The structure is formed using Bellmen-Ford Algorithm which reduces the path between source node and sink node for reducing the energy consumption and increases the network lifetime (Table 2).

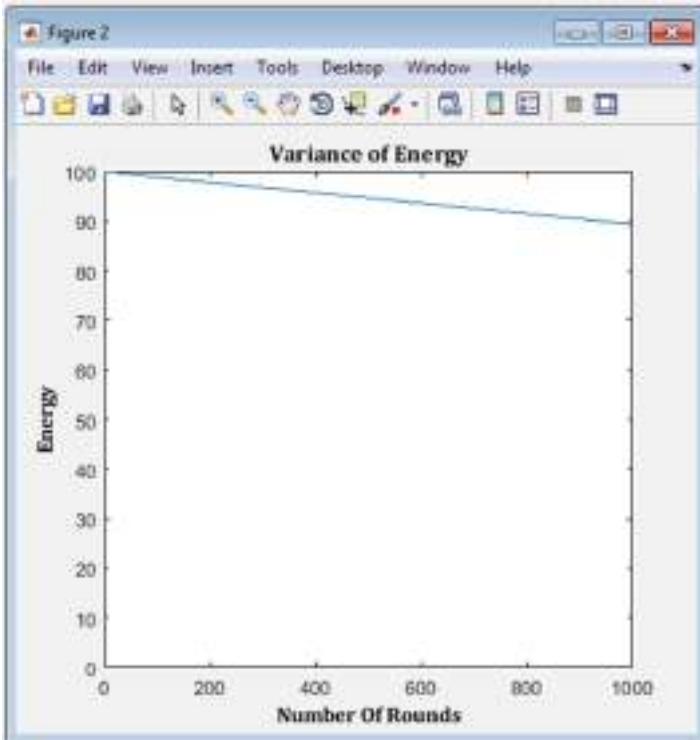


Fig. 5. The variance of energy level rounds

Figure 5 shows the variance of energy consumed by sensor nodes as number of round increases.

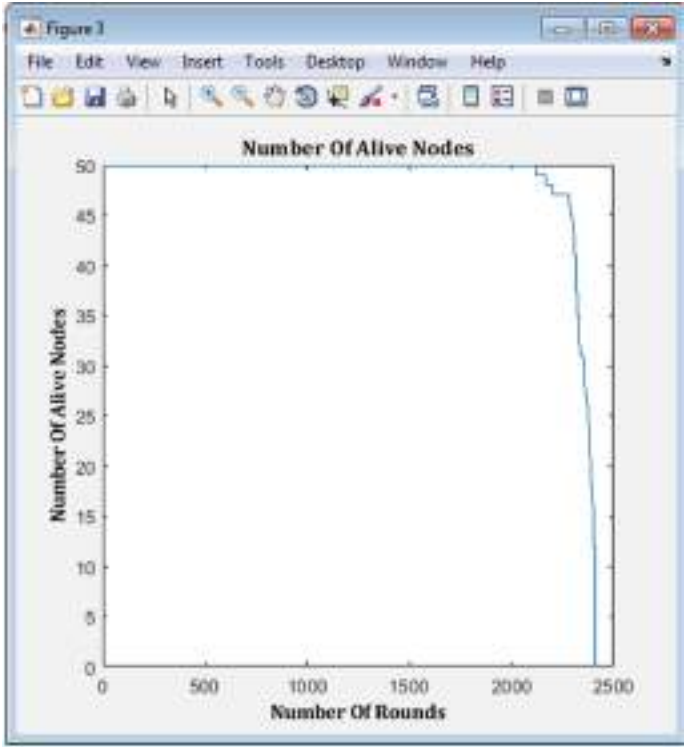


Fig. 6. Number of alive nodes over no. of rounds

Figure 6 shows the decline of alive nodes as number of rounds increases whose difference between first node dead and last node dead determines the network lifetime.

Table 2. Parameters with K-Medoid and Enhanced Bellmen-Ford Algorithm

Parameters	K- Medoid	Enhanced BFA
Energy left	63.973945 J	89.315893 J
First node dead	1201 round	2074 round
Last node dead	1642 round	2402 round

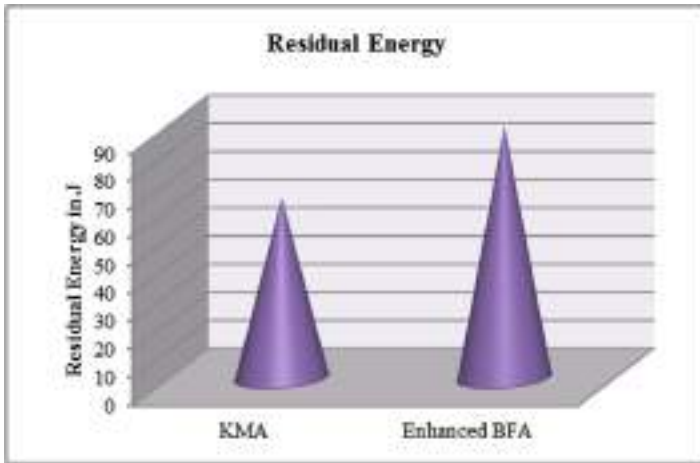


Fig. 7. Residual energy graph

Figure 7 depict the comparison of energy consumption performance of K-Medoid Algorithm versus Enhanced Bellman Ford Algorithm.

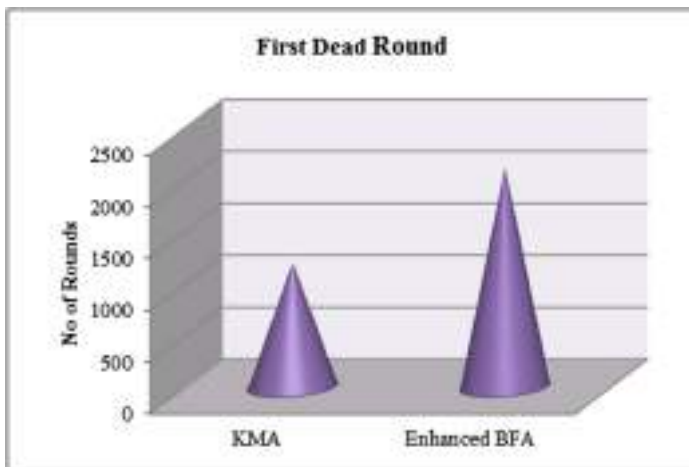


Fig. 8. First dead round graph

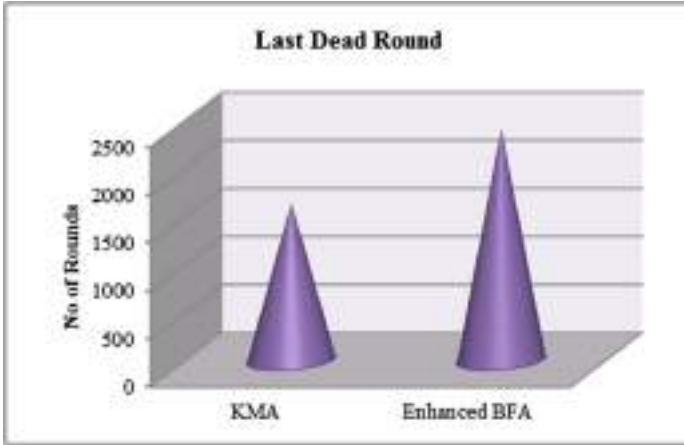


Fig. 9. Last dead round graph

Figures 8 and 9, Depict the first node dead and last dead node of both K-Medoid Algorithm and Enhanced Bellman Ford Algorithm whose difference calculates the lifetime of the network which clearly shows the Enhanced Bellman Ford Algorithm is better than the K-Medoid Algorithm.

6 Results and Discussion

In the proposed work, energy left after 1000 rounds is 89.3158 joules. In this, the actual amount of energy used in the transmission purpose is approximately 10 joules which are comparatively less. A number of round increases, the lifetime of the sensor node increases. Therefore, battery life is long-lasting. In this work, all the sensor nodes are in active mode.

7 Conclusion




Generally, KMA is much more efficient for the huge WSN and performs better than the LEACH and K-means algorithm in clustering formation. In order to maximize the lifetime of WSNs, this paper designs a path planning and it is solved by Enhanced Bellmen-Ford Algorithm. Our method chooses the Shortest Path from optional paths to balance the left out the energy of every node, also can prevent the emergence of dead nodes to extend network lifetime. Simulation output illustrates that the proposed method extends NW lifetime in comparison with the traditional shortest path strategy, and get better NW reliability. The proposed network improved in terms of energy, first dead node, last dead node, and network reliability.

References

1. Koriem, S.M., Bayoumi, M.A. Detecting and measuring holes in wireless sensor network. J. King Saud Univ. Comput. Inf. Sci. (2018), <https://doi.org/10.1016/j.jksuci.2018.08.001>
2. Umale, M., Markande, S.D.: Energy-efficient routing algorithm on the target tracking in wireless sensor network. In: 2015 International Conference on Information Processing (ICIP) (2015). <https://doi.org/10.1109/infop.2015.7489373>
3. Li, P., Xu, S., Sun, K., Qiu, X., Qi, F.: A path planning method of wireless sensor networks based on service priority. In: 2017 13th International Conference on Network and Service Management (CNSM) (2017). <https://doi.org/10.23919/cnsm.2017.8255984>
4. Nanda, A., Rath, A.K.: Cost-effective ModLeach-A* search algorithm for shortest path routing in Wireless Sensor Networks. In: 2016 Sixth International Symposium on Embedded Computing and System Design (ISED) (2016). <https://doi.org/10.1109/ised.2016.7977072>
5. Khediri, S.E., Thaljaoui, A., Dallali, A., Kachouri, A.: Clustering Algorithm in wireless sensor networks based on the shortest path. In: 2018 30th International Conference on Microelectronics (ICM) (2018). <https://doi.org/10.1109/icm.2018.8704059>
6. Li, Y., Wang, J., Zheng, G., Shi, X., Lu, D.: Compressive data gathering in wireless sensor networks based on random path. In: 2018 International Conference on Virtual Reality and Intelligent Systems (ICVRIS) (2018). <https://doi.org/10.1109/icvr.2018.00131>
7. Wang, N., Li, J.: Shortest path routing with risk control for compromised wireless sensor networks. IEEE Access **1**, 19303–19311 (2019). <https://doi.org/10.1109/access.2019.2897339>
8. El Khedira, S., Thaljaoui, A., Dallali, A., Harakti, S., Kachouri, A.: A novel connectivity algorithm based on shortest path for wireless sensor networks. In: 2018 1st International Conference on Computer Applications & Information Security (ICCAIS) (2018). <https://doi.org/10.1109/cais.2018.8442032>
9. Wang, J., Wang, K., Niu, J., Liu, W.: A K-medoids based Clustering Algorithm for wireless sensor networks. In: International Workshop on Advanced Image Technology (IWAIT) (2018)



Wavelet Based Compression of Acne Face Images with Automatic Selection and Lossless Compression of Acne Affected Region

Garima Nain , Ashish Gupta , and Rekha Gupta 

Department of Electronics Engineering, MITS, Gwalior,
Madhya Pradesh, India
garimanain96@gmail.com, agashishietk@gmail.com,
rekha652003@yahoo.com

Abstract. Medical image compression is inevitable part of medical research centers and hospitals. In this paper, compression of acne face images is considered by exploiting the fact that such images normally have some region of interest (ROI) space that contains acne and other space (without acne) as non region of interest. For proper diagnosis and treatment of acne, compression should be performed in such a way that no information loss results for the acne affected region. This paper proposes a new algorithm, in which the acne affected region is automatically selected using K-means clustering and then compressed minimally whereas relatively higher compression is applied on the non region of interest using wavelet transform in RGB colour space. Using this algorithm good Compression Ratio (CR) upto 8-14 is achieved without degradation in image quality of the acne affected region.

Keywords: Medical image processing · Acne face images · Discrete wavelet transform (DWT) · Region of interest · K-means clustering

1 Introduction

The medical images gathered while examining patient, their personal information and diagnostic reports contains huge amount of data. Acne vulgaris or lesions [1] are commonly known as white head, black head, scars, pimples and cysts. Acne vulgaris is a common chronic inflammatory disease which strikes the majority of individuals at certain time in their lives, generally during adolescence [2]. Some of the very popular compression standards available in literature as Joint Photographic Experts Group (JPEG) [3] and JPEG –LS build on Discrete Cosine Transform (DCT) [4] and JPEG2000 [5] based on discrete wavelet transform (DWT) [6] but they consider an evenly compression for all kind of images. Medical images cannot attain superior compression ratios because image quality needs to be maintained which leads to only lossless compression attaining compression ratio (CR) only upto 2–3 [7]. Literature also shows that different compression techniques based on masking, segmentation and clustering have been given for variety medical images such as MRI, CT scan [8], etc. Various methods have been given to segment and classify acne images [9, 10]. So

given concept of image segmentation is applied in compression technique to achieve higher compression. Here an irregular compression method is adopted, that segments the image into various clusters and the cluster with acne lesion or scar is selected, known as ROI. Less compression is applied on ROI and higher compression is applied on non ROI segments. In order to attain segments, K-means clustering is used which helps to segment acne cluster and other background clusters [11, 12]. Clustering is done in CIELAB or $L^*a^*b^*$ colour space where a^* and b^* spaces have colour information and L^* have brightness information [13]. Chromaticity-layer ' a^* ' represents colour falls along the red-green axis, green is in the negative direction and red is in the positive direction similarly ' b^* ' is along the blue-yellow axis, with blue in negative direction and yellow in the positive direction. Three level of DWT iterations [14] are applied to the background image and one level of DWT iteration to the ROI, followed by the arithmetic coding [15]. The cluster has been selected by cluster centre and mean values. The cluster selection has been validated for huge set of images and it was found adequate to be applied to them. Encouraging results achieved in terms of Mean Square Error (MSE), Peak Signal to Noise Ratio (PSNR) and CR in contrast to conventional lossy compression method.

2 Wavelet Based Compression and K-means Clustering

This section gives brief description of image compression using wavelet transform and K-means clustering.

2.1 Wavelet Based Compression

Image decomposition takes place using wavelets as each wavelet has a pair of low and high pass filters and image is decomposed into four sub images [15, 16]. Out of these sub images approximation matrix contains the necessary information which is low pass filtered component. The Fig. 1 shows image decomposition at second iteration level with much reduced image size significantly. The LH, HL and HH components contains high frequency information which is ignored at the image retrieval which leads to lossy compression. In order to apply this lossy compression on acnes, different iteration levels are applied on the ROI and non ROI clusters.



Fig. 1. Two level image decomposition using 2-D wavelet transform.

2.2 K-means Clustering

K-means clustering is a segmentation method (for images and data) into k mutually exclusive clusters [17]. The squared Euclidean metric is used to determine minimum distances. It assigns an index value to each cluster observation. It partitions a given object such that data in each cluster is as close as possible to each other, and also objects in other clusters are as far as possible. K-means uses an iterative technique that minimizes the sum of distances from each object to its cluster centroid, over all clusters [18]. The result of K-means clustering is that obtained a set of clusters that are as compact and as well-separated as achievable.

Figure 2 shows the division of a colour image in 3 clusters. Here black, grey and white colour indicates the areas falling in different clusters. Further these can be seen clearly as Cluster 1, Cluster 2 and Cluster 3.

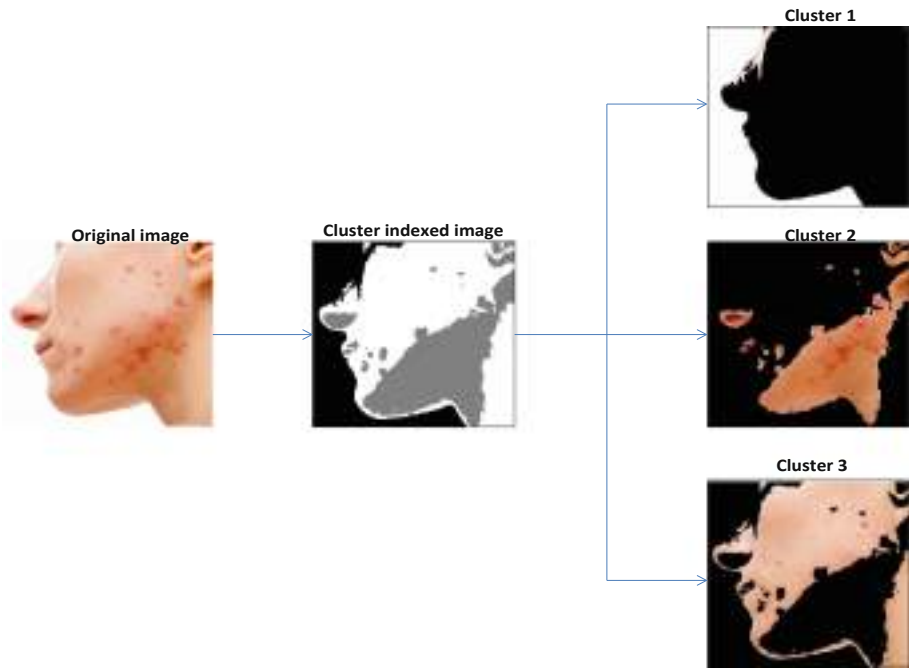


Fig. 2. Image segmentation into three clusters and pixels included by each cluster.

Let the set of data points be $X = \{x_1, x_2, x_3, \dots, x_n\}$ and set of centers as $V = \{v_1, v_2, v_3, \dots, v_c\}$ then the aim of K-means clustering is to minimize squared error which is also known as objective function, given by below equation

$$J(V) = \sum_{i=1}^c \sum_{j=1}^{c_i} \|x_i - v_j\|^2 \tag{1}$$

Where,

$\|x_i - v_j\|$ is the Euclidian distance between x_i and v_j .

c'_i is the number of data points in the i th cluster.

c' is the number of cluster centres.

3 Acne Cluster Identification

K-means clustering is used for the image segmentation into clusters [19, 20]. But the main concern is in finding the one cluster that contains acne (scars), since every time clustering is done it produces different index for the same clusters. To determine the acne cluster following steps are taken:

- (i) Convert a *RGB* acne image to $L^*a^*b^*$ colour space.
- (ii) Apply k-means clustering to divide image into N clusters.
- (iii) Find the cluster centroid or centre values for N clusters, which contains the mean values ' a^* ' and ' b^* ' of the image cluster.
- (iv) Now find the maximum value of the cluster centroid both for ' a^* ' and ' b^* '.
- (v) The above obtained cluster is the acne affected cluster.

The cluster obtained through above steps is the ROI or acne affected cluster. This method of acne selection has been validated by applying it on 20 set of images.

4 Proposed Methodology

This section describes the implementation of acne cluster identification, selection and DWT based compression using MATLAB. The various steps involved are described in the form of flow chart in the Fig. 3.

As shown in flow chart, first an image is read and converted into the CIELAB space or $L^*a^*b^*$ space from the RGB colour space. Further K-means clustering is done and image is segmented into 8 clusters. From these 8 clusters, the one called ROI is selected as described in Sect. 3. Hence from the set of cluster centroid values the one having maximum of both a^* and b^* is selected and the cluster is known as ROI or acne lesion cluster. Image compression is done in the RGB colour space.

Now the compression is attained by implementing one level of DWT iteration on ROI cluster and three level iterations on the overall image. At the receiving end the ROI cluster obtained after image retrieval is superimposed on overall retrieved image with their respective inverse DWT iterations at the time of image repositioning.

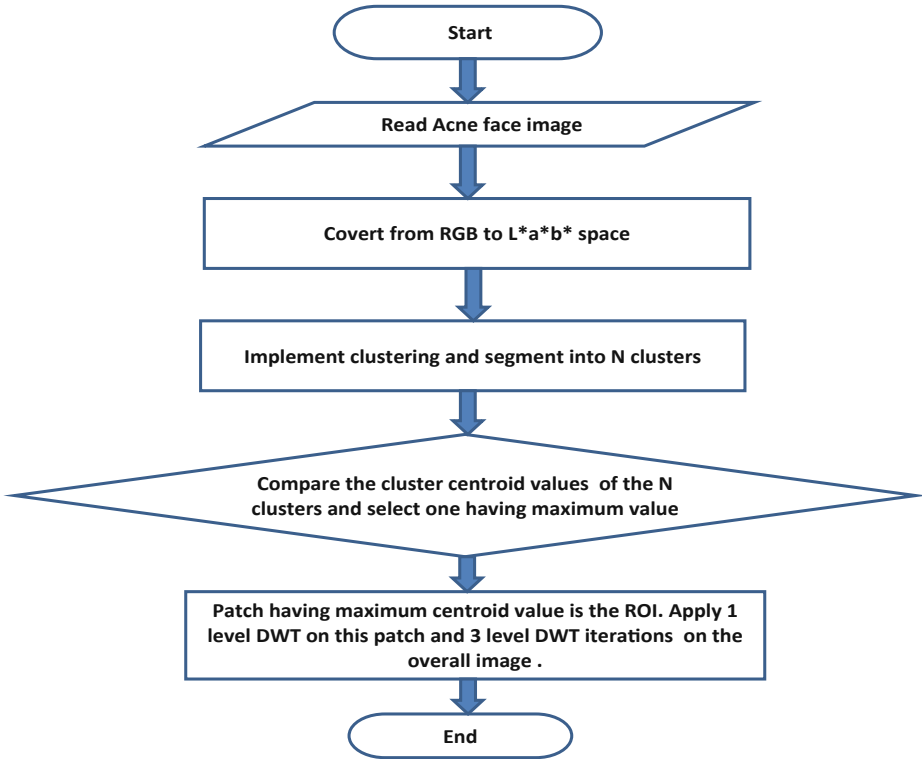


Fig. 3. Flow chart for the proposed methodology

5 Result and Discussion

In current section, the proposed methodology given in the previous section is shown on various images that are really different in terms of skin colour and intensity of acne. The analysis of the proposed method was done on a huge set of images and some of them are shown here to validate the effectiveness of the proposed method. The image quality examination is done using the quality parameters such as MSE and PSNR.

The main aim is to attain a compromise between the CR and quality parameter such that a higher compression can still retain the image quality that can be readily done using this method. Figure 4 gives the set of 3 acne images their 8 cluster and the ROI selected cluster. Following acne face images are taken from free public database [20]. Figure 4 clearly shows that the obtained ROI is an acne affected cluster. Figure 4(ii) shows the cluster index of the acne image in which each grey shade shows area belonging to a single cluster. Here 8 level clustering has been performed. If fewer clusters made then lesser compression is obtained and when more clusters made then area of ROI is less leading to higher compression with the compromise of some acne area.

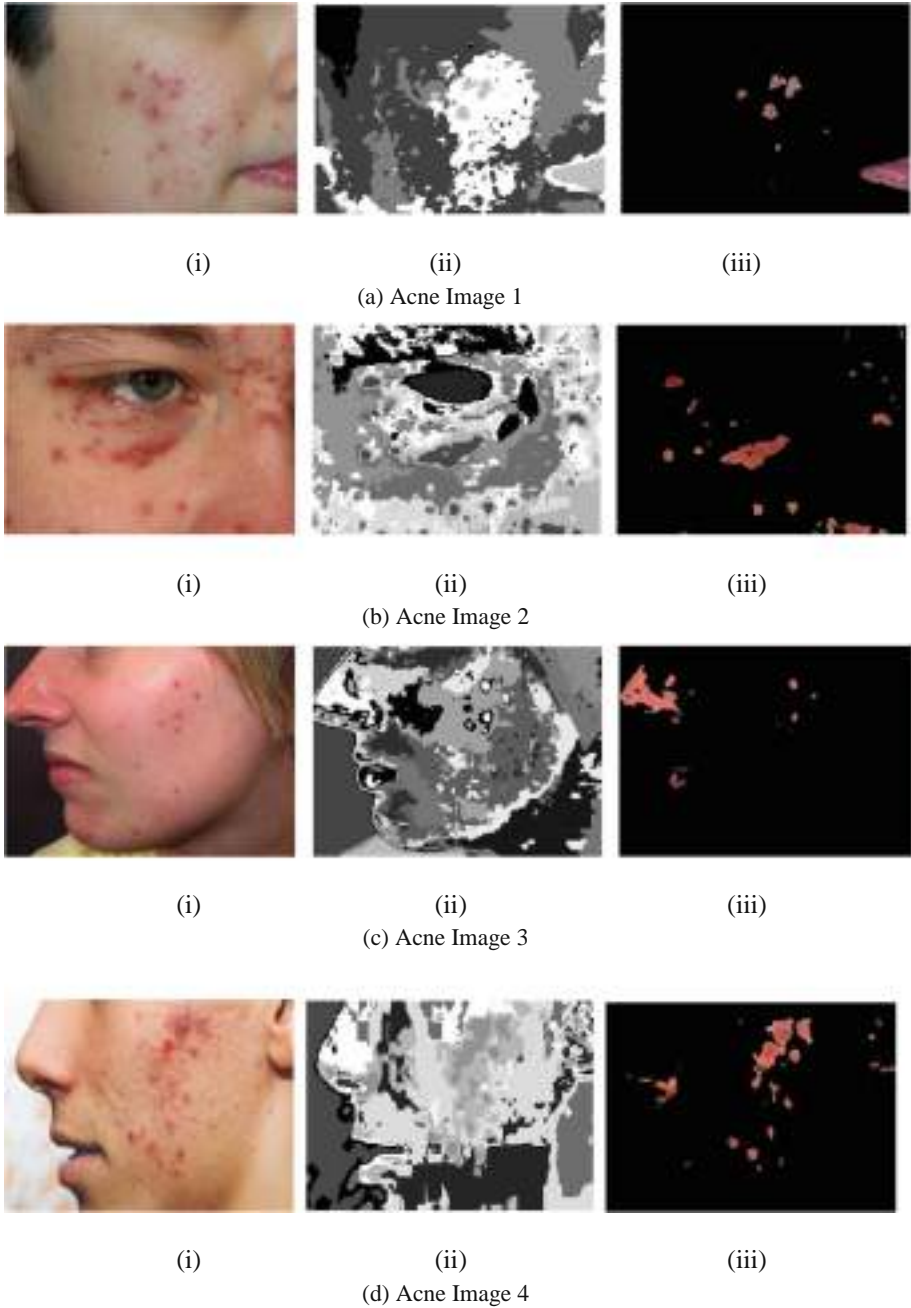


Fig. 4. (i) Various acne images (Source: free public database [20]) (ii) cluster index and (iii) acne cluster (ROI)



(i) Conventional Reconstructed (ii) Reconstructed ROI cluster (iii) overall reconstructed image.

Fig. 5. Acne image 1 reconstruction

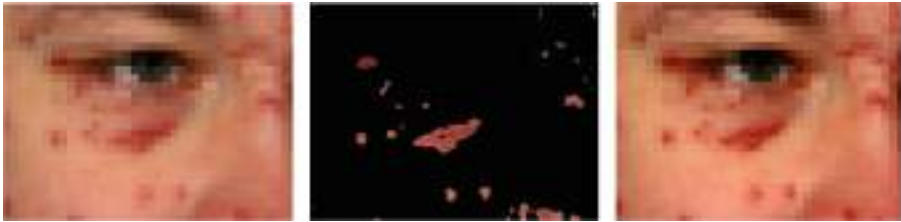
Figure 5 shows the acne image 1 in which the reconstructed images from the conventional method, acne (ROI) cluster and image obtained from proposed method are shown. Clearly this is a lossy compression but in comparison to the reconstructed images from the conventional method the acne is clearer in the reconstructed image from the proposed method.

Table 1. Image quality parameters for the proposed method and conventional method for the acne image 1.

Method	Parameter					
	PSNR (dB)		CR		MSE	
	Overall	Patch	Overall	Patch	Overall	Patch
Proposed	32.67	36.47	13.22	2.97	35.15	14.66
Conventional	34.81		6.63		21.46	

Table 1 tabulates the various image quality parameters obtained for acne image 1. The uncompressed image size is 195804 bytes which is reduced to almost 14805 bytes after compression giving nearly 13.22 CR. CR for the acne part is just 2.97 which is almost lossless giving all the necessary information about the acne. Clearly using the proposed method an increase of 1.66 dB in PSNR is achieved for the acne affected region whereas overall PSNR reduction doesn't cause any effect on the grade of quality of acne. Compression achieved is almost twice using this approach and MSE is significantly less for the acne cluster.

Similar analysis is done for the other set of images and similar results obtained in terms of increment in CR and PSNR. Below are given the reconstructed images obtained for acne image 2 in Fig. 6.



(i) Conventional Reconstructed (ii) Reconstructed ROI cluster (iii) overall reconstructed image.

Fig. 6. Acne image 2 reconstruction

Table 2. Image quality parameters for the proposed method and conventional method for the acne image 2.

Method	Parameter					
	PSNR (dB)		CR		MSE	
	Overall	Patch	Overall	Patch	Overall	Patch
Proposed	28.97	33.94	11.98	2.99	82.47	26.23
Conventional	31.10		6.35		50.41	

Above Table 2 tabulates the parameters obtained for acne image 2. PSNR obtained by conventional method is 31.10 dB but using our approach for acne part PSNR achieved is 33.94 dB. The overall CR obtained by the proposed method is 11.98, which is nearly double to the CR obtained by conventional method for the same image sizes as image 1.



(i) Conventional Reconstructed (ii) Reconstructed ROI cluster (iii) overall reconstructed image.

Fig. 7. Acne image 3 reconstruction

Figure 7 gives the reconstructed images for the acne image 3 for the ROI cluster or acne affected cluster and overall image. Here the acne region is clear in the Fig. 7(iii) than the Fig. 7(ii). Below is Table 3 listing the image quality parameters for acne image 3. Some of the other region is also selected because the features of the face (like lips, nose, etc.) also exist in the image which cannot be ignored if complete face image is considered.

Table 3. Image quality parameters for the proposed method and conventional method for the acne image 3.

Method	Parameter					
	PSNR (dB)		CR		MSE	
	Overall	Patch	Overall	Patch	Overall	Patch
Proposed	29.02	35.22	13.80	2.77	81.59	19.53
Conventional	32.48		5.64		36.66	

From Table 3, the PSNR obtained by conventional method is 32.48 dB but proposed method has 35.22 dB. The overall CR obtained by the proposed method is 13.80 for the same size as image 1, which are more than double to the CR 5.64 that is obtained by conventional method.



(i) Conventional Reconstructed (ii) Reconstructed ROI cluster (iii) overall reconstructed image.

Fig. 8. Acne image 4 reconstruction

Another image 4 given in Fig. 8 is validating the results and the quality parameters for this image are tabulated in the Table 4. It has a compression ratio of nearly 11.60 with PSNR of patch nearly 31.04 dB.

Table 4. Image quality parameters for the proposed method and conventional method for the acne image 4.

Method	Parameter					
	PSNR (dB)		CR		MSE	
	Overall	Patch	Overall	Patch	Overall	Patch
Proposed	25.94	31.04	11.60	2.63	165.37	51.07
Conventional	28.21		6.03		98.16	

Clearly the PSNR that can be obtained by conventional method is calculated for 2 level DWT iterations because further compression would lead to overall degradation of the image quality which is not in the acceptable range of PSNR and hence limits the

Table 5. Tabulated results for the dataset.

S. No.	CR	Patch PSNR (dB)	Percentage images
1.	10–11	Less than 31	3%
2.	11–12	31–32	9%
3.	12–13	32–33	12%
4.	13–14	33–35	79%
5.	14–15	More than 35	1%

DWT iterations only upto 2 levels. But through proposed approach even further compression would not cause any loss to the acne scars. Appreciable compression is obtained using the proposed method, as for acne image 1, increase in the compression achieved is nearly 100%. Clearly image clustering has helped a lot in terms of higher compression achievement (Table 5).

Nearly 79% of the images falls in the range of CR of 13–14 and 12% were giving in the range of 12–13. Also some were giving higher CR whereas some were giving less since the severity of acne varies from image to image. Also the PSNR of the patch in the given CR (12–14) is significantly higher than the image.

6 Conclusion

In this paper K-means clustering is applied for automatic selection of acne affected region. Then, selected area is compressed minimally by applying single wavelet iteration and rest of the image is compressed using three wavelet iterations. The compression ratio thus obtained is compared with conventional method where the complete image is uniformly compressed using two level wavelet iterations. It has been observed that proposed methodology comprising of automatic selection and compression outperforms the conventional method in terms of CR with almost 100% increase in its value leading to higher bandwidth economy. This paper has focused on the qualitative analysis of the acne scar (less compressed) which is sufficient for a doctor to generate essential analysis and diagnosis. From the proposed method future work can be carried out for acne image compression along with acne classification.



References

1. James Fulton, J.: Acne Vulgaris. *Expert Rev. Dermatol.*, 1–21 (2009)
2. Smithard, A., Glazebrook, C., Williams, H.C.: Acne prevalence, knowledge about acne and psychological morbidity in mid-adolescence: a community-based study. *Br. J. Dermatol.* **145**, 274–279 (2001)
3. Zeng, Y., Huang, F., Liao, H.M.: Compression and protection of JPEG images. In: 18th IEEE International Conference on Image Processing, Brussels, pp. 2733–2736 (2011)
4. Chen, Y.-Y.: Medical image compression using DCT-based sub band decomposition and modified SPIHT data organization. *Int. J. Med. Inf.* **76**, 717–725 (2007)

5. Sebastian, S., Manimekalai M.A.P.: Color image compression using JPEG2000 with adaptive color space transforms. In: International Conference on Electronics and Communication Systems (ICECS), pp. 1–5 (2014)
6. Nashat, A., Hassan, N.M.H.: Image compression based upon wavelet transform and a statistical threshold. In: International Conference on Optoelectronics and Image Processing (ICOIP), pp. 20–24 (2016)
7. Shen, L., Rangayyan, R.M.: A segmentation based lossless image coding method for high resolution medical image compression. *IEEE Trans. Med. Imaging* **16**(3), 301–307 (1997)
8. Taquet, J., Labit, C.: Hierarchical oriented predictions for resolution scalable lossless and near-lossless compression of CT and MRI biomedical images. *IEEE Trans. Image Process.* **21**(5), 2641–2652 (2012)
9. Sumithra, R., Suhil, M., Guru, D.S.: Segmentation and classification of skin lesions for disease diagnosis. *Procedia Comput. Sci.* **45**, 76–85 (2015)
10. Alamdari, N., Tavakolian, K., Alhashim, M., Fazel-Rezai, R.: Detection and classification of acne lesions in acne patients a mobile application. In: IEEE International Conference on Electro Information Technology (EIT), Grand Forks, ND, pp. 0739–0743 (2016)
11. Kamdi, S., Krishna, R.K.: Image segmentation and region growing algorithm. *Int. J. Comput. Technol. Electron. Eng. (IJCTEE)* **2**(1), 103–107 (2012)
12. Budhi, G.S., Adipranata, R., Gunawan, A.: Acne segmentation and classification using region growing and self-organizing map. In: International Conference on Soft Computing, Intelligent System and Information Technology (ICSIT), Denpasar, pp. 78–83 (2017)
13. Ohno, Y.: CIE fundamentals for color measurements. In: The IS&TNIP16 Conference, pp. 540–545 (2000)
14. Antonini, M., Barlaud, M., Mathieu, P., Daubechies, I.: Image coding using wavelet transform. *IEEE Trans. Image Process.* **1**, 205–220 (1992)
15. Koya, T., Chandran, S., Vijayalakshmi, K.: Analysis of application of arithmetic coding on DCT and DCT-DWT hybrid transforms of images for compression. In: The International Conference on Networks & Advances in Computational Technologies (NetACT), pp. 288–293 (2017)
16. Gonzalez, R.C., Wood, R.E.: *Digital Image Processing Using MATLAB*, 2nd edn, pp. 331–439. McGraw Hill Companies, Reading (2011)
17. Chen, C.W., Luo, J., Parker, K.J.: Image segmentation via adaptive K-mean clustering and knowledge-based morphological operations with biomedical applications. *IEEE Trans. Image Process.* **7**(12), 1673–1683 (1998)
18. Ramli, R., Malik, A.S., Hani, A.F.M., Jamil, A.: Acne analysis, grading and computational assessment methods: an overview. *Skin Res. Technol.* **18**, 1–14 (2012)
19. Roy, K., Chaudhuri, S.S., Ghosh, S., Dutta, S.K., Chakraborty, P., Sarkar, R.: Skin disease detection based on different segmentation techniques. In: International Conference on Opto-Electronics and Applied Optics (Optronix), Kolkata, India, pp. 1–5 (2019)
20. DermNet NZ: The Dermatology Resource. Dermatological Society New Zealand



Absolute Ionization Cross Sections of Hydrogen Chloride Gaseous Molecule by Electron Impact

Ravinder Sharma^{1,2}  and Satya Prakash Sharma² 

¹ Department of Biomedical Engineering, DCRUST, Murthal, Sonapat, Haryana, India
ravindersharma591@gmail.com

² Department of Chemistry, Baba Mast Nath University, Asthal Bohar, Rohtak, Haryana, India

Abstract. Due to abundant applications of ionization cross sections of gaseous atoms and molecules in various fields of applied sciences, like plasma processes, vacuum technology, fusion reactors, atmospheric sciences, etc. it's desirable to calculate absolute ionization cross-sections of various atoms and molecules. In this literature, we have calculated the partial and absolute total ionization cross sections of HCl gas by electron impact ionization from threshold energy to 10,000 eV. To the best of our knowledge, there are no available data for partial ionization cross sections to compare the results. We compare our results of absolute total ionization cross sections with suitable available data and its find in good agreements from threshold to high incident electron energies.

Keywords: Absolute ionization cross-section · Electron impact ionization · Single and double differential cross-sections

1 Introduction

Electron impact ionization of halogen hydrides plays an important role in low-temperature plasma processes. The ionization cross-section of HCl is applicable in the field of mass spectrometry, plasma etching, fusion reactors, gas discharges, astrophysics, radiation chemistry, etc. [1]. Hydrogen chloride gas has many industrial applications. It is used in the manufacture of rubber, pharmaceuticals, chemicals, in gasoline refining, tanning leather, and metals processing. So, it is necessary to calculate the ionization cross-sections which can be used for the above-said applications.

There is no theoretical and/or experimental data available for partial ionization cross sections except Harper et al. have given experimental results from 30 eV–200 eV only [2]. Jain et al. determine the total ionization cross-section for HCl from 20 eV–5000 eV using the Complex Optical Potential method [3]. Bobeldijk et al. give the ionization cross-sections of polyatomic molecules from 15 eV to 150 eV using a semi-empirical approach [4]. Deutsch derived the theoretical results for HCl from threshold to 200 eV incident electron energy using Modified Additivity Rule [5]. Further Ali et al. give the cross-sections from threshold to 1000 eV by use of Binary Encounter Bethe and Effective Core Potentials methods [6]. After that Vinodkumar et al. give the

ionization cross-section for HCl by combining the Spherical Complex Optical Potential and Complex Optical Potential-ionization contribution formalisms from threshold to 2000 eV [1]. So, there are various theoretical formalisms to determine the partial and total ionization cross sections [7]. For better accuracy and less mechanical computation, we use a modified semi-empirical approach of Jain and Khare [8–17] to determine absolute ionization cross-sections of Hydrogen chloride.

2 Theoretical Methodology

The partial and total ionization cross-section is determined via a modified semi-empirical approach of Jain and Khare [9]. We have developed the MATLAB programming codes for the calculation of ionization cross-sections. This gives the ionization cross-section to the production of an i th type of ion in the ionization of an atom by an incident electron of energy E solving the following equation [9].

$$Q_i(E) = \frac{4\pi a_0^2 R}{E} \left[\frac{E}{E-I_i} \left(M_i^2 - \frac{R}{E} S_i \right) \ln \left[1 + C_i (E - I_i) \right] + \frac{R(E-I_i)}{E} S_i \right] \times \int_0^{(E-I_i)/2} \frac{1}{\varepsilon^3 + \varepsilon_0^3} \left(\varepsilon - \frac{\varepsilon^2}{(E-\varepsilon)} + \frac{\varepsilon^3}{(E-\varepsilon)^2} \right) d\varepsilon \quad (1)$$

Where, W , I_i , a_0 , ε_0 , C_i , S_i , R are energy loss suffered by the incident electron, ionization potential, Bohr radius, mixing parameter, collision parameter, a number of ionizable electrons and Rydberg energy respectively and oscillator strength df_i/dw is the key parameter. We have used the experimental values of absolute dipole oscillator strengths for dissociative ionization of HCl derived by Daviel using (e, e⁺ ion) spectroscopy [18]. Here, data of oscillator strengths are available up to 40 eV of photon energy. Thus, for higher energies, the TRK sum rule has to be used to extrapolate the same data, within 5%–10% error bars [19]. The dissociative ionization potential for Hydrogen chloride is 13 eV, 17 eV and 18 eV for HCl⁺, Cl⁺, H⁺ respectively [18]. The value of the collision parameter and mixing parameter are ($C_i = 0.02124$) and ($\varepsilon_0 = 80$) respectively.

In this literature, we have calculated the partial and absolute total ionization cross sections over the secondary electron energy varying from 0 to $(E-I)/2$ by integrating the Eqs. (2) and derived the Eq. (1) and details are given in the literature [9, 10, 14, 17]. However, Pal [10] used the secondary electron energy varying from 0 to $(E-I)$ for partial differential cross-sections. In partial ionization cross-sections, if we vary secondary electron energy from 0 to $(E-I)$, then results at low incident energy are more as compared to experimental and all other theoretical data. The summation of partial ionization cross sections (PICS) over the system gives the total ionization cross sections (TICS) given by Eq. (3).

$$Q_{i(E,W)} = \frac{4\pi a_0^2 R}{E} \left[\left(1 - \frac{\varepsilon}{E-I_i} \right) \left(\frac{R}{W} \right) \times \frac{df_i(w,0)}{dw} \ln \left[1 + C_i (E - I_i) \right] + \frac{R}{E} S_i \times \frac{(E-I_i)}{\varepsilon^3 + \varepsilon_0^3} \left(\varepsilon - \frac{\varepsilon^2}{(E-\varepsilon)} + \frac{\varepsilon^3}{(E-\varepsilon)^2} \right) \right] \quad (2)$$

$$Q'_i(E) = \sum_i Q_i(E) \quad (3)$$

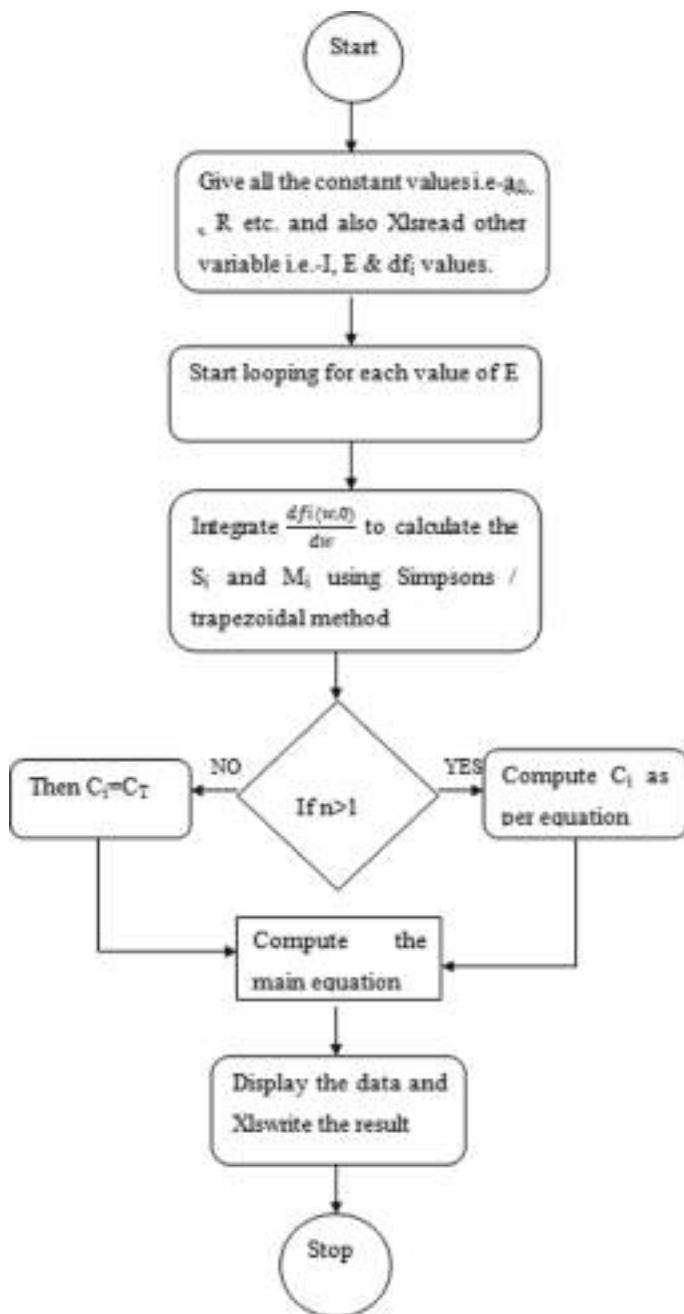


Fig. 1. Algorithm flow chart.

3 Results and Discussion

In this literature, we have calculated the partial and absolute total ionization cross sections of Hydrogen chloride using Eqs. (1), (2), and (3) with the help of MATLAB programming codes and the algorithm flow chart is given in Fig. 1.

The calculated partial and total ionization cross sections from threshold to 10 keV of incident electron energies are tabulated in Table 1.

Table 1. Present result for ionization cross-section of Hydrogen Chloride (10^{-18} cm^2)

Energy (eV)	HCl ⁺	Cl ⁺	H ⁺	Total
18	12.926	14.569	–	27.496
20	20.437	16.509	1.322	38.268
25	148.866	19.424	1.504	169.794
30	227.746	31.109	7.054	265.910
35	277.813	50.760	15.033	343.606
40	310.680	59.224	18.417	388.321
45	332.610	62.744	19.857	415.211
50	347.278	63.832	20.359	431.469
55	356.966	63.650	20.374	440.989
60	363.151	62.784	20.127	446.063
65	366.825	61.554	19.740	448.119
70	368.670	60.337	19.366	448.373
75	369.185	59.111	18.942	447.239
80	368.686	57.767	18.476	444.928
85	367.424	56.376	17.993	441.793
90	365.592	55.030	17.523	438.145
95	363.334	53.639	17.043	434.016
100	360.758	52.328	16.587	429.673
110	354.961	49.778	15.710	420.449
120	348.660	47.416	14.902	410.979
130	342.128	45.245	14.164	401.537
140	335.529	43.254	13.491	392.275
150	328.964	41.429	12.878	383.270
160	322.497	39.752	12.317	374.565
170	316.163	38.208	11.803	366.174
180	309.988	36.783	11.331	358.102
190	303.983	35.465	10.896	350.344
200	298.154	34.247	10.495	342.896
210	292.506	33.113	10.123	335.742
220	287.038	32.055	9.778	328.870
230	281.748	31.065	9.456	322.269
240	276.635	30.134	9.154	315.924

(continued)

Table 1. (continued)

Energy (eV)	HCl ⁺	Cl ⁺	H ⁺	Total
250	271.692	29.263	8.873	309.828
260	266.914	28.444	8.609	303.967
270	262.297	27.671	8.361	298.329
280	257.836	26.942	8.127	292.904
290	253.525	26.250	7.906	287.680
300	249.356	25.596	7.698	282.649
310	245.326	24.976	7.500	277.802
320	241.428	24.386	7.313	273.128
330	237.657	23.826	7.136	268.619
340	234.009	23.291	6.967	264.267
350	230.476	22.782	6.806	260.064
360	227.055	22.295	6.653	256.004
370	223.740	21.831	6.507	252.078
380	220.528	21.386	6.368	248.282
390	217.414	20.960	6.234	244.608
400	214.393	20.552	6.107	241.051
410	211.462	20.160	5.985	237.607
420	208.617	19.784	5.867	234.268
430	205.854	19.422	5.755	231.031
440	203.171	19.074	5.647	227.892
450	200.563	18.739	5.543	224.845
460	198.027	18.417	5.443	221.887
470	195.561	18.106	5.347	219.013
480	193.161	17.806	5.254	216.221
490	190.826	17.516	5.164	213.506
500	188.553	17.236	5.078	210.867
520	184.181	16.704	4.914	205.800
540	180.028	16.206	4.761	200.995
560	176.078	15.739	4.618	196.434
580	172.316	15.299	4.483	192.098
600	168.729	14.884	4.356	187.969
620	165.304	14.493	4.237	184.034
640	162.031	14.123	4.124	180.278
660	158.900	13.773	4.018	176.690
680	155.900	13.440	3.917	173.257
700	153.025	13.124	3.821	169.970
720	150.266	12.824	3.730	166.820
740	147.616	12.538	3.643	163.797
760	145.068	12.265	3.561	160.894
780	142.617	12.004	3.482	158.104

(continued)

Table 1. (continued)

Energy (eV)	HCl ⁺	Cl ⁺	H ⁺	Total
800	140.256	11.755	3.407	155.418
850	134.721	11.178	3.234	149.133
900	129.652	10.658	3.078	143.388
950	124.992	10.187	2.937	138.116
1000	120.691	9.758	2.809	133.258
1050	116.708	9.366	2.692	128.766
1100	113.008	9.005	2.585	124.598
1150	109.560	8.673	2.486	120.720
1200	106.340	8.366	2.395	117.102
1250	103.323	8.082	2.311	113.716
1300	100.491	7.817	2.233	110.540
1350	97.827	7.569	2.160	107.556
1400	95.316	7.338	2.092	104.746
1450	92.944	7.122	2.028	102.093
1500	90.700	6.918	1.968	99.586
1550	88.573	6.726	1.912	97.211
1600	86.554	6.546	1.859	94.958
1650	84.634	6.375	1.809	92.818
1700	82.807	6.213	1.762	90.783
1750	81.066	6.060	1.717	88.843
1800	79.404	5.915	1.675	86.994
1850	77.816	5.777	1.634	85.227
1900	76.296	5.645	1.596	83.538
1950	74.841	5.520	1.560	81.921
2000	73.447	5.401	1.525	80.372
2100	70.823	5.177	1.460	77.460
2200	68.398	4.973	1.401	74.772
2300	66.150	4.784	1.346	72.281
2400	64.060	4.610	1.296	69.966
2500	62.110	4.449	1.249	67.809
2600	60.287	4.300	1.206	65.793
2700	58.578	4.161	1.166	63.904
2800	56.972	4.030	1.129	62.131
2900	55.460	3.909	1.094	60.463
3000	54.035	3.794	1.061	58.890
3100	52.687	3.687	1.030	57.404
3200	51.412	3.586	1.001	55.999
3300	50.202	3.490	0.974	54.666
3400	49.054	3.400	0.948	53.402
3500	47.962	3.314	0.923	52.200

(continued)

Table 1. (continued)

Energy (eV)	HCl ⁺	Cl ⁺	H ⁺	Total
3600	46.922	3.233	0.900	51.055
3700	45.930	3.156	0.878	49.964
3800	44.983	3.083	0.857	48.923
3900	44.078	3.013	0.838	47.929
4000	43.212	2.947	0.819	46.977
4100	42.383	2.883	0.801	46.066
4200	41.587	2.823	0.783	45.193
4300	40.824	2.765	0.767	44.355
4400	40.091	2.709	0.751	43.551
4500	39.386	2.656	0.736	42.778
4600	38.708	2.605	0.721	42.034
4700	38.054	2.556	0.708	41.317
4800	37.425	2.508	0.694	40.627
4900	36.818	2.463	0.681	39.962
5000	36.231	2.419	0.669	39.320
5200	35.118	2.337	0.646	38.101
5400	34.078	2.260	0.624	36.961
5600	33.102	2.188	0.604	35.893
5800	32.185	2.121	0.585	34.891
6000	31.322	2.058	0.567	33.947
6200	30.508	1.999	0.550	33.057
6400	29.739	1.943	0.535	32.216
6600	29.011	1.891	0.520	31.421
6800	28.320	1.841	0.506	30.667
7000	27.664	1.794	0.493	29.951
7200	27.041	1.750	0.480	29.271
7400	26.447	1.707	0.468	28.623
7600	25.881	1.667	0.457	28.006
7800	25.341	1.629	0.446	27.417
8000	24.825	1.593	0.436	26.854
8200	24.331	1.558	0.427	26.315
8400	23.858	1.525	0.417	25.800
8600	23.404	1.493	0.408	25.305
8800	22.969	1.462	0.400	24.831
9000	22.551	1.433	0.392	24.376
9200	22.149	1.405	0.384	23.938
9400	21.763	1.379	0.377	23.518
9600	21.390	1.353	0.369	23.112
9800	21.032	1.328	0.362	22.722
10000	20.686	1.304	0.356	22.346

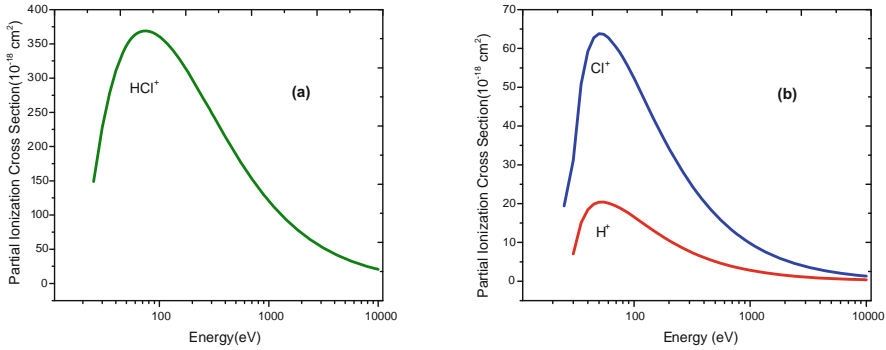


Fig. 2. Partial ionization cross section (a) HCl⁺, (b) H⁺ and Cl⁺.

The calculated partial ionization cross sections for HCl are presented graphically in Fig. 2. We have compared our results of the total ionization cross sections with other theoretical easily available data/results [1, 3, 5, 6] which are presented in Table 2 and shown in Fig. 3. The numerical data is collected from the literature [1, 3, 6] but the other results are derived from graphs within some error bars [5]. Our results are in good agreement with the result of Ashok Jain [3] from threshold to high energy but after peak values; our data slightly overestimates and also matches well with H. Deutsch [5] and BEB Sing and BEB Coun [6]. However, Vinodkumar [1] has little deviations from low to high energy. But all available data are theoretical calculations. To best our knowledge, there are no experimental data available from low to high incident electron energy to compare our results. So, we also compare our results with other theoretical data as discussed above.

Table 2. Compared data for ionization cross-section of Hydrogen Chloride (10⁻¹⁶ cm²)

Energy (eV)	Present result	Ashok Jain	Vinod kumar	BEB Coun	BEB Sing	Deutsch
18	0.275	–	0.960	1.273	1.273	1.531
20	0.383	0.655	1.370	1.624	1.624	1.805
25	1.698	1.365	2.270	2.510	2.510	2.460
30	2.659	2.076	2.880	3.090	3.090	2.991
40	3.883	3.091	3.510	3.794	3.794	3.640
50	4.315	3.656	3.720	4.089	4.089	3.773
60	4.461	3.944	3.760	4.178	4.178	3.823
70	4.484	4.126	3.750	4.162	4.162	3.797
80	4.449	4.261	3.690	4.092	4.092	3.726
90	4.381	4.246	3.620	3.994	3.994	3.616
100	4.297	4.145	3.510	3.884	3.884	3.575
150	3.833	3.498	3.040	3.328	3.328	3.205
200	3.429	2.998	2.640	2.879	2.879	2.796

(continued)

Table 2. (continued)

Energy (eV)	Present result	Ashok Jain	Vinod kumar	BEB Coun	BEB Sing	Deutsch
300	2.826	2.351	2.110	2.266	2.262	–
400	2.411	1.953	1.770	1.876	1.869	
500	2.109	1.682	1.510	1.607	1.597	
600	1.880	1.484	1.360	1.410	1.398	
700	1.700	1.333	1.230	1.259	1.246	
800	1.554	1.213	1.120	1.139	1.125	
900	1.434	1.123	1.030	1.042	1.027	
1000	1.333	1.032	0.960	0.960	0.946	
2000	0.804	0.610	0.570	–	–	
3000	0.589	0.439	–	–	–	
4000	0.470	0.344				
5000	0.393	0.285				
6000	0.339	–				
7000	0.300	–				
8000	0.269	–				
9000	0.244	–				
10000	0.223	–				

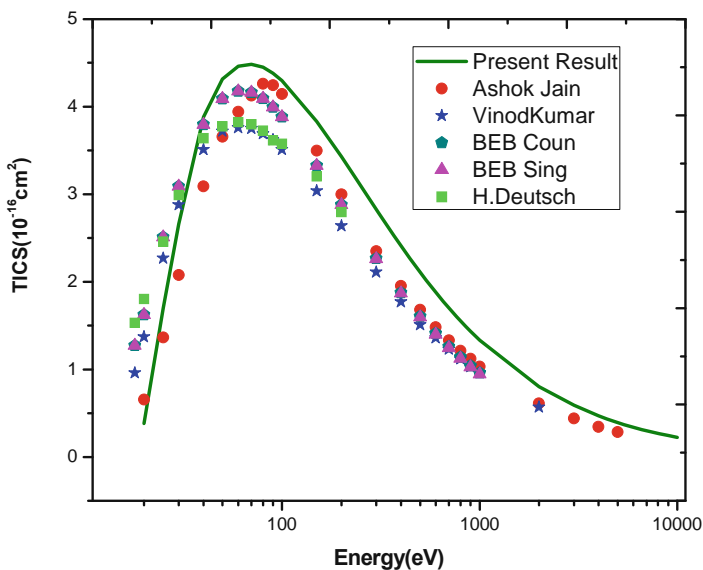


Fig. 3. Hydrogen chloride absolute total ionization cross-section in \AA^2 . Solid line, Present result; Circle, Ashok Jain et al. [3]; star, VinodKumar et al. [1]; Pentagon, BEB Coun [6]; Triangle, BEB Sing [6]; and Square, H. Deutsch MAR [5]

4 Conclusion

Electron impact ionization cross sections of Hydrogen chloride gaseous molecule have been calculated and the absolute ionization cross sections are compared with theoretical available data from threshold energy to high energies [1, 3, 5, 6]. It's clear our results give a satisfactory agreement with other theoretical data. Thus, from the compared data and graph, we can say that the results are very reliable in strength and shape and establish that the present method and developed programming can produce reliable cross sections even for complex molecules also and the data could be used in the plasma processes and other applications.

Acknowledgments. The authors are thankful to the unknown reviewers for their useful comments.

References

1. Vinodkumar, M., Dave, R., Bhutadia, H., Antony, B.K.: Electron impact total ionization cross sections for halogens and their hydrides. *Int. J. Mass Spectrom.* **292**(1–3), 7–13 (2010)
2. Harper, S., Calandra, P., Price, S.D.: Electron impact ionization of hydrogen chloride. *Chem. Phys.* **3**, 741–749 (2001)
3. Jain, A., Baluja, K.L.: Total (elastic plus inelastic) cross-sections for electron scattering from diatomic and polyatomic molecules at 10–5000 eV. *Phys. Rev. A* **45**, 202–218 (1991)
4. Bobeldijk, M., van der Zande, W.J., Kistemaker, P.G.: Simple models for the calculation of photoionization and electron impact ionization cross sections of polyatomic molecules. *Chem. Phys.* **179**(2), 125–130 (1994)
5. Deutsch, H., Becker, K., Märk, T.D.: A modified additivity rule for the calculation of electron impact ionization cross-section of molecules AB_n. *Int. J. Mass Spectrom. Ion Process.* **167–168**, 503–517 (1997)
6. Ali, M.A., Kim, Y.: Ionization cross sections by electron impact on halogen atoms, diatomic halogen, and hydrogen halide molecules. *J. Phys. B: Atomic Mol. Opt. Phys.* **41** (2008)
7. Sharma, R., Sharma, S.P., Kumari, N.: Electron impact ionization cross-section- semi-empirical approach. *J. Bull. Pure Appl. Sci.* **36**(2), 45–53 (2017)
8. Khare, S.P., Prakash, S., Meath, W.J.: Dissociative ionization of NH₃ and H₂O molecule by electron impact. *Int. J. Mass Spectrom. Ion Process.* **88**, 299–308 (1989)
9. Kumar, R.: Electron ionization cross sections of PF₃ molecule. *J. Appl. Math. Phys.* **3**(3), 1671–1678 (2015)
10. Pal, S., Kumar, J., Bhatt, P.: Electron impact ionization cross sections for the N₂ and O₂ molecule. *J. Electron Spectro. Relat. Phenom.* **129**(1), 35–41 (2003)
11. Khare, S.P., Meath, W.J.: Cross sections for the direct and dissociative ionization of NH₃, H₂O, and H₂S by electron impact. *J. Phys. B: Atomic Mol. Phys.* **20**(9), 2101–2116 (1987)
12. Sharma, R., Kumari, N.: Electron impact ionization cross-section of gallium atom. *J. Emerg. Technol. Innov. Res.* **6**(2), 339–344 (2019)
13. Kumar, R.: Double differential cross-sections of ethane molecule. In: *AIP Conference Proceedings*, vol. 1953, no. 1, p. 140039, 2018 May
14. Pal, S., Kumar, M., Singh, R., Kumar, N.: Evaluation of electron-impact ionization cross sections for molecules. *J. Phys. Chem. A* **123**(19), 4314–4321 (2019)

15. Sharma, R.: Absolute electron impact ionization cross sections of oxygen atom. *J. Emerg. Technol. Innov. Res.* **6**(6), 228–245 (2019)
16. Bhatt, P., Sharma, S.P., Sharma, R.: The partial ionization cross-section calculation of O₃ molecules. *Int. J. Adv. Innov. Res.* **6**(May), 66–71 (2019)
17. Kumar, R., Pal, S.: Evaluation of electron ionization cross-sections of methyl halides. *Rapid Commun. Mass Spectrom.* **27**(1), 223–237 (2013)
18. Daviel, S., Iida, Y., Carnovale, F., Brion, C.E.: Absolute oscillator strengths for the partial & photoionization, fragmentation, and photoabsorption of HCl. *J. Chem. Phys.* **83**, 319–406 (1983)
19. Zeiss, G.D., William, J.M., MacDonald, J.C.F., Dawson, D.J.: Dipole oscillator strength distributions, sums, and some related properties for Li, N, H₂, N₂, O₂, NH₃, H₂O, NO, and N₂O. *Can. J. Phys.* **55**(23), 2080–2100 (1977)



A Weight Function RSA Strategy Based on Path Length and Bandwidth Demand for Static Traffic in Elastic Optical Network

Deepak Batham¹  and Dharmendra Singh Yadav² 

¹ Department of Electronics Engineering, Madhav Institute of Technology and Science, Gwalior 474005, India
deepakbatham786@gmail.com

² Department of Electronics and Communication Engineering, Institute of Engineering and Science, IPS Academy, Indore 452012, India
dsyadav_davv@rediffmail.com

Abstract. Worldwide, the emerging grid computing, cloud computing, and Internet of Thing (IoT) applications are dominating the Internet traffic. Such applications require flexible bandwidth and high-speed connectivity. The elastic optical network (EON) is a promising solution to fulfill the present need of growing Internet traffic as a backbone optical network. In EON, the spectrum continuity and contiguity constrains limit the efficiency of spectrum allocation and its utilization, when performing routing and spectrum assignment (RSA). To diminish the effect of spectrum constraints two RSA strategies based on weight function namely lowest weight demand first with first fit (LWDF with FF) and lowest weight demand first with first last fit (LWDF with FLF) is proposed for static traffic. The proposed strategies accords priority to the connection requests having minimum value of weight function in order to utilize optimum network resources, minimum bandwidth blocking probability, and maximize the accepted connection requests. The simulation results show the proposed LWDF with FF and FLF outperforms as compare to the existing strategies.

Keywords: Weight function · Elastic optical network · Routing and spectrum assignment · Bandwidth blocking probability · Resource utilization ratio · Static traffic

1 Introduction

The overwhelming growth of IP traffic mainly comprises of multimedia, cloud computing, grid computing, and Internet of Thing (IoT) services which requires flexible bandwidth and high-speed connectivity [1]. The traditional fixed frequency grid wavelength division multiplexing (WDM) technology based backbone optical networks are infeasible to accommodate such traffic needs. The fixed frequency grid is 50 or 100 GHz channel spacing which supports up to 100 Gbps data rate [2]. Due to the rigid and coarse spectrum granularity, the traditional WDM optical network is inefficient to utilize the complete spectrum bandwidth. However, to fulfill the present need of recently crossed Zettabyte (ZB) threshold of IP traffic whose data rate is beyond 100

Gbps with flexible bandwidth, an elastic optical networks (EON) or flexible optical network (FON) now become a promising solution to replace the conventional fixed grid technology [3–5].

EON is worked on the principle of OFDM (orthogonal frequency division multiplexing) technology which allocates high-speed data stream to several orthogonal low-speed subcarriers. In literature, the smallest size of subcarrier is either 6.25 or 12.5 GHz, also referred as frequency slot (FS) [6]. This has been possible due to the innovations in the bandwidth variable - modulation technology, transponders, and wavelength cross-connects which is abbreviated as BVMT, BVTs, and BV-WXCs, respectively [4]. The BVT offers flexible granularity by using variable modulation format and bit rate configuration that allow the tuning of spectrum resources as per their bandwidth demands. The BV-WXC provides an end-to-end physical optical path connectivity between the source (s) and destination (d) nodes, which is referred as lightpath. For establishing a lightpath, RSA (routing and spectrum assignment) is essential and have been widely explored and reported in [5–12]. In EON, the selection of appropriate route and allocation of spectrum resources (or FSs) for the requested bandwidth to the connection request is known as RSA. The spectrum contiguity and continuity constraints must be followed while performing RSA. In spectrum contiguity, adjacent FSs on a network link must be free, while in spectrum continuity, all links of the selected route follow same FSs.

The RSA problem is NP hard [6] that can be solved individually as routing sub problem, and spectrum allocation (SA) sub problem, or solved as jointly [7]. The appropriate route selection and SA scheme is a key concern to achieve the efficient spectrum utilization. The routing may be of static or dynamic [13] in nature. In static routing, routes are pre-defined which is calculated offline at the time of network planning and designing phase. In dynamic routing, the route selection is online on the basis of current network state information. Fixed routing (FR), fixed alternate routing (FAR) [13], distance adaptive routing [8–10], and fragmentation-aware routing schemes [11, 12] have been proposed and thoroughly investigated for EONs. In FR, only one candidate route, while in FAR, a set of K -alternate routes are search between the s - d node pair. The route can be searched either by hop count or link cost method. After routing, SA is performed either by using first fit (FF), or last fit (LF), or first-last fit (FLF) spectrum allocation scheme [13, 14]. In all SA policies, the FSs are indexed first then a list of unused (free) and used FSs indexes is maintained. When a new lightpath is to be establish, the lowest indexed FSs from the list of unused FSs is assigned for the connection request in FF scheme, while, in LF the highest indexed FS from the list of unused FSs is assigned [13]. In FLF [14], the connection requests are divided into odd and even partition. For odd numbered request, always try to assign lowest indexed FS to the selected route and for even numbered request, always assign the highest indexed FS to the selected route.

The traffic in the network may be of dynamic or static in nature. In dynamic traffic, information related to s - d nodes pair, setup time, and teardown time of the connection requests is completely unknown. In static traffic, the s - d nodes and their setup and teardown time are fixed and known in prior, also referred as scheduled traffic [15–17]. When performing RSA, the spectrum continuity and contiguity constrains limit the efficiency of spectrum allocation and its utilization in EON. To minimize the effects of

these constraints, two weight function based RSA strategies namely lowest weight demand first with first fit (LWDF with FF) and lowest weight demand first with first last fit (LWDF with FLF) under static traffic is proposed for EON. The proposed strategies are then compared with the traditional first come first serve (FCFS) [18], shortest path demand first (SPDF) [19], and minimum bandwidth demand first (MinBwDF) [19] strategies. The performance evaluation of the existing and proposed strategies is on the metrics of accepted connection requests, bandwidth blocking probability (BBP), and resource utilization ratio (RUR). The rest of the paper is arranged in such a manner that the existing and proposed strategies are explained in Sect. 2. Section 3 deals with simulation results and discussion. Conclusion of the research work is reported in Sect. 4.

2 Existing and Proposed RSA Strategies

The existing and proposed strategies for EON under static traffic are presented in this section. The existing strategies are FCFS, SPDF and MinBwDF, and the proposed weight function based RSA strategies are LWDF with FF and LWDF with FLF. All are explained one by one.

2.1 First Come First Serve (FCFS)

In FCFS RSA strategy, the connection requests are served as per their arrived sequence. Earlier the connection requests arrive will serve first [18]. For routing, K-alternate shortest path algorithm, while for assigning spectrum resources FF spectrum allocation scheme is use for establishing the connection requests. A connection request can be established only, when it follows the spectrum contiguity and continuity constraints.

2.2 Shortest Path Demand First (SPDF)

In SPDF RSA strategy [19], first choose the shortest route from the K-alternate routes for each connection request. Next the complete set of connection requests is arranged in ascending order of their path length. This implies that the connection requests having smaller route will serve first. After that, assign spectrum resources one by one to the connection requests. The SPDF, accords priority to the shortest path requests first, this will reduce the spectrum continuity constraint problem and increase the availability of free spectrum resources for future connection requests. But, the spectrum contiguity problem remains constant.

2.3 Minimum Bandwidth Demand First (MinBwDF)

In MinBwDF RSA strategy [19], all incoming connection requests are prioritized as per increasing order of their bandwidth needs. The connection requests having lower value of bandwidth requested will be served first. The MinBwDF is unaware of route length. It may be possible that the connection requests require less bandwidth will traverses larger number of links. Thus, higher number of spectrum resources is used. MinBwDF

strategy reduces the spectrum contiguity problem, but spectrum continuity problem remain unchanged or may be increased.

2.4 Proposed Lowest Weight Demand First (LWDF) RSA Strategies

To minimize the spectrum assignment constrain issues and to use the spectrum resources efficiently in EON, we propose weight function based strategies for solving the RSA problem under static traffic scenario. The parameters used to formulate the weight function are path length and bandwidth demand of the connection requests. The bandwidth demand is also referred as requested bandwidth. The proposed strategies prioritize the connection requests as per the estimated weights, prior to actual provisioning of network resources. The shortest feasible route from the predefined K-alternate routes for all the connection requests is selected first then the weight of each connection request is estimated by using Eq. (1).

$$W_i = \frac{PL_i}{PL_{max}} + \frac{Bw_i}{Bw_{max}} \quad (1)$$

$$\bar{C} = \frac{\sum_{i=1}^N W_i}{N} \quad (2)$$

where,

- W_i : Weight of i^{th} connection request
- PL_i : Path length (number of links) of the selected candidate route used between the s - d node pair for i^{th} connection request in EON
- PL_{max} : Maximum path length of any connection request from the complete set of incoming connection requests in EON
- Bw_i : Requested bandwidth for i^{th} connection requests
- Bw_{max} : Maximum requested bandwidth of any connection request from the set of incoming connection requests in EON
- \bar{C} : Mean of weights
- N : Total number of arrived connection requests in EON

After estimating the weight of each connection request, the requests are arranged in increasing order of their weight then allocate the network resources to them. The lower value of weight indicates the optimal value of path length as well as bandwidth. Each term of weight function is divided by their respective maximums (i.e., PL_{max} and Bw_{max}) to maintain normalization among the solution. To achieve the best performance results of the proposed weight based RSA strategies, FF and FLF spectrum allocation schemes are used. On this basis the proposed strategies named as lowest weight demand first with first fit (LWDF with FF) and lowest weight demand first with first last fit (LWDF with FLF). The FF and FLF spectrum allocation schemes have been already discussed in Sect. 1.

In LWDF with FF policy, arrange all the connection requests in increasing order of their weight then perform RSA and the spectrum allocation is done by using FF (i.e., lowest indexed FS is assigned from the list of unused or free FSs). In LWDF with FLF,

apply FLF spectrum assignment scheme in some different way. After estimating the weight of each connection request, calculate the mean of weights of the given set of connection requests i.e., \bar{C} (see Eq. 2). Now arrange all the connection requests in ascending order of weight function. Before allocating the FSs to the connection requests, check $(W_i \leq \bar{C})$ or $(W_i > \bar{C})$. If $(W_i \leq \bar{C})$, lowest indexed FS is assigned, whereas for $(W_i > \bar{C})$, highest indexed FS is assigned from the list of unused FSs. In FF scheme, FSs always select the lowest indexed FSs from the list of available FSs. It may be possible that FSs are free, but connection requests cannot be establish. This is due to unavailability of contiguous (adjacent) FSs. While in FLF, it avoids such situation and provides more free contiguous FSs.

3 Simulation Results and Discussion

The simulation results and discussion are presented in this section. The simulations of the existing and proposed strategies are performed on NSFNET (14 nodes and 22 links) topology [20] (see Fig. 1) in MATLAB software. Information regarding the number of nodes, links, bandwidth/spectrum capacity per fiber link, and the set of connection requests with their required bit rates are considered as input parameters for the simulation program. The bit rates are assumed to be 25, 50, 75, 100, 125, and 150 (all in Gbps). Each link in EON contains 300 FSs and the width of each FS is assumed to be 12.5 GHz. For the shack of simplicity and reduction in time complexity, a pre-computed K-alternate routes (where, K = 3) is used for each s - d connection request. The performance evaluation of all strategies evaluated on the metric of accepted connection request, BBP, and RUR.

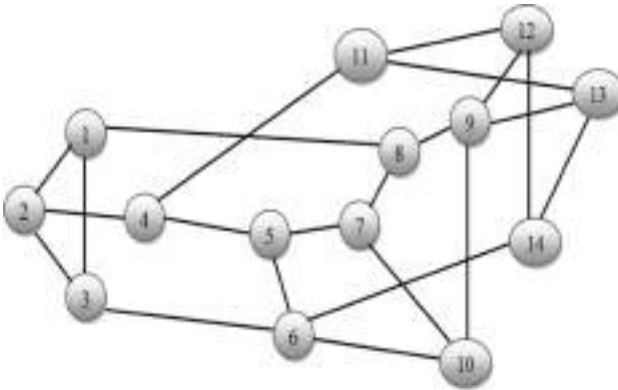


Fig. 1. NSFNET topology (14 Nodes, 22 Links) [20]

Figure 2(a) shows the graph between the accepted connection requests versus the number of connection requests arrived in EON. The curve in figure shows that with the increase in the connection requests arrive, the acceptance of connection requests also increases. This implies that higher number of connection requests is established in the

network. It is evident from the figure that the proposed LWDF with FF and LWDF with FLF strategies establish higher number of connection requests because of the systematic arrangement of connection demands. This leads to uniform FS allocation on each link in the network, resulting to increase the unused FSs availability as compare to other existing strategies. The arrangement of connection requests as weight function yields good result. As compare to traditional FCFS strategy 16.03% and 25.94% improvement is recorded in LWDF with FF and LWDF with FLF strategies, respectively.

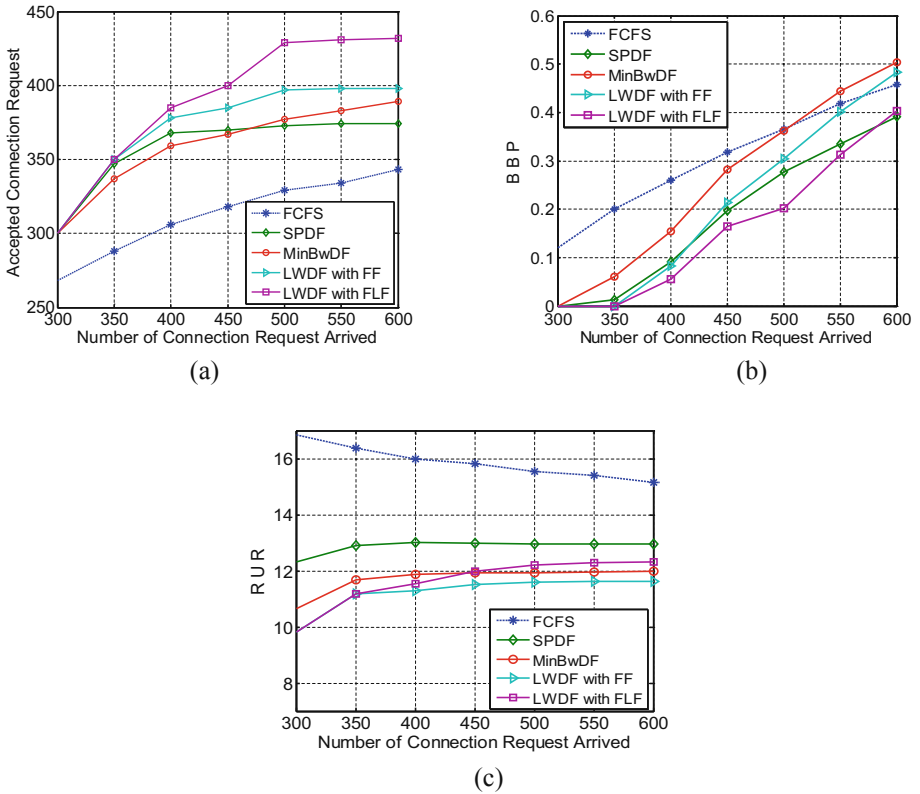


Fig. 2. Illustration of (a) Accepted Connection Requests, (b) BBP, and (c) RUR with increase in the number of connection requests arrived in EON.

Figure 2(b) illustrates the plot of BBP with the variation in number of connection requests arrived. BBP refers to the ratio of blocked/rejected spectrum bandwidth to the total requested bandwidth of the arrived connection requests in EON. The SPDF and LWDF with FLF show noteworthy performance and lower BBP as compared to other strategies. In SPDF, priority given to shortest path requests first, this may reduce spectrum continuity problem and increase availability of free spectrum resources for

future connection requests. In MinBwDF, priority given to lowest bandwidth demand and is unaware of route length, this may results more links traversing and resource consumption. It reduces the spectrum contiguity problem, but spectrum continuity problem remain unchanged or may be increased. In LWDF strategy, both bandwidth and path length are considered simultaneously to estimate the weight of connection requests. However, in LWDF with FF spectrum allocation suffer more bandwidth blocking due to increase in the spectrum fragmentation. This problem is reduced by using FLF spectrum allocation scheme. As compare to FCFS strategy 32.23% and 48.16% reduction of BBP is noted in LWDF with FF and LWDF with FLF policies, respectively.

Another metric parameter is RUR, i.e., how efficiently the network resources are utilized (see Fig. 2(c)). The ratio of total number of FSs used to the accepted connection requests in EON is known as RUR. Smaller the value of RUR indicates better resource utilization in the network. It is predicted from the graph that RUR of the proposed LWDF strategy shows significantly better performance as compare to other strategies. LWDF with FF and LWDF with FLF achieved 42.70% and 41.54% improvement, respectively, as compare FCFS strategy. Figure 3 shows a comparative bar graph of all strategies on all metrics. This shows a clear perspective that the LWDF with FLF performs best in all respect as compare to other strategies. The accepted connection request (CR), average value of BBP (in %) and RUR are given in Table 1.

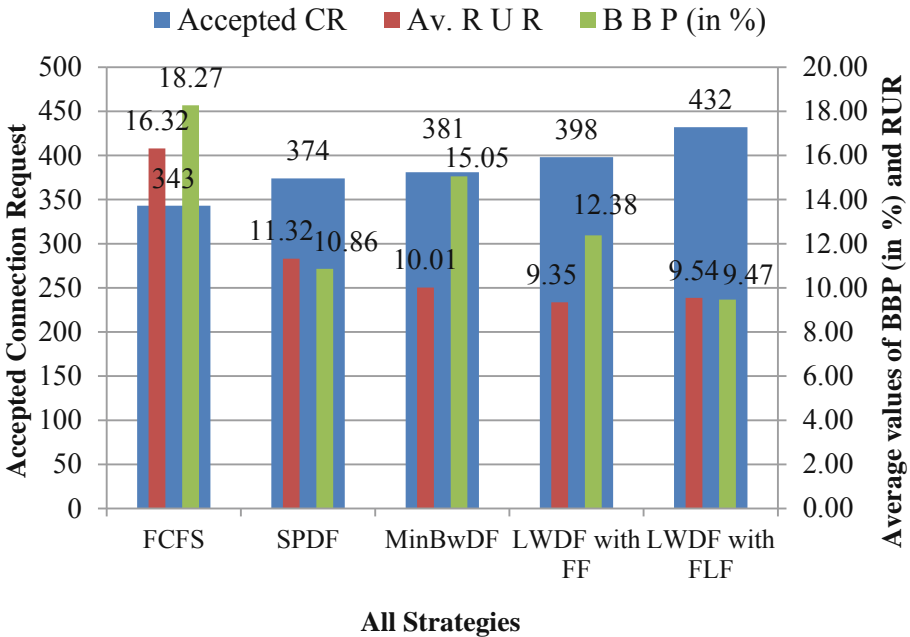


Fig. 3. Illustration of comparative bar graph of all strategies

Table 1. Average values of existing and proposed strategies

Parameters	FCFS	SPDF	MinBwDF	LWDF with FF	LWDF with FL F
Accepted CR	343	374	381	398	432
Average BBP (in %)	18.27	10.86	15.05	12.38	9.47
Average RUR	16.32	11.32	10.01	9.35	9.54

4 Conclusion

The paper deals with the problem of non-uniform allocation of network resources on the network links in EON under the static traffic scenario. The improper arrangement of connection requests and spectrum assignment constraints limit the efficiency of any RSA strategy. The proposed two RSA strategies namely LWDF with FF and LWDF with FLF minimize these issues. The proposed strategies accords priority to the connection requests having minimum weight. These leads to properly arrange the connection requests and to utilize optimum network resources. Simulation results show that the proposed strategies significantly improved the performance on the metrics of connection request acceptance, BBP, and RUR as compare to the existing strategies. The LWDF with FLF outperforms among all strategies. The proposed strategies shall be extended for survivable EONs in near future.




References

1. White Paper: Cisco visual networking index: forecast and trends, 2017–2022. <https://www.cisco.com/c/en/us/solutions/collateral/service-provider/visual-networking-index-vni/white-paper-c11-741490.html>. Accessed 15 July 2019
2. Recalcati, M., Musumeci, F., Tornatore, M., Bregni, S., Pattavina, A.: Benefits of elastic spectrum allocation in optical networks with dynamic traffic. In: Proceedings of Conference on Latin-America Communications (LATINCOM), pp. 1–6. IEEE, Cartagena de Indias (2014)
3. Gerstel, O., Jinno, M., Lord, A., Yoo, S.J.B.: Elastic optical networking: a new dawn for the optical layer? *IEEE Commun. Mag.* **50**(2), s12–s20 (2012)
4. Jinno, M., Takara, H., Kozycki, B., Tsukishima, Y., Sone, Y., Matsuoka, S.: Spectrum-efficient and scalable elastic optical path network: architecture, benefits, and enabling technologies. *IEEE Commun. Mag.* **47**(11), 66–73 (2009)
5. Xavier, A.V.S., Almeida, R.C., Chaves, D.A.R., Bastos-Filho, C.J.A., Martins-Filho, J.F.: Spectrum continuity based routing algorithm for flexible grid optical networks. In: International Microwave and Optoelectronics Conference (IMOC), pp. 1–5. SBMO/IEEE MTT-S, Porto de Galinhas (2015)
6. Chatterjee, B.C., Sarma, N., Oki, E.: Routing and spectrum allocation in elastic optical networks: a tutorial. *IEEE Commun. Surv. Tutor.* **17**(3), 1776–1800 (2015). Third Quarter
7. Zhang, G., De Leenheer, M., Morea, A., Mukherjee, B.: A survey on OFDM-based elastic core optical networking. *IEEE Commun. Surv. Tutor.* **15**(1), 65–87 (2013). First Quarter
8. Ding, Z., Xu, Z., Zeng, X., Ma, T., Yang, F.: Hybrid routing and spectrum assignment algorithms based on distance-adaptation combined coevolution and heuristics in elastic optical networks. *Opt. Eng.* **53**(4), 1–9 (2014)

9. Jinno, M., Kozicki, B., Takara, H., Watanabe, A., Sone, Y., Tanaka, T., Hirano, A.: Distance-adaptive spectrum resource allocation in spectrum-sliced elastic optical path network. *IEEE Commun. Mag.* **48**(8), 138–145 (2010)
10. Izquierdo-Zaragoza, J., Pavon-Marino, P., Bueno-Delgado, M.: Distance-adaptive online RSA algorithms for heterogeneous flex-grid networks. In: *International Conference on Optical Network Design and Modeling (ONDM)*, pp. 204–209. IEEE, Stockholm (2014)
11. Batham, D., Yadav, D.S., Prakash, S.: Least loaded and route fragmentation aware RSA strategies for elastic optical networks. *Opt. Fiber Technol.* **39**, 95–108 (2017)
12. Singh, P.D., Yadav, D.S., Bhatia, V.: Defragmentation based load balancing routing & spectrum assignment (DLBRSA) strategy for elastic optical networks. In: *International Conference on Advanced Networks and Telecommunications Systems (ANTS)*, pp. 1–6. IEEE, Indore, India (2018)
13. Zang, H., Jue, J.P., Mukherjee, B.: A review of routing and wavelength assignment approaches for wavelength routed optical WDM networks. *Opt. Netw. Mag.* **1**, 47–60 (2000)
14. Chatterjee, B.C., Oki, E.: Performance evaluation of spectrum allocation policies for elastic optical networks. In: *17th International Conference on Transparent Optical Networks (ICTON)*, pp. 1–4. IEEE, Budapest (2015)
15. Batham, D., Rajvaidya, M., Yadav, D.S., Prakash, S.: Wavelength indexing based end-to-end routing in multi-domain optical networks under scheduled lightpath demands. In: *International Conference on Signal Processing (ICSP)*, pp. 1–5. IET, Vidisha (2016)
16. Batham, D., Yadav, D.S., Prakash, S.: Greedy RWA algorithm for scheduled traffic in multi-domain optical networks. In: *12th International Conference on Fiber Optics and Photonics (PHOTONICS)*, pp. 1–3. OSA, Kharagpur (2014)
17. Batham, D., Yadav, D.S., Prakash, S.: Efficient resource provisioning using traffic balancing in multi-domain optical networks. *Int. J. Commun Syst* **30**(9), 1–14 (2017)
18. Yadav, D.S., Batham, D., Rajvaidya, M., Prakash, S.: A heuristic load balancing strategy for the static traffic in elastic optical network. In: *International Conference on Optics and Photonics (ICOP)*, Kolkata, India, pp. 1–4 (2015)
19. Batham, D., Jain, A., Gethewale, P., Kherajani, Y., Gupta, U.: Ordering policy based routing and bandwidth assignment algorithms in optical networks. In: *International Conference on Information, Communication, Instrumentation and Control (ICICIC)*, pp. 1–5. IEEE, Indore (2017)
20. Yadav, D.S., Chakraborty, A., Manoj, B.S.: A multi-backup path protection scheme for survivability in elastic optical networks. *Opt. Fiber Technol.* **30**, 167–175 (2016)



GIS and AHP Based Site Suitability Analysis for Desirable Obnoxious Facilities in Sultanpur District in India

Ruchin Agrawal¹(✉) , Amitabh Kumar Srivastava² ,
and Anjani Kumar Nigam² 

¹ Department of Civil Engineering, Kamla Nehru Institute of Technology,
Sultanpur, UP, India

ruchin_eng@yahoo.com

² Department of Civil Engineering, Bundelkhand Institute of Engineering
and Technology, Jhansi, UP, India

aksl07@rediffmail.com, anjani.k.nigam@gmail.com

Abstract. Rapid urbanization (both controlled and uncontrolled) coupled with other factors (such as land acquisition cost being high) is putting up a new sort of challenge for planners and decision-makers. The challenge of how to define and control the land-use for sustainable urban development. Constant clash of interest of various groups of people makes the decision even more difficult. To address this challenge stake-holders can use GIS and AHP based technology.

The present study deals with the problem of site selection for various desirable obnoxious facilities (Landfill and STP). These facilities are necessary to reduce the burden that urban areas put on the environment. The selection of suitable sites for landfill and STP land use has been carried out using GIS and AHP based methods. GIS analysis by taking into account the various spatial and non-spatial criterions provides the various alternatives that can be used for Landfill and STP land-use. These alternatives are then ranked by doing the pair-wise comparison of the various criterions. These ranks then make the job of the planners and decision-makers pretty comfortable in the final selection of a site for Landfill and STP land-use. The Landfill site (LS4) and STP site (SS5) were the top-ranked sites amongst other identified sites in this case study.

Keywords: GIS · AHP · Spatial data · Aspatial data · Landfill · STP

1 Introduction

Urban planning refers to planning with a spatial component. It suggests proposing land-uses, which are better than the otherwise unplanned pattern of land-use.

One of the major concerns of urban planning is to identify land-use suitability [1]. This will, in turn, depend upon a number of factors both spatial and aspatial. The combined effect of these factors will influence our choice of the decision on land-use.

Urban areas, in general, comprise of two types of land-uses:

1. Desirable Innocuous Facilities
2. Desirable Obnoxious Facilities

Desirable Innocuous Facilities (for example residential areas, commercial areas, recreational areas, etc.) are supposed to form the heartland of the urban area. They are required to be placed in the near vicinity of the urban area to be directly used by the public at large.

On the other hand, Desirable Obnoxious Facilities (for example landfill sites, sewage treatment plants, etc.) though necessary are supposed to be placed as far as economically possible from the heartland of the urban area. They are required to be placed far from the vicinity of the public settlement.

GIS proves to be a powerful tool of spatial analysis for the evaluation of site suitability [2]. Alternatives provided by the GIS analysis are then evaluated by the multi-criteria analysis, thus helping the planners in the complex decision-making process [3].

This paper deals with the site suitability evaluation of two desirable obnoxious facilities namely landfill sites and sewage treatment plant sites.

1.1 Landfill Site

A landfill is utilized directly to satisfy waste generated from domestic, commercial and/or industrial activities. Therefore, landfills carry the load of the waste generated by the urban setup. Uncontrolled operation of the landfill sites poses a serious challenge to the environment as they contribute significantly to the soil, water, and air pollution. With rapid urbanization, the exponential rise in the demand for waste disposal has added to the woes of environmental agencies.

Thus making it pertinent for the planners to devise a methodology to identify the most suitable site for landfill operations.

1.2 Sewage Treatment Plant Site

Domestic activities in urban areas generate effluents, which threaten the environmental balance when discharged directly without treatment [4]. Due to rapid urbanization, the threat has snowballed into a menace for the stake-holders. Thus, pressing the authorities hard enough to facilitate installation of STPs to contain the situation.

Now, the site selection for the STP becomes very crucial for the stake-holders [5]. This is due to the fact that their discharge still has the potential to affect the ecosystem [6].

2 Methodology

2.1 Spatial Analysis

Geographic Information System (GIS) is a software that gathers, stores and analyzes both spatial and aspatial data [7–9]. This data when analyzed with reference to some complex problem help in arriving at a solution, which otherwise would have been difficult to deal with [10, 11]. This makes GIS a robust tool [12]. Thereby making it

helpful for stake-holders by providing solutions to a variety of problems. One such problem is the identification of a suitable site for various land uses [13].

Thus making it quite imperative for GIS to be used in the site selection of the desirable obnoxious facilities. This spatial analysis helps in identifying various alternatives that can be taken into consideration.

Advantages:

1. A variety of data (both spatial and aspatial) from various sources can be seamlessly used for analysis.
2. Criteria of analysis can be efficiently used to develop a model for analysis.
3. The model can then be used and reused and also can be tweaked to suit different local conditions.
4. The results obtained are in the form of maps, which make the decision-making process faster, easy to understand and more logical.

Disadvantages:

1. The integrity of data from various sources is very difficult to achieve.
2. The efficiency of the model is very much dependent on how efficiently the criterions are defined.
3. Tweaking of the model for different sites is easier said than achieved. It may require a good amount of rework.
4. The maps obtained as a result may sometimes be very confusing, thereby making the task of the planners and decision-makers even more difficult.

2.2 Multi-criteria Analysis

Spatial analysis delivers alternatives. Multi-Criteria Analysis then helps the stake-holders in final decision-making by ranking the alternative. Analytical Hierarchy Process (AHP) is the tool to carry out Multi-Criteria Analysis [14].

The process begins with establishing the hierarchy of the problem, viz. as follows in the order from top to bottom:

1. Goals
2. Criterions
3. Sub-criterions
4. Decision alternatives

Eigenvectors for each element are then computed and aggregated by pair-wise comparison at each hierarchy level. Composite final vector of weight coefficients for alternatives is then obtained. The weight coefficient is a measure of the relative importance (value) of each alternative in accordance with the stated goals in the hierarchy. The alternatives are then ranked according to the descending order of the weight coefficients.

Advantages:

1. The process ensures the active participation of all the stakeholders, beginning with the finalization of goals at levels and sub-levels.
2. Weights for all the criteria are then decided by the stakeholders.
3. The whole process is rational with no room for ambiguity.
4. The results obtained are in the form of ranked alternatives, which can be suitably compared.

Disadvantages:

1. The participation of stakeholders from a broad domain group free from all sorts of biases ensures the success of this process. This is very hard to achieve.
2. Lack of conscious and focussed efforts of stakeholders can seriously hamper the results achieved.
3. No mathematical model can 100% replicate real-life situations.
4. A very small difference in the percentage suitably (used to compute ranks) may render more confusion to the situation.

3 Case Study

3.1 Study Area

The present study focuses on a semi-urban town 'Kurwar' in the Sultanpur district of U.P. Sprawling across 26° 19' 42.918" N to 26° 25' 20.42" N latitude and 81° 58' 30.897" E to 82° 5' 4.079" E longitude and totaling an area of 112.81 km². Comprising quaternary alluvium as the main soil type and Gomti as the main river. Kurwar is in a state of rapid transition from semi-urban to urban. And hence attracting the attention of planners. Thereby, making it a suitable candidate for the current study (Fig. 1).

3.2 Spatial Data

Following is the list of spatial data generated for carrying out the study:

1. Map representing Land Use/Landcover
2. Map representing Soil Cover
3. Map representing Slope Profile
4. Map representing Transportation Details
5. Map representing Drainage Details
6. Map representing Flood Effects
7. Map representing Geological Features

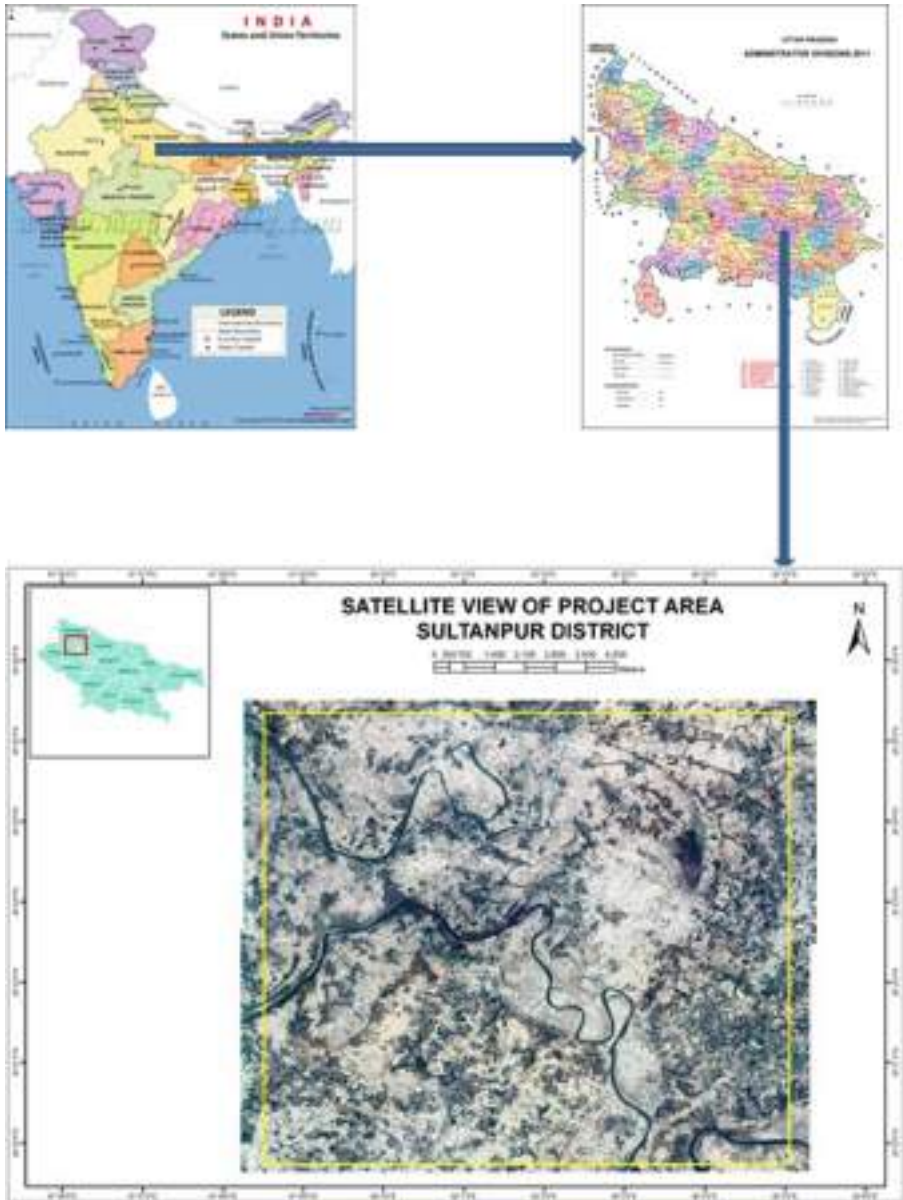


Fig. 1. Study area

3.3 Spatial Analysis

Landfill Site

Firstly, the identification of suitable sites for landfill construction was carried out. A GIS model was created for carrying out the spatial analysis in lieu of the guidelines

laid down by CPHEEO (2016) and with due deliberations amongst the expert group. 41 Representatives from academics, municipal authorities, and research groups constituted the expert group. The following parameters were considered to achieve the first objective and the model was tuned accordingly.

1. Distance from Pond: No Landfill should be constructed within a vicinity of 200 m of any lake or pond to avoid water body contamination.
2. Distance from Road: No Landfill should be constructed within a vicinity of 200 m of the right of way of any state or national highway. Aesthetics is the main reason for this restriction.
3. Distance from River: No Landfill should be constructed within a vicinity of 100 m of any navigable river or stream.
4. Distance from Settlement: No landfill site should be constructed within a vicinity of 500 m of a notified inhabited locality.

A GIS model was developed in accordance with the above-defined criteria. Spatial analysis was then carried out on the spatial data using this GIS model. Suitable sites for landfill construction were then identified.

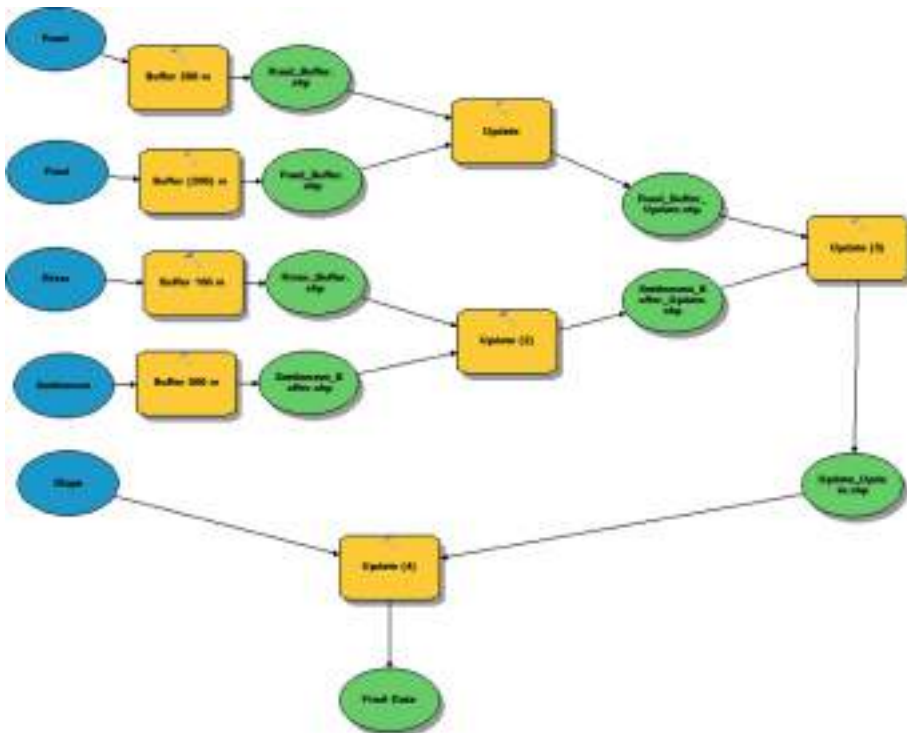


Fig. 2. GIS model for landfill site selection

GIS model (Fig. 2) when applied to the spatial data (created in due course of the study) resulted in eight candidate sites for prospective **Landfill land-use**. Figure 3 shows the map with various landfill candidate sites as per the respective locational criterion. The geographical location detail of these landfill sites along with their designation (i.e. LS1 to LS8 for ease of notation) is given in Table 1. Various spatial parameters for each candidate landfill site are detailed in Table 2.

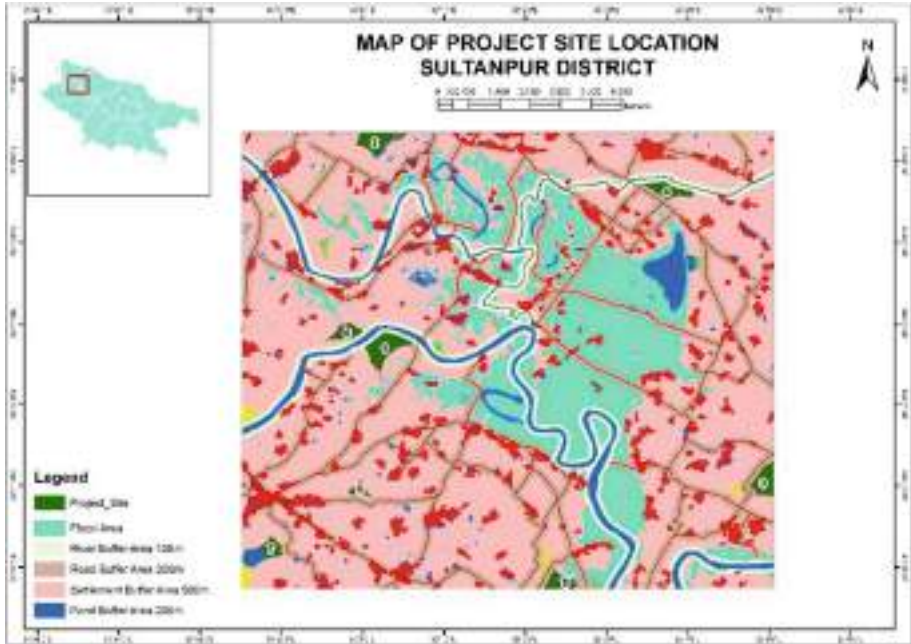


Fig. 3. Map representing candidate landfill site

Table 1. Locational attributes of eight candidate landfill sites

Landfill site	Coordinates	
Landfill Project Site 1 (LS1)	Long.	82° 0' 16.403" E
	Lat.	26° 22' 42.846" N
Landfill Project Site 2 (LS2)	Long.	82° 0' 9.927" E
	Lat.	26° 25' 13.407" N
Landfill Project Site 3 (LS3)	Long.	82° 4' 56.297" E
	Lat.	26° 21' 2.947" N
Landfill Project Site 4 (LS4)	Long.	82° 3' 43.756" E
	Lat.	26° 24' 38.187" N
Landfill Project Site 5 (LS5)	Long.	82° 2' 25.187" E
	Lat.	26° 19' 47.070" N

(continued)

Table 1. (continued)

Landfill site	Coordinates	
Landfill Project Site 6 (LS6)	Long.	81° 59' 49.662" E
	Lat.	26° 22' 53.303" N
Landfill Project Site 7 (LS7)	Long.	81° 58' 52.621" E
	Lat.	26° 20' 13.243" N
Landfill Project Site 8 (LS8)	Long.	81° 59' 57.661" E
	Lat.	26° 20' 57.297" N

Table 2. Various spatial parameters for each candidate landfill site

	Candidate landfill sites							
	LS1	LS2	LS3	LS4	LS5	LS6	LS7	LS8
Level (C1)	89.81766	89.17833	100.5855	93.08073	89.15734	88.85716	101.108	94.63739
Area (C2)	37.30091	28.94903	24.44189	19.91221	16.08631	14.24916	13.95707	7.210163
Slope (C3)	5–10%	5–10%	>10%	>10%	5–10%	5–10%	>10%	>10%
Distance Nearest Pond (m) (C4)	1423.995	423.12	193.08	962.21	885.05	1894.52	373.84	477.46
Distance Nearest Road (m) (C5)	685.0537	767.04	289.70	262.90	716.58	773.82	946.86	231.69
Distance Nearest River (m) (C6)	418.1724	1255.07	1979.60	255.75	1036.68	282.59	2723.57	2414.24
Distance Nearest Settlement (m) (C7)	685.0537	738.57	797.89	959.15	716.58	773.82	1063.07	809.94

Sewage Treatment Plant Site

Secondly, the identification of suitable sites for STP construction was carried out. A GIS model was created for carrying out the spatial analysis in lieu of the guidelines laid down in the available literature and with due deliberations amongst the expert group. 41 Representatives from academics, municipal authorities, and research groups constituted the expert group. The following parameters were considered to achieve the second objective and the model was tuned accordingly.

1. Distance from Settlement: No STP should be constructed within a vicinity of 500 m of a notified inhabited locality.
2. Distance from Road: STP should be constructed within 200 m vicinity of a road to provide easy access.
3. Distance from Pond: No STP should be constructed within a vicinity of 200 m of any lake or pond to avoid water body contamination.

4. Distance from landfill: No STP should be constructed within a vicinity of 300 m of any landfill.
5. Slope: Requirement of the flow of wastewater under gravity within the STP makes it pertinent to choose a site with a slight slope.

A GIS model was developed in accordance with the above-defined criteria. Spatial analysis was then carried out on the spatial data using this GIS model. Suitable sites for STP construction were then identified.

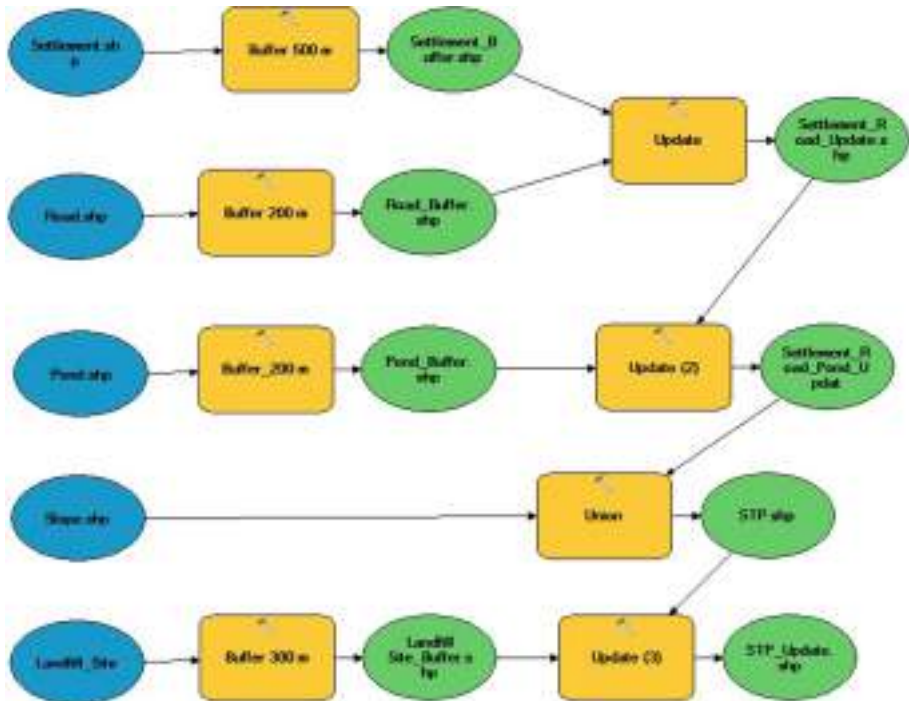


Fig. 4. GIS model for STP site selection

GIS model (Fig. 4) when applied to the spatial data (created in due course of the study) resulted in six candidate sites for prospective **STP land-use**. Figure 5 shows the map with various STP candidate sites as per the respective locational criterion. The geographical location detail of these STP sites along with their designation (i.e. SS1 to SS6 for ease of notation) is given in Table 3. Various spatial parameters for each candidate STP site are detailed in Table 4.

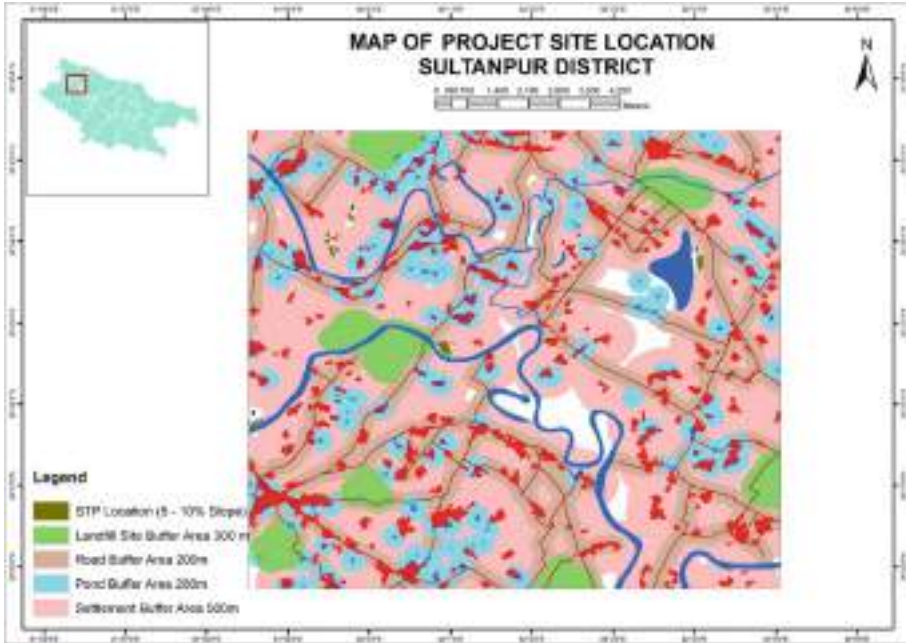


Fig. 5. Map representing candidate STP site

Table 3. Locational Attributes of eight candidate STP sites

STP Site	Coordinates
STP Project Site 1 (SS1)	Long. 82° 0' 55.478" E
	Lat. 26° 22' 41.436" N
STP Project Site 2 (SS2)	Long. 81° 59' 32.183" E
	Lat. 26° 23' 52.914" N
STP Project Site 3 (SS3)	Long. 81° 59' 32.144" E
	Lat. 26° 24' 1.311" N
STP Project Site 4 (SS4)	Long. 81° 59' 46.450" E
	Lat. 26° 24' 17.604" N
STP Project Site 5 (SS5)	Long. 82° 4' 3.746" E
	Lat. 26° 23' 44.695" N
STP Project Site 6 (SS6)	Long. 81° 58' 35.281" E
	Lat. 26° 21' 46.737" N

Table 4. Various spatial parameters for each candidate landfill site

	Candidate STP site					
	SS1	SS2	SS3	SS4	SS5	SS6
Level (C1)	90.860811	89.068882	89.357481	89.080073	89.268392	90.881455
Area in ha (C2)	6.14 ha	2.09 ha	2.34 ha	1.85 ha	3.62 ha	2.40 ha
Slope (C3)	5–10%	5–10%	5–10%	5–10%	5–10%	5–10%
Distance Nearest Pond (m) (C4)	609.65 m	475.11 m	645.14 m	659.28 m	852.52 m	134.78 m
Distance Nearest Road (m) (C5)	285.9 m	995.12 m	804.92 m	743.05 m	313.74 m	200.60 m
Distance Nearest River (m) (C6)	129.96 m	377.10 m	339.86 m	845.13 m	107.49 m	1534.88 m
Distance Nearest Settlement (m) (C7)	500.06 m	590.40 m	507.62 m	501.83 m	701.78 m	500.23 m

3.4 AHP Analysis

To rank the identified landfill and STP sites AHP analysis was carried out. Seven criterions as defined in Table 2 for landfill and Table 4 for STP formed the basis for AHP analysis.

As per the opinions and recommendations of the expert group pair-wise comparison of each criterion for all the candidate sites was carried out. This resulted in weights for each criterion. The percentage suitability of each site for both landfill and STP was then calculated from these weights. Ranks were then assigned to each site by arranging them in descending order on the basis of percentage suitability.

Table 5 represents the Ranks of candidate Landfill sites and Table 6 represents the Ranks of candidate STP sites.

Table 5. Ranks of candidate landfill sites

Candidate sites	Percentage suitability	Rank
LS4	14.51	1
LS6	14.35	2
LS8	12.94	3
LS1	12.47	4
LS3	12.34	5
LS2	11.80	6
LS5	11.52	7
LS7	10.06	8

Table 6. Ranks of candidate STP sites

Candidate sites	Percentage suitability	Rankings
SS5	23.38	1
SS1	21.62	2
SS6	17.23	3
SS3	13.29	4
SS2	12.88	5
SS4	11.59	6

3.5 Results and Discussions

The ranks of all the candidate landfill sites were then fed into the GIS to obtain Final Map showing rank-wise Landfill Sites as shown in Fig. 6 below. With 14.51% of suitability, LS4 ranked 1st among all sites for landfill construction. Favorable values of criterions C4 and C7 made LS4 the most preferable choice. While 10.06% of suitability forced LS7 to appear last in the rank table. Unfavorable values of C2 and C4 made LS7 the least preferable choice.

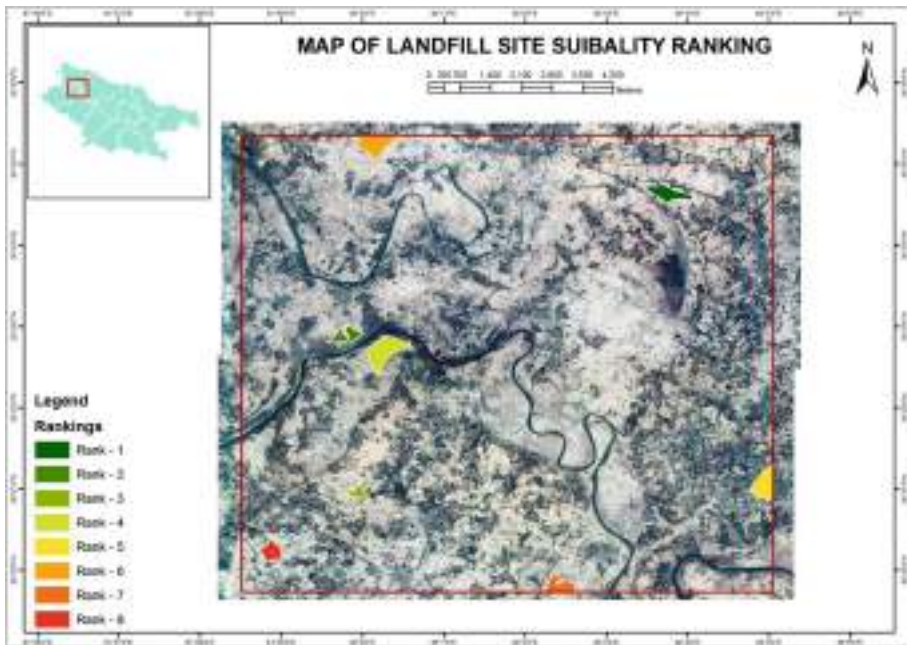


Fig. 6. Final map showing rank-wise landfill sites

The ranks of all the candidate STP sites were then fed into the GIS to obtain Final Map showing rank-wise STP Sites as shown in Fig. 7 below. With 23.38% of suitability, SS5 ranked 1st among all sites for STP construction. Favorable values of

criteria C2, C4, C6, and C7 made SS5 the most preferable choice. While 11.59% of suitability forced SS4 to appear last in the rank table. Unfavorable values of C2, C5 and C6 made SS4 the least preferable choice.



Fig. 7. Final map showing rank-wise STP sites

Kurwar (the region under consideration in the present study) is in the very early stage of urbanization with no formal method of sewage disposal in place. This gives planners and decision-makers an excellent opportunity to create a sustainable modular development of the area in a controlled fashion. The results achieved in the course of the present study can be of much help to the planners and decision-makers in attaining the desired goals of sustainable development.

4 Conclusions

This study has demonstrated that complex decision-making problems involving many influencing factors and conflicting interests of various stake-holders can logically and to an appreciable level of satisfaction be solved using GIS and AHP based decision-making models. Site selection for desirable obnoxious facilities (i.e. landfill and sewage treatment plant) is one such challenging task. Wherein economy, environment, political interests, vested interests of the people involved affected the decision-making process. Due to this a simple linear solution can never satisfy the interests and motives of the project. Thereby, making it pertinent for the technology to intervene and logically

provide a fair solution to attain all aims and objectives of the project and without compromising the interests of the people involved.

Thus the prowess of the GIS-AHP based decision-making tool has been successfully showcased through this study. And also this is a scalable tool and can be used for other decision-making problems as well.

References

1. Kumar, M., Shaikh, V.R.: Site suitability analysis for urban development using GIS based multicriteria evaluation technique. *J. Indian Soc. Remote Sens.* **41**(2), 417–424 (2012)
2. Zhao, Y.W., et al.: GIS-based optimization for the locations of sewage treatment plants and sewage outfalls - a case study of Nansha District in Guangzhou City, China. *Commun. Nonlinear Sci. Numer. Simul.* **14**(4), 1746–1757 (2009)
3. Anagnostopoulos, K.P., Gratziou, M., Vavatsikos, A.P.: Using the fuzzy analytic hierarchy process for selecting wastewater facilities at prefecture level. *Eur. Water* **19**(20), 15–24 (2007)
4. Metcalf and Eddy: *Water Reuse: Issue, Technology and Application*. McGraw Hill, New York (2007)
5. Gambi, C., Frascchetti, S., Terlizzi, A., Danovaro, R., Musco, L., Giangrande, A.: Structural and functional response of meiofauna rocky assemblages to sewage pollution. *Mar. Pollut. Bull.* **52**(5), 540–548 (2005)
6. Hughes, K.A.: Reducing sewage pollution in the Antarctic marine environment using a sewage treatment plant. *Mar. Pollut. Bull.* **49**(9–10), 850–853 (2004)
7. Huber-Sannwald, E., de Galindo Mendoza, M.G., Carrera Hernández, J., de Paz, F.P., García Barrios, L., Ribeiro Palacios, M.: Landscape diversity in a rural territory: emerging land use mosaics coupled to livelihood diversification. *Land use policy* **30**(1), 814–824 (2012)
8. Martínez-Graña, A.M., Goy, J.L., Zazo, C.: Water and wind erosion risk in natural parks - a case study in ‘Las Batuecas-Sierra de Francia’ and ‘Quilamas’ protected parks (Central System, Spain). *Int. J. Environ. Res.* **8**(1), 61–68 (2014)
9. Hijazi, I., Lv, Z., Li, X., Zhong, C., Koenig, R., Schmitt, G.: Assessing essential qualities of urban space with emotional and visual data based on GIS technique. *ISPRS Int. J. Geo-Inf.* **5** (11), 218 (2016)
10. Xie, Z., Liu, J., Ma, Z., Duan, X., Cui, Y.: Effect of surrounding land-use change on the wetland landscape pattern of a natural protected area in Tianjin, China. *Int. J. Sustain. Dev. World Ecol.* **19**(1), 16–24 (2012)
11. Li, X.: Emergence of bottom-up models as a tool for landscape simulation and planning. *Landsc. Urban Plan.* **100**(4), 393–395 (2011)
12. Burrough, P.A., McDonnell, R.A.: *Principles of geographical information systems*. *Econ. Geogr.* **75**(4), 333 (1998)
13. Collins, M.G., Steiner, F.R., Rushman, M.J.: Land-use suitability analysis in the United States: historical development and promising technological achievements. *Environ. Manag.* **28**(5), 611–621 (2001)
14. Saaty, T.L.: Decision making with the analytic hierarchy process. *Int. J. Serv. Sci.* **1**, 83–98 (2008)



Supplementary Cementitious Material: An Elixir for Concrete

Abhishek Kumar Jaiswal¹  and Manoj Kumar Trivedi² 

¹ Gammon Engineers and Contractors Pvt. Ltd., Mumbai, India
jaiswal_1508@rediffmail.com

² Department of Civil Engineering, Madhav Institute of Technology
and Science, Gwalior, MP, India
manojtrivedi@mitsgwalior.in

Abstract. The concrete mix design of high-performance concrete of M-60 grade for the construction of Piers has to be done with as low cement content as possible to minimize the effect of heat during production, pouring and hardening of concrete in hot weather of Ludhiana. The concrete should also be made durable to the extent possible in order to maximize the structure life by providing the shield to reinforcement. The high grade of concrete generally involves higher cement content which in turn have high heat of hydration and may develop cracks which affects the durability and life expectancy of structure. Citing the hot weather of Ludhiana (Punjab) in summers and time constrain, attempt has been made to use supplementary cementing material along with cement in an economical manner so that the desirable compressive strength of concrete can be achieved along with very low permeability in addition to adhering to the concerning IS (Indian Standards) codes and MoRTH (Ministry of Road Transport and Highways) [7].

Keywords: High grade concrete · Heat of hydration · Durability of concrete · Supplementary cementing material

1 Introduction

To ease off the heavy vehicular traffic on the portion falling in municipal limits of Ludhiana (Punjab) of National Highway 5 (old NH95), which frequently leads to traffic jams due to number of busy intersections such as Bhai Bala Chowk, Aarti Chowk, PAU (Punjab Agriculture University) gate number 1 and 2, the 12.951-km elevated road is being constructed by the National Highways Authority of India (NHAI) from the erstwhile Octroi Post on Ferozpur Road (NH 95) to Samrala Chowk at a cost of Rs 756.27 crore.

The project details are as follows:-

“Name of the Project:- Construction of Partially Access Controlled Four Lane Elevated Highway Between Samrala Chowk (Design Chainage Km 0 + 000) to Ludhiana Municipal Limit (Design Chainage Km 12 + 951) of NH-95 (Section Passing Through Ludhiana City) in The State of Punjab On EPC Mode under NHDP IV

Estimated cost:- Rs 756.27 Cr.

Time limit:- 30 Months (Oct 2017 to April 2020)

Maintenance period:- 48 months after completion

Mode of construction:- EPC (engineering, procurement and construction)

Contractor:- M/s Gammon Engineers and Contractors Private Limited – S P Singla Construction Private Limited (JV)”

To cater the need of project structure various grades of concrete is needed among them the highest grade is M-60. In order to minimize the heat of hydration (as the maximum temperature in Ludhiana mostly crosses 45° centigrade in summers) and to enhance the sustainability of structure the use of SCM (Supplementary Cementitious Material) in concrete has been explored.

Usage of supplementary cementitious materials (SCM) helps in designing durable concrete. SCM nowadays being used are fly ash, Ground Granulated Blast-furnace Slag (GGBS), densified silica fume, metakaolin, rice husk ash (RHA), etc. Reaction of these SCMs is mainly pozzolanic.

2 Literature Review

The role of SCM in concrete has been widely discussed and has been established through experimental studies backed by chemical theories, it has been found that certain materials which are byproducts of different processes (like fly ash generation GGBS generation etc.) if selected and treated/refined (if needed) suitably can be used in concrete which not only improves the overall performance of concrete but also lowers the cost of concrete which makes the project more viable along with covering the most burning topic which is saving the environment by utilizing the byproducts and reducing the cement content which again helps in lowering the carbon dioxide emission (as per study up to 8% contribution in producing carbon di oxide is there by cement industries).

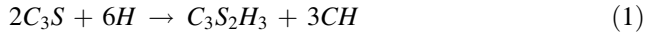
With reference to the paper published by Megat et al. [18] it has been established through experimental studies that the green as well as hardened concrete properties improve if the SCMs are used in concrete judiciously. This not only improves the ease to place but also increases the durability of concrete which in turn improves the longevity of structure by protecting the reinforcement for longer duration in a better manner.

A recent study on the subject has been published in the paper by Junenger and Siddique [17] which includes the enhancement of long-term durability of concrete with the addition of SCMs along with betterment of other desirable concrete properties. The ingress of water, gas and chemicals is slowed down due to lower permeability of concrete which has been attributed to it by SCMs thus slowing the corrosion and environmental attack on structure. Also, the use of SCM not only reduces the cost of concrete but also gives a positive impact on environment by consuming the byproducts and hazardous materials in a constructive manner.

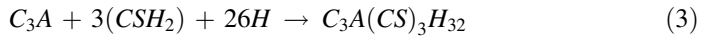
In order to reap the benefits of SCM, the chemical formulation and reactions needed to be discussed which is as below:

Ordinary Portland Cement (OPC) is a product of four principal mineralogical phases. These phases are Tricalcium Silicate - C_3S ($3CaO.SiO_2$), Dicalcium Silicate - C_2S ($2CaO.SiO_2$), Tricalcium Aluminate - C_3A ($3CaO.Al_2O_3$) and Tetracalcium aluminoferrite - C_4AF ($4CaO, Al_2O_3, Fe_2O_3$). The setting and hardening of the OPC takes place as a result of reaction between these principal compounds and water.

The reaction between these compounds and water are shown as under:



The quantity of calcium hydroxide (lime) is more in C_3S as compared to C_2S even though the products from C_3S and C_2S are similar. The reaction between C_3A and water happens due to sulphate ions coming from the dissolution of gypsum present in OPC. This fast pace process can be summarized as below:



Similar to those of C_3A the hydration product is formed by Tetra calcium aluminoferrite with iron which is a partial substitute for alumina in the crystal structures of ettringite and monosulpho-aluminate hydrate. Release of excess lime during hydration of concrete makes the concrete weak by inducing porosity in it, thus, weakening the bond as is evident from the above reaction. SCM when mixed with concrete consumes all the surplus lime and produce C-S-H gel which has good binding properties, thus boosting the binding.

Coal-fired power station provides fly ash as a byproduct, which is electrostatically precipitated from the exhaust gases. Fly ash is the most common form of artificial pozzolana. Therefore, fly ash is the most economically viable option for the project.

The chemical properties of fly ash depend on the following factors:-

- i. Properties of Coal used for burning
- ii. Furnace's temperature
- iii. Degree of pulverization of coal
- iv. ESP's efficiency

Following are the principal constituents of fly ash:-

- (a) Silica (25–60%),
- (b) Alumina (10–30%)
- (c) Ferric Oxide (5–25%)

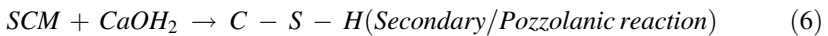
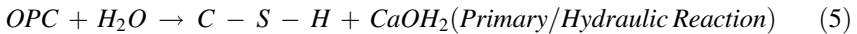
Fly Ash can be categorized as:-

- i. Class F (the sum of the three constituents is $\geq 70\%$ and reactive calcium oxide is $< 10\%$)
- ii. Class C (the sum of the three constituents is $\geq 50\%$ and reactive calcium oxide is $> 10\%$)

Class F fly ash contains Calcium Alumino-Silicate glass, Free Lime, Anhydrate, Tri-Calcium Aluminate and Calcium Silicate as the active constituents. Therefore, Class F fly ash has been used for the project under consideration. The extra strength gain of fly ash concrete is attributed to the cementitious gel which is formed by the reaction of alkali hydroxides and calcium obtained from cement-fly ash system with the glassy materials found in fly ash. Low carbon and high glass content characterize good quality of fly ash, with 75% or more particles finer than 45 μm .

Slag based SCM, Ultrafine Slag (Alccofine 1203) has optimized particle size distribution, which renders it ultra-fineness. It is obtained by process of controlled granulation of GGBFS (Ground granulated blast-furnace slag). Chilling the molten slag by quenching in water produces glassy sand like granulated product material when grounded to less than 45 microns, the granulated material can acquire specific surface area of about 1000 to 1200 m^2/kg .

2.1 Hydration Reaction



Notations:

OPC: Ordinary Portland Cement; H_2O : Water; $\text{Ca}(\text{OH})_2$: Calcium hydroxide (traditionally called slaked lime); C-S-H: Calcium Silicate Hydrate; SCM: Supplementary Cementitious Material;

C-S-H gel is the compound which imparts strength and impermeability to the concrete. In primary/hydraulic reaction, when water is added to the OPC, C-S-H gel and $\text{Ca}(\text{OH})_2$ are formed. In secondary/pozzolanic reaction when SCM is used, Calcium Hydroxide $\text{Ca}(\text{OH})_2$, which is otherwise a weak element in concrete, gets replaced with C-S-H, it helps concrete to gain strength even after 28 days. Thus, concrete with SCMs progressively gain strength and impermeability over the time.

A replacement of OPC by these SCMs has to be restricted as per the Codal provisions, noted in Table below (Table 1):

Table 1. Upper permissible limits of SCMs in concrete

SCMs in concrete	Upper permissible limits for use in concrete as per,					
	Indian standards				British standards	American standards
	IS 456: 2000 (Fourth Revision) [3]	IRC 112: 2011 [12]	MoRTH: 2013 (5 th Revision) [7]	IRS: 2003	BSEN 450 [11]-2012 and BS 4246 [10]-1996	ACI 232.2 R-18 [13] and ACI 233 R-17 [14]
Fly ash	Permissible upper limit is specified as min. OPC content to be 65% of min. Cementitious materials content specified (IS 456:2000, Amendment No. 4) [3] based on environment condition, balance could be fly ash	Max. 35%	35% (For structural concrete)	Not permitted	55% (BSEN 450 [11] - 2012)	35% for general concrete and can be higher for mass concrete. (ACI 232.2R-18)
GGBS	Permissible upper limit is specified as min. OPC content to be 30% of min. Cementitious materials content specified (IS 456:2000, Amendment No. 4) [3] based on environment condition, balance could be GGBS	Max. 70%	Max. 70% (For structural concrete)	Not permitted	85% (BS 4246-199 Morth 6) [7]	50% (ACI 233R-17)

(continued)

Table 1. (continued)

SCMs in concrete	Upper permissible limits for use in concrete as per,					
	Indian standards				British standards	American standards
	IS 456: 2000 (Fourth Revision) [3]	IRC 112: 2011 [12]	MoRTH: 2013 (5 th Revision) [7]	IRS: 2003	BSEN 450 [11]-2012 and BS 4246 [10]-1996	ACI 232.2 R-18 [13] and ACI 233 R-17 [14]
Ultrafine SCMs	No limits specified Usually 5–12% for SF, 3–12% for UFS and 6–20% for UFFA)	No limits specified usually 5–12% for SF, 2–20% for UFS and 6–20% for UFFA)	–	–	–	–
Composite cement	As per Table-1 Clause 5.1 of IS 16415:2015 [9], Combined fly ash and GGBS content shall be max. 65% and min. OPC content shall be 35%				–	–

Adhering the project tender documents, the use of fly ash can be done in between 20–35% as per MoRTH [7]. Citing the availability along with suitability of materials, the use of Fly ash and Ultra-fine GGBS (Alccofine 1203 commercial name) has been explored along with cement as Pozzolanic material for M-60 grade of concrete.

3 Practical Work and Results

(See Tables 2, 3, 4, 5 and 6).

Table 2. Physical properties of cementitious material

Material		Specific surface area (m ² /kg)	Average particle size (µm)	Bulk density (kg/m ³)	Specific gravity
Fine pozzolanic materials	Cement	260–300	20	1300–1400	3.15
	Fly ash (FA)	300–500	20	900–1100	2.15
	Ultrafine Slag (UFS) (Alccofine 1203)	1000–1200	3	600–700	2.87

Table 3. Cement properties

Brand of cement: ultratech cement (grade: OPC 53)			
Sr. no.	Characteristics	Codal requirement IS 269-2015 [1]	Test results
Chemical properties			
1	Lime saturation factor CaO-0.7 SO 2.8 SiO ₂ + 1.2 Al ₂ O ₃ + 0.65 Fe ₂ O ₃	0.80–1.02	0.84
2	Ratio of % alumina to that of iron oxide Al ₂ O ₃ + Fe ₂ O ₃	0.66 Min	1.25
3	Insoluble residue (% by mass)	5.00 Max	1.18
4	Magnesia (% by mass)	6.0 Max	2.2
5	Sulphuric anhydride (% by mass)	3.5 Max	3.33
6	Total loss on ignition (%)	4.0 Max	1.65
7	Chloride (%) (for prestressed concrete 0.05 Max)	0.1 Max	0.018
Physical properties			
1	Normal consistency %		29.5
2	Fineness (m ² /kg)	225 Min	338
3	Setting time (minutes)		
	Initial	30 Min	140
	Final	600 Max	215
4	Soundness		
	Le-chat expansion (mm)	10 Max	1
	Auto clave (%)	0.80 Max	0.2
5	Compressive strength (MPa)		
	72 ± 1 h (3 days)	27 Min	31
	168 ± 2 h (7 days)	37 Min	39.5
	672 ± 4 h (28 days)	53 Min	55.5

Table 4. Fly ash properties

Source of fly ash: Rajpura			
Sr. no.	Characteristics	Requirement as per IS 3812-2013 [2]	Test results
Chemical properties			
1	SiO ₂ + Al ₂ O ₃ + Fe ₂ O ₃	70% Min	78.67
2	Silicon dioxide SiO ₂	35% Min	48.5
3	Reactive silica	20% Min	21.78
4	Magnesium oxide MgO	5% Max	4.02
5	Total sulphur as SO ₃	3% Max	2.11
6	Available alkalis as Na ₂ O	1.5% Max	0.5
7	Loss on ignition	5% Max	1.52
8	Total chloride	0.5% Max	0.01
Physical properties			
1	Fineness (m ² /kg)	320 Min	388
1	Fineness by wet sieving	34% (Max)	28
2	Lime reactivity (Mpa)	4.5 Min	5.42
3	Compressive strength at 28 days (Mpa)	Not less than 80% of corresponding plain cement mortar cubes	87.6
4	Soundness by autoclave	0.8% Max	0.1

Table 5. Ultrafine slag properties

Source of Ultrafine Slag (UFS): Ambuja cement; product name: Alccofine 1203			
Sr. no.	Characteristics	IS 12089 [8]	Test results
Chemical analysis			
1	Manganese oxide	5.5% Max	2.00
2	Magnesium oxide	17% Max	9.30
3	Sulphide sulphur	2% Max	0.95
Physical analysis			
1	Bulk density (Kg/m ³)		630.00
2	Specific gravity		2.87

Table 6. Mix design for M 60 grade (PIER/RCC-structure) concrete

Table 6 (A) STIPULATIONS FOR PROPORTIONING			
S.No.	Parameters	Requirements	Applicable Standards clause
1	Grade Designation	M 60	As per approved Design and Drawing
2	Type of Cement	OPC Grade 53	IS: 269-2015
3	Type of Mineral Admixture	Siliceous Pulverised Fuel Ash (Flyash + Alccofine)	IS: 3812 (Part 1)
4	Type of Coarse Aggregate	Crushed angular type	IS: 383
5	Type of Fine Aggregate	Natural Sand and Crusher Dust (Zone II)	IS: 383
6	Chemical Admixture Type	Super plasticizer (Type F)	IS: 9103
7	Maximum nominal size of aggregate	20 mm	As per approved Design and Drawing
8	Exposure condition	Severe	IS: 456-2000 (Table 3)
9	Min. Cementitious content	380 Kg/m ³	MoRTH (1715.2) [7]
10	Max. w/c ratio	0.33	MoRTH (1715.2) [7]
11	Slump	75-125 mm	MoRTH (Table 1700-4) [7]
12	Mode of placement	Pump	As per Methodology
13	Degree of Workability	Medium	IS: 456-2000 (Clause 7.1)
14	Slump of concrete	120 mm	-
15	Degree of supervision	Good	-
16	Maximum Cement content	450 Kg/m ³	IS: 456-2000 (Clause 8.2.4.2)

Table 6 (B) Mix Design Calculations and Results

Mix Details		Ingredients Details	Ratio CA: FA	Individual %age	Source Name	Combined Specific gravity	Material Property		
							Specific Gravity	Water Absorption	Moisture Content
Grade	M60	20 mm (60 %)	63	37.8 %	Pathankot	2.670	2.67	0.41	0.41
		10 mm (40 %)		25.20 %	Pathankot		2.67	0.45	0.45
Target Mean Strength	74.00	Natural Sand (90%)	37	3.70 %	Pathankot	2.586	2.60	1.26	1.26
		Crusher Dust (10 %)		33.30 %	Pathankot		2.47	2.56	2.56
Water Cement Ratio	0.29	Average SpG					2.638		

Cementitious Material in 'kg/cum'	501	Binder Material Details		
% of Flyash	21.96	Material	Source Name	Specific Gravity
Free Water content	145.30	Cement	Ultratech OPC 53 G	3.15
Admixture Dosages	1.00%	Fly Ash	Rajpura	2.15
% of M.A.	2.49%	Mineral Admixture	Alcofine 1203	2.87
		Admixture	ATPL-CARPOL 303 L	1.08

Mix Proportion				Weight in Kg (in SSD condition)	Moisture Content in %age	Correction in Kgs	Corrected Design Mix in Kgs
Material	%age	Volume of ingredients in 'Cum'					
20 mm	63	Ca and Fa	0.673	680	0.41	0.00	680
10 mm				453	0.45	0.00	453
Natural sand	37	Ca and Fa	0.673	580	1.26	0.00	580
Crusher Dust				64	2.56	0.00	64
Volume of Concrete Mix design in Cum	1.00	Cement	0.120	378.5	-	-	378.5
		Fly Ash	0.051	110	-	-	110
		M.A.	0.004	12.5	-	-	12.5
		Admixture	0.006	6.5	-	-	6.5
		Water	0.145	145.3	-	-	145.3
Fresh Density of Mix in 'Kg/Cum'				2430			2430

Wt. of Material in 'kg' for 0.04 Cum		Trial data						
40 mm	0.00	Starting time of trial				10:00AM		
20mm	27.20							
10 mm	18.12	Ambient temperature in 'deg'	36		Concrete temperature in 'deg'		Density of Green Concrete in kg/m ³	
Natural Sand	23.20				29			2446
Crusher Dust	2.56		Initial	30Min	60Min	90 Min	120 Min	150 Min
Cement	15.16	Slump in 'mm'	Collapse	Collapse	Collapse	180	140	100
Fly Ash	4.40							
Mineral Admixture	0.52	Mix Condition	Cohesive	Cohesive	Cohesive	Cohesive	Cohesive	Cohesive
Admixture	0.260							
Water	5.80	Numbers of Cube Casted				9		

No of specimen tested of Size 150X150X150 mm	Age in days	Compressive Strength							
		Wt. of Cube in Kg	Load in KN Sample1	Wt. of Cube in Kg	Load in KN Sample2	Wt. of Cube in Kg	Load in KN Sample 3	Average in KN	Average in N/mm ²
3	7	8.128	1490	8.09	1440	8.308	1490	1473.33	65.48
3	28	8.142	1700	8.177	1730	8.121	1690	1706.67	75.85
3	56	8.214	1840	8.206	1890	8.223	1870	1866.67	82.96
RCPT Test Result		298 Coulombs		Permeability Test Result		5 mm			

4 Conclusions

After carrying out this study following points can be concluded about the use of SCM in cement concrete:-

- The use of SCM is environment friendly as it reduces the consumption of cement which in turn reduces carbon–dioxide emission.
- Also it utilizes the byproducts of various processes (e.g. fly ash and Ultra-fine slag) which are harmful to environment, if not disposed-off properly.
- Use of SCMs reduces bleeding and segregation (effect of fly ash is more prominent) in the concrete mix and makes it more cohesive (Alccofine 1203 play a lead role in this due to its fineness).
- The lime released from hydration of OPC gets converted into additional binding material by SCM, thus providing the additional strength to concrete.

- Use of SCM also reduces the heat of hydration considerably due to slow rate of reaction. Thereby, reducing thermal cracking, this in turn gives sound concrete.
- Rounded shape and finer particle size of SCMs make the mix more impermeable, thus concrete shows better resistance against freeze and thaw action.
- Water reducing property of SCMs (Fly ash play major role) and reduction in total cementitious content (effect of Alccofine 1203) also result in less drying shrinkage strain and creep strain.
- Reaction between SCMs and liberated lime improves impermeability by improving pore refinement and grain refinement. This, in turn, increases the resistance for the moisture movement and other environmental elements (gases and chemicals) resulting in improved sustainability.
- Consumption of excess lime by SCM imparts uniform color. Hence, efflorescence will be lesser.
- Reduced requirement of cement for same strength thus reduces cost of concrete (Table 7).

Table 7. Bi-furcation of effect of fine and ultrafine SCMs on fresh and hardened of concrete:

Material	Property	Results
Fly ash	Water demand	Reduces
	Workability	Increases, due to spherical particle shape
	Bleeding and segregation	Reduces, as mix becomes cohesive
	Heat of hydration	Reduces
	Setting time	Increases
	Pumpability	Improves
	Slump retention period	Increases
	Early strength gain	Reduces, delayed strength gain observed up to 7 to 10 days
	Long term strength gain	Increases
Ultrafine slag (Alccofine 1203)	Permeability	Reduces
	Heat of hydration	Neutral, due to low % of UFS
	Cohesiveness	Increases
	Early strength gain	No substantial impact
	Long term strength gain	Improves
	Permeability	Reduces significantly

For producing sustainable and cost-effective concrete, it is essential to use supplementary cementitious materials individually or in combination. As can be inferred from the above results most of the desirable concrete properties have been improved with addition of SCM in concrete.

References

1. IS 269-2015-Specification for Ordinary Portland Cement
2. IS 3812 Part-1-2013-Specification for Pulverized Fuel Ash-For Use as Pozzolona in Cement
3. IS 456-2000-Plain and Reinforced Concrete
4. IS 383-2016-Specification for Coarse and Fine Aggregate
5. IS 10262-2009-Guideline For Concrete Mix Design
6. IS 9103-1999-Specification For Concrete Admixture
7. MoRTH-Specification for Road and Bridges Work
8. IS 12089-Specification for granulated Slag for the manufacture of Portland slag cement
9. IS 16415-2015-Composite Cement Specification
10. BS 4246-Specification For High Slag blast furnace Cement
11. BS EN450-2012-Flyash For Concrete
12. IRC-112-2011-Code of practice for Concrete Road Bridges
13. ACI 232.2R-18-Use of Flyash in Concrete
14. ACI 233R-17-Guide to use of Slag Cement in Concrete and Mortar
15. Properties of Concrete by AM NEVILLE
16. Nayak, N.V., Manish, M.: Handbook on Quality and Productivity Improvement of Concrete. Alpha Science International Limited, Oxford (2019)
17. Juenger, M.C., Siddique, R.: Recent advances in understanding the role of supplementary cementitious materials in concrete. *Cem. Concr. Res.* **78**(Part A), 71–80 (2015)
18. Joharia, M.M., Brooks, J.J., Kabira, S., Rivard, P.: Influence of supplementary cementitious materials on engineering properties of high strength concrete. *Constr. Build. Mater.* **25**(5), 2639–2648 (2011)



A Two Variable Adjustable Window Function Approach to Design FIR Filter

Awadhesh Gupta^(✉), Juhi Afridi, Shikha Shrivastava,
and Vandana Vikas Thakre

Department of Electronics, MITS, Gwalior, India
awadhesh2911@mitsgwalior.in

Abstract. This work suggested a new window function with adjustable spectral characteristics. The suggested window is a combination of Blackman-Harris, Hamming and Gaussian window function. Gaussian, Kaiser, Lanczos-L and Hamming window function have been used to compare the proposed window functions. Observations from the MATLAB simulation shows that suggested window provides better ripple-ratio, main-lobe width and side-lobe roll-off ratio compared to Gaussian window function. While comparing with Kaiser, Lanczos L and Hamming window, suggested window gives better spectral performance with a very small compromise of one of the spectral characteristics.

Keywords: FIR filter · Window function · Ripple ratio · Side-lobe roll-off ratio · Main-lobe width

1 Introduction

A filter is a frequency selective device. Digital filters show a lot of applications in speech processing, noise suppression [1] and image enhancement etc. FIR filters are highly preferable if no phase distortion is required. Various researchers across the globe have proposed a various approaches for FIR filter design which provides a closed form solutions. Windowing is a truncation of the IIR filter impulse response [9]. Truncation of the impulse response $h_d[n]$ is equivalent to product of the $h_d[n]$ by a rectangular window $w[n]$.

$$h[n] = h_d[n]w[n] \quad (1)$$

Window method of digital FIR filter design is the best efficient design method. Windows function is used to provide zero-valued outside of certain interval. We can change the value of adjustable window by changing the one or more variable parameter [1, 5]. Several windows have been suggested for better spectral specifications than commonly used windows [3].

There are three desired specifications for any window function. They must have smaller main-lobe width, high ripple-ratio (in negative sense) and high side-lobe roll-off ratio. But these properties oppose each other [7]. For a fixed duration, a window having higher side lobes has smaller main-lobes width and vice versa [2]. Gaussian, Kaiser and Lanczos window are commonly used adjustable window functions [7, 9].

Kaiser window has higher computational complexity due to inclusion of Bessel functions [8].

There are three desired specifications for any window function. They must have smaller main-lobe width, high ripple-ratio (in negative sense) and high side-lobe roll-off ratio. But these properties oppose each other [7]. For a fixed duration, a window having higher side lobes has smaller main-lobes width and vice versa [2]. Gaussian, Kaiser and Lanczos window are commonly used adjustable window functions [7, 9]. Kaiser window has higher computational complexity due to inclusion of Bessel functions [8].i.e. Gaussian, Kaiser and Hamming window. By adjusting the value of adjustable parameters ‘a’ and ‘r’, desired specification for the digital filter can be achieved. The suggested window suggests better spectral traits with some window with a very small compromisation of one of the spectral characteristics.

The normalized frequency domain of a generalized window characteristic is presented in Fig. 1.

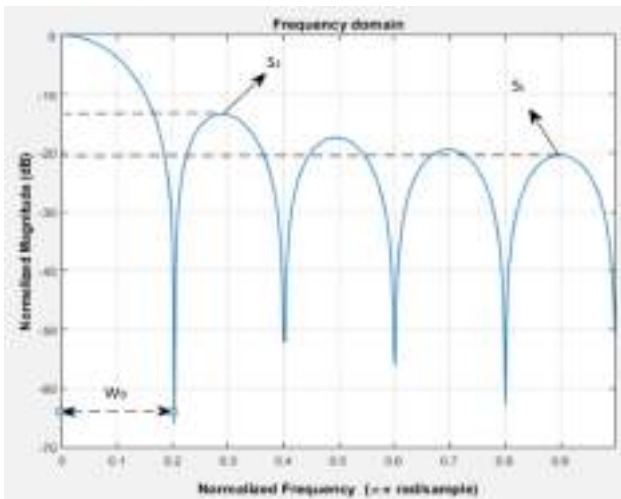


Fig. 1. A general normalized window characteristics

There are three desired specifications for a window function which are defined as:

$$\text{Main-lobe width (MLW)}(W_B) \stackrel{\text{def}}{=} \text{Width of the main-lobe} \times 2\pi$$

$$\text{Ripple-Ratio (RR)} \stackrel{\text{def}}{=} \text{Maximum side-lobe amplitude (in dB)} - \text{Main-lobe amplitude (in dB)} = S_1$$

$$\text{Side-lobe roll-off ratio (SLRR)} \stackrel{\text{def}}{=} \text{Maximum side-lobe amplitude (in dB)} - \text{Minimum side-lobe amplitude (in dB)} = S_1 - S_L.$$

2 Suggested Window Function

The composite of the Blackman-Harris, Blackman and Hamming and window function in the suggested window function provided in Eqs. (2), (3) and (4) respectively.

$$w_1[n] = 0.35875 - 0.48829 \cos\left(\frac{2\pi n}{N-1}\right) + 0.14128 \cos\left(\frac{4\pi n}{N-1}\right) - 0.01168 \cos\left(\frac{6\pi n}{N-1}\right) \tag{2}$$

$$w_2[n] = 0.54 - 0.46 \cos\left(\frac{2\pi n}{N-1}\right) \tag{3}$$

$$w_3[n] = \exp\left(-0.5\left(\frac{\alpha n}{N/2}\right)^2\right) \tag{4}$$

where N is the length of FIR filter required.

The suggested window functions given by Eq. (5)

$$w[n] = \begin{cases} \left[w_1 - w_1 \left\{ \left(\frac{1}{a} \right) (\cosh(w_2))^{0.1} w_3^2 \right\}^r \right]^r & 0 \leq n \leq N - 1 \\ 0 & \text{otherwise} \end{cases} \tag{5}$$

where ‘a’ setup the gain of the window and ‘r’ is the spectral control parameter.

Figure 2 present such suggested window width reduces in time domain while increasing ‘a’ and ‘r’. The reduction of window width in time domain causes higher main-lobe width in frequency domain [9].

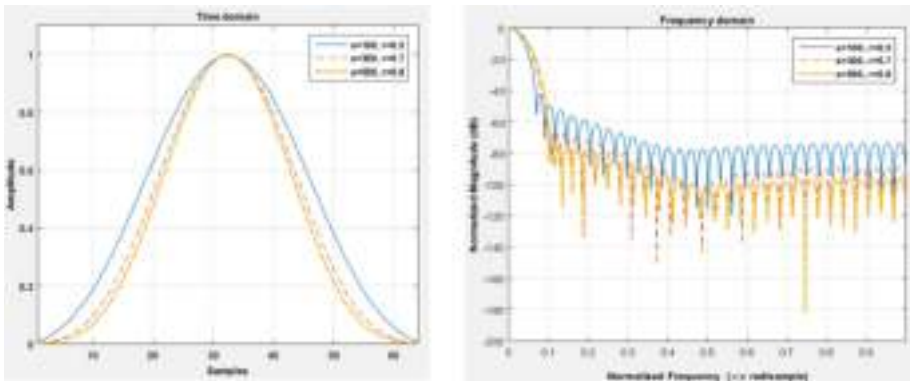


Fig. 2. Time domain and frequency domain behavior of suggested window for specific expense of ‘a’ and ‘r’

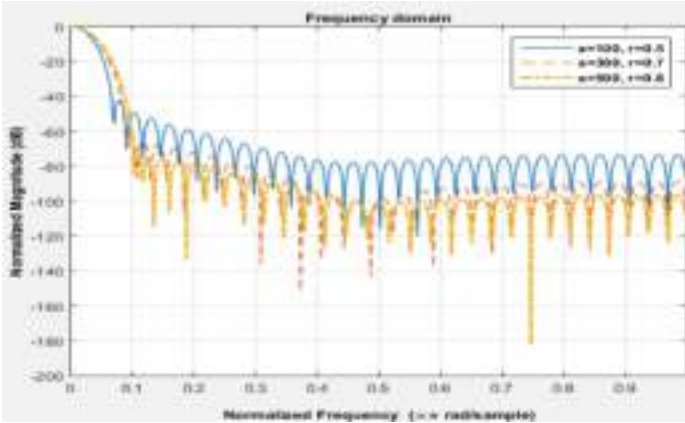


Fig. 3. Frequency domain response of the suggested window for specific expense of ‘a’ and ‘r’

Table 1 and Fig. 3 indicates that increasing ‘a’ and ‘r’ increases the RR and MLW smaller. But SLRR increases upto some extent than decreases.

Table 1. Frequency domain characteristics of suggested window for specific ‘a’ and ‘r’

Parameter ‘a’ and ‘r’	MLW	RR (dB)	SLR R (dB)
a = 70, r = 0.4	$0.0605 \times 2\pi$	-35.95	30.64
a = 100, r = 0.5	$0.0703 \times 2\pi$	-42.49	35.38
a = 300, r = 0.7	$0.0898 \times 2\pi$	-60.18	41.19
a = 500, r = 0.8	$0.1015 \times 2\pi$	-70.95	29.83

3 Performance and Comparisons

Comparison of the proposed window with the empirical available window function is presented in this section.

3.1 Gaussian Window

The Gaussian window function is defined as Eq. 3 (Fig. 4):

$$w[n] = \exp\left(-0.5\left(\frac{\alpha n}{N}\right)^2\right)$$

Figure 5 and Table 2 shows that suggested window (a = 100, r = 0.55) gives smaller main-lobe width, smaller ripple-ratio and higher side-lobe roll-off ratio

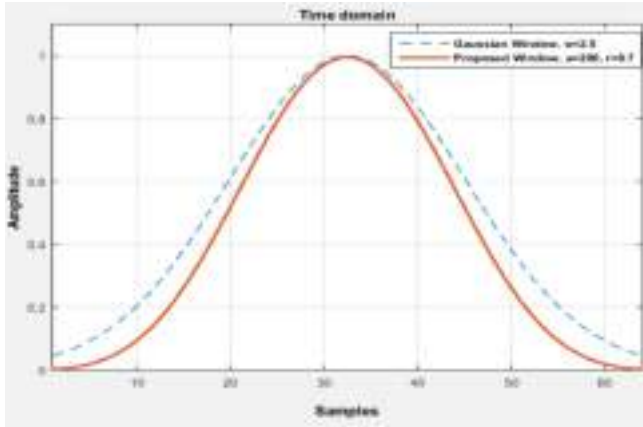


Fig. 4. Gaussian window comparison with proposed window in time domain

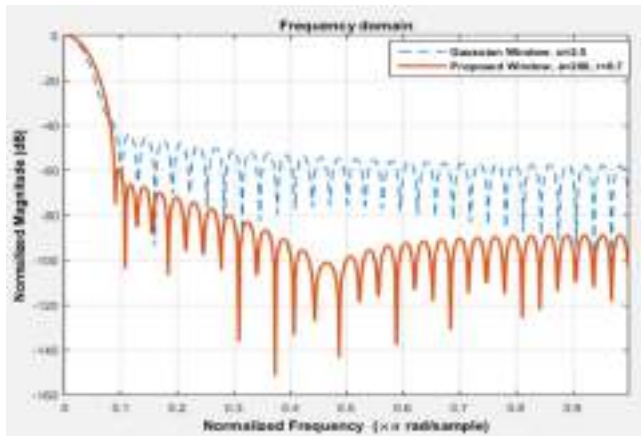


Fig. 5. Gaussian window comparison with proposed window in frequency domain

compared to Gaussian window as desired. Even for $a = 200$, $r = 0.75$ the suggested window gives better frequency domain characteristics as compared to Gaussian window.

Table 2. Frequency domain characteristics comparison of proposed window with Gaussian window

Window function	MLW	RR (dB)	SLRR (dB)
Gaussian, $\alpha = 2.5$	$0.1018 \times 2\pi$	-43.29	13.90
Proposed window $a = 100, r = 0.55$	$0.07421 \times 2\pi$	-46.59	38.16
Proposed window $a = 200, r = 0.70$	$0.0898 \times 2\pi$	-59.4	41.96
Proposed window $a = 200, r = 0.75$	$0.0957 \times 2\pi$	-64.02	36.92

3.2 Kaiser Window

Kaiser window function is defined as:

$$w[n] = \frac{I_0\left(\pi\alpha\sqrt{1-\left(\frac{2n}{N-1}\right)^2}\right)}{I_0(\pi\alpha)} \text{ for } 0 \leq n \leq N - 1$$

where I_0 is the zero-th order modified Bessel function of the first kind.

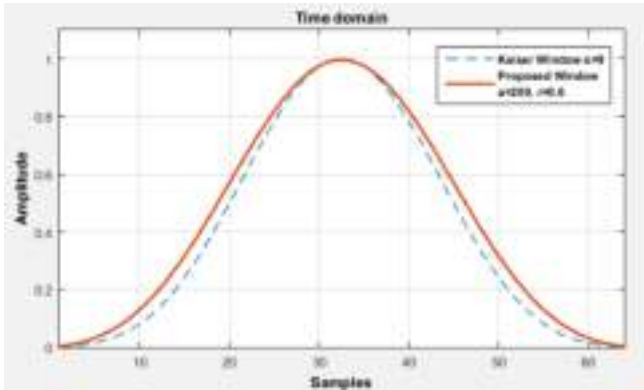


Fig. 6. Kaiser window comparison with proposed window in time domain

Figure 6 and Table 3 indicates that suggested window ($a = 200, r = 0.60$) gives smaller MLW and higher SLRR compared to Kaiser window as desired. But there is a compromise of 14 dB in RR. For $a = 200, r = 0.75$ the suggested window provides almost same MLW as Kaiser window and higher SLRR (approx. 5 dB) with a very small compromise of RR (approx. 2 dB). Though the suggested window does not include any complex function like Bessel function hence its complexity is less compared to Kaiser window.

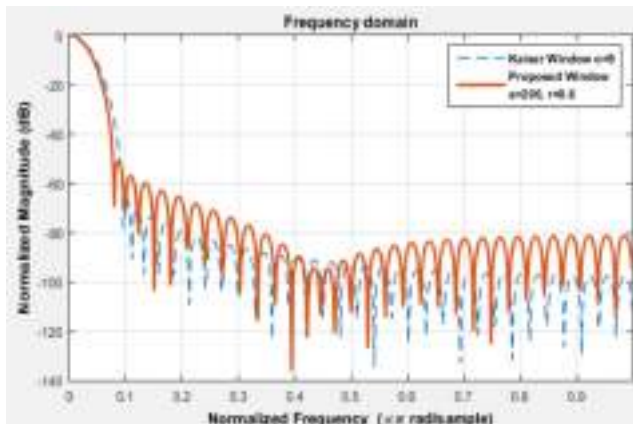


Fig. 7. Kaiser window comparison with proposed window in frequency domain

Table 3. Frequency domain characteristics comparison of proposed window with Kaiser window

Window function	MLW	RR (dB)	SLRR (dB)
Kaiser, $\alpha = 2.5$	$0.0957 \times 2\pi$	-65.95	31.90
Proposed window $a = 200, r = 0.60$	$0.0800 \times 2\pi$	-51.05	44.33
Proposed window $a = 200, r = 0.70$	$0.0898 \times 2\pi$	-59.40	41.96
Proposed window $a = 200, r = 0.75$	$0.0957 \times 2\pi$	-64.02	36.92

3.3 Summary Comparisons with Other Window Functions

Table 4 indicates that suggested window ($a = 200, r = 0.70$) gives smaller MLW and RR compared to Lanczos-L window as desired. But there is a compromise of approximate 34 dB in SLRR.

Table 4. Frequency domain characteristics comparison of proposed window with Lanczos L window

Window function	MLW	RR (dB)	SLRR (dB)
Lanczos L = 3	$0.0976 \times 2\pi$	-53.79	76.41
Proposed window $a = 200, r = 0.70$	$0.0898 \times 2\pi$	-59.40	41.96

Table 5. Comparison of the frequency domain characteristics of the suggested window with Hamming window

Window function	MLW	RR (dB)	SLRR (dB)
Hamming	$0.0644 \times 2\pi$	-42.82	9.77
Proposed window $a = 200, r = 0.43$	$0.0625 \times 2\pi$	-37.71	32.04

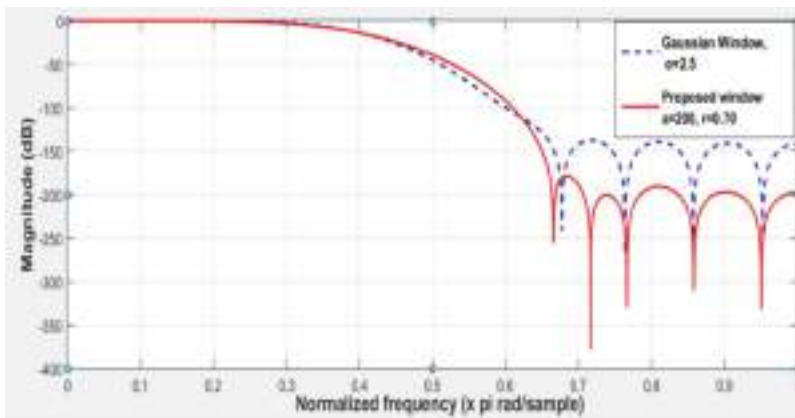
Table 5 indicates that proposed window ($a = 200, r = 0.43$) gives smaller MLW and SLRR as desired. But there is a compromise of approximate 5 dB in RR.

4 Application

In this section, FIR low-pass filter is designed using proposed window and the same is compared with the low-pass filter designed using Gaussian window function [6] as shown in Fig. 7.

Impulse response of the FIR filter $h[n]$ may be calculated from Eq. 1, in which impulse response of a low-pass filter $h_d[n]$ may be given as:

$$h_d[n] = \begin{cases} \frac{\omega_c}{\pi}, & n = 0 \\ \frac{\sin(\omega_c n)}{\pi n}, & n \neq 0 \end{cases}$$

**Fig. 8.** FIR filter design comparison between suggested window and Gaussian window of length $N = 21$.

The comparative study of the FIR filter design of Gaussian window and suggested window in Fig. 8 concluded that suggested window gives better frequency domain characteristics than Gaussian window.

5 Conclusion

The suggested window function can adjust the spectral characteristics i.e. RR, MLW, and SLRR by using two parameters 'a' and 'r'. It shows better performance than Gaussian window in all desired specifications. The proposed window has better MLW and RR than Kaiser Window but with a very small compromisation of SLRR (approx. 2 dB). While comparing with Lanczos L window we have concluded that suggested window gives better RR and MLW and but with a compromisation of SLRR. The comparative study with Hamming window shows that suggested window provides better MLW and SLRR with a small compromisation of RR. Finally to show the application of proposed window, FIR filter has been designed using proposed window and compared with filter designed using Gaussian window. It has been shown that proposed window gives far better performance than Gaussian window function.

References

1. Rakshit, H., Ullah, M.A.: An adjustable novel window function with its application to FIR filter design. In: Proceedings of International Conference on Computer and Information Engineering (ICCIE), pp. 36–41 (2015)
2. Nuttall, A.: Some windows with very good sidelobe behavior. *IEEE Trans. Acoust. Speech Signal Process. ASSP* **29**(1), 84–91 (1981)
3. Ha, Y.H., Pearce, J.A.: A new window and comparison to standard windows. *IEEE Trans. Acoust. Speech Signal Process.* **37**(2), 298–301 (1989)
4. Roberts, R.A., Mullis, C.T.: *Digital Signal Processing*, pp. 135–136. Addison-Wesley, Boston (1987)
5. Shil, M., Rakshit, H., Ullah, H.: An adjustable window function to design an FIR filter. In: proceedings of IEEE International Conference on Imaging, Vision & Pattern Recognition (icIVPR), pp. 1–5 (2017)
6. Khatun, M.: Implement a new window function and design FIR filters by using this new window. *IJECS* **3**(3), 4087–4090 (2014)
7. Oppenheim, A., Schafer, R., Buck, J.: *Discrete-Time Signal Processing*, 2nd edn. Prentice-Hall, Upper Saddle River (1999)
8. Kaiser, J.F., Schafer, R.W.: On the use of the I_0 -sinh window for spectrum analysis. *IEEE Trans. Acoust. Speech Signal Process.* **28**(1), 105–107 (1980)
9. Proakis, J., Manolakis, D.G.: *Digital Signal Processing*, 4th edn. Prentice Hall, Upper Saddle River (2007)



Performance Analysis of a Twin Rotor MIMO System Using Fuzzy Logic Controller

Piyali Das ^(✉) , Pema Rinzing Bhutia , Ram Krishna Mehta ,
and Om Prakash Roy 

North Eastern Regional Institute of Science and Technology,
NERIST, Nirjuli 791109, AP, India
pd@nerist.ac.in

Abstract. This study explains about the MIMO plant statistics of fuzzy logic based control of a electro-mechanical system. An intelligent control system is proposed here in this paper to observe all the response of both the planes horizontal and vertical. The controller was established for pitch and yaw planes separately which determines the desired output responses. A triangular response was selected in fuzzy logic controller to mitigate complexity of calculation and produce faster and smoother output stabilization which leads to better robustness. The model is highly nonlinear and model controller design is done by MATLAB simulation functions.

Keywords: TRMS · Fuzzy set · Fuzzy logic controller · Pitch response · Yaw response

1 Introduction

The modern fuzzy logic concept was first introduced in 1965, by Zadeh [1] in his research work on “fuzzy sets”, the detail mathematical expressions of fuzzy set theory was provided by him, in 1968 he proposed his theory of “fuzzy algorithms”. Before the introduction of fuzzy logic mathematics was confined to only two conclusions that is true or false (0 or 1). But fuzzy logic allows the input to exist with varying degree at more than one state at a time, describing the system in more than natural terms. In [2] basic fuzzy set applications were illustrated by Zadeh where to apply fuzzy logic for a control technology was described. The fuzzy logic controller (FLC) was used in [4] to overcome the complex coupling effect of the multiple input multiple output (MIMO) system. In 2014, a neuro-fuzzy controller was established by Aras and Kayank [5] for a 2- DOF MIMO TRMS system. A brief review of fuzzy logic controller is shown in [6, 7] where the plant was a multiple input and multiple output system. The objective of designing an intelligent controller for the multiple input multiple output scheme to overcome the limitations of conventional control. In modern control FLC is a developed and authentic controlling unit. Various FLC research topics are experienced on several areas of engineering, medicine, bio-technology etc. A self-learning based FLC was used for missile autopilot system in [7] which describe using Lyapunov Stability fuzzy parametric rules decided. The tracking as well as stability was performed by

using this control strategy. An MEMS gyroscope sensor was controlled by using an adaptive fuzzy sliding mode control in [8]. The tracking of the system as controlled by sliding mode controller An observer based robust fuzzy controller was investigated in [9]. The plant was nonlinear and model parameters were unmeasurable which was estimated by the fuzzy observer controller. Many researchers have been established various precise results using TRMS model in [11–14], where in some of the cases to avoid coupling effect decoupled model was used (Fig. 1).

2 Model Description

In this exclusive study the laboratory helicopter model is used, it is very difficult to control the model for its complex coupling effect in both the planes. Two planes as well as motors are used to furnish the model realization, first is pitch rotor and second one is tail rotor. The model is from the company name M/s Feedback, prototype of a helicopter. This model follows the aerodynamic law of motion where 2D control is being applicable. All mathematical expressions are trying to establish the exact model of real object. These two planes are designed with the help of two individual propellers, where the motion freedom is till 360° . All the model depicted identification provided by the company is given in Table 1, for the further calculations. Due to the complex model parameters the system is segregated in two parts one is vertical and the other is horizontal plant.

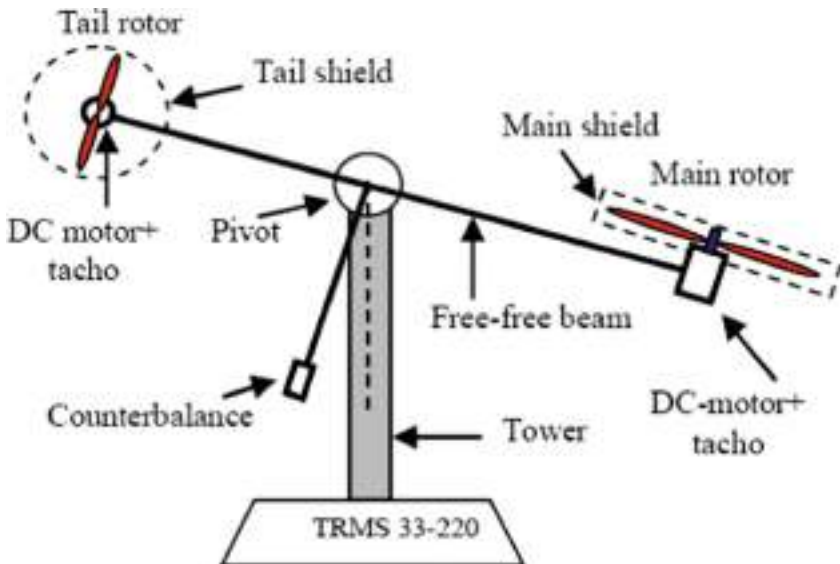


Fig. 1. Laboratory model of the TRMS

Table 1. 2-DOF laboratory model parameters [2]

	Depiction	Numbers
G_a	Inertia of main motor	$6.8 \times 10^{-2} \text{ kg} \cdot \text{m}^2$
G_b	Inertia of tail motor	$2 \times 10^{-2} \text{ kg} \cdot \text{m}^2$
A_1	Fixed constant for main	0.0135
B_1	Fixed constant for tail	0.02
A_2	Fixed constant for main 2	0.02
B_2	Fixed constant for tail 2	0.09
m_g	gMomentum	0.32 N . m
$B_{1\psi}$	Tail rotor friction momentum	$6.8 \times 10^{-3} \text{ N-m-s/rad}$
$B_{1\phi}$	Main rotor friction momentum	$1 \times 10^{-1} \text{ N-m-s/rad}$
k_{gy}	Gyroscopic effect momentum	0.05 rad/s
k_1	Motor 1	1.1
k	Motor 2	0.8
t_{11}	Margin of the denominator for motor 1	1.1
t_{10}	Margin of the numerator for motor 1	1
t_{21}	Margin of the denominator for motor 2	1
t_{20}	Margin of the numerator for motor 2	1
k_c	Cross reaction momentum gain	-0.2

Now here in Eq. (1) the main system plant mathematical modeling is provided. Here A, B, C, D may be considered as the state matrices

$$\begin{aligned} \dot{X} &= Ax + Bu \\ Y &= Cx + Du \end{aligned} \tag{1}$$

$$\text{Where, } A = \begin{bmatrix} 0 & 1 & 0 & 0 & 0 & 0 \\ A_{21} & A_{22} & 0 & 0 & A_{25} & 0 \\ 0 & 0 & 0 & 1 & 0 & 0 \\ 0 & 0 & 0 & A_{44} & A_{45} & A_{46} \\ 0 & 0 & 0 & 0 & A_{55} & 0 \\ 0 & 0 & 0 & 0 & 0 & A_{66} \end{bmatrix}$$

$$B = \begin{bmatrix} 0 & 0 & 0 & 0 & B_{15} & 0 \\ 0 & 0 & 0 & 0 & 0 & B_{26} \end{bmatrix}^T, C = \begin{bmatrix} 1 & 0 & 0 & 0 & 0 & 0 \\ 0 & 1 & 0 & 0 & 0 & 0 \end{bmatrix}, A = \begin{bmatrix} 0 & 0 \\ 0 & 0 \\ 0 & 0 \\ 0 & 0 \end{bmatrix} \tag{2}$$

Where $A_{21} = -\frac{m_g}{G_a}$, $A_{22} = \frac{B_{1\psi}}{G_a}$, $A_{25} = \frac{A_1}{G_a}$, $A_{44} = \frac{B_{1\phi}}{G_b}$, $A_{45} = \frac{-1.75k_c B_1}{G_a}$, $A_{46} = \frac{B_2}{G_b}$,
 $A_{55} = \frac{-t_{10}}{t_{11}}$, $A_{66} = \frac{-t_{20}}{t_{21}}$, $B_{15} = \frac{k_1}{t_{11}}$, $B_{26} = \frac{k_2}{t_{21}}$

After defining various mathematical expressions it has been seen that the model possess six states and these states are provide by Eq. 3 for a 2-DOF TRMS system [3].

$$\begin{aligned}
 \frac{d\phi}{dt} &= \dot{\phi} = x_1; \\
 \frac{d\psi}{dt} &= \dot{\psi} = x_2; \\
 \frac{d\dot{\phi}}{dt} &= \frac{a_1}{G_a} \rho_1^2 + \frac{b_1}{G_a} \rho_1 - \frac{m_g}{G_a} \sin(\psi) + \frac{0.0326}{2G_a} \sin(2\psi) \phi^2 - \frac{B_1 \psi}{G_a} \dot{\psi} - \frac{k_{gy}}{G_a} \cos(\psi) \phi (a_1 \rho_1^2 + \\
 b_1 \rho_1) &= x_3; \quad \frac{d\dot{\psi}}{dt} = \frac{a_2}{G_b} \rho_2^2 + \frac{b_2}{G_b} \rho_2 - \frac{B_1 \phi}{G_b} \dot{\phi} - \frac{1.75K_c}{G_b} \cos(\psi) \phi (a_1 \rho_1^2 + \\
 b_1 \rho_1) &= x_4 \\
 \frac{d\rho_1}{dt} &= -\frac{t_{10}}{t_{11}} \rho_1 + \frac{k_1}{t_{11}} u_v = x_5 \\
 \frac{d\rho_2}{dt} &= -\frac{t_{20}}{t_{21}} \rho_2 + \frac{k_2}{t_{21}} u_h = x_6
 \end{aligned} \tag{3}$$

The different states are $(\dot{\phi}, \ddot{\phi}, \dot{\psi}, \ddot{\psi}, \rho_1, \rho_2)$ where $\dot{\phi}(x_1)$ is the first derivative of main rotor location, $\ddot{\phi}(x_2)$ is the acceleration of main rotor location, $\dot{\psi}$ & $\ddot{\psi}$ can be mentioned as tail rate of change of position and its acceleration, ρ_1 & ρ_2 are the main rotor and tail rotor time constants. Using the values from Table 1 state space equations can be established, now to find the transfer function of the non linear model MATLAB is used and the result appeared as Eq. 5. After simplifying the transfer function matrix of the TRMS the segregated matrix looks like Eq. 4 [3].

$$G(s) = \begin{bmatrix} g_{11}(s) & g_{12}(s) \\ g_{21}(s) & g_{22}(s) \end{bmatrix} \tag{4}$$

Using $g_{11}(s)$ and $g_{22}(s)$ a 1-DOF decoupled model may be designed, now some of the coupled factors has less effect due to the mechanical construction of the model, the horizontal to vertical system transfer function $g_{12}(s)$ can be neglected, the vertical to horizontal transfer functions cannot be neglected as it has some impact due to the state matrix equations of the main rotor.

$$\begin{aligned}
 g_{11}(s) &= \frac{1.36}{s^3 + 0.9973s^2 + 4.79s + 4.28} \\
 g_{12}(s) &= 0 \\
 g_{21}(s) &= \frac{1.617}{s^3 + 5.909s^2 + 4.546s} \\
 g_{22}(s) &= \frac{3.6}{s^3 + 6s^2 + 5s}
 \end{aligned} \tag{5}$$

System model for the horizontal angle position can be illustrated as Eq. 6.

$$\frac{\Psi(s)}{U_v(s)} = \frac{1.359}{s^3 + 0.9973s^2 + 4.786s + 4.278} \tag{6}$$

System model for the vertical angle position can be illustrated as Eq. 7.

$$\frac{\varphi(s)}{U_h(s)} = \frac{3.6}{s^3 + 6s^2 + 5s} \tag{7}$$

The transfer function g_{12} denotes from horizontal to vertical coupled system and g_{21} denotes the vertical to horizontal coupled system.

2.1 Model Identification

This identification method may be achieved by the matlab least mean square identification method. This procedure enhances the modeling of controller. The plant is nonlinear so to design a controller for such plants is very difficult task. The TRMS may be used as a linearised model while is it actually a non-linear one. The controller should be able to balance both the rotors and should follow the reference angle provided by the user.

The pitch angle tentative transfer function is provided in (4) where $g_{11}(s)$ represents the same and yaw angle tentative transfer function is denoted by $g_{22}(s)$, the cross couplings of horizontal and vertical axis are respectively provided by $g_{12}(s)$ and $g_{21}(s)$.

2.2 Controller Design

Here after plant identification the controller may be decided where to stabilize such nonlinear model is very difficult. For TRMS control a Fuzzy Logic Controller (FLC) has been opted as a controller [10]. The simulation and real time models are shown in the next section. Now for the pitch control and yaw stabilization similar controller may be witnessed in the next sections. As an introduction to the FLC the classical fuzzy control may be formulate to the fuzzy inputs, outputs, rules and defuzzification. This FLC reduces the deviation in state trajectories of a system while maintaining minimum control effort (Fig. 2).

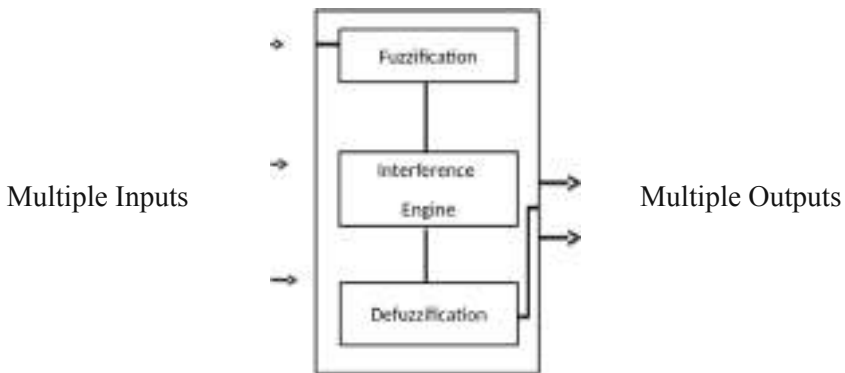


Fig. 2. Open-loop system using fuzzy logic controller

Fuzzyfication is a process which may convert the crisp values into fuzzy set values later on which may be applied in a suitable operation like as [8]. The next step is to decide the rules, where the decision made by fuzzy logic controller are derived from the rules known as fuzzy rules and is discussed in terms of ‘If’ and ‘Then’ statements.

2.3 Coupled Control Effect

In this paper two separate FLC has been considered and in an nonlinear plant. The block diagram of the close loop unity feedback control is shown in Fig. 3, where $G_{hplant}(s)$, $G_{vplant}(s)$, $G_{v1plant}(s)$, and $G_{h1plant}(s)$ denotes the four plant TF, $C_h(s)$ FLC defines the horizontal controller TF, $C_v(s)$ FLC defines the vertical controller TF where $U_1(s)$ and $U_2(s)$ are two input responses, $E_1(s)$ and $E_2(s)$ represents the error signals. Two separate disturbance was injected in different planes of the helicopter. In this study of 2-DOF helicopter two different fuzzy controllers has been developed, one is for horizontal plane and another for vertical plane. Both the controllers work simultaneously to using similar fuzzy rules provides desired output. One is for pitch control and the other controls yaw. Both these controllers are developed using Mamdani Inference [15] which is designed using MATLAB. To establish the multiple input and multiple output it is very difficult to set the rules of both the controllers. The inputs are considered to be beam angle error and the first-time derivative of beam angle error. Figure 4 illustrates the membership functions of the inputs and outputs for beam angle error. The most important part of fuzzy controller design is the determination of fuzzy rule base.

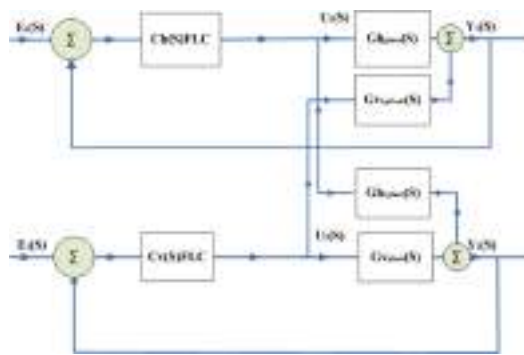


Fig. 3. Block diagram for the FLC used in MIMO system

After considering the system behavior in both vertical and horizontal planes the fuzzy rules were decided for these two controllers. The identical rule bases have been used for vertical and horizontal plane two identical controllers of similar rules were tried to establish which possibly suits the output response behavior for both the plants (Figs. 5 and 6).

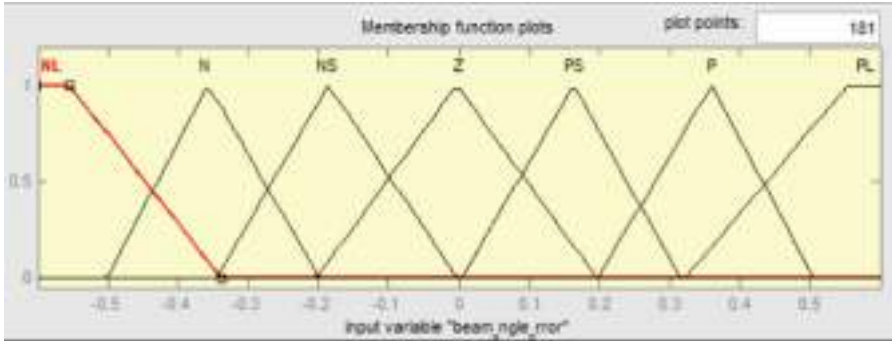


Fig. 4. Beam angle error (E_r) membership function

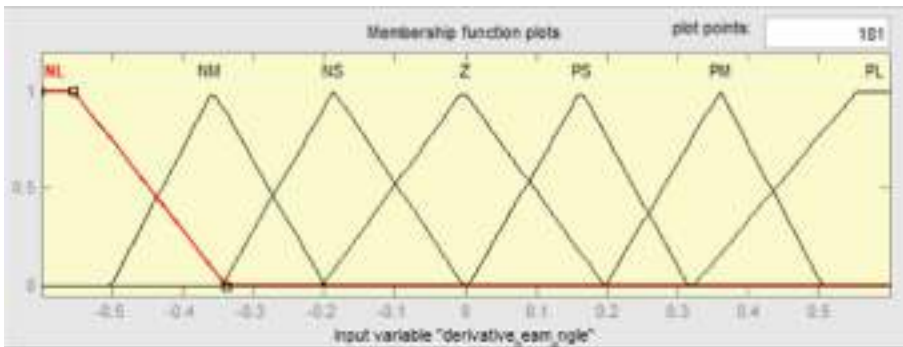


Fig. 5. Rate of change of beam angle error (ΔE_r) membership function

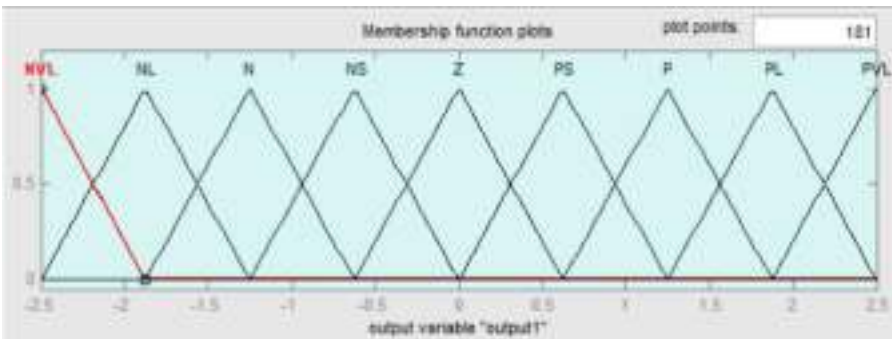


Fig. 6. Output controller membership function

In this fuzzy logic controller (FLC) triangular membership function designing is not intricate but the output is precise and accurate, so to avoid the complexity of the controller this membership function is used. Using triangular membership function (MF) arithmetic operations becomes easier. The triangular MFs are formed using straight lines, these straight line membership functions have the advantage of simplicity. In order to maximize their performance, it is often necessary to undertake a design optimization process in which the adjustable parameters defining a particular fuzzy system are tuned to maximize a given performance criterion. Triangular shapes are simple to implement and fast for computation, triangular shapes represent fuzzy numbers only. Comparing other MFs triangular MFs are effortless when bifurcated variables (low, medium, high) are measured. Based on extensive review on many literatures, it can be concluded that the triangular MF is widely used because of its simplicity (Table 2).

Table 2. The rules based on the behaviour of both the fuzzy controllers [14].

$\Delta E_r \setminus E_r$	nl	nm	ns	z	ps	pm	pl
nl	nvl	nvl	nl	nm	ns	ns	z
n	nvl	nl	nm	nm	ns	z	ps
ns	nl	nm	ns	ns	z	ps	pm
z	nm	ns	ns	z	ps	ps	pm
ps	nm	ns	z	ps	ps	pm	pl
p	ns	z	ps	pm	pm	pl	pvl
pl	z	ps	ps	pm	pl	pvl	pvl

3 Illustrative Example

3.1 Simulation Result

The TRMS system horizontal and vertical plane responses are being discussed in this section, where from the Fig. 7 it can be easily detected that the desired and the original response converges very fast to the stability. In [4, 5, 13] different types of FLC approaches are being introduced, where some of them are neuro-fuzzy combined system. The simulink model is shown in Fig. 7 which shows how to design the controller for a coupled MIMO system. It is very complex problem to be decided still the desired output has a less steady state error. New fuzzy controller gains were introduced in both the plants to maintain the sustainability to track the specified trajectory with rapid and precise action.

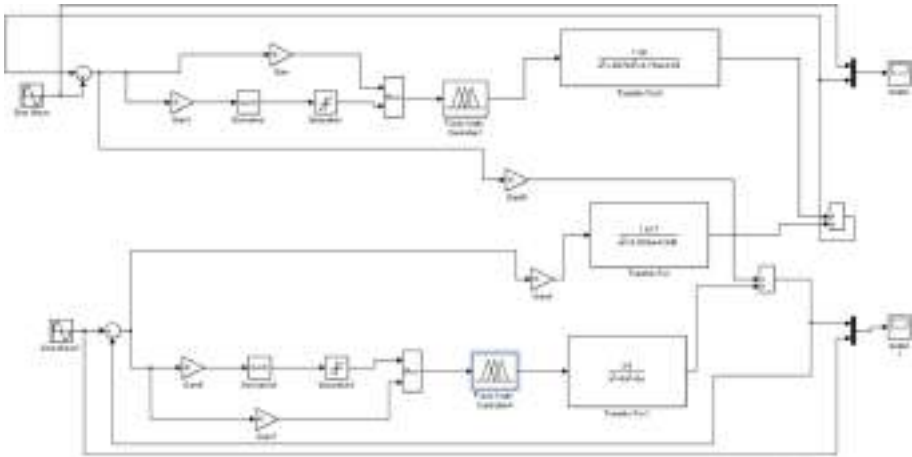


Fig. 7. Fuzzy control of the TRMS horizontal part and vertical parts.

Figures 8 and 9 are showing the simulated plant results of pitch and yaw respectively after a periodic sinusoidal reference, where in Fig. 9 the real model MATLAB implementation is discussed, where it is clearly shown that two FLC has been designed for different planes. Figures 13 and 15 showing the system open loop transfer function response for two different plants of pitch and yaw respectively. The steady state error for both the plants in periodic sinusoidal is less than 0.2 (Figs. 10 and 11).

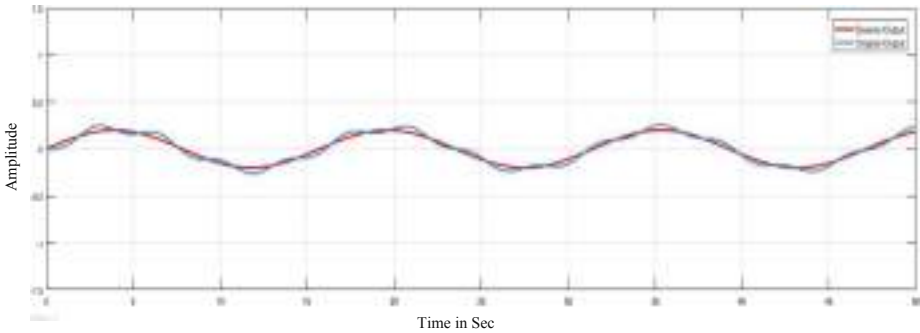


Fig. 8. FLC response of the TRMS horizontal part

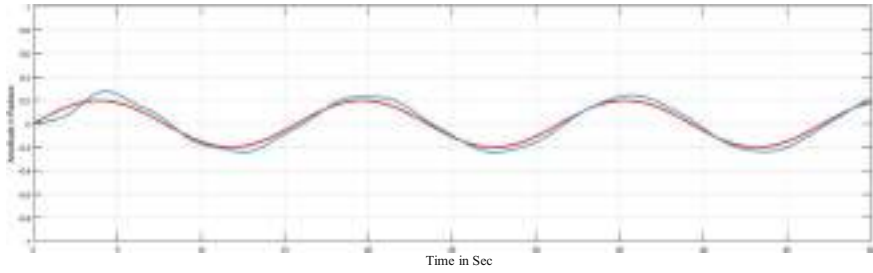


Fig. 9. FLC response of the TRMS vertical part

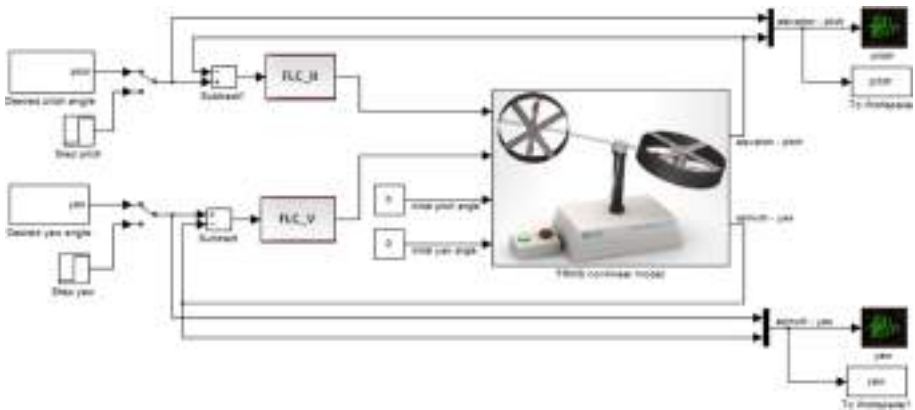


Fig. 10. Real model implementation for both the planes

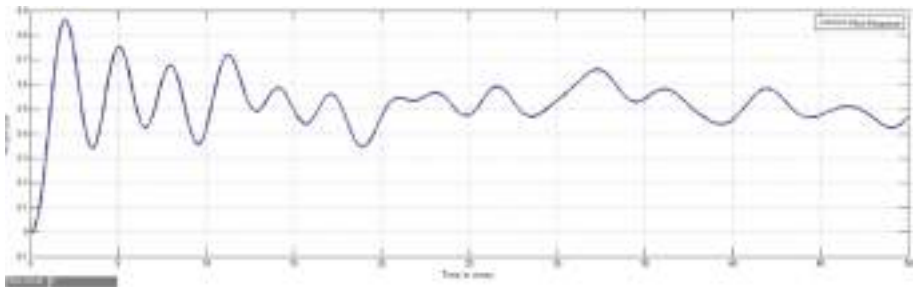


Fig. 11. Real Plant 2-DOF TRMS Pitch open loop response

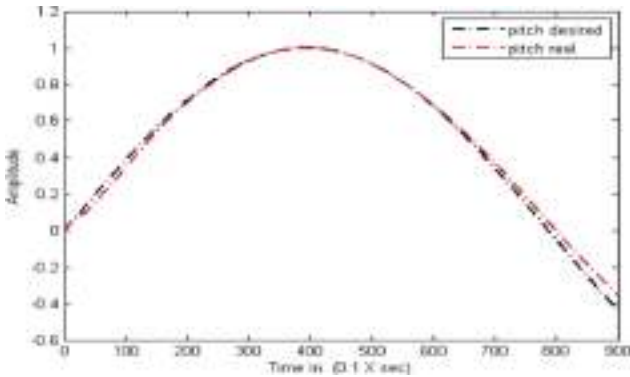


Fig. 12. Real plant 2-DOF TRMS Pitch FLC response

In real plant of TRMS for both horizontal and vertical planes FLC is been implemented. In [10] the coupled TRMS model rise time responses for pitch and yaw are 1.22 s and 1.188 s, where as in this section it has been seen that it is 1.1 s and 1.08 s respectively. A comparative statement of various results is show in Table 3.

Table 3. Comparative statement with [10] and [16]

		[10]	[16]	FLC
Rise time (sec)	P	1.22	4.1	1.1
	Y	1.188	2.01	1.08
Overshoot (%)	P	-	-	0.03
	Y	-	-	5.2
Settling time (sec)	P	1.596	6.2	7.3
	Y	1.529	4.1	2.5
Steady state error	P	0.373	0.23	0.211
	Y	0.1151	0.01	0.06

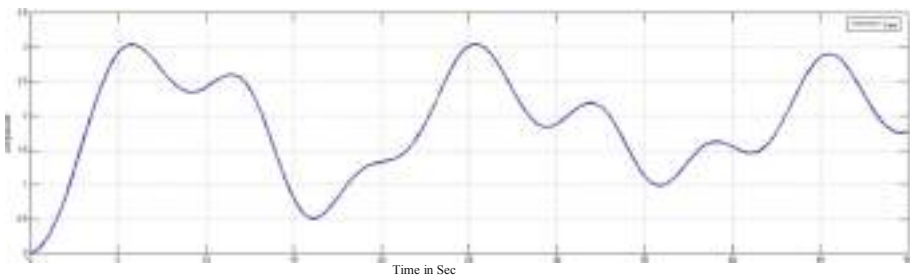


Fig. 13. Real Plant 2-DOF TRMS Yaw open loop

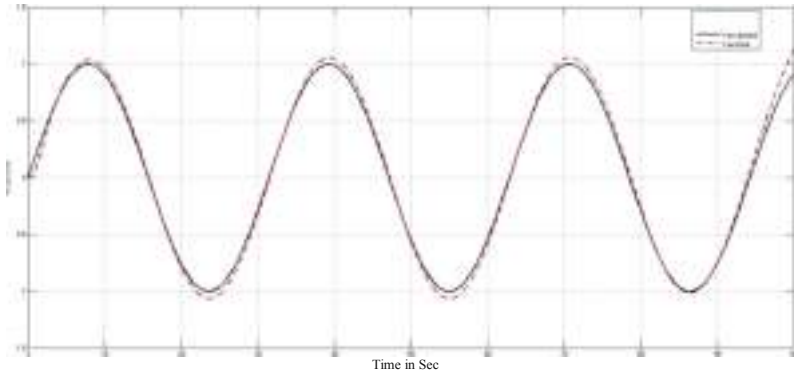


Fig. 14. Real plant 2-DOF TRMS Yaw FLC response

The real model 2-DOF responses of both the plants are shown in the Figs. 12 and 14, which implies a great convergence to the desired response. The selection criteria of beam angle error and rate of change of beam angle error is quite definite and stabilizing both the horizontal and vertical planes very rapidly. The reference signal was considered as random sinusoidal but periodic waves for both the plants. Now in case of step response being fed to the system is shown in Figs. 15 and 16, which implicates that the steady state error is very less after using the controllers for both the plants. The convergence is very fast towards stability for both the systems i.e. yaw and pitch. The controller response is synchronised with the reference signal in such a manner that the error becomes less than 0.1 for both the plants.

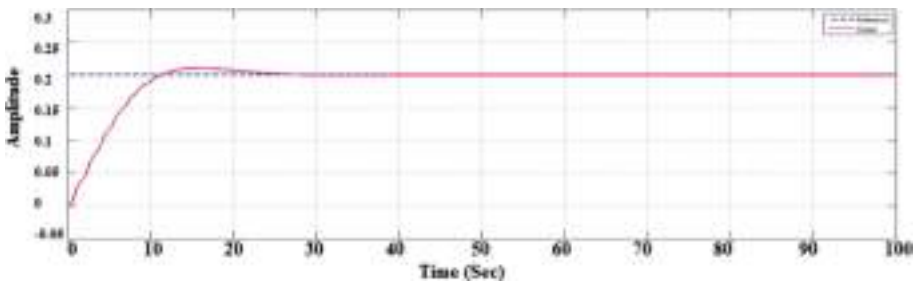


Fig. 15. Real plant 2-DOF TRMS Pitch FLC response for Step response at 0.2

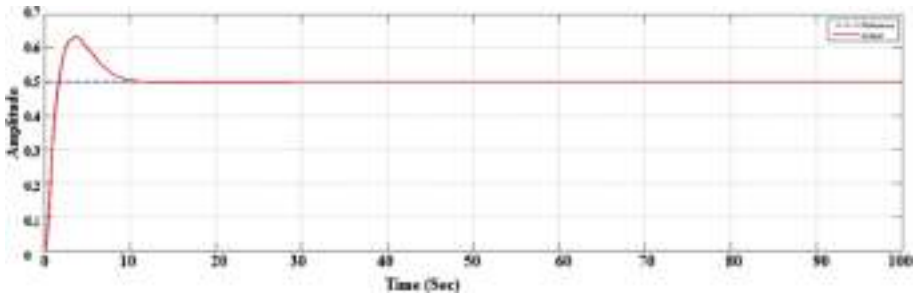


Fig. 16. Real plant 2-DOF TRMS Yaw FLC response for Step response at 0.5

4 Conclusion

In this paper it has been tried to establish a simple and effective control via intelligent method to a very complex nonlinear problem. Although it has been shown with the suitable variables and rules set the problem is controllable. A simple and non-complicated FLC was used for both the planes of pitch and yaw position control which is working very effectively. A triangular membership function was introduced to converge the system responses very rapid and precise. Accordingly, the shape of MFs are important for a this problem since it effects the fuzzy inference system. The beam error and the rate of change of beam error was the variable parameters to set fuzzy rules for this coupled system of TRMS. The steady state error is mitigated here in this paper using the simple coupled FLC in both the planes.





References

1. Zadeh, L.A.: Fuzzy sets. *Inf. Control* **8**, 338–353 (1965)
2. Zadeh, L.A.: Fuzzy algorithms. *Inf. Control* **12**, 94–100 (1968)
3. TRMS 33–949S User Manual. Feedback Instruments Ltd., East Sussex, U.K. (2006)
4. Wen, P., Lu, T.-W.: Decoupling control of a twin rotor MIMO system using robust deadbeat control technique. *IET Control Theory Appl.* **2**(11), 999–1007 (2008)
5. Aras, A., Kaynak, O.: Trajectory tracking of a 2-DOF helicopter system using neuro-fuzzy system with parameterized conjunctors. In: *IEEE/ASME International Conference on Advanced Intelligent Mechatronics* (2014)
6. Goodwin, G.C., Graebe, S.F., Salgado, M.E.: *Control System Design*. Pearson, London (2000)
7. Nguyen, C.H., Leonessa, A.: Predictor-based adaptive output feedback control: application to functional electrical stimulation of a human arm model. *ASME J. Dyn. Syst. Measur. Control* **138**(8), 111014 (2016)
8. Rong, H., Yang, Z., Wong, P.K., Vong, C.M.: Adaptive self-learning fuzzy autopilot design for uncertain bank-to-turn missiles. *ASME. J. Dyn. Sys., Measur. Control* **139**(4), 041002 (2017)
9. Ghorbel, H., El Hajjaji, A., Souissi, M., Chaabane, M.: Robust tracking control for Takagi–Sugeno fuzzy systems with unmeasurable premise variables: application to tank system. *ASME. J. Dyn. Syst. Measur. Control* **136**(4), 041011 (2014)

10. Taskin, Y.: Improving pitch and yaw motion control of twin rotor MIMO system. *J. Vibroengineering* **16**(4), 1650–1660 (2014)
11. Nguyen, Q.V., Hyun, C.-H.: Multiple sliding surface control approach to twin rotor MIMO systems. *Int. J. Fuzzy Logic Intell. Syst. Int. J. Fuzzy Logic Intell. Syst.* **14**(3), 171–180 (2014)
12. Zeghlache, S., Kara, K., Saigaa, D.: Type-2 fuzzy logic control of a 2-DOF helicopter (TRMS system). *Cent. Eur. J. Eng.* **303**(4) (2014)
13. Kar, A., Hui, N.B.: Control of two-axis helicopter model using fuzzy logic. *Comput. Intell. Commun. Bus. Anal.* **776**, 585–598 (2017)
14. Hashim, H.A., Abido, M.A.: Fuzzy controller design using evolutionary techniques for twin rotor MIMO system: a comparative study. *Comput. Intell. Neurosci.* **2015**, 704301 (2015)
15. Assilian, S., Mamdani, E.H.: Learning control algorithms in real dynamic systems. In: *Proceedings of the 4th International IFAC/IFIP Conference on Digital Computer Applications to Process Control*, Zürich, March 1974
16. Singh, A., Sharma, S., Yadav, S.A.: Fuzzy Logic Based Control of a Dual Rotor MIMO. <https://amity.edu/UserFiles/ajjem/IFuzzy%20Logic.pdf>



Solar Cell Efficiency Enhancement Using Embedded Surface Plasmonic Nanoparticles in Various Medium

Diptanu Dey , Amit Chakraborty , Anurendra Singh  ^(✉),
and Priyanath Das 

Electrical Engineering Department, National Institute of Technology,
Agartala, Agartala, India
ddiptanu.career@gmail.com,
amitchakraborty.agartala@gmail.com,
anurendrasingh7046@gmail.com, priyanath70@gmail.com

Abstract. The paper deals with mainly two objectives, first the study of silver surface plasmonic nanoparticles embedded in the various substrates and how they can improve the efficiency of a solar cell. Here silver nanoparticles embedded in different substrates of a solar cell we found out the various types of light scattering and light absorption with the help of MIE scattering software. The secondary objective is to study the effect of nanoparticle size and standard deviation on light scattering and absorption. Also to find which of the plasmonic nanoparticle is the best suitable to improve the performance of the solar cell. The methodology used in this work can be summarized as follows: The literature review on surface plasmons and how it enhances solar cell efficiency is done. The research study on MIE Scattering and MIE theory is also done. The analysis of a silver sample with different mediums and comparing the variations in peak wavelength using MIE PLOT software and graphs were plotted. The effect of particle size and standard deviation on Cscattering, Cabsorption, Qscattering and Qabsorption were done.

Keywords: MIE scattering · Glass medium · Scattering · Absorption · Deviation

1 Introduction

This paper deals with the study of improving solar cell efficiency by using plasmonic nanoparticles on the surface embedded in the silver substrates. With the help of MIE scattering software we can find out the various types of light scattering and absorption shown by silver in different embedded substrates like glass, cSi, aSi, pSi, etc. [1].

Importance of Plasmon in Improving Solar Cells Efficiency

The Plasmonic solar cells using plasmons convert the light photons into electricity.

This is done by two methods.

- On the upper surface of the absorber layer is formed by metal nanoparticles so particles can couple and trap freely propagating plane waves from the sun [2].

- The consistent oscillation of conduction electrons at a metal/dielectric interface is surface plasmons. The light absorption and efficiency can be improved in the solar cell by using the surface plasmons with the support of metallic nanostructures on the back surface of absorber using a corrugated metallic film [3].

2 MIE Scattering

The maxima and minima in the plot of intensity with angle are explained by MIE theory [4].

Conditions for MIE Theory

- Only monochromatic light is considered-theory applies to the formation of scattering pattern by a single wavelength of light.
- The particle is isotropic - no matter which direction the light radiation comes.
- The particle is spherical.
- Incident light consists of 2 plane waves.

In this project, we analyze the results for Silver sample by changing the nanoparticle size from 20 nm–200 nm and comparing the

1. $C_{ext}/C_{sca}/C_{abs}$ Vs wavelength
2. $Q_{ext}/Q_{sca}/Q_{abs}$ VS wavelength where
 - C_{ext} - Coefficient of Extinction which is the sum of absorption and scattering.
 - C_{abs} - Coefficient of absorption.
 - C_{sca} - Coefficient of scattering.
 - Q_{SCA} - Efficiency of scattering.
 - Q_{ABS} - Efficiency of absorption [5, 6].

3 Analysis of SILVER Sample

Procedure

1. Select the ($C_{ext}/C_{sca}/C_{abs}$ Vs wavelength) & ($Q_{ext}/Q_{sca}/Q_{abs}$ Vs Wavelength) option in the MIEPLOT software.
2. Select DISPERSE and standard deviation 5% and nanoparticle size 20nm.
3. Keep Number of particles (N)=50
4. Go to advanced setting and - select drop size in terms of diameter, Refractive index-sphere (silver) and surrounding medium-user defined.
5. The peak wavelength range should be from 300 nm–1200 nm as we are interested in the visible region.
6. Select the Number of steps in the range 1000.
7. The horizontal and intensity scale should be linear.
8. Save the file as a text file.

3.1 Four Different Silver Samples

3.1.1 Analysis of SILVER in Glass Medium

Firstly we are analyzing the results of silver on glass medium by varying the nanoparticle size from 20 nm–200 nm and compare $C_{ext}/C_{sca}/C_{abs}$ Vs wavelength & $Q_{ext}/Q_{sca}/Q_{abs}$ Vs wavelength. An example has been done here. Ex: silver in glass medium (20 nm nanoparticle size) [7] (Fig. 1).

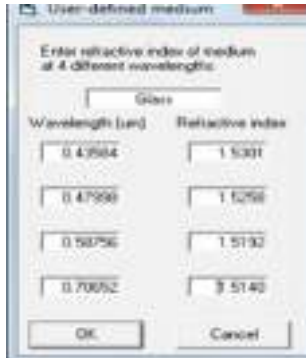


Fig. 1. Refractive index corresponding to different wavelength in the glass medium

Result Obtained

See Figs. 2, 3, 4 and 5.



Fig. 2. MIE scattering, silver in glass ($C_{ext}/C_{sca}/C_{abs}$ Vs wavelength)



Fig. 3. MIE scattering, silver in glass ($Q_{ext}/Q_{sca}/Q_{abs}$ Vs wavelength)

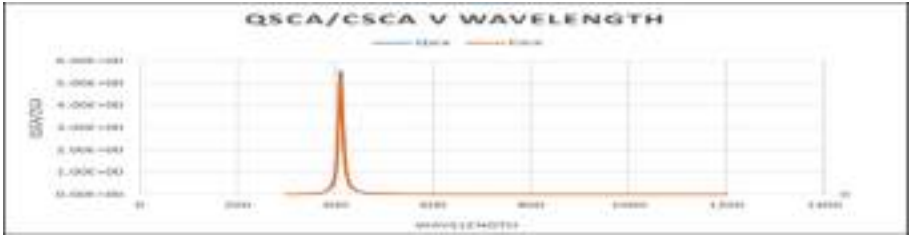


Fig. 4. Graph of Qsca/Csca Vs Wavelength

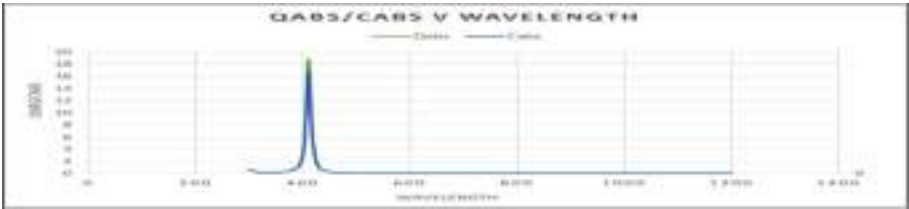


Fig. 5. Graph of Qabs/Cabs Vs Wavelength

3.1.2 Analysis of Silver on cSi Medium

Here we analyze the results of silver on cSilicon medium by varying the nanoparticle size from 20 nm–200 nm and comparing Cext/Csca/Cabs VS wavelength & Qext/Qsca/Qabs VS wavelength [8].

Result Obtained

See Figs. 6, 7, 8 and 9.

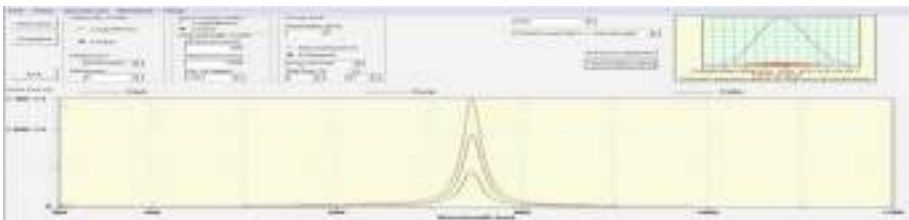


Fig. 6. MIE scattering, silver in cSi (Cext/Csca/Cabs Vs wavelength)

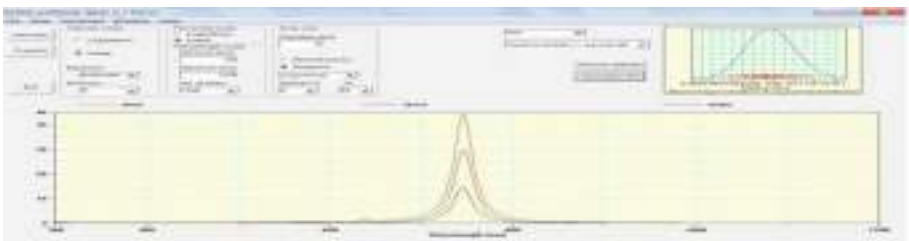


Fig. 7. MIE scattering, silver in cSi (Qext/Qsca/Qabs Vs wavelength)

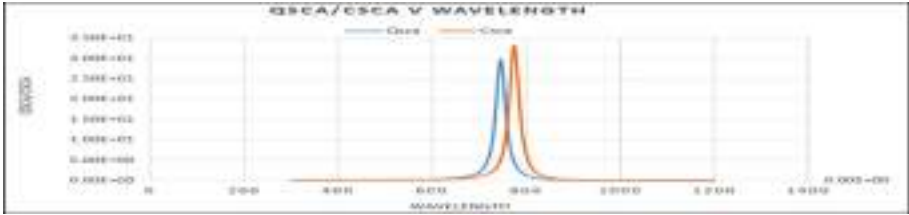


Fig. 8. Graph of Q_{sca}/C_{sca} Vs Wavelength

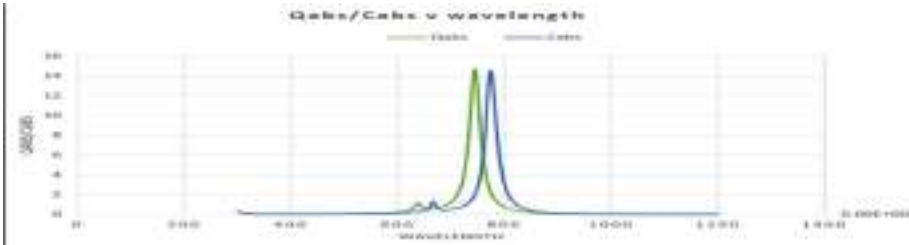


Fig. 9. Graph of Q_{abs}/C_{abs} Vs Wavelength

3.1.3 Analysis of Silver on pSi Medium

Here we analyze the results of silver on pSi medium by varying the nanoparticle size from 20 nm–200 nm and comparing $C_{ext}/C_{sca}/C_{abs}$ Vs wavelength & $Q_{ext}/Q_{sca}/Q_{abs}$ Vs wavelength [9].

Result Obtained

See Figs. 10, 11, 12 and 13.

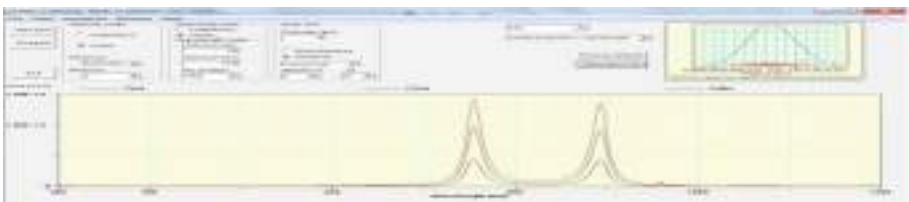


Fig. 10. MIE scattering, silver in pSi ($C_{ext}/C_{sca}/C_{abs}$ Vs wavelength)

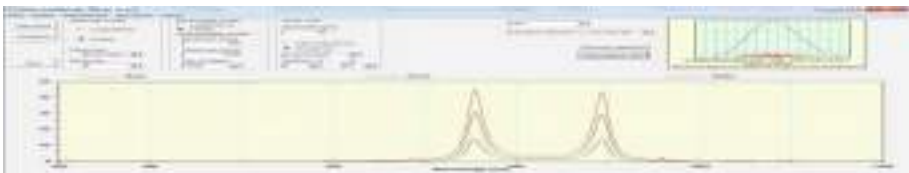


Fig. 11. MIE scattering, silver in pSi ($Q_{ext}/Q_{sca}/Q_{abs}$ Vs wavelength)

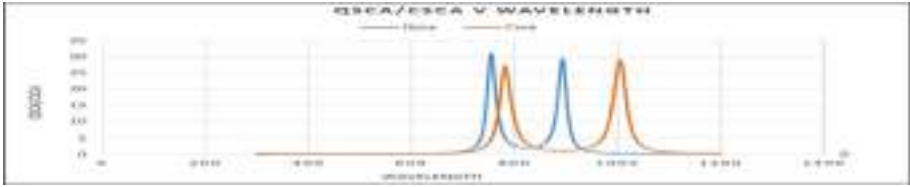


Fig. 12. Graph of Qsca/Csca Vs Wavelength

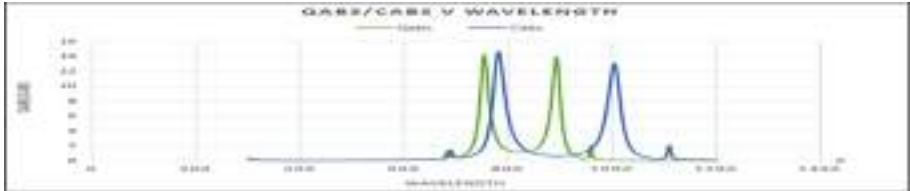


Fig. 13. Graph of Qabs/Cabs Vs Wavelength

3.1.4 Analysis of Silver on aSi Medium

Here we analyze the results of silver on aSi medium by varying the nanoparticle size from 20 nm–200 nm and comparing Cext/Csca/Cabs Vs wavelength & Qext/Qsca/Qabs Vs wavelength [10].

Result Obtained

See 14, 15, 16, 17.

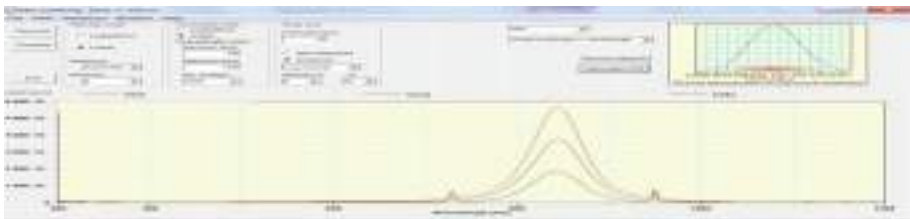


Fig. 14. MIE scattering, silver in aSi (Cext/Csca/Cabs Vs wavelength)

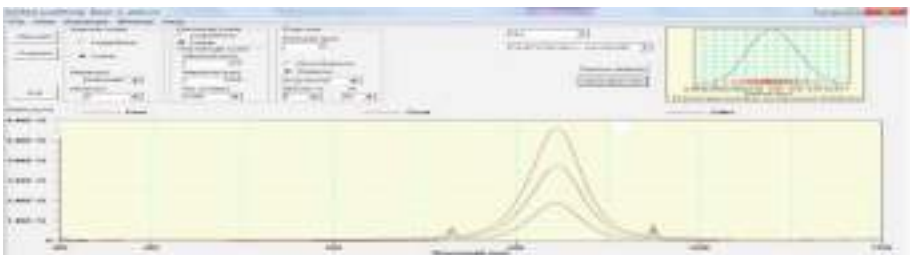


Fig. 15. MIE scattering, silver in aSi (Qext/Qsca/Qabs Vs wavelength)

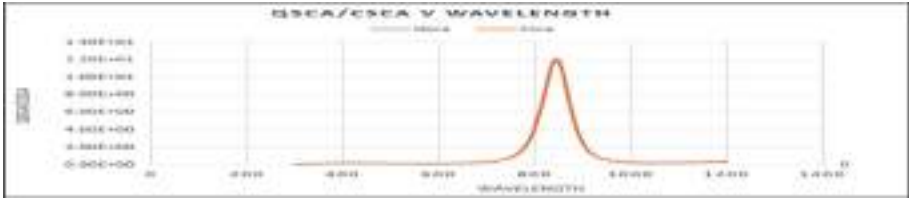


Fig. 16. Graph of Qsca/Csca vs Wavelength

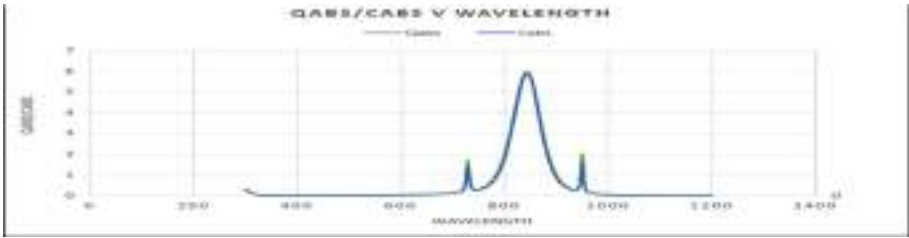


Fig. 17. Graph of Qabs/Cabs Vs Wavelength

Graphs of all the samples from 20 nm to 200 nm particle size are plotted in an excel file. Then the comparative study of how particle size affects the C Scattering of Silver in glass medium, Silver in cSi, Silver in pSi and Silver in aSi was done and graphs plotted.

The comparison of Qsca/Csca and Qabs/Cabs is also shown above for 4 different silver samples.

Variation of Qscattering and Qabsorption by SILVER samples at 20 nm, 5% Standard Deviation

See Figs. 18 and 19.

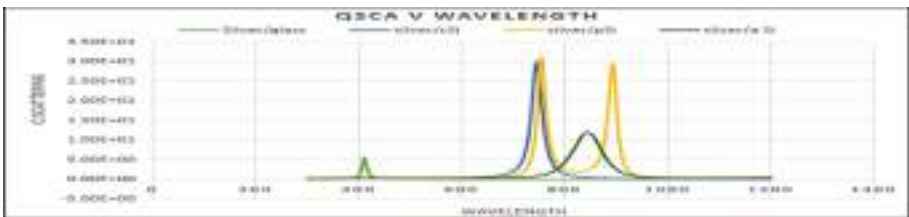


Fig. 18. Graph of Qsca Vs Wavelength

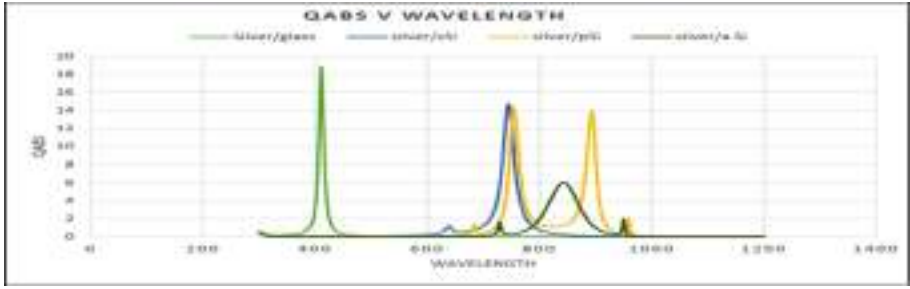


Fig. 19. Graph of Q_{abs} Vs Wavelength

Effect of Particle Size on Cscattering

See Figs. 20, 21, 22 and 23.

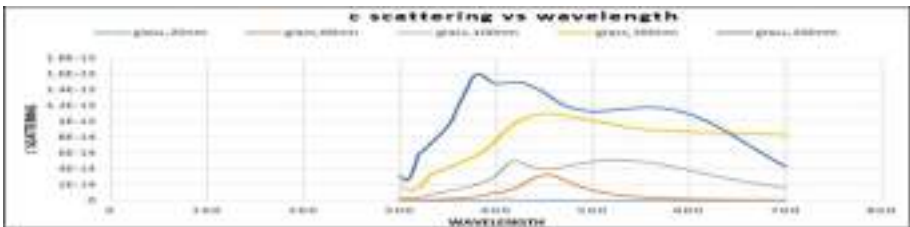


Fig. 20. Silver with glass medium (10% standard deviation)

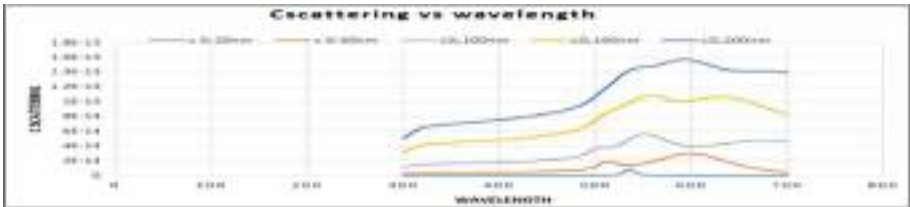


Fig. 21. Silver with cSi medium (10% standard deviation)

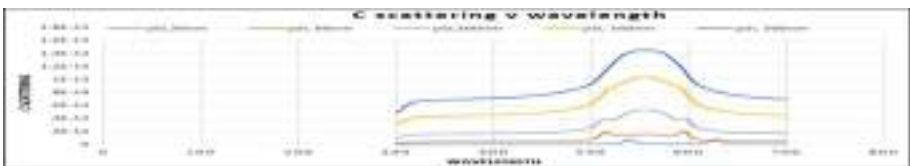


Fig. 22. Silver with pSi medium (10% standard deviation)

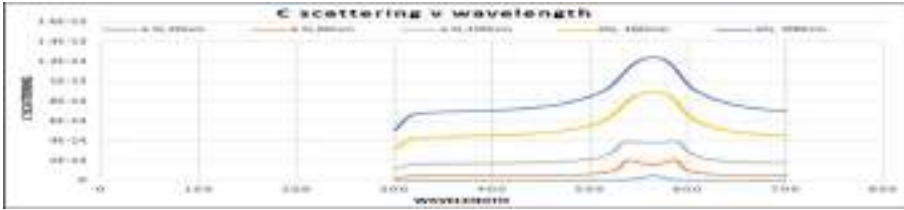


Fig. 23. Silver with aSi medium (10% standard deviation)

Result among these different mediums used, Silver (200 nm) with glass and cSi give the max Cscattering. As particle size increases, the C scattering increases in all samples. Thus nanoparticle size of the sphere directly proportional to the scattering of light.

In the PV cells market worldwide, cSi PV cells are the popular ones and they give the highest energy conversion efficiency. In the comparative study, Silver nanoparticles with cSi medium showed better light scattering compared to all other samples.

Variation of Cscattering By All Silver Samples at One Particular Nanoparticle Size and Standard Deviation

See Figs. 24, 25, 26, 27, 28.

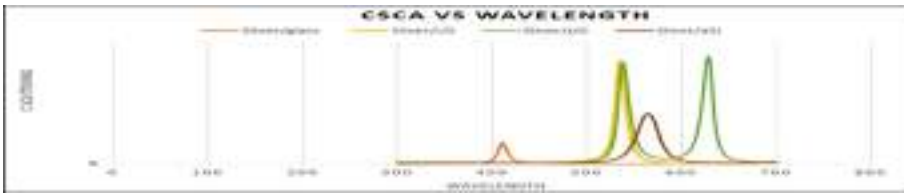


Fig. 24. Cscattering at 20 nm nanoparticle size and 10% standard deviation

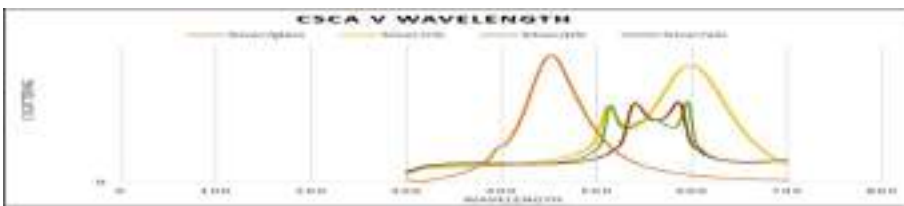


Fig. 25. Cscattering at 60 nm nanoparticle size and 10% standard deviation

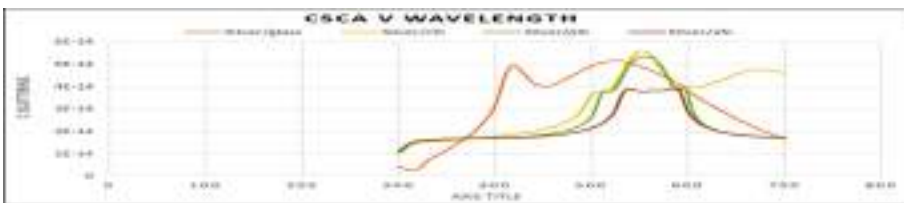


Fig. 26. Cscattering at 100 nm nanoparticle size and 10% standard deviation

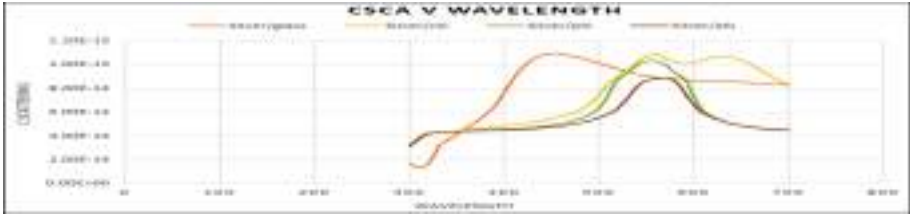


Fig. 27. Cscattering at 160 nm nanoparticle size and 10% standard deviation

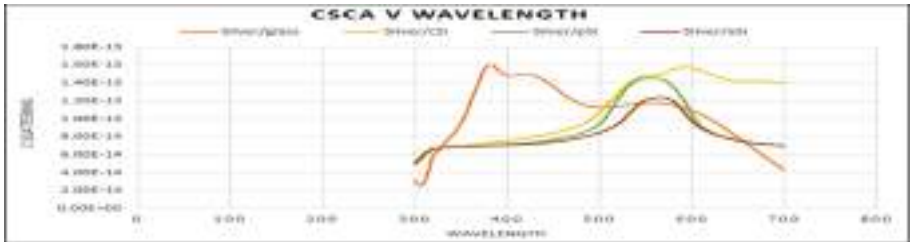


Fig. 28. Cscattering at 200 nm nanoparticle size and 10% standard deviation

Result

Comparing the above graphs, we find

At the smallest nanoparticle size 20 nm, 10% standard deviation, Silver/glass sample showed the least Cscattering and Silver/pSi showed the max. As the nanoparticle size increases (at 200 nm) we can see the Silver/glass sample showing max Cscattering and Silver/aSi sample showing the least. Silver/glass sample gives the best light scattering at a larger nanoparticle size of Silver.

Effect of Standard Deviation on C_{scattering}

See Figs. 29, 30, 31 and 32.

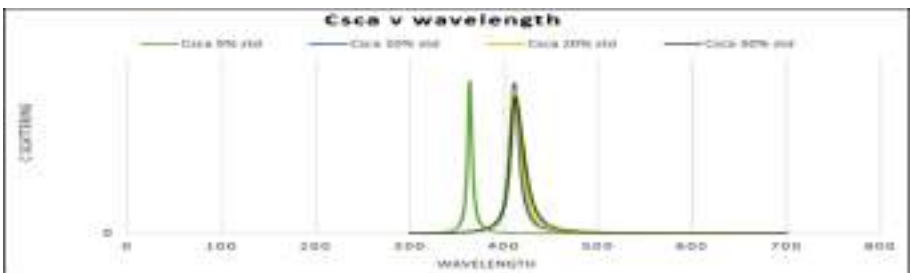


Fig. 29. Silver in glass medium (20 nm particle size)



Fig. 30. Silver in cSi medium (20 nm particle size)

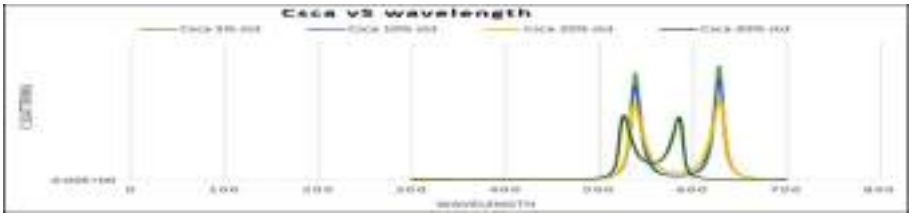


Fig. 31. Silver in pSi medium (20 nm particle size)

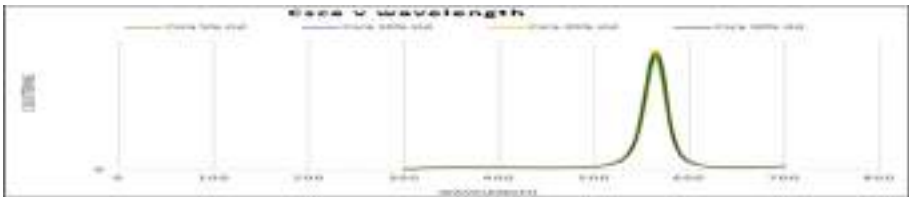


Fig. 32. Silver in aSi medium (20 nm particle size)

Result

At 5% standard deviation, all the samples showed max light scattering except Silver/aSi which showed max light scattering at 20% standard deviation. The common trend observed was light scattering inversely proportional to the standard deviation.

Effect of Particle Size on $C_{\text{absorption}}$

See Figs. 33, 34, 35 and 36.

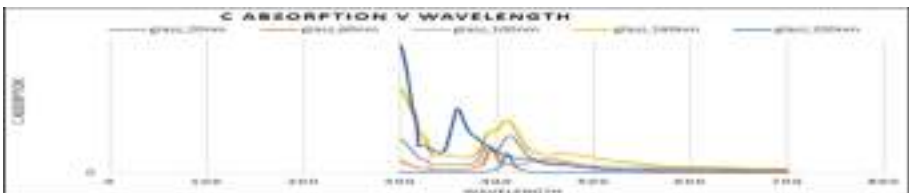


Fig. 33. Silver with glass medium (10% standard deviation)

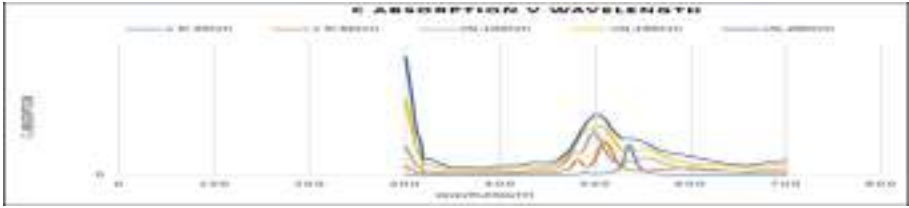


Fig. 34. Silver with cSi medium (10% standard deviation)

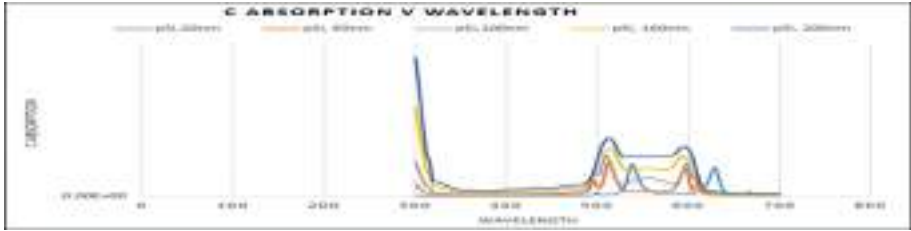


Fig. 35. Silver with pSi medium (10% standard deviation)

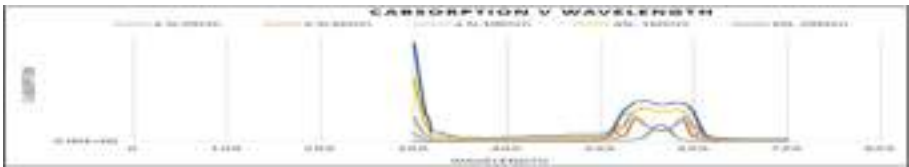


Fig. 36. Silver with aSi medium (10% standard deviation)

Result

Among these different mediums used, Silver (200 nm) with cSi gives the max Cabsorption. As particle size increases, the Cabsorption increases in all samples. Thus nanoparticle size of the sphere directly proportional to the absorption of light.

Variation of Cabsorption By All Silver Samples at a Particular Nanoparticle Size and Standard Deviation

See Figs. 37, 38, 39, 40 and 41.

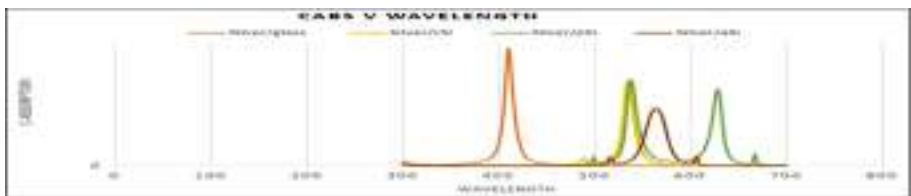


Fig. 37. Cabsorption at 20 nm nanoparticle size and 10% standard deviation

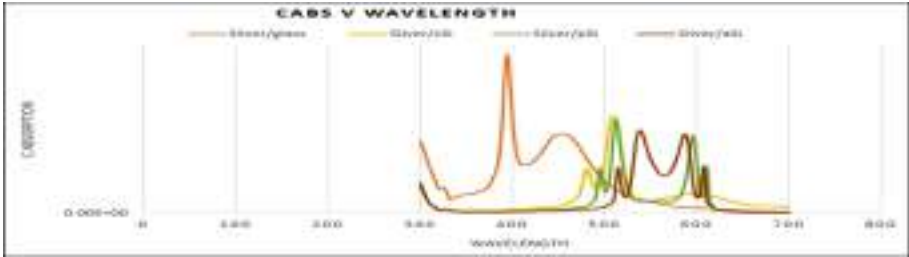


Fig. 38. Cabsorption at 60 nm nanoparticle size and 10% standard deviation

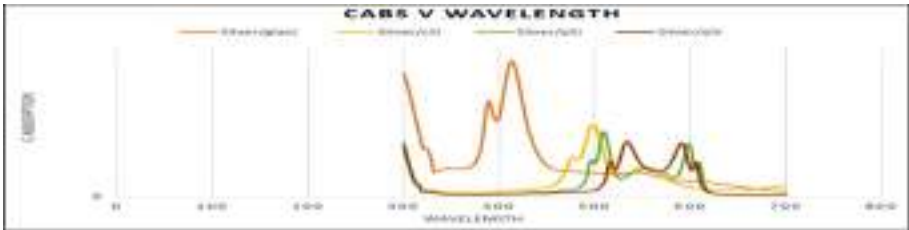


Fig. 39. Cabsorption at 100 nm nanoparticle size and 10% standard deviation

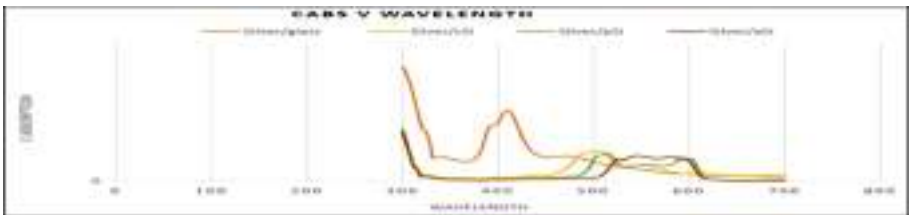


Fig. 40. Cabsorption at 160 nm nanoparticle size and 10% standard deviation



Fig. 41. Cabsorption at 200 nm nanoparticle size and 10% standard deviation

Result

In all the above graphs, the Silver-glass sample showed the highest light absorption. With an increase in nanoparticle size of Silver, the light absorption also increases in the Silver-glass sample.

At the smallest nanoparticle size 20 nm, 10% standard deviation, Silver/glass sample showed the most Cabsorption and Silver/aSi showed the least.

Effect of Standard Deviation on $C_{\text{absorption}}$

See Figs. 42, 43, 44 and 45.

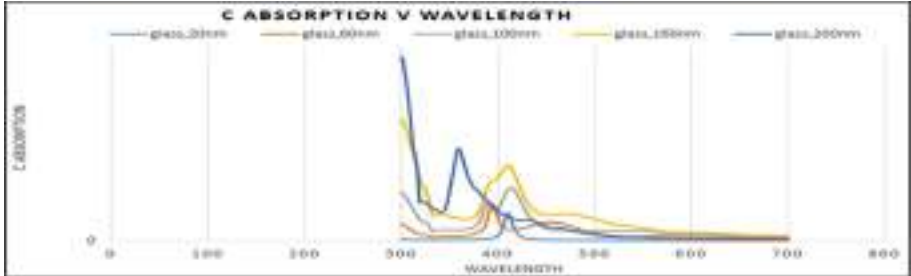


Fig. 42. Silver in glass medium (20 nm particle size)

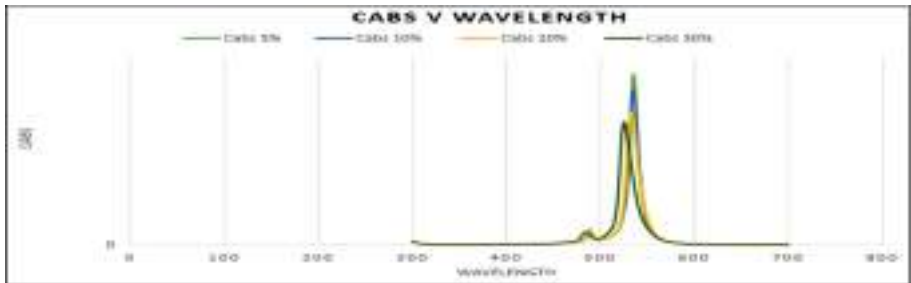


Fig. 43. Silver in cSi medium (20 nm particle size)

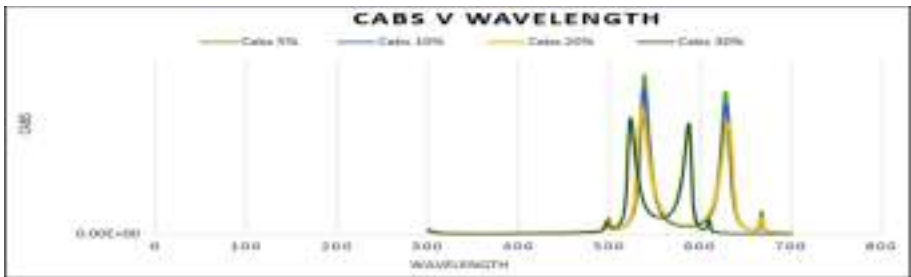


Fig. 44. Silver in pSi medium (20 nm particle size)



Fig. 45. Silver in aSi medium (20 nm particle size)

Result

At 5% standard deviation, all the samples showed max light absorption except Silver/aSi which showed max light absorption at 30% standard deviation. Silver/glass sample showed the max light absorption at 5% standard deviation among all the samples. The common trend observed was light absorption inversely proportional to the standard deviation.

Variations of C_{sca}, Q_{sca}, C_{abs}, Q_{abs} (Silver/Glass Sample)

(See Fig. 46).

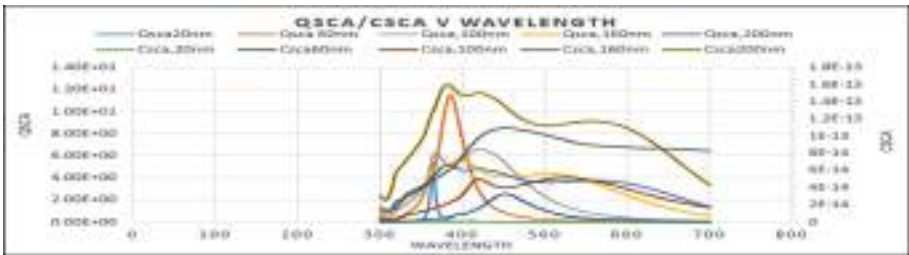


Fig. 46. Effect of particle size on Qsca and Csca

Here We See Qsca Decreasing Rapidly for Higher Wavelengths, Under 100 nm Particle Size. Almost Similar Behaviour is Shown by Csca

See Figs. 47, 48, 49 and 50.

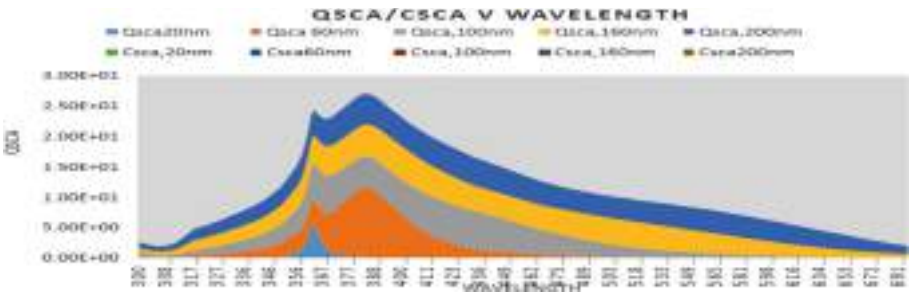


Fig. 47. Area curve under Qsca

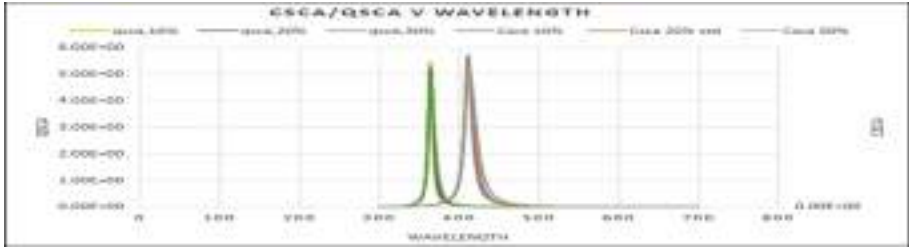


Fig. 48. Effect of standard deviation on Csca and Qsca

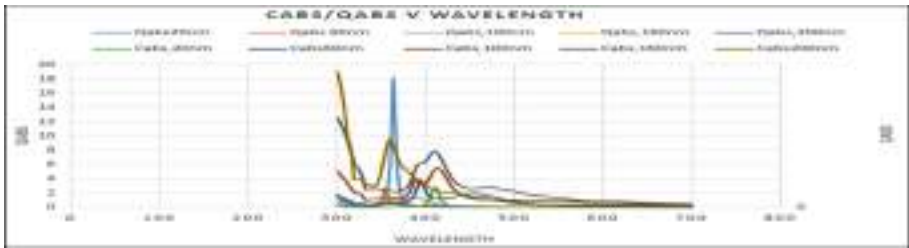


Fig. 49. Effect of particle size on Cabs and Qabs

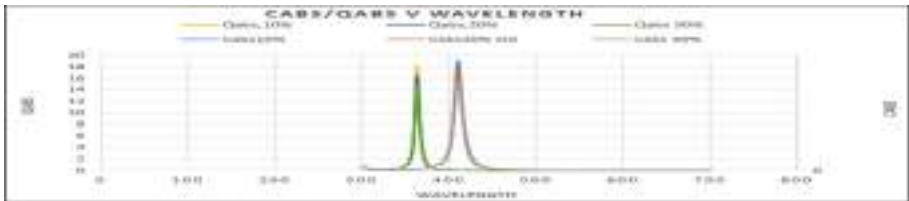


Fig. 50. Effect of standard deviation on Cabs and Qabs.

Results from Analysis on Silver Samples

Qsca and Csca both are inversely proportional to the standard deviation. Qsca and Csca are directly proportional to the size of the nanoparticle. Both quickly reduce to zero when the particle size is less than 100 nm at higher wavelengths. Qabs and Cabs are directly proportional to nanoparticle size. Qabs and Cabs are inversely proportional to the standard deviation.

4 Conclusion

This paper work not only gives valuable research experience in the field of plasmonic solar cells but it also helps in learning how to work with the new MIE plot software. In this paper numerous graphs on the effect of particle size and standard deviation on

$C_{\text{SCATTERING}}$, $C_{\text{ABSORPTION}}$, $Q_{\text{SCATTERING}}$, and $Q_{\text{ABSORPTION}}$ are shown. For the first objective, the glass shows maximum $Q_{\text{SCATTERING}}$ and $Q_{\text{ABSORPTION}}$ and so it has maximum efficiency in the silver nanoparticle [11].

We can conclude the findings from the analysis done in the paper work:

Analysis of Silver Sample Showed:

- $C_{\text{SCATTERING}}$ and $Q_{\text{SCATTERING}}$ inversely proportional to the standard deviation.
- $C_{\text{SCATTERING}}$ and $Q_{\text{SCATTERING}}$ directly proportional to the size of the nanoparticle. Both quickly reduce to zero when the particle size is less than 100 nm at higher wavelengths.
- $C_{\text{ABSORPTION}}$ and $Q_{\text{ABSORPTION}}$ directly proportional to nanoparticle size.
- $C_{\text{ABSORPTION}}$ and $Q_{\text{ABSORPTION}}$ inversely proportional to the standard deviation.

References

1. Derkacs, D., Lim, S.H., Matheu, P., Mar, W., Yu, E.T.: Improved performance of amorphous silicon solar cells via scattering from surface plasmon polaritons in nearby metallic nanoparticles. *Appl. Phys. Lett.* **89**, 093103 (2006)
2. Sayeed, Md.N., Al Razi, A., Hossain, Md.N., Das, S.: Effects of different parameters in enhancing the efficiency of plasmonic thin film solar cell. *Int. J. Adv. Mater. Sci. Eng. (IJAMSE)* **2**(1), 1–7 (2013)
3. Akimov, Yu.A., Koh, W.S., Ostrikov, K.: Enhancement of optical absorption in thin-film solar cells through the excitation of higher-order nanoparticle plasmon modes, vol. 17, pp. 10195–10205 (2009)
4. Hahn, D.W.: *Light Scattering Theory* (2009)
5. Tan, H., Santbergen, R., Smets, A.H.M., Zeman, M.: Plasmonic light trapping in thin-film silicon solar cells with improved self-assembled silver nanoparticles. *Nano Lett.* **12**, 4070–4076 (2012)
6. Cheng, Y., et al.: Localized surface plasmon resonances caused by Ag nanoparticles on SiN for solar cell applications. *J. Korean Phys. Soc.* **56**(5), 1488–1491 (2009)
7. Catchpole, K.R., Polman, A.: Plasmonic solar cells. *Opt. Express* **16**, 21793–21800 (2008)
8. Shah, V., Schade, H., Vanecek, M., Meier, J., Vallat-Sauvain, E., Wyrsh, N., Kroll, U., Droz, C., Bailat, J.: Thin-film silicon solar cell technology. *Progress Photovoltaics: Res. Appl.* **12**, 113–142 (2004)
9. Kim, J.: Surface plasmon resonance for photoluminescence and solar cell applications. *Electron. Mater. Lett.* **8**, 351–364 (2012)
10. Beck, F.J.: Tunable light trapping for solar cells using localized surface plasmons. *J. Appl. Phys.* **105**, 114310 (2009)
11. Chakraborty, A., Dey, D., Das, P.: Investigation of energy consumption and reservation scheme using energy auditing techniques. In: 2018 International Conference on Smart Systems and Inventive Technology (ICSSIT), Tirunelveli, India, pp. 34–38 (2018)



Age Estimation and Gender Prediction Using Convolutional Neural Network

Bulbul Agrawal^(✉)  and Manish Dixit 

Department of Computer Science and Engineering and Information Technology,
Madhav Institute of Technology and Science, Gwalior, India
bulbulag04@gmail.com, dixitmits@gmail.com

Abstract. A face of a person plays a very crucial part to identify the person uniquely. Two important traits namely age and gender can enhance the performance of face recognition. From the human perspective, it is very easy to estimate the person's gender and age on the basis of visualization but if we see from the machine perspective they can't. To estimate the age and gender from the facial image is a challenging task for a machine due to variations, lighting and other conditions in the face. This paper proposed the estimation of age and predict the gender of a person from the facial image using the convolutional neural network. In the proposed methodology before the training and testing, also apply the PCA to reduce the extracted features dimensions. This work is done on the publicly available IMDB-WIKI dataset as well as own dataset using the MATLAB platform for the implementation purpose.

Keywords: Computer vision · Gender recognition · Age estimation · Machine learning · Deep learning · Convolutional Neural Network · Neural network · Principal Component Analysis

1 Introduction

In the field of computer vision [11], analysis of facial images can be supposed as a most researched zone. In real life, visualization appearance plays a very crucial role to identify the gesture, posture, age, gender, ethnicity, and emotions like happy, sad, anger, neutral, etc., of the person. Recognition of the facial image is very important whenever you work with any type of face [3]. A facial image contains lots of features point [27] based on textures, shapes, and colors. It is very difficult to find interesting points from the face [25]. If you want to work with any topic which is related to human face then recognition of face is the very first and mandatory step.

There are lots of applications available in the real world which is related to age estimation and gender prediction namely sale of the product, biometrics, cosmetology, forensic field, entertainment, etc.

A good application of face recognition is in the biometrics [17]. In today's era, biometric techniques are very useful and gain a hot topic as research because of their convenience. Using the biometric approaches there is no need for the person to remember the password, any type of key or number pattern. To identify the person using behavioral or physiological characteristics gain much attention as well as it also

makes the security system more powerful [4]. There are various traits available in biometric that can be used for identifying the person like iris, signature, voice, fingerprint, etc. but still face recognition is the important trait in the human as well as demanded topic in biometrics. Since if someone wants to identify the person so in this situation primarily facial recognition plays a crucial role [6].

Generally recognizing the face is a very simple procedure. It consists of mainly two steps. Firstly capture the image of a face using the capturing device camera in the visible light then evaluate the features of the facial image. The main advantage of face recognition is there is no need of any machine, tool or device to capture the image whereas iris scanner and fingerprint scanner need a particular device [4]. But there is a disadvantage of face recognition, Facial images are changed by the expression, pose variation, aging, etc. that is the reason behind the low accuracy in the face recognition system.

In the soft biometric traits are hairstyle, age, gender, ethnicity, hair color, etc. it does not always give the relevant information about the person. But the set of these traits can show useful information in the person authentication. So to improve the accuracy of face recognition use the combination of soft biometrics and face recognition [4].

In this paper, we focus on the two things i.e. estimate the age of a person and gender prediction. There are lots of techniques and methods proposed in the till date [5, 8, 15, 30]. So this paper proposed an effective method to estimate the age and prediction of gender using (Convolutional Neural Network) CNN [12]. In the field of image analysis, CNN introduced a new paradigm [1, 24]. So in this project used the pre-trained CNN model to extract the features from the images on the basis of gender and estimate the age. In this proposed system, there are mainly three constraints i.e. it works only with the facial images, frontal images and should not be a group image. After extracted features dimension reduced by applying Principal Component Analysis (PCA) algorithm [9, 10].

For predict the gender of a person, we classify the network for the two results i.e. one for male and other for female [16]. For the purpose of age estimation, we classify the ages in the four groups [19]. Groups can be categorized as the group of children, group of young people, group of adult people and group of old people which is organized in the first, second, third, and fourth group respectively. For the classification purpose, if the age of the person lies between the 0–20 then it will go for the first group. If the age of a person lies between 21–40 then it will go for the second group. If the age of a person lies between 41–60 then it will go for the third group and if the person age is higher than 60 then it will be classified as the last group [21].

The remainder of this paper is organized as: Sect. 2 shows the related study, Sect. 3 shows the experimental details, Sect. 4 discusses the proposed methodology, Sect. 5 analyzed the result and Sect. 6 discusses the conclusion.

2 Related Study

Haider et al. [1] present the paper on gender classification at real-time using deep learning. The input of CNN is prepared to apply such pre-processing techniques: firstly detect the face from the input image then remove the noise if any after that align or

resize the face. The simple CNN architecture follows by four convolution layers and three max-pool layers within the two FC layers and single multinomial regression layer for the classification purpose. This paper also discusses the architecture of the server and smartphone. The overview system also tested for the smartphone and basically its architecture gives the knowledge about how to upload or test the trained or tested system in the smartphones. CAS-PEAL or FEI is all about the dataset which is used by this paper for training and testing purpose (as a static dataset).

Mane et al. [2] discusses the identification of the gender and recognition of facial and expression. Used the six different datasets for experiment namely JAFFE, CK, PSL, FER2013, IMDB-Wiki and Real-world dataset. Used the four different methodologies on all above-mentioned dataset namely CNN, Feature engineering, Transfer learning, and Amazon Recognition. So, in short, it is recognized the face by facial landmark, amazon recognition, and transfer learning. Similarly, recognition of facial expression is done by transfer learning, HOG descriptor, CNNs, and facial landmark. And finally, gender recognition is done by using the only CNNs. It is shown that amazon recognition is performed better on facial recognition and facial expression.

Ito et al. [4] predict the age and gender from the facial image using CNN. They used the IMDB-WIKI dataset for age and gender prediction. Using the AlexNet, VGG-16, ResNet-152 and WRN-16-8 net architecture age and gender is predicted. Each and every net have own properties. This paper shows the which net is performing well on the IMDB-WIKI dataset. It gives the comparison summary among all the net architecture and the accuracy is evaluated by the mean absolute error. They conclude that the WideResNet work well as compares the all above-mentioned net. For improving the accuracy of this model and reduce the time complexity, they used the multi-task learning to predict the age and gender.

Zhang et al. [16] present the deep CNN collection of Gnet and Snet for gender and smile classification respectively. VGG architecture is followed by the 16 convolution layer, maximum pooling, and ReLu within the SoftMax function used for classification. In this approach firstly detect the face and its five landmarks than apply the pre-processing as crop the face. After that one face is going to Gnet for gender classification purpose and another two faces (from face crop) are going for two Snet to classify the smile of the face. Take the average of both Snet and predict as a result. They experiment the proposed method on the ChaLearn 16 FoTfW dataset that shows the effective result.

Rothe et al. [18] discuss the age classification using deep learning. Its CNN used the VGG-16 architecture and ImageNet is used for the pre-trained purpose for image classification. In the proposed method firstly detect the face and crop the input image after that extract the features using the VGG-16 and SoftMax function is applied to predict the age of the person. An experiment is done on IMBD, WIKI and LAP dataset for age estimation. The performance is evaluated by mean absolute error and ϵ -error.

Sang et al. [22] this paper discusses the smile detection, gender classification, and emotion recognition. It used the deep CNN Vgg model to obtain the result over the WIKI, IMDB, GENKI-4 K, FER-2013 dataset.

Rai et al. [25] present a review on the techniques of gender classification. It illustrates the gender classification processing steps on the basis of the frontal face image. Lots of the application such as computer-human interface and facial recognition

can improve the performance of the system if predicted age and gender is true. In the system overview, there are two phases i.e. training phase and testing phase. In the training phase just extract the features and at the testing phase basically, classify the result. At the end of feature extraction, it presents the two methods which are geometry-based and appearance-based. At the other end, it discusses the gender classification method using multilayer NN, SVM, Discrete Adaboost, LDA, etc. It also shows the comparison among different feature extraction technique with classifying techniques within the classification rate. It attempts to provide the basic knowledge of the gender classification.

Gupta et al. [26] PCA is the certain case of factor analysis. Here is an example that shows the step by step process of finding the value of the principal component. PCA has a little fundamental assumption like principal components, variances, linearity are orthogonal. Data classification and dimensionality reduction techniques used the concept of principal component analysis. This paper shows the importance of biomedical signal processing. PCA has applicable to both batch process and continuous process.

3 Experimental Details

3.1 Programming Environment and Toolboxes

MATLAB: MATLAB stands for Matrix Laboratory which is high-level programming language developed by MathWorks. It provides an interactive environment for programming, computation, and visualization. For the computational purpose, MATLAB is widely used in the tool. It contains the lots of features and application in the all field including image processing, signal processing, optimization, machine learning, control system, etc. the reason behind the popularity of the MATLAB is unique applications i.e. toolboxes. It offers such valuable toolbox like Image processing toolbox, NN (Neural Network) toolbox, Optimization toolbox, Signal processing toolbox, etc. In the image processing field, we can use the MATLAB for the image segmentation, image enhancement, object detection, etc. One more feature of MATLAB makes it very different from other tools i.e. GUI toolbox. Using the GUI we can make our work very attractive as well as simple. MATLAB also offer the work with deep learning. If you are a beginner for MATLAB then don't worry it is very user-friendly. It helps window give you all the necessary information to execute the program. So in this project, used the MATLAB 2019a for the implementation purpose along with the NN toolbox for the training purpose.

3.2 Image Dataset

The experiment is done on the Wiki dataset which is one of the publicly available largest datasets of the face image. In this dataset, it contains the 62K+ images. In which using the below 8 details, age and gender label can be found [2, 4, 7] (Fig. 1).



Fig. 1. Sample images from the WIKI dataset

dob: It gives information about the date of birth of all the 62K+ images.

photo_taken: It shows the year of when the photo was taken.

full_path: shows the file path.

gender: It shows the knowledge of gender for the all 62K+ image. Here 0 is used for Female and 1 is used for male whereas NaN is used for unknown.

name: Show the name of each image.

face_location: Show the face location.

face_score: Detect the score of the face. Inf is showing that no face is present in the image.

second_face_score: Detect the second-highest score of the face. If more than one facial image is present then it is used to avoid it. If the return value is NaN it means that no second face is detected

Secondly, some sample images from the own dataset are also tested over the proposed system.

4 Proposed Methodology

4.1 Proposed Methodology

In this paper, we proposed an effective methodology for an estimate the age and gender prediction using the convolutional neural network [14]. In the proposed method used the CNN for feature extraction and also used the PCA algorithm to reduce the dimensionality of the data. It follows the basic building block of image processing which is used to classify an image. The flow of the proposed method is followed; firstly upload the dataset as an input and applying some pre-processing to the dataset that makes it relevant. Then extract the features from the images using the CNN and just train or test the system to plot all observations using the FFNN.

4.2 Proposed Work

The flow graph of the proposed method is shown in Fig. 2. Which is discussed deeply below.

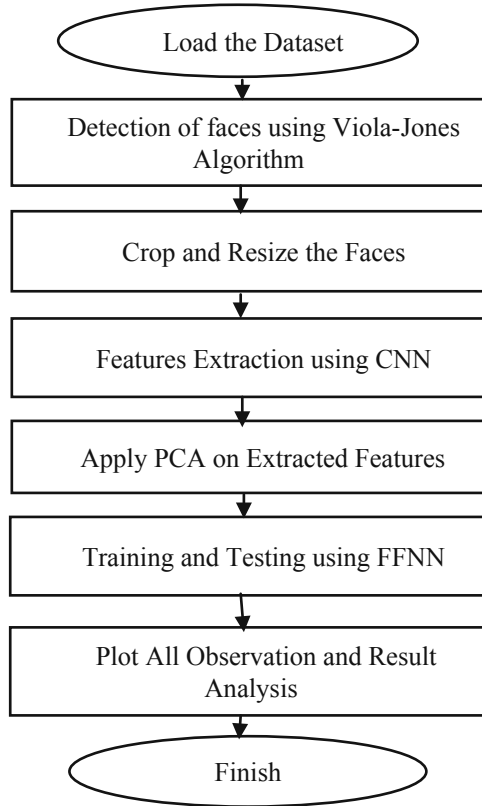


Fig. 2. Flow diagram of the proposed methodology

Step 1: Load the Dataset

In this paper, all the experiments are done in the WIKI dataset which is publicly available largest dataset [18] as well as own dataset.

Step 2: Excluded the Incorrectly Labeled Images

For calculating the age of the person in the WIKI dataset subtracting the date of photo taken to the date of birth. In this case, we found that the age of some identities are negative and some identities were very high like 130–1800 i.e. not possible in real life. So to avoid the misclassification, removed the identities that age are greater than 120.

Step 3: Detection of the Face Using the Viola-Jones Algorithm

It is the primary and important part of any facial images. In some case, an image may contain the different things rather than face examples are shown by below Fig. 3 from the WIKI dataset.



Fig. 3. Non-frontal and non-facial images

So here detection of the face is very important [16]. In this paper, the face detection Viola-Jones algorithm is used because of its fastest detection property. It is requisite to learn the features from only the detected facial image skin rather than other parts of the images.

Step 4: Crop the Detected Face Image and Resize It

Before applying the input to CNN, firstly cropped the facial images then resize it to the $227 \times 227 \times 3$. Each input image is resized before extracted the features to match the input format of CNN.



Fig. 4. The output of face detection, cropped face and resized the image from the sample image

The output of face detection using Viola-Jones algorithm cropped face image and resized an image is shown in Fig. 4 from the WIKI dataset.

Step 5: Feature Extraction

In this phase, resized input is given to the feature extraction phase which extracts the features using the CNN [18]. The architecture of the network is given by Fig. 6 in which the whole process is defined from taking the input image to the result. The knowledge about the used layers, filters and FC layers is given by the network architecture.

Network Architecture for Feature Extraction:

CNN used the different no. of filters to each image in each convolutional layer in the network. These filters are responsible for extracting the features of an image. The weights in the layer are trained to recognize the colour, edges, shapes, etc. This CNN net has a total of 8 layers in which 5 layers are convolutional layers and the remaining 3 layers are FC layers. The proposed work network receives the input of $227 \times 227 \times 3$ of size. The first convolutional layer contains the 96 no. of filters with the filter of size 11×11 using 4 pixels of stride and max pooling. Basically, the output of the first layers goes to the input as a second convolutional layer which contains the 256 no. of filters with the filter of size 5×5 . Convolutional layers third and fourth don't connect with the pooling and normalization layers. The third convolutional layer contains the 384 no. of the filter with the size of the filter is 3×3 . The fourth convolutional layer contains the 384 no. of the filters with the size of the filter is 3×3 and finally last convolutional layer contains the 256 no. of the filters with the size of the filter is 3×3 . After that perform the max-pooling over the last convolutional layer. At the end of the FC layers [13], 4096 neurons have each. All of the layers are followed by ReLu [20]. Here provided the additionally schematic diagram to understand the architecture of the network which is shown in Fig. 6. In the proposed work, we used the fc7 layer which is works with the texture of an image. Also used the dropout layer and cross channel normalization along with the network. This is a standard typical architecture of the AlexNet [4].

An example that is based on a CNN architecture is shown in Fig. 5 that depicts the whole process of CNN.

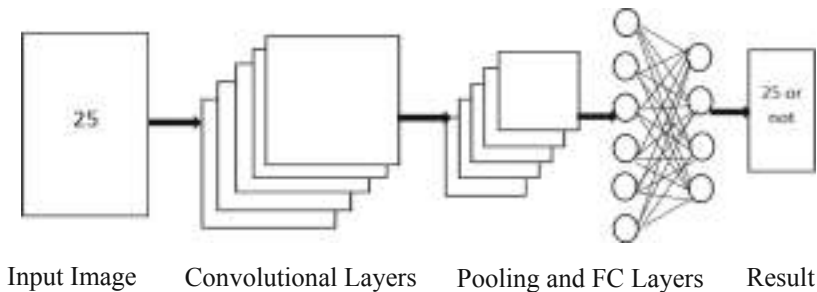


Fig. 5. An example based architecture of CNN

Step 6: Apply PCA to Extracted Features

To reduce the dimensionality of the features, PCA is used [23]. PCA is attained by fragment the co-variance matrix of the eigenvalues and eigenvector [26]. The process of identifying the lesser number of uncorrelated variables i.e. principal components from a huge set of data is known as Principal Component Analysis (PCA). PCA just removes correlation and not higher-order dependency as it works only in second-order statistics. The technique is widely used to emphasize variation and capture strong patterns in a dataset [28]. PCA is a technique that used in predictive models and

exploratory data analysis was invented by Karl Pearson in 1901 [29], PCA is considered as a useful statistical method and used in fields such as image compression, face recognition, neuroscience, and computer graphics. In the proposed method, we create a training set file by reduced the features from 4096 to 500.

Step 7: Training and Testing of NN

For the training purpose, used the Feed Forward Neural Network to classify the age and gender of the human in which input of FFNN is given by values of extracted features from the above CNN layers. So, here FFNN is just used for the classification purpose and finally testing is done.

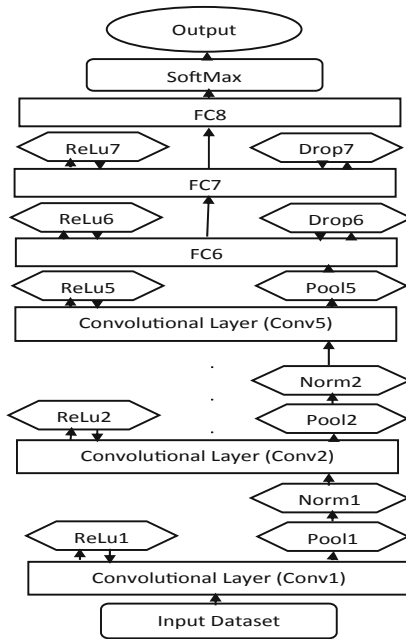


Fig. 6. Semantic diagram of a used network for feature extraction

Step 8: Plot all Observations and Result Analysis

In this phase, we plot all the observation to analysis the performance of the proposed method.

5 Result Analysis

In the proposed method, we take the sample images for the testing purpose to estimate the age and predict the gender. For the classification purpose, we used the feed-forward neural network which takes the reduced features from PCA. It is finely tuned for 500 features with the 30 no. of neurons in a hidden layer at the appropriate epochs using the

NN toolbox. We also calculate the different number of parameters for measuring the performance. In the end, we achieve a better classification result for the gender prediction and age estimation on WIKI dataset as well as own dataset using the CNN with PCA. The accuracy and value of MAE can be defined as;

5.1 Rate of Classification/Accuracy

Accuracy can be described as;

$$\text{Accuracy} = \frac{\text{TP} + \text{TN}}{\text{TP} + \text{TN} + \text{FP} + \text{FN}} \quad (1)$$

5.2 Mean Absolute Error (MAE)

As the name depicted, it gives the error as a mean of the absolute difference between the prediction and target values. The value of MAE can be determined as;

$$\text{MAE} = \frac{1}{N} \sum_{i=1}^N |y_i - \hat{y}_i| \quad (2)$$

Here, y_i and \hat{y}_i is the actual expected output and predicted output respectively. Since Absolute error is determined by the total amount of error in measurement (Tables 1 and 2).

Table 1. Result analysis for gender prediction on WIKI dataset

Gender prediction	CNN	AlexNet	KNN	Vgg	Our
Accuracy	96%	91.53%	84.89%	96.33%	96.50%

Table 2. Result analysis for age estimation on WIKI dataset

Age estimation	AlexNet	Vgg16	ImageNet	Our
MAE	9.44	8.15	3.349	0.1441

The result obtained from the proposed method over the WIKI dataset is shown in Fig. 7.



Fig. 7. The output of age estimation and gender prediction from the WIKI dataset

Table 3. Result analysis for gender prediction from the own dataset

Parameters	Value
Accuracy	95%
Recall	90%
Precision	100%
F-measure	94.73%
TNR	100%
FPR	0%
FNR	10%
MAE	0.1269
MSE	0.5698

Table 4. Result analysis for age estimation from the own dataset

Parameters	Value
Accuracy	85%
MAE	0.1623
MSE	0.4573

Result analysis on the own dataset is achieved the 95% accuracy for the gender prediction and 85% accuracy along with 0.1623 value of MAE for the age estimation and different no. of parameters are also calculated which is represented by Tables 3 and 4.

The result obtained from the proposed method over own dataset is shown in Fig. 8.

**Fig. 8.** The output of age estimation and gender prediction from the own dataset

6 Conclusion

In this paper, we evaluate the CNN architecture for gaining good performance. The proposed methodology of this paper is age estimation and gender prediction using the convolutional neural network. We also used the type of post-processing which is used to reduce the dimension of extracted features. For extracting the features from the image, used the pre-trained CNN model. This proposed methodology valuated on the

publicly available WIKI dataset as well as own dataset. Here our result is also compared with existing methods which demonstrates the satisfactory result.

References

1. Haider, K.Z., et al.: Deepgender: real-time gender classification using deep learning for smartphones. *J. Real-Time Image Process.* **16**(1), 15–29 (2019)
2. Mane, S., Shah, G.: Facial recognition, expression recognition, and gender identification. In: *Data Management, Analytics and Innovation*, pp. 275–290. Springer, Singapore (2019)
3. Fang, J., et al.: Multi-stage learning for gender and age prediction. *Neurocomputing* **334**, 114–124 (2019)
4. Ito, K., et al.: Age and gender prediction from face images using convolutional neural network. In: *2018 Asia-Pacific Signal and Information Processing Association Annual Summit and Conference (APSIPA ASC)*. IEEE (2018)
5. Hosseini, S., et al.: Age and gender classification using wide convolutional neural network and Gabor filter. In: *2018 International Workshop on Advanced Image Technology (IWAIT)*. IEEE (2018)
6. Ke, P., et al.: A novel face recognition algorithm based on the combination of LBP and CNN. In: *2018 14th IEEE International Conference on Signal Processing (ICSP)*. IEEE (2018)
7. Lee, S.H., et al.: Age and gender estimation using deep residual learning network. In: *2018 International Workshop on Advanced Image Technology (IWAIT)*. IEEE (2018)
8. Verma, S., Jariwala, K.N.: Age & gender classification using histogram of oriented gradients and back propagation neural network (2018)
9. Ait-Sahalia, Y., Xiu, D.: Principal component analysis of high-frequency data. *J. Am. Stat. Assoc.* **114**, 1–17 (2018)
10. Dabiri, Z., Lang, S.: Comparison of independent component analysis, principal component analysis, and minimum noise fraction transformation for tree species classification using APEX hyperspectral imagery. *ISPRS Int. J. Geo-Inf.* **7**(12), 488 (2018)
11. Sze, V., et al.: Efficient processing of deep neural networks: a tutorial and survey. In: *Proceedings of the IEEE105.12*, pp. 2295–2329 (2017)
12. Dehghan, A., et al.: Dager: deep age, gender and emotion recognition using convolutional neural network. arXiv preprint [arXiv:1702.04280](https://arxiv.org/abs/1702.04280)(2017)
13. Liu, W., et al.: A survey of deep neural network architectures and their applications. *Neurocomputing* **234**, 11–26 (2017)
14. Lapuschkin, S., et al.: Understanding and comparing deep neural networks for age and gender classification. In: *Proceedings of the IEEE International Conference on Computer Vision* (2017)
15. Mansanet, J., Albiol, A., Paredes, R.: Local deep neural networks for gender recognition. *Pattern Recogn. Lett.* **70**, 80–86 (2016)
16. Zhang, K., et al.: Gender and smile classification using deep convolutional neural networks. In: *Proceedings of the IEEE Conference on Computer Vision and Pattern Recognition Workshops* (2016)
17. Santarcangelo, V., Farinella, G.M., Battiato, S.: Gender recognition: methods, datasets and results. In: *2015 IEEE International Conference on Multimedia & Expo Workshops (ICMEW)*. IEEE (2015)

18. Rothe, R., Timofte, R., Van Gool, L.: Dex: deep expectation of apparent age from a single image. In: Proceedings of the IEEE International Conference on Computer Vision Workshops (2015)
19. Levi, G., Hassner, T.: Age and gender classification using convolutional neural networks. In: Proceedings of the IEEE Conference on Computer Vision and Pattern Recognition Workshops (2015)
20. van de Wolfshaar, J., Karaaba, M.F., Wiering, M.A.: Deep convolutional neural networks and support vector machines for gender recognition. In: 2015 IEEE Symposium Series on Computational Intelligence. IEEE (2015)
21. Kalansuriya, T.R., Dharmaratne, A.T.: Neural network based age and gender classification for facial images. *ICTer* 7(2), 1–10 (2014)
22. Sang, D.V., Cuong, L.T.B., Van Thieu, V.: Multi-task learning for smile detection, emotion recognition and gender classification. In: Proceedings of the Eighth International Symposium on Information and Communication Technology. ACM (2014)
23. Shang, H.L.: A survey of functional principal component analysis. *AStA Adv. Stat. Anal.* 98(2), 121–142 (2014)
24. Ng, C.-B., Tay, Y.-H., Goi, B.-M.: A convolutional neural network for pedestrian gender recognition. In: International Symposium on Neural Networks. Springer, Heidelberg (2013)
25. Rai, P., Khanna, P.: Gender classification techniques: a review. In: Advances in Computer Science, Engineering & Applications, pp. 51–59. Springer, Heidelberg (2012)
26. Gupta, V., et al.: An introduction to principal component analysis and its importance in biomedical signal processing. In: International Conference on Life Science and Technology, IPCBEE, vol. 3 (2011)
27. Gunay, A., Nabyev, V.V.: Automatic age classification with LBP. In: 2008 23rd International Symposium on Computer and Information Sciences. IEEE (2008)
28. Luo, B., et al.: Comparison of PCA and ICA in face recognition. In: 2008 International Conference on Apperceiving Computing and Intelligence Analysis. IEEE (2008)
29. Draper, B.A., et al.: Recognizing faces with PCA and ICA. *Comput. Vis. Image Underst.* 91(1–2), 115–137 (2003)
30. Moghaddam, B., Yang, M.-H.: Gender classification with support vector machines. In: Proceedings Fourth IEEE International Conference on Automatic Face and Gesture Recognition (Cat. No. PR00580). IEEE (2000)



Pattern Based Detection and Mitigation of DoS Attacks in MANET Using SVM-PSO

Divya Gautam¹  and Vrinda Tokekar²

¹ Department of Computer Science and Engineering,
Amity University Madhya Pradesh, Gwalior, India
divyagautam06@gmail.com

² Department of Information and Technology,
Institute of Engineering and Technology, DAVV, Indore, India
vrindatokekar@yahoo.com

Abstract. In today's world where most of the communication is done through Internet using wireless networking, it is important to protect the communication from external attacks. Mobile Ad Hoc Network (MANET) is a type of wireless networks in which automatically connected devices share information for communication using wireless links. Each device cooperates with each other in a distributed manner to facilitate communication in infrastructure less environment. Due to unfixed architecture of network it is quite vulnerable for various attacks. One of the prominent attacks is Denial of Service attack (DoS). It is a type of attack in which nodes are going to be compromised even without knowing of becoming victim of the attacker node. In DoS attacks, the machines stop responding for giving services to the legitimate user as they become busy in responding the attacker's request. This research work is mainly focused on detecting the DoS attacks in the traffic coming to a node in Mobile ad Hoc Networks. This research work is also focused on identifying the attacked node in the adhoc network. The classification algorithm SVM (Support Vector Machine) is used along with optimization technique PSO (Particle Swarm Optimization) to identify the attacked and non-attacked node in the network. The Simulation is done on NS 2 using LIBSVM and JAVA Script.

Keywords: LIBSVM · NS 2 · MANET · DoS · SVM · PSO

1 Introduction

MANET is a type of network where individual device is responsible for routing and communication without any external access point. In this network each device is independent to move in any direction. So mobile devices used in this system is self-governing device. Every device in such network is free to move in any direction and therefore the topology is not fixed at any point of time. The network density is dependent on the usage of the MANETs. The example of MANET like WSN are (Wireless Networks), Tactical Networks, Data Networks, Device Networks etc. Ad Hoc networks are more vulnerable in comparison to wired network because of its Mobile nature which leads to dynamic topology and hence makes it more prone to attacks from compromised nodes inside the network.

There are three generations of MANETs. The first generation came in early 1970s was sponsored by DARPA and called as PRNET (Packet Radio Networks). Second Generation came in early 1980's. Radios were improved by Survival Adaptive Radio Networks. The main goal was to make devices smaller, cheaper and power saver and resilient to various attacks. Global Mobile Information System (Glo Mo) and Near-Term Digital Radio (NTDR) were the two main developments done in this period. In 1990's third generation came in market and names as "commercial network" along with notebook computers, open source software. In this time period only, ad hoc networks became a part of IEEE 802.11; hence forth commercial ad hoc networking came. Within the IETF, the Mobile Ad Hoc Networking (MANET) working group was horn and sought to standardize routing protocols for ad hoc networks.

Ad Hoc networks started coming in use when the use of wireless communication increases and lots of portable devices emerged. It has started getting more popularity when its applications came in market for commercial, military purposes. Ad Hoc networks are widely used in private sectors also. The ad hoc networks in military areas take the advantage of common place network technology to maintain an information network between the soldiers, vehicles, and military information headquarters. The basic techniques of ad hoc network came from this field. In commercial sector such networks are used during rescue operations or in any emergency like fire, earthquake or flood etc. Reason behind using such networking is that during disaster it may be possible that existing infrastructure may not work, or the region is far away. In such cases rescue team can communicate with each other to passing messages. Other examples of Ad Hoc network are ship to ship ad hoc mobile communication, law enforcement etc. Ubiquitous computing is involved in MANETs (Mobile ad hoc networks) In such network it is quite much possible to extend networks at any extent due to independency of the devices on fixed infrastructure.

1.1 Mobile Ad Hoc Network (MANET)

A MANET is a decentralized form of ad hoc network which does not depend on any existent infrastructure such as routers or access points. In these kinds of networks, the task of routing and forwarding of packets are taken up by each node participating in the network and packets are forwarded dynamically depending on connectivity and routing algorithms implemented. These networks have the ability to add more nodes anytime as there is no need for set up as in infrastructure based wireless networks. Thus, these networks are also referred to as self-configuring, self-organized networks. The IEEE 802.11 Wi-Fi protocol supports ad hoc networks. MANETs have gained importance due to this decentralized mode that it facilitates.

1.2 Characteristics of MANETs

MANETs have several important characteristics:

Dynamic Topologies: Network Topology is defined as the arrangement of nodes in a network and their links. As a MANET is a decentralized version of a wireless network,

the nodes can move in and out of the network at any given time thereby giving rise to a rapidly changing dynamic network.

Limited Bandwidth and Non-uniform Capacity Links: In general, wireless links have lower bandwidth than their wired counterparts. In MANETs the bandwidth and the network throughput depend on the bandwidth of each individual nodes. Also, in MANETs as the network is rapidly changing, there is a lack of uniform capacity links.

Constrained Physical Security: MANETs are more vulnerable to physical security threats than wired networks. Risks of eavesdropping, spoofing and Denial-of-Service (DoS) attacks are more in MANETs. Also due to its decentralized nature, detection of point of failure sometimes becomes a complicated.

1.3 Advantages of MANETs

The advantages of MANETs include the following:

Access Independent of Geographical Position: MANETs can provide access to information and services irrespective of the geographic position of a node due to its dynamic nature.

Independent Network: MANETs provide higher degree of independence due to no involvement of pre-existing network administrating infrastructure. Each node can forward and route packets thereby acting as independent routers.

Scalable: New nodes can join or leave the network at any point of time.

Economical: As there is no involvement of the infrastructure, MANETs are and have the potential in future to be more commercially viable than other infrastructure networks

1.4 Challenges in MANETs

Some of the challenges faced with MANETs are:

Constrained Bandwidth: As with other wireless networks, MANETs also face the problem of constrained bandwidth as compared to their wired counterparts.

Dynamic Topology: The dynamic topology can be a challenge as an attack on one node can disturb the trust relationship between the nodes in the MANET.

Hidden Terminal Problem: The hidden terminal problem can be referred to as the clash between the packets at the receiving node due to simultaneous transmission of the same packets which are not in the vicinity of the sender but are in range to the receiving node.

Loss of Packets Due to Erroneous Transmission: Due to existence of hidden terminals, network interferences etc. packets are lost in this type of network.

Constrained Physical Security: MANETs are more vulnerable to physical security threats than wired networks. Risks of eavesdropping, spoofing and Denial-Of-Service

(DoS) attacks are more in MANETs. Also due to its decentralized nature, detection of point of failure sometimes becomes a complicated.

1.5 Applications of MANETs

In the recent past MANETs have become popular due to the advantages it offers. Also, MANETs are highly adaptive systems and thus, in future they have the potential to make wireless communication technology more advanced.

Application of MANETs can be seen in the following sectors:

Defense: MANETs are used by the military to maintain connectivity between military personnel, vehicles and command centers. In fact, this sector has a huge contribution to the development of the MANET systems. As MANETs don't require any pre-existing infrastructure, a network can be set up with ease and is very cheap which is one of the biggest advantages for military operations as generally time available is less in case of an emergency.

Automobile: MANETs are also used in automobile for various purposes like vehicular information systems, traffic information and tracking. MANETs can help to provide more accurate geographical locations as often it is seen that GPS satellites cannot pinpoint vehicles in remote areas like caves and tunnels. MANETs provide better triangulation for locating. Also, in case of traffic information systems, drivers can be informed about the real-time traffic conditions by the means of relaying information between cars connected in a MANET network thereby eliminating the need for expensive, massive infrastructure i.e. servers, databases etc.

Disaster Management: MANETs are also being used in disaster relief, search and rescue operations. In case of any disaster it is seen that almost all of the time, the infrastructure networks are destroyed due to natural calamities etc. and it becomes extremely important to restore the communication process for proceeding with rescue operations. MANETs can be proved to be extremely useful in these situations as they are easy and fast to set up and they require no infrastructure.

Local Level: MANETs can also be used to broadcast files or information in classrooms, library etc. A MANET can be set up between various nodes in a school or college in which students and teachers can communicate between themselves without the involvement of any infrastructure. MANETs can even be used in homes for the same reason. Thus, this will eliminate the need of cables and infrastructure connecting and setting up of which is a problem for a lot of users. As MANETs work on cooperation between the nodes, users can easily join a network, complete their required tasks and leave the network without any hassle.

1.6 Vulnerabilities in MANETs

Although MANETs provide us with a lot of advantages, still it has a certain degree of exposure to attacks due to their decentralized and dynamic nature. Some of the vulnerabilities of MANETs are:

Wireless Links Between Nodes: The use of wireless links between nodes introduces the possibility of passive attacks like eavesdropping and active interference as there is no need for an attacker to have physical access to the network. This is not a vulnerability of MANETs only but in general for wireless networks.

Dynamic Topology: The dynamic nature of MANETs allow nodes to join the network or leave the network at any point of time. Thus, there is a frequent change in the network topology which makes it hard to tell in case of any suspicious behavior of the nodes.

Cooperation Among Nodes: The whole idea of a MANET revolves around the notion of cooperation between the nodes. Thus, if a malicious node becomes a part of the network, this node can be treated as an important node for routing and forwarding packets which can be detrimental.

Lack of Designated Line of Defense: Due to the fact that MANETs can cover a wide geographical boundary and the fact that they are decentralized, there is no clear boundary for the network which makes it hard to set up preventive measures for attacks or detect attacks.

1.7 Attacks on MANETs

Every network tries to ensure the following goals when it comes to security of the network:

Confidentiality: Confidentiality in terms of network security means that the information contained in a packet which is transmitted through the network should only be accessed by the receiver and shall be kept secret from other intermediate nodes.

Authentication: Authentication of a node is the process of identifying the node based on certain credentials.

Integrity: Integrity means that data should be the same throughout its life cycle without any tampering or loss. In other it means the data should be consistent throughout.

Availability: Availability means information should be ready to be accessed as and when required by any node given that it is authorized to access it.

Non-repudiation: Non-repudiation gives a guarantee that information once sent cannot be denied later.

We can classify the type of attacks broadly based on the layer of the network protocol stack it works on:

Application Layer - Data corruption, Virus, Worms, Repudiation.

Transport Layer - TCP/UDP SYN Flood.

Network Layer - Blackhole, Wormhole, Sinkhole, Link Spoofing, Rushing Attack, Resource Consumption.

Data Link Layer - Traffic Analysis, Selfish misbehavior, Monitoring.

Physical Layer - Eavesdropping, Active Interference, Jamming.

2 Methodology

The main objective of the intended research is to identify the attacked node in the mobile adhoc network. For achieving the objectives, experiments are carried out to detect the attack and identify the attacked nodes based on pattern-based approach using LIBSVM and NS-2.

2.1 Early Detection of DoS Attacks in MANET

Early detection of attack is possible if pattern-based approach is applied. To generate the patterns, it is required to have the dataset of the traffic. This dataset is generated on NS-2 simulator. Two scenarios are created in mobile Adhoc environment. One is normal scenario where no attack is performed and second one is attacked scenario where attack is performed in the network. In attacked environment, the traffic behaves unexpectedly on certain parameters.

The parameters bitrate, entropy and packet delivery ratio [1, 2] are taken as the input to carry out this work are having lower computational cost and captures both instantaneous and the longer-term statistical behavior of the traffic.

It is clearly visible from the patterns [3] that if proper monitoring of the system is done on the given parameters after every new entry of the node in the Adhoc Networks then it is quite much possible to detect attacks in earlier stages [4].

2.2 Identification of DoS Attacks in the Network Using Support Vector Machine

After understanding about the attack in the network it is necessary to confirm about the impact of the attack. For achieving this, support vector machine is applied to obtain the accuracy and classified data for further optimization [5]. When SVM is applied on the two scenarios i.e. normal and attacked then the different accuracies are obtained when is quite comparable to understand the impact of the attack in the network.

For identifying the attack in the network more accurately total six parameters are taken in consideration. The parameters are bit rate, entropy, delay, packet delivery ratio, increased bit rate and increased delay.

2.3 Identification of the Attacked Node Using SVM-PSO

The objective of the work is to identify the attacked node as soon as possible to stop the consequences of the attack in the network and machine. For achieving this it is very much required to have a pattern for identifying the attacked node. This is applicable only when the attack is confirmed in the network. Once the attack is confirmed in the network, the attacked node must be identified. In this work, PSO (Particle Swarm Optimization) [6] is applied along with SVM (Support Vector Machine) to identify the attacked node in the network. PSO is an algorithm which is population-based. It is initialized with a population of random solutions called particles. The concept is based on the behavior of the particles in the search space. The particles adjusted in search

space as per their historical behaviors. It is a heuristic search technique that simulates the movements of a flock of birds which aim to find food.

For identifying the attacked node, it is necessary to analyze the traffic of every node in the network. This is done by classification of the traffic coming on every node using SVM after optimizing the SVM parameters by calculating the particle best value (pBest) and global best value (gBest) for every node in the ad-hoc network. On analyzing the obtained values, a range of threshold values based on SVM is calculated. After analyzing the threshold values a min-max range of threshold is obtained. The pattern of min-max threshold based on fitness is helpful in the early detection of the attacked nodes in the Adhoc network.

3 Simulation and Results After Applying PSO with SVM

To carry out this work, LIBSVM is used for classification purpose and further for detecting the attack impact on the traffic. NS-2 simulator is used to generate the dataset in normal scenario and attack scenario. To create a mobile ad hoc environment, total 11 nodes are used to generate the dataset. Dataset is created using listed parameters (bit rate, entropy, delay, packet delivery ratio, increased bit rate and increased delay) and then this dataset is converted in the format accepted by LIBSVM. The dataset is created in normal scenario and obtained the simulation results (Accuracy). Then 3 malicious nodes are introduced in the scenario (total nodes are still 11) and got new traffic (dataset). While applying SVM with PSO on both the dataset, the ratio between training and the testing dataset is kept as 7:3. On comparing the two; attack and normal traffic, it has been found that accuracies in normal traffic achieved is very high (upto 97%) in comparison to the accuracy achieved in attack traffic (upto 96%).

The entire work is mainly focused on detecting the attack in the network and then identifying the attacked node in the network. The motive is to find a pattern to identify the attacked node as early as possible after confirming the attack. Once the attack is confirmed SVM-PSO is applied on the dataset (traffic) of the individual node to classify the data. On analyzing the fitness values of all the nodes a pattern is identified. This pattern is very useful in detecting the attack as early as possible. The fitness value is mostly within the threshold range called as min-max threshold range (Lower and Upper Threshold), but sometimes they are either less or greater than the range. During the situation when the node's fitness value increases or decreases from the range of the threshold then these nodes are concluded as attacked nodes.

The Fig. 1 shows the comparison of fitness values for the individual nodes in normal and attack scenarios. The analysis found is as follows:

1. The Min-Max Threshold Range obtained is in between +6 to -6.

Interpretation: The fitness value obtained for the node 1 in the normal and attack scenario is 89 and 88 then the difference of the two values for the same node is +1, which is in the range of Min-Max Threshold hence the traffic is legitimate.

Pattern-Based Detection and Mitigation of DoS Attacks 7. But in case of Node 2, Node 3 and Node 8 the difference obtained is out of the range of Min-Max Threshold i.e. +7, +10 and -7 respectively. It is concluded that these nodes are attacked nodes and have malicious traffic.

2. Accuracy of the obtained results.

The obtained malicious nodes are those nodes which were made malicious to perform DoS attack in the network. Hence the mechanism used for identifying the DoS attacks on a given node is proved correct.

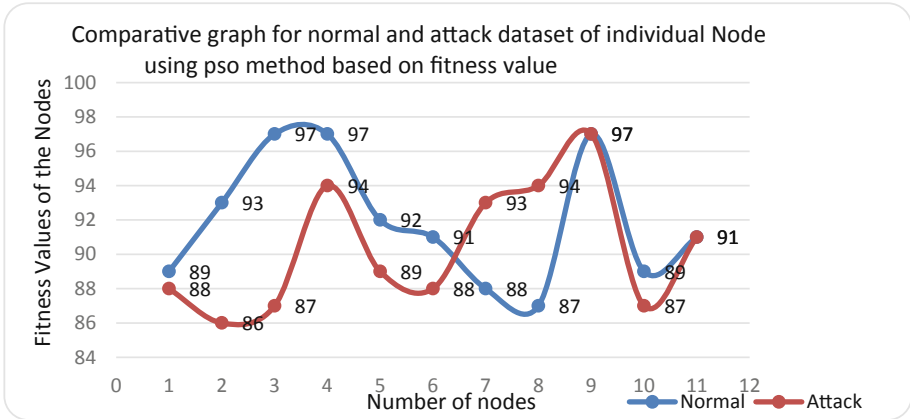


Fig. 1. Comparative graph for normal and attack dataset on individual value based on fitness value.

4 Mitigating the Effect of DoS Attacks in MANET Based on Detection of Attack

Based on simulation done for normal and attack traffic using SVM it has been found that there is a difference in attack traffic patterns and normal traffic patterns, which confirms the attack in the network. After confirming for the attack based on the patterns, it is necessary to find which are nodes exactly affected from the attack. For this SVM-PSO is applied on an individual node to get the fitness value. Once the fitness value obtained is going to be compared with the Min-Max Threshold value range. If the obtained value is in the range of the threshold then the node is not affected by the attacker. But if the fitness value crosses the range in either way then the concerned node is having the attacked traffic. Hence it is necessary to block the traffic coming from different nodes for the stipulated time period. After the next refresh, the traffic can be open for the node.

5 Conclusion and Future Work

5.1 Conclusion

The main aim of the proposed work is to identify the DoS attacked nodes in Mobile Adhoc environment. The identification of the attack in the network is the first

requirement before identifying the attacked nodes and then mitigating the attack effects. The proposed methodology for detecting the attack in the traffic is based on Support Vector Machine and Particle swarm optimisation.

In this work, a pattern is identified after analyzing the fitness values of the nodes in the mobile ad-hoc environment. A min-max threshold range is identified for the adhoc network. If the individual node's fitness value falls within the min-max threshold range, then it is observed that it is a non-attacked node. If the fitness value of the node crosses the upper or lower range of the threshold, then its an attacked node. Upon identifying the attacked node, it is required to block the node in order to keep the node safe from the crash. The node can be reactivated after the next refresh in the network.

5.2 Future Work

The entire work done is to overcome from some of the limitations of earlier work and generated a new method to detect DoS attacks in MANET environment. As a result, this research work has highlighted more work to be done for further clarifications of the attack. In DDoS attacks many of the machines are unaware of being compromised and acting as a zombie for third party attacker. If further the traffic of generated by sender can be optimised, then it can be predicted that the node is a zombie and is compromised by the attacker. Once if it possible to optimise the behaviour of the sender node, the attack can be stopped in initial stages.

References

1. Loukas, G., Oke, G., Gelenbe, E.: Defending against denial of service in a self-aware network: a practical approach. In: NATO Symposium on Information Assurance for Emerging and Future Military Systems, At Ljubljana, Sloveni (2008)
2. Kim, M., Na, H., Chae, K., Bang, H., Na, J.: A combined data mining approach for DDoS attack detection. In: Lecture Notes in Computer Science, vol. 3090, pp. 943–950 (2004)
3. Duda, R.O., Hart, P.E., Stork, D.G.: Pattern Classification. Wiley, New York (2001). pp. xx + 654, ISBN 0-471-05669-3
4. Gautam, D., Tokekar, V.: Detection of DoS attacks in MANET using LIBSVM. *Int. J. Eng. Adv. Technol. (IJEAT)* **8**(5), 1568–1573 (2019)
5. Manekar, V., Waghmare, K.: Intrusion detection system using support vector machine (SVM) and particle swarm optimization (PSO). *Int. J. Adv. Comput. Res.* **4**, 808 (2014)
6. Alam, M.: Particle swarm optimization: algorithm and its codes in MATLAB (2016). <https://doi.org/10.13140/rg.2.1.4985.3206>
7. Gautam, D., Tokekar, V.: Pattern based detection of DDoS attacks in MANET. *Int. J. Innov. Technol. Explor. Eng. (IJITEE)* **8**(8), 270–273 (2019)



Exploring the Optimal Path for Supply Chain System Using Queueing Models

Jitendra Kumar^(✉)  and Vikas Shinde^(✉) 

Department of Applied Mathematics, Madhav Institute of Technology
and Science, Gwalior, M.P., India
jkmuthete@gmail.com, v_p_shinde@rediffmail.com

Abstract. In this paper, we are exploring the optimal path for the supply chain system by using queueing models. We analyze different optimal paths are designed using various optimal channels from a different location. This article aims to obtain the best optimal path so that the delivery of the system makes more effective. The various performance measures have been determined such as queue length, response time and waiting time corresponding to store, packing, and transportation by adopting different paths. Numerical results have been obtained using MATLAB which validates for our model.

Keywords: Queueing models · Queue length · Response time · Waiting time · Optimal path

1 Introduction

The supply chain system is coordination among the buying, producing, delivering and maintaining products and ultimately origin to customers which placed in different locations. The modeling approach is considered to analyze the performance of the delivery system. To achieve the shortest path and success rate of the supply chain system. Queueing model is used to evaluate performance measures. Queueing model is used as a tool to provide the best cost-effective business model. Performances of the supply chain system have been analyzed by many authors. Xu et al. [1] examined the online seller's e-service offerings and customer cumulative ratings and demand. Kvasnicova et al. [2] compared known definitions and classifications of e-services. Kumar and Shinde [3] established a modeling approach to analyze the network for Five- input, Five-stage for better delivery of items. Zhou et al. [4] taken into consideration a two-stage tandem community with Markov arrival manner (MAP) to derive the overall performance measure of the deliver chain, along with stock stage and un-fill price. Taherdoost et al. [5] analyzed the three echelon inventory model for the supply chain system. Mokaddis et al. [6] developed a supply chain system, which involves a single manufacturer and several retail outlets. The manufacturer makes several products in batches and stores than in different warehouses after production. Sahraeian et al. [7] tested a supply chain network design (SCND) method with consideration of strategic and operational selection. This determines plant and distribution facilities (DF) as well as product cargo; however, the shipment has to attend in the

queue for transportation from followers to distribution facilities. Bhaskar and Lallement [8] obtained the optimal path for the delivery of products to the destination with the least response time. Kerbachea et al. [9] proposed a three-stage supply chain model that incorporates sale, production and buy logistics planning. Scott et al. [10] investigated the full cost gain which executed by using providers and warehouses through the elevated worldwide visibility provided by way of an included device. Viswanadhan [11] discussed an analytical model for evaluating the average lead time. Medjkoune and Aissau [12] estimated for the proximately of the performance measures of the M/G/1 queueing system. Zhang and Hou [13] analyzed the vacation interruption with M/G/1 queueing model using the supplementary variable and the matrix-analytic method and also obtained queue length under steady-state conditions. Onazine and Abbhan [14] discussed the computational approach based on a Taylor series for numerical evaluation of the M/G/1/N queue model with vacation interruptions.

2 Notations

n = Number of customers in the system (in queue plus in service),

λ = Arrival rate per order to customer for any things,

μ = Service rate per order to customer for any things

C = Number of Servers to reach things to customers corresponding to order,

$C\mu$ = Serving rate when $C > 1$ in a system,

P_n = Steady-state probability of exactly n customers in the system,

ρ = The utilization factor ($= \lambda/(C\mu)$)

P_0 = Steady-state probabilities of all idle servers in the system,

L_q = Queue length,

R_t = Response time order to customer for any things,

W_t = Waiting time for next order to customer.

O = Order to customer,

S = Store things as (Digital, Clothing, Kitchen, Health, Footwear & Accessories and others),

P = Packing section

T = Transportation (order to customers).

3 Model Description

The supply chain system has come to be very important, is handling hazards, dynamism, and complexities of worldwide sourcing. A completely integrated supply chain is required for the company to get the most advantage. Supply chain process from complex interconnections between production agencies and carrier vendors consisting of uncooked cloth, providers, unique device manufacturers, logistics operators, warehouse operators, vendors, stores and clients (see Fig. 1).

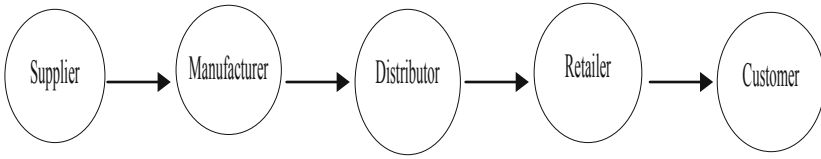


Fig. 1. Supply chain system

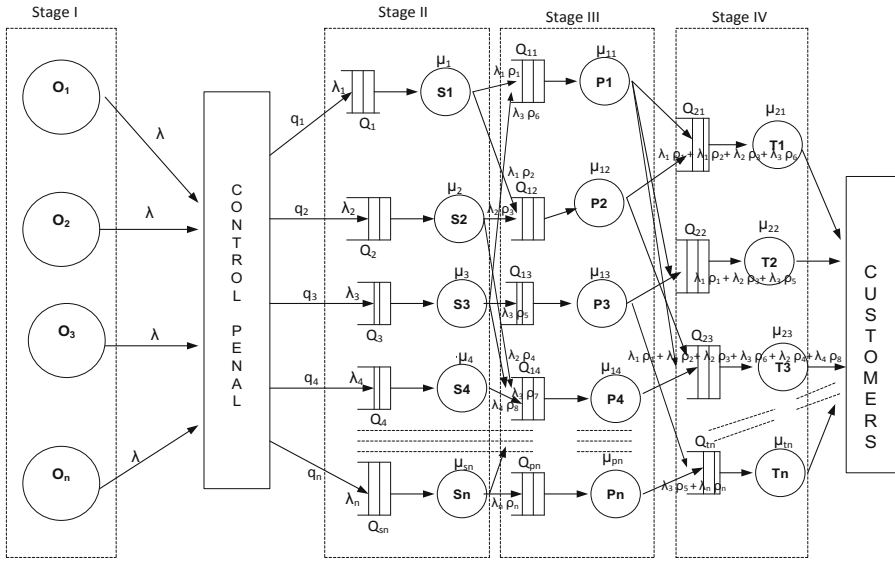


Fig. 2. Structure origin to customer with different stages

4 Performance Measures

In this section, we obtain response time, waiting for time and queue length corresponding to order to customers and using queueing models. We evaluate the different optimal paths in two cases (i) single server queueing model and (ii) multi-server queueing model. To obtained performance analysis as utilization, response time and waiting time and queue length, with different sections (store section, making section, and packing section and transportation section) to a destination from Fig. 2.

4.1 Utilization Systems

Applying M/M/1 and M/M/C queueing model to obtained performance analysis as utilization, queue length, response time and waiting time with different sections (store section, packing section and transportation section) as given Tables 1, 2 and 3.

Table 1. System utilization with different stages corresponding single – server

Stage II (S ₁ , S ₂ , S ₃ , …, S _n)	Stage III (P ₁ , P ₂ , P ₃ , …, P _n)	Stage IV (T ₁ , T ₂ , …, T _n)
$\rho_1^{(s_1)} = \frac{\lambda_1}{\mu_1}$ where $\lambda_1 = \lambda \cdot q_1$	$\rho_1^{(P_1)} = \frac{\lambda_1 \rho_1 + \lambda_3 \rho_6}{\mu_{11}}$	$\rho_1^{(T_1)} = \frac{\lambda_{T_1}}{\mu_{21}}$
$\rho_2^{(s_2)} = \frac{\lambda_2}{\mu_2}$ where $\lambda_2 = \lambda \cdot q_2$	$\rho_2^{(P_2)} = \frac{\lambda_1 \rho_2 + \lambda_2 \rho_3}{\mu_{12}}$	$\rho_2^{(T_2)} = \frac{\lambda_{T_2}}{\mu_{22}}$
$\rho_3^{(s_3)} = \frac{\lambda_3}{\mu_3}$ where $\lambda_3 = \lambda \cdot q_3$	$\rho_3^{(P_3)} = \frac{\lambda_2 \rho_4 + \lambda_3 \rho_5 + \lambda_3 \rho_9}{\mu_{13}}$	$\rho_3^{(T_3)} = \frac{\lambda_{T_3}}{\mu_{23}}$
$\rho_4^{(s_4)} = \frac{\lambda_4}{\mu_4}$ where $\lambda_4 = \lambda \cdot q_4$	$\rho_4^{(P_4)} = \frac{\lambda_4 \rho_8 + \lambda_3 \rho_7}{\mu_{14}}$	$\rho_4^{(T_4)} = \frac{\lambda_{T_4}}{\mu_{24}}$
$\rho_n^{(s_n)} = \frac{\lambda_n}{\mu_n}$ where $\lambda_n = \lambda \cdot q_n$	$\rho_n^{(P_n)} = \frac{\lambda_{2n} \rho_{4n} + \lambda_{2n-1} \rho_{4n-1}}{\mu_{1n}}$	$\rho_n^{(T_n)} = \frac{\lambda_{T_n}}{\mu_{2n}}$

Table 2. System utilization with different stages corresponding multi- server

Stage II (S ₁ , S ₂ , S ₃ , …, S _n)	Stage III (P ₁ , P ₂ , P ₃ , …, P _n)	Stage IV (T ₁ , T ₂ , …, T _n)
$\rho_1^{(s_1)} = \frac{\lambda_1}{C\mu_1}$ where $\lambda_1 = \lambda \cdot q_1$	$\rho_1^{(P_1)} = \frac{\lambda_1 \rho_1 + \lambda_3 \rho_6}{C\mu_{11}}$	$\rho_1^{(T_1)} = \frac{\lambda_{T_1}}{C\mu_{21}}$
$\rho_2^{(s_2)} = \frac{\lambda_2}{C\mu_2}$ where $\lambda_2 = \lambda \cdot q_2$	$\rho_2^{(P_2)} = \frac{\lambda_1 \rho_2 + \lambda_2 \rho_3}{C\mu_{12}}$	$\rho_2^{(T_2)} = \frac{\lambda_{T_2}}{C\mu_{22}}$
$\rho_3^{(s_3)} = \frac{\lambda_3}{C\mu_3}$ where $\lambda_3 = \lambda \cdot q_3$	$\rho_3^{(P_3)} = \frac{\lambda_2 \rho_4 + \lambda_3 \rho_5 + \lambda_3 \rho_9}{C\mu_{13}}$	$\rho_3^{(T_3)} = \frac{\lambda_{T_3}}{C\mu_{23}}$
$\rho_4^{(s_4)} = \frac{\lambda_4}{C\mu_4}$ where $\lambda_4 = \lambda \cdot q_4$	$\rho_4^{(P_4)} = \frac{\lambda_4 \rho_8 + \lambda_3 \rho_7}{C\mu_{14}}$	$\rho_4^{(T_4)} = \frac{\lambda_{T_4}}{C\mu_{24}}$
$\rho_n^{(s_n)} = \frac{\lambda_n}{C\mu_n}$ where $\lambda_n = \lambda \cdot q_n$	$\rho_n^{(P_n)} = \frac{\lambda_{2n} \rho_{4n} + \lambda_{2n-1} \rho_{4n-1}}{C\mu_{1n}}$	$\rho_n^{(T_n)} = \frac{\lambda_{T_n}}{C\mu_{2n}}$

Table 3. Performance measures for queuing models

Description	Single-server queueing model	Mutli- server queueing model
Queue length (Lq)	$E[N_i] = \frac{\rho_i}{1-\rho_i}$	$\frac{1}{(C-1)!} \left[\left(\frac{\lambda}{\mu}\right)^c * \frac{\lambda\mu}{(C\mu-\lambda)^2} \right] \times P_0$
Response time (Rt)	$E[R_i] = \frac{E[N_i]}{\lambda_i}$	$\frac{1}{\mu} + \frac{1}{(C)!} \left[\frac{\rho}{\lambda} * \frac{(C\rho)^2}{(1-\rho)^2} \right] \times P_0$
Waiting time (Wt)	$E[W_i] = E[R_i] = \frac{1}{\mu_i}$	$\frac{1}{(C-1)!} \left[\left(\frac{\lambda}{\mu}\right)^c * \frac{\lambda\mu}{(C\mu-\lambda)^2} \right] \times P_0$ Where $P_0 = \left[\sum_{n=0}^{C-1} \frac{1}{n!} \left(\frac{\lambda}{\mu}\right)^n + \frac{1}{(C)!} \left(\frac{\lambda}{\mu}\right)^c * \left(\frac{C\mu}{C\mu-\lambda}\right) \right]^{-1}$

Queue length for stage II

$$E[N_1^{(s_1)}] = \frac{\rho_1^{(s_1)}}{(1 - \rho_1^{(s_1)})} = \frac{\lambda_1}{(\mu_1 - \lambda_1)} \tag{1}$$

$$E[N_2^{(s_2)}] = \frac{\rho_2^{(s_2)}}{(1 - \rho_2^{(s_2)})} = \frac{\lambda_2}{(\mu_2 - \lambda_2)} \quad (2)$$

$$E[N_3^{(s_3)}] = \frac{\rho_3^{(s_3)}}{(1 - \rho_3^{(s_3)})} = \frac{\lambda_3}{(\mu_3 - \lambda_3)} \quad (3)$$

$$E[N_4^{(s_4)}] = \frac{\rho_4^{(s_4)}}{(1 - \rho_4^{(s_4)})} = \frac{\lambda_4}{(\mu_4 - \lambda_4)} \quad (4)$$

Response time for stage II

$$E[R_1^{(s_1)}] = \frac{1}{\lambda_1} E[N_1^{(s_1)}] = \frac{1}{(\mu_1 - \lambda_1)} \quad (5)$$

$$E[R_2^{(s_2)}] = \frac{1}{\lambda_2} E[N_2^{(s_2)}] = \frac{1}{(\mu_2 - \lambda_2)} \quad (6)$$

$$E[R_3^{(s_3)}] = \frac{1}{\lambda_3} E[N_3^{(s_3)}] = \frac{1}{(\mu_3 - \lambda_3)} \quad (7)$$

$$E[R_4^{(s_4)}] = \frac{1}{\lambda_4} E[N_4^{(s_4)}] = \frac{1}{(\mu_4 - \lambda_4)} \quad (8)$$

Waiting time for stage II

$$E[W_1^{(s_1)}] = E[R_1^{(s_1)}] - \frac{1}{\mu_1} = \frac{\lambda_1}{\mu_1(\mu_1 - \lambda_1)} \quad (9)$$

$$E[W_2^{(s_2)}] = E[R_2^{(s_2)}] - \frac{1}{\mu_2} = \frac{\lambda_2}{\mu_2(\mu_2 - \lambda_2)} \quad (10)$$

$$E[W_3^{(s_3)}] = E[R_3^{(s_3)}] - \frac{1}{\mu_3} = \frac{\lambda_3}{\mu_3(\mu_3 - \lambda_3)} \quad (11)$$

$$E[W_4^{(s_4)}] = E[R_4^{(s_4)}] - \frac{1}{\mu_4} = \frac{\lambda_4}{\mu_4(\mu_4 - \lambda_4)} \quad (12)$$

Queue length for stage III

$$E[N_1^{(p_1)}] = \frac{\rho_1^{(p_1)}}{(1 - \rho_1^{(p_1)})} = \frac{\lambda_1 \rho_1 + \lambda_3 \rho_6}{[\mu_{11} - (\lambda_1 \rho_1 + \lambda_3 \rho_6)]} \quad (13)$$

$$E\left[N_2^{(P_2)}\right] = \frac{\rho_2^{(P_2)}}{\left(1 - \rho_2^{(P_2)}\right)} = \frac{\lambda_1 \rho_2 + \lambda_2 \rho_3}{\left[\mu_{12} - (\lambda_1 \rho_2 + \lambda_2 \rho_3)\right]} \tag{14}$$

$$E\left[N_3^{(P_3)}\right] = \frac{\rho_3^{(P_3)}}{\left(1 - \rho_3^{(P_3)}\right)} = \frac{\lambda_2 \rho_4 + \lambda_3 \rho_5 + \lambda_3 \rho_9}{\left[\mu_{13} - (\lambda_2 \rho_4 + \lambda_3 \rho_5 + \lambda_3 \rho_9)\right]} \tag{15}$$

$$E\left[N_4^{(P_4)}\right] = \frac{\rho_4^{(P_4)}}{\left(1 - \rho_4^{(P_4)}\right)} = \frac{\lambda_4 \rho_8 + \lambda_3 \rho_7}{\left[\mu_{14} - (\lambda_4 \rho_8 + \lambda_3 \rho_7)\right]} \tag{16}$$

Response time for stage III

$$E\left[R_1^{(P_1)}\right] = \frac{1}{\lambda_1 \rho_1 + \lambda_3 \rho_6} E\left[N_1^{(P_1)}\right] = \frac{1}{\left[\mu_{11} - (\lambda_1 \rho_1 + \lambda_3 \rho_6)\right]} \tag{17}$$

$$E\left[R_2^{(P_2)}\right] = \frac{1}{\lambda_1 \rho_2 + \lambda_2 \rho_3} E\left[N_2^{(P_2)}\right] = \frac{1}{\left[\mu_{12} - (\lambda_1 \rho_2 + \lambda_2 \rho_3)\right]} \tag{18}$$

$$E\left[R_3^{(P_3)}\right] = \frac{1}{\lambda_2 \rho_4 + \lambda_3 \rho_5 + \lambda_3 \rho_9} E\left[N_3^{(P_3)}\right] = \frac{1}{\left[\mu_{13} - (\lambda_2 \rho_4 + \lambda_3 \rho_5 + \lambda_3 \rho_9)\right]} \tag{19}$$

$$E\left[R_4^{(P_4)}\right] = \frac{1}{\lambda_4 \rho_8 + \lambda_3 \rho_7} E\left[N_4^{(P_4)}\right] = \frac{1}{\left[\mu_{14} - (\lambda_4 \rho_8 + \lambda_3 \rho_7)\right]} \tag{20}$$

Waiting time for stage III

$$E\left[W_1^{(P_1)}\right] = E\left[R_1^{(P_1)}\right] - \frac{1}{\mu_{11}} = \frac{\lambda_1 \rho_1 + \lambda_3 \rho_6}{\mu_{11} \left[\mu_{11} - (\lambda_1 \rho_1 + \lambda_3 \rho_6)\right]} \tag{21}$$

$$E\left[W_2^{(P_2)}\right] = E\left[R_2^{(P_2)}\right] - \frac{1}{\mu_{12}} = \frac{\lambda_1 \rho_2 + \lambda_2 \rho_3}{\mu_{12} \left[\mu_{12} - (\lambda_1 \rho_2 + \lambda_2 \rho_3)\right]} \tag{22}$$

$$E\left[W_3^{(P_3)}\right] = E\left[R_3^{(P_3)}\right] - \frac{1}{\mu_{13}} = \frac{\lambda_2 \rho_4 + \lambda_3 \rho_5 + \lambda_3 \rho_9}{\mu_{13} \left[\mu_{13} - (\lambda_2 \rho_4 + \lambda_3 \rho_5 + \lambda_3 \rho_9)\right]} \tag{23}$$

$$E\left[W_4^{(P_4)}\right] = E\left[R_4^{(P_4)}\right] - \frac{1}{\mu_{14}} = \frac{\lambda_4 \rho_8 + \lambda_3 \rho_7}{\mu_{14} \left[\mu_{14} - (\lambda_4 \rho_8 + \lambda_3 \rho_7)\right]} \tag{24}$$

Queue length for stage IV

$$E\left[N_1^{(T_1)}\right] = \frac{\rho_1^{(T_1)}}{\left(1 - \rho_1^{(T_1)}\right)} = \frac{\lambda_{T_1}}{\left(\mu_{21} - \lambda_{T_1}\right)} \tag{25}$$

$$E\left[N_2^{(T_2)}\right] = \frac{\rho_2^{(T_2)}}{\left(1 - \rho_2^{(T_2)}\right)} = \frac{\lambda_{T_2}}{\left(\mu_{22} - \lambda_{T_2}\right)} \tag{26}$$

$$E\left[N_3^{(T_3)}\right] = \frac{\rho_3^{(T_3)}}{\left(1 - \rho_3^{(T_3)}\right)} = \frac{\lambda_{T_3}}{\left(\mu_{23} - \lambda_{T_3}\right)} \tag{27}$$

Response time for stage IV

$$E\left[R_1^{(T_1)}\right] = \frac{1}{\lambda_{T_1}} E\left[N_1^{(T_1)}\right] = \frac{1}{\left(\mu_{21} - \lambda_{T_1}\right)} \tag{28}$$

$$E\left[R_2^{(T_2)}\right] = \frac{1}{\lambda_{T_2}} E\left[N_2^{(T_2)}\right] = \frac{1}{\left(\mu_{22} - \lambda_{T_2}\right)} \tag{29}$$

$$E\left[R_3^{(T_3)}\right] = \frac{1}{\lambda_{T_3}} E\left[N_3^{(T_3)}\right] = \frac{1}{\left(\mu_{23} - \lambda_{T_3}\right)} \tag{30}$$

Waiting time for stage IV

$$E\left[W_1^{(T_1)}\right] = E\left[R_1^{(T_1)}\right] - \frac{1}{\mu_{21}} = \frac{\lambda_{T_1}}{\mu_{21}\left(\mu_{21} - \lambda_{T_1}\right)} \tag{31}$$

$$E\left[W_2^{(T_2)}\right] = E\left[R_2^{(T_2)}\right] - \frac{1}{\mu_{22}} = \frac{\lambda_{T_2}}{\mu_{22}\left(\mu_{22} - \lambda_{T_2}\right)} \tag{32}$$

$$E\left[W_3^{(T_3)}\right] = E\left[R_3^{(T_3)}\right] - \frac{1}{\mu_{23}} = \frac{\lambda_{T_3}}{\mu_{23}\left(\mu_{23} - \lambda_{T_3}\right)} \tag{33}$$

4.2 Case I: Evaluation of Performance with Single Server

To evaluate the various performance such as queue length (Lq) response time (Rt) and waiting time (Wt) corresponding to different sections as (S₁, P₁, T₁), (S₁, P₁, T₃), (S₁, P₂, T₁), (S₁, P₂, T₂), (S₁, P₂, T₃), (S₂, P₂, T₁), (S₂, P₂, T₂), (S₂, P₂, T₃), (S₂, P₄, T₃), (S₂, P₄, T₃), (S₃, P₁, T₁), (S₃, P₁, T₃), (S₃, P₃, T₂), (S₃, P₄, T₃) & (S₄, P₄, T₃).

The average number of order to customers in way X₁ (S₁, P₁, T₁)

$$E[X_1] = E\left[N_1^{(S_1)}\right] + E\left[N_1^{(P_1)}\right] + E\left[N_1^{(T_1)}\right]$$

$$L_q = \frac{\lambda_1}{\left(\mu_1 - \lambda_1\right)} + \frac{\lambda_1 \rho_1 + \lambda_3 \rho_6}{\left[\mu_{11} - \left(\lambda_1 \rho_1 + \lambda_3 \rho_6\right)\right]} + \frac{\lambda_{T_1}}{\left(\mu_{21} - \lambda_{T_1}\right)} \tag{34}$$

$$R_t = \frac{1}{\left(\mu_1 - \lambda_1\right)} + \frac{1}{\left[\mu_{11} - \left(\lambda_1 \rho_1 + \lambda_3 \rho_6\right)\right]} + \frac{1}{\left(\mu_{21} - \lambda_{T_1}\right)} \tag{35}$$

$$W_t = \frac{\lambda_1}{\mu_1(\mu_1 - \lambda_1)} + \frac{\lambda_1\rho_1 + \lambda_3\rho_6}{\mu_{11}[\mu_{11} - (\lambda_1\rho_1 + \lambda_3\rho_6)]} + \frac{\lambda_{T_1}}{\mu_{21}(\mu_{21} - \lambda_{T_1})} \tag{36}$$

The average number of order to customers in way X₂ (S₁, P₁, T₃)

$$E[X_2] = E[N_1^{(S_1)}] + E[N_1^{(P_1)}] + E[N_1^{(T_3)}]$$

$$L_q = \frac{\lambda_1}{(\mu_1 - \lambda_1)} + \frac{\lambda_1\rho_1 + \lambda_3\rho_6}{[\mu_{11} - (\lambda_1\rho_1 + \lambda_3\rho_6)]} + \frac{\lambda_{T_3}}{(\mu_{23} - \lambda_{T_3})} \tag{37}$$

$$R_t = \frac{1}{(\mu_1 - \lambda_1)} + \frac{1}{[\mu_{11} - (\lambda_1\rho_1 + \lambda_3\rho_6)]} + \frac{1}{(\mu_{23} - \lambda_{T_3})} \tag{38}$$

$$W_t = \frac{\lambda_1}{\mu_1(\mu_1 - \lambda_1)} + \frac{\lambda_1\rho_1 + \lambda_3\rho_6}{\mu_{11}[\mu_{11} - (\lambda_1\rho_1 + \lambda_3\rho_6)]} + \frac{\lambda_{T_3}}{\mu_{23}(\mu_{23} - \lambda_{T_3})} \tag{39}$$

The average number of order to customers in way X₃ (S₁, P₂, T₁)

$$E[X_3] = E[N_1^{(S_1)}] + E[N_1^{(P_2)}] + E[N_1^{(T_1)}]$$

$$L_q = \frac{\lambda_1}{(\mu_1 - \lambda_1)} + \frac{\lambda_1\rho_2 + \lambda_2\rho_3}{[\mu_{12} - (\lambda_1\rho_2 + \lambda_2\rho_3)]} + \frac{\lambda_{T_1}}{(\mu_{21} - \lambda_{T_1})} \tag{40}$$

$$R_t = \frac{1}{(\mu_1 - \lambda_1)} + \frac{1}{[\mu_{12} - (\lambda_1\rho_2 + \lambda_2\rho_3)]} + \frac{1}{(\mu_{21} - \lambda_{T_1})} \tag{41}$$

$$W_t = \frac{\lambda_1}{\mu_1(\mu_1 - \lambda_1)} + \frac{\lambda_1\rho_2 + \lambda_2\rho_3}{\mu_{12}[\mu_{12} - (\lambda_1\rho_2 + \lambda_2\rho_3)]} + \frac{\lambda_{T_1}}{\mu_{21}(\mu_{21} - \lambda_{T_1})} \tag{42}$$

The average number of order to customers in way X₄ (S₁, P₂, T₂)

$$E[X_4] = E[N_1^{(S_1)}] + E[N_1^{(P_2)}] + E[N_1^{(T_2)}]$$

$$L_q = \frac{\lambda_1}{(\mu_1 - \lambda_1)} + \frac{\lambda_1\rho_2 + \lambda_2\rho_3}{[\mu_{12} - (\lambda_1\rho_2 + \lambda_2\rho_3)]} + \frac{\lambda_{T_2}}{(\mu_{22} - \lambda_{T_2})} \tag{43}$$

$$R_t = \frac{1}{(\mu_1 - \lambda_1)} + \frac{1}{[\mu_{12} - (\lambda_1\rho_2 + \lambda_2\rho_3)]} + \frac{1}{(\mu_{22} - \lambda_{T_2})} \tag{44}$$

$$W_t = \frac{\lambda_1}{\mu_1(\mu_1 - \lambda_1)} + \frac{\lambda_1\rho_2 + \lambda_2\rho_3}{\mu_{12}[\mu_{12} - (\lambda_1\rho_2 + \lambda_2\rho_3)]} + \frac{\lambda_{T_2}}{\mu_{22}(\mu_{22} - \lambda_{T_2})} \tag{45}$$

The average number of order to customers in way X₅ (S₁, P₂, T₃)

$$E[X_5] = E[N_1^{(S_1)}] + E[N_1^{(P_2)}] + E[N_1^{(T_3)}]$$

$$L_q = \frac{\lambda_1}{(\mu_1 - \lambda_1)} + \frac{\lambda_1 \rho_2 + \lambda_2 \rho_3}{[\mu_{12} - (\lambda_1 \rho_2 + \lambda_2 \rho_3)]} + \frac{\lambda_{T_3}}{(\mu_{23} - \lambda_{T_3})} \quad (46)$$

$$R_t = \frac{1}{(\mu_1 - \lambda_1)} + \frac{1}{[\mu_{12} - (\lambda_1 \rho_2 + \lambda_2 \rho_3)]} + \frac{1}{(\mu_{23} - \lambda_{T_3})} \quad (47)$$

$$W_t = \frac{\lambda_1}{\mu_1(\mu_1 - \lambda_1)} + \frac{\lambda_1 \rho_2 + \lambda_2 \rho_3}{\mu_{12}[\mu_{12} - (\lambda_1 \rho_2 + \lambda_2 \rho_3)]} + \frac{\lambda_{T_3}}{\mu_{23}(\mu_{23} - \lambda_{T_3})} \quad (48)$$

The average number of order to customers in way X₆ (S₂, P₂, T₁)

$$E[X_6] = E[N_1^{(S_2)}] + E[N_1^{(P_2)}] + E[N_1^{(T_1)}]$$

$$L_q = \frac{\lambda_2}{(\mu_2 - \lambda_2)} + \frac{\lambda_1 \rho_2 + \lambda_2 \rho_3}{[\mu_{12} - (\lambda_1 \rho_2 + \lambda_2 \rho_3)]} + \frac{\lambda_{T_1}}{(\mu_{21} - \lambda_{T_1})} \quad (49)$$

$$R_t = \frac{1}{(\mu_2 - \lambda_2)} + \frac{1}{[\mu_{12} - (\lambda_1 \rho_2 + \lambda_2 \rho_3)]} + \frac{1}{(\mu_{21} - \lambda_{T_1})} \quad (50)$$

$$W_t = \frac{\lambda_2}{\mu_2(\mu_2 - \lambda_2)} + \frac{\lambda_1 \rho_2 + \lambda_2 \rho_3}{\mu_{12}[\mu_{12} - (\lambda_1 \rho_2 + \lambda_2 \rho_3)]} + \frac{\lambda_{T_1}}{\mu_{21}(\mu_{21} - \lambda_{T_1})} \quad (51)$$

The average number of order to customers in way X₇ (S₂, P₂, T₂)

$$E[X_7] = E[N_1^{(S_2)}] + E[N_1^{(P_2)}] + E[N_1^{(T_2)}]$$

$$L_q = \frac{\lambda_2}{(\mu_2 - \lambda_2)} + \frac{\lambda_1 \rho_2 + \lambda_2 \rho_3}{[\mu_{12} - (\lambda_1 \rho_2 + \lambda_2 \rho_3)]} + \frac{\lambda_{T_2}}{(\mu_{22} - \lambda_{T_2})} \quad (52)$$

$$R_t = \frac{1}{(\mu_2 - \lambda_2)} + \frac{1}{[\mu_{12} - (\lambda_1 \rho_2 + \lambda_2 \rho_3)]} + \frac{1}{(\mu_{22} - \lambda_{T_2})} \quad (53)$$

$$W_t = \frac{\lambda_2}{\mu_2(\mu_2 - \lambda_2)} + \frac{\lambda_1 \rho_2 + \lambda_2 \rho_3}{\mu_{12}[\mu_{12} - (\lambda_1 \rho_2 + \lambda_2 \rho_3)]} + \frac{\lambda_{T_2}}{(\mu_{22}(\mu_{22} - \lambda_{T_2}))} \quad (54)$$

The average number of order to customers in way X₈ (S₂, P₂, T₃)

$$E[X_8] = E[N_1^{(S_2)}] + E[N_1^{(P_2)}] + E[N_1^{(T_3)}]$$

$$L_q = \frac{\lambda_2}{(\mu_2 - \lambda_2)} + \frac{\lambda_1 \rho_2 + \lambda_2 \rho_3}{[\mu_{12} - (\lambda_1 \rho_2 + \lambda_2 \rho_3)]} + \frac{\lambda_{T_3}}{(\mu_{23} - \lambda_{T_3})} \tag{55}$$

$$R_t = \frac{1}{(\mu_2 - \lambda_2)} + \frac{1}{[\mu_{12} - (\lambda_1 \rho_2 + \lambda_2 \rho_3)]} + \frac{1}{(\mu_{23} - \lambda_{T_3})} \tag{56}$$

$$W_t = \frac{\lambda_2}{\mu_2(\mu_2 - \lambda_2)} + \frac{\lambda_1 \rho_2 + \lambda_2 \rho_3}{\mu_{12}[\mu_{12} - (\lambda_1 \rho_2 + \lambda_2 \rho_3)]} + \frac{\lambda_{T_3}}{(\mu_{23}(\mu_{23} - \lambda_{T_3}))} \tag{57}$$

The average number of order to customers in way X₉ (S₂, P₄, T₃)

$$E[X_9] = E[N_1^{(S_2)}] + E[N_1^{(P_4)}] + E[N_1^{(T_3)}]$$

$$L_q = \frac{\lambda_2}{(\mu_2 - \lambda_2)} + \frac{\lambda_4 \rho_8 + \lambda_3 \rho_7}{[\mu_{14} - (\lambda_4 \rho_8 + \lambda_3 \rho_7)]} + \frac{\lambda_{T_3}}{(\mu_{23} - \lambda_{T_3})} \tag{58}$$

$$R_t = \frac{1}{(\mu_2 - \lambda_2)} + \frac{1}{[\mu_{14} - (\lambda_4 \rho_8 + \lambda_3 \rho_7)]} + \frac{1}{(\mu_{23} - \lambda_{T_3})} \tag{59}$$

$$W_t = \frac{\lambda_2}{\mu_2(\mu_2 - \lambda_2)} + \frac{\lambda_4 \rho_8 + \lambda_3 \rho_7}{\mu_{14}[\mu_{14} - (\lambda_4 \rho_8 + \lambda_3 \rho_7)]} + \frac{\lambda_{T_3}}{(\mu_{23}(\mu_{23} - \lambda_{T_3}))} \tag{60}$$

The average number of order to customers in way X₁₀ (S₃, P₁, T₁)

$$E[X_{10}] = E[N_1^{(S_3)}] + E[N_1^{(P_1)}] + E[N_1^{(T_1)}]$$

$$L_q = \frac{\lambda_3}{(\mu_3 - \lambda_3)} + \frac{\lambda_1 \rho_1 + \lambda_3 \rho_6}{[\mu_{11} - (\lambda_1 \rho_1 + \lambda_3 \rho_6)]} + \frac{\lambda_{T_1}}{(\mu_{21} - \lambda_{T_1})} \tag{61}$$

$$R_t = \frac{1}{(\mu_3 - \lambda_3)} + \frac{1}{[\mu_{11} - (\lambda_1 \rho_1 + \lambda_3 \rho_6)]} + \frac{1}{(\mu_{21} - \lambda_{T_1})} \tag{62}$$

$$W_t = \frac{\lambda_3}{\mu_3(\mu_3 - \lambda_3)} + \frac{\lambda_1 \rho_1 + \lambda_3 \rho_6}{\mu_{11}[\mu_{11} - (\lambda_1 \rho_1 + \lambda_3 \rho_6)]} + \frac{\lambda_{T_1}}{\mu_{21}(\mu_{21} - \lambda_{T_1})} \tag{63}$$

The average number of order to customers in way X₁₁ (S₃, P₁, T₃)

$$E[X_{11}] = E[N_1^{(S_3)}] + E[N_1^{(P_1)}] + E[N_1^{(T_3)}]$$

$$L_q = \frac{\lambda_3}{(\mu_3 - \lambda_3)} + \frac{\lambda_1 \rho_1 + \lambda_3 \rho_6}{[\mu_{11} - (\lambda_1 \rho_1 + \lambda_3 \rho_6)]} + \frac{\lambda_{T_3}}{(\mu_{23} - \lambda_{T_3})} \tag{64}$$

$$R_t = \frac{1}{(\mu_3 - \lambda_3)} + \frac{1}{[\mu_{11} - (\lambda_1 \rho_1 + \lambda_3 \rho_6)]} + \frac{1}{(\mu_{23} - \lambda_{T_3})} \tag{65}$$

$$W_t = \frac{\lambda_3}{\mu_3(\mu_3 - \lambda_3)} + \frac{\lambda_1\rho_1 + \lambda_3\rho_6}{\mu_{11}[\mu_{11} - (\lambda_1\rho_1 + \lambda_3\rho_6)]} + \frac{\lambda_{T_3}}{\mu_{23}(\mu_{23} - \lambda_{T_3})}. \tag{66}$$

The average number of order to customers in way X₁₂ (S₃, P₃, T₂)

$$E[X_{12}] = E[N_1^{(S_3)}] + E[N_1^{(P_3)}] + E[N_1^{(T_2)}]$$

$$L_q = \frac{\lambda_3}{(\mu_3 - \lambda_3)} + \frac{\lambda_2\rho_4 + \lambda_3\rho_5 + \lambda_3\rho_9}{[\mu_{13} - (\lambda_2\rho_4 + \lambda_3\rho_5 + \lambda_3\rho_9)]} + \frac{\lambda_{T_2}}{(\mu_{22} - \lambda_{T_2})} \tag{67}$$

$$R_t = \frac{1}{(\mu_3 - \lambda_3)} + \frac{1}{[\mu_{13} - (\lambda_2\rho_4 + \lambda_3\rho_5 + \lambda_3\rho_9)]} + \frac{1}{(\mu_{22} - \lambda_{T_2})} \tag{68}$$

$$W_t = \frac{\lambda_3}{\mu_3(\mu_3 - \lambda_3)} + \frac{\lambda_2\rho_4 + \lambda_3\rho_5 + \lambda_3\rho_9}{\mu_{13}[\mu_{13} - (\lambda_2\rho_4 + \lambda_3\rho_5 + \lambda_3\rho_9)]} + \frac{\lambda_{T_2}}{\mu_{22}(\mu_{22} - \lambda_{T_2})} \tag{69}$$

The average number of order to customers in way X₁₃ (S₃, P₄, T₃)

$$E[X_{13}] = E[N_1^{(S_3)}] + E[N_1^{(P_4)}] + E[N_1^{(T_3)}]$$

$$L_q = \frac{\lambda_3}{(\mu_3 - \lambda_3)} + \frac{\lambda_4\rho_8 + \lambda_3\rho_7}{[\mu_{14} - (\lambda_4\rho_8 + \lambda_3\rho_7)]} + \frac{\lambda_{T_3}}{(\mu_{23} - \lambda_{T_3})} \tag{70}$$

$$R_t = \frac{1}{(\mu_3 - \lambda_3)} + \frac{1}{[\mu_{14} - (\lambda_4\rho_8 + \lambda_3\rho_7)]} + \frac{1}{(\mu_{23} - \lambda_{T_3})} \tag{71}$$

$$W_t = \frac{\lambda_3}{\mu_3(\mu_3 - \lambda_3)} + \frac{\lambda_4\rho_8 + \lambda_3\rho_7}{\mu_{14}[\mu_{14} - (\lambda_4\rho_8 + \lambda_3\rho_7)]} + \frac{\lambda_{T_3}}{\mu_{23}(\mu_{23} - \lambda_{T_3})} \tag{72}$$

The average number of order to customers in way X₁₄ (S₄, P₄, T₃)

$$E[X_{14}] = E[N_1^{(S_4)}] + E[N_1^{(P_4)}] + E[N_1^{(T_3)}]$$

$$L_q = \frac{\lambda_4}{(\mu_4 - \lambda_4)} + \frac{\lambda_4\rho_8 + \lambda_3\rho_7}{[\mu_{14} - (\lambda_4\rho_8 + \lambda_3\rho_7)]} + \frac{\lambda_{T_3}}{(\mu_{23} - \lambda_{T_3})} \tag{73}$$

$$R_t = \frac{1}{(\mu_4 - \lambda_4)} + \frac{1}{[\mu_{14} - (\lambda_4\rho_8 + \lambda_3\rho_7)]} + \frac{1}{(\mu_{23} - \lambda_{T_3})} \tag{74}$$

$$W_t = \frac{\lambda_4}{(\mu_4 - \lambda_4)} + \frac{\lambda_4\rho_8 + \lambda_3\rho_7}{\mu_{14}[\mu_{14} - (\lambda_4\rho_8 + \lambda_3\rho_7)]} + \frac{\lambda_{T_3}}{\mu_{23}(\mu_{23} - \lambda_{T_3})} \tag{75}$$

4.3 Case II: Evaluation of Performance with Multi-server

To construct some paths corresponding to different sections (store, packing and transportation) with different stages (II, III & IV) as (S₁, S₂), (S₂, S₃, S₄), (P₁, P₂), (P₁, P₄), (P₂, P₄), (P₂, P₃), (P₂, P₃, P₄), (T₁, T₂), (T₁, T₃), (T₂, T₃) and (T₁, T₂, T₃) and using multi-server queueing model and also obtained queue length (Lq), response time (Rt) and waiting time (Wt).

Path-I: For stage II (S₁, S₂) with servers (C = 2) and arrival rate $\lambda = \lambda_1 + \lambda_2$ and service rate $\mu = \mu_1 + \mu_2$.

$$Lq = \frac{1}{(C - 1)!} \left[\left(\frac{\lambda_1}{\mu_1} \right)^C \frac{\lambda_1 \mu_1}{(C \mu_1 - \lambda_1)^2} + \left(\frac{\lambda_2}{\mu_2} \right)^C \frac{\lambda_2 \mu_2}{(C \mu_2 - \lambda_2)^2} \right] \times P_0 \tag{76}$$

$$Rt = \left(\frac{1}{\mu_1} + \frac{1}{\mu_2} \right) + \frac{1}{(C)!} \left[\frac{\rho^{(S_1)}}{\lambda_1} \frac{(C \rho^{(S_1)})^2}{(1 - \rho^{(S_1)})^2} + \frac{\rho^{(S_2)}}{\lambda_2} \frac{(C \rho^{(S_2)})^2}{(1 - \rho^{(S_2)})^2} \right] \times P_0 \tag{77}$$

$$Wt = \frac{1}{\lambda} \left[\frac{1}{(C - 1)!} \left[\left(\frac{\lambda_1}{\mu_1} \right)^C \frac{\lambda_1 \mu_1}{(C \mu_1 - \lambda_1)^2} + \left(\frac{\lambda_2}{\mu_2} \right)^C \frac{\lambda_2 \mu_2}{(C \mu_2 - \lambda_2)^2} \right] \times P_0 \right] \tag{78}$$

where $P_0 = \left[\sum_{n=0}^{c-1} \frac{1}{n!} \left(\frac{\lambda}{\mu} \right)^n + \frac{1}{(C)!} \left(\frac{\lambda}{\mu} \right)^c \left(\frac{c\mu}{c\mu-1} \right) \right]^{-1}$

Path-II: For stage II (S₂, S₃, S₄) with servers (C = 3) and arrival rate $\lambda = \lambda_2 + \lambda_3 + \lambda_4$ and service rate $\mu = \mu_2 + \mu_3 + \mu_4$.

$$Lq = \frac{1}{(C - 1)!} \left[\left(\frac{\lambda_2}{\mu_2} \right)^C \frac{\lambda_2 \mu_2}{(C \mu_2 - \lambda_2)^2} + \left(\frac{\lambda_3}{\mu_3} \right)^C \frac{\lambda_3 \mu_3}{(C \mu_3 - \lambda_3)^2} + \left(\frac{\lambda_4}{\mu_4} \right)^C \frac{\lambda_4 \mu_4}{(C \mu_4 - \lambda_4)^2} \right] \times P_0 \tag{79}$$

$$Rt = \left(\frac{1}{\mu_2} + \frac{1}{\mu_3} + \frac{1}{\mu_4} \right) + \frac{1}{(C)!} \left[\frac{\rho^{(S_2)}}{\lambda_2} \frac{(C \rho^{(S_2)})^2}{(1 - \rho^{(S_2)})^2} + \frac{\rho^{(S_3)}}{\lambda_3} \frac{(C \rho^{(S_3)})^2}{(1 - \rho^{(S_3)})^2} + \frac{\rho^{(S_4)}}{\lambda_4} \frac{(C \rho^{(S_4)})^2}{(1 - \rho^{(S_4)})^2} \right] \times P_0 \tag{80}$$

$$Wt = \frac{1}{\lambda} \left[\frac{1}{(C - 1)!} \left[\left(\frac{\lambda_2}{\mu_2} \right)^C \frac{\lambda_2 \mu_2}{(C \mu_2 - \lambda_2)^2} + \left(\frac{\lambda_3}{\mu_3} \right)^C \frac{\lambda_3 \mu_3}{(C \mu_3 - \lambda_3)^2} + \left(\frac{\lambda_4}{\mu_4} \right)^C \frac{\lambda_4 \mu_4}{(C \mu_4 - \lambda_4)^2} \right] \times P_0 \right] \tag{81}$$

where $P_0 = \left[\sum_{n=0}^{c-1} \frac{1}{n!} \left(\frac{\lambda}{\mu} \right)^n + \frac{1}{(C)!} \left(\frac{\lambda}{\mu} \right)^c \left(\frac{c\mu}{c\mu-1} \right) \right]^{-1}$

Path-III: For in stage II (P₁, P₂) with servers (c = 2) and arrival rate $\lambda_{P_1} = \lambda_1 \rho_1 + \lambda_3 \rho_6$ & $\lambda_{P_2} = \lambda_1 \rho_2 + \lambda_2 \rho_3$ and service rate μ_{11} & μ_{12} where $\mu = \mu_{11} + \mu_{12}$.

$$Lq = \frac{1}{(C-1)!} \left[\left(\frac{\lambda_{P_1}}{\mu_{11}} \right)^C \frac{\lambda_{P_1} \mu_{11}}{(C\mu_{11} - \lambda_{P_1})^2} + \left(\frac{\lambda_{P_2}}{\mu_{12}} \right)^C \frac{\lambda_{P_2} \mu_{12}}{(C\mu_{12} - \lambda_{P_2})^2} \right] \times P_0 \quad (82)$$

$$Rt = \left(\frac{1}{\mu_{11}} + \frac{1}{\mu_{12}} \right) + \frac{1}{(C)!} \left[\frac{\rho^{(P_1)} (C\rho^{(P_1)})^2}{\lambda_{P_1} (1 - \rho^{(P_1)})^2} + \frac{\rho^{(P_2)} (C\rho^{(P_2)})^2}{\lambda_{P_2} (1 - \rho^{(P_2)})^2} \right] \times P_0 \quad (83)$$

$$Wt = \frac{1}{\lambda} \left[Lq = \frac{1}{(C-1)!} \left[\left(\frac{\lambda_{P_1}}{\mu_{11}} \right)^C \frac{\lambda_{P_1} \mu_{11}}{(C\mu_{11} - \lambda_{P_1})^2} + \left(\frac{\lambda_{P_2}}{\mu_{12}} \right)^C \frac{\lambda_{P_2} \mu_{12}}{(C\mu_{12} - \lambda_{P_2})^2} \right] \times P_0 \right] \quad (84)$$

where $P_0 = \left[\sum_{n=0}^{C-1} \frac{1}{n!} \left(\frac{\lambda}{\mu} \right)^n + \frac{1}{(C)!} \left(\frac{\lambda}{\mu} \right)^C \left(\frac{c\mu}{c\mu-1} \right) \right]^{-1}$ and $\lambda = \lambda_{P_1} + \lambda_{P_2}$.

Path-IV: For stage II (P_1, P_4) with servers ($C = 2$) and arrival rate $\lambda_{P_1} = \lambda_1\rho_1 + \lambda_3\rho_6$ & $\lambda_{P_4} = \lambda_2\rho_4 + \lambda_3\rho_5 + \lambda_3\rho_9$ and service rate μ_{11} & μ_{14} where $\mu = \mu_{11} + \mu_{14}$.

$$Lq = \frac{1}{(C-1)!} \left[\left(\frac{\lambda_{P_1}}{\mu_{11}} \right)^C \frac{\lambda_{P_1} \mu_{11}}{(C\mu_{11} - \lambda_{P_1})^2} + \left(\frac{\lambda_{P_4}}{\mu_{14}} \right)^C \frac{\lambda_{P_4} \mu_{14}}{(C\mu_{14} - \lambda_{P_4})^2} \right] \times P_0 \quad (85)$$

$$Rt = \left(\frac{1}{\mu_{11}} + \frac{1}{\mu_{14}} \right) + \frac{1}{(C)!} \left[\frac{\rho^{(P_1)} (C\rho^{(P_1)})^2}{\lambda_{P_1} (1 - \rho^{(P_1)})^2} + \frac{\rho^{(P_4)} (C\rho^{(P_4)})^2}{\lambda_{P_4} (1 - \rho^{(P_4)})^2} \right] \times P_0 \quad (86)$$

$$Wt = \frac{1}{\lambda} \left[\frac{1}{(C-1)!} \left[\left(\frac{\lambda_{P_1}}{\mu_{11}} \right)^C \frac{\lambda_{P_1} \mu_{11}}{(C\mu_{11} - \lambda_{P_1})^2} + \left(\frac{\lambda_{P_4}}{\mu_{14}} \right)^C \frac{\lambda_{P_4} \mu_{14}}{(C\mu_{14} - \lambda_{P_4})^2} \right] \times P_0 \right] \quad (87)$$

where $P_0 = \left[\sum_{n=0}^{C-1} \frac{1}{n!} \left(\frac{\lambda}{\mu} \right)^n + \frac{1}{(C)!} \left(\frac{\lambda}{\mu} \right)^C \left(\frac{c\mu}{c\mu-1} \right) \right]^{-1}$ and $\lambda = \lambda_{P_1} + \lambda_{P_4}$

$$\mu = [(\mu_{21} + \mu_{22}) + \mu_{23}] \text{ \& } \lambda = [(\lambda_{T_1} + \lambda_{T_2}) + \lambda_{T_3}]$$

Path-V: For stage II (P_2, P_4) with servers ($C = 2$) and arrival rate $\lambda_{P_2} = \lambda_1\rho_2 + \lambda_2\rho_3$ & $\lambda_{P_4} = \lambda_2\rho_4 + \lambda_3\rho_5 + \lambda_3\rho_9$ and service rate μ_{12} & μ_{14} where $\mu = \mu_{12} + \mu_{14}$.

$$Lq = \frac{1}{(C-1)!} \left[\left(\frac{\lambda_{P_2}}{\mu_{12}} \right)^C \frac{\lambda_{P_2} \mu_{12}}{(C\mu_{12} - \lambda_{P_2})^2} + \left(\frac{\lambda_{P_4}}{\mu_{14}} \right)^C \frac{\lambda_{P_4} \mu_{14}}{(C\mu_{14} - \lambda_{P_4})^2} \right] \times P_0 \quad (88)$$

$$Rt = \left(\frac{1}{\mu_{12}} + \frac{1}{\mu_{14}} \right) + \frac{1}{(C)!} \left[\frac{\rho^{(P_2)} (C\rho^{(P_2)})^2}{\lambda_{P_2} (1 - \rho^{(P_2)})^2} + \frac{\rho^{(P_4)} (C\rho^{(P_4)})^2}{\lambda_{P_4} (1 - \rho^{(P_4)})^2} \right] \times P_0 \quad (89)$$

$$Wt = \frac{1}{\lambda} \left[\frac{1}{(C-1)!} \left[\left(\frac{\lambda_{P_2}}{\mu_{12}} \right)^C \frac{\lambda_{P_2} \mu_{12}}{(C\mu_{12} - \lambda_{P_2})^2} + \left(\frac{\lambda_{P_4}}{\mu_{14}} \right)^C \frac{\lambda_{P_4} \mu_{14}}{(C\mu_{14} - \lambda_{P_4})^2} \right] \times P_0 \right] \quad (90)$$

where $P_0 = \left[\sum_{n=0}^{c-1} \frac{1}{n!} \left(\frac{\lambda}{\mu} \right)^n + \frac{1}{(C)!} \left(\frac{\lambda}{\mu} \right)^c \left(\frac{c\mu}{c\mu-1} \right) \right]^{-1}$ and $\lambda = \lambda_{P_2} + \lambda_{P_4}$.

Path-VI: For stage II (P_2, P_3) with servers ($C = 2$) and arrival rate $\lambda_{P_2} = \lambda_1 \rho_2 + \lambda_2 \rho_3$ & $\lambda_{P_3} = \lambda_1 \rho_1 + \lambda_3 \rho_6$ and service rate μ_{12} & μ_{13} where $\mu = \mu_{12} + \mu_{13}$.

$$Lq = \frac{1}{(C-1)!} \left[\left(\frac{\lambda_{P_2}}{\mu_{12}} \right)^C \frac{\lambda_{P_2} \mu_{12}}{(C\mu_{12} - \lambda_{P_2})^2} + \left(\frac{\lambda_{P_3}}{\mu_{14}} \right)^C \frac{\lambda_{P_3} \mu_{13}}{(C\mu_{13} - \lambda_{P_3})^2} \right] \times P_0 \quad (91)$$

$$Rt = \left(\frac{1}{\mu_1} + \frac{1}{\mu_2} \right) + \frac{1}{(C)!} \left[\frac{\rho^{(P_2)} (C\rho^{(P_2)})^2}{\lambda_{P_2} (1 - \rho^{(P_2)})^2} + \frac{\rho^{(P_3)} (C\rho^{(P_3)})^2}{\lambda_{P_3} (1 - \rho^{(P_3)})^2} \right] \times P_0 \quad (92)$$

$$Wt = \frac{1}{\lambda} \left[\frac{1}{(C-1)!} \left[\left(\frac{\lambda_{P_2}}{\mu_{12}} \right)^C \frac{\lambda_{P_2} \mu_{12}}{(C\mu_{12} - \lambda_{P_2})^2} + \left(\frac{\lambda_{P_3}}{\mu_{14}} \right)^C \frac{\lambda_{P_3} \mu_{13}}{(C\mu_{13} - \lambda_{P_3})^2} \right] \times P_0 \right] \quad (93)$$

where $P_0 = \left[\sum_{n=0}^{c-1} \frac{1}{n!} \left(\frac{\lambda}{\mu} \right)^n + \frac{1}{(C)!} \left(\frac{\lambda}{\mu} \right)^c \left(\frac{c\mu}{c\mu-1} \right) \right]^{-1}$ and $\lambda = \lambda_{P_2} + \lambda_{P_3}$.

Path-VII 7: For stage II (P_2, P_3, P_4) with servers ($C = 3$) and arrival rate $\lambda_{P_2} = \lambda_1 \rho_2 + \lambda_2 \rho_3$, $\lambda_{P_3} = \lambda_1 \rho_1 + \lambda_3 \rho_6$ & $\lambda_{P_4} = \lambda_2 \rho_4 + \lambda_3 \rho_5 + \lambda_3 \rho_9$ and service rate μ_{12}, μ_{13} , & μ_{14} where $\mu = \mu_{12} + \mu_{13} + \mu_{14}$.

$$Lq = \frac{1}{(C-1)!} \left[\left(\frac{\lambda_{P_2}}{\mu_{12}} \right)^C \frac{\lambda_{P_2} \mu_{12}}{(C\mu_{12} - \lambda_{P_2})^2} + \left(\frac{\lambda_{P_3}}{\mu_{14}} \right)^C \frac{\lambda_{P_3} \mu_{13}}{(C\mu_{13} - \lambda_{P_3})^2} + \left(\frac{\lambda_{P_4}}{\mu_{14}} \right)^C \frac{\lambda_{P_4} \mu_{14}}{(C\mu_{14} - \lambda_{P_4})^2} \right] \times P_0 \quad (94)$$

$$Rt = \left(\frac{1}{\mu_{12}} + \frac{1}{\mu_{13}} + \frac{1}{\mu_{14}} \right) + \frac{1}{(C)!} \left[\frac{\rho^{(P_2)} (C\rho^{(P_2)})^2}{\lambda_{P_2} (1 - \rho^{(P_2)})^2} + \frac{\rho^{(P_3)} (C\rho^{(P_3)})^2}{\lambda_{P_3} (1 - \rho^{(P_3)})^2} + \frac{\rho^{(P_4)} (C\rho^{(P_4)})^2}{\lambda_{P_4} (1 - \rho^{(P_4)})^2} \right] \times P_0 \quad (95)$$

$$Wt = \frac{1}{\lambda} \left[\frac{1}{(C-1)!} \left[\left(\frac{\lambda_{P_2}}{\mu_{12}} \right)^C \frac{\lambda_{P_2} \mu_{12}}{(C\mu_{12} - \lambda_{P_2})^2} + \left(\frac{\lambda_{P_3}}{\mu_{14}} \right)^C \frac{\lambda_{P_3} \mu_{13}}{(C\mu_{13} - \lambda_{P_3})^2} + \left(\frac{\lambda_{P_4}}{\mu_{14}} \right)^C \frac{\lambda_{P_4} \mu_{14}}{(C\mu_{14} - \lambda_{P_4})^2} \right] \times P_0 \right] \quad (96)$$

where $P_0 = \left[\sum_{n=0}^{c-1} \frac{1}{n!} \left(\frac{\lambda}{\mu} \right)^n + \frac{1}{(C)!} \left(\frac{\lambda}{\mu} \right)^c \left(\frac{c\mu}{c\mu-1} \right) \right]^{-1}$ and $\lambda = \lambda_{P_2} + \lambda_{P_3} + \lambda_{P_4}$.

Path-VIII: For stage II (T_1, T_2) with servers ($C = 2$) and arrival rate $\lambda_{T_1} = \lambda_1 \rho_1 + \lambda_1 \rho_2 + \lambda_2 \rho_3 + \lambda_3 \rho_6$ & $\lambda_{T_2} = \lambda_1 \rho_2 + \lambda_2 \rho_3 + \lambda_3 \rho_5$ and service rate μ_{21} & μ_{22} .

$$Lq = \frac{1}{(C-1)!} \left[\left(\frac{\lambda_{T_1}}{\mu_{21}} \right)^C \frac{\lambda_{T_1} \mu_{21}}{(C\mu_{21} - \lambda_{T_1}^2)} + \left(\frac{\lambda_{T_2}}{\mu_{22}} \right)^C \frac{\lambda_{T_2} \mu_{22}}{(C\mu_{22} - \lambda_2^2)} \right] \times P_0 \quad (97)$$

$$Rt = \left(\frac{1}{\mu_{21}} + \frac{1}{\mu_{22}} \right) + \frac{1}{(C)!} \left[\frac{\rho^{(T_1)} (C\rho^{(T_1)})^2}{\lambda_{T_1} (1 - \rho^{(T_1)})^2} + \frac{\rho^{(T_2)} (C\rho^{(T_2)})^2}{\lambda_{T_2} (1 - \rho^{(T_2)})^2} \right] \times P_0 \quad (98)$$

$$Wt = \frac{1}{\lambda} \left[\frac{1}{(C-1)!} \left[\left(\frac{\lambda_{T_1}}{\mu_{21}} \right)^C \frac{\lambda_{T_1} \mu_{21}}{(C\mu_{21} - \lambda_{T_1}^2)} + \left(\frac{\lambda_{T_2}}{\mu_{22}} \right)^C \frac{\lambda_{T_2} \mu_{22}}{(C\mu_{22} - \lambda_2^2)} \right] \times P_0 \right] \quad (99)$$

Where $P_0 = \left[\sum_{n=0}^{c-1} \frac{1}{n!} \left(\frac{\lambda}{\mu} \right)^n + \frac{1}{(C)!} \left(\frac{\lambda}{\mu} \right)^c \left(\frac{c\mu}{c\mu-1} \right) \right]^{-1}$ & $\mu = \mu_{21} + \mu_{22}$ & $\lambda = \lambda_{T_1} + \lambda_{T_2}$.

Path-IX: For stage II (T_1, T_3) with servers ($C = 2$) and arrival rate $\lambda_{T_1} = \lambda_1\rho_1 + \lambda_1\rho_2 + \lambda_2\rho_3 + \lambda_3\rho_6$ & $\lambda_{T_3} = \lambda_1\rho_1 + \lambda_3\rho_7 + \lambda_2\rho_4 + \lambda_3\rho_6 + \lambda_4\rho_8$ and service rate μ_{21} & μ_{23} .

$$Lq = \frac{1}{(C-1)!} \left[\left(\frac{\lambda_{T_1}}{\mu_{21}} \right)^C \frac{\lambda_{T_1} \mu_{21}}{(C\mu_{21} - \lambda_{T_1}^2)} + \left(\frac{\lambda_{T_3}}{\mu_{23}} \right)^C \frac{\lambda_{T_3} \mu_{23}}{(C\mu_{23} - \lambda_{T_3}^2)} \right] \times P_0 \quad (100)$$

$$Rt = \left(\frac{1}{\mu_{21}} + \frac{1}{\mu_{23}} \right) + \frac{1}{(C)!} \left[\frac{\rho^{(T_1)} (C\rho^{(T_1)})^2}{\lambda_{T_1} (1 - \rho^{(T_1)})^2} + \frac{\rho^{(T_3)} (C\rho^{(T_3)})^2}{\lambda_{T_3} (1 - \rho^{(T_3)})^2} \right] \times P_0 \quad (101)$$

$$Wt = \frac{1}{\lambda} \left[\frac{1}{(C-1)!} \left[\left(\frac{\lambda_{T_1}}{\mu_{21}} \right)^C \frac{\lambda_{T_1} \mu_{21}}{(C\mu_{21} - \lambda_{T_1}^2)} + \left(\frac{\lambda_{T_3}}{\mu_{23}} \right)^C \frac{\lambda_{T_3} \mu_{23}}{(C\mu_{23} - \lambda_{T_3}^2)} \right] \times P_0 \right] \quad (102)$$

where $P_0 = \left[\sum_{n=0}^{c-1} \frac{1}{n!} \left(\frac{\lambda}{\mu} \right)^n + \frac{1}{(C)!} \left(\frac{\lambda}{\mu} \right)^c \left(\frac{c\mu}{c\mu-1} \right) \right]^{-1}$ & $\mu = \mu_{21} + \mu_{23}$ & $\lambda = \lambda_{T_1} + \lambda_{T_3}$.

Path-X: For stage II (T_2, T_3) with servers ($C = 2$) and arrival rate $\lambda_{T_2} = \lambda_1\rho_2 + \lambda_2\rho_3 + \lambda_3\rho_5$ & $\lambda_{T_3} = \lambda_1\rho_1 + \lambda_3\rho_7 + \lambda_2\rho_4 + \lambda_3\rho_6 + \lambda_4\rho_8$ and service rate μ_{22} & μ_{23} .

$$Lq = \frac{1}{(C-1)!} \left[\left(\frac{\lambda_{T_2}}{\mu_{22}} \right)^C \frac{\lambda_{T_2} \mu_{22}}{(C\mu_{22} - \lambda_2^2)} + \left(\frac{\lambda_{T_3}}{\mu_{23}} \right)^C \frac{\lambda_{T_3} \mu_{23}}{(C\mu_{23} - \lambda_{T_3}^2)} \right] \times P_0 \quad (103)$$

$$Rt = \left(\frac{1}{\mu_{22}} + \frac{1}{\mu_{23}} \right) + \frac{1}{(C)!} \left[\frac{\rho^{(T_2)} (C\rho^{(T_2)})^2}{\lambda_{T_2} (1 - \rho^{(T_2)})^2} + \frac{\rho^{(T_3)} (C\rho^{(T_3)})^2}{\lambda_{T_3} (1 - \rho^{(T_3)})^2} \right] \times P_0 \quad (104)$$

$$Wt = \frac{\frac{1}{(C-1)!} \left[\left(\frac{\lambda_{T_2}}{\mu_{22}} \right)^C \frac{\lambda_{T_2} \mu_{22}}{(C\mu_{22} - \lambda_2^2)} + \left(\frac{\lambda_{T_3}}{\mu_{23}} \right)^C \frac{\lambda_{T_3} \mu_{23}}{(C\mu_{23} - \lambda_{T_3}^2)} \right] \times P_0}{\lambda} \quad (105)$$

where $P_0 = \left[\sum_{n=0}^{c-1} \frac{1}{n!} \left(\frac{\lambda}{\mu} \right)^n + \frac{1}{(C)!} \left(\frac{\lambda}{\mu} \right)^c \left(\frac{c\mu}{c\mu-1} \right) \right]^{-1}$ & $\mu = \mu_{22} + \mu_{23}$ & $\lambda = \lambda_{T_2} + \lambda_{T_3}$.

Path-XI: For stage II (T_1, T_2, T_3) with servers ($C = 3$) and arrival rate $\lambda_{T_1} = \lambda_1\rho_1 + \lambda_1\rho_2 + \lambda_2\rho_3 + \lambda_3\rho_6$, $\lambda_{T_2} = \lambda_1\rho_2 + \lambda_2\rho_3 + \lambda_3\rho_5$ & $\lambda_{T_3} = \lambda_1\rho_1 + \lambda_3\rho_7 + \lambda_2\rho_4 + \lambda_3\rho_6 + \lambda_4\rho_8$ and service rate μ_{21}, μ_{22} , & μ_{23} .

$$Lq = \frac{1}{(C-1)!} \left[\left(\frac{\lambda_{T_1}}{\mu_{21}} \right)^C \frac{\lambda_{T_1}\mu_{21}}{(C\mu_{21} - \lambda_{T_1}^2)} + \left(\frac{\lambda_{T_2}}{\mu_{22}} \right)^C \frac{\lambda_{T_2}\mu_{22}}{(C\mu_{22} - \lambda_{T_2}^2)} + \left(\frac{\lambda_{T_3}}{\mu_{23}} \right)^C \frac{\lambda_{T_3}\mu_{23}}{(C\mu_{23} - \lambda_{T_3}^2)} \right] \times P_0 \tag{106}$$

$$Rt = \left(\frac{1}{\mu_{21}} + \frac{1}{\mu_{22}} + \frac{1}{\mu_{23}} \right) + \frac{1}{(C)!} \left[\frac{\rho^{(T_1)} (C\rho^{(T_1)})^2}{\lambda_{T_1} (1 - \rho^{(T_1)})^2} + \frac{\rho^{(T_2)} (C\rho^{(T_2)})^2}{\lambda_{T_2} (1 - \rho^{(T_2)})^2} + \frac{\rho^{(T_3)} (C\rho^{(T_3)})^2}{\lambda_{T_3} (1 - \rho^{(T_3)})^2} \right] \times P_0 \tag{107}$$

$$Wt = \frac{1}{\lambda} \left[\frac{1}{(C-1)!} \left[\left(\frac{\lambda_{T_1}}{\mu_{21}} \right)^C \frac{\lambda_{T_1}\mu_{21}}{(C\mu_{21} - \lambda_{T_1}^2)} + \left(\frac{\lambda_{T_2}}{\mu_{22}} \right)^C \frac{\lambda_{T_2}\mu_{22}}{(C\mu_{22} - \lambda_{T_2}^2)} + \left(\frac{\lambda_{T_3}}{\mu_{23}} \right)^C \frac{\lambda_{T_3}\mu_{23}}{(C\mu_{23} - \lambda_{T_3}^2)} \right] \times P_0 \right] \tag{108}$$

Where $P_0 = \left[\sum_{n=0}^{c-1} \frac{1}{n!} \left(\frac{\lambda}{\mu} \right)^n + \frac{1}{(C)!} \left(\frac{\lambda}{\mu} \right)^c \left(\frac{c\mu}{c\mu-1} \right) \right]^{-1}$ & $\mu = \mu_{21} + \mu_{22} + \mu_{23}$ & $\lambda = \lambda_{T_1} + \lambda_{T_2} + \lambda_{T_3}$.

Path-XII: For stage II (P_2, P_3, P_4) with servers ($c = 3$) and arrival rate $\lambda_{P_2}, \lambda_{P_3}$ & λ_{P_4} and service rate μ_{12}, μ_{13} & μ_{14} .

$$Lq = \frac{1}{(C-1)!} \left[\left\{ \left(\frac{\lambda_{P_2}}{\mu_{12}} \right)^C \frac{\lambda_{P_2}\mu_{12}}{(C\mu_{12} - \lambda_{P_2}^2)} + \left(\frac{\lambda_{P_3}}{\mu_{14}} \right)^C \frac{\lambda_{P_3}\mu_{13}}{(C\mu_{13} - \lambda_{P_3}^2)} \right\} + \left(\frac{\lambda_{P_4}}{\mu_{14}} \right)^C \frac{\lambda_{P_4}\mu_{14}}{(C\mu_{14} - \lambda_{P_4}^2)} \right] \times P_0 \tag{109}$$

$$Rt = \left(\frac{1}{\mu_{12}} + \frac{1}{\mu_{13}} + \frac{1}{\mu_{14}} \right) + \frac{1}{(C)!} \left[\left\{ \frac{\rho^{(P_2)} (C\rho^{(P_2)})^2}{\lambda_{P_2} (1 - \rho^{(P_2)})^2} + \frac{\rho^{(P_3)} (C\rho^{(P_3)})^2}{\lambda_{P_3} (1 - \rho^{(P_3)})^2} \right\} + \frac{\rho^{(P_4)} (C\rho^{(P_4)})^2}{\lambda_{P_4} (1 - \rho^{(P_4)})^2} \right] \times P_0 \tag{110}$$

$$Wt = \frac{1}{\lambda} \left[\frac{1}{(C-1)!} \left[\left\{ \left(\frac{\lambda_{P_2}}{\mu_{12}} \right)^C \frac{\lambda_{P_2}\mu_{12}}{(C\mu_{12} - \lambda_{P_2}^2)} + \left(\frac{\lambda_{P_3}}{\mu_{14}} \right)^C \frac{\lambda_{P_3}\mu_{13}}{(C\mu_{13} - \lambda_{P_3}^2)} \right\} + \left(\frac{\lambda_{P_4}}{\mu_{14}} \right)^C \frac{\lambda_{P_4}\mu_{14}}{(C\mu_{14} - \lambda_{P_4}^2)} \right] \times P_0 \right] \tag{111}$$

where $P_0 = \left[\sum_{n=0}^{c-1} \frac{1}{n!} \left(\frac{\lambda}{\mu} \right)^n + \frac{1}{(C)!} \left(\frac{\lambda}{\mu} \right)^c \left(\frac{c\mu}{c\mu-1} \right) \right]^{-1}$ and $\mu = [(\mu_{12} + \mu_{13}) + \mu_{14}]$ & $\lambda = [(\lambda_{P_2} + \lambda_{P_3}) + \lambda_{P_4}]$

Path-XIII: For stage II (T_1, T_2, T_3) with servers ($c = 3$) and arrival rate $\lambda_{T_1}, \lambda_{T_2}$ & λ_{T_3} and service rate μ_{21}, μ_{22} & μ_{23} where $\mu = [(\mu_{21} + \mu_{22}) + \mu_{23}]$.

$$Lq = \frac{1}{(C-1)!} \left[\left\{ \left(\frac{\lambda_{T_1}}{\mu_{21}} \right)^C \frac{\lambda_{T_1} \mu_{21}}{(C\mu_{21} - \lambda_{T_1}^2)} + \left(\frac{\lambda_{T_2}}{\mu_{22}} \right)^C \frac{\lambda_{T_2} \mu_{22}}{(C\mu_{22} - \lambda_{T_2}^2)} \right\} + \left(\frac{\lambda_{T_3}}{\mu_{23}} \right)^C \frac{\lambda_{T_3} \mu_{23}}{(C\mu_{23} - \lambda_{T_3}^2)} \right] \times P_0 \tag{112}$$

$$Rt = \left(\frac{1}{\mu_{21}} + \frac{1}{\mu_{22}} + \frac{1}{\mu_{23}} \right) \frac{1}{(C)!} \left[\left\{ \frac{\rho^{(T_1)} (C\rho^{(T_1)})^2}{\lambda_{T_1} (1 - \rho^{(T_1)})^2} + \frac{\rho^{(T_2)} (C\rho^{(T_2)})^2}{\lambda_{T_2} (1 - \rho^{(T_2)})^2} \right\} + \frac{\rho^{(T_3)} (C\rho^{(T_3)})^2}{\lambda_{T_3} (1 - \rho^{(T_3)})^2} \right] \times P_0 \tag{113}$$

$$Wt = \frac{1}{\lambda} \left[\frac{1}{(C-1)!} \left[\left\{ \left(\frac{\lambda_{T_1}}{\mu_{21}} \right)^C \frac{\lambda_{T_1} \mu_{21}}{(C\mu_{21} - \lambda_{T_1}^2)} + \left(\frac{\lambda_{T_2}}{\mu_{22}} \right)^C \frac{\lambda_{T_2} \mu_{22}}{(C\mu_{22} - \lambda_{T_2}^2)} \right\} + \left(\frac{\lambda_{T_3}}{\mu_{23}} \right)^C \frac{\lambda_{T_3} \mu_{23}}{(C\mu_{23} - \lambda_{T_3}^2)} \right] \times P_0 \right] \tag{114}$$

where $P_0 = \left[\sum_{n=0}^{c-1} \frac{1}{n!} \left(\frac{\lambda}{\mu} \right)^n + \frac{1}{(C)!} \left(\frac{\lambda}{\mu} \right)^c \left(\frac{c\mu}{c\mu-1} \right) \right]^{-1}$ & $\mu = [(\mu_{21} + \mu_{22}) + \mu_{23}]$ & $\lambda = [(\lambda_{T_1} + \lambda_{T_2}) + \lambda_{T_3}]$.

5 Optimal Path Corresponding Case I and Case II

In this section, we are exploring the best optimal path by using different paths with single- server and multi-server queueing models as described in the previous section case I and case II. According to Fig. 2, to obtained performance measures of queue length, response time and waiting time with different sections (Fig. 3).

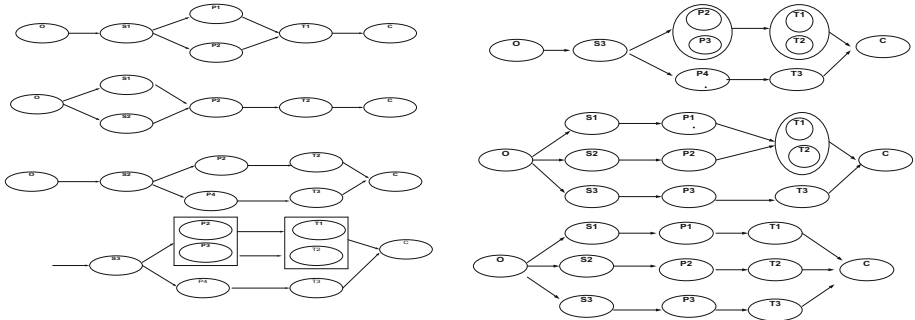


Fig. 3. Different paths with single and multi-servers

Path-I: (S₁, P₁, T₁):

$$Lq = \frac{\lambda_1}{(\mu_1 - \lambda_1)} + \frac{\lambda_1 \rho_1 + \lambda_3 \rho_6}{[\mu_{11} - (\lambda_1 \rho_1 + \lambda_3 \rho_6)]} + \frac{\lambda_{T_1}}{(\mu_{21} - \lambda_{T_1})} \tag{115}$$

$$Rt = \frac{1}{(\mu_1 - \lambda_1)} + \frac{1}{[\mu_{11} - (\lambda_1 \rho_1 + \lambda_3 \rho_6)]} + \frac{1}{(\mu_{21} - \lambda_{T_1})} \tag{116}$$

$$Wt = \frac{\lambda_1}{\mu_1(\mu_1 - \lambda_1)} + \frac{\lambda_1 \rho_1 + \lambda_3 \rho_6}{\mu_{11}[\mu_{11} - (\lambda_1 \rho_1 + \lambda_3 \rho_6)]} + \frac{\lambda_{T_1}}{\mu_{21}(\mu_{21} - \lambda_{T_1})} \tag{117}$$

Path-II: (S₁, (P₁, P₂), T₁)

$$Lq = \frac{\lambda_1}{(\mu_1 - \lambda_1)} + \left\{ \frac{1}{(C-1)!} \left[\left(\frac{\lambda_{P_1}}{\mu_{11}} \right)^C \frac{\lambda_{P_1} \mu_{11}}{(C\mu_{11} - \lambda_{P_1})^2} + \left(\frac{\lambda_{P_2}}{\mu_{12}} \right)^C \frac{\lambda_{P_2} \mu_{12}}{(C\mu_{12} - \lambda_{P_2})^2} \right] \times P_0 \right\} + \frac{\lambda_{T_1}}{(\mu_{21} - \lambda_{T_1})} \tag{118}$$

$$Rt = \frac{1}{(\mu_1 - \lambda_1)} + \left\{ \left(\frac{1}{\mu_{11}} + \frac{1}{\mu_{12}} \right) + \frac{1}{(C)!} \left[\frac{\rho^{(P_1)} (C\rho^{(P_1)})^2}{\lambda_{P_1} (1 - \rho^{(P_1)})^2} + \frac{\rho^{(P_2)} (C\rho^{(P_2)})^2}{\lambda_{P_2} (1 - \rho^{(P_2)})^2} \right] \times P_0 \right\} + \frac{1}{(\mu_{21} - \lambda_{T_1})} \tag{119}$$

$$Wt = \frac{1}{\lambda} \left\{ \frac{\lambda_1}{(\mu_1 - \lambda_1)} + \frac{\lambda_1 \rho_1 + \lambda_3 \rho_6}{[\mu_{11} - (\lambda_1 \rho_1 + \lambda_3 \rho_6)]} + \frac{\lambda_{T_1}}{(\mu_{21} - \lambda_{T_1})} \right\} \tag{120}$$

where $\lambda = \lambda_1 + (\lambda_1 \rho_1 + \lambda_3 \rho_6) + \lambda_{T_1}$.

Path-III: (S₁, S₁, P₂, T₂)

$$Lq = \left\{ \frac{1}{(C-1)!} \left[\left(\frac{\lambda_1}{\mu_1} \right)^C \frac{\lambda_1 \mu_1}{(C\mu_1 - \lambda_1)^2} + \left(\frac{\lambda_2}{\mu_2} \right)^C \frac{\lambda_2 \mu_2}{(C\mu_2 - \lambda_2)^2} \right] \times P_0 \right\} + \frac{\lambda_1 \rho_2 + \lambda_2 \rho_3}{[\mu_{12} - (\lambda_1 \rho_2 + \lambda_2 \rho_3)]} + \frac{\lambda_{T_2}}{(\mu_{22} - \lambda_{T_2})} \tag{121}$$

$$Rt = \left\{ \left(\frac{1}{\mu_1} + \frac{1}{\mu_2} \right) + \frac{1}{(C)!} \left[\frac{\rho^{(S_1)} (C\rho^{(S_1)})^2}{\lambda_1 (1 - \rho^{(S_1)})^2} + \frac{\rho^{(S_2)} (C\rho^{(S_2)})^2}{\lambda_2 (1 - \rho^{(S_2)})^2} \right] \times P_0 \right\} + \frac{1}{[\mu_{12} - (\lambda_1 \rho_2 + \lambda_2 \rho_3)]} + \frac{1}{(\mu_{22} - \lambda_{T_2})} \tag{122}$$

$$Wt = \frac{1}{\lambda} \left\{ \left\{ \frac{1}{(C-1)!} \left[\left(\frac{\lambda_1}{\mu_1} \right)^C \frac{\lambda_1 \mu_1}{(C\mu_1 - \lambda_1)^2} + \left(\frac{\lambda_2}{\mu_2} \right)^C \frac{\lambda_2 \mu_2}{(C\mu_2 - \lambda_2)^2} \right] \times P_0 \right\} + \frac{\lambda_1 \rho_2 + \lambda_2 \rho_3}{[\mu_{12} - (\lambda_1 \rho_2 + \lambda_2 \rho_3)]} + \frac{\lambda_{T_2}}{(\mu_{22} - \lambda_{T_2})} \right\} \tag{123}$$

where $\lambda = (\lambda_1 + \lambda_2) + (\lambda_1 \rho_2 + \lambda_2 \rho_3) + \lambda_{T_2}$.

Path-IV: (S₂, (P₂, P₄), (T₂, T₃))

$$Lq = \left[\frac{\lambda_2}{(\mu_2 - \lambda_2)} + \left\{ \frac{1}{(C-1)!} \left[\left(\frac{\lambda_{P_2}}{\mu_{12}} \right)^C \frac{\lambda_{P_2} \mu_{12}}{(C\mu_{12} - \lambda_{P_2})^2} + \left(\frac{\lambda_{P_4}}{\mu_{14}} \right)^C \frac{\lambda_{P_4} \mu_{14}}{(C\mu_{14} - \lambda_{P_4})^2} \right] \times P_0 \right\} \right. \\ \left. + \left\{ \frac{1}{(C-1)!} \left[\left(\frac{\lambda_{T_2}}{\mu_{22}} \right)^C \frac{\lambda_{T_2} \mu_{22}}{(C\mu_{22} - \lambda_{T_2})^2} + \left(\frac{\lambda_{T_3}}{\mu_{23}} \right)^C \frac{\lambda_{T_3} \mu_{23}}{(C\mu_{23} - \lambda_{T_3})^2} \right] \times P_0 \right\} \right] \tag{124}$$

$$Rt = \frac{1}{(\mu_2 - \lambda_2)} + \left\{ \left(\frac{1}{\mu_{12}} + \frac{1}{\mu_{14}} \right) + \frac{1}{(C)!} \left[\frac{\rho^{(P_2)} (C\rho^{(P_2)})^2}{\lambda_{P_2} (1 - \rho^{(P_2)})^2} + \frac{\rho^{(P_4)} (C\rho^{(P_4)})^2}{\lambda_{P_4} (1 - \rho^{(P_4)})^2} \right] \times P_0 \right\} + \left\{ \left(\frac{1}{\mu_{22}} + \frac{1}{\mu_{23}} \right) + \frac{1}{(C)!} \left[\frac{\rho^{(T_2)} (C\rho^{(T_2)})^2}{\lambda_{T_2} (1 - \rho^{(T_2)})^2} + \frac{\rho^{(T_3)} (C\rho^{(T_3)})^2}{\lambda_{T_3} (1 - \rho^{(T_3)})^2} \right] \times P_0 \right\} \tag{125}$$

$$Wt = \frac{1}{\lambda} \left[\frac{\lambda_2}{(\mu_2 - \lambda_2)} + \left\{ \frac{1}{(C-1)!} \left[\left(\frac{\lambda_{P_2}}{\mu_{12}} \right)^C \frac{\lambda_{P_2}\mu_{12}}{(C\mu_{12} - \lambda_{P_2})^2} + \left(\frac{\lambda_{P_4}}{\mu_{14}} \right)^C \frac{\lambda_{P_4}\mu_{14}}{(C\mu_{14} - \lambda_{P_4})^2} \right] \times P_0 \right\} + \left\{ \frac{1}{(C-1)!} \left[\left(\frac{\lambda_{T_2}}{\mu_{22}} \right)^C \frac{\lambda_{T_2}\mu_{22}}{(C\mu_{22} - \lambda_2)^2} + \left(\frac{\lambda_{T_3}}{\mu_{23}} \right)^C \frac{\lambda_{T_3}\mu_{23}}{(C\mu_{23} - \lambda_{T_3})^2} \right] \times P_0 \right\} \right] \tag{126}$$

where $\lambda = (\lambda_2) + \lambda_{T_3} + \lambda_{T_2}$.

Path-V: $\{S_3, \{P_2, P_3, P_4\}, \{T_1, T_2, T_3\}$

$$Lq = \frac{\lambda_3}{(\mu_3 - \lambda_3)} + \left[\frac{1}{(C-1)!} \left[\left\{ \left(\frac{\lambda_{P_2}}{\mu_{12}} \right)^C \frac{\lambda_{P_2}\mu_{12}}{(C\mu_{12} - \lambda_{P_2})^2} + \left(\frac{\lambda_{P_3}}{\mu_{14}} \right)^C \frac{\lambda_{P_3}\mu_{13}}{(C\mu_{13} - \lambda_{P_3})^2} \right\} + \left(\frac{\lambda_{P_4}}{\mu_{14}} \right)^C \frac{\lambda_{P_4}\mu_{14}}{(C\mu_{14} - \lambda_{P_4})^2} \right] \times P_0 \right] + \left[\frac{1}{(C-1)!} \left[\left\{ \left(\frac{\lambda_{T_1}}{\mu_{21}} \right)^C \frac{\lambda_{T_1}\mu_{21}}{(C\mu_{21} - \lambda_{T_1}^2)^2} + \left(\frac{\lambda_{T_2}}{\mu_{22}} \right)^C \frac{\lambda_{T_2}\mu_{22}}{(C\mu_{22} - \lambda_2)^2} \right\} + \left(\frac{\lambda_{T_3}}{\mu_{23}} \right)^C \frac{\lambda_{T_3}\mu_{23}}{(C\mu_{23} - \lambda_{T_3})^2} \right] \times P_0 \right] \tag{127}$$

$$Rt = \frac{1}{(\mu_3 - \lambda_3)} + \left[\left(\frac{1}{\mu_2} + \frac{1}{\mu_3} + \frac{1}{\mu_4} \right) + \frac{1}{(C)!} \left[\left\{ \frac{\rho^{(P_2)} (C\rho^{(P_2)})^2}{\lambda_{P_2} (1 - \rho^{(P_2)})^2} + \frac{\rho^{(P_3)} (C\rho^{(P_3)})^2}{\lambda_{P_3} (1 - \rho^{(P_3)})^2} \right\} + \frac{\rho^{(P_4)} (C\rho^{(P_4)})^2}{\lambda_{P_4} (1 - \rho^{(P_4)})^2} \right] \times P_0 \right] + \left[\left(\frac{1}{\mu_{21}} + \frac{1}{\mu_{22}} + \frac{1}{\mu_{23}} \right) + \frac{1}{(C)!} \left[\left\{ \frac{\rho^{(T_1)} (C\rho^{(T_1)})^2}{\lambda_{T_1} (1 - \rho^{(T_1)})^2} + \frac{\rho^{(T_2)} (C\rho^{(T_2)})^2}{\lambda_{T_2} (1 - \rho^{(T_2)})^2} \right\} + \frac{\rho^{(T_3)} (C\rho^{(T_3)})^2}{\lambda_{T_3} (1 - \rho^{(T_3)})^2} \right] \times P_0 \right] \tag{128}$$

$$Wt = \frac{1}{\lambda} \left[\frac{\lambda_3}{(\mu_3 - \lambda_3)} + \left[\frac{1}{(C-1)!} \left[\left\{ \left(\frac{\lambda_{P_2}}{\mu_{12}} \right)^C \frac{\lambda_{P_2}\mu_{12}}{(C\mu_{12} - \lambda_{P_2})^2} + \left(\frac{\lambda_{P_3}}{\mu_{14}} \right)^C \frac{\lambda_{P_3}\mu_{13}}{(C\mu_{13} - \lambda_{P_3})^2} \right\} + \left(\frac{\lambda_{P_4}}{\mu_{14}} \right)^C \frac{\lambda_{P_4}\mu_{14}}{(C\mu_{14} - \lambda_{P_4})^2} \right] \times P_0 \right] + \left[\frac{1}{(C-1)!} \left[\left\{ \left(\frac{\lambda_{T_1}}{\mu_{21}} \right)^C \frac{\lambda_{T_1}\mu_{21}}{(C\mu_{21} - \lambda_{T_1}^2)^2} + \left(\frac{\lambda_{T_2}}{\mu_{22}} \right)^C \frac{\lambda_{T_2}\mu_{22}}{(C\mu_{22} - \lambda_2)^2} \right\} + \left(\frac{\lambda_{T_3}}{\mu_{23}} \right)^C \frac{\lambda_{T_3}\mu_{23}}{(C\mu_{23} - \lambda_{T_3})^2} \right] \times P_0 \right] \right] \tag{129}$$

where $\lambda = \lambda_3 + \lambda_{T_1} + \lambda_{T_3} + \lambda_{T_2}$.

Path-VI: $\{(S_1, S_2, S_3)\} \{P_1, P_2, P_3\}, \{(T_1, T_2), T_3\}$

$Lq =$

$$\begin{aligned} & \left\{ \frac{1}{(C-1)!} \left[\left(\frac{\lambda_1}{\mu_1} \right)^C \frac{\lambda_1 \mu_1}{(C\mu_1 - \lambda_1)^2} + \left(\frac{\lambda_2}{\mu_2} \right)^C \frac{\lambda_2 \mu_2}{(C\mu_2 - \lambda_2)^2} + \left(\frac{\lambda_3}{\mu_3} \right)^C \frac{\lambda_3 \mu_3}{(C\mu_3 - \lambda_3)^2} + \right] \times P_0 \right\} \\ & + \left\{ \frac{1}{(C-1)!} \left[\left(\frac{\lambda_{P_1}}{\mu_{11}} \right)^C \frac{\lambda_{P_1} \mu_{11}}{(C\mu_{11} - \lambda_{P_1})^2} + \left(\frac{\lambda_{P_2}}{\mu_{12}} \right)^C \frac{\lambda_{P_2} \mu_{12}}{(C\mu_{12} - \lambda_{P_2})^2} + \left(\frac{\lambda_{P_3}}{\mu_{14}} \right)^C \frac{\lambda_{P_3} \mu_{13}}{(C\mu_{13} - \lambda_{P_3})^2} + \right] \times P_0 \right\} \\ & + \left\{ \frac{1}{(C-1)!} \left[\left\{ \left(\frac{\lambda_{T_1}}{\mu_{21}} \right)^C \frac{\lambda_{T_1} \mu_{21}}{(C\mu_{21} - \lambda_{T_1}^2)^2} + \left(\frac{\lambda_{T_2}}{\mu_{22}} \right)^C \frac{\lambda_{T_2} \mu_{22}}{(C\mu_{22} - \lambda_2)^2} \right\} + \left(\frac{\lambda_{T_3}}{\mu_{23}} \right)^C \frac{\lambda_{T_3} \mu_{23}}{(C\mu_{23} - \lambda_{T_3})^2} \right] \times P_0 \right\} \end{aligned} \tag{130}$$

$Rt =$

$$\begin{aligned} & \left\{ \left(\frac{1}{\mu_1} + \frac{1}{\mu_2} + \frac{1}{\mu_3} \right) + \frac{1}{(C)!} \left[\frac{\rho^{(S_1)}}{\lambda_1} \frac{(C\rho^{(S_1)})^2}{(1 - \rho^{(S_1)})^2} + \frac{\rho^{(S_2)}}{\lambda_2} \frac{(C\rho^{(S_2)})^2}{(1 - \rho^{(S_2)})^2} + \frac{\rho^{(S_3)}}{\lambda_3} \frac{(C\rho^{(S_3)})^2}{(1 - \rho^{(S_3)})^2} \right] \times P_0 \right\} \\ & + \left\{ \left(\frac{1}{\mu_{11}} + \frac{1}{\mu_{12}} + \frac{1}{\mu_{13}} \right) + \frac{1}{(C)!} \left[\left\{ \frac{\rho^{(P_1)}}{\lambda_{P_1}} \frac{(C\rho^{(P_1)})^2}{(1 - \rho^{(P_1)})^2} + \frac{\rho^{(P_2)}}{\lambda_{P_2}} \frac{(C\rho^{(P_2)})^2}{(1 - \rho^{(P_2)})^2} + \frac{\rho^{(P_3)}}{\lambda_{P_3}} \frac{(C\rho^{(P_3)})^2}{(1 - \rho^{(P_3)})^2} \right\} \right] \times P_0 \right\} \\ & + \left\{ \left(\frac{1}{\mu_{21}} + \frac{1}{\mu_{22}} + \frac{1}{\mu_{23}} \right) + \frac{1}{(C)!} \left[\left\{ \frac{\rho^{(T_1)}}{\lambda_{T_1}} \frac{(C\rho^{(T_1)})^2}{(1 - \rho^{(T_1)})^2} + \frac{\rho^{(T_2)}}{\lambda_{T_2}} \frac{(C\rho^{(T_2)})^2}{(1 - \rho^{(T_2)})^2} \right\} + \frac{\rho^{(T_3)}}{\lambda_{T_3}} \frac{(C\rho^{(T_3)})^2}{(1 - \rho^{(T_3)})^2} \right] \times P_0 \right\} \end{aligned} \tag{131}$$

$Wt =$

$$\begin{aligned} & \frac{1}{\lambda} \left\{ \left[\frac{1}{(C-1)!} \left[\left(\frac{\lambda_1}{\mu_1} \right)^C \frac{\lambda_1 \mu_1}{(C\mu_1 - \lambda_1)^2} + \left(\frac{\lambda_2}{\mu_2} \right)^C \frac{\lambda_2 \mu_2}{(C\mu_2 - \lambda_2)^2} + \left(\frac{\lambda_3}{\mu_3} \right)^C \frac{\lambda_3 \mu_3}{(C\mu_3 - \lambda_3)^2} + \right] \times P_0 \right\} \\ & + \left\{ \frac{1}{(C-1)!} \left[\left(\frac{\lambda_{P_1}}{\mu_{11}} \right)^C \frac{\lambda_{P_1} \mu_{11}}{(C\mu_{11} - \lambda_{P_1})^2} + \left(\frac{\lambda_{P_2}}{\mu_{12}} \right)^C \frac{\lambda_{P_2} \mu_{12}}{(C\mu_{12} - \lambda_{P_2})^2} + \left(\frac{\lambda_{P_3}}{\mu_{14}} \right)^C \frac{\lambda_{P_3} \mu_{13}}{(C\mu_{13} - \lambda_{P_3})^2} + \right] \times P_0 \right\} \\ & + \left\{ \frac{1}{(C-1)!} \left[\left\{ \left(\frac{\lambda_{T_1}}{\mu_{21}} \right)^C \frac{\lambda_{T_1} \mu_{21}}{(C\mu_{21} - \lambda_{T_1}^2)^2} + \left(\frac{\lambda_{T_2}}{\mu_{22}} \right)^C \frac{\lambda_{T_2} \mu_{22}}{(C\mu_{22} - \lambda_2)^2} \right\} + \left(\frac{\lambda_{T_3}}{\mu_{23}} \right)^C \frac{\lambda_{T_3} \mu_{23}}{(C\mu_{23} - \lambda_{T_3})^2} \right] \times P_0 \right\} \end{aligned} \tag{132}$$

Finally, we have got six optimal paths for searching best optimal path corresponding to paths (I to VI).

6 Numerical Illustration

In this section, we analyzed queue length, response time and waiting time v/s number of order to customer for any product is considered for searching optimal path through different section with stages. Let λ be the arrivals number of order to customers and μ is service rate corresponding different stages with different ways. Consider the arrival rate, $\lambda = 5, 10, 15, \dots, 100$. The other parameters are assumed as follows:

- Probability of entering $\lambda_1, \lambda_2, \lambda_3$ & λ_4 networks from the original source to q_1, q_2, q_3 and q_4 , respectively.

- Probability of arrival at queues (Q₁, Q₂), (Q₃, Q₄), (Q₅, Q₆), (Q₇, Q₈), (Q₉, Q₁₀) are (q₁, q₂) = (0.3, 0.7), (q₃, q₄) = (0.6, 0.4), (q₄, q₅) = (0.5,0.5), (q₆, q₇) = (0.2, 0,8) & (q₉, q₁₀) = (0,1,0.9) respectively.
- Here, C is the number of servers and for C = 2 & 3 (Tables 4, 5, 6, 7, 8 and 9).
- The service rate for servers with different paths are as given:

$$\begin{aligned} \mu_1 &= 2.5, \mu_2 = 3.4, \mu_3 = 5.5, \mu_4 = 12.4, \mu_5 = 6.5, \mu_6 = 9.4, \\ \mu_7 &= 8.5, \mu_8 = 10.4, \mu_9 = 9.5, \mu_{10} = 15.4, \mu_{11} = 6.5, \mu_{12} = 4.5, \\ \mu_{13} &= 10.5, \mu_{14} = 3.6, \mu_{21} = 7.5, \mu_{22} = 4.2 \& \mu_{23} = 8.2. \end{aligned}$$

Table 4. For optimal path-I

Arrival rate (λ)	5	10	15	20	25	30	35	40	45	50	55	60	65	70	75	80	85	90	95	100
(Lq)	250	240	220	210	198	189	210	185	165	157	180	135	110	85	65	49	40	20	11	15
(Rt)	255	235	225	229	215	193	210	182	175	165	145	172	120	80	75	48	36	20	20	25
(Wt)	240	241	228	215	209	200	195	211	190	175	155	175	111	85	72	54	41	21	15	10

Table 5. For optimal path-II

Arrival rate (λ)	5	10	15	20	25	30	35	40	45	50	55	60	65	70	75	80	85	90	95	100
(Lq)	250	230	215	205	191	180	175	160	145	131	120	101	99	80	72	60	45	30	25	15
(Rt)	255	225	145	220	190	179	170	155	160	150	130	110	105	91	84	75	50	42	35	20
(Wt)	260	240	225	220	190	200	180	155	142	125	111	99	89	75	69	51	40	49	53	12

Table 6. For optimal path-III

Arrival rate (λ)	5	10	15	20	25	30	35	40	45	50	55	60	65	70	75	80	85	90	95	100
(Lq)	250	240	220	230	210	199	215	195	165	157	140	135	110	85	65	49	40	20	15	10
(Rt)	230	215	205	200	220	212	190	180	175	165	170	124	120	80	75	48	36	20	20	15
(Wt)	260	251	238	240	209	190	200	201	190	175	155	123	111	85	72	54	41	21	10	20

Table 7. For optimal path-IV

Arrival rate (λ)	5	10	15	20	25	30	35	40	45	50	55	60	65	70	75	80	85	90	95	100
(Lq)	235	240	220	210	198	189	199	185	165	157	179	135	110	85	65	49	40	20	15	10
(Rt)	255	235	215	225	220	190	200	180	175	165	185	124	120	80	75	48	36	20	20	15
(Wt)	251	241	218	215	209	190	195	201	190	175	195	123	111	85	72	54	41	21	10	20

Table 8. For optimal path-V

Arrival rate (λ)	5	10	15	20	25	30	35	40	45	50	55	60	65	70	75	80	85	90	95	100
(Lq)	259	240	228	220	200	199	189	185	175	167	139	125	110	85	65	49	40	20	15	10
(Rt)	260	238	230	222	215	201	190	182	175	165	148	124	115	80	73	48	38	21	16	11
(Wt)	261	241	231	216	209	195	190	184	180	175	152	123	111	85	72	51	41	19	14	11

Table 9. For optimal path-VI

Arrival rate (λ)	5	10	15	20	25	30	35	40	45	50	55	60	65	70	75	80	85	90	95	100
(Lq)	255	240	220	210	198	189	199	185	165	157	139	135	110	85	64	49	44	20	15	10
(Rt)	220	235	225	205	215	190	205	184	176	165	145	124	120	90	85	42	36	25	22	3
(Wt)	210	241	218	215	209	190	195	201	190	175	155	123	118	95	72	54	45	28	18	5

7 Graphical Interpretation

According to the above tables and graphs are indicated the performance measures. Figure 5 shows the best optimal path as for the queue length (Lq), the response time (Rt) and waiting Time (Wt) vs arrival rate (Figs. 4, 6, 7, 8 and 9).

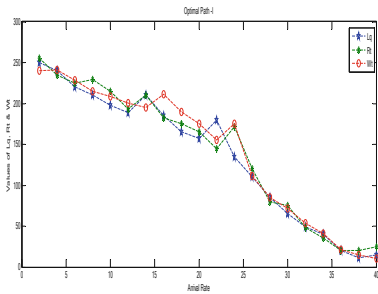


Fig. 4. Optimal path 1

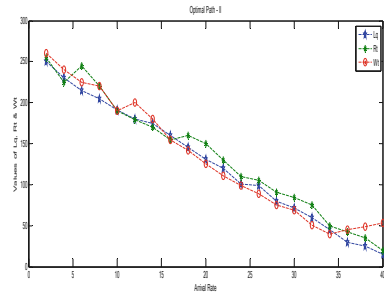


Fig. 5. Optimal path 2

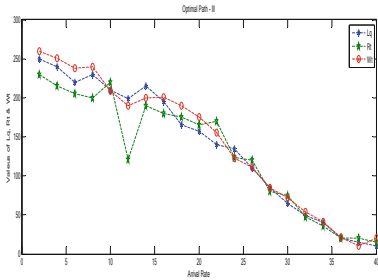


Fig. 6. Optimal path 3

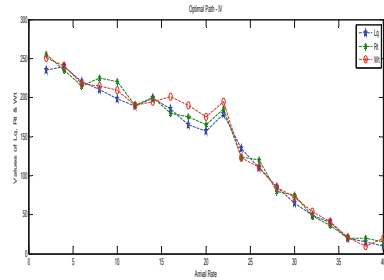


Fig. 7. Optimal path 4

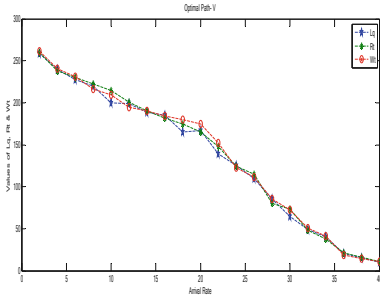


Fig. 8. Optimal path 5

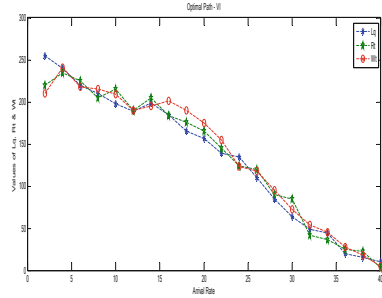


Fig. 9. Optimal path 6

8 Conclusion

In this investigation, we determined the optimal path based on the numerical evaluation of the response time, waiting time and queue length of queuing models. We evaluated the shortest path for each stage of the network and identified that path-V is provided a more accurate path. Various performance indices have been obtained viz. average the number of items in queue length, average response time, and average waiting time along with numerical results and graphs. The present article may help to reduce the lead time, delivery of effectiveness and consumer satisfaction using a supply chain system.

Acknowledgement. The authors of this paper extend their Gratitude to the Director MITS GWALIOR and TEQIP III under AICTE New Delhi for extending their necessary support.

References

1. Xu, X., Munson, C.L., Zeng, S.: The impact of e-service offering on the demand of online customers. *Int. J. Prod. Econ.* **184**, 231–244 (2017)
2. Kvasnicova, T., Kremenova, I., Fabus, J.: From an analysis of e-services definitions and classifications to the proposal of new e-service classification. *Proc. Econ. Financ.* **39**, 192–196 (2016)
3. Kumar, J., Shinde, V.: Study of industrial model for five-input, five-stage network. In: *Optimal Inventory Control and Management Techniques*, Chap. 15, pp. 300–339. IGI Global, USA (2016). <https://doi.org/10.4018/978-1-4666-9888-8>
4. Zhou, W., Huang, W., Zhang, R.: A two-stage queuing network on form postponement supply chain with correlated demands. *Appl. Math. Model.* **38**, 2734–2743 (2014)
5. Taherdoost, H., Sahibuddin, S., Ibrahim, S., Kalantari, A.: A review paper of e-services, technology concepts. In: *8th International Conference Interdisciplinary in Engineering, INTER-ENG-2014, Romania* (2014)
6. Mokaddis, G.S., Ismail, A., Metry, M.K.: A queueing model for solving three layer supply chain. *J. Math. Comput. Sci.* **2**, 226–240 (2012)
7. Sahraeian, R., Bashiri, M., Ramezani, M.: A stochastic multi-product, multi-stage supply chain design considering products waiting time in the queue. In: *Proceedings of the International Conference on Industrial Engineering and Operations Management* (2010)

8. Bhaskar, V., Lallement, P.: Modeling a supply chain using a network of queues. *Appl. Math. Model.* **34**, 2074–2088 (2010)
9. Kerbachea, L., James, Mac-Gregor S.: Networks and the topological design of supply chain systems. *Int. J. Prod. Econ.* **91**, 251–272 (2004)
10. Scott, J., Mason, P., Mauricio, R., Jennifer, A.F.: Integrating the warehousing and transportation functions of the supply chain. *Transp. Res. Part E* **39**, 141–159 (2003)
11. Viswanadhan, N., Raghavan, N.R.S.: Performance modeling of supply chains using networks. In: *Proceeding of the 2001 IEEE. In: International Conference on Robotics & Automation Seoul*, 21–26 May 2001, pp. 529–534 (2001)
12. Medjkoune, L.B., Aissoui, D.: Performance analysis approximation in a queueing system of type M/G/1. *Math. Methods Oper. Res.* **63**, 341–356 (2006)
13. Zhang, M., Hou, Z.: Performance analysis of M/G/1 queue with working vacations and vacation interruption. *J. Comput. Appl. Math.* **234**(10), 2971–2985 (2010)
14. Onazine, S., Abbhan, K.: A numerical analysis of the M/G/1/N queue with vacations. In: *12th IFAC/IEEE Workshop on Discrete Event Systems Caching*, 14–16 May 2004, France (2004). 978-3-902823-61-8/2014



Thermal Aging Analysis of Nomex Paper Solid Insulation Impregnated in Ester Insulation Oil for Possible Use in Transformer

Rajesh Roshan, Manisha Sharma^(✉), and Raj Kumar Jarial

Electrical Engineering Department, National Institute of Technology,
Hamirpur 177005, India
rajesh.roshan1993@gmail.com, manisha@nith.ac.in

Abstract. This paper encompasses experimental investigations carried out on two different properties like electrical and mechanical properties of Nomex paper insulations immersed in ester oil (rapeseed-based) by adopting accelerated thermally aged process. For sake of comparison, two different types of paper insulation (Nomex paper and Kraft insulation paper) of 5mil thick each have been used. Experimental testing like $\tan \delta$ test and Tensile strength test were performed for time interval of 48, 72 & 96 h respectively to undergo impact of ageing due to thermal stresses. Test results acquired from electrical and mechanical tests at 120 °C & 150 °C considering thermally aged procedure has been analyzed and presented in this paper to highlight efficacy of such solid insulations for possible futuristic use in modern transformers.

Keywords: Accelerated thermal aging · Dissipation factor · Kraft paper · Nomex · Power transformer · Rapeseed ester oil · Tensile strength

1 Introduction

Transformer is a static device which plays an important role in transmission or distribution from one voltage level to another voltage level which make possible smooth transmission of AC power over longer distances. One of the most important parameter which decides the operating life of transformer is its integrated insulation system. Insulating oil serves some important functions like providing insulation, dissipates heat from the transformer windings to its surrounding by some cooling equipment such as radiator and cooling fan [1, 2]. Other uses of insulating liquid media are in detection of oil paper degradation level and prevent arcing etc. Apart from that its used in high voltage capacitor, bushings, circuit breakers, tap changer. Transformer oil should have good insulating properties such as lesser moisture content, lesser dissipation factor, higher BDV (breakdown voltage), higher temperature tolerance and stable in chemical properties [3]. Basically, normal transformer oil is crude- based-petroleum which are treated by the process of fractional distillation. India has been using mineral oil for more than a century even though it is facing criticism. Mineral oil has some drawbacks such as when transformer bursts, it may release poly-nuclear aromatic hydrocarbon which may pollute the environment, hardly degradable, rate of deterioration is higher,

and the last but not the least it is non-renewable in nature as crude petroleum stocks are limited in nature [4, 5]. Hence to minimize the problem, many researchers are working on next alternative to normal transformer oil (Mineral insulating oil). Many researchers have done experimentation on synthetic ester oil and vegetable-based oil such as natural ester oil and have concluded that these oils may be next alternative to mineral oil. This paper highlights the use of natural ester oil (Rapeseed based) which is vegetable-based product. This oil is eco-friendly, non-toxic, higher BDV, lesser inflammability, higher flash point [3, 6]. These types of vegetable oils are utilized in some small or medium transformers. Thermal stress bearing capability for vegetable-based oil is from 70 °C to 190 °C which is better than mineral insulating oil.

This paper presents comparison of performance for both Nomex and Kraft insulation papers immersed in ester oil. Solid Paper insulation **basically contains 75–80%** cellulose and the rest of the part is lignin [1]. Kraft papers which are used generally in transformer shows lesser stability at higher temperatures as compared to Nomex paper. Kraft paper shows higher tensile strength. Generally during the normal operation of transformer, it is subjected to various stress like mechanical, electrical, chemical, environmental stresses. But this paper conveys about thermal stresses which has been taken to perform experimental analysis. By conducting two kind of tests like tensile strength and $\tan \delta$ at different temperatures for different aging duration, comparative analysis has been done on the basis of changes observed in the their electrical and mechanical characteristics after subjecting two insulating papers immersed in liquid insulation to thermal aging procedure.

2 Experimental Setup

2.1 Sample Preparation

In the present experimental work, insulating paper-Nomex 410 (5 mil thick) and other one is Kraft papers (5mil) while natural ester oil as liquid dielectrics has been taken for performing accelerated thermal aging procedure. Firstly, boro-silicate conical flask of 250 ml was cleaned with water and heated at 100 °C in electric oven for 1day to prevent the ingress of moisture present in the flask. It was then taken out from the oven to allow it to cool down at lower temperature below 250 °C. Conical flask was filled with 250 ml of ester oil which was put in oven for 1 day so that no moisture should remain in the insulating fluid. Kraft and Nomex papers was kept in the oven for drying so that moisture is removed. Copper strip was put in flask containing ester oil and insulating paper in order to imitate the real working conditions of the transformer. Kraft paper and Nomex paper were immersed separately in different ester oil samples. Oil to paper insulation in the ratio of 1:20 (mass in grams) was taken according to IEEE C57.154-2012 [7]. Conical flask was covered by using Aluminum and rubber cork. The materials which were taken during experimental work are mentioned in the Table 1.

Table 1. Materials used in testing.

Materials	Description
Insulating oil	Natural ester oil (Rapeseed based)
Insulating paper	Nomex 410 & Kraft paper(5mil thick each)
Conical flask	250 ml capacity
Cork	Rubber
Copper strip	35 mm × 20 mm × 2 mm

2.2 Thermally Aged Procedure

Different types of ageing occur in transformer like thermal, chemical, electrical, mechanical, environmental ageing. But in this work, only thermal aging has been included in accordance to IEEE Std. C57.100-2011. This experimental work has been done at temperature of 120 °C & 150 °C for time interval of 48, 72 and 96 h. Initially both Nomex paper and Kraft insulating paper of 5 mil thick impregnated in Rapeseed-based ester oil was placed in hot electric oven at 120 °C, 150 °C. After that every sample was taken out from the electric oven one by one after aging duration for 48 h, 72 h, 96 h separately. After the samples exposed to thermal stress, the variation in the properties of electrical and mechanical were noticed [8] by conducting tests like Tensile strength and $\tan \delta$ or dissipation factor. In this, $\tan \delta$ was done at 120 °C & 150 °C for 48 h, 72 h and 96 h (Figs. 1 and 2).



Fig. 1. Oil and paper insulation samples in Electric Oven.

2.3 Tensile Strength Test

Solid insulation such as paper insulation consists of cellulosic material which is formed from fibres. Tensile strength of insulating material decides the reliable operation of transformer. Aging affects the tensile property of insulating paper because it will reduce



Fig. 2. Universal testing machine Test kit.

the strength of glucose ring and hence it breaks after it reaches to its critical limit. It also reduces the value of DP (Degree of polymerization) which results in further release of Furanic compounds and other by-products. Since the value of DP and tensile strength is directly proportional. Hence by knowing the tensile strength of paper, one can analyse the actual health status of paper insulation. The testing kit which was used to measure the tensile strength of insulating paper is Universal Testing machine. ASTM D828-16 Standard method [10] was adopted to conduct this test. Cellulose fibres are used in the manufacturing of paper which influences the mechanical properties of paper. So tensile strength is most useful property of paper insulation. Tensile strength is defined as the maximum tensile force which exerts on the paper and results in the tearing of paper when it reaches above its threshold value. Threshold value is the value above which paper starts to break or start losing its mechanical strength. Due to overload in the transformer, short circuit may occur in the windings which results in the tearing or bursting of insulating paper. Thus it will result in the failure of transformer.

2.4 The Tan δ Test

The tan δ test can also be termed as dissipation factor test. When prepared thermally aged oil is placed in between live part and neutral part of the oil test cell then very less current flows. Since insulating oil shows dielectric property hence that current will lead the voltage in phase by 90° . But all insulating materials are not perfectly dielectric in nature because it contains some impurities, water content. Therefore, current doesn't lead the voltage by exactly 90° (Fig. 3).

The amount of degree by which it is short of exact 90° can be called as loss tangent. It can also be termed as dissipation factor. For good insulating oil it should be lesser than 0.005. It is achieved when it has lesser amount of moisture and dust or impurities. These are the factors which influence the properties of insulating oil. In the other word it can be said that if resistivity of oil is higher lesser amount of leakage current will flow. The tan δ test kit consists of two components which are discussed in brief.



Fig. 3. Tan δ Test kit

Oil Test Cell

It consists of 3 terminals which are high voltage terminal, low voltage and ground terminal. It helps in knowing the electrical properties of insulating oil. Electrodes should be arranged to give uniform stress to have good results.

Oil Cell Heater

It heats the oil sample and raises the temperature to 90 °C in 15 min. After attaining this temperature heater cell is automatically turned OFF. Tan δ test is done at 90 °C so that it does not get influenced by atmospheric temperature.

3 Experimental Results and Analysis

3.1 Tensile Strength

Table 2 shows the results acquired by conducting experimental testing of tensile strength at two different temperatures kept in oven for thermal aging process to occur for time interval of 0, 48, 72 and 96 h. The tensile strength of different paper is showing different values at different temperatures.

Table 2. Tensile strength (N/Mm) of insulating paper.

Temperature (°C)	Insulating paper	0 h	48 h	72 h	96 h
120°	Nomex-410	12.62	12.36	12.31	12.25
150°			12.17	12.07	11.29
120°	Kraft paper	3.502	3.106	3.04	2.790
150°			2.715	2.347	2.216
120°	Nomex-910 [11]	2.82	2.746	2.460	2.421
150°			2.669	2.460	2.389

Nomex-910 paper [11] immersed in soya-based natural ester oil has been taken as base for comparing the two insulating papers Nomex-410 and kraft papers impregnated in Rapeseed-based natural ester oil. Tensile strength for both samples has been compared in Fig. 4. From Table-2, it is clearly shown that Nomex-910 [11] immersed in soya-based ester oil [11] shows lesser tensile strength than Nomex-410 paper impregnated in rapeseed-based ester oil.

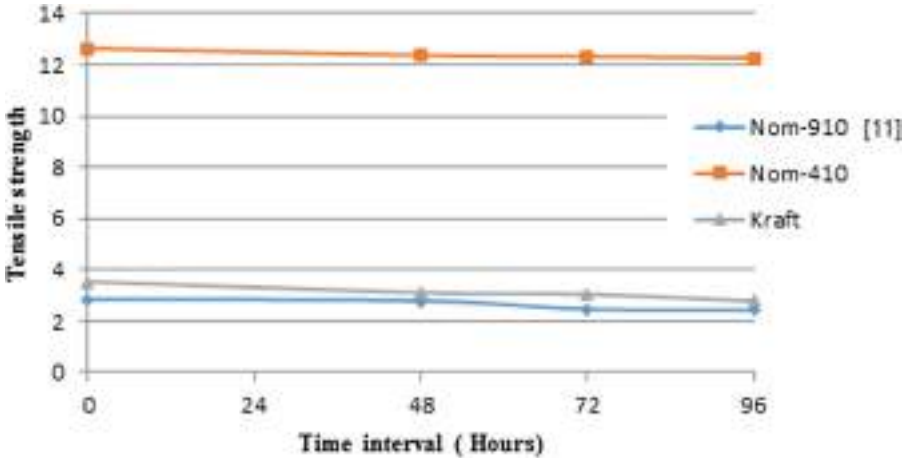


Fig. 4. Tensile strength with time at 120 °C

Figure 4 depicts how tensile strength is undergoing variation with duration of ageing (in hours). Tensile strength value for pure Nomex paper is 12.62 N/mm but the tensile strength of pure Kraft insulated paper recorded was 3.502 N/mm. So Nomex paper is almost four times mechanically stronger than the other paper insulation. After conducting thermal stressed procedure some noticeable variations were observed in the properties of insulating material. When the time duration for thermal stress is made to increase, then tensile strength of both the paper decreases. Since it is known that insulating paper mainly comprises of cellulosic material. weakening of cellulosic bonds and it causes it to break down due to the thermal stress forced in insulating paper. Hence tensile strength of both paper shows gradual decrease. When the cellulosic bonds become weaker and finally undergoes breakdown then it results to form furanic compounds and other decaying products. Tensile strength parameter has a direct relation to degree of polymerization. It can be concluded that when higher temperature is applied to insulating papers, force due to elongation on insulating papers increases and its strength decreases after the reach of threshold limit of paper, it starts to break. It can also be understood in the other way that stress due to tensile force its bearing capability decreases and hence furanic compounds are formed at a very high rate. Thermal stress exerted on the paper lowers its mechanical strength and therefore insulating material initiate the deterioration process. A comparison between the two different kinds of Nomex paper and Kraft paper has been done. Tensile strength for

Nomex paper-910 [11] of 5mil thickness and nomex-410 paper of similar thickness are 2.82 N/mm and 12.62 N/mm respectively before aging process of sample. After aging duration of 96 h, it can be observed that tensile strength of Nomex-410 has better mechanical strength than Nomex-910 [11] paper in appropriate liquid insulating media.

From Fig. 5, it is stated that Nomex 410 paper bears more tensile stress than Kraft paper. Mechanical strength for Nomex paper shows lesser decrement in value with gradual rise in temperature and ageing duration of paper. Hence on the basis of Fig. 410, Nomex-410 paper shows highest mechanical strength than both kraft paper and Nomex-910 insulating paper.

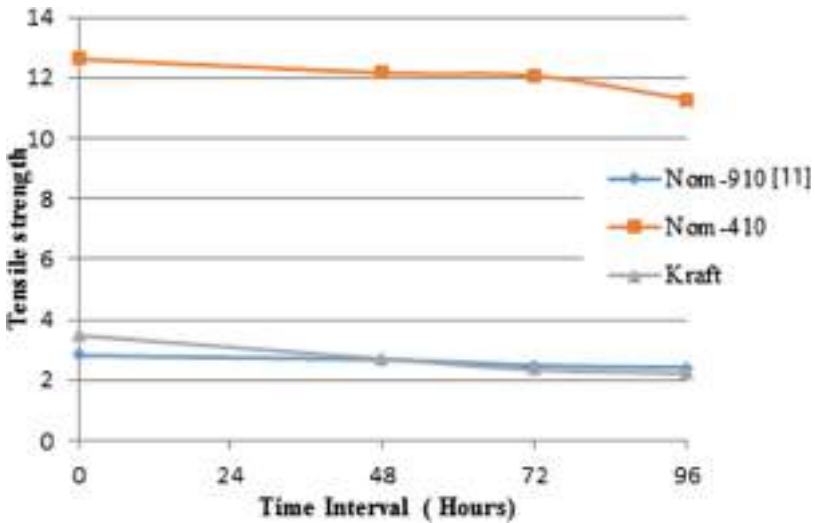


Fig. 5. Tensile strength with time at 150 °C

3.2 Electrical Tanδ Test

Figure 6 depicts the changing pattern of tan δ with time and temperature. The tan δ of virgin oil sample is 0.00742. When Nomex paper and other paper insulation as kraft paper is impregnated in natural ester oil and also thermal stress duration is operated for 0 to 96 h then tan δ for that samples starts increasing. When time duration for the prepared samples is increased then deterioration rate of oil increases. It can be observed from the graph at 120 °C that as the thermal duration for the samples is increased from 48 to 96 h insulating oil deteriorates which can be noticed by the increased value of tan δ. The tan δ for transformer oil should be very low. The tan δ of insulating oil should be 0.005 for better insulating property [3] (Table 3).

Figure 7 depicts how tan δ test of Kraft paper is changing with duration. The kraft paper is compared between two temperatures i.e. at 120 °C and 150 °C. Prepared oil samples starts deteriorating at higher rate for duration around 96 h. Also the increase in temperature of samples shows some increment in tan δ. This indicates more deterioration of oil occurs during this process. Greater the dissipation factor, higher rate of

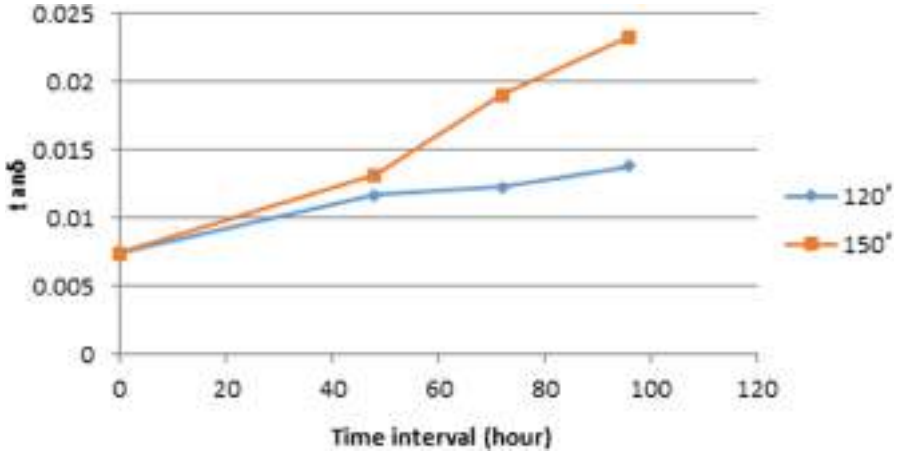


Fig. 6. The tan δ test results of Nomex-410 with time.

Table 3. Tan δ for oil sample

Temperature (°C)	Insulating paper	0 h	48 h	72 h	96 h
120°	Nomex-410	0.00742	0.0117	0.0123	0.01384
150°		0.00742	0.01315	0.01905	0.02334
120°	Kraft paper	0.00742	0.00949	0.01048	0.01264
150°		0.00742	0.01263	0.01533	0.0169

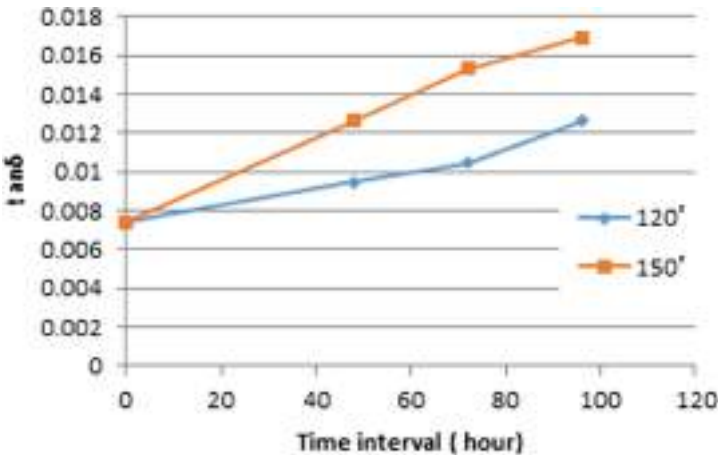


Fig. 7. The tan δ test results of Kraft paper with time.

deterioration of insulating oil is observed. The $\tan \delta$ test is used to check the status of insulation or how much deterioration has taken place which finally indicates the time for replacement of oil for operation in transformer. This electrical property of insulating oil is affected by impurities, moisture content which degrades the insulating property and hence impairs life of transformers.

4 Conclusion

This paper highlights experimental investigations related with accelerated thermal ageing of solid insulation impregnated in ester based insulating oil using tensile strength, and dissipation factor test. Both kind of solid insulating paper of identical thickness has been exposed to different temperatures kept for 0, 48, 72 and 96 h respectively by thermally aged process. It can be inferred that Nomex-410 has better mechanical strength than Kraft insulation paper. When the thermal stress increases tensile force bearing capability of paper also decreases. TUK (Thermally upgraded Kraft insulated paper) in terms of $\tan \delta$ shows better performance as compared to Nomex paper insulation. Its value increases with the higher temperature. Also Nomex-910 paper immersed in soya-based oil has been taken as base which has been used here to compare the results of Nomex-410 paper immersed in rapeseed-based ester oil. It was found that Nomex-410 paper has higher tensile strength than Nomex-910 paper and hence can be suitably selected while designing futuristic transformers based on ester based liquid dielectrics which has higher thermal stability and enviro- friendly attributes as compared to conventional mineral insulating oil.

References

1. CIGRE Brochure 323: Ageing of Cellulose in Mineral Oil Insulated Transformers, October 2007
2. IEEE Standard for the design, testing and application of liquid immersed distribution, power and regulating transformers using high temperature insulation system and operating at elevated temperatures, IEEE Std. C57.154-2012
3. Mehta, D.M., Kundu, P.: A review on critical evaluation of natural ester Vis-a-Vis mineral oil insulating liquid for use in transformer: part 2. IEEE Trans. Dielectr. Insul. **24**(2) (2016)
4. Oommen, T.V.: Vegetable oils for liquid-filled transformers. IEEE Electr. Insul. Mag. **18**(1), 6–11 (2002)
5. Oommen, T.V., Claiborne, C.C., Mullen, J.T.: Biodegradable electrical insulation fluids. In: Electric Systems Technology Institute, ABB Power T & D Company Inc. (1997)
6. Hamid, M.H.A., Ishak, M.T., Din, M.M.: Dielectric properties of natural ester oil used for transformer application under temperature variation. In: IEEE International Conference on Power and Energy, pp. 54–57 (2016)
7. Verma, P., Roy, M., Verma, M., Bhanot, V.: Change in electrical and chemical properties of transformer oil with accelerated thermal stress and its service life. Int. J. Cond. Monit. Diagn. Eng. Manag. **8**, 42–48 (2015)

8. Singh, J., Sood, Y.R., Verma, P.: Experimental investigation using accelerated aging factors on dielectric properties of transformer insulating oil. *Electr. Power Compon. Syst.* **39**, 1045–1059 (2011)
9. Saha, T.K.: Review of modern diagnostic techniques for assessing the insulation condition in aged transformers. *IEEE Trans. Dielectr. Electr. Insul.* **10**, 903–917 (2013)
10. Standard Test Method for Tensile Properties of Paper and Paperboard using Constant Rate of Elongation Apparatus, ASTM D828-16
11. Ankit, C.: Comparative evaluation of Nomex-910 and TUK Insulating paper thermally aged in Soya-based Natural Ester oil. M. tech dissertation, N.I.T Hamirpur, pp. 56–57, July 2018



Retrieval of Content-Based Images by Fuzzified HSV and Local Textural Pattern

Punit Kumar Johari^(✉)  and R. K. Gupta 

Madhav Institute of Technology and Science, Gwalior, M.P., India
{pkjohari, rkg}@mitsgwalior.in

Abstract. An efficient recognition of texture color pattern information from the image under shifting condition is still an open problem. Quite a lot of features extraction methods have been proposed for this purpose, ranging from available descriptors to features extracted with machine learning tools. Upon this stage, it is not totally clear under what situations a feature behave better than the others. In this paper, we propose combination of two methods under the region and present a novel descriptor to decide color and texture features using a structured fuzzy-color and Local Ternary pattern (LTP), which we call the Fuzzified Color Local Ternary Pattern Feature descriptor (FCLTP). In the suggested method, A combined of local ternary pattern feature descriptor with histograms obtained through Hue, Saturation and Value (illumination) channels, HSV color space, provides the entire coverage of global data.

Keywords: Content Based Image Retrieval (CBIR) · Local Binary Pattern (LBP) · Local Ternary Pattern (LTP) · Color Histogram (CH) · FCLTP

1 Introduction

In the field of image processing, a huge intensification has developed large image databases used in several applications. In the literature the role of color dominance and extraction of wide variety of texture patterns which are available in the images has been widely debated. Even though wide variety of depth in verifications of the experiments, it is still not completely apparent how much and what circumstances how color variations can be effective.

Images are searched in the data bases on the basis of the visual contents (color, shape, texture, etc.), using contents-based image retrieval techniques. The image visual contents are defined by multi-dimensional vectors in typical content-based image retrieval methods. The feature vectors of the images form a database of features. To obtain images, a user must provide an example image or sketched image, which is converted by a system into its feature vectors compared to the available feature vectors in the database. The indexing system can further improve the efficiency as an effective means of searching the image database is provided by the indexing schema.

The image content describing the types of characteristics and must be correctly chosen by the user-related image domain. This visual content produces a new space called the feature space. The satisfactory findings on the basis of categories of features applied to the CBIR system are achieved.

2 Related Work

A texturization description was conceived with the lately suggested local binary pattern (LBP). LBPs suggested by Ojala et al. [1] and these LBPs are transformed to a texture classification rotational invariant [2]. Pietikainen et al. [3] suggested an invariant classification of rotational texture with feature distributions. The LBP facial expressive analyses and recognition operator used Ahonen et al. [4] and Zhao et al. [5]. The background modelling and detection was suggested by Heikkila et al. using LBP [6]. The expanded LBP for shape localisation was suggested by Huang et al. [7]. For interest region description Heikkila et al. [8] used the LBP. For texture segmentation Li et al. [9] used the Gabor filter combination with LBP. The local derivative patterns for face recognition were suggested by Guo et al. [10]. They regard LBP as a local first order non-directional pattern, which are the binary results of the first order image derivatives.

Yet another variant of LBP, called Local Transitional Pattern, was proposed by Jabid et al. [11] where the texture code computes by comparing the intensity shift transition of adjacent pixels in various directions. To decide the bit value of the code, LBP compares intensity value of a neighbour in a particular direction with the intensity of centre pixel. In contrast, in LTP, the intensity of the pixel centre is compared to the intensity of its two neighbours to set a single bit value in a specific direction.

2.1 Local Binary Pattern (LBP)

It is a straightforward but very effective texture operator, which labels an image pixel by thresholding each pixel's neighborhood and considers it as a binary. The LBP texture operator became popular in multiple applications thanks to their discrimination power and computational simplicity [1]. The traditionally divergent statistic and structural models for texture analysis could be viewed as a unifying strategy. Maybe its robustness to monotonic gray modifications, for instance, induced by illumination differences, is the LBP Operator's key feature for real-world application. The computing simplicity that enables images to be analyzed under difficult real time environments is another significant property. For encoding intensity differences, LBP uses 0 and 1 values. The three valued LBP are calculated for 3×3 neighborhood as

$$f_1(p, c) = \begin{cases} 1, & \text{if } p \geq c \\ 0, & \text{if } p < c \end{cases} \quad (1)$$

where p is pixel value and c is centre pixel from 3×3 matrix. Figure 1 shows the calculation of LBP operator.

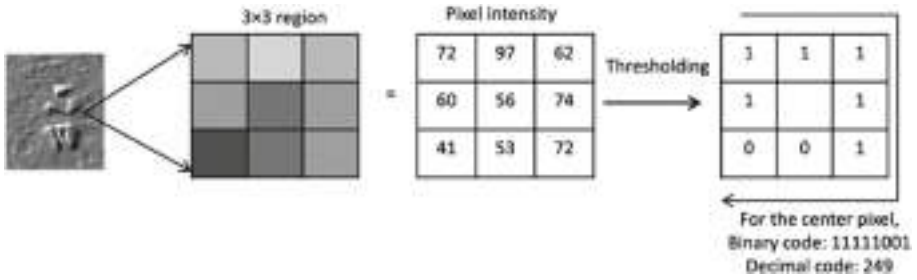


Fig. 1. LBP calculation

2.2 Local Ternary Pattern (LTP)

For encoding intensity differences, LTP uses -1, 0 and +1 values in place of 0 and 1 used in LBP. It's a local binary pattern expansion [12]. The ternary pattern acquired is subdivided into the upper and lower binary patterns, taking p as a neighborhood pixel, k as the boundary constant and c as the center pixel value then the outcome is computed as:

$$f_2(p, c, k) = \begin{cases} 1, & \text{if } p > c + k \\ 0, & \text{if } p > c - k \text{ and } p < c + k \\ -1, & \text{if } p < c - k \end{cases} \quad (2)$$

The upper pattern will be obtained by substituting 0 for -1 and 0 and maintaining 1. The lower binary pattern is obtained by substituting 0 for 1 and 0 & -1 for 1. Figure 2 depicts the operation working of Local Ternary Pattern on a 3×3 section of a channel from image.

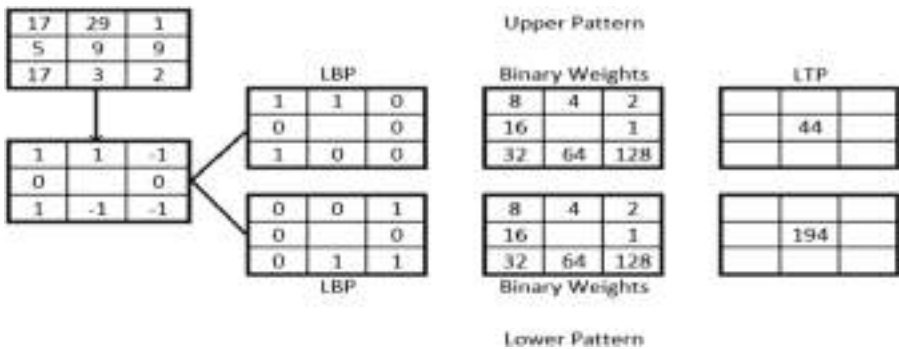


Fig. 2. LTP calculation

3 Proposed Methodology

Researchers have proposed several improved methods for retrieving relevant images according to the user prospects. These methods differ in the ways of extracting the features using CBIR techniques and the way in which they can use the different properties according to the user intention and query support. Another element where the retrieval method differs in the way in which they handle the database i.e. a new ensemble is constructed with “one against-all” strategy in order to improve the target search and how they retrieve the images from the feature vector processed. Ultimate objective is to improve the performance of the image retrieval method is to fast and accurate result.

In the suggested method (Fig. 3), we regarded a variety in the technique of Local Ternary patterns with addition of fuzzified H, S, V HSV-color space elements to accurately extract chromatic information from input images and for obtaining maximum information from input image an additional color space is augmented. Here Local Ternary patterns for capturing textured data are applied on gray space. Local textural information is obtained here by splitting gray image into a pixel map of the neighborhood of 3×3 , then LTP is applied for texture feature extraction. Besides the textured information obtained from the proposed feature, hue and saturation channels provide useful information on color changes in the image. In order to find chromatic characteristics, color data is obtained by working on H, S, V components of HSV channels. H channel of HSV color space is divided in 12 segments to extract the dominant colors (DC), because Hue (H) is the color tone (red, blue, etc.) and for each component of colour, the fuzzy membership functions and linguistic labelling are defined. Similarly, HSV color space elements S and V are divided into 3 segments: low, medium, high saturation level for S component and dark, light and bright for V component. 8 dominant Hue wheel colors were chosen for experimentation purposes. The histogram is calculated on the basis of segmentation for each HSV channel component.

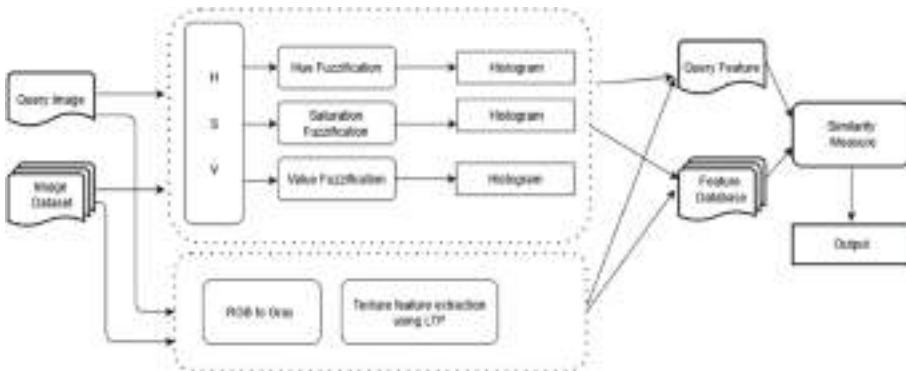


Fig. 3. Proposed system architecture

Consequently, the entire coverage is accomplished through a concatenating local ternary pattern descriptor with histograms acquired through the HSV color space channels of fuzzified Hue, saturation and value (illumination).

3.1 Fuzzification Based Color Histogram Creation Method

One reason why the HSV color space has been chosen is that it is a color space that is perceptibly uniform and approximates how people perceive color. However, the primary reason is that in different retrieval experiments, HSV color space has been discovered to be better than other color spaces. The fuzzy-linking is used to form a histogram in the descriptor. An output histogram of more than one histogram is defined by a word “fuzzy-linking”. The channels of input are defined in the following fuzzy sets:

- Channel hue (H) is split into ten fuzzy areas,
- The channel of saturation (S) is split into three fuzzy areas,
- The channel value (V) is split into three fuzzy regions.

$$\mu_A(x) = \begin{cases} 0, & (x < a) \text{ or } (x > d) \\ \frac{x-a}{b-a}, & a \leq x \leq b \\ 1, & b \leq x \leq c \\ \frac{d-x}{d-c}, & c \leq x \leq d \end{cases} \quad (3)$$

where lower limit is denoted as a, an upper limit as d, a lower support limit b, upper support limit as c and $a < b < c < d$. The membership features are shown in Fig. 4, 5 and 6. The final fuzzy histogram includes only 10 bins for the H channel out of 12 bins.

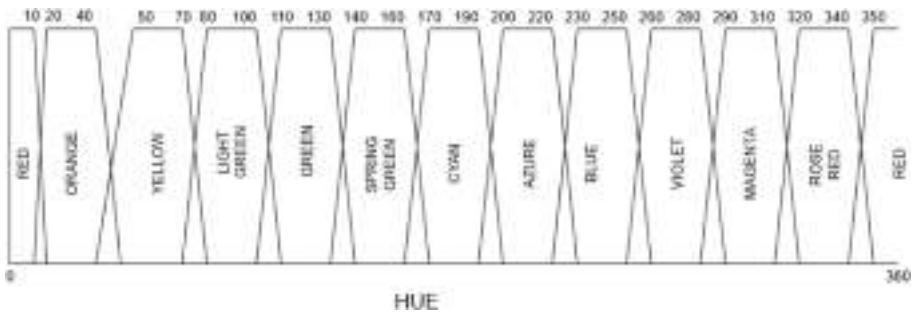


Fig. 4. Membership function of Hue color

The histogram bins are displayed in the Figs. 4, 5 and 6 is in reference to: (1) Red, (2) Orange, (3) Yellow, (4) Light Green, (5) Green, (6) Spring Green, (7) Cyan, (8) Azure, (9) Blue, (10) Violet, (11) Magenta and (12) Rose Red for H Channel. Similarly, for S channel bins are: (1) Low, (2) Medium and (3) High Saturation. And for V Channel bins are: (1) Dark, (2) Light and (3) Bright. The dominant colors in each

picture can readily be noticed. As described in the following section, the histogram in the suggested system has proven to be an instrument for exact image retrieval.

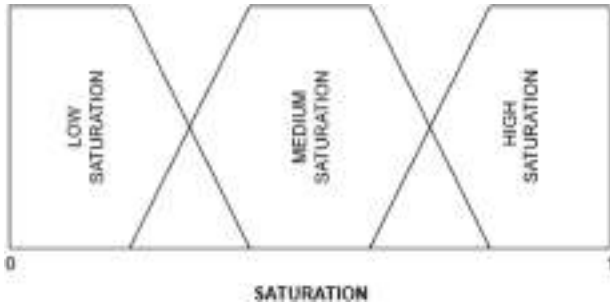


Fig. 5. Membership function of saturation channel

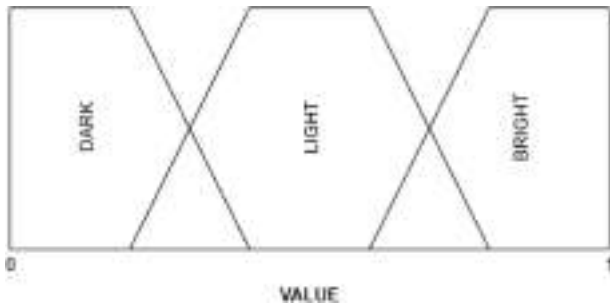


Fig. 6. Membership function of value channel

4 Results and Discussion

4.1 Evaluation Measures

The Two performance measures assess the discriminating ability and efficiency of each method: average precision AP and average recall AR. With the image Q of a query, its precision P_Q is calculated as

$$P_Q = \frac{\text{Number of relevant images retrieved}}{\text{Total number of images retrieved}}, \tag{4}$$

Where the images concerned applies to images of the same type. With a query image Q, its precision P_Q is determined as

$$AP = \frac{1}{|DB|} \sum_{Q=1}^{|DB|} P_Q \quad (5)$$

where $|DB|$ is the size of the database.

In similar lines, the database average recall is calculated as

$$AR = \frac{1}{|DB|} \sum_{Q=1}^{|DB|} RR_Q \quad (6)$$

where query image Q recall is represented as RR_Q , i.e.,

$$RR_Q = \frac{\text{Number of relevant images retrieved}}{\text{Total number of relevant images present in database}}, \quad (7)$$

Average Recall sometimes refers to the average database retrieval rate [13].

4.2 Experimental Results

The experiment is performed on the data set of Corel 1000 [14] for performance analysis. The collection includes 1000 pictures in ten different categories, including food, mountain, horse, beach, bus, flowers, tribes of Africa, elephants and more (Tables 1, 2, 3 and 4).



Fig. 7. Sample images from corel 1000 database

In experiment the Precision Percentage is computed and is compared with existing methods at 10, 20, 30 and up to 100 retrieved images. Few example images from the dataset are shown in Fig. 7. All images are in JPEG format with resolution of 256×384 or 384×256 .

Table 1. Average retrieval of image using LBP+FCH

Category	Number of image retrieved (average)		
	10	20	30
African Tribe	8.3	16	24
Beach	8	13.6	15.3
Monuments	8.5	15.5	21.5
Buses	10	19	29
Dinosaurs	10	20	30
Elephants	7.4	12	16
Flowers	9	18	28
Horses	8	17	24
Mountains	6.7	12	20
Food	6.3	11.4	15

Table 2. Average retrieval of image using LTP+FCH

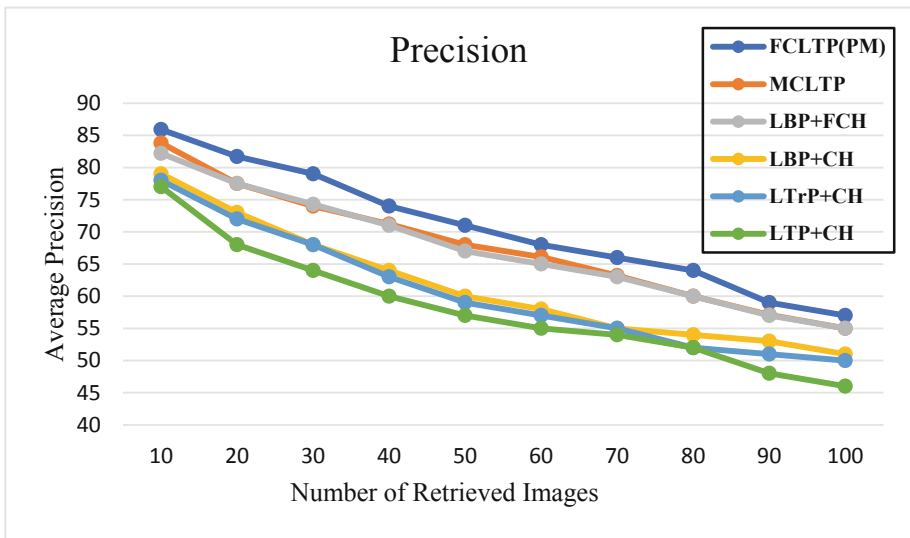
Category	Number of image retrieved (average)		
	10	20	30
African Tribe	8.3	17	24.8
Beach	8	14.1	16.1
Monuments	8.6	16.1	21.8
Buses	10	19	29
Dinosaurs	10	20	30
Elephants	7.5	12.2	18
Flowers	9	18	28
Horses	9	17.1	24.5
Mountains	7.4	14	22
Food	8.1	16	23

Table 3. Comparison of precision between existing methods and proposed technique

No. of retrieved images	FCLTP (PM)	MCLTP [15]	LBP +FCH	LBP+CH [15]	LTrP +CH [15]	LTP+CH [15]
10	85.9	83.3	82.2	79	78	77
20	81.7	77.5	77.5	73	72	68
30	79	74	74.26	68	68	64
40	74	71.2	71	64	63	60
50	71	68	67	60	59	57
60	68	66.1	65	58	57	55
70	66	63.2	63	55	55	54
80	64	60	60	54	52	52
90	59	57.1	57	53	51	48
100	57	55	55	51	50	46

Table 4. Comparison of recall between existing methods and proposed technique

No. of retrieved images	FCLTP (PM)	MCLTP [15]	LBP +FCH	LBP+CH [15]	LTrP +CH [15]	LTP+CH [15]
10	8	7	7	6	6	6
20	16	16	16	12	11	10
30	23	22	22	18	17	17
40	29	27	27	23	22	21
50	34	34	33	30	28	27
60	40	38	37	35	33	33
70	46	44	43	38	36	35
80	51	47	47	42	41	40
90	53	51	50	46	44	42
100	57	55	55	48	48	45

**Fig. 8.** COREL 1000 average precision

Average accuracy and recall values obtained based on the number of images retrieved are evaluated for the retrieval performance of the FCLTP (PM) method. The proposed method shows average accuracy and average recall of 85.9% and 57% in Figs. 8 and 9, which is outperforming the existing techniques such that MCLTP, LBP +CH, LTrP+CH, LTP+CH, where CH indicates the color histogram. The results validate the strength of our proposed method.

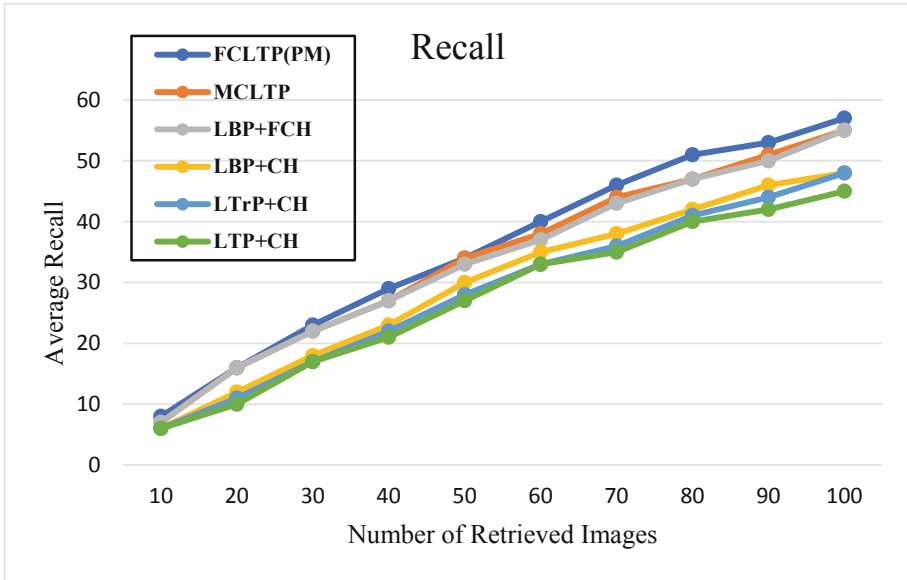


Fig. 9. COREL 1000 average recall

5 Conclusion

A fresh technique for creating histograms is suggested. The histogram is produced by HSV color space components which are regarded as fuzzy sets. By combining these fuzzy sets into 18 fuzzy rules the histogram is obtained. Very few bins are used to describe the distribution of the color in image which results in a much faster comparison of histograms and improved algorithm robustness. The approach was compared to other histogram methods that showed that multiple image retrieval tests were considerably more precision and robust. However, this does not mean that it cannot be enhanced (e.g. insertion of spatial data). Experimental data show that the suggested method can lead to accurate image retrieval.

References

1. Ojala, T., Pietikäinen, M., Harwood, D.: A comparative study of texture measures with classification based on featured distributions. *Pattern Recognit.* **29**(1), 51–59 (1996)
2. Ojala, T., Pietikainen, M., Maenpaa, T.: Multiresolution gray-scale and rotation invariant texture classification with local binary patterns. *IEEE Trans. Pattern Anal. Mach. Intell.* **24**(7), 971–987 (2002)
3. Pietikainen, M., Ojala, T., Scruggs, T., Bowyer, K.W., Jin, C., Hoffman, K., Marques, J., Jacsik, M., Worek, W.: Overview of the face recognition using feature distributions. *J. Pattern Recognit.* **33**(1), 43–52 (2000)

4. Ahonen, A., Hadid, A., Pietikainen, M.: Face description with local binary patterns: applications to face recognition. *IEEE Trans. Pattern Anal. Mach. Intell.* **28**(12), 2037–2041 (2006)
5. Zhao, G., Pietikainen, M.: Dynamic texture recognition using local binary patterns with an application to facial expressions. *IEEE Trans. Pattern Anal. Mach. Intell.* **29**(6), 915–928 (2007)
6. Heikkila, M., Pietikainen, M.: A texture based method for modeling the background and detecting moving objects. *IEEE Trans. Pattern Anal. Mach. Intell.* **28**(4), 657–662 (2006)
7. Huang, X., Li, S.Z., Wang, Y.: Shape localization based on statistical method using extended local binary patterns, In: Third International Conference Image and Graphics, (ICIG'04), Hong Kong, China, pp. 184–187 (2004)
8. Heikkila, M., Pietikainen, M., Schmid, C.: Description of interest regions with local binary patterns. *Pattern Recognit.* **42**(3), 425–436 (2009)
9. Li, M., Staunton, R.C.: Optimum gabor filter design and local binary patterns for texture segmentation. *J. Pattern Recognit.* **29**(5), 664–672 (2008)
10. Guo, Z., Zhang, L., Zhang, D.: Rotation invariant texture classification using LBP variance with global matching. *Pattern Recognit.* **43**(3), 706–716 (2010)
11. Jabid, T., Chae, O.S.: Facial expression recognition based on local transitional pattern. *Int. J. Inf.* **15**(5), 2007–2018 (2011)
12. Tan, X., Triggs, B.: Enhanced local texture feature sets for face recognition under difficult lighting conditions. *IEEE Trans. Image Process.* **19**(6), 1635–1650 (2010)
13. Murala, S., Wu, Q.M.J.: Spherical symmetric 3D local ternary patterns for natural, texture and biomedical image indexing and retrieval. *Neurocomputing* **149**(C), 1502–1514 (2015)
14. Li, J., Wang, J.Z.: Automatic linguistic indexing of pictures by a statistical modeling approach. *IEEE Trans. Pattern Anal. Mach. Intell.* **25**(9), 1075–1088 (2003)
15. Agrawal, M., Singhal, A., Lall, B.: Multi-channel local ternary pattern for content-based image retrieval. *Pattern Anal. Appl.* **22**, 1585–1596 (2019)



A Novel Meta-material Based Mirco-strip Patch Antenna

Vikas Mahor^(✉) and Madhav Singh

Department of Electronics, MITS, Gwalior, India
vikas@mitsgwalior.in

Abstract. The research work presents a smaller size rectangular mirco-strip patch antenna. In this work, a smaller size patch antenna designed using meta-material. In the work, antenna's resonate frequency is 1.815 GHz, normally designing a rectangular mirco-strip patch antenna at this frequency required more space but with the help of meta-material minimize the size of patch and also base structure of the antenna. The designed antenna is fit when required less size antenna, at 1.815 GHz frequency.

Keywords: Left-Handed Meta-material (LH MTM) · Rectangular micro-strip patch antenna · Return loss · Nicolson Ross Weir

1 Introduction

Left handed metamaterial is an artificial materials. The term Metamaterials were first coined in 1967 [1]. The unique properties of metamaterial such as negative permittivity and negative permeability makes it capable of suitable candidate for antenna design [2, 3]. Due these properties, this is called left handed metamaterial. Because of these properties, the metamaterial is capable to improve the properties of microstrip patch antenna.

Rectangular mircostrip patch antenna is easy to fabricate, it is a larger sheet of metal which is flat rectangular in shape and is fixed and known as a ground plane. In designing microstrip antennas, a number of substrate can be used. In this work FR-4 lossy substrate is used. This substrate is situated between smaller sheet of metal and larger sheet of metal.

For the purpose of antenna simulation a Computer Simulation Technology is used known as Micro Wave Simulator (MWS - CST) Software. MS Excel Software has been used for plotting the results and verifying the negative permittivity and permeability of the used meta-material cover.

2 Formulae and Designing

For the designing of patch of Microstrip patch antenna some formulae are used, which are given below.

Desired Formulae [4, 5]:

Width (W):

$$W = \frac{1}{2f_r \sqrt{\mu_0 \epsilon_0}} \sqrt{\frac{2}{\epsilon_r + 1}} = \frac{c}{2f_r} \sqrt{\frac{2}{\epsilon_r + 1}} \quad (1)$$

Effective dielectric constant:

$$\epsilon_{\text{eff}} = \frac{\epsilon_r + 1}{2} + \frac{\epsilon_r - 1}{2} \left(\frac{1}{\sqrt{1 + \left(\frac{12 \times h}{W} \right)^2}} \right) \quad (2)$$

The actual length of the Patch (L):

$$L = L_{\text{Eff}} - 2 \times \Delta L \quad (3)$$

Where,

$$L_{\text{Eff}} = \frac{c}{2f_r \sqrt{\epsilon_{\text{eff}}}} \quad (4)$$

Calculation of Length Extension:

$$\frac{\Delta L}{h} = 0.412 \times \frac{(\epsilon_{\text{eff}} + 0.3) \left(\frac{W}{h} + 0.264 \right)}{(\epsilon_{\text{eff}} - 0.258) \left(\frac{W}{h} + 0.8 \right)} \quad (5)$$

Where,

- c = free space velocity of light,
- ϵ_r = Dielectric constant of substrate,
- f_r = Resonating frequency,
- ϵ_{eff} = Effective dielectric constant,
- h = Height of dielectric substrate,
- W = Width of patch,
- L = Length of patch and
- ΔL = Effective Length.

3 Patch Antenna Design

The fabrication material which has been used in this material is a FR4 lossy sheet, whose dielectric constant is $\epsilon_r = 4.3$ and thickness of (h = 1.6 mm) at matching impedance of 50 Ω . Size of FR4 and ground lossy substrate is same with the length = 80 mm and

width = 80 mm. The Physical layout of the proposed patch antenna is illustrated in Fig. 1 along with its dimensions. The parameters are given in the measurement of millimeter (mm) (Fig. 2).

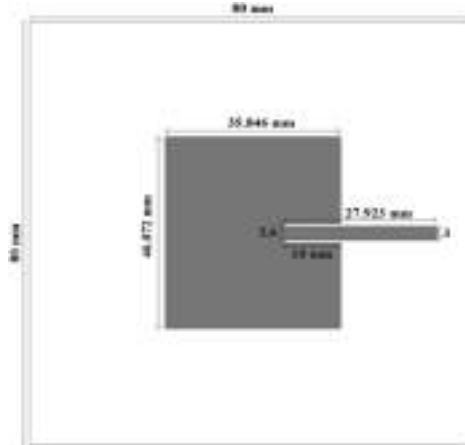


Fig. 1. Dimensions of the microstrip patch antenna (all dimensions are in mm).

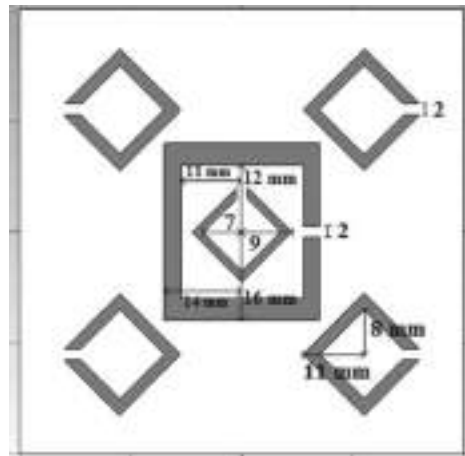


Fig. 2. Dimensional view of the meta-material cover (all dimensions in mm).

MWS-CST software is used for the purpose of micro-strip patch antenna simulation in transient mode. The antenna resonates at an operating frequency of 1.815 GHz. From the simulation results, the return loss of antenna is illustrated in Fig. 3.

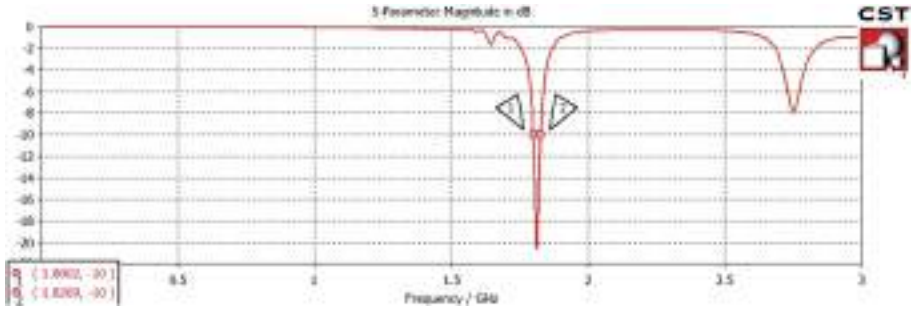


Fig. 3. Return loss of -20 dB at resonating frequency of 1.815 GHz frequency.

Figure 4 illustrates the radiation pattern of the designed antenna. It also illustrates the directivity of 6.668 dBi and total efficiency of 54.51% . Here, the Radiation pattern is defined as power radiated the function of the angular position and radial distance from the antenna.

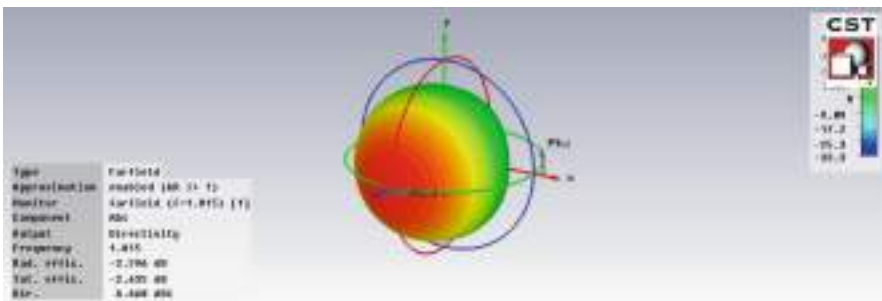


Fig. 4. Radiation pattern of the RMPA with directivity & total efficiency

Now the designed meta-material based antenna is placed between the two ports of a waveguide along the X-Axis. This is done for the calculation of S_{11} and S_{21} parameters. It is assumed here that the surrounding is air [6, 7]. The direction of electromagnetic signal is along the structure. Here the Z-plane acts as a magnetic boundary while Y-plane acts as electric boundary. The transmission of wave takes place from the Port 1 to Port 2. RMPA with waveguide ports is shown below Fig. 5.

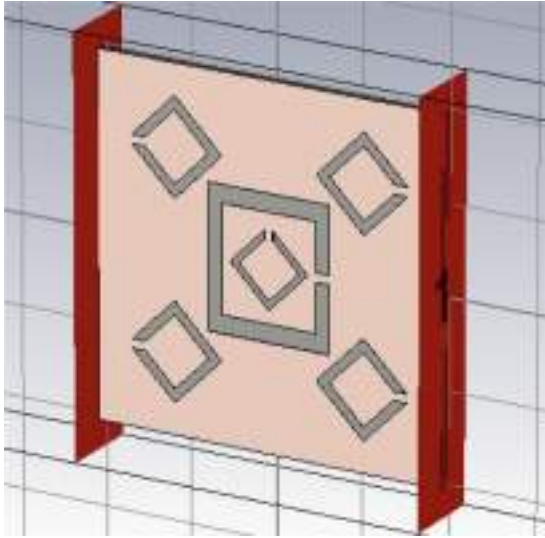


Fig. 5. Meta-material cover used in the micro-strip patch antenna design.

As per this process the parameters S_{11} and S_{21} are in complex form, these parameters are plotted in excel for verifying the negative permeability and permittivity of the micro-strip antenna. This is achieved with the NRW approach.

Equation for deriving the values of μ_r and ϵ_r using NRW Method is given as [8]:

$$\mu_r = \frac{2 \cdot c(1 - v_2)}{\omega \cdot d \cdot i(1 + v_2)} \tag{6}$$

$$\epsilon_r = \mu_r + \frac{2 \cdot S_{11} \cdot c \cdot i}{\omega \cdot d} \tag{7}$$

Where,

$$v_1 = S_{11} + S_{21} \text{ and } v_2 = S_{21} - S_{11}$$

v_1 = maximum measured voltage

and v_2 = minimum voltage measured

The parameters permittivity (ϵ) and permeability (μ) are obtained from Eqs. (6) and (7) [9–11]. The negative permittivity and negative permeability of meta-material based patch antenna is illustrated in Figs. 6 and 7.

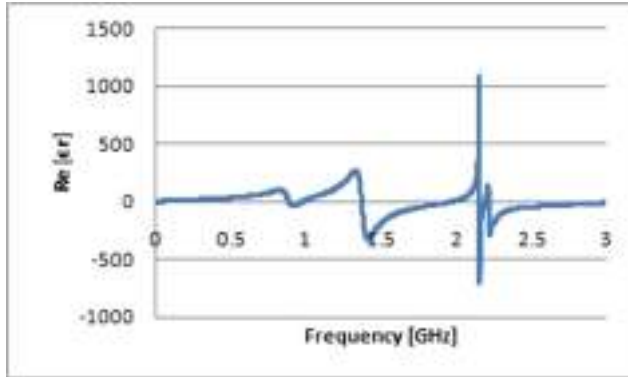


Fig. 6. Relative permittivity of the meta-material based antenna.

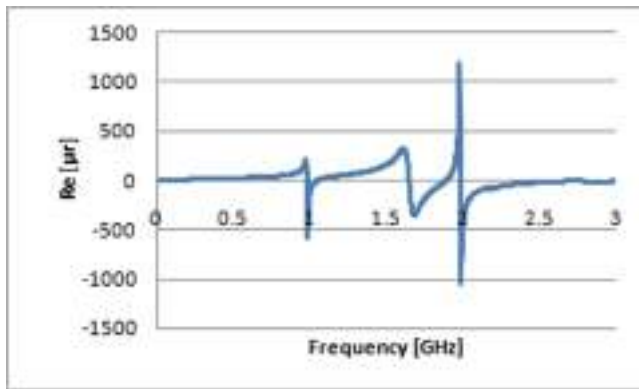


Fig. 7. Relative permeability of the meta-material based antenna.

Table 1 illustrates the negative permeability and permittivity of meta-material based patch antenna operating in the frequency range 1.800–1.827 GHz.

Table 1. Measured values of permittivity (ϵ_r) and permeability (μ_r) in the operating frequency range

Frequency (GHz)	Real value of permittivity $Re(\epsilon_r)$	Real value of permeability $Re(\mu_r)$
1.800	-40.47825592	-99.0554163
1.806	-39.17853177	-92.2725816
1.812	-37.8257407	-85.3903918
1.818	-36.44228849	-78.4134796
1.824	-35.07479546	-71.5210824
1.827	-34.41042488	-68.1682156

Comparison between lone patch antenna dimension and proposed Metamaterial based patch antenna is shown in Table 2.

Table 2. Dimension comparison of prevalent patch antenna and proposed patch antenna with meta-material

Parameter	Dimension of prevalent patch antenna (mm)	Dimension of patch antenna with meta-material (mm)
Length (L)	39.552	35.846
Width (W)	50.768	46.072
Length of substrate	110	80
Width of substrate	110	80

4 Conclusion

The objective of this research work is to provide a smaller size Metamaterial based patch antenna for requiring applications. It is clearly prove by Table 2 that the desired operating frequency can be achieved with smaller size antenna. Finally, in this work found a small size antenna at operating frequency 1.815 GHz with -20 dB return loss, 6.668 dBi directivity and 54.51% total efficiency.

References

1. Veselago, V.G.: The electrodynamics of substances with simultaneously negative value ϵ and μ . *Sov. Phys. Uspekhy*. **10**(4), 509–514 (1968)
2. Smith, D.R., Padilla, W.J., Vier, D.C., et al.: Composite medium with simultaneously negative permeability and permittivity. *Phys. Rev. Lett.* **84**, 4184–4187 (2000)
3. Pendry, J.B.: Negative refraction makes a perfect lens. *Phys. Rev. Lett.* **85**, 3966–3996 (2000)
4. Balanis, C.A.: *Antenna Theory and Design*. Wiley, Hoboken (1997)
5. Stutzman, W.L., Thiele, G.A.: *Antenna Theory and Design*, 2nd edn. Wiley, New York (1998)
6. Lovat, G., Burghignoli, P., Capolino, F., Jackson, D.R., Ziolkowski, R.W.: Combinations of low/high permittivity and/or permeability substrates for highly directive planar metamaterial antennas. *IET Microw. Antennas Propag.* **1**, 177 (2007)
7. Sulaiman, A.A., Nasaruddin, A.S.: Bandwidth enhancement in patch antenna by metamaterial substrate. *Eur. J. Sci. Res.* **44**, 493–501 (2010)
8. Mazid, H.A., Rahim, M.K.A., Masri, T.: Left-handed metamaterial design for microstrip antenna application. In: *IEEE International RF and Microwave Conference* (2008)
9. Mahor, V., Pattanaik, M.: A state-of-the-art current mirror-based reliable wide fan-in FinFET domino OR gate design. *Circuits Syst. Signal Process.* **37**(2), 475–499 (2018)
10. Kundu, S., Mahor, V., Gupta, R.: A highly accurate fire detection method using discriminate method. In: *2018 International Conference on Advances in Computing, Communications and Informatics (ICACCI)*. IEEE (2018)
11. Mahor, V., Pattanaik, M.: An aging-aware reliable FinFET-based low-power 32-word x 32-bit register file. *Circuits Syst. Signal Process.* **36**(12), 4789–4808 (2017)



A Study on Sampling-Based Parameter Estimation Techniques in Big Data Analytics Environment

Abdul Alim^(✉)  and Diwakar Shukla

Department of Computer Science and Applications,
Dr. Harisingh Gour Vishwavidyalaya, Sagar, MP, India
abdulaleem1990@gmail.com, diwakarshukla@rediffmail.com

Abstract. In a big data environment, there are lots of large datasets are arising from the data processing complexity regarding the user's query. We cannot imagine how many datasets are generating within a second. Those datasets are coming from different sources like social media, health sectors, weather department, insurance companies, share market, and more, in which the social media such as facebook, WhatsApp, Instagram are producing more and more data that is called big data. Basically big data have three very important pillars which are known as volume, variety, and velocity. It is also called as big data parameters. When the availability of data in huge volume then it is not possible to process all huge datasets, so in this case, we have opportunities to apply the sampling techniques and estimate the big data parameters. The sampling techniques are more powerful in capered to traditional techniques because the small dataset (sample) can select from entire data or population and then process it. Due to a small dataset, we can process easily and then can reduce process time and cost. In this paper, we have to study the different types of sampling techniques suitable for big data parameters. This paper has discussed sampling-based parameter estimation techniques in the big data environment. Furthermore, we have suggested one big data analytics model based on stratified sampling. The main objective of this paper is to find out the reliable sampling techniques for big data parameter estimation.

Keywords: Big data · Big data analytics · Big data parameters · Parameter estimation · Sampling techniques

1 Introduction

The sampling-based big data parameter estimation techniques can be classified into seven different types, which are listed as - 1: Simple Random sampling (SRS) 2: Stratified Sampling Techniques (SST) 3: Systematic Sampling (SS) 4: Multistage Sampling (MS) 5: Simple Cluster Sampling (SCS) 6: Multistage Cluster Sampling (MCS) and 7: Quota sampling (QS). The estimation problem will be necessary when the source of additional information is in huge amount and there are some parameters are unknown. The estimation problem is a burning area in social-economical and where the data is so large. The estimation problem may be looked upon into two aspects

deterministic and non-deterministic, the deterministic approach were given inputs estimate the unknown parameters [1] with accuracy assessment. The accuracy assessment is an important step in data analytics within the data prediction model. Due to the variety of data that are producing by the users by various sources where accuracy is the major factor. The simple random sampling is a technique in which selecting n (sample) units from the population (data) N units, here the distinct sample has an equal chance of being selected [2]. Furthermore, the sampling techniques can be divided into two types - probability and non-probability sampling method in which all subjects in the entire population have an equal chance to be selected in the sample and non-probability sampling methods where the sample of the population is a nonsystematic process. The non-probability sampling does not guarantee an equal chance for each subject in the population and some non-probability sampling is a convenience, judgmental and snowball sampling [3]. The following Fig. 1 has categorized the different probability and non-probability sampling.

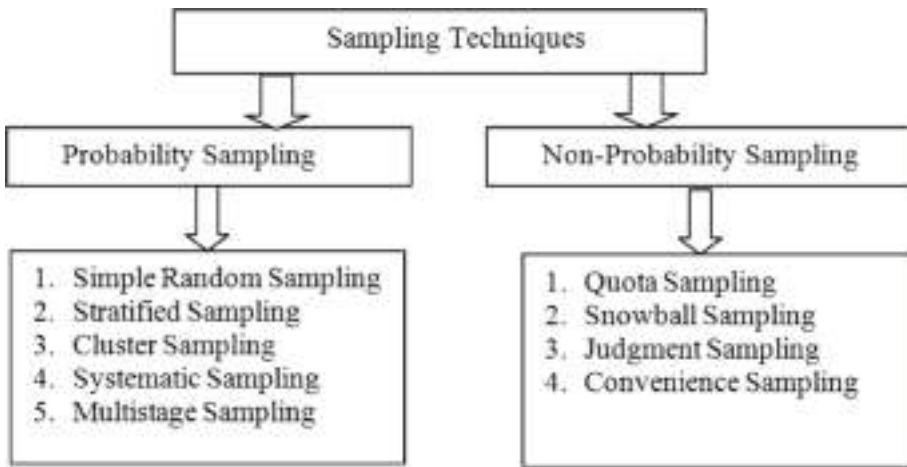


Fig. 1. Categories and types of sampling techniques.

The above figure represents some important probability and non-probability sampling.

2 Big Data Analytics

The analytical mechanism in big data is to process huge heterogeneous data within sufficient time. On the other hand, the traditional relational database system has a lack of scalability and expandability. The RDBMS (Relation Database Management System) could not meet the performance requirement [4]. Big data analytics is one of the burning and current trading research in related areas. The best example of big data analytics is to used in the prediction train delay system for large scale railway networks [5], prediction of diabetes patients in the health sector [6] and also used in weather

forecast systems. Big data analytics is capable to handle that dataset which is coming from different sources and has different characteristics such as an unstructured dataset. The traditional data processing application software is not sufficient to handle large and unstructured data [7]. Big data has various tools and frameworks for processing a large amount of data in a distributed manner such as Hadoop is widely popular which an open-source and it can store and process large datasets. MapReduce is another programming model that is used by Hadoop for breaking the entire task into two parts, one is Mapper and the second is Reducers. There is also a big data processing paradigm available with different models [8]. Furthermore, big data analytics can be used in health informatics, business, future investment, etc.

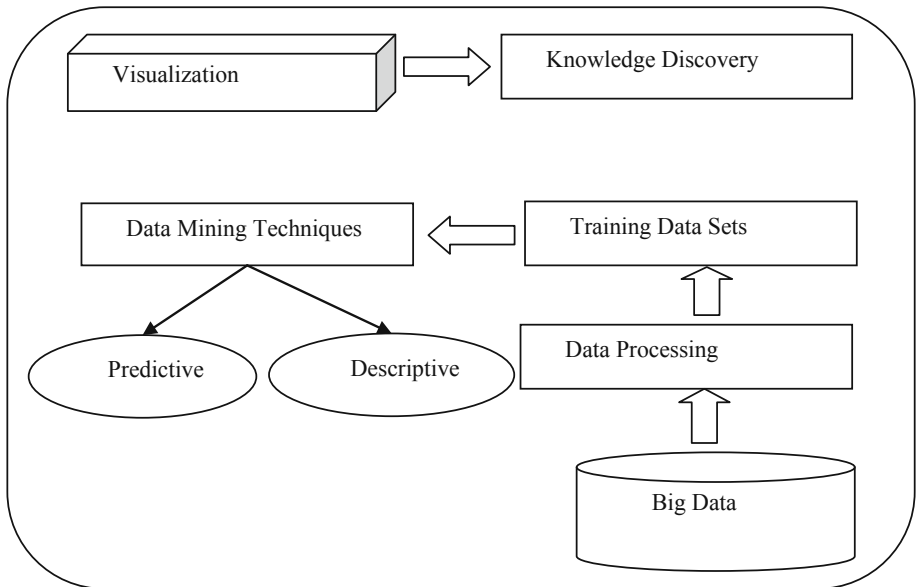


Fig. 2. The overview of big data analytics framework.

Furthermore, big data analytics can be used in health informatics, business, future investment, and more. Figure 2 has represented the process of big data analytics and knowledge discovery [9].

3 Sampling Techniques Regarding Big Data Parameters Estimation

We are living in a modern society where users constantly interact with each other through the rapid development of social computing and other media devices these devices are continuously increasing the large dataset in every second in different formats such as structured, unstructured and semi-structured. These types of complex datasets called big data. Big data has different parameters which are showing in the following Fig. 3.

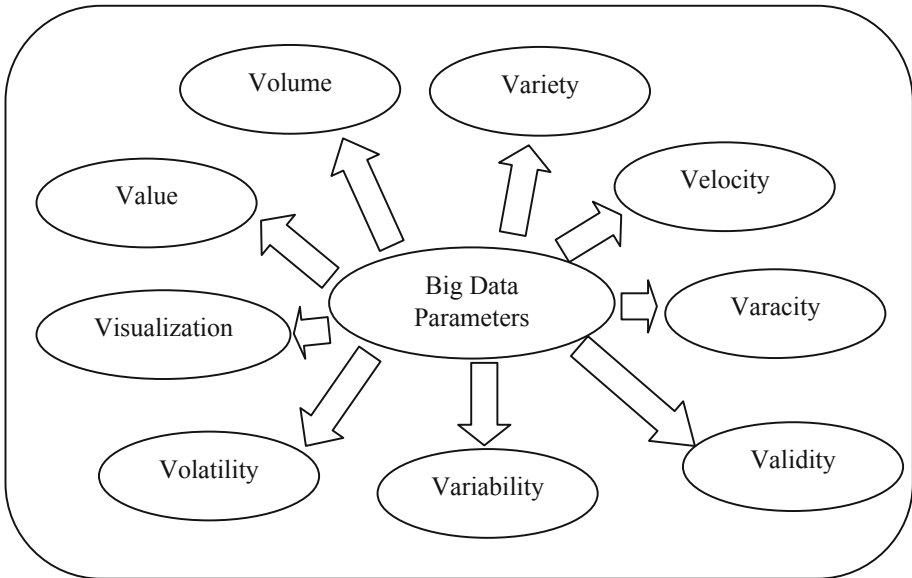


Fig. 3. The different parameters of big data.

In the above Fig. 3, there are nine parameters of big data which also known as 9Vs of big data. In Table 1, has given an explanation of all these parameters.

Table 1. Description of big data parameters.

Parameter name	Description
Veracity	It is referred to the biases, noise, and abnormality in data
Variety	Various types of data like structured, semi-structured and unstructured
Velocity	It is referred to, how fast data is to be produced and processed to meet the demand
Volume	Volume is a size of data such as terabyte, petabyte, Exabyte, zettabyte etc.
Validity	The data is correct and accurate for the intended
Variability	Along with the velocity, the data flows may be highly inconsistent with the data. The need to be found by anomaly and outlier detection methods in order for any meaningful analytics to occur
Volatility	Recall the retention policy of structured data that the implement every day in the businesses
Visualization	It makes all that huge amount of data comprehensible and easy to understand and read
Value	It has a low-value density as a result of extracting value from massive data

In the above Table 1 represents the big data parameters and its values [10].

3.1 Simple Random Sampling (SRS)

A simple random sampling concerned within two stages with replacement and without replacement. In with replacement procedure, the previous sample drawn from the population is replaced back before the chosen next sample and without replacement, procedure concerned with not replacement back when drawing a sample from the population. It is the most basic method where each and every member of the dataset has the same chance of being selected in the sample. The probability of in which sample has an equal chance $P = \frac{1}{(N_{c_n})}$ being included [11]. Here the population can be any data center which has stored heterogeneous data sets (population) like the downloading and uploading the file in a particular time.

3.2 Stratified Random Sampling (SRS)

The simple random sampling does not provide a good representation of the data sets, that's why a high chance is likely to occur from estimate to be inaccurate. In the stratified sampling method, the population has to divide into a different group which is known as strata. A stratum is a group of a homogeneous unit of the population, in the dataset (population) of N units is divided into K strata, each of size, $N_1, N_2, \dots, N_K; \sum_{i=1}^K N_i = N$. The sample which is taken from the population is also further divide into strata in K parts, $n_1, n_2, \dots, n_k; \sum_{i=1}^k n_i = n, n_i$ group is randomly selected from N_i using simple random sampling without replacement. The sample allocation can be proportional allocation, Neyman allocation and optimal allocation or n_i may arbitrary [12]. The following figure shows that the procedure of sample selection from data centers in SRS (Fig. 4).

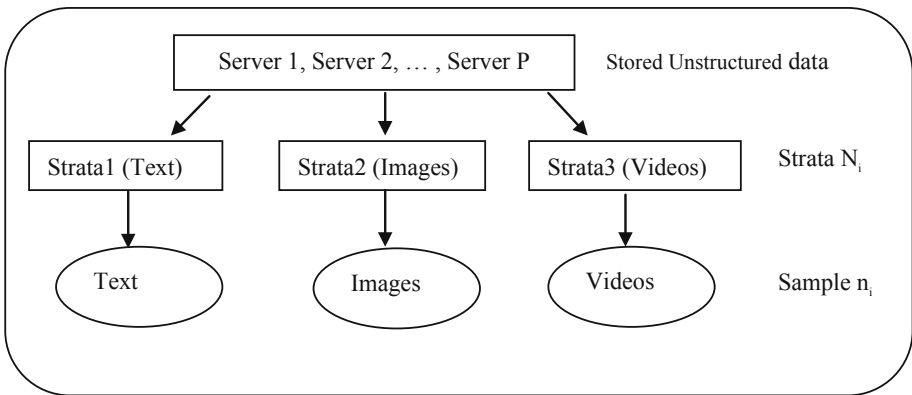


Fig. 4. The graphical representation of sample selection in SRS.

3.3 Systematic Sampling

The systematic sampling can provide more precise estimators than simple random sampling when at the time of design the sampling frame. In the systematic sampling first unit is randomly selected and the remaining being automatically selected according to a predetermined pattern. In order to systematic sampling procedure for N population unit is to compute $K = \frac{N}{n}$, where K should be a complete integer and that is called sampling interval. For select any i^{th} unit of the population by randomly such that $1 \leq i \leq K$; and then the systematic sample of n units is $\{i, i+K, i+2K, \dots, i+(n-1)K\}$. Some researchers tried to estimate the finite population variance ($V(y)$) from a systematic sample through the multi-start approach [1, 13].

3.4 Multistage Sampling

The multistage sampling is a type in which dividing the population in two or more stages of random sampling that is based on the hierarchical structure [14], it is widely used for health surveys and household when the population is expanded over a wide area. Multistage sampling usually applied where the population is so large and the selection of final sample units need in small size [15]. Through the use of a multistage sampling technique, the large dataset can be reduced again and again, due to big data the data mining techniques take more time for processing large datasets. For better efficiency and reduction in computing time for data mining techniques, multistage sampling plays a very important role by reducing data size at different stages [16].

3.5 Cluster Sampling

When we have a huge amount of digitalized data sets and it is very difficult to apply simple random sampling techniques then we can divide whole data sets into small clusters just like groups, each sampling unit is a cluster of elements. There are many clustering-based algorithms is available for data mining like k-means. Under two conditions cluster sampling can be used, when the population cannot be easy sampled any other way and the second condition is when can only observe in a cluster like a blog interaction which is by definition comprised of a cluster of the post, the structured data set N consists of data items N_1, N_2, \dots, N_m and the sample is n_1, n_2, \dots, n_n [17, 18].

3.6 Multistage Cluster Sampling

The multistage cluster sampling concerned with the produced better result through the effect of stage clustering. Basically, it is an extension of cluster sampling, these units are established in hierarchically such as primary, secondary, tertiary, etc. if there are k stage of sub-sampling, there will be the k sources of variability, estimation is also done at this stages. The variance and variance estimators for multistage cluster sampling with k different stages starting with the last units [19, 20]. Due to more efficiency and usefulness information in dynamic nature datasets, multistage sampling techniques able to classified the data within different stages and process the result can improve and a multistage clustering-based algorithm will achieve a good performance [21].

3.7 Quota Sampling

Quota sampling is similar to stratified sampling the only difference is that quota sampling is based on nonprobability sampling and stratified sampling is based on probability sampling. When the population is available in heterogeneous such as social media has stored data in the form of text, images, videos, etc. then the subgroup are formed that are homogeneous, and the samples are selected non randomly from each subgroup, or quota [22].

4 Summarization of Sampling Techniques Regarding Big Data Parameter Estimation

The following Table 2 has summarized all sampling techniques which we have discussed in previous sections [11–13, 16, 18, 21, 23].

Table 2. Brief description of sampling techniques.

Sampling techniques	Description	Advantages	Limitations
Simple random sampling	Draw sample from the whole population	High representation	Bears difficulty in the selection of sample units from large data sets
Stratified random sampling	Draw sample from identifiable non-homogeneous strata	Ensure about the specific groups are presented high accuracy	The required greater effort, more complex, strata must be carefully designed
Systematic sampling	Draw the first sample at random and remaining will be systematic	Selection of sample is easy	If the size of the population is unknown then it is very difficult to create systematic samples
Multistage sampling	Based on stages like state, district, villages, households	The estimation process is easy because population dividing or breaking again and again in the form of stages	It has high-level subjectivity, expensive and time-consuming
Cluster sampling	The population are dividing into clusters or small groups	Not more expensive in comparison to another sampling, reduce variability	Due to sampling design may occur higher sampling error, biases in the sample
Multistage cluster sampling	Draw samples in stages by using a smaller unit at every stage	more accurate in comparison to cluster sampling, takes less time with more cost	Not accurate in that situation when the sample size is equal, testing is difficult
Quota sampling	Population divide into small group and sample selected from each group	Take less time, it is powerful when time is limited	Maybe biased in the case of nonprobability sampling

5 Suggested Model of Big Data Analytics Based on Stratified Sampling

The stratified sampling is one of the most effective sampling techniques which provides useful knowledge of the important aspects of the large dataset because the entire population (N) units are divided into different strata of size N_h where $h = 1, 2, \dots, n$ [24]. In our study, we have found that stratified sampling is most suitable for the big data parameter estimation. Here we have suggested one model for big data analytics based on stratified sampling techniques.

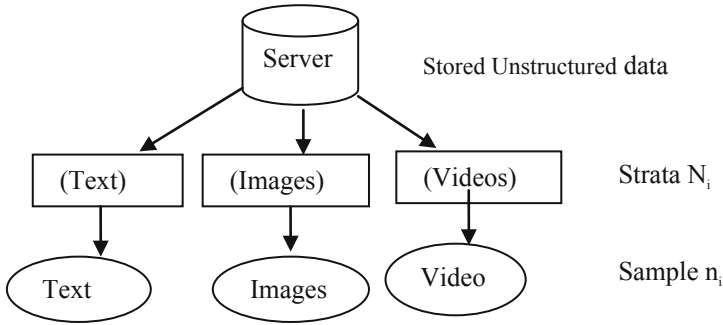


Fig. 5. The graphical representation of suggested model.

The stratified sampling already has discussed in Sect. 3.2. In our suggested model, we have studied the assumptions like the average size of the picture, the average size of videos, the average size of text messages. Figure 5 has described an overview of the suggested model.

Let there are T time interval for any server, then

$$N = \sum_{i=1}^k N_i \tag{1}$$

A total n sample has to be taken through the random sample technique. The size of the sample in different strata considering the phased operation as stratification criteria will be-

$$n = \sum_{i=1}^h n_i \tag{2}$$

if the dataset is dynamic nature then the general weight is-

$$W_i = \frac{N_i}{N} \tag{3}$$

Estimation of mean and variance for the proposed method, to estimate the population (data) mean- $\bar{Y} = \sum_{i=0}^n W\bar{Y}_i$ of the study parameter Y, the estimator used is given by-

$$\bar{y}_{st} = \sum_{i=1}^L W_i \bar{y}_i \tag{4}$$

Which is an unbiased estimator of the population mean and the variance of y_{st} under proportional allocation is given by-

$$V(\bar{y}_{st}) = \sum_{i=1}^L \left(\frac{1}{n_i} - \frac{1}{N_i} \right) W_i^2 S_i^2 \tag{5}$$

Where $S_i^2(t) = \frac{1}{N_i-1} \sum_{i=1}^N (Y_{ij} - \bar{y}_i)^2$
 The confidence interval (C.I.) is-

$$(\bar{y}_{st})_T \pm 3 \left[\sqrt{V(\bar{y}_{st})_T} \right] \tag{6}$$

The pooling estimated mean value of the sample-

$$(\bar{y}_{st})_T = \sum_{i=1}^n \theta_i (\bar{y}_{st})_{t_i} \tag{7}$$

The pooling estimated variance value of the sample-

$$V(\bar{y}_{st})_T = \sum_{i=1}^n V(\bar{y}_{st})_{t_i} \tag{8}$$

In stratified sampling, before taking a sample, the sample has to decide about the allocation of the sample size to the strata (equal, proportional, arbitrary and optimum) [25, 26].

6 Simulation Study

Let the population has stored dynamic population with three types of files such as images, videos and text file, this file are given into Megabyte on time t_1, t_2 and t_3 and the total population size is - $\sum_{i=1}^k N_i = 717$. The population dataset be divided into k homogeneous strata and $n_h (h = 1, 2, 3)$ be the number of sample unit which is drawn 70% from each strata of t_i by the simple random sampling without replacement and the sample allocation method is arbitrary an sample allocation method. So first we have divided the entire population into three strata for each time interval (t_i). The following Fig. 6 are showing the population and each time interval strata. There are total nine strata of and three time interval t_1, t_2 and t_3 .

```

Python 3.7.4 (tags/v3.7.4:1e0939112e, Jul 8 2019, 19:29:22) [MSC v.1916 32 bit
Type "help", "copyright", "credits" or "license()" for more information.
>>>
===== RESTART: C:\Users\Manager\Desktop\working1.py =====
   User ID(t1)  Image Size(t1)  ...  Video Size(t3)  Text Size(t3)
0             1.0           300.0  ...           1270           218
1             2.0           400.0  ...           1220           238
2             3.0           280.0  ...             770           128
3             4.0           900.0  ...             970           328
4             5.0           100.0  ...             770           438
..           ...           ...     ...           ...           ...
82           NaN           NaN     ...             720           105
83           NaN           NaN     ...             720           105
84           NaN           NaN     ...             720           105
85           NaN           NaN     ...             720           105
86           NaN           NaN     ...             720           105

[87 rows x 14 columns]
>>>
    
```

Fig. 6. The pictorial visualization of dynamic population (t_i).

The following Table 3 is showing the properties of sample like n_i - sample strata, w_i - each strata weights, \bar{y} - each strata mean, σ - each strata standard deviation, S_i^2 - each strata variance, $(\bar{y}_{st})_{t_i}$ - estimated mean of each time interval t_i , $V(\bar{y}_{st})_{t_i}$ - estimated variance of each time interval t_i , $(\bar{y}_{st})_T$ - estimated pooling sample mean, $V(\bar{y}_{st})_T$ - estimated pooling variance of sample. Every t_i has different population such as $t_1 = 213$, $t_2 = 240$ and $t_3 = 264$. Further we have taken the sample (70%) of each t_i strata and estimate the mean (\bar{y}_{st}) of each t_i . After that we have pooling the all mean and calculate the estimated mean $(\bar{y}_{st})_T$. After the calculating confidence interval we have compared to estimated value with the true value of population mean $(\bar{Y}_{st})_T = 561.93$, and the estimated value is $(\bar{y}_{st})_T = 634.18$. We have calculated 99% confidence interval and the confidence interval (CI) are $- [520 - 743]$ by Eq. 6. So the true value (population estimated mean $(\bar{Y}_{st})_T$) will lies between in our calculated confidence interval. The unit of final result will be in Megabyte because the all files in dataset are given in MB. Due to the dynamic population $N t_1, t_2$ and t_3 has some weights $(\theta_i) - \theta_1 = 0.1, \theta_2 = 0.4$ and $\theta_3 = 0.5$ these weights are arbitrary and it is used in Eq. 7 for calculate pooled value of estimated mean. So we can say that the our proposed big data parameter estimation method is applicable to estimate dynamic population mean at different time.

Table 3. The simulation study of samples.

Time	n_i	w_i	\bar{y}	σ	S_i^2	$(\bar{y}_{st})_{t_i}$	$V(\bar{y}_{st})_{t_i}$	$(\bar{y}_{st})_T$	$V(\bar{y}_{st})_T$
t_1	n1 = 50	w1 = 0.33	524.36	288.13	83016.28	623.58	4755.45	634.18	1458.19
	n2 = 50	w2 = 0.33	1253.44	2051.62	4209135.52				
	N3 = 50	w3 = 0.33	106.54	178.37	31814.78				
t_2	n1 = 56	w1 = 0.33	397.55	284.95	81196.54	486.63	4249.91		
	n2 = 56	w2 = 0.33	959.59	1937.43	3753631.48				
	N3 = 56	w3 = 0.33	113.46	169.48	28724.54				
t_3	n1 = 62	w1 = 0.33	560.02	351.66	123665.92	754.34	4118.38		
	n2 = 62	w2 = 0.33	1517.47	1892.90	3583087.43				
	N3 = 62	w3 = 0.33	208.39	192.55	37229.42				

7 Conclusion

In this research article, we have studied some important sampling techniques regarding sampling-based parameter estimation for big data and also have discussed the various parameters of big data. This paper has focused on to use and importance of sampling techniques in big data parameter estimation. Furthermore, we have suggested a stratified sampling based parameter estimation model for big data analytics. The proposed model can predict the average size of Text, Videos, and Images in a particular time interval with respect to the dynamic dataset and for simulation study; we have implemented the proposed analytics model on a dynamic Internet traffic dataset (each file size in MB). After that have calculated confidence interval for comparing the estimated result and true value, and we have found that true value lies within range of the our calculated 99% confidence interval. The future work may proceed with the implementation of other sampling techniques also.

References

1. Shukla, D., Rajput, Y.S.: Graph Sampling, 1st edn. Aman Prakashan, Sagar (2010). ISBN 978-93-80296-03-6
2. Hashemian, M.S., Abkar, A.A., Fatemi, S.B.: Study of sampling methods for accuracy assessment of classified remotely sensed data. In: International Congress for Photogrammetry and Remote Sensing, pp. 1682–1750 (2004)
3. Elfil, M., Negida, A.: Sampling methods in clinical research an educational review. *Emergency* **5**(1), e52 (2017)
4. Chen, M., Mao, S., Liu, Y.: *J. Mob. New Appl.* **19**, 171–209 (2014)
5. Oneto, L., Fumeo, E., Clerico, G., Canepa, R., Papa, F., Dambra, C., Mazzino, N., Anguita, D.: Train delay prediction systems: a big data analytics perspective. *J. Big Data Res.* **11**, 54–64 (2018)
6. Razavian, N., Blecker, S., Schmidt, A.M., Smith-McLallen, A., Nigam, S., Sontag, D.: Population-level prediction of type 2 diabetes from claims data and analysis of risk factors. *J. Big Data* **3**, 277–287 (2015)

7. Das, N., Pandey, M., Rautaray, S.S.: A big step for prediction of HIV/AIDS with big data tools. In: Bhatia, S., Tiwari, S., Mishra, K., Trivedi, M. (eds.) *Advances in Computer Communication and Computational Sciences. Advances in Intelligent Systems and Computing*, vol. 760, pp. 37–46. Springer, Singapore (2019)
8. Singh, D., Reddy, C.: A survey on platforms for big data analytics. *J. Big Data* **1**(8), 1–20 (2014)
9. Chauhan, R., Kaur, H.: A spectrum of big data applications for data analytics. In: *Computational Intelligence for Big Data Analysis: Frontier Advances and Applications*, vol. 19, pp. 165–179 (2015)
10. Alim, A., Shukla, D.: Big data: myth, reality and parametric relationship. *Int. J. Adv. Manag. Technol. Eng. Sci.* **8**(3), 1235–1244 (2018)
11. West, P.: Simple random sampling of individual items in the absence of a sampling frame that lists the individuals. *NZ J. Forest. Sci.* **46**(15), 1–7 (2016)
12. Alim, A., Shukla, D.: An application approach of stratified sampling in analytic-predictive environments of big data. In: *Proceedings of International Conference on Sustainable Computing in Science, Technology and Management (SUSCOM)*, pp. 1340–1346. Amity University Rajasthan, Jaipur - India, 26–28 February 2019
13. Mostafa, S.A., Ahmad, I.A.: Recent developments in systematic sampling: a review. *J. Stat. Theory Pract.* **12**(2), 290–310 (2018)
14. Sedgwick, P.: Multistage sampling. *BMJ* (online) **351**, h4155, 1–2 (2015)
15. Hauvet, G.: Coupling methods for multistage sampling. *J. Ann. Stat.* **43**(6), 2484–2506 (2015)
16. Cebeci, Z., Yildiz, F.: Efficiency of random sampling based data size reduction on computing time and validity of clustering in data mining. *J. Agric. Inform.* **7**, 53–64 (2016)
17. Kurasova, O., Marcinkevicius, V., Medvedev, V., Rapecka, A., Stefanovic, P.: Strategies for big data clustering. In: *2014 IEEE 26th International Conference on Tools with Artificial Intelligence, Limassol*, pp. 740–747 (2014)
18. Webb, L., Wang, Y.: Techniques for sampling online text-based data sets (2013). <https://doi.org/10.4018/978-1-4666-4699-5.ch005>
19. Shimizu, I.: Multistage sampling. In: Armitage, P., Colton, T. (eds.) *Encyclopedia of Biostatistics* (2005). <https://doi.org/10.1002/0470011815.b2a16041>
20. Nafiu, L.: Generalization of multistage cluster sampling using finite population. *J. Eng. Appl. Sci.* **3**(1), 17–20 (2013)
21. Abdullah, M., Al-Anzi, F., Al-Sharhan, S.: Hybrid multistage fuzzy clustering system for medical data classification. In: *2018 International Conference on Computing Sciences and Engineering (ICCSE)*, Kuwait City, pp. 1–6 (2018)
22. Alvi, M.: A Manual for Selecting Sampling Techniques in Research (2016). <https://mpr.ub.uni-muenchen.de/70218/>. Accessed 05 June 2019
23. Sampling techniques: Advantages and disadvantages. https://www.researchgate.net/profile/Krishnan_Umachandran/post/Is_it_appropriate_to_apply_multiple_sampling_methods_sampling_techniques_in_data_collection_in_social_science/attachment/59d630e6c49f478072ea0b61/AS%3A273611233521667%401442245410745/download/Sampling+techniques.pdf. Accessed 05 June 2019
24. Khowaja, S., Ghufuran, S., Ahsan, M.J.: Multi-objective optimization for optimum allocation in multivariate stratified sampling with quadratic cost. *J. Stat. Comput. Simul.* **82**(12), 1789–1798 (2012)
25. Pandey, R., Verma, M.R.: Samples allocation in different strata for impact evaluation of developmental programme. *Rev. Bras. Biom.* **26**(4), 103–112 (2008)
26. Ozgul, N.: New calibration estimator in stratified sampling. *J. Stat. Comput. Simul.* **18**(13), 2561–2572 (2018)



Development of Framework for Greenness Identification

Chandrika Dabariya^(✉)  and Rajeev Kumar Singh 

Department of Computer Science & Engineering and Information Technology,
Madhav Institute of Technology and Science, Gwalior, India
chandrika.dabl5@gmail.com, rajeev.mitsl@gmail.com

Abstract. In this paper, an enhanced approach for greenness identification from organic carrot crop while the carrot plants were in the initial phase of authentic leaf development is proposed. This paper proposes an enhancement gamma correction and optimization contrast techniques which is worked with vegetation index-based methods for identification of greenness. In this paper, the enhancement of vegetation index-based methods examined its efficiency by comparing it with performances of vegetative index-based methods that have lately been commonly used. The findings showed that the accuracy of vegetation extraction was considerably better than existing methods by the proposed method.

Keywords: Carrot plant · Vegetation index · Image thresholding · Enhancement techniques · Morphological operations

1 Introduction

To date, due to the growing use of artificial vision sensors in precision agriculture (PA), the research of distinct methods for precise data is becoming increasingly essential. These sensors are in self-contained vehicles and should provide independent responses [1].

More and more nations are considering precise agriculture for better crop yields [2]. To understand the precise farming philosophy, the most significant task for crops to be recognized as a preliminary step is to obtain crop data at each point of growth. The segmentation of pictures is a significant problem linked to the implementation of artificial vision techniques. Effective and automatic segmentation of vegetation from soil pictures is a significant move for many applications, such as weed identification, determining the development phase of the plant, among others, nutrients were always needed for site-specific treatments to minimize manufacturing expenses or to avoid unnecessary contamination of the soil or environment during herbicide applications [3].

In order to classify plants and weeds, numerous scientists have implemented image processing methods based on various characteristics including color, texture and shape. Some have shown excellent efficiency, particularly under controlled circumstances, but precise detection remains a challenge for uncontrolled circumstances.

2 Related Work

Distinctive strategies and methodologies have been applied for plant distinction tests. One is the basic method of the color index-based methods: [4] the excess of green index method (ExG) was examined, which was more valuable to distinguish the plant districts. In any case, luminous soil or residual pixels containing a high green substance (despite not showing green color to the human eye) tend to provide erroneous data about the plant [5]. [6] analysis of the RGB focused on the images and subsequently a strategy called Color Index Vegetation Extraction (CIVE) substance.

In any event, the varying light that can trigger disappointment when the green plant is isolated from the background readily influences pictures captured by external circumstances. The other is the strategy based on learning: [7] applied the EASA within its color space (saturation intensity) to treat light inconstancy. [8] uses a supervised mean-shift algorithm to distinguish greenery. [9] applied the fuzzy clustering method to identify green. [10] have approached the AP-HI method that combines the chromatic model of hue-intensity and affinity propagation clustering algorithm. [11] suggested a technique of vegetative index (VEG), that produces a large contrast between the plant and the soil. [12] uses this strategy to evaluate the crop or the grass.

ExGR method was introduced by [5] combining two color index methods, specifically, Excess Green Index (ExG) and Excess Red Index (ExR) [13] a combined index (COM) technique has been suggested. All color-based indices are based on the premise that crops display a large degree of green and that the soil includes a low-green. Specific approaches based on the threshold, including the dynamic limit. In general, these techniques presuppose a problem of two kinds in which plants and soil must be identified. [14] estimated a decision function based on the premise that Gaussian distributions were accompanied by classes. The Otsu method [15] an issue of two was also implemented [16, 17].

These algorithms apply to gray images. [18] also applied the segmentation limit when transforming RGB images to grayscale intensity. Subsequently, this algorithm was enhanced with local homogeneity and morphological operations in [19]. [20] a combination of green and intensity obtained from red and green spectral bands was applied and an automatic limit for a two-class issue was calculated by assuming two Gaussian probability density functions related to soil and vegetation respectively. This operation needs a preliminary angle estimate to rotate the greenery hypothetical axis

3 Proposed Methodology

The Propose Method uses Enhanced techniques to identify greenness in the plant. This method is capable to handle the problem arises during the review of previous techniques and detection of greenness. This method can be visualized more precisely with the help of flow diagram as shown in Fig. 1.

3.1 Flow Graph

Proposed method using the above mentioned is shown in Fig. 1.

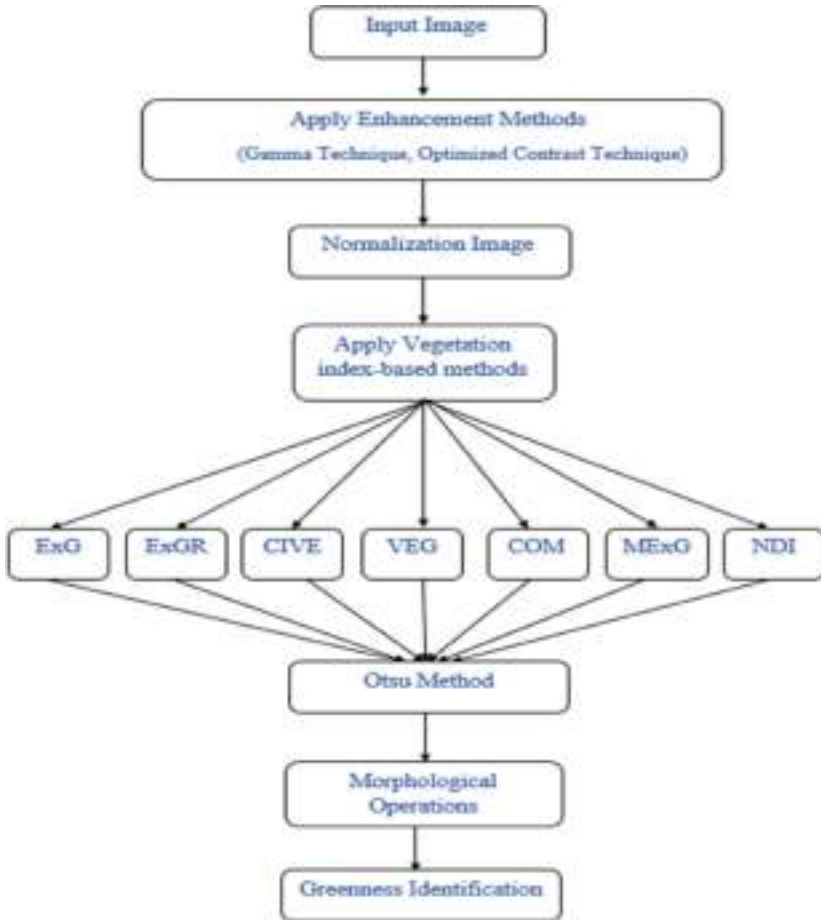


Fig. 1. Flow graph of proposed method

3.2 Proposed Algorithm

In the proposed methodology, it follows the certain number of steps which is using in the proposed method. All the required steps in this proposed method discussed here as a proposed algorithm.

Step1: Take the original image as input image from the dataset.

Step2: Apply enhanced two sub-techniques the first is gamma correction and the second is the optimized contrast technique for enhancing the images.

- Step3:** Normalized the enhanced RGB image, with the normalization the RGB image obtain the grayscale image. The grayscale image represents greenness identification through the pixels.
- Step4:** After normalization than calculate the vegetation index-based methods for identification of greenness.
- Step5:** Following this, vegetation indices are thresholded by applying the Otsu’s method, obtaining a binary image that determine which pixels belong to green plants and which pixels belong to other elements present in the grayscale image.
- Step6:** Apply morphological operations, for removing small pixels and filled the holes.
- Step7:** Greenness identifies in the binary image.

3.3 Enhancement Techniques

We will use two sub-techniques in this method, the first is image correction and the second is the contrast technique, and we will perform enhancement techniques in pictures by combining correction and contrast technique.

3.3.1 Gamma Correction Technique

It is a non-linear procedure that operates on the bad quality picture encoding and decoding operations, helping to show a picture on the computer screen properly. It controls the complete brightness of an image. A picture that is not corrected correctly may stand out, or discolored dark too. If we try to reproduce the colors correctly, we should have a strong gamma understanding. By varying the quantity of gamma in a picture, it can result in image brightness and corresponding colors of red to green to blue [21]. For all digital imaging systems, gamma correction is essential. It describes the ratio of numerical pixels to their luminance. Gamma correction can enhance the method of exposure and assist editing images. All picture information from the world includes Gamma Correction. It has the slope of the curve’s linear range, the relationship between the logarithmic light intensity and the resulting film density. The graph of gamma correction at the different values of gamma is shown in Fig. 2.

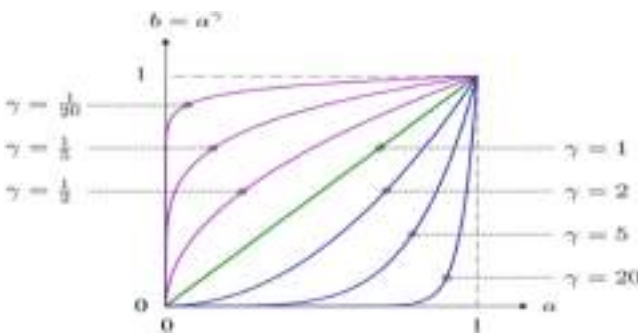


Fig. 2. Graph of gamma correction at different values of gamma

3.3.2 Optimized Technique of Contrast

Based on the finding that a poor quality image usually shows low contrast, we re-store the poor quality image by enhancing its contrast. It is used to make the picture more sensitive and more specific. Contrast is the image quality assessment. The contrast is the distinction in visual quality and characteristics that distinguish object from other objects [22]. Contrast is the determination with other things attached to the distinction between the object's color and brightness. In particular, a bad quality picture shows low contrast, where the bad quality picture was stored by improving its contrast. However, degraded comparison overcompensation can truncate pixel values and cause information loss. Hence, we formulate a cost function composed of the comparison period and the information loss period. By minimizing the cost function, the suggested algorithm enhances contrast and optimally retains information.

3.4 Normalization Image

The primary step is to get a grayscale picture of the past RGB picture once the picture is captured by the camera in the RGB color model. Separating green plants (crops and weeds) from the rest (soil, stones, and others) is the focus of this segmentation method. The grayscale image represents the original picture's greenness so that the higher the value of the pixel, the higher the likelihood of a plant being.

The normalized colour r , g , and b in the RGB colour space, where R , G , and B are the colour components of the RGB crop picture.

After normalizing the conspiracy, which is normally applied in the agronomic image division, the original input image within the RGB colour space [23], we apply normalized r , g and b elements extending to $[0, 1]$ as per (1),

$$r = \frac{R_n}{R_n + G_n + B_n}, g = \frac{G_n}{R_n + G_n + B_n}, b = \frac{B_n}{R_n + G_n + B_n} \quad (1)$$

Where R_n, G_n, B_n are standardized using RGB spectral channels with a value range $[0, 1]$.

$$R_n = \frac{R}{R_{\max}}, G_n = \frac{G}{G_{\max}}, B_n = \frac{B}{B_{\max}} \quad (2)$$

Where for our 24-bit color pictures $R_{\max} = G_{\max} = B_{\max} = 255$ for. The combined vegetation indices are calculated as follows.

3.5 Vegetation Index-Based Approaches

Vegetation is one of the most popular techniques of distinguishing crops from computer vision background clutter. Several scientists used vegetation index to distinct crops from the soil, such as color features, to differentiate green plants from the soil and to estimate the leaf region [24, 25] and [20]. It is possible to accentuate the color of a region of concern, thus attenuating the undesired area (soil background region). The pictures are produced in the standard RGB color space for most standard visible spectrum cameras. Due to similar grayscale values in plant and soil background

images, the transformation of RGB values into greyscale did not lead to outstanding segmentation. Therefore, to demonstrate great segmentation, the RGB space is often converted into alternative color spaces

Green excess:

$$ExG = 2g - r - b \quad (3)$$

Green excess minus red excess:

$$ExGR = ExG - (1.4r - g) \quad (4)$$

Vegetation extraction colour index:

$$CIVE = 0.441r - 0.881g + 0.385b + 18.78745 \quad (5)$$

Vegetative parameter:

$$VEG = \frac{g}{r^a b^{1-a}}, \text{ with a range to } 0.667 \text{ as in [12] combined:} \quad (6)$$

$$COM = w_{ExG}ExG + w_{ExGR}ExGR + w_{CIVE}CIVE + w_{VEG}VEG \quad (7)$$

In order to separate crops from soil and residue background pictures, other colour vegetation indices have been suggested. For instance, the standardized vegetation difference index (NDI) only utilizes green and red channels by [26] and is given as:

$$NDI = G - R / G + R \quad (8)$$

Modified Excess Green (MExG) Index was developed and is defined as follows:

$$MExG = 1.262G - 0.884G - 0.311B \quad (9)$$

3.6 Otsu Thresholding

Among these methods, [15] one of the major thresholding methods is the Otsu threshold. Otsu's technique is applied in many applications for segmentation. After the acquired vegetation index-based, which is thresholded by applying the Otsu method, a binary image is acquired, where black pixels recognize masked crops, i.e. crops not contaminated by soil-sectioned products.

3.7 Morphological Operations

After binarization of the picture, in the following order, the following two morphological operations are carried out:

3.7.1 Opening

Small patches are removed.

3.7.2 Closing

For both operations, the closing operation dilates the image and then erodes the dilated image using the same element of structure. Morphological closure is useful for filling small holes in the image while preserving the shape and size of the objects in the image.

3.8 Greenness Identification in Binary Image

According to Fig. 1, once the complete method is finished, we get the final segmented image, the binary image, where unmasked as well as masked crops are recognized. So we have enough knowledge about the distribution of their field, which was the objective of this work.

4 Result

For comparative study purpose, we have selected sample 5 organic carrots images from the data set of 60 photos were captured in a commercial crop of natural carrots in northern Germany in 2013 [27]. This dataset provides source image as well as vegetation mask image we use these images as ground truth images for comparison. The greenness identification methods performance is being evaluated by objective, subjective, comprehensive, and comparative study of various low light images and the results obtained will tell you about the removal of low contrast, increase brightness, and the natural color balancing capabilities of the methods. Finally, we will test and prove the use of defined approaches for the different scenes and environmental conditions of the crop images. The digital images were stored as 24-bit color images with 1296×966 pixels resolutions and saved in PNG format in the RGB color space. The algorithms were programmed in MATLAB.

Then we compare the various image quality assessment parameters with the original image and enhanced image which is shown in Tables 1 and 2.

Table 1. Evaluation of original image by quality assessment parameters





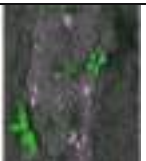


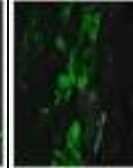
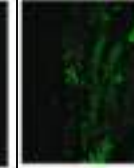
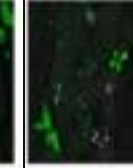
Quality Assessment Parameters					
PSNR	13.887	13.77	14.08	13.9107	14.550
SNR	22.0907	21.3801	21.99	22.4411	22.563
MSE	2677.79	2750.94	2561.74	2663.25	2298.92
RMSE	51.7474	52.450	50.614	51.607	47.947
AG	3.05234	2.707	2.9244	2.9220	2.69224
MAE	27.784	27.807	27.3075	28.1906	26.347

Table 2. Evaluation of enhanced image by quality assessment parameters by combination of GC and OC techniques

Quality Assessment Parameters					
PSNR	25.444	30.968	26.812	31.157	25.316
SNR	24.96	22.597	25.573	27.30	27.18
MSE	187.12	52.3	136.55	50.21	192.7
RMSE	13.68	7.24	11.7	7.09	13.9
AG	1.726	1.21	1.40	1.14	1.29
MAE	7.27	3.72	5.88	3.67	7.02

The quality of the enhanced picture is better than the original image and the parameters of quality assessments give better result a comparison to the original image. Evaluation of enhanced image by quality assessment parameters by the combination of GC and OC techniques is shown in Table 2.

The result of segmentation on the sample image which is taken from the data set which is represent in Table 3. The segmentation findings of the proposed algorithm were superior to the outcomes of vegetation-based index-based techniques, as vegetation-based techniques misclassified most background pixels (including ash) as plant based. Greenness identification from visualization the proposed method gives the far better result than to existing methods.

4.1 Accuracy Measures of Vegetation Indices

In this experiment, segmentation accuracy was evaluated on segmented pictures against ground truth by computing the Jaccard Index.













4.1.1 Jaccard Index

The Jaccard Index, also known as Jaccard’s similarity coefficient, is a statistical metric used to compare the similarity and diversity of sample sets. The Jaccard coefficient measures resemblance between finite sample sets and is described as the intersection size divided by sample size union:

$$(A, B) = \frac{|A \cap B|}{|A \cup B|} \tag{10}$$

The average vegetation similarity over the number of pictures tested against our suggested techniques based on the respective ground truth. By comparing the

Table 3. Comparison of proposed method and existing method

Vegetation index based methods	Proposed Method	Existing Method[28]
ExG		
ExGR		
CIVE		
COM		
MExG		
NDI		

segmentation accuracies of various techniques in Table 4, it was found that the proposed algorithm had better outcomes in segmentation than the other techniques on average. VEG cannot get correct results for all conditions (like different environmental conditions and when dealing with those images with ash or stem).

Table 4. Parametric evaluation using vegetation index-based method of Jaccard’s similarities index accuracy for proposed method and existing method

Proposed method	Existing method	Vegetation index-based method
98.3%	97.6%	ExG
98.3%	97.6%	ExGR
98.1%	97.6%	CIVE
98.32%	97.6%	COM
0%	0%	VEG
99.3%	97.6%	MExG
98.42%	97.6%	NDI

The average mean accuracy value of proposed method is better than existing method which is shown in Table 5.

Table 5. Parametric evaluation using vegetation index-based method for proposed method and existing method

Proposed method		Existing method		Vegetation index-based method
Mean	Standard deviation	Mean	Standard deviation	
89.4%	30.4%	87.9%	31.5%	ExG
89.4%	30.4%	87.9%	31.5%	ExGR
89.2%	30.4%	88.9%	31.4%	CIVE
89.4%	30.6%	88.4%	31.2%	COM
89.4%	30.4%	87.9%	31.5%	MExG
88.6%	30.7%	87.1%	32.4%	NDI

5 Conclusion

In this paper, the problem related to greenness identification for finding the visibility of green color in crops in different lighting and different types of images is a great challenge for us, and the presence of field images of growing crops and estimating their greenness, little brightness phenomenon in crop pictures that results in the poor visibility create difficulties. We have worked on few enhancement algorithms which have been specifically developed for the greenness pictures and find results from the output image. We have compared the previously developed methods and evaluated the performance of all the techniques in relations to various calculations, these methods work on all the greenness identification images.



References

1. Davis, G., Casady, W., Massey, R.: Water Quality. Precision Agriculture: An Introduction, pp. 1–7 (1998)
2. Pierpaoli, E., Carli, G., Pignatti, E., Canavari, M.: Drivers of precision agriculture technologies adoption: a literature review. *Procedia Technol.* **8**(Haicta), 61–69 (2013)
3. Riomoros, I., Pajares, G., Herrera, P.J., Guijarro, M., Burgos-Artizzu, X.P., Ribeiro, A.: Automatic image segmentation of greenness in crop fields. In: Proceedings of 2010 International Conference of Soft Computing and Pattern Recognition, SoCPaR 2010, pp. 462–467 (2010)
4. Woebbecke, D.M., Meyer, G.E., Von Bargaen, K., Mortensen, D.A.: Color indices for weed identification under various soil, residue, and lighting conditions. *Trans. ASAE* **38**(1), 259–269 (2013)
5. Meyer, G.E., Neto, J.C., Jones, D.D., Hindman, T.W.: Intensified fuzzy clusters for classifying plant, soil, and residue regions of interest from color images. *Comput. Electron. Agric.* **42**(3), 161–180 (2004)
6. Kataoka, T., Kaneko, T., Okamoto, H., Hata, S.: Crop growth estimation system using machine vision. In: IEEE/ASME International Conference on Advanced Intelligent Mechatronics, AIM, vol. 2, no. Aim, pp. 1079–1083 (2003)
7. Ruiz-Ruiz, G., Gómez-Gil, J., Navas-Gracia, L.M.: Testing different color spaces based on hue for the environmentally adaptive segmentation algorithm (EASA). *Comput. Electron. Agric.* **68**(1), 88–96 (2009)
8. Zheng, L., Shi, D., Zhang, J.: Segmentation of green vegetation of crop canopy images based on mean shift and fisher linear discriminant. *Pattern Recognit. Lett.* **31**(9), 920–925 (2010)
9. Romeo, J., Pajares, G., Montalvo, M., Guerrero, J.M., Guijarro, M., De La Cruz, J.M.: A new expert system for greenness identification in agricultural images. *Expert Syst. Appl.* **40**(6), 2275–2286 (2013)
10. Yu, Z., et al.: Automatic image-based detection technology for two critical growth stages of maize: Emergence and three-leaf stage. *Agric. For. Meteorol.* **174–175**, 65–84 (2013)
11. Marchant, J.A., Onyango, C.M.: Shadow-invariant classification for scenes illuminated by daylight. *J. Opt. Soc. Am. A* **17**(11), 1952 (2007)
12. Hague, T., Tillett, N.D., Wheeler, H.: Automated crop and weed monitoring in widely spaced cereals. *Precis. Agric.* **7**(1), 21–32 (2006)
13. Guijarro, M., Pajares, G., Riomoros, I., Herrera, P.J., Burgos-Artizzu, X.P., Ribeiro, A.: Automatic segmentation of relevant textures in agricultural images. *Comput. Electron. Agric.* **75**(1), 75–83 (2011)
14. Reid, J.F., Searcy, S.W.: Vision-based guidance of an agricultural tractor. *IEEE Control Syst. Mag.* **7**(2), 39–43 (1987)
15. Smith, P., Reid, D.B., Environment, C., Palo, L., Alto, P., Smith, P.L.: Ostu Algorithm 79, vol. C, no. 1, pp. 62–66 (1979)
16. Ling, P.P., Ruzhitsky, V.N.: Machine vision techniques for measuring the canopy of tomato seedling. *J. Agric. Eng. Res.* **65**(2), 85–95 (1996)
17. Shrestha, D.S., Steward, B.L., Birrell, S.J.: Video processing for early stage maize plant detection. *Biosyst. Eng.* **89**(2), 119–129 (2004)
18. Gebhardt, S., Schellberg, J., Lock, R., Kühbauch, W.: Identification of broad-leaved dock (*Rumex obtusifolius* L.) on grassland by means of digital image processing. *Precis. Agric.* **7**(3), 165–178 (2006)

19. Gebhardt, S., Kühbauch, W.: A new algorithm for automatic *Rumex obtusifolius* detection in digital images using colour and texture features and the influence of image resolution. *Precis. Agric.* **8**(1–2), 1–13 (2007)
20. Kirk, K., Andersen, H.J., Thomsen, A.G., Jørgensen, J.R., Jørgensen, R.N.: Estimation of leaf area index in cereal crops using red-green images. *Biosyst. Eng.* **104**(3), 308–317 (2009)
21. Chiang, J.Y., Chen, Y.C.: Underwater image enhancement by wavelength compensation and dehazing. *IEEE Trans. Image Process.* **21**(4), 1756–1769 (2012)
22. Lu, H., et al.: Underwater image enhancement method using weighted guided trigonometric filtering and artificial light correction. *J. Vis. Commun. Image Represent.* **38**, 504–516 (2016)
23. Gée, C., Bossu, J., Jones, G., Truchetet, F.: Crop/weed discrimination in perspective agronomic images. *Comput. Electron. Agric.* **60**(1), 49–59 (2008)
24. Rasmussen, J., Nørremark, M., Bibby, B.M.: Assessment of leaf cover and crop soil cover in weed harrowing research using digital images, pp. 299–310 (2007). <http://orgprints.org/11007>
25. Meyer, G.E., Neto, J.C.: Verification of color vegetation indices for automated crop imaging applications. *Comput. Electron. Agric.* **63**(2), 282–293 (2008)
26. Pérez, A.J., López, F., Benlloch, J.V., Christensen, S.: Colour and shape analysis techniques for weed detection in cereal fields. *Comput. Electron. Agric.* **25**(3), 197–212 (2000)
27. Agapito, L., Bronstein, M.M., Rother, C.: *Computer Vision - ECCV 2014 Workshops: Zurich, Switzerland, September 6–7 and 12, 2014 Proceedings, Part IV. Lecture Notes in Computer Science (including Subseries Lecture Notes in Artificial Intelligence and Lecture Notes in Bioinformatics)*, vol. 8928, pp. 105–116 (2015)
28. Yang, W., Wang, S., Zhao, X., Zhang, J., Feng, J.: Greenness identification based on HSV decision tree. *Inf. Process. Agric.* **2**(3–4), 149–160 (2015)



Wideband Crossed Dipole Antenna for Base Station Antenna

Anshul Agarwal^(✉) , P. K. Singhal , and V. V. Thakare 

Department of Electronics, Madhav Institute of Technology and Science,
Gwalior, M.P., India

agarwal.2712@gmail.com, pks_65@yahoo.com,
vandanavt_19@rediffmail.com

Abstract. Wideband crossed dipole antenna for base station antenna has been proposed in the present article. Impedance bandwidth of the dipole antenna has been enhanced by using the gap-coupling technique, whereas the gain of the proposed antenna is enhanced by using the reflector. Meanwhile, omnidirectional radiation patterns in E-plane & H-plane are also achieved. The proposed antenna with reflector provides 1.52 GHz–3.08 GHz impedance bandwidth and 5.98 dB to 7.16 dB antenna gain which is very useful for GSM application.

Keywords: Dipole antenna · Base station antenna · Omnidirectional antenna

1 Introduction

Antenna geometries having miniaturized dimensions, wide bandwidth and high gain are the requirements of a present wireless communication system. Various structure of planar antenna is extensively investigated and designed to meet these requirements. From previously reported designs, printed dipole antennas are very much feasible as base station antenna for mobile communication due to a compact size, bi-directional radiation pattern, low cost, etc. Various printed dipole structures are already reported and discussed for their performance parameters viz. wider impedance bandwidth, circular & dual-polarization radiation pattern, high gain, required half-power beamwidth, miniaturized dimensions with proper impedance matching with co-axial feed [1–7].

A planar half-circular with tapered rectangular shape dipole antenna is published [1] for wide impedance bandwidth of 1.265 GHz to 3.98 GHz but measured radiation pattern is not matched with a simulated radiation pattern. Nie et al. [2] presents a dual-band dipole antenna array with dual-polarization for 2G/3G/4G. Impedance bandwidth is enhanced by four shorting strips resulting into wide impedance bandwidths of 0.82 GHz–0.99 GHz and 1.68 GHz–2.86 GHz. A wideband dipole antenna for 2G/3G/4G is proposed by Cui et al. [3]. By using four parasitic disks on the antenna, a wide bandwidth of 1.39–2.8 GHz is achieved. Also gain of 17 dBi is achieved by 8 element antenna array. The wideband omnidirectional printed dumbbell-shaped dipole antenna is published [4] and wider bandwidth of 0.89 to 2.39 GHz is achieved by open sleeves parasitic patches. Two strip dipole antenna connected in series is presented in [5] with 49% (1.7–2.8 GHz) impedance bandwidth with 5.5–6.3 dBi gain. The proposed

antenna obtained a wide bandwidth of 1.71 GHz–2.69 GHz by loading long and short dipoles in the design of [6] with good performance parameters. In [7], a combination of magnetic and electric dipoles dipole antenna is developed by Luk et al. Besides, the antenna has a wide bandwidth of 1.718 GHz–3.409 GHz, high port isolation of 36 dB but the antenna is bulky due to its metallic structure.

In the present work, a wideband crossed folded dipole antenna is designed which can be used as a base station antenna. Techniques such as gap-coupling technique which is loading the parasitic patch with dipole structure and metal sheet as a reflector are proposed to achieve wider bandwidth and high gain. The designed antenna is optimized using a finite integral method based CST Microwave Studio Software [8].

2 Antenna Design and Analysis

The proposed antenna structure is printed on FR-4 glass epoxy substrate of relative permittivity 4.4 with a loss tangent 0.025 and a thickness 1.6 mm. The geometry of the proposed design dipole antenna is shown in Fig. 1.

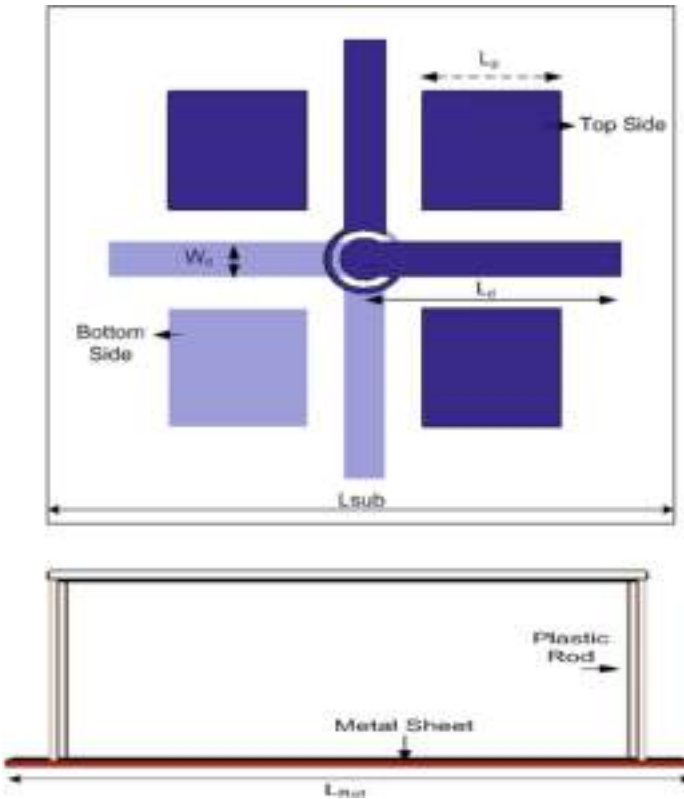


Fig. 1. Top view & side view of crossed dipole antenna.

A pair of two orthogonal microstrip dipoles and three parasitic square patches have printed both sides of the substrate. Two orthogonal microstrip dipoles are connected by a partially circular ring at the one end of dipoles. Three square parasitic patches are placed symmetrically 4.2 mm away from straight dipoles to enhance the impedance bandwidth of proposed antenna structure.

Antenna dimensions are $L_d = 28.8$ mm, $W_d = 4.5$ mm and $L_p = 15.5$ mm, $L_{sub} = 70$ mm, $L_{Ref} = 80$ mm. A small circular patch is attached with the straight dipole at the one end to provide the flat transition from dipole antenna input impedance to coaxial probe which created a capacitive load to neutralize the dipole inductivity and produce approximately pure resistive input impedance. Thereafter, antenna gain & impedance bandwidth are enhanced by a square metal sheet is placed 36 mm away from the substrate. The metal sheet is attached to the substrate by using four plastic pods. The optimization of the designed antenna structure in various dimensions is performed by varying one parameter and manually fixing the other.

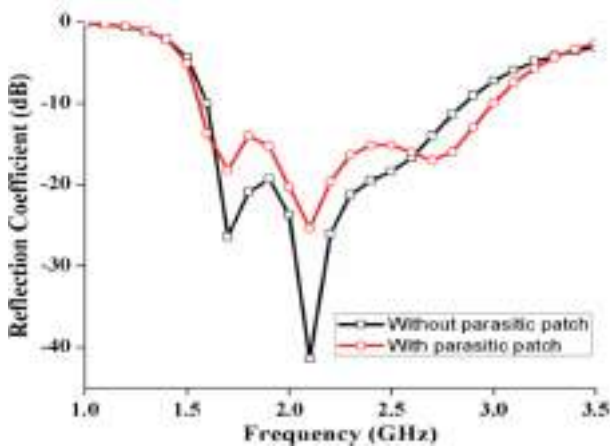


Fig. 2. The simulated reflection coefficient of crossed dipole antenna (CDA) with & without parasitic patches.

The reflection coefficient of a proposed antenna structure with & without parasitic patches is shown in Fig. 2 and listed in Table 1. From Fig. 2 and Table 1, it is observed that the impedance bandwidth at -10 dB of proposed antenna structure with parasitic patches is enhanced by 190 MHz as compared to proposed antenna structure without parasitic patches. The improvement in impedance bandwidth is due to the effect of increasing the electrical length by gap-coupling technique. In both cases, two resonant frequencies of 1.7 GHz & 2.1 GHz are achieved.

Table 1. Comparison of bandwidths of proposed structure with & without parasitic patches.

Structure	Bandwidth (GHz)
Without parasitic patch	1.26 (1.60–2.86)
With parasitic patch	1.45 (1.55–3.00)

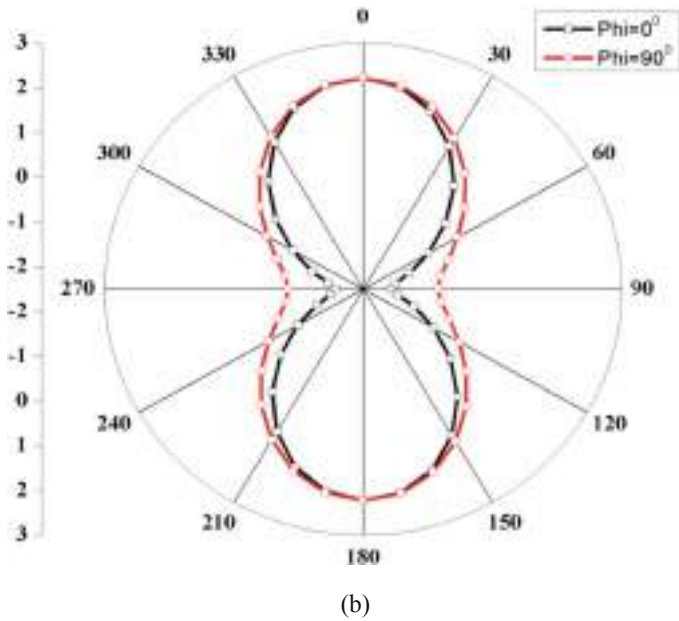
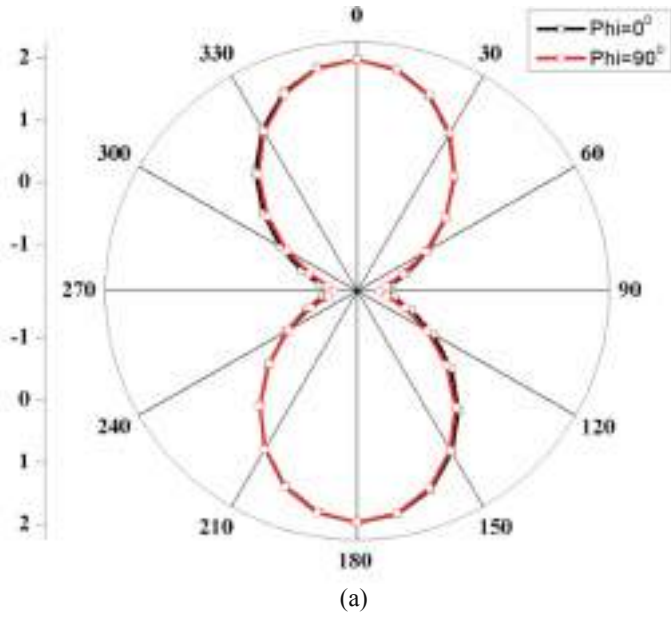


Fig. 3. The simulated radiation pattern of crossed dipole antenna (CDA) in E & H planes. (a) at 1.7 GHz, and (b) at 2.1 GHz.

The simulated radiation pattern of proposed CDA at both the resonance frequencies are shown in Fig. 3 in both E-plane (at $\phi = 0^\circ$) and H-plane (at $\phi = 90^\circ$). It is observed from Fig. 3(a) for 1.7 GHz that both the planes are similar to each other and produced bidirectional radiation. In the case of 2.1 GHz resonance which is depicted in Fig. 3(b), H-plane radiation pattern slightly moves in quasi-omnidirectional while H-plane is still bidirectional in nature.

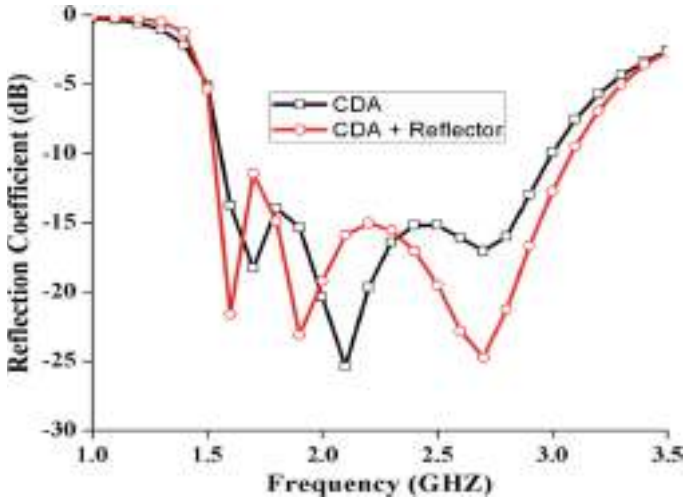


Fig. 4. The simulated reflection coefficient of crossed dipole antenna (CDA) with & without a reflector.

The impedance bandwidth and gain of the CDA are improved by the metal sheet which works as a reflector. The reflection coefficient of the CDA with and without a reflector is shown in Fig. 4 and the effect of the reflector on the impedance bandwidth is listed in Table 2. It is clearly observed from Fig. 4 that enhancement in the impedance bandwidth of CDA with reflector is improved and excited the 3rd resonance frequency of 2.7 GHz. The proposed antenna design has resonance at the frequencies of 1.6 GHz, 1.9 GHz, and 2.7 GHz. Enhance bandwidth of proposed antenna design as compare with CDA is listed in Table 2.

Table 2. Comparison of bandwidths for CDA with & without a reflector.

Antenna design	Bandwidth (GHz)
CDA	1.45 (1.55–3.00)
CDA + reflector	1.56 (1.52–3.08)

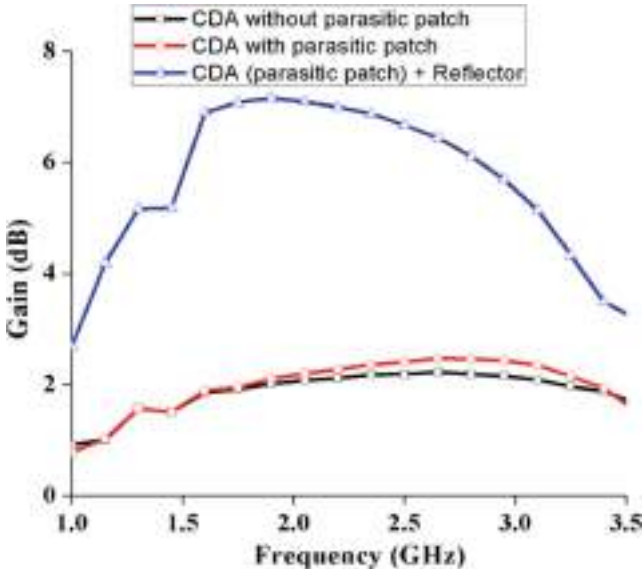


Fig. 5. Simulated antenna gain of CDA with & without parasitic patch and with reflector.

Variation of simulated gain of CDA with and without parasitic patch & reflector for comparison is shown in Fig. 5. It is observed from Fig. 5 that the gain of CDA with reflector is first increasing from 5.98 dB to 7.16 dB in the frequency range from 1.52 GHz to 2nd resonance frequency of 1.9 GHz and then decreasing 7.16 dB to 5.20 dB in the remaining operating band while gain of CDA is increasing continuously from 1.76 dB to 2.46 dB within the operating band. The gain of CDA with reflector is almost 5 dB more as compare with proposed CDA, as the backside radiation is reflected back due to the reflector which increases the radiation in the front side and therefore bidirectional radiation becomes unidirectional radiation pattern.

3 Simulated and Measured Results

The antenna is fabricated after the parametric analysis to obtain the optimized results of the proposed design is shown in Fig. 6. The simulated & measured results of CDA are shown in Fig. 7 which represent the measured result is agreed with the simulated result. The measured impedance bandwidth is 1.37 GHz (1.51–2.88 GHz) whereas 1.45 GHz (1.55–3.00 GHz) is simulated impedance bandwidth. Loss of bandwidth in measured results is due to impedance mismatching between the patch & coaxial cable.

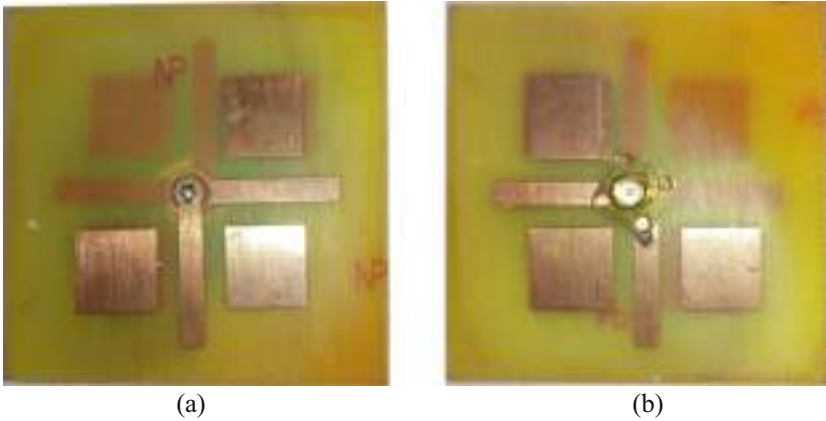


Fig. 6. A prototype of the designed antenna. (a) Top view and (b) Bottom view.

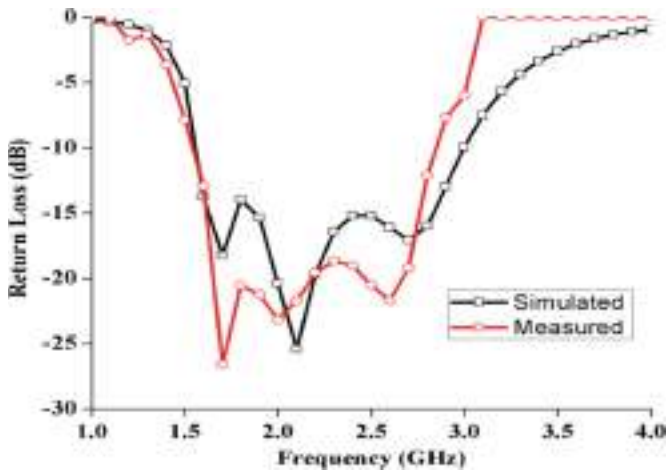
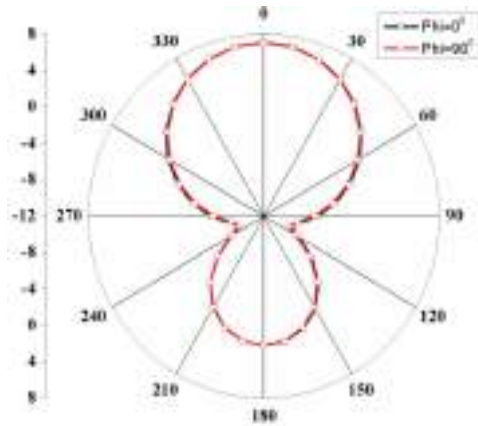
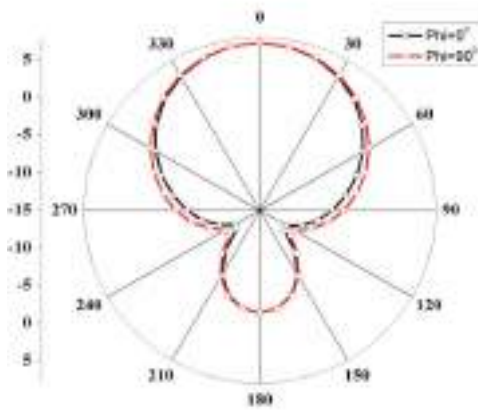


Fig. 7. Simulated & measured return loss of the proposed CDA.

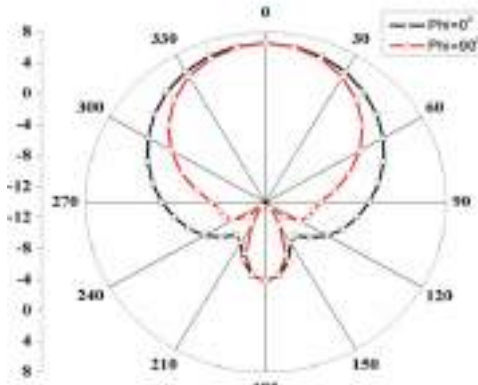
Figure 8 shows the radiation pattern of CDA with reflector in both the fields at the three resonance frequencies viz. 1.6 GHz, 1.9 GHz & 2.7 GHz. It is observed and confirmed from Fig. 8(a)–(c) that in all the three resonant frequencies, bidirectional radiation changes into unidirectional radiation with small back lobes due to the reflector. Also, the pattern in both planes is almost similar to each other except the third resonance. The HPBWs in E-plane & H-plane are listed in Table 3.



(a)



(b)



(c)

Fig. 8. The simulated radiation pattern of CDA with reflector in E & H planes, (a) at 1.6 GHz, (b) at 2.1 GHz, and (c) at 2.7 GHz.

Table 3. Comparison of simulated HPBWs in both the planes at three resonance frequencies.

Frequency (GHz)	Plane	HPBW (degree)
1.6	E-plane	80.3
	H-plane	79.1
1.9	E-plane	79.6
	H-plane	84.9
2.7	E-plane	102.2
	H-plane	75.8

Comparing the proposed structure with the dipole antenna earlier mentioned is depicted in Table 4. Table 4 indicates that the proposed structure has a wider bandwidth over other dipoles structure present in the literature.

Table 4. Comparison of proposed structure with other reported dipole structure.

Antenna	Bandwidth
[2]	1.18 GHz (1.68–2.86 GHz)
[3]	1.41 GHz (1.39–2.80 GHz)
[4]	1.5 GHz (0.89–2.39 GHz)
[5]	1.1 GHz (1.70–2.80 GHz)
[6]	0.98 GHz (1.71–2.69 GHz)
Proposed	1.56 GHz (1.52–3.08 GHz)

4 Conclusion

A crossed dipole antenna with reflector is investigated in the proposed work. The effect of parasitic elements of the dipole antenna on the antenna performance is also analyzed. The technique to enhance the bandwidth and gain are utilized and found very efficient. The reflector is used to improve the impedance matching resulting into an impedance bandwidth of 1.52 GHz–3.08 GHz and the antenna gain of 5.98 dB to 7.16 dB within the operating band. The proposed antenna may be used in many applications such as Weather satellites (1670 MHz–1710 MHz), GSM (1710 MHz–1785 MHz), Radio microphones (1785 MHz–1804.8 MHz), MFCN (1900 MHz–1980 MHz), PMSE (2010 MHz–2500 MHz), etc. and hence very much required from the commercial point of view.



References

1. Yeganeh, A.N., Mahan, A., Sedighy, S.H.: Design of a new compact planar wide band dipole antenna. *Microw. Opt. Technol. Lett.* **59**(12), 3189–3197 (2017)
2. Nie, L.Y., Lin, X.Q., Chen, Y.J., Zhang, J., Wang, B., Yang, Z.Q., Fan, Y.: A low-profile coplanar dual-polarized and dual-band base station antenna array. *IEEE Trans. Antennas Propag.* **66**(12), 6921–6929 (2018)

3. Cui, Y.H., Wu, L., Li, R.L.: Bandwidth enhancement of a broadband dual-polarized antenna for 2G/3G/4G and IMT base stations. *IEEE Trans. Antennas Propag.* **66**(12), 7368–7373 (2018)
4. Zhang, Z.Y., Yang, X.D., Zuo, S.L., Fu, G.: Wideband omnidirectional printed dipole antenna with dumbbell-shaped open sleeve for wireless communication applications. *IET Microw. Antennas Propag.* **8**(15), 1299–1304 (2014)
5. Yeo, J., Lee, J.I.: Broadband series-fed two dipole array antenna with an integrated balun for mobile communication applications. *Microw. Opt. Technol. Lett.* **54**(9), 2166–2168 (2012)
6. Luo, Y., Chu, Q.X.: Oriental crown-shaped differentially fed dual-polarized multi dipole antenna. *IEEE Trans. Antennas Propag.* **63**(11), 4678–4685 (2015)
7. Wu, B.Q., Luk, K.M.: A broadband dual-polarized magneto-electric dipole antenna with simple feeds. *IEEE Antennas Wirel. Propag. Lett.* **8**, 60–63 (2009)
8. CST (Computer Simulation Technology) Microwave Studio (2010)



Automated Diagnosis of Optic Atrophy Using Empirical Wavelet Transform

K. Sneha^(✉)  and T. P. Byjubai 

Government Engineering College, Kozhikode, Kerala, India
ksnehaclt@gmail.com

Abstract. Optic atrophy is an ocular disorder that causes damage to optic tract and is the final result of many of the eye diseases like glaucoma, diabetic retinopathy etc. The accessible scanning strategies are Heidelberg retinal pictorial representation, scanning laser polarimetry, and optical coherence pictorial representation. These strategies are terribly expensive and need practiced clinicians to use them. So, diagnosing optic atrophy at early stages is very necessary for an appropriate medical treatment of the sickness. This paper proposes a novel methodology for an automatic identification of optic atrophy using digital fundus images using empirical wavelet transform (EWT). Empirical wavelet transform is employed to decompose the input image, and also the correntropy features are obtained from these of the decomposed EWT elements. These extracted features are arranged based on the t-value and extremely discriminated features are chosen using student t-test algorithm. These features are employed for the classification of normal and optic atrophy images using least-squares support vector machine (LS-SVM) classifier.

Keywords: Optic atrophy · Empirical wavelet transform (EWT) · Correntropy · Least-squares support vector machine (LS SVM) classifier

1 Introduction and Background

Optic atrophy is the end result of many of the eye diseases that damages nerve cells between the retinal ganglion cells and the lateral anterior visual system. The optic nerve transmits information about the image formed on retina to the brain, optic atrophy leads to vision loss. Optic disorders causes damage to the optic nerve due to many reasons, the most common one is poor blood flow. Eye diseases such as glaucoma, can also cause a form of optic nerve atrophy and is known a glaucomatous optic atrophy. The condition can also be caused by diseases of the brain and central nervous system. A pale optic nerve is main feature of long-standing optic atrophy.

The existing method for diagnosing optic atrophy are expensive and it requires experienced physicians to use them. So, it is necessary to diagnose optic atrophy fast and accurately. Glaucoma diagnosis can be done using the fundus images based on the empirical wavelet transform (EWT) [1]. The EWT is used to decompose an input image. It decomposes the input into different frequency bands. Correntropy features are extracted from these decomposed EWT components. The HOS bispectrum features [2] and wavelet energy features are the other features which are used for glaucoma

diagnosis. Unlike other wavelet transform such as DWT, empirical wavelet transform [3] is a signal-dependent decomposition technique. The features thus produced are classified into normal and glaucoma image using LS-SVM [4].

Based on the exiting method for diagnosis of Glaucoma, we propose a novel method for diagnosis of optic atrophy using empirical wavelet transform. In order to reduce the search space and thus to reduce the time required for computation the proposed method uses optic disc segmentation. There are different methods for OD segmentation, among them the method which effectively segment the optic disc with less time is used here. Empirical wavelet transform is used for decomposing the segmented optic disc to obtain different bands of frequency. Then the correntropy features are extracted from these decomposed EWT components [5]. From the extracted features highly discriminated features are selected using student t-test algorithm. Features with higher t-values are more discriminatory. This features thus extracted are used for the classification of normal and optic atrophy images using Least Square Support Vector machines (LS-SVM) classifier.

The proposed method includes optic disc segmentation in order to achieve fast diagnosis. The optic disc segmentation technique consist of mainly three steps. First step is Preprocessing and elimination of blood vessels, then center detection is performed, and finally the OD region is segmented successfully. In pre-processing green component of image is considered as it contains most of the structural information about OD. Preprocessing consist of adaptive histogram equalisation and is performed on green channel of image to enhance the contrast of an image. Then the blood vessels in the retinal image are removed using equiripple LPF. Detection of OD center and segmentation of OD is done followed by blood vessel elimination [6]. After segmentation EWT is used to decompose the signal as it is a signal-dependent decomposition technique. Then the correntropy features [7] are extracted and these extracted features are then classified using least square version of support vector machine. Classification can be also performed using other classifiers, where as the proposed method uses Least-square SVM as it provides the better classification accuracy.

The organization of paper is described below. General introduction of the project with overview of proposed methods are given in Sect. 1. Section 2 describes the design of the system and describes in detail about methodology, design etc. Section 3 contains the details about datasets used in the proposed method. Section 4 explains the result and analysis of proposed system with public and private database.

2 Proposed Method

The block diagram for the proposed method is given in Fig. 1. RGB components of image are extracted. The optic disc segmentation technique consist of mainly three steps. First step is Preprocessing and blood vessel elimination, then OD center detection is performed, and finally segmentation of the OD region is carried out. In preprocessing green component of image is considered as it contains most of the structural information about OD. Preprocessing consist of adaptive histogram equalisation and is applied on green component of image to enhance the contrast of an image.

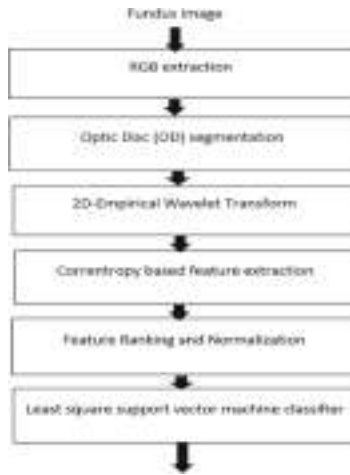


Fig. 1. Block diagram for the proposed method

Then the blood vessels are removed using equiripple low pass filter. A maximum Intensity Pixel is Computed and a region of 15 by 15 pixels around the reference point is considered for threshold calculation. Segmentation of the filtered image has been carried out using this threshold value. Detection of OD center and segmentation of OD is done followed by blood vessel elimination. After segmentation 2D Littlewood-Paley EWT is used for signal decomposition in the proposed methodology.

2.1 Empirical Wavelet Transform

The proposed method uses empirical wavelet transform for signal decomposition. EWT is a signal-dependent method and it does not use any predefined basis functions like other transforms. EWT is an adaptive method of signal decomposition based on the information content of the signal. 2D-EWT is applied on this segmented fundus image and is converted into sub band images. Steps involved in EWT are discussed below,

1. Let x denote the image. Find out 1-D Fourier transform of each row and column separately. Let $X(r, \Omega)$ be the FT of rows r of x and $X(c, \Omega)$ be the FT of columns c of x . Calculate the mean row and column spectrum magnitudes as given below:

$$X_R = \frac{1}{N_r} \sum_{r=0}^{N_r} X(r, \Omega)$$

And

$$X_C = \frac{1}{N_c} \sum_{c=0}^{N_c} X(c, \Omega)$$

where N_r and N_c denote number of rows and columns respectively.

2. Perform boundaries detection on X_R and X_C and build the corresponding filter bank
3. Filter the image along the rows to produce $(N_r + 1)$ output images.
4. Filter $(N_r + 1)$ output images along the columns with this provides $(N_r + 1)$ $(N_c + 1)$ subband images.

where N_r and N_c are the number of mean row and column subband, respectively. 2D-EWT is applied on this segmented fundus image and is converted into sub band images. There are four decomposed components from each input image.

2.2 Feature Extraction and Selection

The correntropy features are extracted from each of the decomposed components. Correlation and entropy together known as correntropy. Three correntropy features are computed from each single decomposed component. Total 12 feature are extracted from a single image. All these features are subjected to Students t-test process to determine highly discriminatory features. The processed features are arranged in decreasing order of their t-values and six features having highest t-values are selected. These are highly discriminatory features and are normalized using z-score normalization. These features are then classified using least square support vector machine (LS SVM).

2.3 Feature Standardization

Feature standardization means, the correntropy features are standardized with zero mean and unit standard deviation. This process of feature standardization is also named as z-score normalization. Here the normalization is done by subtracting mean from the given data and then using the standard deviation the resultant is being. Then the normalized data obtained will have unit standard deviation and zero mean. Let \bar{x} be mean and \tilde{x} be the standard deviation of data x , respectively; Then normalized data \hat{x} can be expressed as follows:

$$\hat{x} = \frac{x - \bar{x}}{\tilde{x}}$$

2.4 LS-SVM Classifier

Least square SVM is used for classification of the standardized features [8]. The least square support machine uses different types of wavelet kernals such as Morelet wavelet, Radial basis function (RBF) [9], and Mexican-hat wavelet [10, 11]. LS-SVM is a supervised machine learning algorithm. Commonly it is used to discriminate different classes based on linear or non-linear hyperplanes. The different types of such as support vector machine, artificial neural network etc are widely used in different biomedical classifiers applications. The proposed method uses LS-SVM for classification as it provides more classification accuracy than other classifiers for glaucoma diagnosis.

3 Datasets Used in the Experiments

The proposed method for diagnosis of optic atrophy is applied on two databases, private and public database. We have collected the optic atrophy and normal fundus images from Government medical college kozhikode. The efficiency of proposed method are checked using both the databases. The images were divided into two groups, a training set and a test set with 20 images in each group. A brief description about this two databases are given below,

1. A. Private database: The database contains fundus images of 45 normal and 40 optic atrophy affected persons. These images are obtained from Government medical college, Kozhikode.
2. B. Public database: The database contains fundus images of 30 normal and 30 optic atrophy affected persons. It is available online publicly at <http://medimrg.webs.uill.es/>.

4 Results and Discussions

In this section, the experimental results of the proposed method are discussed. To verify the effectiveness of the proposed method, various performance measures are used. Results obtained for various stages of the proposed method is given below. Fundus images of healthy and optic atrophy affected persons are collected from Government medical college kozhikode. Figure 2(a) & (b) shows fundus images of abnormal person and optic atrophy affected person respectively.

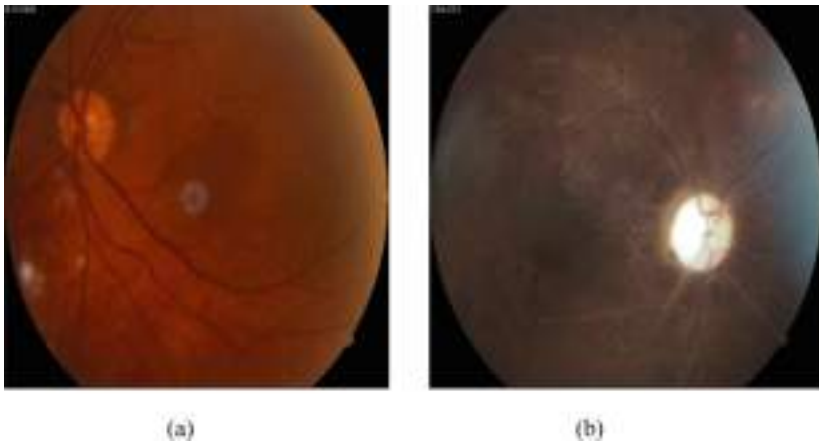


Fig. 2. Fundus image of (a) healthy person and (b) optic atrophy affected person

Each of the input image is segmented using the optic disc segmentation methods as described in the Sect. 2. Segmented fundus image of normal person and optic atrophy affected person are given in Fig. 3(a) & (b) respectively.

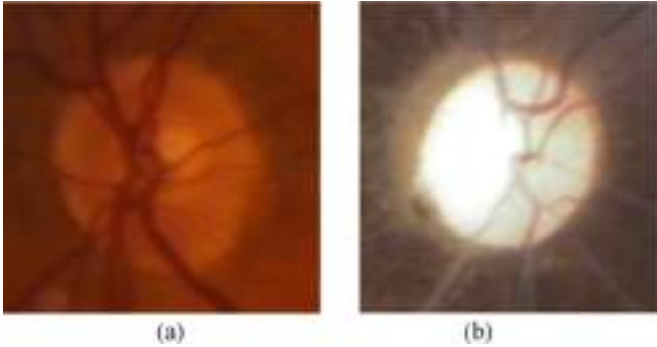


Fig. 3. Segmented fundus of (a) healthy person & (b) optic atrophy affected person

2D empirical wavelet transform is applied on the red component of the segmented optic disc and it decomposed into four different wavelet bands, similarly four images are obtained from green, blue and gray component of the segmented optic disc. Thus a total of 16 sub images. Four decomposed EWT components of red channel of healthy and optic atrophy affected fundus image are shown in Fig. 4(a) & (b) respectively.

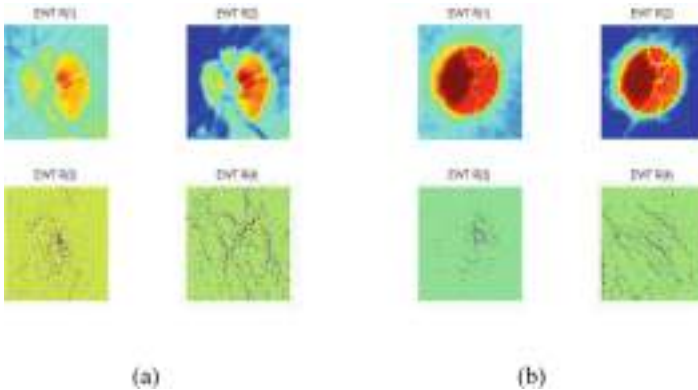


Fig. 4. Four EWT components of red channel of (a) healthy & (b) optic atrophy affected fundus image

Four decomposed EWT components of green channel of healthy and optic atrophy affected fundus image are shown in Fig. 5(a) & (b) respectively. Four decomposed EWT components of blue channel of healthy and optic atrophy affected fundus image are shown in Fig. 6(a) & (b) respectively. Four decomposed EWT components of gray channel of healthy and optic atrophy affected fundus image are shown in Fig. 7(a) & (b) respectively.

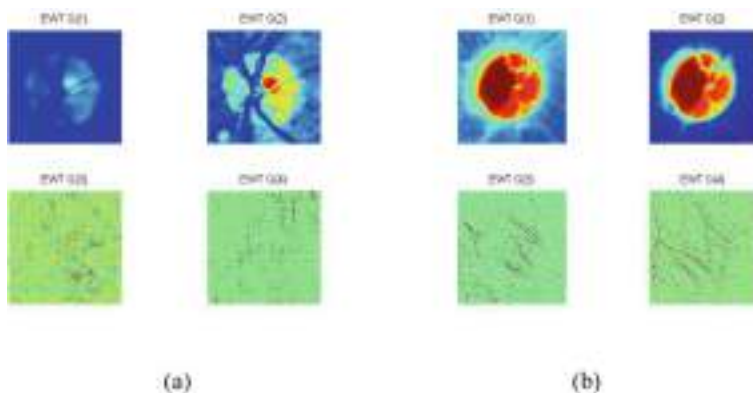


Fig. 5. Four EWT components of green channel of (a) healthy & (b) optic atrophy affected fundus image

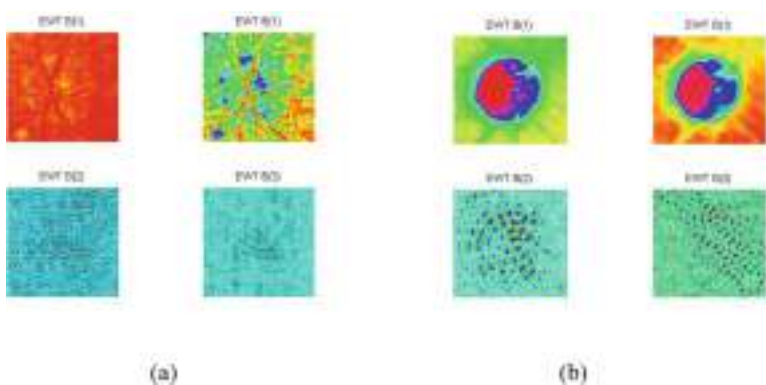


Fig. 6. Four EWT components of blue channel of (a) healthy & (b) optic atrophy affected fundus image

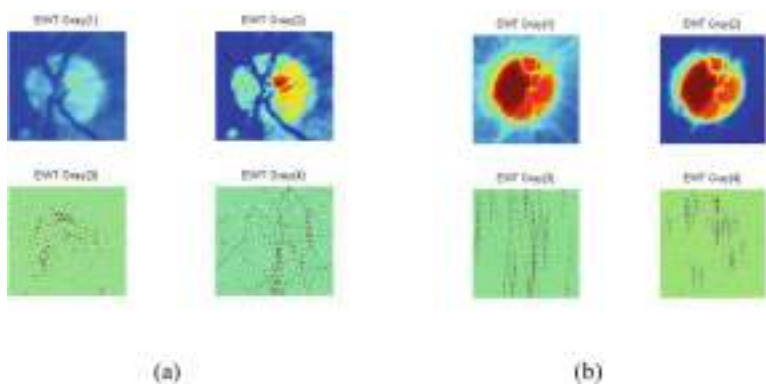


Fig. 7. Four EWT components of gray channel of (a) healthy & (b) optic atrophy affected fundus image

Four EWT components are computed from each of the input image and from each of these single decomposed components three correntropy features are calculated. Thus total 12 correntropy features are computed from each image. All these computed features are further subjected to Student’s test process. The processed features are then arranged in decreasing order of their t-values and six features having highest t-values are selected. These features are classified using least square support vector machine classifier with different kernals such as RBF kernal, Mexican hat and morelet wavelet. The accuracy obtained by using different kernals are given in Table 1. Among these three kernals RBF kernal has highest accuracy of 93.93%.

4.1 Performance of the Proposed System for Public Database

The proposed system performs the classification of the data into normal and optic atrophy affected using least square support vector machine classifier. The LS-SVM supports different types of kernals such as RBF, mexican hat, morelet wavelet etc. We compare the performance of our system with all these three kernals. Performance comparison of the proposed method using different kernals with $\sigma = 0.6$ is given in Table 1.

Table 1. Performance comparison of LS-SVM using different kernals for public database

Kernal	Accuracy (%)	Sensitivity (%)	Specificity (%)
RBF	93.93	100	80
Morelet	90.90	95.65	80
Mexican hat	90.65	91.30	90

Among the three types of wavelets kernals, the system has got highest accuracy for RBF kernal. The highest accuracy obtained is 93.93%. Table 2 shows accuracy of proposed method using different kernals under three fold cross validation. In three fold cross validation third fold has the highest classification accuracy.

Table 2. Accuracy of proposed method using different kernals under three fold cross validation for public database

Kernal	Fold1 (%)	Fold2 (%)	Fold3 (%)
RBF	93.93	90.95	96.96
Morelet	89.85	87.65	93.50
Mexican hat	87.65	84.88	90.91

Classification accuracy is higher for the third fold under 3 fold cross validation, which indicates that third fold is the best fold among the three folds. Table 3 shows the variation in the accuracy with increasing number of features. The accuracy of the proposed system has only a slight variation when the number of features used for

classification was doubled. Thus the proposed system is capable to classify the images as normal and disease affected using only 6 number of features, i.e. the system has got maximum accuracy with minimum number of features.

Table 3. Performance variation with no. of features for public database

Kernal	No. of features	Accuracy (%)	Sensitivity (%)	Specificity (%)
RBF	6	93.93	100	80
Morelet	6	90.90	95.65	80
Mexican hat	6	90.65	91.30	90
RBF	12	94.25	100	85
Morelet	12	91.00	96	82
Mexican hat	12	91.50	93	90

4.2 Performance of the Proposed System for Private Database

The proposed system performs the classification of the data into normal and optic atrophy affected using least square support vector machine classifier. The LS-SVM supports different types of kernals such as RBF, mexican hat, morelet wavelet etc. We compare the performance of our system with all these three kernals. Performance comparison of the proposed method using different kernals with $\sigma = 0.6$ is given in Table 4. Among the three types of wavelets kernals, the system has got highest accuracy for RBF kernal. The highest accuracy obtained is 96.47%. Table 5 shows accuracy of proposed method using different kernals under three fold cross validation. In three fold cross validation third fold has the highest classification accuracy.

Table 4. Performance comparison of LS-SVM using different kernals for private database

Kernal	Accuracy (%)	Sensitivity (%)	Specificity (%)
RBF	96.47	100	92.50
Morelet	94.11	93	95
Mexican hat	91.65	91.30	95

Table 5. Accuracy of proposed method using different kernals under three fold cross validation for public database

Kernal	Fold1 (%)	Fold2 (%)	Fold3 (%)
RBF	94.75	92.16	95.50
Morelet	92.34	89.65	89.50
Mexican hat	91.65	87.88	90.91

Classification accuracy is higher for the first fold under 3 fold cross validation, which indicates that first fold is the best fold among the three folds. Table 6 shows the

variation in the accuracy with increasing number of features. The accuracy of the proposed system has only a slight variation when the number of features used for classification was doubled. Thus the proposed system is capable to classify the images as normal and disease affected using only 6 number of features, i.e. the system has got maximum accuracy with minimum number of features.

Table 6. Performance variation with no. of features for public database

Kernal	No. of features	Accuracy (%)	Sensitivity (%)	Specificity (%)
RBF	6	96.47	100	92.50
Morelet	6	94.11	93	95
Mexican hat	6	91.65	91.30	95
RBF	12	96.95	100	93
Morelet	12	95.25	96	92
Mexican hat	12	92	93.46	91

5 Conclusion

This work proposes an automated diagnosis of optic atrophy by using limited number of correntropy features. Unlike the existing works where the features are considered from the complete fundus or a sub image of the fundus, this work is based on feature extraction from the segmented optic disc to improve the accuracy of identification and to reduce the execution time. Classification is performed using various kernels such as RBF, Mexican hat and morelet wavelets, among this classification using RBF kernel has got highest accuracy for both private and public database. Classification accuracy is higher for the third fold in three-fold cross validation process of public database and first fold has got highest accuracy for private database. Performance of the system slightly increases as the number of features used was doubled. Here classification is done with and without optic disc segmentation, without OD segmentation it requires 0.9850 s where as with OD segmentation it requires only 0.0865 s. Experimental results shows that the proposed method achieves better accuracy by using RBF kernel with a limited number of correntropy features.

References

1. Maheshwari, S., Pachori, R.B., Acharya, U.R.: Automated diagnosis of glaucoma using empirical wavelet transform and correntropy features extracted from fundus images. *IEEE J. Biomed. Health Inform.* **21**(3), 803–813 (2016)
2. Acharya, U.R., Dua, S., Du, X., Chua, C.K., et al.: Automated diagnosis of glaucoma using texture and higher order spectra features. *IEEE Trans. Inf. Technol. Biomed.* **15**(3), 449–455 (2011)
3. Dua, S., Acharya, U.R., Chowriappa, P., Sree, S.V.: Wavelet-based energy features for glaucomatous image classification. *IEEE Trans. Inf Technol. Biomed.* **16**(1), 80–87 (2011)

4. Suykens, J.A., Vandewalle, J.: Least squares support vector machine classifiers. *Neural Process. Lett.* **9**(3), 293–300 (1999)
5. Khandoker, A.H., Lai, D.T., Begg, R.K., Palaniswami, M.: Waveletbased feature extraction for support vector machines for screening balance impairments in the elderly. *IEEE Trans. Neural Syst. Rehabil. Eng.* **15**(4), 587–597 (2007)
6. Almazroa, A., Burman, R., Raahemifar, K., Lakshminarayanan, V.: Optic disc and optic cup segmentation methodologies for glaucoma image detection: a survey. *J. Ophthalmol.* **2015** (2015)
7. Gunduz, A., Principe, J.C.: Correntropy as a novel measure for nonlinearity tests. *Sig. Process.* **89**(1), 14–23 (2009)
8. Suykens, J., Van Gestel, T., De Brabanter, J., De Moor, B., Vandewalle, J.: *Least Squares Support Vector Machines*, vol. 4. World Scientific, Singapore (2002)
9. Zhang, L., Zhou, W., Jiao, L.: Wavelet support vector machine. *IEEE Trans. Syst. Man Cybern. B Cybern.* **34**(1), 34–39 (2004)
10. Zavar, M., Rahati, S., Akbarzadeh-T, M.-R., Ghasemifard, H.: Evolutionary model selection in a wavelet-based support vector machine for automated seizure detection. *Expert Syst. Appl.* **38**(9), 10751–10758 (2011)
11. Bajaj, V., Pachori, R.B.: Classification of seizure and nonseizure EEG signals using empirical mode decomposition. *IEEE Trans. Inf Technol. Biomed.* **16**(6), 1135–1142 (2011)



Improvement of Pavement Soil Sub-grade Using Industrial Waste: Cement Kiln Dust & Brick Kiln Dust

Vikas Shukla^(✉)  and M. K. Trivedi 

Department of Civil Engineering, Madhav Institute of Technology and Science,
Gwalior, India

vikas.shukla183@gmail.com

Abstract. For performing any kind of Engineering work the primary concern is to have information about the type of soil. India is having clayey soil cover in most of the part, its cover is around 20 to 25% of the surface area of the country. Clayey soil is always known for its behavior of swelling and shrinkage under the moisture content variation, because of which cause severe damage to the structures causing economic loss. Clayey soil is highly unpredictable in nature when it comes in contact with the moisture and it needs either modification or replacement for performing any kind of constructional activity. For pavement construction, engineers are keen to know the engineering properties of soil underlying because subgrade is primarily composed of locally available soil which needs to be strengthen for providing effective base for pavement overlying. Swelling and shrinkage needs to be reduced, subgrade needs to be strengthen by increasing the CBR value of soil. The modification in engineering properties of such soil needs to be done keeping in mind the criteria of strength and cost management. The idea of utilization of waste in soil enhancement is quite popular in today's scenario. So the modification of soil subgrade by waste material can be done which provide solution to the problem of disposal and is also effective in terms of cost of alteration. In this study the modification of lacking engineering properties of clayey soil is being done by stabilizing the soil with industrial waste such as Cement Kiln Dust (C.K.D) and Brick Kiln Dust (B. K.D). Clayey soil properties are being determined by performing number of experiments. Modification of properties is being observed at varying percentage of CKD (5%, 10%, 15%, 20%, 25%) and the optimum dose of CKD is treated with varying dose of BKD (5%, 10%, 15%, 20%, 25%). Soil samples are further tested for the blend combination of (Soil+ BKD+ CKD) and the modification of the engineering properties are noted. The tests performed are Atterberg Limit, Free Swell Index, Optimum Moisture Content Test and Maximum Dry Density test and California Bearing Test, Unconfined Compressive strength test. The results revealed that the enhancement in the physical state of clayey specimen is being observed, swelling is highly reduced, improvement of CBR value & shear strength is being observed by the addition of (BKD & CKD).

Keywords: California Bearing Ratio (CBR) · Unconfined Compressive Strength (UCS) · Cement Kiln Dust (CKD) · Brick Kiln Dust (BKD)

1 Introduction

The sub-grade comprises layer of local soil, that provide support and stability to the material placed above it. The loads on the pavement are ultimately received by the soil below. It is mandatory that the subgrade is free from the stresses for carrying the resultant load. For the construction of a highway project stability of the wearing layer is of primary importance. The performance evaluation of a soil subgrade is primarily dependent on the load bearing capacity, water content and expansion and contraction characteristics of soil subgrade. These criteria need to be checked well before the commencement of any project. The need for soil modification is increasing due to pressures to build and rehabilitate infrastructure and other civil works on sites with marginal soils (Marginal soil usually may has little potential for infrastructure development). If the infrastructure cannot be relocated or adapted to the soil conditions as in case of clayey soil than modification is done. Soil stabilization methods are mechanically or chemically based. Chemical changes have been used generally to enhance the missing properties in soil. The Appian Way, built during the Roman Time was often considered the first lime modified road (ASCE 1978). Chemical soil stabilization has been extensively used in the every corner of the world. Traditional chemical amendments have been extensively researched and are commonly used: cement, lime, fly ash, and asphalt emulsion. Cement and lime are frequently used in road sub grades for the modification of engineering properties.

Industrial waste is threatening when we talk of its clearance or effective dumping, different researches are being carried out on the waste that are generated on daily basis to check their feasibility as road pavement material. The introduction of Industrial waste in the area of soil improvement is quite general in present scenario. Environmental hazards are being caused by the waste exhaust of industries, so the utilization of exhaust material can be done in construction industry. The industrial effluent if used in engineering activities provides basic feasible solution to the problem of utilization of waste and is also cost effective measure to the problem of modifying the soil.

1.1 Methods of Soil Stabilization

Generally soil stabilization methods falls under following basic categories:

- **According to the process of stabilization:** Under this compaction, dewatering, reinforcement, admixturing or grouting is being done.
- **According to the material or chemicals used:** Under this falls lime stabilization, cement stabilization, bitumen stabilization, polymer, stabilization is being done.
- **Industrial waste stabilization:** Under this industrial waste or effluent are used to modify the soil, such as ckd, bkd, fly ash etc. are being used.
- **Polymer stabilization:** Some of the most common non-traditional additives are polymers which are also being used in stabilization. Two common polymer products used for soil stabilization are vinyl acetate and acrylic based copolymers. Both vinyl acetate and acrylic copolymers are hydrophobic and have had moderate success in bonding to a range of soils (Srikanth Reddy 2018).

2 Literature Review

2.1 Soil Modification Using Cement Kiln Dust

At different temperature level compacted specimens were checked for UCS value after 7days curing, 28days curing and 90 days of curing period. The specimens tested for road sub-bases gave satisfactory results. These tests include test of durability, C.B.R. test and split tension. The experiments recommended that ckd between 12%–50% may be satisfactory for modifying the soil (Baghdadi et al. 1995). Expansive soil of high plasticity is being modified using CKD & (CKD+Lime) limits their heaving properties and improves the stability. The observations revealed that the of CKD and CKD+ lime made to increase dry density & decrease in its moisture content. With 7 days of curing UCS values enhanced using CKD and CKD with lime. (Ismail 2013). A review on research of ckd and waste stabilization is being done. The pH of sludge above 10 is being brought by using 34% Ckd. The results revealed that of 34% CKD is suitable enough to stabilize the sludge. The aggregate blocks were examined for strength test with addition of Ckd in the mix. (Keerthi et al. 2013).

2.2 Soil Modification Using Brick Kiln Dust

Research is being done to reduce expansion phenomena in clayey soil by using the blend combination of marbledust powder and brickdust powder. The enhancement or modification of soil is being done by 30% replacement with both the waste-stabilizers. The blend 70% soil + 30% waste-stabilizer is being made. A comparative statement of clay-soil & blended soil is being provided. The paper reveals the soil physical enhancement as well as modification to be used in soil-subgrade (Ankit J. Patel IJSR). The Review is being performed in order to understand the changes in the physical behavior of soil-sample with increasing amount of burnt-brick-dust (ranging from 30%–50%). Swelling-nature is found to be degraded almost nil at 50% concentration of BBD (Sachin N. Bhawasar).

2.3 Literature Summary

A portion of the data published upto date displays potential for enhancing soil properties with the addition of CKD and BKD individually. These waste also highly contributed in reducing the heaving & contraction of clayey soil and also enhancing CBR value in case of soil subgrade. As observed from the literature review there is further scope to study the blend combination of CKD, BKD and soil to enhance engineering property of the soil. Therefore, a test program is needed that will evaluate the combined action of BKD and CKD at different percentages with the soil. In view of above the clayey soil is stabilized using different percentage of CKD (5%, 10%, 15%, 20%, 25%) and further the optimum dose is treated with varying percentages of BKD. Further the blend combination of BKD and CKD is being done and the series of laboratory experiments are conducted. The test conducted includes Atterberg limits determination; free swell index determination, OMC and M.D.D determination, and C. B.R. and UCS value determination.

3 Material and Methodology

3.1 Material

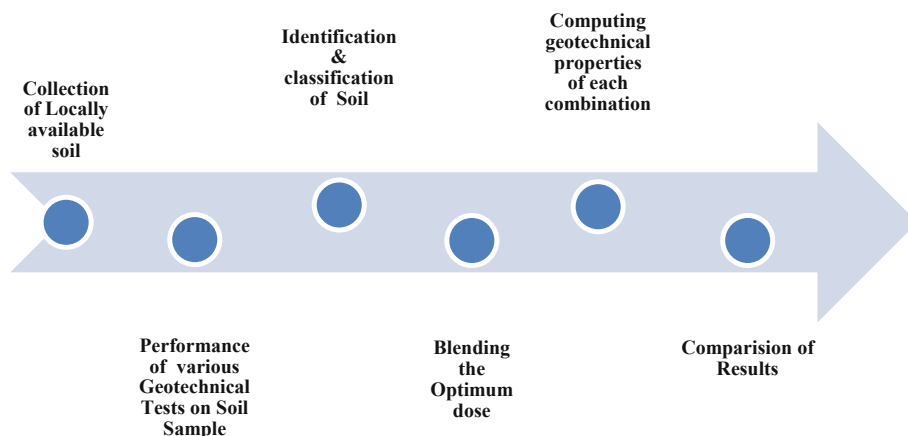
Experimentation is being done to evaluate the potential of BKD, CKD amended soil. The following material is being used in study are:

Brick Kiln Dust: It is a by product of brick manufacturing kilns which is accumulated during the process of brick production. It is being collected from Mau village lying in Banmore, District Morena (MP).

Cement Kiln Dust: It is a waste product which is generated during the manufacturing of cement by dry process, at the time of clinker formation the accumulation of dust takes places. It has got high concentration of alkali because of which it is not fit to be reused in cement. It is being collected from the plant of Rewa District (MP).

Soil Sample: The soil which is put to test is being collected from Badagaon Morar Gwalior (M.P.).

3.2 Proposed Methodology Flowchart



3.3 Experimental Programs

Testing was performed keeping in consideration all applicable Indian Standard Codes. Initially Index property test are being done, then the soil Optimum moisture Content and Dry density tests is being done & at OMC, MDD, the tests are performed. Soil is observed for LL, PL, and Specific gravity in order to identify and classify the soil-sample. Than CBR Test, UCS Test, FSI test is being carried out. The experiments conducted are divided in three groups:

1. The first series of experiments were performed on raw soil sample for identifying the soil properties such as specific gravity, natural moisture content, plastic limit, liquid limit, plasticity index, optimum moisture content, maximum dry density, free swelling index, CBR, unconfined compressive strength, permeability test.

2. Second series of experiments were conducted on soil mixed with different percentages (5%, 10%, 15%, 20%, 25%, 30%) of cement kiln dust and brick kiln dust (5%, 10%, 15%, 20%, 25%) after seven days of curing to find the optimum dose of CKD and BKD.
3. In third series experiments were conducted on the blend combination of (Soil+ BKD+ CKD) keeping the optimum dose of CKD and varying percentage of BKD to observe the enhancement in soil. The tests conducted to check the swelling potential, optimum moisture content, increase in maximum dry density, CBR, UCS value were conducted.

4 Results and Discussions

4.1 Atterberg Limits

The nature and quantity of clay mineral largely influences the LL and PL of soil-sample & provides platform for the soil-categorization for cohesive-soil based on the Atterberg limit observations. The plasticity test gives information about the cohesive property of soil-sample and the presence of water in due to capillary action of soil-sample (Figs. 1, 2, 3 and Table 1).

Table 1. Atterberg’s limit

Sample	Liquid limit % (LL)	Plastic limit % (PL)	Plasticity index
1. Clayey soil	63.60	31.16	32.44
2. Clayey soil+20%ckd+5%bkd	59.90	30.61	29.29
3. Clayey soil+20%ckd+10%bkd	56.20	29.26	26.94
4. Clayey soil+20%ckd+15%bkd	50.32	27.91	22.41
5. Clayey soil+20%ckd+20%bkd	48.3	26.32	21.98

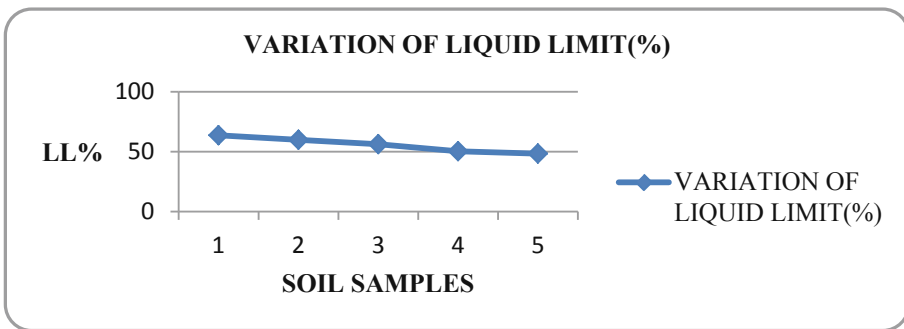


Fig. 1. Variation of liquid limit

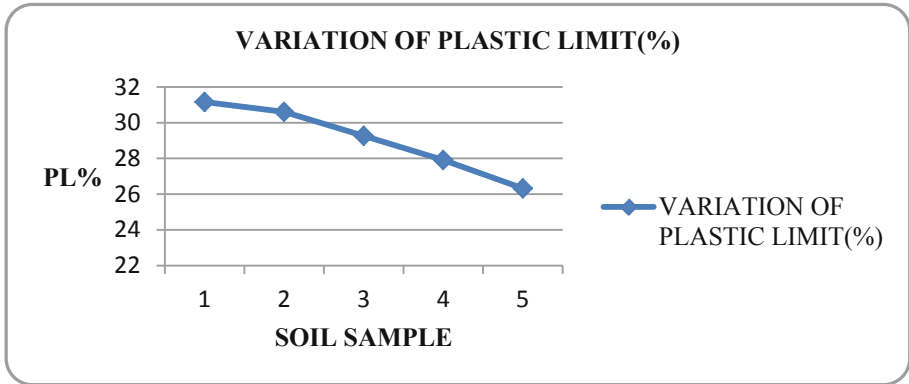


Fig. 2. Variation of plastic limit

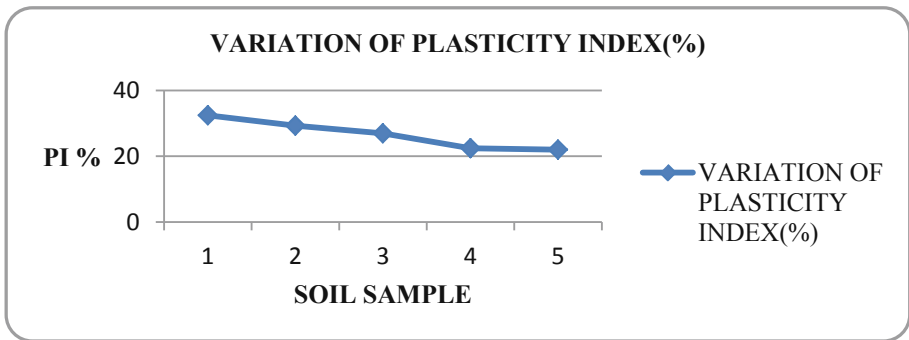


Fig. 3. Variation of plasticity index

4.2 IS Heavy Weight Compaction Test

Compaction is basically a process in which the expulsion of air from voids takes place by means of controlled amount of compaction. This is generally indicated by enhancement of dry density. For a given amount compaction effort every soil attains the maximum dry density at a particular water content which is known as optimum moisture content (Table 2).

Table 2. Calculation of OMC and MDD

Sample	OMC (%)	MDD (KN/m ³)
Clayey Soil	18.01	21.80
Clayey Soil+20%ckd+5%bkd	17.32	22.62
Clayey Soil+20%ckd+10%bkd	16.31	23.24
Clayey Soil+20%ckd+15%bkd	15.40	24.82
Clayey Soil+20%ckd+20%bkd	15.50	23.20

4.3 CBR Test

The role of CBR Test in the pavement design is remarkable. At the time of overlaying of pavement this test is being used fetching the strength of Sub-base, subgrade and other materials needed for the construction of pavement. The test is performed at 4 days and 7 days soaking period. CBR is the ratio of force needed per unit area in order to ensure that standard circular piston at 1.25 mm/min penetrates the soil mass to that is required to penetrate standard material. This generally determines the ratio needed at 2.5 mm & 5 mm penetration. The ratio in correspondence to 2.5 mm penetration is generally taken as CBR value. But if 5 mm penetration value constantly comes higher that can also be the required CBR value (Fig. 4 and Table 3).

$$\text{CBR value} = (\text{Test load} / \text{Standard load}) \times 100$$

Table 3. CBR values at 4 & 7 days curing

Percentages of BKD+CKD	CBR(%) at 4 days curing	CBR(%) at 7 days curing
1. Clayey soil	2	3
2. Soil + 20 CKD + 5% BKD	5	7
3. Soil + 20% CKD + 10% BKD	9	10
4. Soil + 20% CKD + 15% BKD	12	14
5. Soil + 20% CKD + 20% BKD	11	12

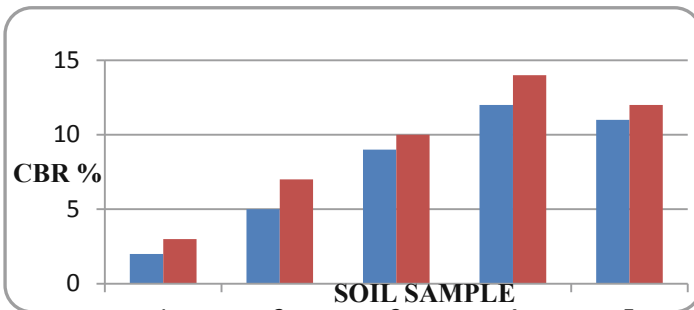


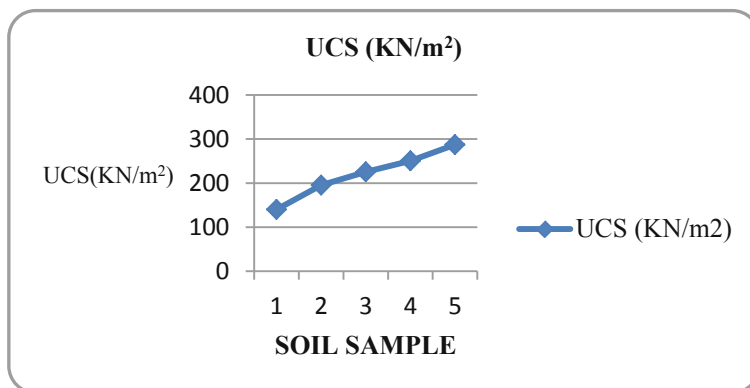
Fig. 4. CBR variation

4.4 Unconfined Compressive Strength

It is basically a type of triaxial test in which confining pressure is kept zero, it is uniaxial compression process. It proves easier as compared to the triaxial test in setup and procedure. At a constant rate of strain, a cylindrical specimen is tested which is without support for compression. In this test, a cylinder of soil without lateral support is tested to failure in simple compression. Unconfined Compressive Strength of the soil is basically load per unit area required to fail the specimen under compression (Table 4 and Fig. 5):

Table 4. Unconfined compressive strength

Sample	UCS (KN/m ²)
Clayey Soil	140
Clayey Soil+20%ckd+5%bkd	195.15
Clayey Soil+20%ckd+10%bkd	225.50
Clayey Soil+20%ckd+15%bkd	250.33
Clayey Soil+20%ckd+20%bkd	287.20

**Fig. 5.** Unconfined compressive strength

4.5 Free Swell Index

Differential free swell also known as free swell index, is the increase in the volume of soil without any external constraint when submerged in water. It's important to investigate the swelling nature of expansive soil which possess the undesirable expansion characteristics. The free swell index is calculated as follows:

$$\text{Free swell index}(\%) = (V_d - V_k) / V_k \times 100$$

where, V_k = volume of soil specimen read from the graduated cylinder containing kerosene. V_d = volume of soil specimen read from the graduated cylinder containing distilled water (Table 5 and Fig. 6).

Table 5. Free swell index

Sample	Mix proportions	Clayey soil	Clayey soil +20%ckd+5% Bkd	Clayey soil +20%ckd+10% bkd	Clayey soil +20%ckd+15% bkd	Clayey soil +20%ckd+20% bkd
1	Initial vol.	10 ml	10 ml	10 ml	10 ml	10 ml
2	Final vol.	13.1 ml	12.1 ml	11.9 ml	11.6 ml	10.1 ml
3	Free swell index	31%	21%	19%	14%	1%

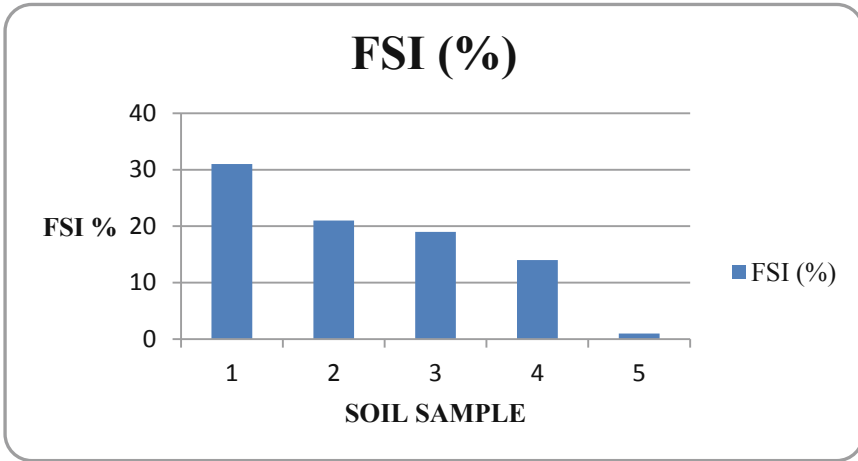


Fig. 6. Variation of FSI

5 Conclusion

This investigation provides the results of observation performed on suitability of material such as (CKD) & (BKD) for improving the characteristics of clayey soil used for subgrade formation. Use of waste material in engineering activities provide a cost effective solution to the problem of dumping the waste, utilization of such industrial waste in constructional activities helps to provide cheap alternative as used in soil modification. This research is being performed to evaluate impact of improvement in the soil property by using BKD and CKD. Results are discussed below.

The specific gravity of soil is 2.70, plastic limit, liquid limit is 32.18%, 63.60% respectively, the plasticity index is 31.42%. Therefore the specimen is Clay soil of high compressibility (CH). The Free Swell Index of soil is 31%, O.M.C and M.D.D is 18% and 16.81 Kn/m². California Bearing Ratio of soil is 1.98%. The blend of optimum result of CKD (20%) and different percentage of BKD (5%, 10%, 15%, 20%, and 25%) with the soil. Further upliftment in the properties is being observed. FSI conducted on the different combinations of Soil +20%CKD+varying percentage of BKD as (5% BKD), (10% BKD), (15%BKD), (20% BKD). The results showed that the FSI value is highly reduced to 1% at (Soil+20% BKD+20% CKD) which is remarkable improvement.

The OMC and MDD at (Soil +20%ckd+15%bkd) is 15.40% and 24.82 KN/m³ respectively. The CBR test conducted on the blend samples to evaluate variation in the CBR value. At the blend combination (Soil+20%CKD+15%BKD) the CBR at 4 day curing reported is 12% and at 7 days curing it is 14% which is remarkable improvement. CBR increases from a value of 2% for raw soil to 14% which is suitable to be used in pavement subgrade according to the IRC guidelines. Decreasing pattern of Atterberg limits is being observed. The unconfined compressive strength is also improved with highest magnitude at (Soil+20% BKD+20% CKD) i.e. 287.20 kn/m². Hence from all

observations it is concluded that waste material such as Cement Kiln dust and brick kiln dust can be used effectively for enhancing soil properties and helping, it to be used in soil subgrade of Pavement.

References

- Onyejekwe, S., Ghataora, G.S.: Soil stabilization using proprietary liquid chemical stabilizers: sulphonated oil and a polymer. *Bull. Eng. Geol. Environ.* **74**(2), 651–665 (2015)
- Kolay, P.K., Dhakal, B., Kumar, S., Puri, V.K.: Effect of liquid acrylic polymer on geotechnical properties of fine-grained soils. *Int. J. Geosynth. Ground Eng.* **2**(4), 29 (2016)
- Azzam, W.R.: Durability of expansive soil using advanced nanocomposite stabilization. *Int J. GEOMATE* **7**(1), 927–937 (2014)
- Naeini, S.A., Naderinia, B., Izadi, E.: Unconfined compressive strength of clayey soils stabilized with waterborne polymer. *KSCE J. Civil Eng.* **16**(6), 943–949 (2012)
- Baghdadi, Z.A., Fatani, M.N., Sabban, N.A.: Soil modification by cement kiln dust. *J. Mater. Civil Eng.* **7**(4), 218–222 (1995)
- Keerthi, Y., Divya Kanthi, P.: Stabilization of clayey soil using cement kiln waste. *Int. J. Adv. Struct. Geotech. Eng.* **2**(2), 77–81 (2013)
- Ismail, H.A.: Cement kiln dust chemical stabilization of expansive soil exposed at El-Kawther Quarter, Sohag Region, Egypt. *J. Adv. Civil Eng.* **4**, 1416–1424 (2013)
- Srikanth Reddy, S., Prasad, A.C.S.V., Vamsi Krishna, N.: Lime stabilized black cotton soil and brick powder mixture as subbase material. *J. Adv. Civil Eng.* **2018**, 1–5 (2018)
- Bhawasari, S.N., Joshi, H.B., Shrof, P., Patel, A.J.: Effect of burnt brick dust on engineering properties of expansive soil. *IJERT* **3**(4), 433–441



Schedule Compression of Construction Project: A Review

Manish Bharadwaj¹, M. K. Trivedi¹, and Vikas Shinde²

¹ Department of Civil Engineering, Madhav Institute of Technology and Science, Gwalior, India

manishbharadwaj.684@mitsgwalior.in

² Department of Applied Mathematics, Madhav Institute of Technology and Science, Gwalior, India

Abstract. Construction projects are complex nature wise which having different types of task and risk. This requires the need of proper schedule planning and team work which complete the project within the specified time duration. Much time project management had to reduce the project duration because of many factors that raise the demand of compressing schedule. The construction management provides the various methods to project practitioner so that they can accomplish their task by reducing the estimated duration. The various methods including crashing, Time Cost Trade-Off, substitution of activity, resource reallocation, and overlapping are the best strategy which reduces the project duration in efficient way. The research represented in this paper aims to represent factors causing compression of schedule and overview the techniques to compress the schedule and comparing them under different criteria.

Keywords: Project management · Project schedule · Critical path · Crashing resource reallocation · Overlapping

1 Introduction

In now a days the modern Project management system look out their project in such a way which deliver maximum benefits and more reliability and satisfaction to their clients and it increase their market growth and value. The construction project is executed in three phases as shown in Fig. 1.

(i) *Pre-construction phase*- It is a very first step of project in which a team management is setup and planning is done. The total duration is also calculated in this phase only. The project to-do list is prepared and the teams are allocated with their task in this phase.

(ii) *Construction phase*- It is the most time consuming stage in which many amendments in prior planning is done due to various causes. In some cases the project delivery time has to be reduce due to client demand which require the methodology to be implanted by which project duration can be reduce. Cost is also escalated in this phase.

(iii) *Post-construction phase*- In this phase the projects is delivered to corresponding client and satisfies them with their needs and make the technical team to be setup which look out the project until the warranty period and resolve the outstanding issues.



Fig. 1. Project 3-phase

The project in a single manner is a big task therefore the project is breakdown in small group of work packages which is defined as activity. The activities are performed in a sequential manner which is formed by interconnecting these activities in logical manner using network diagram. In this network there exist many paths. The path which is of maximum duration is selected which is defined as critical path and the activity associated with this path is defined as critical activity. This maximum duration is defined as shortest possible time required in finishing the project. This duration can be further reduce as per the needs of client or any circumstances, which can be done by Schedule Compression TeChniques (SCT)- crashing, Time Cost Trade-Off, substitution, resource reallocation, and overlapping. In this paper the factors which are responsible for schedule compression are highlighted and the SCT are studied. The different SCT are compared under various criteria which help project practitioner to reduce the delivery time. These criteria are mainly responsible for adopting SCT. The project execution under different aspects may accelerate as-

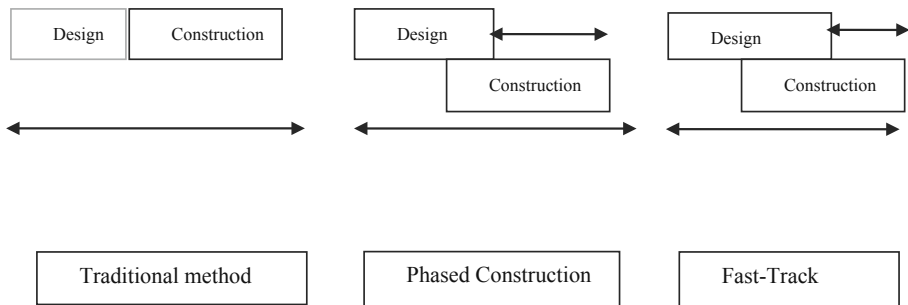


Fig. 2. Effects of different project delivery systems on project acceleration.

2 Literature Review

Many researchers have been explored the theory on schedule compression techniques in project management. Many schedule and resource constrained scheduling (RCS) techniques are introduced to apply resource constraints to project schedules. These methods create schedules that contain resource dependencies between activities

as well as their technological relationships [1–3]. Kim and de la Garza [4] have further upgraded resource-constrained scheduling methods by recalculating late start and finish times of activities through a backward pass, considering both technological and resource links [4]. States that project time and resources are the two most important components of a construction project that are subjected to constraints. Considering these constraints is required not only in the initial scheduling stage, but also it should dynamically be considered during execution phase of construction projects since some resources are highly limited and also each project has timely deadlines that cannot be passed. Schedule is another project component that can highly be bounded to constraints. Accordingly, [5] have divided schedule compression to planned schedule compression which is planned before the execution of construction starts. Further studied were carried on overlapping in which many authors have worked and deliver the possible methods for compression of duration of project and execute it in fast-tracking manner. Theory of [6] is useful to shorten the duration of project by overlapping activities. There are many other techniques by which schedule can be compressed and all mechanisms are described and compared in this paper (Table 1).

3 Schedule Compression Factors and Its Benefit

Schedule compression is said to be reducing the needed time period for fixing one or more of the engineering, procurement, construction or start-up in order to get following:

- (1) Decreasing total design and construction period as compared to normal.
- (2) For the owner accelerated schedule is being prepared
- (3) If the project is short of schedule it resolves lost time, in order to meet the demand of owner and contractors because both have their different need as contractors usually tend to perform schedule compression.

Benefits of SC from Contractor view-

- Contractual times are decided.
- Resolves the clause of bonus, penalty in case of early and delayed construction.
- Delay recovery enhanced productivity is being assured during the project.
- Weather conditions if adverse are being avoided.

Benefits of SC from owner view-

- Financial considerations are being satisfied.
- Any changes in order and schedule if causing delay is being reduced.
- To make sure any delays because of delayed supply of materials from owners are being eliminated.
- Total project cost is being reduced.

Factors which are responsible for schedule compression include-

- (1) **Resource availability-** Resource escalation is the main cause for escalating schedule. If the critical activity resources are depreciating then the other critical

activity should be deployed with additional resource so that the activity can be finish before the expected duration.

- (2) **Contractors-** Some time contractor leverage on subcontractors who are selected to carry out the accelerated work,
- (3) **Additional direct cost required to crash each activity from its normal duration state-** Some time crashing may require the need for additional cost which increase the duration of project because the additional cost need time to sanctioned from higher authorities.
- 4) **Risk-** This factor can be outcome in any phase of construction.
- (5) **Complexity and logistics of the work involved,**
- (6) **Environmental cause-** Bad weather may cause the project to be delayed, hence contractor may reduce the duration of some activity which are exposed to weather.
- (7) **Bonus/Penalty-** This factor can motivate the contractor to execute the project fast, hence the schedule compression is require.
- (8) **Activity Duration-** Duration if passed and work is not completed as per the schedule or if task achieved is more than the duration of activity than duration of activity can be compressed.

These factors had led to increase the demand for formation of schedule compression techniques by project management researchers. These techniques by which the project duration can be compressed are called Schedule Compression Technique (SCT).

4 Schedule Compression Techniques

The SCT which can be efficiently reduce the project duration are-

Table 1. Techniques of schedule Compression

Schedule compression techniques
1. Crashing
2. Time cost trade off
3. Resource re-allocation
4. Substitution of activity
5. Overlapping

i. Crashing

This methodology was invented by Siemens in 1971 as a technique with implementing cost model efficiently and thus named as SAM (Siemens Approximation Method). This methodology focus on reduction of project duration by reducing schedule of critical activities in a proposed manner, the schedule is reduced below the normal time. This phenomenon of time reduction is known as Crashing in project management (Table 1).

The method adopts linear, piecewise linear, discontinuous, hyperbolic or discrete relations between activity's direct cost and its duration and tends to shorten project total

duration by crashing the activity with the lowest cost slope on the critical path by one unit of time in each iteration. Thus the method is continued in trial cycle manner. This method is suitable for small scale construction work involving less number of activities. The activity-based (direct) cost of crashing selected activity (or activities) and indirect cost savings is associated with reducing overall project duration by involving crashing. This procedure terminates when no further crashing can be done.

As project cost is an important aspect thus the procedure is to be adopted to attain minimum cost at optimal duration. The methodology can be used by analytical or graphical method. The method also involve risks that can be incurred during or after crashing which may come forward as a increase cost, lack of material, disputes etc. Considering that the main purpose of time-cost trade-off analysis is to find the least additional cost required to crash project schedules into a targeted duration, the risk associated with that cost should be identified and quantified to help generate a realistic crashing plan.

ii. Overlapping

The techniques where two activities are executed in parallel in order to reduce the duration are referred as overlapped activity and the methodology is called overlapping. The methodology is also defined as fast-tracking of Construction projects. This is an aspect of Concurrent engineering.

Overlapping allow the compression of schedule and is now frequently used by project practitioner because despite of many risks the potential benefits are high in this. The comparison of crashing and overlapping is shown in Table 2.

Table 2. Comparison of crashing and overlapping

Schedule compression by crashing-	Schedule compression by overlapping-
Overall duration of the work can be highly reduced by employing addition manpower or resource to an activity. Care needs to be taken while employing and deploying resources. Compression process shall be employed after analyzing the direct cost and the specified activity duration of the project. In other words, it needs to be kept in mind how the direct cost relates with the employment of additional resource. Scheduled compression can be applied after analyzing time cost relation of the different activities	Overlapping is a schedule based methodology: since its inception in 1997 in Krishnan et al. theory, overlapping has involved in reducing duration without additional resources which increase the economy of technique. The problem requires the handling of risk called rework generated due to overlapping. This can be applied to activities which are behind schedule and by careful analysis of project activities relationship For this it should be noted that the dependent activity if overlapped may not generate risk. After each activities relation has been determined, the process of schedule compression should be started

Other used techniques are-

I. Time-cost trade-off-

This analysis typically leads to rational estimation of project least cost duration, which is not necessarily identical to the original contractual duration. The need also can arise from the fact that “originally estimated project duration is not necessarily the least time solution nor is the least cost schedule for the project, in spite of the fact that each activity within the project was originally planned to be done in the most efficient manner” [7] (Fig. 3).

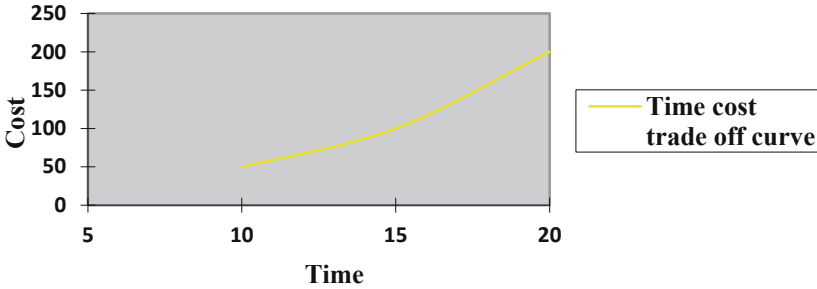
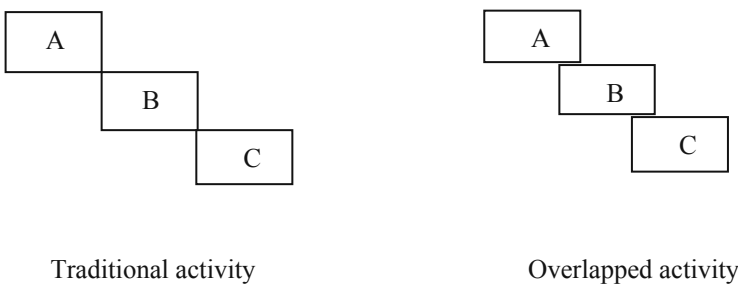


Fig. 3. Time cost trade-off curve

Substitution of activity- For the early completion of task slow going activity is being replaced by the fast going activity. The need of rearranging and recalculation of activity arise in it.

II. Resource re-allocation- In this technique more resources are allocated or resources are transferred among different activity so that duration can be shorten and activity can complete earlier. Identification of activities is being made which are need to optimize the work duration. Activities for example excessive working, overtime employing additional resources makes the delayed project to fall within the deadline of the project. Above techniques are similar in contrast to both schedule and resource constraints as per the need of project acceleration (Fig. 4).

These methods allow the project activity to execute faster than if executed in serial way.



Traditional activity

Overlapped activity

Fig. 4. Sequential performance of activity in different phase

5 Comparison of Schedule Compression Techniques

The criteria under which SCT compared are-

- I. **Cost increment-** The additional cost incurred due to schedule compression is cost increment of project. It is an outcome of risk associated with schedule compression.
- II. **Resource increment-** The amount of resources which has to be increase in order to achieve the task of schedule compression is defined as Resource increment.
- III. **Degree of schedule compression-** The duration amount which has compressed is defined as degree of schedule compression.
- IV. **Calculation-** The procedure involve in technique is defined as calculation. Ease of calculation lead to simplicity for project practitioner to compress the schedule.

Each technique had different response from different criteria. The criteria’s are related to the techniques and the amount that is resulted is shown in Table 2.

This result is the study of many examples of construction project which allow the contractor to adopt the suitable method to compress the schedule (Table 3).

Table 3. Comparison of criteria of SCT

Schedule compression techniques	Criteria				
		Cost increment	Resource increment	Degree of schedule compression	Calculation
Crashing	0	15%–20%	18%–20%	High	High
Substitution	5%–10%	10%–15%	5%–10%	Low	High
Resource re-allocation	10%–12%	20%–25%	0–5%	High	Low
Overlapping	0–5%	5%–10%	15%–20%	Medium	Medium

From the above Table the method which is best suitable for compression of schedule is Overlapping because it involve less calculation, extra resources and schedule is also compressed more, after this the one for which project practitioner can go is crashing, in which schedule is compressed more which is the key demand for project practitioner. But the method which project practitioner use regularly is crashing. Now a day’s overlapping is also a frequently adopted technique which is applied more rapidly. The crashing and overlapping technique comparison is shown in Table 2.

6 Conclusion

Reduction of time of a scheduled project needs effective decision making and complete analysis needs to be made in order to decide where the additional resources are to be deployed to enhance the effectiveness of activity management with respect to the time management. Minimization of such increased direct cost and finding the point of least-cost duration has always been of interest to researchers and professionals alike. Project



should look out closely at the contractors and owners issues and factors that arises the demand for schedule compression. And the technique which is more suitable should be applied. The best technique to be used is according to the condition and in which duration is reducing more but it should be handled carefully and under proper supervision and management because every technique is having the risk. This research work will help project management to deliver the project fast before the proposed duration.

References

1. Kelly, J.E.: Critical-path planning and scheduling: mathematical basis. *Oper. Res. J.* **9**(3), 296–320 (1961)
2. Moder, J.J., Phillips, C.R., Davis, E.W.: *Project management with CPM, PERT, and precedence diagramming*. Van Nostrand Reinhold, New York (1983)
3. Aslani, P.: *Dynamic resource-constrained scheduling*. Ph.D. Thesis, Civil Engineering, Polytechnic University (2007)
4. Kim, K., de la Garza, J.M.: Evaluation of the resource-constrained critical path method algorithms. *ASCE, J. Constr. Eng. Manage.* **131**(5), 522–532 (2005)
5. Noyce, D.A., Hanna, A.S.: Planned and unplanned schedule compression: the impact on labour. *Constr. Manage. Econ. J.* **16**, 79–90 (1998)
6. Dehghan, R., Ruwnapura, J.Y.: Model of trade-off between overlapping and rework. *J. Constr. Eng. Manage.* **140**(2), 04013043-1–04013043-13 (2014)
7. Hinze, J.W.: *Construction Planning and Scheduling*. Prentice Hall, Upper Saddle River (2008)



A Hybrid Approach to Decision Support Environment: Onto-DM-DSS Model

Aastha Mishra¹(✉) , Amit Yadav², and Preetvanti Singh¹ 

¹ Department of Physics and Computer Science,
Dayalbagh Education Institute, Agra, India

aasthamishra006@yahoo.in, preetvantisingh@gmail.com

² Faculty of Engineering, Dayalbagh Education Institute, Agra, India
amitphd2@gmail.com

Abstract. The present paper focuses on integrating Ontology with in a DSS for extracting efficient knowledge. The paper carried out the process of building an integrated model through integrating the knowledge management and decision support processes by making use of knowledge discovery. The paper explains an approach for integrating decision support model and ontology that can be reused and contributes to several decision making tasks and activities. Based on the approaches for building decision support environment using ontologies an integrative framework is presented. This framework is expected to be helpful in guiding future research work on the development and evolvement of decision support environments of the next generation.

Keywords: Ontology · Knowledge management · Data mining · Decision support system

1 Introduction

Decision Support System (DSS), a computerized system, enables a decision maker to arrive at a more knowledgeable and scientific decision. It conveys the decision support information through synthesis and interpretation of quantifiable and scientific data. A DSS helps in making effective decisions that involve optimizing trade-offs and also in dealing with human cognitive deficiencies which provides improved knowledge to the decision maker.

Ontology plays a vital role in developing knowledge framework. It helps in explaining the structure of knowledge. Ontology, within a domain, is set of concepts and relationships between them [1]. Ontologies help in dealing with various complex knowledge handling problems of the modern decision making age.

It is possible that a decision maker may not be able to extract knowledge regarding the decision making processes from the existing inadequate databases. Use of ontology based DSS can therefore be helpful in extracting meaningful knowledge to increase the reasoning capability of a DSS.

Thus the aim of this paper is to demonstrate how DSS and Ontology can be integrated to make the decision support process more effective and efficient.

2 Literature Review

Researchers have constructed ontology to solve domain specific problems. [2] integrated network analysis into the OntoDM for explaining of data mining concepts. [3] investigated the method of incorporating formal semantics in ontologies into the data mining process. [4] proposed an enhanced EEG-based emotion assessment system exploiting a collection of ontological models representing EEG feature sets and arousal–valence space. [5] developed a DM3 ontology to translate the business requirements into model selection criteria and measurements. [6] built an ontology-based data access paradigm for the actual log extraction. [7] proposed a novel interactive search method for extracting disease information by using data mining-based ontology. [8] focused on a specific paradigm for semantic data integration, called Ontology-Based Data Access using various techniques of ontology engineering and the design science methodology. [9] developed a reusable, extensible and adaptable artifact in the form of an ontology. [10] proposed an architecture to process big data, including heterogeneous sources of information and defined an ontology-oriented architecture. [11] focused on the use of ontology for efficient knowledge management.

[12] proposed a DSS based on integrated ontology-based text mining, self-organizing maps and cost optimization for identifying manufacturing faults. [13] explained a method to develop intelligent decision support system using ontology knowledge bases. [14] discussed construction of the sensitivity and specificity of a decision support system based on ontologies for infectious disease diagnosis and antibiotic therapy. [15] implemented a semantically interpretable Fuzzy rule-based systems framework for diabetes diagnosis to provide intuitive and accurate design.

3 Ontology-DSS

This section presents the proposed Ontology-DSS Model. The developed Ontology-DSS Model will help in providing most suitable ontology to the decision making process for extracting the domain knowledge.

An introductory version of ontologies for the Knowledge Base component of DSS is developed using Protégé. The model also re-uses already existing ontologies present at different level of Ontology structure to determine potential re-use, estimate their usability, and personalize ontology to be integrated and re-used with different decision support component. The components of DSS are integrated with the ontology (Fig. 1) in following fashion:

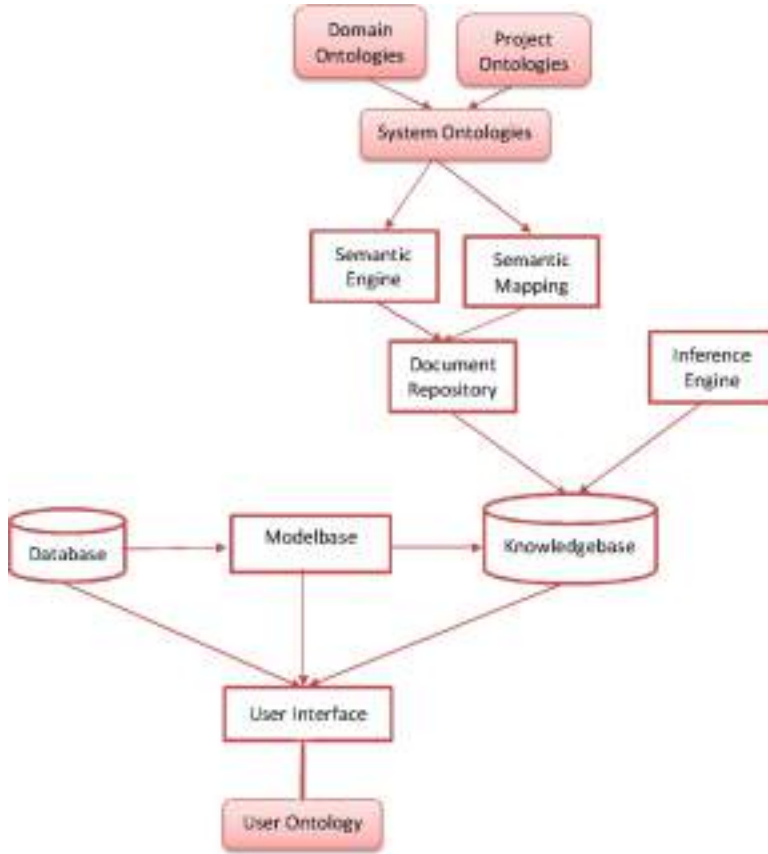


Fig. 1. Onto-DSS model

Model Base

For model based management system which stores and accesses models that managers use to make decisions, the classes can be used are <Type> that define the types of model which can be used by a DSS developer. The sub-classes of <Type> class are <Strategic>, <Tactical> and <Operational>. These are the three types of model available for the use. The next class is <MCDM>. These are the techniques used for multi-criteria decision making and consist of sub-classes that explain each method for MCDM such as <AHP>, <CBR> etc. Another class is used for optimization method with two sub-classes <Linear_programming> and <Nonlinear_programming>. Functions of Model-based system are explained in <Function> class (Fig. 2).

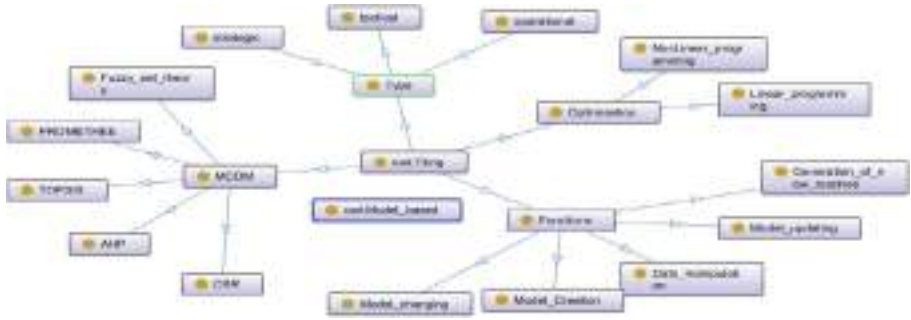


Fig. 2. Model based ontology

Knowledge Base

Knowledge Base is the information storehouse, where the concepts and relations are explained. This can be done using an ontology framework of instances in order to manage data and collect it for future use.

The modeling of such type of knowledge is done by the domain ontology which represents the formal structure and activities of agencies. Domain ontologies provide formal conceptualization and vocabularies to act as a support for the knowledge base of a given domain. In order to retrieve domain knowledge and the resources of information, there are many systems which uses domain ontology. The classes on top are extended in is-a hierarchies and by using limited set of non-standard relations the relations between them are expressed. Despite of that it already had a ontology present to re-use a new ontology is developed that is more easier to understand for the developer. The ontology consist of classes <Techniques>, <Feature> and <Application> (Fig. 3).



Fig. 3. Knowledge based ontology

The above ontologies are at an introductory level, which can further be expanded to more generalized form explaining all the relationship between classes and class mappings.

The mapping is performed at each level of the Ontology-DSS Model is as follows:

- a. **User interface:** The most suitable ontology that can be used with this level is User Ontology. User ontology presents a valuable and more specific representation of the user's interests in the target domain.
- b. **Semantic Engine:** Semantic search denotes search with meaning. It enables user to find documents presents in semantic space. For semantic search purpose the most favorable ontology used is Babelnet ontology [16].
BabelNet [17] is the largest encyclopedic dictionary multilingual network. It provides the meaning to the queries which are search by Semantic engine.
- c. **Inference Engine:** It is the system component that applies logical rules to deduce new information to the knowledge base. DAML+OIL [18] Ontology may be used by inference engine.
- d. **Knowledge Base:** It is the information storehouse, where the concepts and relations are explained using an ontology framework of instances in order to manage data and collect it for future use. The modeling of such type of knowledge is done by the domain ontology which provide formal conceptualization and vocabularies to act as a support for the knowledge base of a given domain.
- e. **Semantic Mapping:** The main purpose of semantic mapping is to obtain a estimator that is capable to conquer only the information important to the assurance of the semantic relationships among elements of language.
PROTON [19] is best suitable for this purpose because it serves as a foundation of domain independent and other more specific ontologies that consists of generic concepts.
- f. **Document Repository:** It is defined as the group of documents that share common features among which several field and their properties which can be retrieved.
Dublin core is simple upper-level ontology for documents and publishing. It lies in Information Artifact Ontology category. To enable intelligent resource discovery systems this ontology gives a semantic vocabulary.
- g. **System Ontologies:** These ontologies are used by the system to perform its task or provide a solution to a problem. System Ontology comprises of two main types of ontologies Project and Domain Ontology.
Domain Ontology is used in characterization of the environment and it is organized as a set of relations and concepts in which the system works.
The project ontology is used to define important features of company projects. The project provides explanation on solving a given problem and is defined as a set of formal descriptions.

As the use of DSS helps in retrieving efficient knowledge this paper can be useful for the decision maker to develop a DSS with more specific knowledge.

4 Conclusion

An extremely important component of the entire decision making process is identifying consequences for each alternative as decision maker has to consider the direct as well as indirect consequences. Ontology mapping is one such representation. The proposed

Onto-DSS model allows to derive new knowledge by studying direct and indirect relationships between concepts of the DSS model. DSS are formalize in the ontology along with their properties. In future, the constructed ontology can be used to developed evaluation technique in other decision support approaches.



References

1. Ford, F.N.: Decision support systems and expert systems: a comparison. *Inf. Manag.* **8**(1), 21–26 (1985)
2. Kralj, J., Panov, P., Džeroski, S.: Expanding the OntoDM ontology with network analysis tasks and algorithms. In: 18th International Multi-Conference Information Society-Intelligent Systems Conference (2015)
3. Dou, D., Wang, H., Liu, H.: Semantic data mining: a survey of ontology-based approaches. In: Proceedings of the 2015 IEEE 9th International Conference on Semantic Computing, IEEE ICSC 2015, pp. 244–251. IEEE (2015)
4. Chen, J., Hu, B., Moore, P., Zhang, X., Ma, X.: Electroencephalogram-based emotion assessment system using ontology and data mining techniques. *Appl. Soft Comput.* **30**, 663–674 (2015)
5. Li, Y., Thomas, M.A., Osei-Bryson, K.M.: Ontology-based data mining model management for self-service knowledge discovery. *Inf. Syst. Front.* **19**(4), 925–943 (2017)
6. Calvanese, D., Kalayci, T.E., Montali, M., Tinella, S.: Ontology-based data access for extracting event logs from legacy data: the onprom tool and methodology. In: International Conference on Business Information Systems, pp. 220–236. Springer, Cham (2017)
7. Nguyen, H.S., Le, M.H., Lam, C.Q.L., Duong, T.H.: Smart interactive search for Vietnamese disease by using data mining-based ontology. *J. Inf. Telecommun.* **1**(2), 176–191 (2017)
8. De Giacomo, G., Lembo, D., Lenzerini, M., Poggi, A., Rosati, R.: Using ontologies for semantic data integration. In: A Comprehensive Guide Through the Italian Database Research Over the Last 25 Years, pp. 187–202. Springer, Cham (2018)
9. Volk, M., Pohl, M., Turowski, K.: Classifying big data technologies-an ontology-based approach (2018)
10. Peral, J., Ferrandez, A., Gil, D., Munoz-Terol, R., Mora, H.: An ontology-oriented architecture for dealing with heterogeneous data applied to telemedicine systems. *IEEE Access* **6**, 41118–41138 (2018)
11. Behnaz, A., Bandara, M., Rabhi, F.A., Peat, M.: A statistical learning ontology for managing analytics knowledge. In: International Workshop on Enterprise Applications, Markets and Services in the Finance Industry, pp. 180–194. Springer, Cham (2018)
12. Alkahtani, M., Choudhary, A., De, A., Harding, J.A.: A decision support system based on ontology and data mining to improve design using warranty data. *Comput. Ind. Eng.* **128**, 1027–1039 (2019)
13. Lytvyn, V., Vysotska, V., Dosyn, D., Lozynska, O., Oborska, O.: Methods of building intelligent decision support systems based on adaptive ontology. In: 2018 IEEE Second International Conference on Data Stream Mining & Processing (DSMP), pp. 145–150. IEEE (2018)
14. Shen, Y., Yuan, K., Chen, D., Colloc, J., Yang, M., Li, Y., Lei, K.: An ontology-driven clinical decision support system (IDDAP) for infectious disease diagnosis and antibiotic prescription. *Artif. Intell. Med.* **86**, 20–32 (2018)

15. El-Sappagh, S., Alonso, J.M., Ali, F., Ali, A., Jang, J.H., Kwak, K.S.: An ontology-based interpretable fuzzy decision support system for diabetes diagnosis. *IEEE Access* **6**, 37371–37394 (2018)
16. Biniz, M., El Ayachi, R., Fakir, M.: Ontology matching using BabelNet dictionary and word sense disambiguation algorithms. *Indones. J. Electr. Eng. Comput. Sci.* **5**(1), 196–205 (2017)
17. Navigli, R., Ponzetto, S.P.: BabelNet: building a very large multilingual semantic network. In: *Proceedings of the 48th Annual Meeting of the Association for Computational Linguistics*, pp. 216–225. Association for Computational Linguistics (2010)
18. McGuinness, D.L., Fikes, R., Hendler, J., Stein, L.A.: DAML+OIL: an ontology language for the Semantic Web. *IEEE Intell. Syst.* **17**(5), 72–80 (2002)
19. Damova, M., Kiryakov, A., Simov, K., Petrov, S.: Mapping the central LOD ontologies to PROTON upper-level ontology. In: *Ontology Matching*, p. 61 (2010)



Immiscible Liquid-Liquid Flow in Coiled Tube

Nazim Ali  and Monisha Mridha Mandal 

University School of Chemical Technology,
Guru Gobind Singh Indraprastha University,
New Delhi 110078, India
monishamridhal@gmail.com

Abstract. Immiscible liquid-liquid flows are frequently encountered in process industries such as petroleum, chemical, polymer and pharmaceutical. Energy efficient designs of such process are requisites for any process plant. However, very few research works have been reported in literature for coiled tubular flow reactors. Therefore, present experimental study was conducted to gain insight of the flows of different immiscible liquids flowing in coiled tube. Effect of ratio of viscosities of liquids and curvature of coiled tube on the pressure drop has been reported here. Different flow patterns were observed and mapped at various volume fractions of liquids. This work may help in better understanding of the hydrodynamics of liquid-liquid flows in equipment having curved geometries which are widely used in industries as reactors, heat exchangers, etc. Energy losses in such devices can be estimated and thus will be helpful in designing equipment in various process plants.

Keywords: Flow pattern · Pressure drop · Liquid-liquid flow · Viscosity ratio · Coiled tube

1 Introduction

Two or more immiscible liquid flow through a conduit is considered to be multiphase flow. These types of flows are frequently found in the industries such as food, chemical and petrochemical industries. These systems are found in processes for instance transportation and production of various products. The two immiscible phases of the oil and water flowing in pipeline show distinct phases because of difference in their properties such as densities and have diverse physical distribution at different flow rates. This leads to different patterns of flow i.e. emulsion, annular flow, stratified flow, etc. The occurrence of flow patterns are depended on forces for instance buoyant force, inertial force, viscous and interfacial tension. Prediction of flow patterns in the pipes is difficult for various applications in contrast to single-phase flows [1–10]. Knowledge of flow patterns is essential to predict the pressure drop behavior is found from the change in the ratio of oil and water [2].

The major parameters that decide the type of flow patterns are flow velocity, characteristics of tube, such as roughness, diameter and inclination angle; liquid properties. Liquid properties for example viscosity, density, surface tension, fluid

wettability has a prominent effect on systems with multiphase flow. These properties affect the flow of immiscible liquids flow significantly. Moreover, gravity increases the tendency of phase separation in the pipe for liquids with different densities. This is the reason why their behavior is found to be quite different from that of the gas-liquid systems. Fluid properties such as density and viscosity of gas phase greatly differ from that of liquid phase. For instance, the immiscible liquid-liquid flows have density ratio nearly equal to one and viscosity ratio may vary from unity to several thousands. Wetting characteristics and surface tension of liquids influences the interfacial forces which in turn affect the phase inversion. The complex mechanisms such as phase inversions make liquid-liquid flows system difficult for the development of predictive tools [11]. The knowledge of hydrodynamics of immiscible liquid mixtures is vital for the design of pipelines, production lines in oil fields and methods of artificial lifting. Understanding the characteristics of water and oil flow in pipes is essential to determine the quantity of water in contact with the walls of the pipe which may give rise to corrosion and erosion problems [12]. As the petroleum industry ventures to exploit oil in harsher environment (the Polar Regions and deep sea waters for instance) the deployment of separating equipment to these producing water, oil and gas has become very expensive and in most of the cases either economically or technically unfeasible. Thus, to overcome these problems multiphase transportation lines for petroleum recovery systems are being designed to cover longer distances every year. Thus, the study of multiphase flow in pipes has become crucial for the development of new frontier in oil industry [13, 14].

Coiled tubes are used as equipment such as heat exchangers, reactors and mixers. Basic modes of heat transfer and mass transfer are affected by advection and convection of fluid. i.e. the net movement of fluids. The transport phenomenon of fluid and transfer of energy between the fluids is dependent on fluids motion and momentum. Therefore, the need for reliable multiphase flow design techniques is the driving force for comprehensive research in this area. Nevertheless, little works have been reported to explore energy losses of immiscible liquids flow in coiled tube. Thus, the aim of current experimental work is to experimentally explore the effect of vital process parameters i.e. viscosity, velocity of flow of two immiscible liquids and curvature of coiled tube on flow pattern as well as pressure drop of flow in coiled tube.

2 Methodology

The set up to conduct the experiments is illustrated in Fig. 1. It consist of two separate tanks (10 L each) for containing water and oil separately. The properties of oils used are given in Table 1. Two gear pumps of $\frac{1}{2}$ HP and single phase were used for pumping each fluid into a vertically coiled test section. A separation tank (20 L) was connected with the outlet of coiled tube test section. It was used to separate oil and water. The pump delivered oil and water at desired velocity. Two Acrylic Rotameter of 0–2 Lpm range were used to measure the flowrates of liquids. Two Dimmerstats

(controller) were connected with both the pumps to get desired flow rate of oil and water. A T-shaped mixing section was used to mix the two immiscible liquids before it entered coiled test sections with a diameter of 0.007 m. The connecting pipes are transparent, flexible pipes. The test section was transparent coiled tube which was coiled around a cylindrical pipe. Total length of coiled tube was 1 m and internal diameter was 0.007 m. Inlet and outlet of the coiled tube were connected to manometer with mercury. It was installed vertically and was used for pressure drop measurement. Pressure drop, ΔP was calculated using below mentioned equation.

$$\Delta P = g \rho (\Delta h) \quad (1)$$

Here, $\rho = (\rho_{\text{mercury}} - \rho_{\text{mixture}})$, ρ_{mercury} is density of mercury, ρ_{mixture} is density of water and oil mixture. ρ_{mixture} was found out by using equation,

$$\rho_{\text{mixture}} = \rho_o \phi_o + (1 - \phi_o) \rho_w \quad (2)$$

Where, $\phi_o = \text{inlet oil flow rate} / \text{flow rate of all liquids}$, $\rho_o = \text{oil density}$

$\phi_w = \text{inlet water flow rate} / \text{flow rate of all liquids}$, $\rho_w = \text{water density}$

The viewing section of the vertically coiled flow included a DSLR camera Nikon 5300D and a light source to record the flow pattern. Two different dyes which were soluble in the oil and water phase were added into the feed tanks for better visualization of flow patterns. The dyes were selected in such a way that it was soluble in only one phase. Fluorescein Sodium which is green in colour, was chosen as the dye for water. Biebrich Scarlett R which is red in colour, was taken for oil phase. Two pumps were connected with separator to recycle back the liquids to its respective storage tanks.

Table 1. Physical property of liquids

Liquids	Property	Value
Kerosene oil	Density	800 kg/m ³
	Viscosity @ 27 °C	1.67 cP
Transformer oil	Density	890 kg/m ³
	Viscosity @ 27 °C	16.2 cP
Motor oil	Density	870 kg/m ³
	Viscosity @ 27 °C	85 cP

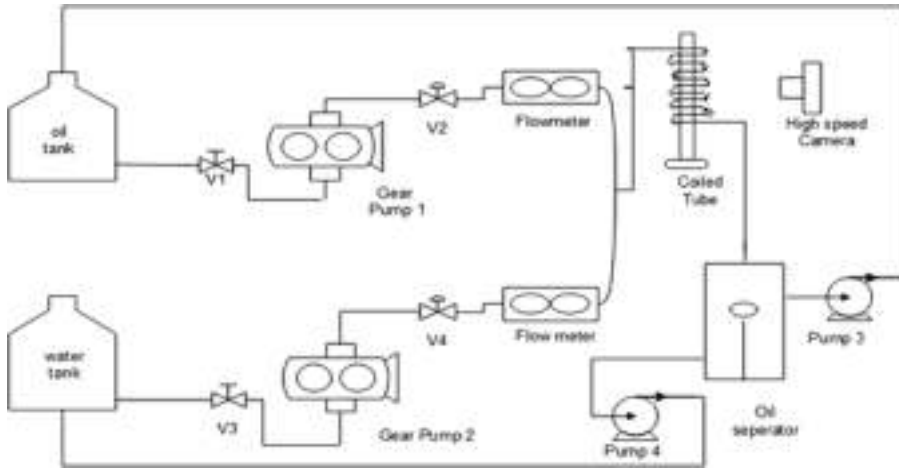


Fig. 1. Experimental set up

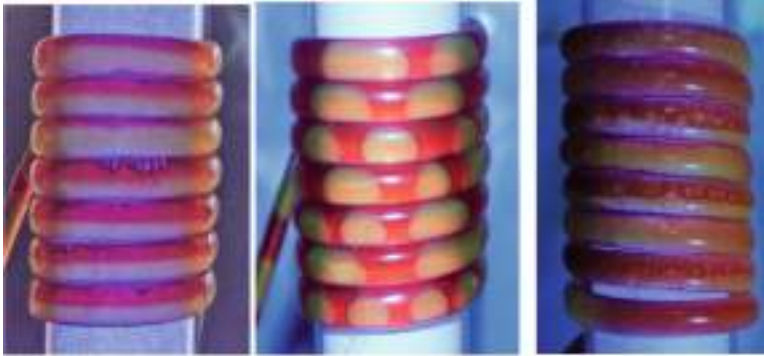
3 Result and Discussion

3.1 Flow Pattern

In the present experimental study, various patterns of flows for both the oil i.e. Kerosene-water and Transformer-water have been visually observed and recorded at varying input rates of mixture flows ranging from 0.2 to 2 lpm. For the case of water-kerosene oil mixture flowing in coiled tube, seven different flow regimes were observed. The seven patterns of flow were observed. They were

- (1) Stratified Flow (ST)
- (2) Mixed stratified Flow (MST)
- (3) Intermittent Flow (IT)
- (4) Emulsion of kerosene oil in water (Eo/w)
- (5) Dispersed flow with kerosene oil in water and water in kerosene oil (Do/w & Dw/o)
- (6) Emulsion of water in kerosene oil (Ew/o)
- (7) Dispersed flow with water in kerosene oil and kerosene oil layer (Dw/o & o)

Figure 2 depicts the pictures of different flow patterns observed in coiled tube. On comparing with work reported by Trallero et al. [11] for oil-water flow in straight tube, it was found that a new flow pattern, Intermittent flow, was observed for kerosene oil and water flow in coiled tube at low oil-water velocity and water fraction. The flow patterns were then mapped based on kerosene and water velocities and is depicted in Fig. 3.



(a) Stratified flow(ST)

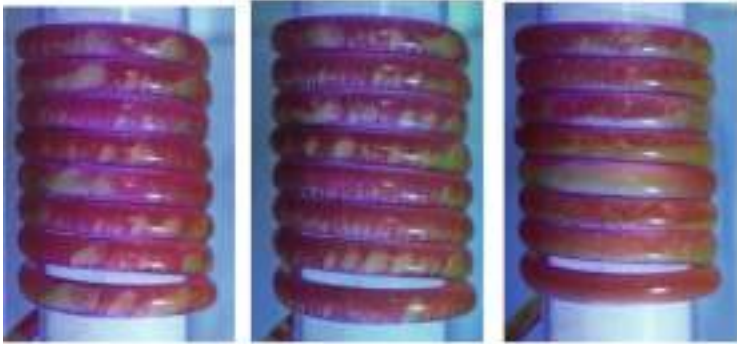
(b) Intermittent Flow (IT)

(c) Mixed stratified Flow (MST)

$U_o=0.216\text{m/s}, U_w=0.216\text{m/s};$

$U_o=0.129\text{m/s}, U_w=0.086\text{m/s};$

$U_o=0.302\text{m/s}, U_w=0.346\text{m/s}$



(d) Emulsion water in kerosene, layer (Dw/o & o)

(e) Dispersion of water in kerosene and kerosene in kerosene (Do/w & Dw/o)

(f) Dispersed flow with kerosene in water and water in kerosene

$U_o=0.173\text{m/s}, U_w=0.043\text{m/s};$

$U_o=0.302\text{m/s}, U_w=0.129\text{m/s};$

$U_o=0.259\text{m/s}, U_w=0.173\text{m/s}$



(g) Emulsion of oil in water (Eo/w)

$U_o=0.259\text{m/s}, U_w=0.605\text{m/s}$

Fig. 2. Kerosene oil-water flow patterns in coiled tube

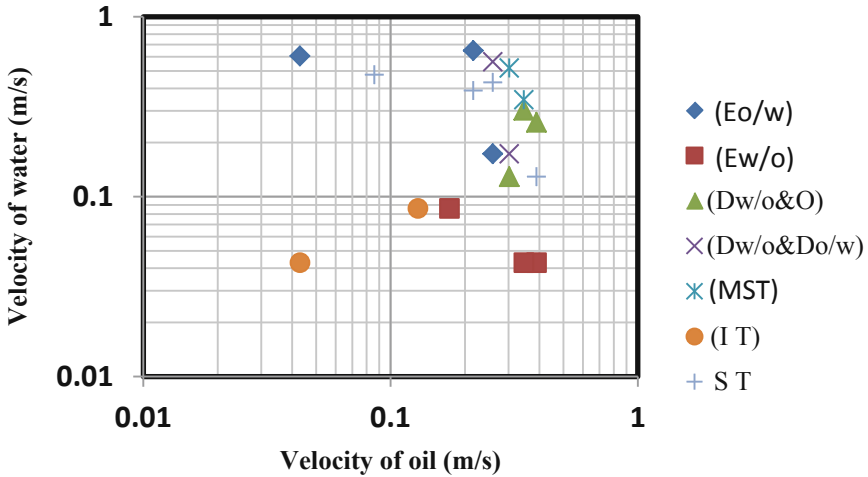


Fig. 3. Flow pattern map for Kerosene and water flowing in coiled tube

Four flow patterns were observed visually in when there was transformer oil and water mixture flow in a coiled tube. They are illustrated in Fig. 4. The patterns of flow were

- (1) Intermittent flow (IT)
- (2) Emulsion of transformer oil within water (Eo/w)
- (3) Emulsion of water within transformer oil (Ew/o)
- (4) Dispersed flow of transformer oil within water and water layer (Do/w&w)

At low velocity of flows and very little water input fraction, intermittent flow (IT) pattern was observed. When the flow velocity was augmented further, emulsion flow patterns were observed due to turbulence and droplet formation. When the velocity of water was increased to 0.649 m/s, dispersed flow with water layer at the bottom was observed. When the water velocity was low and oil velocity ($U_o = 0.389$ m/s $U_w = 0.043$ m/s) was high then dispersed flow of water in transformer oil with transformer oil layer (Dw/o&o) was observed. Figure 5 shows the pattern of flow map developed at different velocity of oil and water for transformer oil and water in vertically placed coiled tube.



(a) Intermittent flow (IT),



(b) Emulsion of transformer oil in water,



(c) Dispersed flow of transformer oil in water with water layer (Do/w&w)

$U_o=0.129\text{m/s}, U_w=0.086\text{m/s}; U_o=0.216\text{m/s}, U_w= 0.432\text{m/s}; U_o= 0.216\text{m/s} U_w=0.649\text{m/s}$



Dispersed flow of water in transformer oil and transformer oil layer (Dw/o&o), $U_o= 0.389 \text{ m/s} U_w= 0.043 \text{ m/s}$

Fig. 4. Flow patterns for transformer oil-water flowing in coiled tube

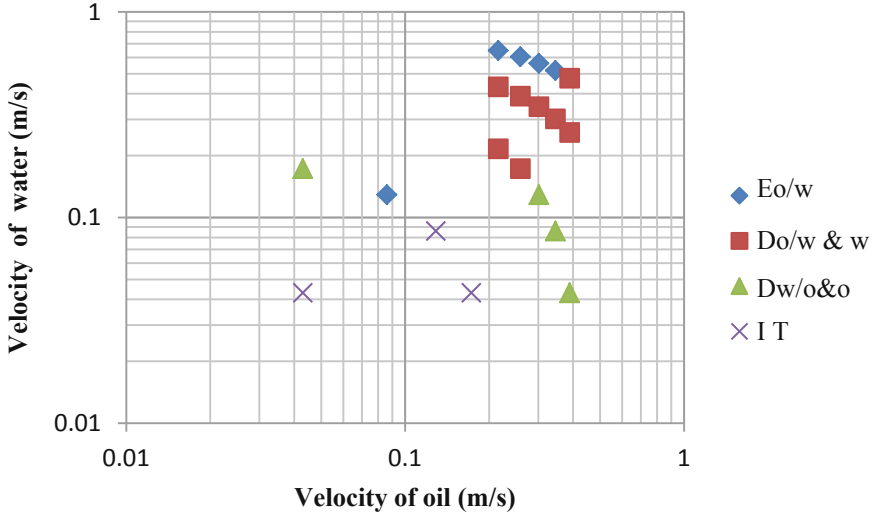


Fig. 5. Flow pattern map for transformer oil-water flowing in coiled tube

3.2 Pressure Drop

The motivation for studying the pressure drop of different oil and water systems was to predict the reduction of the pumping power resulting from the injection of water in lines that transport highly viscous oils. Majority of previous studies for pressure drop (ΔP) calculations were performed in vertical coiled tube are for single phase fluid. Limited works have been carried out for exploration of pressure drop calculation for two immiscible liquid-liquid flow in coiled tube. In the present study pressure drop for both oils i.e. Kerosene oil-water and Transformer oil-water was evaluated by U tube manometer.

In order to study the effect of variation of flow rate and oil fraction on pressure drop, the scattered graph of ΔP verses oil fraction at different flow rates were plotted as shown in Fig. 6. It was found that as we increase the total flow rate of kerosene oil-water from 0.2 lpm to 2 lpm, the pressure drop increased due to overall increase in inertial forces. It was also found that with increase in oil fraction, pressure drop increased because of increase in overall viscous forces of liquid-liquid flow. Similarly, pressure drop measurement for different input rates of transformer oil-water at five different total flow rates. Scattered graph of ΔP verses oil fraction at different flow rates were plotted as shown in Fig. 7. It was found that with increase in flow rate, velocity and oil fraction increased the pressure drop across the coiled tube.

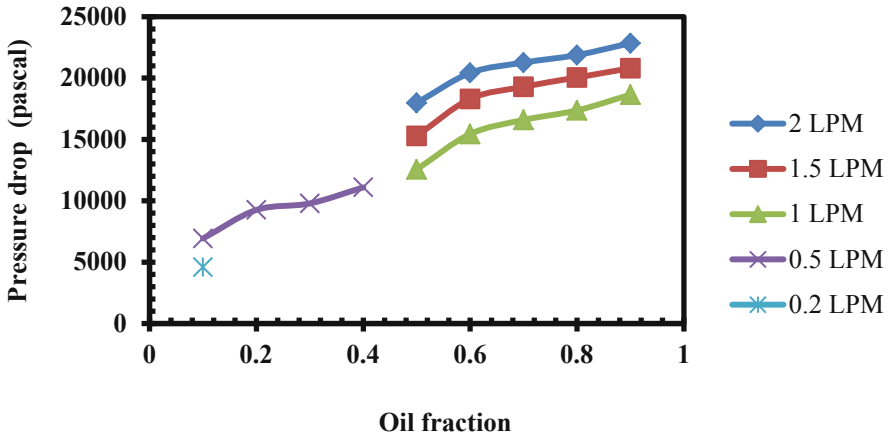


Fig. 6. Pressure drop vs. oil fraction for kerosene-water flowing in coiled tube

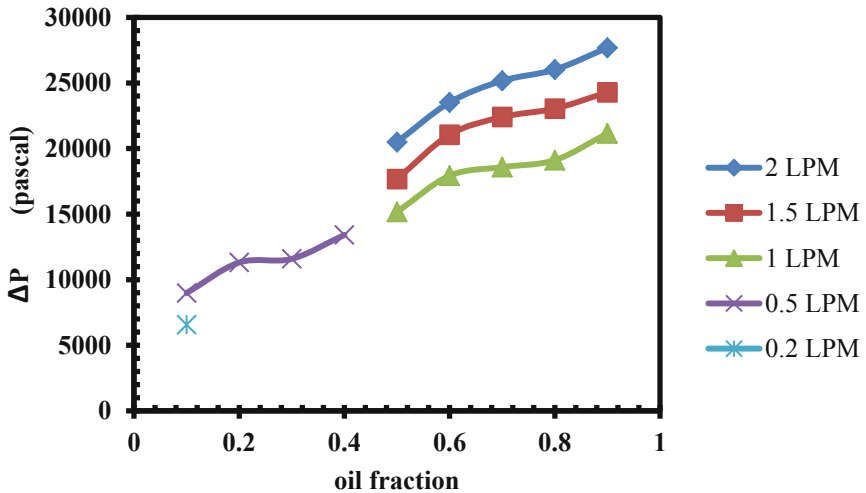


Fig. 7. Pressure drop vs. oil fraction for transformer oil-water flowing in coiled tube

Curvature ratio is the ratio of diameter of tube (d_i) to the diameter of coil (D). The curvature ratio of coiled tube affects the potential of secondary forces generated due to the curvature of coiled tube. Therefore, in the present study, the effect of curvature ratio on pressure drop of two immiscible liquid for kerosene oil –water, two different curvature ratio i.e. (a) $d_i/D = 0.1$ and (b) $d_i/D = 0.14$ were investigated experimentally. Pressure drop calculation with different input flow rate of Kerosene oil and water at three different total flow rates i.e. (a) at 2 LPM (b) at 1 LPM (c) at 0.5 LPM for both curvature ratios were performed. ΔP and oil fraction were plotted for the different curvature ratios with different flow rates as shown in Fig. 8. It was found that as the

curvature ratio was increased pressure drop increased. This was due to increase effect of secondary forces which acts perpendicular to the direction of primary liquid flow.

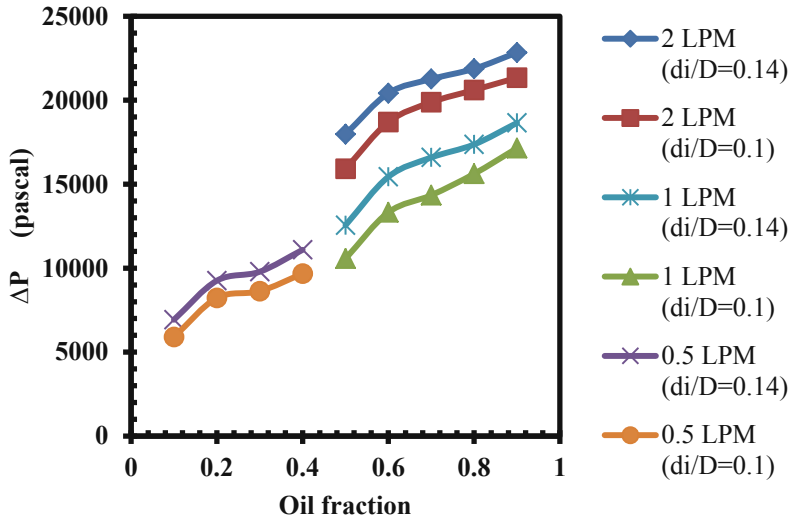


Fig. 8. Pressure drop vs. oil fraction at different curvature ratio for kerosene-water flowing in coiled tube

Pressure drop calculation with different input flow rate of transformer oil and water at three different total flow rates i.e. (a) at 2 LPM (b) at 1 LPM (c) at 0.5 LPM for both curvature ratios (i.e. $d_i/D = 0.1$ and $d_i/D = 0.14$) were performed separately and plotted graphically as shown in Fig. 9. It was again found that as the curvature ratio was increased pressure drop of liquids also increased.

Pressure drop for different viscosity ratio i.e. $\mu_o/\mu_w = 1.67$ (kerosene oil-water) and 16.2 (transformer oil-water) was evaluated experimentally with different input rates of oil and water at three different total flow rates and shown in Fig. 10. It was found that with increase in viscosity ratio, pressure drop increased due to increase in viscous forces. Experiment was further conducted with one more type of oil i.e. Motor oil ($\mu = 85$ cP). The effect of viscosity ratio on pressure drop was compared and plotted as Fig. 11. There was 21% increase in pressure drop as the viscosity ratio was increased from 1.67 to 85 at total flowrate of 2 LPM and oil volume fraction = 0.5. The pressure drop was found to be increased 29% when the viscosity ratio was increased from 1.67 to 85 at oil volume fraction 0.9 and total flow rate 2 LPM.

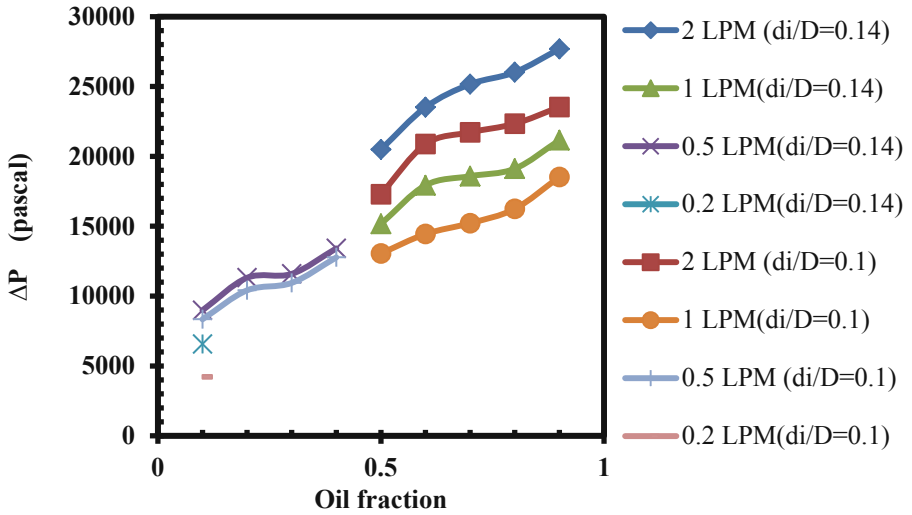


Fig. 9. Pressure drop vs. oil fraction at different curvature ratio for transformer oil-water flow in coiled tube

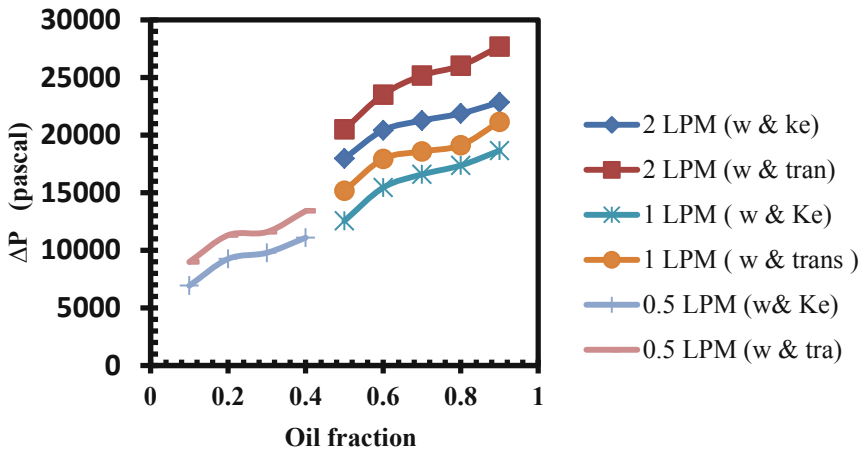


Fig. 10. Effect of oil fraction on pressure drop for different viscosity ratio

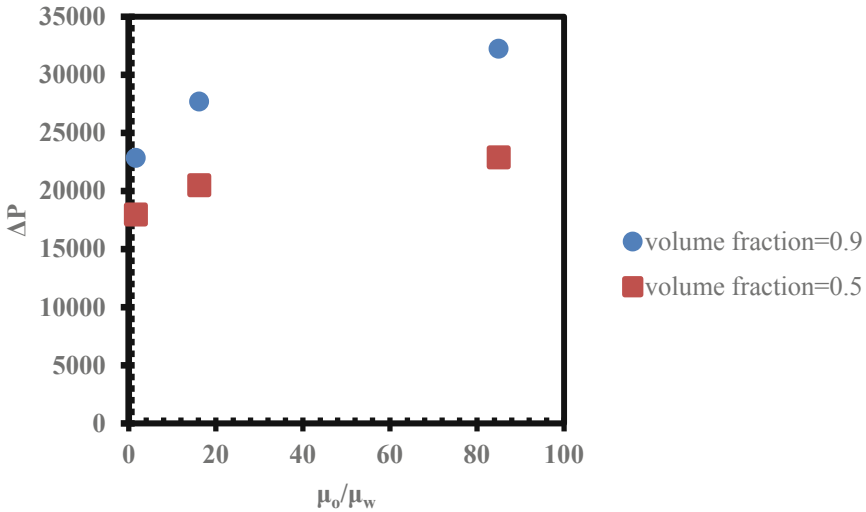


Fig. 11. Effect of viscosity ratio on pressure drop at total flow rate of 2 lpm

4 Conclusions

Present experimental study was conducted to investigate the effect of ratio of viscosity of oil to water, oil fraction of immiscible liquid-liquid flows in coiled tube. Seven types of flow patterns were observed for kerosene oil and water flow and are reported here. Four types of flow patterns were detected for transformer oil and water. The pressure drop of immiscible liquids increased with increase in viscosity ratio, curvature ratio and oil fraction. This work may give better understanding of estimation of energy losses due to combined effect of viscous force, inertial forces and centrifugal forces acting on liquid-liquid flows in coiled tubes.

Acknowledgement. The authors would like to acknowledge Guru Gobind Singh Indraprastha University, New Delhi, for the financial as well as administrative support to carry out this research work.





References

1. Mukhaimer, A.A., Ahmed, W.H., Al-Hadhrami, L.: Pressure drop and flow pattern of oil-water flow for low viscosity oils: role of mixture viscosity. *Int. J. Multiph. Flow* **73**, 90–96 (2015)
2. Luo, X., Lü, G., Zhang, W., He, L., Lü, Y.: Flow structure and pressure gradient of extra heavy crude oil-water two phase flow. *Exp. Therm. Fluid Sci.* **82**, 174–181 (2017)
3. Jose, M., Remacha, N., Kulkarni, A.A., Jenas, K.F.: Hydrodynamics of liquid-liquid dispersion in an advanced-flow reactor. *Ind. Eng. Chem. Res.* **51**, 16251–16262 (2012)
4. Mandal, T.K., Chakrabarti, D.P., Das, G.: Oil water flow through different diameter pipes: similarities and differences. *Chem. Eng. Res. Des.* **85**, 1123–1128 (2007)

5. Perera, K., Mylvaganam, S., Time, R.W.: Characterization of oil-water plug related flow in slightly inclined pipe. *Int. J. Comput. Methods Exp. Meas.* **2**, 373–384 (2018)
6. Vashishth, S., Kumar, V., Nigam, K.D.P.: A review of potential applications of curved geometries in process industry. *Ind. Eng. Chem. Res.* **47**, 3291–3337 (2008)
7. Al-Yaari, M., Soleimani, A., Abu-Sharkh, B., Al-Mubaiyedh, U., Al-sarkhi, A.: Effect of drag reducing polymers on oil–water flow in a horizontal pipe. *Int. J. Multiph. Flow* **35**, 516–524 (2009)
8. Brauner, N., Moalem Maron, D.: Flow pattern transitions in two-phase liquid-liquid flow in horizontal tubes. *Int. Multiph. Flow J.* **18**, 123–140 (1992)
9. Charles, M.E., Lilleth, L.U.: Correlation of pressure gradients for the stratified laminar-turbulent pipeline flow of two immiscible liquids. *Can. J. Chem. Eng.* **44**, 47–49 (1966)
10. Ibarra, R., Markides, C.N., Matar, O.K.: A review of liquid-liquid flow patterns in horizontal and slightly inclined pipes. *Multiph. Sci. Technol.* **26**(3), 171–198 (2014)
11. Trallero, J.L., Sarica, C., Brill, J.P.: A study of oil/water flow patterns in horizontal pipes. *Soc. Petrol. Eng.* **12**(3), 165–172 (1997)
12. Tan, J., Jing, J., Hu, H., You, X.: Experimental study of the factors affecting the flow pattern transition in horizontal oil–water flow. *Exp. Therm. Fluid Sci.* **98**, 534–545 (2018)
13. Kumar, V., Aggarwal, M., Nigam, K.D.P.: Mixing in curved tubes. *Chem. Eng. Sci.* **61**, 5742–5753 (2006)
14. Mandal, M., Aggarwal, P., Nigam, K.D.P.: Liquid -liquid mixing in coiled flow inverter. *Ind. Eng. Chem. Res.* **50**, 13230–13235 (2011)



Numerical Analysis of Joukowski ($T = 12\%$) Airfoil by $k-\epsilon$ Turbulence Model at High Reynolds Number

Ravi Jain¹, Mohd. Yunus Sheikh¹, Dharmendra Singh¹,
and Manoj Tripathi²

¹ Department of Mechanical Engineering, Government Engineering College,
Bikaner, Rajasthan Technical University, Bikaner 334004, Rajasthan, India
ravijain845482@gmail.com, mysbkn03@gmail.com,
dharmendra3103@gmail.com

² Department of Physics and Materials Science and Engineering, Jaypee Institute
of Information Technology, Noida 201309, India
tripmanoj@gmail.com

Abstract. In aerodynamics, the role of an airfoil is vastly dominant to generate the adequate lift to transport the aircraft. Aerodynamically characteristic of an airfoil is construct on the design yet still its desire performance of an airfoil is ground on design yet its result is not simple in present days [1]. In present scenario airfoil design is observe arbitrary for the flows of an aircrafts and a very early time in history Orville and Wilbur brothers made and design camber or asymmetrical airfoil and In before days NACA define a proper way to describe the definition of an airfoil and tells about their characteristics or how airfoil efficient. In present study about NACA4412, NACA0012 and JOUKOWSKI ($t = 12\%$) airfoil, at different Angle of attack and velocity of flow is 43.822 m/s in CFD [2]. The salient feature of present work study is to knows about their behavior of fluid flow located on each and every sides of an airfoil and calculate the characteristics of aerodynamic performances at very high Reynolds Number (3 million) and angle of attacks varies from 2° to 18° . The coefficients of drag and lift for all the airfoil is determined by seeing the surface pressure on different airfoil. In present research work performance of aerodynamics of an airfoil are plot against Angle of attack and how the results area unit getting ready to the experimental results. During this work we have a tendency to calculate and observe the comparison of $k-\epsilon$ turbulence model along with experimental results [3].

Keywords: NACA airfoil · Joukowski airfoil · CFD · k -epsilon turbulence model · ANSYS

1 Introduction

1.1 Overview

In previous days, Transportation is completely based on the all locomotive as: Rails, Buses, Motorbikes, in presents days what we want, more efficient, fastest bikes and comfortable and high standard luxury travelling it can be possible by only air

transportations. Basically the surface could be a cross-sectional of a wing of associate craft. Its necessary aim is to provide adequate raise for associate aero-plane throughout take-off time [2].

1.2 Airfoil Theory – Definitions

The work study of several term in airfoil are listed and describe below in the Fig. 1.

- **Leading edge:** It is the edge of the airfoil facing the direction of motion of Associate in aircraft [3].
- **Trailing edge:** It's the sting or sharp corner of Associate in nursing surface that is set and pointed within the nature or air.
- **Chord line:** It is delineated because the line that use to joins the leading edge to trailing edge.
- **Angle of attack:** It's described as the angle which makes between the chord line and the direction of an aircraft [4].
- **Lift:** It is the perpendicular element to the entire force to the air.
- **Drag:** It is the parallel element to the entire force to the air.

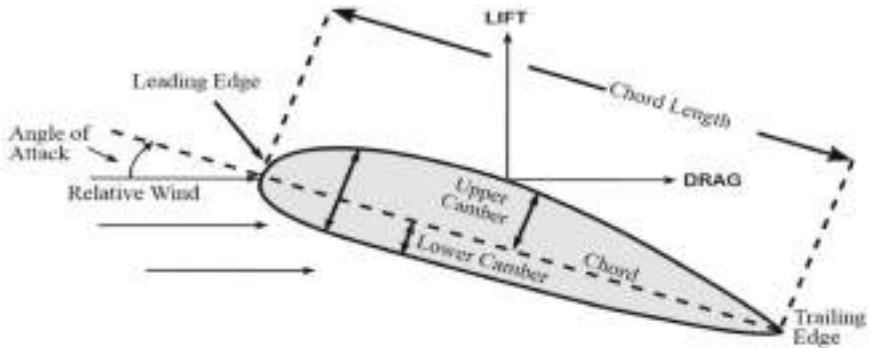


Fig. 1. Sectional view of an airfoil [1]

2 Objective of Study

This study, understand and describe working principle and phenomena behind the need of airfoil design. Airfoil shape are used in aircraft, automobile and production sectors e.g. turbo machinery, wind turbines, and wing etc. Airfoil are used for generate lift for an aircraft as well as drag force. It is totally depend upon the shape and the proper or actual design of an airfoil [5].

The objective of this study to know the design parameter of many airfoil and their working principle of flow simulation to understand how they work and some points are written below.

- Symmetric and Asymmetric airfoil modeling in ANSYS.
- JUOKOWSKI ($t = 12\%$) airfoil modeling in ANSYS.
- Examine the comparison between aerodynamics performances of same thickness airfoil.
- Determine the surface pressure distribution and velocity profile of various airfoils.
- Determine the coefficients of drag and lift of the NACA and JUOKOWSKI ($t = 12\%$) airfoil and examine their variation with AOA.
- Examine lift forces and drag force on NACA and JUOKOWSKI ($t = 12\%$) airfoil for each AOA.
- Examine the turbulent kinetic energy for airfoil in K-EPSILON model.
- Angle of attack varies from 2 to 18 degree and free stream velocity ranges is 43.822 m/s.

3 Literature Review

In this Paper determined all the literature reviews on various airfoils are presented. Different turbulence model are used for increasing lift coefficient of the airfoil by different researcher have been discussed.

Bhargava et al. [2] have determined the pressure distribution on airfoil profiles enables to understand the dynamic flow characteristics around the surface of wings or blades. The pressure distribution of NACA airfoil profiles is calculated using the numerical panel method for 2D lifting air flow conditions. The analysis of airfoil geometry subjected to various 14AOA (angle of attack) including the stalling angles is considered to observe the variation in pressure coefficients along the chord.

He et al. [3] performed a linear Global modal stability analysis on the separated flow around a NACA 4415 airfoil at low Reynolds numbers ($Re = 300-1000$) and a high angle of attack ($\alpha = 20$), with a focus on the effect of the airfoil's proximity to two different types of ground: a stationary ground and a moving ground.

D'Souza et al. [4] provides an overview of the design parameters of a low speed wind tunnel and then the study of coefficient of lift (C_L) and coefficient of drag (C_D) for different length to diameter (L/D) ratios of a NACA 4412 airfoil section shaped as per the NACA standards of Airfoil design. It was observed through flow visualization test that flow remained un separated throughout the test section for 70% of its characteristic dimension i.e. The breadth or height of the test section in this case.

4 Boundary Condition for Solving the Problem

It is requiring for satisfaction of the all parts of the boundary regions in which observed by differential equation conditions is to be investigated. Table 1. Represents the all input parameters which is required to solve this airfoil problem.

Table 1. Input parameters of the airfoil

Input parameters	NACA0012	NACA4412	JOUKOWSKI ($T = 12\%$)
Velocity of flow	43.822 m/s	43.822 m/s	43.822 m/s
Operating temp.	288.16 C	288.16 C	288.16 C
Operating pressure	101325 Pa	101325 Pa	101325 Pa
Turbulence model	$k-\epsilon$	$k-\epsilon$	$k-\epsilon$
Density of fluid	1.225 kg/m ³	1.225 kg/m ³	1.225 kg/m ³
Dynamic viscosity	$1.7894 * 10^{-5}$ kg/m	$1.7894 * 10^{-5}$ kg/m	$1.7894 * 10^{-5}$ kg/m
Reynolds no.	3 million	3 million	3 million
Chord length	1 m	1 m	1 m
Angle of attack	2 to 18°	2 to 18°	2 to 18°
Fluid	Air	Air	Air
Turbulent viscosity ratio	10	10	10
Momentum	Second Order upwind	Second Order upwind	Second Order upwind
Pressure velocity coupling	Simple	Simple	Simple
Residual	1.00E-06	1.00E-06	1.00E-06
No. of iteration	10000	10000	10000
No. of elements	73999	74361	65831
No. of nodes	74736	75103	65909
Orthogonal quality	0.26535	0.39182	$2.9741e^{-002}$
Skewness	$8.5388 * e^{-005}$	$5.0151e^{-005}$	$1.2041e^{-004}$
Aspect ratio	Max - 33.116	Max - 33.069	Max - 76.637
Surface area	557.86 m ²	557.85 m ²	557.87 m ²
Dimension	2D	2D	2D
Solver	Pressure based steady state	Pressure based steady state	Pressure based steady state
Ratio of specific heats	1.4	1.4	1.4
Initialization methods	Standard	Standard	Standard

5 Results and Discussion

5.1 Grid Independency Test

This environment consist of two squares and one semicircle around the NACA0012, NACA4412 and JOUKOWSKI ($T = 12\%$) airfoil. In this study the meshing is done to a very fine region closer to all airfoils, and more coarser to the surface away from all the airfoils. In this geometry quadratic meshing was used for solving the problem.

Coefficient of lift is determined at AOA 10°. Compare the final results for different mesh (No. of elements and nodes) show the minimum changes of result with the quadratic meshing having numbers of element 73999 for NACA0012, 74361 for NACA4412 and 65831 for JOUKOWSKI (T = 12%) airfoil shown above in Table 2. After this meshing result are not affect by following meshing up so that all simulation will complete on the same meshing files and all the final result are validating with experimentally data.

Table 2. Grid independency test for NACA0012, NACA4412, JOUKOWSKI (T = 12%) airfoil

Order	No. of elements			Lift coefficients (C_L)		
	NACA0012	NACA4412	JOUKOWSKI	NACA0012	NACA4412	JOUKOWSKI
1	45268	46258	45021	0.875954	1.2846256	0.9262821
2	52256	51236	49025	0.925625	1.3262565	0.9925326
3	58020	57503	54265	0.992565	1.3652549	1.0256253
4	69526	68592	59203	1.012456	1.3923569	1.0562552
5	71256	72362	62352	1.023658	1.4023561	1.0692525
6	73999	74361	65831	1.049895	1.4235183	1.0870212

5.2 Numerical Results of NACA0012, NACA4412 and Joukowski (T = 12%) Airfoil

The k- ϵ models solve for two variables, the first one is 'k' is known as the turbulence kinetic energy and second one is ' ϵ ' is known as the rate of dissipation of turbulence kinetic energy.

5.2.1 NACA0012 Airfoil

Tables 3, 4 and 5 represent that how lift and drag coefficient is varying by AOA and where is the maximum C_L/C_D ratio for NACA0012, NACA4412, JOUKOWSKI (T = 12%) airfoil. Lift and Drag force are calculated by formula which is given below (Fig. 2).

$$\text{Lift Force}(L) = \frac{1}{2} \rho_C C_L v^2 \quad (1)$$

$$\text{Drag Force}(D) = \frac{1}{2} \rho_C C_D v^2 \quad (2)$$

Table 3. Numerical results of NACA0012 airfoil

AOA (α)	Coefficient of lift (C_L)	Coefficient of drag (C_D)	C_L/C_D	Lift force	Drag force
2	0.21616083	0.009391026	23.01780788	254.2538169	11.04596138
4	0.43016895	0.010467346	41.09627694	505.975562	12.31195621
6	0.64098345	0.012200114	52.53913611	753.9408908	14.35008161
8	0.84682993	0.014637271	57.85435892	996.0627092	17.2167271
10	1.049895	0.018411725	57.02317409	1234.912963	21.65633504
12	1.2375598	0.023512735	52.63359622	1455.649031	27.65627158
14	1.4076691	0.029467722	47.76986494	1655.735878	34.66067739
16	1.5495289	0.038576279	40.16792029	1822.59495	45.37439173
18	1.6163117	0.051188357	31.57576829	1901.146563	60.20903578

5.2.2 NACA4412 Airfoil

Table 4. Numerical results of NACA4412 airfoil

AOA (α)	Coefficient of lift (C_L)	Coefficient of drag (C_D)	C_L/C_D	Lift force	Drag force
2	0.64825046	0.011184021	57.96219982	762.4885311	13.15492741
4	0.85540892	0.012882737	66.3996261	1006.153534	15.15299999
6	1.0582718	0.0153451	68.9648031	1244.765966	18.04929342
8	1.2423949	0.018760403	66.22431832	1461.336198	22.06645889
10	1.4235183	0.022816316	62.39036574	1674.378106	26.837126
12	1.5937527	0.028707254	55.51742079	1874.612099	33.76619576
14	1.7396664	0.034800748	49.98933931	2046.23947	40.933517
16	1.855017	0.043005256	43.13465777	2181.917754	50.58386612
18	1.9062048	0.056406135	33.79428142	2242.126134	66.34631779

5.2.3 JOUKOWSKI (T = 12%) Airfoil

Table 5. Numerical results of JOUKOWSKI (t = 12%) airfoil

AOA	Coefficient of lift (C_L)	Coefficient of drag (C_D)	C_L/C_D	Lift force	Drag force
2	0.2246402	0.00968051	23.2054188	264.227559	11.3864594
4	0.44868715	0.010771937	41.6533396	527.7571356	12.67022382
6	0.66978499	0.012742316	52.56383455	787.8179881	14.98783327
8	0.88526278	0.01590001	55.67686939	1041.268396	18.70199254
10	1.0870212	0.020617468	52.7233121	1278.581735	24.25078555
12	1.2530329	0.027389769	45.74820985	1473.848881	32.2165367
14	1.3393019	0.041411983	32.34092654	1575.320654	48.70981825
16	1.4094153	0.056029278	25.1549788	1657.789802	65.90304908
18	1.2772281	0.10407361	12.27235319	1502.307886	122.4140034

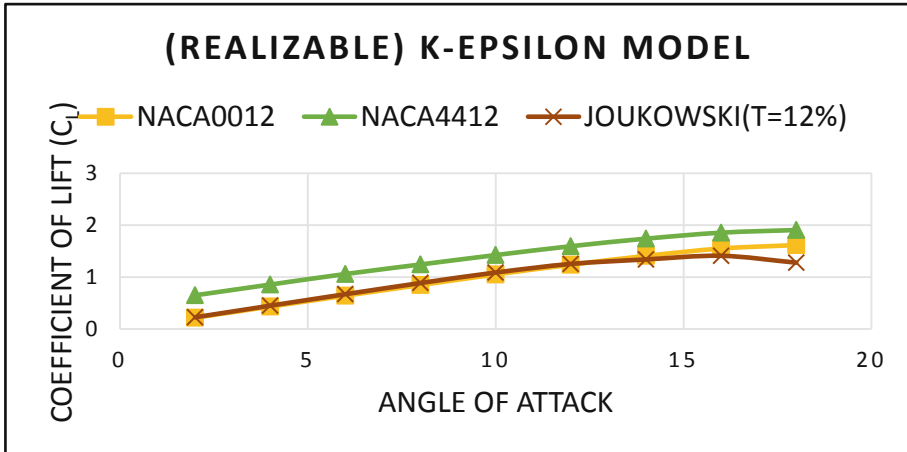


Fig. 2. Lift coefficient (CL) vs Angle of attack

5.3 Distribution of Surface Pressure

Figures 3 and 4 shows relationship between pressure coefficient along with Chord length (Meter) of separately, NACA0012, JOUKOWSKI (t = 12%) airfoil in k-epsilon turbulence model.

The distribution of pressure over the upper surface and lower surface of an airfoil is determined by the dimensionless Parameters called as coefficient of pressure

$$C_p = \frac{Pressure}{0.5 * 1.225 \text{ kg/m}^3 * 43.822 \text{ m/s}^2} \tag{3}$$

The pressure coefficient having high suction zenith on the side of suction surface close to leading edge and further it is moderately increasing in the pressure of suction. The pressure coefficient (Cp) determines maximum values at the side of pressure which is close to the top leading edges. At α = 2°, Pressure varies on the suction side on all the airfoil. The value of the suction pressure surface side were ranging from -0.50 to -12.50 for NACA0012 and -0.50 to -8.50 for JOUKOWSKI (t = 12%) airfoil with the help of k-epsilon turbulence model from

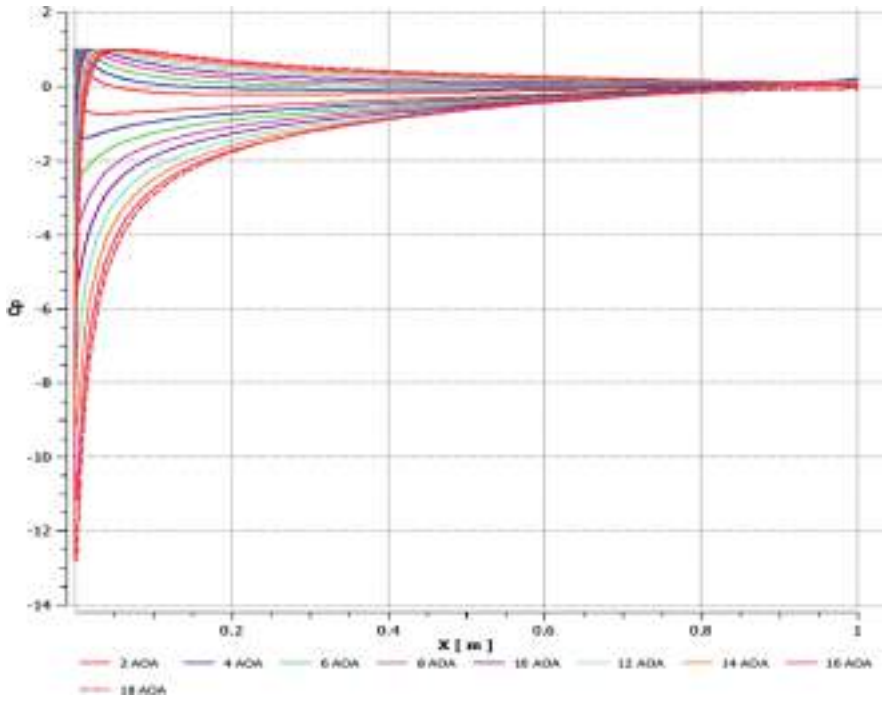


Fig. 3. C_p vs AOA for NACA0012

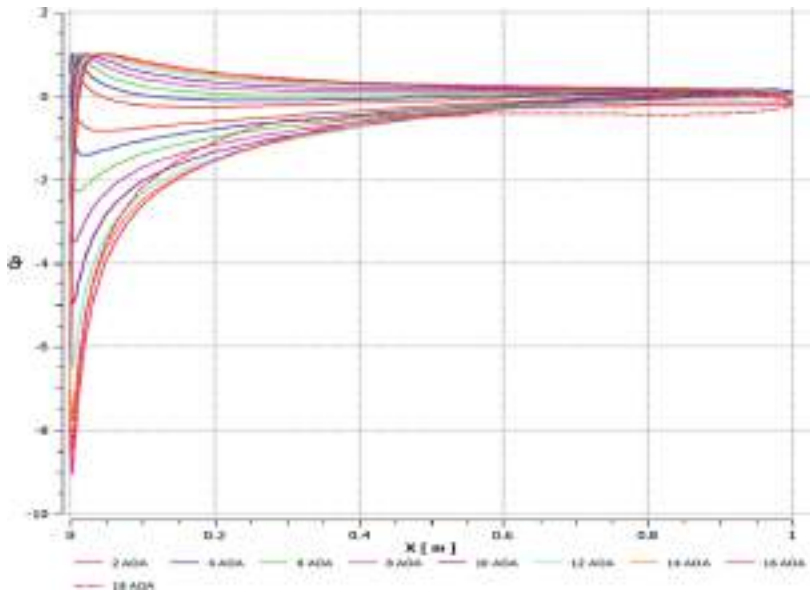


Fig. 4. C_p vs AOA for JOUKOWSKI ($t = 12\%$) airfoil

6 Conclusions

According to the numerical result of NACA4412, NACA0012 and JOUKOWSKI ($t = 12\%$) airfoil, there are various point as shown below:

This study shows mean flow numerical study of NACA4412, NACA0012 and JOUKOWSKI ($t = 12\%$) airfoil, covers all physical phenomenon formation round the airfoil surface.

- It's clearly observed that the less or more negative pressure developed more on the top surface for all airfoil. The values of pressure is -15098.0 Pa in NACA0012 airfoil, -12917.0 Pa in NACA4412airfoil and -9983.0 Pa in JOUKOWSKI ($t = 12\%$) airfoil.
- It's also observed that there is max. Velocity value generated on the top surfaces for all the airfoil. Velocity is 155.775 m/s in NACA0012 airfoil, 144.843 m/s in NACA4412 airfoil along with 128.829 m/s in JOUKOWSKI ($t = 12\%$) airfoil.
- It's described and calculated the max. Ratio of C_L/C_D generated by the 57.85435893 in NACA0012 airfoil, 68.9648032 in NACA4412airfoil and 55.67686929 JOUKOWSKI ($t = 12\%$) airfoil.
- It is already defined that the airfoil will be better, if it's having high ratio of C_L/C_D with another airfoil. In this study, It calculated that NACA 4412 having more higher ratio of C_L/C_D other than NACA0012 and JOUKOWSKI ($t = 12\%$) airfoil that's why it's observed that NACA4412airfoil is superior satisfactory airfoil for the all aerodynamics applications than NACA0012airfoil and JOUKOWSKI ($t = 12\%$) airfoil and it's define highest ratio of C_L/C_D and lowest wake and eddies generation.
- It's also seems that some Joukowski ($t = 12\%$) airfoil result are close to NACA0012 airfoil (symmetrical airfoil). That why it may say that within the future if we are going to work on the design or planning section of the Joukowski ($t = 12\%$) airfoil. It would describe close and better result for the same thickness of all NACA symmetrically airfoil and furthermore it would be used in modern and latest aircraft.


References

1. Jain, R., Mohammad, U.: CFD approach of Joukowski airfoil ($T = 12\%$), comparison of its aerodynamic performance with NACA airfoils using k- ϵ turbulence model with 3 million reynolds number. *IRJET* **5**(10), 1414–1418 (2018)
2. Bhargava, V., Rao, Ch.K., Dwivedi, Y.D.: Pressure distribution & aerodynamic characteristics of NACA airfoils using computational panel method for 2D lifting flow. *Int. J. Eng. Res.* **5**(11), 2347–5013 (2017)
3. He, W., Yu, P., Li, L.K.B.: Ground effects on the stability of separated flow around a NACA 4415 airfoil at low Reynolds numbers. *Aerosp. Sci. Technol.* **72**, 63–76 (2018)
4. D'Souza, A.G., Concessao, J.I., Quadros, J.: Study of airfoil design parameters for low speed wind tunnel. *J. Mech. Eng. Autom.* **5**(3B), 47–54 (2015)
5. Şahin, I., Acir, A.: Numerical and experimental investigations of lift and drag performances of NACA 0015 wind turbine airfoil. *Int. J. Mater. Mech. Manuf.* **3**(1), 22–25 (2015)

6. Ceyhan, C.: Towards 20MW wind turbine: high reynolds number effects on rotor design. In: 50th AIAA Aerospace Sciences Meeting including the New Horizons Forum and Aerospace Exposition 09–12 January 2012 (2012)
7. Camarius, A., et al.: Numerical study of the optimization of separation control (2007)
8. Wong, C., Kontis, K.: Flow control by spanwise blowing on a NACA 0012. *J. Aircr.* **44**(1), 337–340 (2007)
9. Huang, L., et al.: Numerical study of blowing and suction control mechanism on NACA0012 airfoil. *J. Aircr.* **41**(5), 1005–1013 (2004)
10. Joslin, R.D., Miller, D.N.: *Fundamentals and Applications of Modern Flow Control*. American Institute of Aeronautics and Astronautics, Reston (2009)
11. Abbott, I.H., Von Doenhoff, A.E.: *Theory of Wing Sections*. Dover Publications, NewYork (1959)
12. Gad-el-Hak, M.: *Control Flow: Passive, Active and Reactive Flow Management*, pp. 25–35. Cambridge University Press, Cambridge (2000)
13. Liu, Y., et al.: Computational evaluation of the steady and pulsed jet effects on the performance of a circulation control wing section. In: AIAA, p. 56 (2004)
14. Ekaterinaris, J.A.: Prediction of active flow control performance on airfoils and wings. *Aerosp. Sci. Technol.* **8**(5), 401–410 (2004)
15. Wu, J.Z., et al.: Post-stall flow control on an airfoil by local unsteady forcing. *J. Fluid Mech.* **371**(1), 21–58 (1998)
16. Anders, S.G., Sellers, W.L., Washburn, A.: Active flow control activities at NASA Langley. In: AIAA 2623, no. 2 (2004)



FDTM Modeling to Analyze Flow Circulation Inside a Lid-Driven Cavity

Siddhartha Kosti^(✉) 

Department of Mechanical Engineering, Rajkiya Engineering College,
Banda 210201, India
siddharth.kosti@gmail.com

Abstract. Flow circulation analysis is conducted in the present work inside a lid-driven cavity. To analyze the flow circulation, Navier-Stokes (N-S) equation is solved using FDTM (finite difference time domain) modeling. As the N-S equation involves the pressure term, Stream-vorticity approach is utilized which eliminates the pressure terms from governing equation (GEs). After non-dimensionlization of equations, Reynolds number (Re) comes as a governing parameter of the problem. Three values of Re are considered. Contours of horizontal & vertical velocities, stream-function and vorticity are presented to analyze the flow circulation inside the cavity for different Re values. It is found that increment in the Re results in increment in the flow circulation strength of horizontal and vertical velocities. Increment in the velocity profiles peak values is also observed with increased values of Re.

Keywords: FDTM scheme · Re · Flow circulation · Contours · Navier-Stokes equation

1 Introduction

A lot of research is available on lid-driven-cavity analysis [1–6]. Researchers have also studied the effect of different nanofluids on the flow circulation inside cavity [7–13]. Solving an N-S equation inside a cavity is difficult, but it can be made easy if one adopted the stream-vorticity approach to solving it. Stream-vorticity approach removes the pressure term from the N-S equation which makes the final equation easy to solve. The problem can be made difficult by adding energy equation and temperature-dependent properties [14–22], these researchers have studied natural convection while some have studied forced convection inside a cavity, and they have further added the effect of nanomaterials in the flow circulation, velocity profiles, and heat transfer enhancement. In the present study stream-vorticity approach is adopted to solve the N-S equation for three different values of Re. Three values of Re are considered to analyze its effect on the flow circulation and velocity profiles.

2 Problem Statement

The geometry of the lid-driven cavity is shown in Fig. 1. It can be observed that only the top lid or boundary wall of the cavity has a non-zero velocity while on the other walls velocities are zero. These zero-velocity boundary conditions are also called as no-slip boundary conditions.

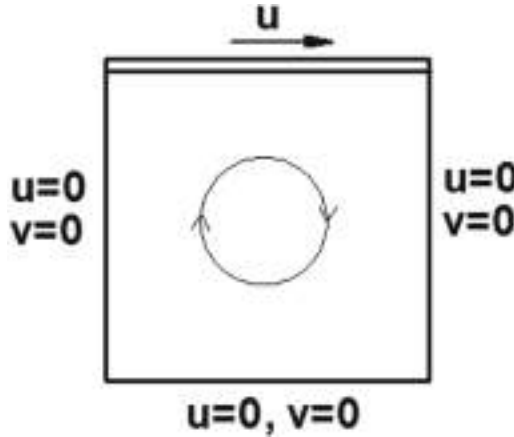


Fig. 1. Schematic of lid-driven cavity

3 Governing Equations (GEs)

Equation 1 to 3 shows the GEs involved in the present problem. Equation 1 is the continuity equation or conservation of mass, Eqs. 2 and 3 are the conservation of momentum equation for X-direction and Y-direction respectively. As can be seen that Eqs. 2 and 3 involve pressure term, and to solve there is no direction equation available for pressure, to eliminate this stream-vorticity approach is adopted and solve the above GEs.

$$\frac{\partial u}{\partial x} + \frac{\partial v}{\partial y} = 0 \tag{1}$$

$$\frac{\partial u}{\partial t} + u \frac{\partial u}{\partial x} + v \frac{\partial u}{\partial y} = -\frac{1}{\rho} \frac{\partial p}{\partial x} + \frac{\mu}{\sigma} \left(\frac{\partial^2 u}{\partial x^2} + \frac{\partial^2 u}{\partial y^2} \right) \tag{2}$$

$$\frac{\partial v}{\partial t} + u \frac{\partial v}{\partial x} + v \frac{\partial v}{\partial y} = -\frac{1}{\rho} \frac{\partial p}{\partial y} + \frac{\mu}{\rho} \left(\frac{\partial^2 v}{\partial x^2} + \frac{\partial^2 v}{\partial y^2} \right) \tag{3}$$

As can be seen that Eqs. 2 and 3 involve pressure term, and to solve there is no direction equation available for pressure, to eliminate this stream-vorticity approach is adopted and solve the above GEs. Equation 4 is the relationship between the

stream-function and horizontal & vertical velocities. Equation 5 is the relationship between the vorticity and stream-function. Equation 6 is the Vorticity transport equation which includes the Re term in it.

$$u = \frac{\partial \psi}{\partial x}, v = -\frac{\partial \psi}{\partial y} \tag{4}$$

$$\omega = \frac{\partial v}{\partial x} - \frac{\partial u}{\partial y} = -\left(\frac{\partial^2 \psi}{\partial x^2} + \frac{\partial^2 \psi}{\partial y^2}\right) \tag{5}$$

$$\frac{\partial \omega}{\partial t} + u \frac{\partial \omega}{\partial x} + v \frac{\partial \omega}{\partial y} = \frac{1}{Re} \left(\frac{\partial^2 \omega}{\partial x^2} + \frac{\partial^2 \omega}{\partial y^2}\right) \tag{6}$$

In the above equations, ψ represents the stream-function and ω represents the vorticity

4 Finite Difference Time Domain (FDTM) Scheme

FDTM scheme is adopted to discretize the partial differential Eqs. 4–6. As FDTM scheme helps in converting the partial terms (spatial and temporal) into algebraic terms which are easier to solve. FDTM scheme is based on Taylor’s series expansion, forward, backward, as well as central discretization differencing schemes, are considered as required. To analyze the flow circulation, different nodes inside the cavity are considered. Fine mesh is adopted to achieve an accurate solution at different discrete nodes. To do this cavity is divided into the small number of nodes. Using the FDTM scheme we can rewrite the Eqs. 4–6 into algebraic form as shown in Eqs. 7–9.

$$u_{i,j} = \frac{\partial \psi}{\partial y} = \frac{\psi_{i,j+1} - \psi_{i,j-1}}{2\Delta y}, v_{i,j} = -\frac{\partial \psi}{\partial x} = -\frac{\psi_{i+1,j} - \psi_{i-1,j}}{2\Delta x} \tag{7}$$

$$\omega_{i,j} = -\left(\frac{\partial^2 \psi}{\partial x^2} + \frac{\partial^2 \psi}{\partial y^2}\right) = -\left(\frac{\psi_{i+1,j} + \psi_{i-1,j} - 2\psi_{i,j}}{(\Delta x)^2} + \frac{\psi_{i,j+1} + \psi_{i,j-1} - 2\psi_{i,j}}{(\Delta y)^2}\right) \tag{8}$$

$$\begin{aligned} &\frac{\omega_{i,j}^{n+1} - \omega_{i,j}^n}{\Delta t} + u_{i,j} \frac{\omega_{i+1,j}^n - \omega_{i-1,j}^n}{2\Delta x} + v_{i,j} \frac{\omega_{i,j+1}^n - \omega_{i,j-1}^n}{2\Delta y} \\ &= \frac{1}{Re} \left(\frac{\omega_{i+1,j}^n + \omega_{i-1,j}^n - 2\omega_{i,j}^n}{(\Delta x)^2} + \frac{\omega_{i,j+1}^n + \omega_{i,j-1}^n - 2\omega_{i,j}^n}{(\Delta y)^2}\right) \end{aligned} \tag{9}$$

Equations 8 and 9 can be rewritten as,

$$\psi_{i,j} = \frac{\left(\omega_{i,j} + \frac{\psi_{i+1,j} + \psi_{i-1,j}}{(\Delta x)^2} + \frac{\psi_{i,j+1} + \psi_{i,j-1}}{\Delta y^2}\right)}{2\left(\frac{1}{(\Delta x)^2} + \frac{1}{(\Delta y)^2}\right)} \quad (10)$$

$$\begin{aligned} \omega_{i,j}^{n+1} = \omega_{i,j}^n - \Delta t & \left[\frac{\psi_{i,j+1} - \psi_{i,j-1}}{2\Delta y} \times \frac{\omega_{i+1,j}^n - \omega_{i-1,j}^n}{2\Delta x} + \frac{\psi_{i+1,j} - \psi_{i-1,j}}{2\Delta x} \right. \\ & \times \frac{\omega_{i,j+1}^n - \omega_{i,j-1}^n}{2\Delta y} \\ & \left. + \frac{1}{Re} \left(\frac{\omega_{i+1,j}^n + \omega_{i-1,j}^n - 2\omega_{i,j}^n}{(\Delta x)^2} + \frac{\omega_{i,j+1}^n + \omega_{i,j-1}^n - 2\omega_{i,j}^n}{(\Delta y)^2} \right) \right] \end{aligned} \quad (11)$$

5 Boundary Condition

Initially, the cavity is assumed to be non-moving that means velocities, stream-function and vorticity are zero as shown in Eq. 12. Equation 13 shows the boundary conditions at the two vertical walls ($x = 0$ & $x = L$). Equations 14 and 15 show the boundary conditions at the bottom and top wall respectively. One can observe that the only difference is in the horizontal velocity.

$$\text{at } t = 0 \rightarrow u = 0, v = 0, \psi = 0, \omega = 0 \quad (12)$$

$$u = 0, v = 0, \psi = 0, \omega = -\frac{\partial^2 \psi}{\partial x^2} \quad (13)$$

$$u = 0, v = 0, \psi = 0, \omega = -\frac{\partial^2 \psi}{\partial y^2} \quad (14)$$

$$u = u, v = 0, \psi = 0, \omega = -\frac{\partial^2 \psi}{\partial y^2} \quad (15)$$

6 Result and Discussion

Flow circulation is analyzed by studying the contours of horizontal & vertical velocities, stream-functions, and vorticity. Figures 2, 3, 4 represents flow circulation of horizontal velocity, vertical velocity, stream-function and vorticity for three values of Reynolds number inside the lid-driven cavity. Stream-function contours also called

streamlines and they represent the flow distribution. Results indicate that increment in the Re increases the intensity of the flow circulations inside the cavity, this may be due to the fact that increment in the Re results in increment in the velocity inside the cavity as other parameters (density, height/length, and viscosity) are all constant. This increased velocity increases the flow velocity and increases the intensity of the flow inside the cavity. It can be noticed that increment in Re circulations in the lower part of the cavity increases, this may be due to the fact that increases Re values increase the strength of the contours in the lower part of the cavity due to the backflow of water, this can be easily observed by increment in the triangular contours of steam-functions.

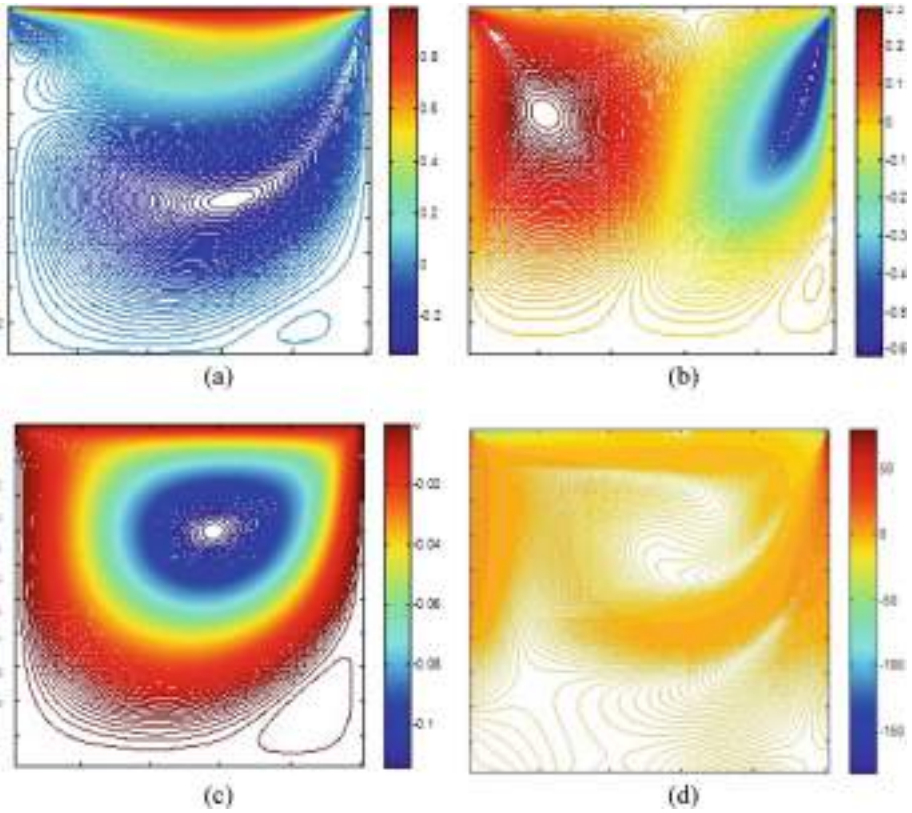


Fig. 2. Flow circulation for $Re = 300$ (a) horizontal velocity (b) vertical velocity (c) stream-function (d) vorticity

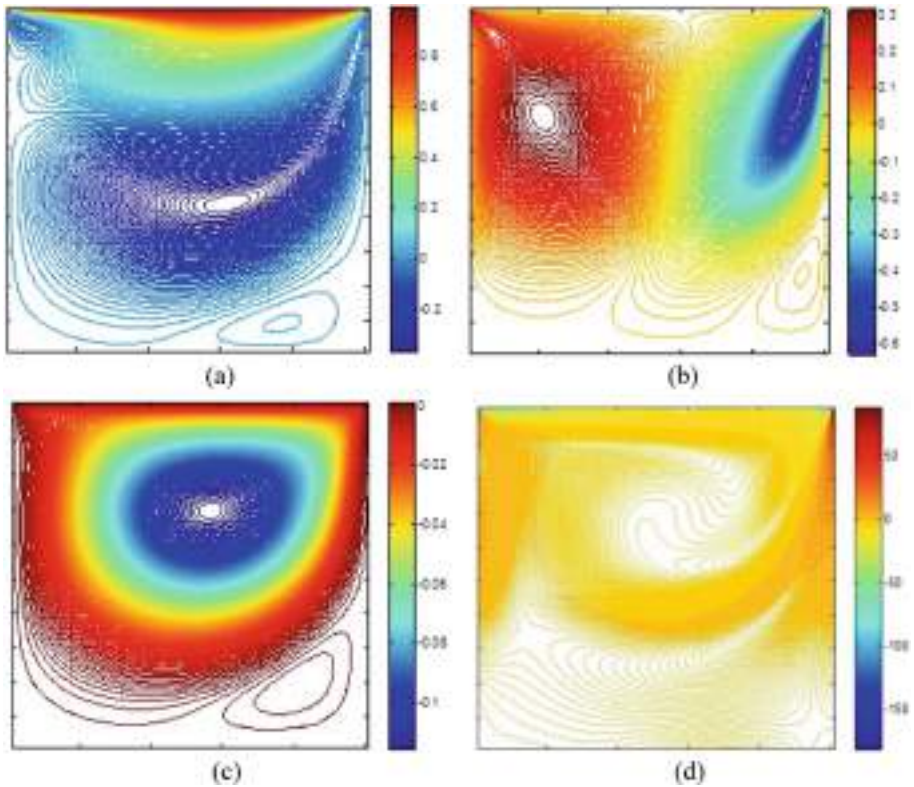


Fig. 3. Flow circulation for $Re = 400$ (a) horizontal velocity (b) vertical velocity (c) stream-function (d) vorticity

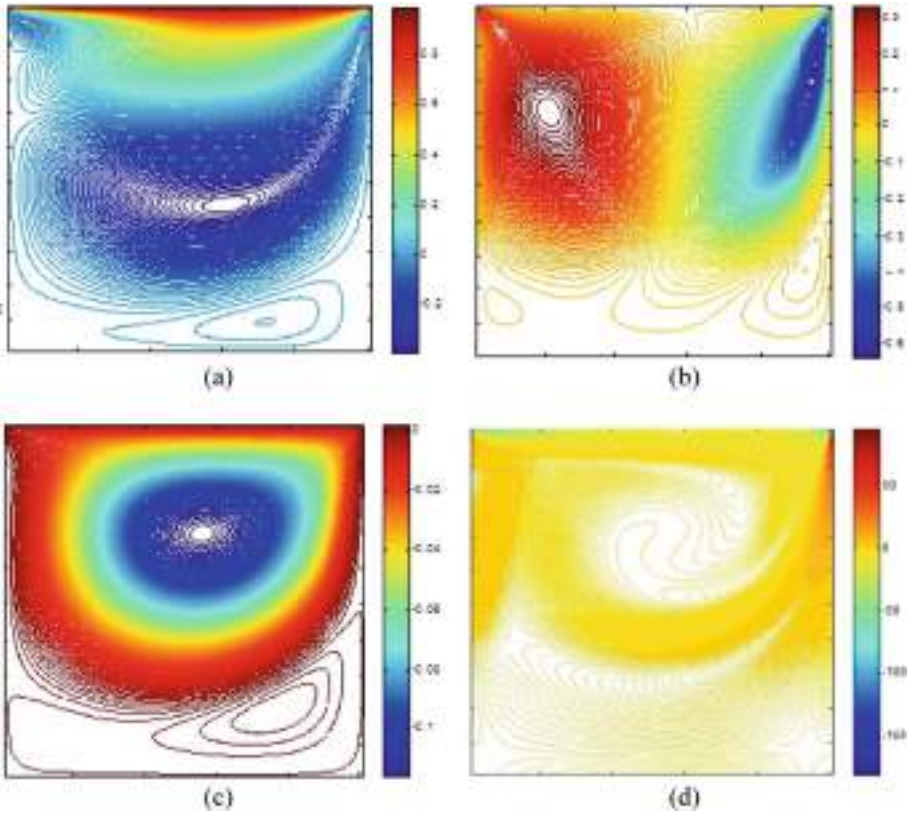


Fig. 4. Flow circulation for $Re = 500$ (a) horizontal velocity (b) vertical velocity (c) stream-function (d) vorticity

Figures 5 and 6 represents the horizontal and vertical velocity profile for three different Re values. Velocity profiles are plotted along the length and height respectively. One can easily observe the difference between the velocity profiles. Increment in the Re results in increment in the highest values.

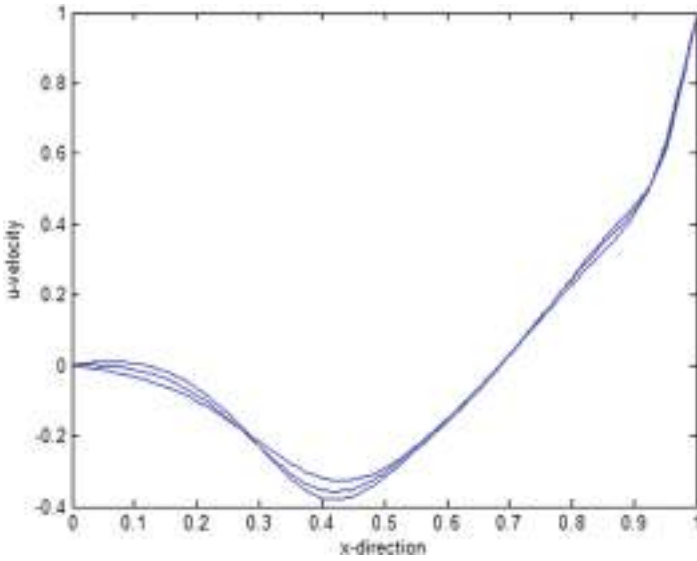


Fig. 5. Horizontal velocity profiles for different Re values

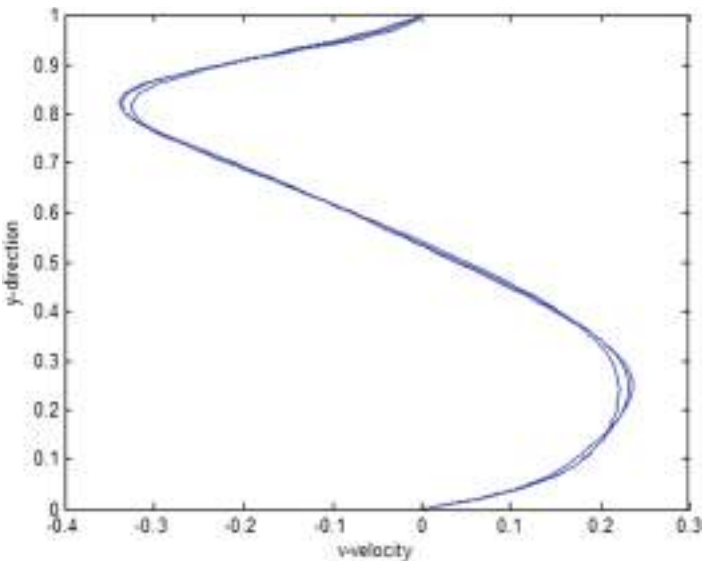


Fig. 6. Vertical velocity profile for different Re values

7 Conclusion

- FDTM scheme gives good results for all the values of Re considered.
- Increment in Re increases the intensity of the flow circulation inside the cavity.

- Increment in Re increases the highest values of horizontal and vertical velocity profiles.
- Thinner vortices start to form near the lower lid with increment in the Reynolds number.

References

1. Chen, S.: Large-eddy-based lattice Boltzmann model for turbulent flow simulation. *Appl. Math. Comput.* **215**, 591–595 (2009)
2. Sidik, N.A.C., Attarzadeh, S.M.R.: An accurate numerical prediction of solid particle fluid flow in a lid-driven cavity. *Int. J. Mech.* **5**(3), 123–128 (2011)
3. Li, S.L., Chen, Y.C., Lin, C.A.: Multi relaxation time lattice Boltzmann simulations of deep lid driven cavity flows at different aspect ratios. *Comput. Fluids* **45**(1), 233–240 (2011)
4. Chamkha, A.J.: Hydromagnetic combined convection flow in a vertical lid-driven cavity with internal heat generation or absorption. *Numer. Heat Transf. Part A* **41**, 529–546 (2002)
5. Khanafer, K.M., Al-Amiri, A.M., Pop, I.: Numerical simulation of unsteady mixed convection in a driven cavity using an externally excited sliding lid. *Eur. J. Mech. B/Fluids* **26**, 669–687 (2007)
6. Batchelor, G.K.: On steady laminar flow with closed streamlines at large Reynolds numbers. *J. Fluid Mech.* **1**, 177–190 (1956)
7. Kosti, S., Das, M.K., Saha, A.K.: Buoyancy-driven flow and heat transfer in a nanofluid-filled enclosure. *Nanomater. Energy* **2**(4), 200–211 (2013)
8. Kosti, S.: Numerical study of heat flux boundary in nanofluid-filled cavity. *Nanomater. Energy* **3**(6), 193–205 (2014)
9. Kosti, S.: Nanoparticle reinforcement effect on the MMC's. In: *Advances in Interdisciplinary Engineering*, pp. 459–469. Springer (2019)
10. Kosti, S., Das, M.K., Saha, A.K.: Effect of nano-fluids on buoyancy-driven flow in a two-dimensional rectangular cavity. In: *Proceedings of 22nd National and 11th International ISHMT-ASME Heat and Mass Transfer Conference*, 28–31 December, IIT Kharagpur, India (2013)
11. Kosti, S.: Heat-flux and convective boundary influence on nano-fluids filled cavity. *Emerg. Mater. Res.* **8**(4), 1–9 (2019)
12. Kosti, S.: Natural convection in nanofluid-filled enclosure with heat flux boundary. *J. Mech. Eng. Technol.* **6**(2), 1–12 (2014)
13. Kosti, S., Malvi, C.S.: Cumulative influence of nanoparticles on MMCs time-temperature history curve. *Nanomater. Energy* **7**(1), 1–10 (2018)
14. Kosti, S., Pathak, P.: Genetic algorithm based finite difference simulation of solidification process of MMC's. *Mater. Today: Proc.* **5**, 8271–8279 (2018)
15. Rubel, A., Landis, F.: Numerical study of natural convection in a vertical rectangular enclosure. *Phys. Fluids* **12**, 208–213 (1969)
16. Khanafer, K., Vafai, L., Lightstone, M.: Buoyancy-driven heat transfer enhancement in a two-dimensional enclosure utilizing nano-fluids. *Int. J. Heat Mass Transf.* **46**, 3639–3653 (2003)
17. Turan, O., Poole, R.J., Chakraborty, N.: Influences of boundary conditions on laminar natural convection in rectangular enclosures with differentially heated side walls. *Int. J. Heat Fluid Flow* **33**, 131–146 (2012)

18. Lai, F.H., Yang, Y.T.: Lattice Boltzmann simulation of natural convection heat transfer of Al_2O_3 /water nano-fluids in a square enclosure. *Int. J. Therm. Sci.* **50**, 1930–1941 (2011)
19. Bilgen, E., Muftuoglu, A.: Natural convection in an open square cavity with slots. *Int. Commun. Heat Mass Transf.* **35**, 896–900 (2008)
20. Tiwari, R.K., Das, M.K.: Heat transfer augmentation in a two-sided lid-driven differentially heated square cavity utilizing nano-fluids. *Int. J. Heat Mass Transf.* **50**, 2002–2018 (2007)
21. Talebi, F., Mahmoudi, A.H., Shahi, M.: Numerical study of mixed convection flows in a square lid-driven cavity utilizing nano-fluid. *Int. Commun. Heat Mass Transf.* **37**, 79–90 (2010)
22. Kosti, S., Kundu, J.: Numerical modelling of nanocomposites using GA and FD techniques. *Mater. Sci. Forum* **969**, 478–483 (2019)



Adsorptive Removal of Cadmium Using Agro-Residue

Chavi Tomar, Vinita Khandegar^(✉), and Perminder Jit Kaur

University School of Chemical Technology,
Guru Gobind Singh Indraprastha University, Dwarka, New Delhi, India
chavitomar05@gmail.com, vinita@ipu.ac.in,
perminder.dua@gmail.com

Abstract. The presence of heavy metals and toxins in the eco-system is a matter of concern for environmentalists and researchers globally. Heavy metals like Cadmium is hazardous not only for human health, but also for the whole environment. It leads to various diseases like dysfunction of the kidney in human beings and contamination of the whole food chain. This work concerns the use of sugarcane bagasse for the adsorption of cadmium Cd (II) metal from an aqueous solution. Experiments were performed using a batch process with raw biochar prepared by sugarcane bagasse at 700 °C pyrolysis. Effect of parameters including contact time, adsorbent dosage, initial concentration and pH of the aqueous solution on removal efficiency were investigated and optimized. Higher removal efficiency (98%) has been achieved at 1 (mg/l) Cd (II) concentration in 4 h of time at 4 mg of adsorbent dose and pH 9.2. It was observed that the sugarcane bagasse can be used as an alternative, attractive, effective, economical, and environmentally friendly adsorbent for Cd (II) removal from wastewater.

Keywords: Agro-residue · Adsorption · Cadmium · Removal

1 Introduction

Increasing human population and urbanization have led to a deterioration in the quality of eco-system as a whole. Heavy metals and toxins from industrial effluents, municipal sewage waste have caused a severe global environmental problem. [1]. One of the most toxic metal is Cadmium obtained from electronic waste, industrial effluents, etc. The hazardous effect of this metal on human health as well on the environment are well-known. On accumulation in human body especially in the kidneys, it causes its dysfunction of the kidney. Uptake of metal through the soil to plants can contaminate the whole food chain [2]. Cadmium is known to affect the leaf litter decomposition [3].

Unlike organic pollutants, natural degradation of heavy metals is not possible. There are certain well-developed metal remediation techniques like chemical precipitation, membrane treatment, adsorption on activated carbon. However, their associated high cost makes them unattractive techniques. Thus, researchers are trying to remediate metals using various innovative new techniques, which are under the development stages [4].

The agricultural residue is a problem to dispose of. There are efforts to utilize various value-added products using them. Thus the present study makes an effort towards the development of cost-effective adsorbent from agricultural waste (sugarcane bagasse) for the removal of cadmium metal from aqueous waste. Parameters such as contact time, pH, adsorbent dose, the concentration of cadmium (II) on metal removal efficiency have been studied and analyzed.

2 Materials and Method

2.1 Preparation of Biochar

Sugarcane bagasse was first washed with water sundried and then dried in oven 75 °C for 12 h. A mini tubular reactor was designed and fitted inside a bench-top furnace (paralyzer). It was purged with nitrogen gas at 10 psi. 100 g of dried bagasse was charged into the furnace. The reactor was equipped with an oxygen sensor to maintain the oxygen content in the reactor was less than 0.5% [5]. The reactor was again purged with nitrogen along with the furnace and sealed for pyrolysis of 100 g of dried bagasse. The controller of the furnace was maintained at 700 °C temperature and increased was at a rate of 100 °C/min. It was held at peak temperature for 2 h before cooling to room temperature. Biochar thus produced was crushed and sieved through 2.2 mm sieve.

2.2 Preparation of Synthetic Solution

Aqueous solution of cadmium was prepared by dissolving an appropriate amount of cadmium nitrate procured from Qualigens fine chemicals, India. Dilution of 1000 mg/L of Cd (II) solutions of lower concentrations was done using distilled water. The samples are shown in Fig. 2. Sodium hydroxide and sulphuric acid solutions were obtained from Merck, India. They were used to adjust the pH of the initial solution. All solutions were prepared from analytical grade chemical reagents. Adsorption experiment

2.3 Experimental Set-up

Batch studies of adsorption properties of sugarcane bagasse (SCB) were conducted. A 100 mL of different ppm Cd (II) solution was taken in 250 mL flask. A known amount of 1 mg of SCB was mixed in different concentration of cadmium (II) solution. Mixing was done using an agitator maintained at 100 rpm for different duration of time. Similarly, solutions of different pH solution were prepared and were agitated in an incubator shaker at 100 rpm for 4 h. The content from the flask was taken separately and filtered. The residual concentration of filtrate was analyzed using

spectrophotometrically against blank. The cadmium removal efficiency and equilibrium biosorption capacity were calculated as follows:

$$C_E = \left(\frac{C_o - C_i}{C_o} \right) \times 100 \quad (1)$$

where C_E = Cadmium removal efficiency (%)

C_o and C_i = Initial and final concentrations of cadmium (mg/L)

C_e = Equilibrium concentrations of cadmium (mg/L)

3 Results and Discussion

3.1 Characterization of Biochar

Figure 1 shows the SEM images which showed significant changes in the surface of biochar before and after adsorption. The SEM images in Fig. 1(a) showing fibrous channels in biochar before adsorption. In Fig. 1(b) biochar's structure consisted of a highly complex network of pores filled with cadmium ions.

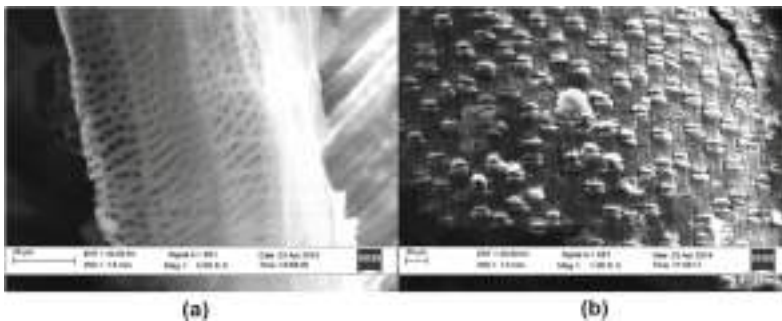


Fig. 1. SEM images of biochar (a) before adsorption (b) after adsorption: parametric study

3.2 Effect of PH

The experiment has been conducted for cadmium removal efficiency with SCB as an adsorbent. The pH was varied from different range (3.2, 5.2, 7.2, and 9.2) for SCB and the other parameters remained constant. The pH of the solution was adjusted by adding NaOH or H₂SO₄ to get the desired pH. The initial concentration of Cd (II) in the solution was 1 mg/L and the mixture was agitated at 100 rpm for 4 h SCB respectively. Results are shown in Fig. 2.

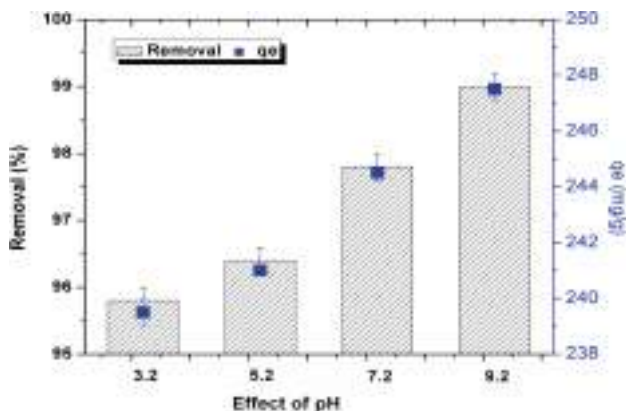


Fig. 2. Effect of pH on metal removal efficiency

3.3 Effect of Dose

The experiment has been conducted for cadmium removal efficiency with SCB as an adsorbent. The initial concentration was varied from different range 1 to 4 mg/L for SCB and the other parameters remained constant. The adsorbent dosages efficiency for cadmium removal of Cd (II) are shown in Fig. 3. The removal efficiency of Cd (II) was found to be increased as the dosage was increased due to the greater availability of adsorption sites [6].

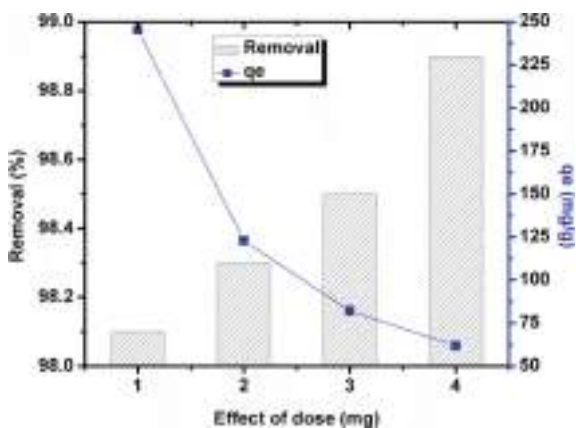


Fig. 3. Effect of dose on metal removal efficiency

3.4 Effect of Time

The experiment has been conducted for cadmium removal efficiency with sugarcane bagasse as an adsorbent at a different time interval. The contact time was varied from

1 h to 4 h for sugarcane bagasse and the other parameters remained constant and the results are shown in Fig. 4. The Cd (II) removal efficiency was found to increase significantly (92.2, 94.2, 97, 99) respectively. Similar finding was reported by [4, 7].

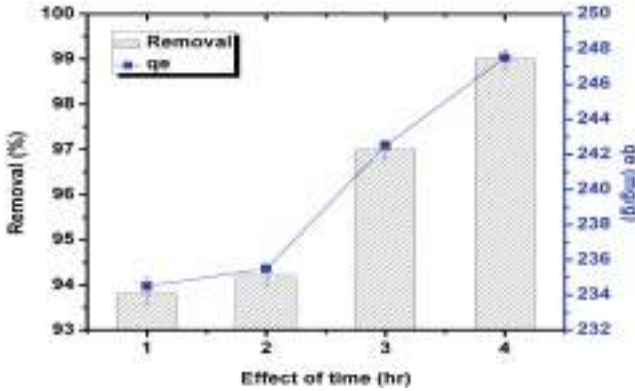


Fig. 4. Effect of time on metal removal efficiency

3.5 Comparison with the Literature

Results of the present study was compared with the study reported by other researchers and the comparison is shown in Table 1. It can be observed from the Table 1 that biochar used in the present study has the potential to remove Cd (II).

Table 1. Comparison with previous study

Reference	Biochar	Conditions	Pollutant and removal (%)
[8]	Pinewood	–	Diclofenac (500 µ/L), (43)
[8]	Pig manure	–	Diclofenac (500 µ/L), (95)
[9]	Pineapple waste	2 h and dosage of 1 g	Cd(II) (1 mg/L), (90)
[9]	Sugarcane bagasse	2 h and dosage of 1 g	Cd(II) (1 mg/L), (55)
[9]	Activated carbon	2 h and dosage of 1 g	Cd(II) (1 mg/L), (30)
Present study	Sugarcane bagasse	2 h and dosage of 4 mg	Cd(II) (1 mg/L), (94)

4 Conclusions

This study has a special significance in Indian perspective. The adsorbent can be obtained at a very low cost, as the raw material required to prepare adsorbent is waste material left after the production of sugarcane juice. The development of process can serve a dual purpose. Locally available waste material is used to remove toxic metal like cadmium. The optimum value of pH was found to be 9.2. The percentage removal

of Cd (II) was found to be increased with increasing the adsorbent dose. Further experiments can be performed to improve the metal removal efficiency of bagasse and scale-up studies of the same.

References

1. Tyagi, U., Khandegar, V.: Biosorption potential of *Vetiveria zizanioides* for the removal of chromium (VI) from synthetic wastewater. *J. Hazard. Toxic Radioact. Waste* **22**, 1–8 (2018)
2. Chaudhary, A.J., Ganguli, B., Grimes, S.M.: The use of chromium waste sludge for the adsorption of color from dye effluent streams. *J. Chem. Technol. Biotechnol.* **77**, 767–770 (2002)
3. Xu, L., Cao, G., Xu, X., Liu, S., Duan, Z., He, C., Wang, Y., Huang, Q.: Simultaneous removal of cadmium, zinc and manganese using electrocoagulation: influence of operating parameters and electrolyte nature. *J. Environ. Manag.* **204**, 394–403 (2017)
4. Sharma, A., Syed, Z., Brighu, U., Gupta, A.B., Ram, C.: Adsorption of textile wastewater on alkali-activated sand. *J. Clean. Prod.* **220**, 23–32 (2019)
5. Liu, Z., Singer, S., Tong, Y., Kimbell, L., Anderson, E., Hughes, M., Zitomer, D., McNamara, P.: Characteristics and applications of biochars derived from wastewater solids. *Renew. Sustain. Energy Rev.* **90**, 650–664 (2018)
6. Singh, H., Chauhan, G., Jain, A.K., Sharma, S.K.: Adsorptive potential of agricultural wastes for removal of dyes from aqueous solutions. *J. Environ. Chem. Eng.* **5**, 122–135 (2017)
7. Tyagi, U., Khandegar, V.: Bio-Sorption Potential of *V. zizanioides* Grass and Roots for the Removal of Cr (VI). *J. Surf. Sci. Technol.* **34**, 19–29 (2018)
8. Lonappan, L., Rouissi, T., Brar, S.K., Verma, M., Surampalli, R.Y.: Adsorption of diclofenac onto different biochar microparticles: dataset – characterization and dosage of biochar. *Data Br.* **16**, 460–465 (2018)
9. Rosmi, M.S., Azhari, S., Ahmad, R.: Adsorption of cadmium from aqueous solution by biomass: comparison of solid pineapple waste, sugarcane bagasse and activated carbon. *Adv. Mater. Res.* **832**, 810–815 (2014)



Optimization of EC Variable for Removal of Acid Violet 17 Dye

Anupam Pathak, Vinita Khandegar^(✉), and Arinjay Kumar

University School of Chemical Technology,
Guru Gobind Singh Indraprastha University, Dwarka, New Delhi, India
pathakanupam911@gmail.com, {vinita, arinjay}@ipu.ac.in

Abstract. Efforts have made to explore the potential of electrocoagulation (EC) process in order to remove Acid Violet 17 (AV 17) dye from synthetic solution. Effect of EC variables such as voltage, time, and spacing was optimized in terms of dye removal efficiency. The maximum (92% and 94%) dye removal efficiency achieved in 3 h at 10 V using Al and Fe electrodes in monopolar configuration. It can be concluded from the present study that the EC process can be a viable method for dye removal.

Keywords: Dyes · Electrocoagulation · Acid Violet 17 · Removal

1 Introduction

In terms of pollution, the textile industry is the second-largest industries in terms of production and among the top polluting sectors with sizeable large volume consumptions of chemicals and water in wet processing [1]. More than 15% of the lost dye released into wastewaters during cloth dyeing and finishing of fibers [2]. Dye containing wastewater consumes dissolved oxygen and responsible for chemical as well as biochemical changes which is harmful to aquatic life [3]. Therefore removal of color from effluents has great attention in nowadays [4, 5]. The processes such as flocculation, adsorption, and ultrafiltration are comparatively expensive than conventional process. Other processes are adsorption and precipitation which are very time intensive and gives less efficiency. Use of chemicals in the chemical process causes secondary pollution also [6]. The most favorable method based on electrochemical technique is electrocoagulation in which metallic hydroxide flocs are created in situ via electrode dissolution in solution and remove the pollutant through flocculation and adsorption [7]. Excessive coagulants addition can be avoided by electrocoagulation. EC process considered an efficacious tool for the management of textile effluent by various researchers due to its high removal efficiency.

2 Materials and Method

2.1 Dye Solution and Analysis

Dye samples were prepared using distilled water and the wavelength for maximum absorption was found to be 540 nm using the wavelength scan via UV spectrophotometer (Hitachi UV2500). The standard calibration curve was plotted against concentration vs. absorbance and a straight line was achieved. Unknown concentrations in the dye solution were calculated using a calibration curve. The following equation was used to compute the removal efficiency, where C_i and C_f are initial and final dye concentrations in the solution (mg/L).

$$\text{Dye removal (\%)} = \left[\frac{(C_i - C_f)}{C_i} \right] \times 100 \quad (1)$$

2.2 EC Experiments

Batch experiments were performed in 200 mL glass beaker using aluminium and iron electrodes. The electrode pair was immersed in the prepared dye solution(s) up to 4 cm and the spacing between both the electrodes was kept as 1 cm. EC assembly was associated with a power source (Sciencetech 4074, India) and provide the required current for the coagulation process. The dye solution(s) was agitated continuously at 300 rpm using magnetic stirrer (Neuation, India) to maintain uniformity. Figure 1 shows the laboratory experimental setup.



Fig. 1. EC experimental setup

3 Results and Discussion

3.1 Voltage Effect on Dye Removal

Voltage is an important parameter to be studied while performing EC, experiments but high voltage lead to too much electricity expenditure as a result high operating cost attain which is not accepted, therefore, in the present study only two voltages 5 V and 10 V were considered for optimization experiments. In each experiments 200 mL dye solution, containing 10 mg/L dye concentration was used. EC run is carried out for 3 h and after EC, solution allowed for sludge settling. The supernatant liquid was centrifuged. The centrifuged supernatants were analyzed for dye concentration using UV spectrophotometer at 540 nm. The results are shown in Fig. 2. It can be depicted from Fig. 2 that voltage has a linear relationship with a removal efficiency of dye. A similar finding was also reported by [8, 9].

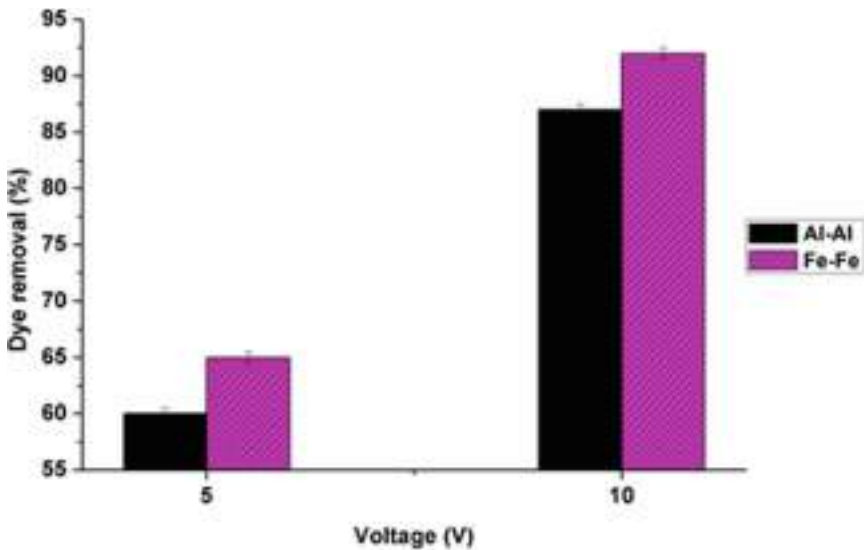


Fig. 2. Effect of voltage

3.2 Time Effect on Dye Removal

One of the most important parameters of electrocoagulation is time, i.e. for how long the dye sample is treated electrochemically would affect the amount of dye removal. The experiment was carried out at discrete intervals of time from 60 to 180 min and the results are shown in Fig. 3. It can be noticed from Fig. 3, that dye removal efficiency increases by increasing the time up to a certain level afterward no more removal recorded. The result indicated that the maximum removal was observed at 180 min.

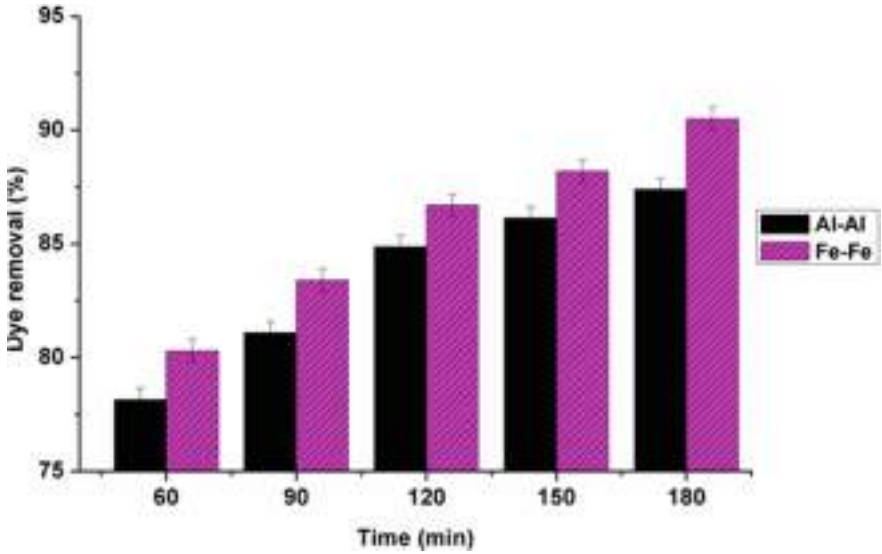


Fig. 3. Time effect

3.3 Spacing Effect on Dye Removal

The effect of spacing between the anode and cathode was investigated by varying the electrode gap from 1–2 cm and the results are shown in Fig. 4. It was estimated from the experiment that on increasing the spacing between the anode and cathode the current density decreased. The possible reason is that the IR resistance increases due to the increase in inter-electrode spacings which increases the cell voltage and adversely affects the dye removal. Low current noticed at minimum inter-electrode spacing in the solution [10]. Therefore, the optimum electrode spacing was found to be 1 cm.

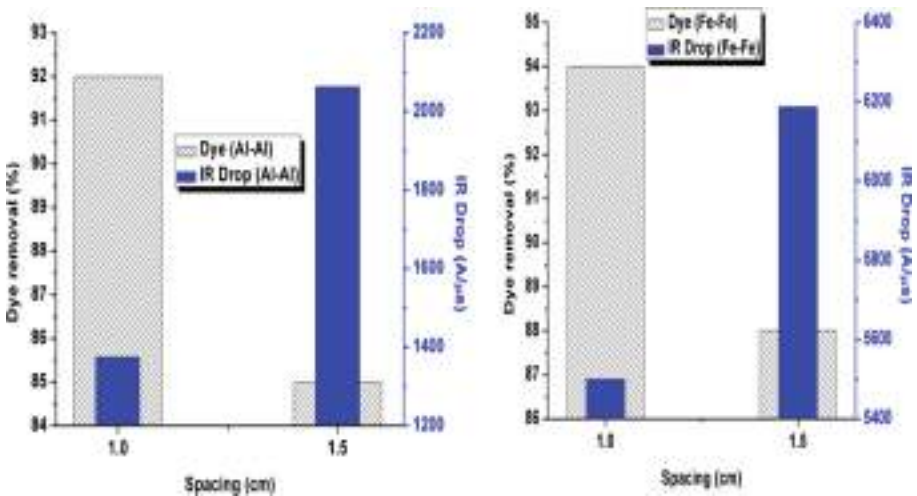


Fig. 4. Spacing effect

4 Conclusions

From the present work, it can be concluded that EC is a fast and economical method for removal of pollutants especially dyes. Also from the present study results, it can be clearly substantiated that electrocoagulation process can be a viable technique for the removal of dyes from the effluents of textile, food and printing mills. The optimum electrolysis time was obtained to be 3 h at which 92% and 94% dye removal efficiency obtained using Al-Al and Fe-Fe electrode respectively at 10 V. Hence it can be stated that EC using Fe-Fe electrodes in monopolar configuration was the most efficient mode for dye removal.

References

1. Tyagi, N., Mathur, S., Kumar, D.: Electrocoagulation process for textile wastewater treatment in continuous upflow reactor. *J. Sci. Ind. Res. (India)* **73**, 195–198 (2014)
2. Daneshvar, N., Oladegaragoze, A., Djafarzadeh, N.: Decolorization of basic dye solutions by electrocoagulation: an investigation of the effect of operational parameters. *J. Hazard. Mater.* **129**, 116–122 (2006)
3. Khandegar, V., Saroha, A.K.: Electrocoagulation for the treatment of textile industry effluent: a review. *J. Environ. Manag.* **128**, 949–963 (2013)
4. Katheresan, V., Kansedo, J., Lau, S.Y.: Efficiency of various recent wastewater dye removal methods: a review. *J. Environ. Chem. Eng.* **6**, 4676–4697 (2018)
5. Yaseen, D.A., Scholz, M.: Textile dye wastewater characteristics and constituents of synthetic effluents: a critical review. *Int. J. Environ. Sci. Technol.* **16**, 1193–1226 (2019)
6. Pajootan, E., Arami, M., Mahmoodi, N.M.: Binary system dye removal by electrocoagulation from synthetic and real colored wastewaters. *J. Taiwan Inst. Chem. Eng.* **43**, 282–290 (2012)
7. Mollah, M.Y.A., Morkovsky, P., Gomes, J.A.G., Kesmez, M., Parga, J., Cocke, D.L.: Fundamentals, present and future perspectives of electrocoagulation. *J. Hazard. Mater.* **114**, 199–210 (2004)
8. Ghernaout, D., Naceur, M.W., Aouabed, A.: On the dependence of chlorine by-products generated species formation of the electrode material and applied charge during electrochemical water treatment. *Desalination* **270**, 9–22 (2011)
9. Singh, A., Srivastava, A., Tripathi, A., Dutt, N.N.: Optimization of brilliant green dye removal efficiency by electrocoagulation using response surface methodology. *World J. Environ. Eng.* **4**, 23–29 (2016)
10. Ghosh, D., Solanki, H., Purkait, M.K.: Removal of Fe(II) from tap water by electrocoagulation technique. *J. Hazard. Mater.* **155**, 135–143 (2008)



Optimal Weight Design of a Spur Gear Train Using Rao Algorithms

R. Venkata Rao^(✉) and Rahul B. Pawar

Department of Mechanical Engineering, S. V. National Institute of Technology,
Surat, Gujarat, India

ravipudirao@gmail.com, rahulp287@gmail.com

Abstract. In many power transmission high-performance applications, the weight of the gear train is required to be minimized. The weight minimization of a spur gear train as an objective function is considered in this work. This problem contains six mixed type design variables such as four continuous variables, one discrete variable, and one integer variable. The optimum design of this gear train is verified with eight non-linear design constraints. In this work, a spur gear train problem is solved for two different sets of design variables' ranges. Each design of a gear train obtained using the recently proposed Rao algorithms is compared with the designs obtained using other advanced optimization algorithms in previous studies such as particle swarm optimization (PSO), genetic algorithm (GA), simulated annealing (SA), and grey wolf optimizer (GWO). The comparison revealed that the Rao algorithms gave better designs of the spur gear train with minimum weight.

Keywords: Spur gear train · Weight optimization · Engineering design optimization · Rao algorithms

1 Introduction

Gear is one of the commonly used power transmission elements in various mechanical systems such as automobiles, aerospace, machine tools, etc. Two or more meshing gears that are working in a sequence are called transmission or a gear train. Generally, gears are employed to change direction, speed, and also the torque of a power source. The design of a gear train is a difficult task due to its complex geometry. The optimization of gear train design is an important task to intensify the performance of various power transmission systems. A design of a gear train involves so many design parameters, empirical formulas of various factors, standard tables and graphs, and the number of constraints. So that the optimization of a gear train design becomes a difficult and complex process for designers. The researchers are working to solve such complex design optimization problems and to improve their performance using various advanced optimization algorithms.

Tamboli *et al.* (2014) proposed a helical gear pair design optimization of the heavy-duty application using particle swarm optimization (PSO) technique. Miler *et al.* (2017) studied the spur gear train optimization using GA with consideration of the profile shift. Rai *et al.* (2018) presented the volume minimization of a helical gear pair having

design variables as the module, the face width, the number of teeth, and the coefficients of profile shift using a real coded genetic algorithm (RCGA). Patil et al. (2019) proposed a helical gearbox optimization using a non-dominated sorting GA (NSGA-II) considering a bi-objective case. Artoni (2019) presented an optimization of hypoid gear using a direct-search global optimization algorithm. Dorterler *et al.* (2019) solved an optimization problem of the spur gear train for minimum weight using a grey wolf optimization (GWO) algorithm. The authors had compared the results obtained using GWO with the results of simulated annealing (SA), GA, and PSO available in the literature.

From literature studies, it is observed that advanced optimization algorithms require the population size along with the number of generations as common controlling parameters. In addition, most of the optimizations algorithms depend on its own algorithm-specific control parameters such as GA depends on the selection operator, the crossover probability, and the mutation probability; Harmony Search algorithm (HSA) depends on the rate of pitch adjusting, the improvisations number and the consideration rate of harmony memory; PSO algorithm depends on its social parameter, cognitive parameter, and inertia weight; Ant Bee Colony (ABC) algorithm depends on the number of scout bees, onlooker bees, employed bees, and its limit. The improper values of algorithm-specific control parameters affects the performance of these optimization algorithms. The precise tuning of algorithm-specific control parameters is a difficult task which increases the computational efforts. Also, the working procedure of these advanced optimization algorithms is difficult to understand for newly coming designers and researchers. There is a need to develop new optimization algorithms that are simple to understand and independent of algorithm-specific parameters. Keeping these points in view, Rao (2020) proposed three algorithms which are simple, algorithm-specific parameter-less and metaphor-less optimization algorithms. In this work, the performance of three Rao algorithms is investigated on a complex engineering design problem of a gear train. For validation purposes, the designs obtained using proposed Rao algorithms are compared with the same obtained using other different advanced optimization algorithms in previous studies, such as PSO, SA, GA, and GWO algorithms. The next section gives a description of Rao algorithms (Rao 2020).

2 Rao Algorithms

The searching path of the Rao algorithms for optimal solution depends on the *best* and *worst* candidate solutions within its entire candidate solutions, and the random interactions between the candidate solutions. Let $f(x)$ be the fitness function which is to be optimized (minimized or maximized). At any n^{th} iteration, there are ' d ' number of design parameters, and ' k ' number of populations (i.e. candidate solutions, $l = 1, 2, 3, \dots, k$). Let x_{best} is the best value of candidate variables corresponding to the best fitness function value (i.e. f_{best}) and x_{worst} be the worst value of candidate variables corresponding to the worst fitness function value (i.e. f_{worst}). If $X_{l,m,n}$ is the value of the l^{th} candidate for the m^{th} variable during the n^{th} iteration, the new updated value of $X_{l,m,n}$ is calculated using any one of the following three equations.

$$X'_{l,m,n} = X_{l,m,n} + r_{1,l,m,n}(X_{best,m,n} - X_{worst,m,n}), \tag{1}$$

$$X'_{l,m,n} = X_{l,m,n} + r_{1,l,m,n}(X_{best,m,n} - X_{worst,m,n}) + r_{2,l,m,n}(|X_{l,m,n} \text{ or } X_{L,m,n}| - |X_{L,m,n} \text{ or } X_{l,m,n}|), \tag{2}$$

$$X'_{l,m,n} = X_{l,m,n} + r_{1,l,m,n}(X_{best,m,n} - |X_{worst,m,n}|) + r_{2,l,m,n}(|X_{l,m,n} \text{ or } X_{L,m,n}| - (X_{L,m,n} \text{ or } X_{l,m,n})), \tag{3}$$

where, $X_{best,m,n}$ is the value of the best candidate for the variable m and $X_{worst,m,n}$ is the value of the worst candidate for the variable m during the n^{th} iteration. $X'_{l,m,n}$ is the updated value of $X_{l,m,n}$, and $r_{1,l,m,n}$ and $r_{2,l,m,n}$ are the two random numbers for the l^{th} candidate of m^{th} variable during the n^{th} iteration in the range of 0 to 1.

In Eqs. (2) and (3), the term $X_{l,m,n}$ or $X_{L,m,n}$ denotes that the l^{th} candidate solution is compared with any random L^{th} candidate solution and there is an interaction between their fitness function values. If value of the fitness function of an l^{th} candidate solution is better than the value of the fitness function of an L^{th} candidate solution then the term “ $X_{l,m,n}$ or $X_{L,m,n}$ ” becomes $X_{l,m,n}$ and the term “ $X_{L,m,n}$ or $X_{l,m,n}$ ” becomes $X_{L,m,n}$. The same condition as above is to be applicable *vice versa*.

The global optimum searching process is carried out using Eqs. (1), (2) and (3) in Rao-1 algorithm, Rao-2 algorithm and Rao-3 algorithm respectively. The simplified form of the Eqs. (1)–(3) can be expressed as,

$$x_{new} = x_{old} + r_1(x_{best} - x_{worst}) \tag{4}$$

$$x_{new} = x_{old} + r_1(x_{best} - x_{worst}) + r_2(|x_{old} \text{ or } x_{random}| - |x_{random} \text{ or } x_{old}|), \tag{5}$$

$$x_{new} = x_{old} + r_1(x_{best} - |x_{worst}|) + r_2(|x_{old} \text{ or } x_{random}| - (x_{random} \text{ or } x_{old})) \tag{6}$$

In Eqs. (4)–(6), x_{new} means the new updated value of the candidate solution x_{old} for a corresponding variable. The main merit of these Rao algorithms is that these are independent of the algorithm-specific control parameters which reduce the computational efforts. The TLBO algorithm (Rao *et al.* 2011) and the Jaya algorithm (Rao 2016; Rao 2019) also do not need algorithm-specific control parameters. However, the Rao algorithms are much simpler than the TLBO algorithm and the Jaya algorithm. For more details and the MATLAB codes of the Rao algorithms, one can go through a research paper by Rao (2020). The next section describes the mathematical formulations of a single-stage spur gear train design optimization problem and presents optimal solutions obtained using proposed three Rao algorithms for a considered spur gear train problem.

3 Spur Gear Train Optimization Problem

In this work, the model of a spur gear train with single-stage as shown in Fig. 1 given by Dorterler *et al.* (2019) is considered. The basic model of this spur gear train was formulated initially by Yokota *et al.* (1998). This basic model of this spur gear train consists

of an objective function of weight and five mixed type design variables such as b, d_1, d_2, Z_1 , and m with five non-linear constraints. Further, this basic model of a spur gear train was modified by Savsani *et al.* (2010) considering more factors that are required in the real practical case. The revised design consists of six design variables such as b, d_1, d_2, m, Z_1 , and H . Among these six design variables, four are continuous types design variables such as b, d_1, d_2 and H , an integer type variable as Z_1 , and a discrete type variable as m . In this work, the modified model of a spur gear train design with a single-stage is considered. The nomenclature of this design problem is given in the *Appendix*. The mathematical formulation of considered design problem is as follows:

$$\text{Design parameters, } \{x\} = [b, d_1, d_2, Z_1, m, H] \tag{7}$$

Objective function:
Minimize Weight,

$$f(x) = \frac{\pi \rho}{4 \cdot 1000} \left[bZ_1^2 m^2 (a^2 + 1) - (D_i^2 - d_o^2)(l - b_w) - nb_w d_p^2 - b(d_1^2 + d_2^2) \right] \tag{8}$$

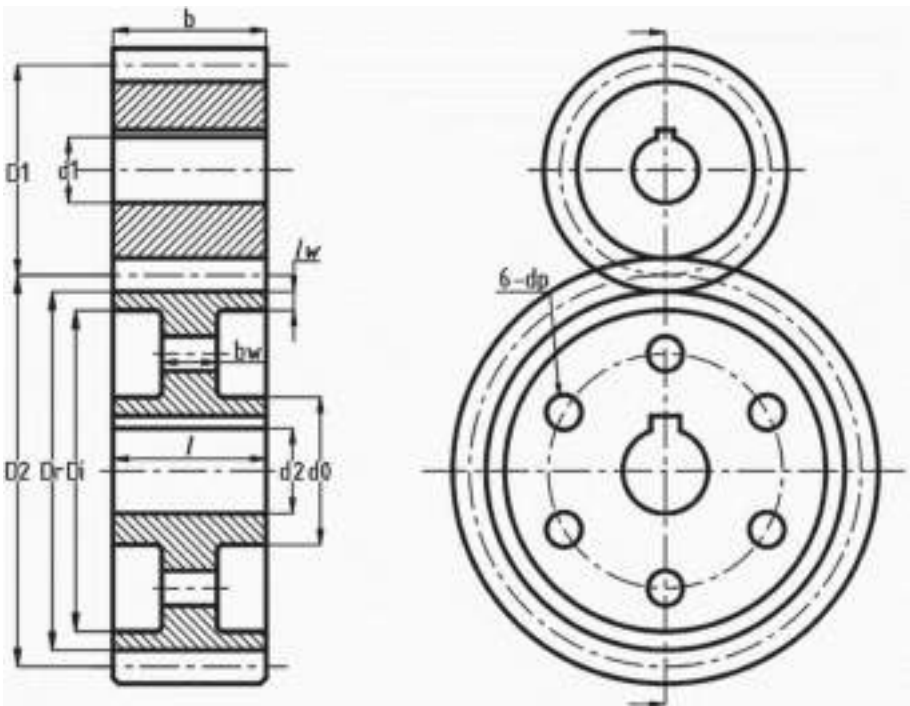


Fig. 1. Schematic diagram of a spur gear train (Source: Dorterler *et al.* 2019)

subjected to the constraints:

$$C_1(x) = \frac{S_n C_s K_r K_{ms} b J m}{K_v K_o K_m} - b_1 \geq 0 \quad (9)$$

$$C_2(x) = \frac{D_1 I S_{fe}^2 C_l^2 C_r^2 b}{K_v K_m K_o C_p^2} - b_1 \geq 0 \quad (10)$$

$$C_3(x) = \frac{D_1 (2D_2 + D_1) \sin^2 \phi}{4m} - (1 + D_2) \geq 0 \quad (11)$$

$$C_4(x) = b - 8m \geq 0 \quad (12)$$

$$C_5(x) = 16m - b \geq 0 \quad (13)$$

$$C_6(x) = b_3 \leq d_3^3 \quad (14)$$

$$C_7(x) = b_4 \leq d_2^3 \quad (15)$$

$$C_8(x) = b_5 - \frac{Z_1(1+a)m}{2} \geq 0 \quad (16)$$

The formulations and values of parameters used in an objective function and the constraints are as follows:

$a = 4$, $\rho = 8 \text{ mg/m}^3$, $P = 7.5 \text{ kW}$, $n = 6$, $\tau = 19.62 \text{ MPa}$, $N_1 = 1500 \text{ rpm}$,
 $D_r = amZ_1 - 2.5 \text{ m}$, $l_w = 2.5 \text{ m}$, $b_w = 3.5 \text{ m}$, $D_i = D_r - 2l_w$, $D_1 = mZ_1$, $D_2 = amZ_1$,
 $d_o = d_2 + 25$, $d_p = 0.25(D_i - d_o)$, $Z_2 = Z_1 D_2 / D_1$, $N_2 = N_1 / a$, $v = \pi D_1 N_1 / 60000$,
 $b_5 = 151.5$, $b_4 = (48.68e6P) / N_2 \tau$, $b_3 = (48.68e6P) / N_1 \tau$, $b_1 = (1000P / v)$,
 $K_r = 0.814$, $C_r = 1$, $K_{ms} = 1.4$, $K_m = 1.3$, $K_o = 1$, $C_l = 1$, $C_p = 191$, $\phi = 25$, $S_n =$
 $1.7236 \times H$, $K_v = \left(\frac{78 + \sqrt{(196.85 \times v)}}{78} \right)$, $S_{fe} = 28H - 69$, $I = \left(\frac{a \sin \phi \cos \phi}{2(a+1)} \right)$

To obtain Lewis geometry factor J corresponding to a different number of teeth, a 3rd order polynomial is fitted ($R^2 = 0.993$) as shown in Fig. 2 for standard values given in AGMA information sheet 908-B89. Also, to obtain surface factor C_s with respect to the hardness of gear material, a straight line is fitted ($R^2 = 0.9865$) as shown in Fig. 3 for the standard curve of machined or cold-drawn materials given by Juvinal and Marshek (2000). This problem is solved using two cases considering different design parameters' ranges provided by Yokota et al. as well as Savsani et al. as follows:

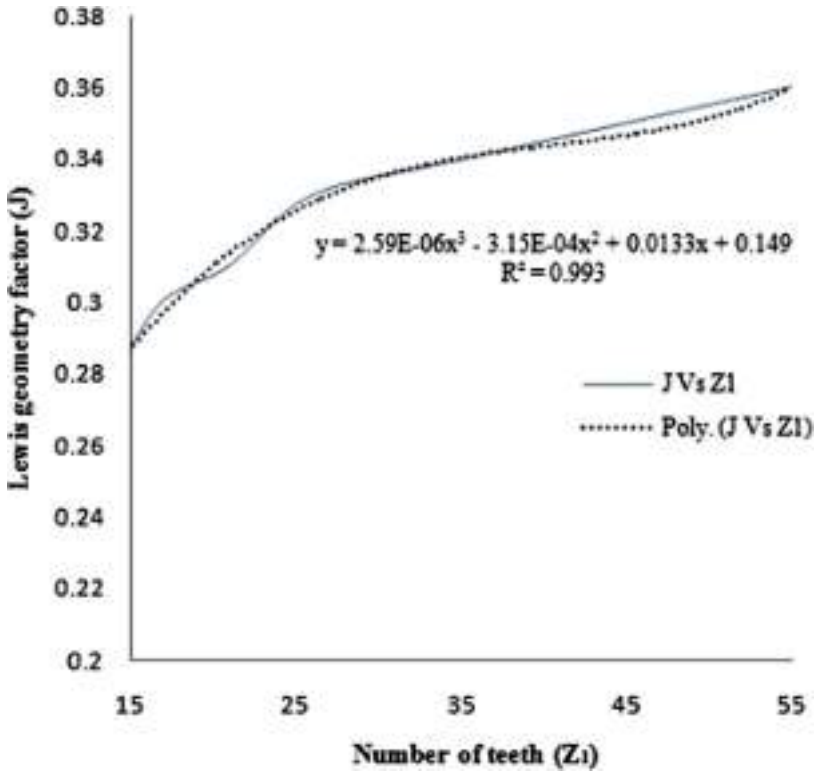


Fig. 2. A plot of the Lewis geometry factor with a 3rd order polynomial fit

3.1 Case 1: Considering the Design Parameters’ Ranges Provided by Yokota *et al.*

In case 1, the optimal solution for the minimum weight of single-stage spur gear is searched within the ranges of design variables given by Yokota *et al.* as follows:

$$\begin{aligned}
 32 &\geq b \geq 20, \\
 30 &\geq d_1 \geq 10, \\
 40 &\geq d_2 \geq 30, \\
 25 &\geq Z_1 \geq 18, \\
 m &\in \{2.75, 3, 3.5, 4\} \text{ and} \\
 400 &\geq H \geq 200.
 \end{aligned}$$

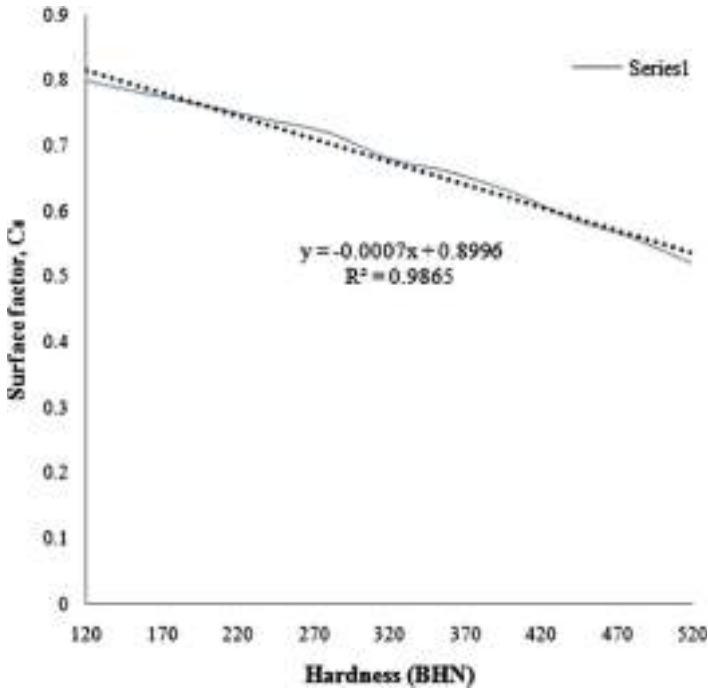


Fig. 3. A plot of the surface factor with a straight-line fit

The Rao algorithms are coded in the R2016b version of the MATLAB tool. A Laptop with processor specification of 1.90 GHz Intel Core i3-4030U and 8 GB RAM is used for computational experiments. To handle the various constraints, a penalty approach is used in this work. Table 1 presents the comparison of the best design solutions for minimum weight in case 1 obtained using the Rao algorithms with the same obtained using other advanced optimization algorithms such as GA, SA, PSO and GWO.

Table 1. Comparison of optimum designs of a spur gear train for case 1

	GA ^{1*}	GA ^{2*}	SA*	PSO*	GWO*	Rao-1	Rao-2	Rao-3
Weight (g)	3512.6	2993.7 ^a	2993.56 ^a	2993.56 ^a	2958.3 ^a	2993.7539	2993.7539	2993.7539
b (mm)	24	21.999	21.997	21.999	22.00384	22	22	22
d_1 (mm)	30	30	30	30	30	30	30	30
d_2 (mm)	30	36.751	36.742	36.768	30	36.7475	36.7475	36.7475
Z_1	18	18	18	18	18	18	18	18
M	2.75	2.75	2.75	2.75	2.75	2.75	2.75	2.75
H (BHN)	–	341.46	350	338	347.8356	273.6882	399.8665	398.1133
Active constraints	–	4, 7	4, 7	4, 7	2, 4, 6	4,7	4,7	4,7
Function evaluated	20000	6000	3300	3000	1990	1720	2190	1860
Time taken (s)	NA	9.99	5.84	1.82	NA	0.37	0.41	0.43

*GA¹ (Yokota *et al.* 1998); GA², SA and PSO (Savsani *et al.* 2010); GWO (Dortlerler *et al.* 2019)

^aInfeasible solutions due to violation of one or two constraint(s).

In case 1 for the execution of the Rao algorithms, the number of populations as 10 and the maximum function evaluations as 3000 are considered. The results given by GA² algorithm violates the $C_4(x)$ constraint, the results given by SA algorithm violates the $C_4(x)$ and $C_7(x)$ constraints, the results given by PSO algorithm violates the $C_4(x)$ constraint, and the design given by GWO algorithm violates the $C_7(x)$ constraint. Due to constraint violation, the results of SA, PSO, GA and GWO algorithm are infeasible and need to be solved again with a precise penalty approach to avoid constraint violation. It is observed from Table 1 that the optimal weight of a gear train obtained using all three Rao algorithms in case 1 is the same.

The functions evaluated to reach the optimal solution by the Rao-1 algorithm in case 1 are less than all other optimization algorithms considered. Also, the computational time taken by the Rao algorithms in case 1 is 0.37 s, 0.41 s, and 0.43 s respectively which are very less than the time taken by other considered advanced optimization algorithms. So, it is observed that the results obtained using the Rao algorithms are better than SA, PSO, GA and GWO algorithms. Figure 4 presents the convergence plot of the Rao algorithms for case 1. From Fig. 4, it is observed that the

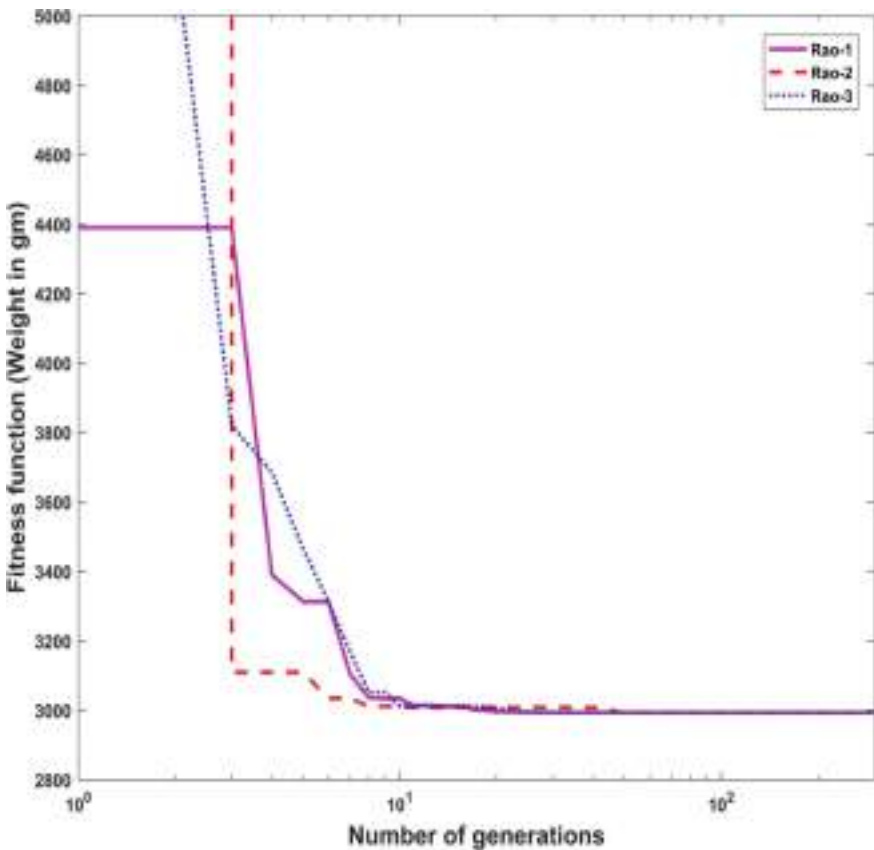


Fig. 4. A plot of convergence of Rao algorithms for case 1

solutions using the Rao-1 and Rao-3 algorithms are converged within 30 generations whereas the solution using the Rao-2 algorithm is converged within 50 generations. Also, it can be perceived that the speed of convergence of the Rao-1 algorithm is higher than the Rao-2 and Rao-3 algorithms in case 1.

3.2 Case 2: Considering the Design Variables with Expanded Ranges

In case 2, the optimal design for the weight minimization of single-stage spur gear is searched within the expanded ranges of design variables given by Savsani *et al.* as follows:

$$\begin{aligned}
 35 &\geq b \geq 10, \\
 30 &\geq d_1 \geq 10, \\
 40 &\geq d_2 \geq 10, \\
 25 &\geq Z_1 \geq 18, \\
 m &= \{1, 1.25, 1.5, 2, 2.75, 3, 3.5, 4\} \text{ and} \\
 400 &\geq H \geq 200.
 \end{aligned}$$

Same as case 1, in case 2 also the Rao algorithms are coded in the R2016b version of MATLAB tool. Also, the same Laptop as described in case 1 is used for computational experiments. A static penalty approach is considered to manage the constraints in this case too. Table 2 presents the comparison between the best design solutions of the spur gear train in case 2 obtained using the Rao algorithms and other optimization algorithms such as PSO, GA, SA and GWO.

Table 2. Comparison of optimal designs of a spur gear train for case 2

	GA*	SA*	PSO*	GWO*	Rao-1	Rao-2	Rao-3
Weight (g)	1664.3	1661.11	1661.1	1292.7656	953.8502	953.8502	953.8502
<i>b</i> (mm)	26.87	26.74	26.73	20.38403	22.6552	22.6552	22.6552
<i>d</i> ₁ (mm)	30	30	30	30	30	30	30
<i>d</i> ₂ (mm)	36.75	36.743	36.74	16.85222	36.7475	36.7475	36.7475
<i>Z</i> ₁	18	18	18	18	20	20	20
<i>M</i>	2	2	2	2	1.5	1.5	1.5
<i>H</i> (BHN)	400	400	400	400	400	400	400
Active constraints	2, 7	2, 7	2, 7	2,4,5,6,7	1,7	1,7	1,7
Function evaluated	6000	3300	3000	8926	2590	2180	2300
Time taken (s)	12.29	6.81	2.01	NA	0.39	0.42	0.45

*GA, SA and PSO (Savsani *et al.* 2010); GWO (Dortlerler *et al.* 2019)

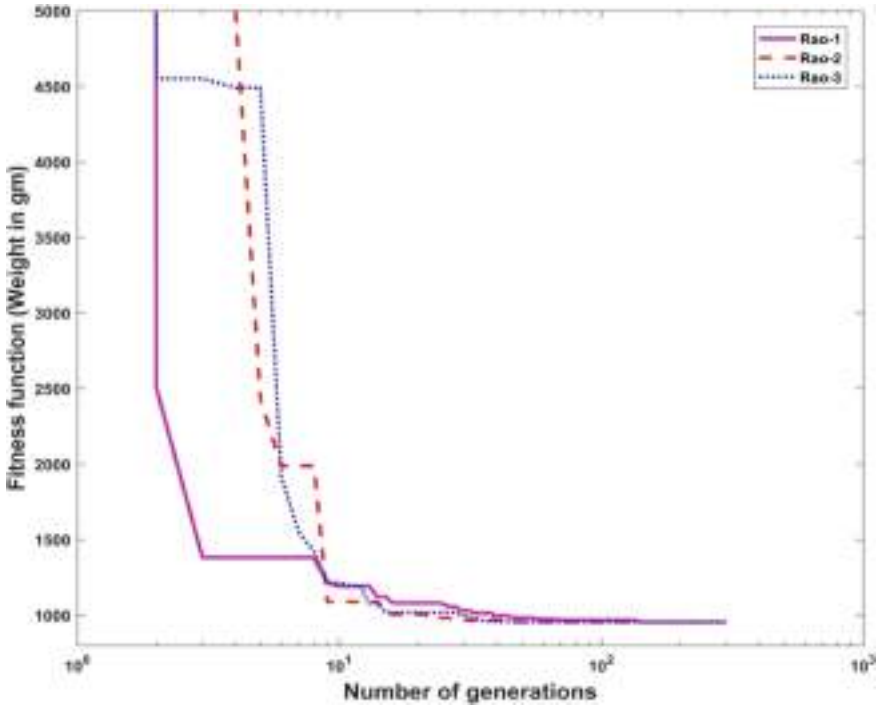


Fig. 5. A plot of convergence of Rao algorithms for case 2

In case 2 for the execution of the MATLAB codes of the Rao algorithms, the maximum function evaluations are considered as 3000 with the size of the population as 10. From Table 2, it is revealed that the same results are obtained using Rao algorithms, and these results are superior to SA, PSO, GA, and GWO algorithms. Also, it can be noted that the Rao algorithms are suggested a new optimal design of a single-stage spur gear train for a minimum weight with the module of 1.5 mm. The functions evaluated to reach the optimal solution by Rao algorithms in case 2 are 2590, 2180, and 2300 respectively which are less than all other optimization algorithms considered. Also, the computational time is taken by the Rao algorithms in case 2 is 0.39 s, 0.42 s, and 0.45 s respectively which are also very less as compared to the other algorithms considered.

Figure 5 shows the convergence plot of the Rao algorithms for case 2. It can be noticed from Fig. 5 that the solutions using the Rao-2 and Rao-3 algorithms are converged within 50 generations whereas the solution using the Rao-1 algorithm is converged within 105 generations. Also, the speed of convergence of the Rao-3 algorithm is higher than the Rao-1 and Rao-2 algorithms in case 2. The next section presents the conclusions of this study and the future studies which will be carried out.

4 Conclusions

The performance of the proposed Rao algorithms is investigated in this work over a complex mechanical design optimization problem of a single-stage spur gear train. It can be concluded that the weight of a gear train designed in case 1 using Rao algorithms is reduced by 14.77% than the one designed using the GA algorithm. Also, it can be concluded that the weight of a gear train designed in case 2 using the Rao algorithms is 42.69% less than the one designed using GA algorithm, 42.58% less than the one designed using SA and PSO algorithms, and 26.22% less than the one designed using GWO algorithm. The results revealed that the proposed Rao algorithms have significant potential to find better solutions for complex engineering design problems in comparatively very less computational time. Also, the proposed Rao algorithms have the ability to handle mixed-type design variables, such as discrete, integer, and continuous variables simultaneously. Furthermore, the computational efforts have significantly reduced using Rao algorithms due to the simplicity and absence of algorithm-specific parameters. In future studies, these Rao algorithms will be used for design optimization of other types of gear trains as well as to optimize more engineering complex design problems of mechanical components and systems. Also, the multi-objective design optimization problems of mechanical elements will be attempted using Rao algorithms.

Appendix

Nomenclature

a	Gear transmission ratio
b	Face width
b_w	Web thickness
d_1, d_2	Pinion and gear shaft diameter
D_1, D_2	Pitch diameter of pinion and gear
D_i	Rim inner diameter
d_o	Boss outer diameter
d_p	Diameter of drilled hole
D_r	Diameter of gear dedendum circle
H	Hardness
I	Geometry factor
K_m	Factor for mounting
K_{ms}	Factor for mean stress
K_o	Factor for overload
K_r	Factor for bending reliability
K_v	Factor for velocity
l	Boss length
l_w	Rim thickness
m	Module
n	No. of drilled holes

N_1, N_2	Pinion and gear shaft speed
S_{fe}	Surface fatigue strength
Z_1, Z_2	Pinion and gear teeth
ρ	Gear material density
τ	Shear strength of shafts
ϕ	Pressure angle

References

- Artoni, A.: A methodology for simulation-based, multi-objective gear design optimization. *Mech. Mach. Theory* **133**, 95–111 (2019)
- Dortlerler, M., Sahin, I., Gokce, H.: A grey wolf optimizer approach for optimal weight design problem of the spur gear. *Eng. Optim.* **51**(6), 1013–1027 (2019)
- Juvinall, R.C., Marshek, K.M.: *Fundamentals of Machine Components Design*. Wiley, New York (2000)
- Miler, D., Loncar, A., Žeželj, D., Domitran, Z.: Influence of profile shift on the spur gear pair optimization. *Mech. Mach. Theory* **117**, 189–197 (2017)
- Patil, M., Ramkumar, P., Shankar, K.: Multi-objective optimization of the two-stage helical gearbox with tribological constraints. *Mech. Mach. Theory* **138**, 38–57 (2019)
- Rai, P., Agrawal, A., Saini, M.L., Jodder, C., Barman, A.G.: Volume optimization of helical gear with profile shift using real coded genetic algorithm. *Procedia Comput. Sci.* **133**, 718–724 (2018)
- Rao, R.V., Savsani, V.J., Vakharia, D.P.: Teaching-learning-based optimization: a novel method for constrained mechanical design optimization problems. *Comput.-Aided Des.* **43**(3), 303–315 (2011)
- Rao, R.V.: Jaya: a simple and new optimization algorithm for solving constrained and unconstrained optimization problems. *Int. J. Ind. Eng. Comput.* **7**(1), 19–34 (2016)
- Rao, R.V.: *Jaya: An Advanced Optimization Algorithm and Its Engineering Applications*. Springer, Heidelberg (2019)
- Rao, R.V.: Rao algorithms: three metaphor-less simple algorithms for solving optimization problems. *Int. J. Ind. Eng. Comput.* **11**, 107–130 (2020)
- Savsani, V., Rao, R.V., Vakharia, D.P.: Optimal weight design of a gear train using particle swarm optimization and simulated annealing algorithms. *Mech. Mach. Theory* **45**, 531–541 (2010)
- Tamboli, K., Sunny Patel, S., George, P.M., Sanghvi, R.: Optimal design of a heavy duty helical gear pair using particle swarm optimization technique. *Procedia Technol.* **14**, 513–519 (2014)
- Yokota, T., Taguchi, T., Gen, M.: A solution method for optimal weight design problem of the gear using genetic algorithms. *Comput. Ind. Eng.* **35**(3–4), 523–526 (1998)



Image Enhancement Techniques: An Exhaustive Review

Shradha Dubey^(✉)  and Manish Dixit 

Department of CSE and IT, Madhav Institute of Technology and Science,
Gwalior, India

shradha290594@gmail.com, dixitmits@gmail.com

Abstract. The various image enhancement techniques are used as a pre-processing step in the image processing task to make the image more productive to be processed in the computer. In this work, the brief study of the various image enhancement methods like Histogram Equalization, Adaptive Histogram Equalization, Contrast Limited Adaptive Histogram Equalization is done. These techniques are verified based on MATLAB an image processing toolbox along with their corresponding images and histograms. Different techniques have their own pros and cons so here the juxtaposition of the various methods have been done along with the calculation of the different image parameters like - Standard Deviation, Mean, Mode, Medians, Mean Squared Error for these enhancement techniques.

Keywords: Spatial domain · Transform domain · Histogram Equalization · Adaptive Histogram Equalization · Contrast Limited Adaptive Histogram Equalization · Peak Signal to Noise Ratio · Mean Square Error

1 Introduction

The quality of an imaging device may not be good [1], the enlightenment of the operator, and the untimely external conditions at the acquisition time [10].

Image enhancement methods can be broadly categorized as [3]

- (i) Spatial Domain Method
- (ii) Transform Domain Method

The desired enhancement can be achieved by manipulating the pixel values and this can be done by the spatial domain method as this method directly operates on pixels [9]. The benefit of the spatial domain method is that it is easily understandable and has low complexity [4] but sufficient robustness cannot be achieved which is a major drawback of this technique.

The Spatial domain is further classified into three categories:

- (i) Point operation
- (ii) Mask operation
- (iii) Global operation

In point operation, every pixel is transformed with the help of an equation which is independent of the values of the other pixels when point operation is used.

$$g(a, b) = T[f(a,b)] \quad (1)$$

Here, T works on single pixel value, or among the input (f (a, b)) and the output image (g (a, b)) and there is the existence of one to one mapping.

In mask operation, every pixel is transformed based on their values in a small neighborhood and in global operation, the values of all the pixels in an image are taken into discussion. Generally, global operations are considered as frequency domain operations.

Firstly, in the method of transform domain, the frequency domain approach is applied for the image transformation. Therefore, the Fourier transform is calculated for the image. The resultant Fourier Transform and a filter transfer function is multiplied and then to get the required image to perform inverse Fourier Transform of the image which we get after multiplying the result with filter transfer function.

So, the image is improved by modifying the frequency components of the image. This includes image power data is transformed by using different approaches, for example, DFT, DCT, and so forth into a particular area. Image Enhancement operations can be categorized mainly as follows [10]

- Using Filtering
- Using Histogram Equalization Techniques.

2 Literature Review

Haris Ackar, Abd Almisreb et al. [1] Image Enhancement is one of the most significant and complex procedures in image preparing innovation. The primary point of image enhancement is to improve the visual appearance on an image and to offer a superior portrayal of the image for Computer Vision Algorithms. In this paper, a couple of utilization fields of image improvement with different images is secured like grayscale, shading, infrared and even with recordings. The principle goal of this paper is to feature the downsides of the condition of the image enhancement procedures.

Sara et al. [2] In this the author compares the different image quality metrics like PSNR, SSIM, MSE, FSIM and also derives a mathematical relationship between them. To give a better understanding of these metrics they have tested these techniques on various images and compare them.

Mallikeswari et al. [3] this work presents different image enhancement strategies and techniques utilized by scientists, to draw out the plans to conquer the downsides by utilizing mixes of calculations which is proficient and efficient in terms of cost. To acquire the better image quality, it is essential to implement an algorithm which is a combination of more than one algorithm. The fundamental goal of this paper is to utilize the calculation which is productive. So it is critical to get the best quality image, it is ideal to build an algorithm that gives an improved image from a unique image of any sort like low differentiate image, infrared image and furthermore night image.

Oktavianta et al. [4] in this paper the discussion is about the utilization of advanced images which is expanding a direct result of the points of interest controlled by advanced images, among others, in the picture, image handling, and others. Be that as it may not every single advanced image have a visual appearance that fulfills the human eye. Disappointment can emerge because of commotion, absence of enlightenment quality in the images where it either excessively dull or excessively brilliant. So we need strategies to upgrade the nature of advanced images. To improve the image quality from the red shading side we can offer consideration to the histogram. The treatment alluded to in this article is an image balance histogram at the dim level (grayscale). A decent picture histogram when it includes every single imaginable level or levels on a dark level. Obviously the objective to have the option to show the detail on the image for simple perception. One strategy to improve computerized images is to utilize the evening out of histogram technique, where the level or dark in the image can spread equally overall degrees of the dark.

Muhammad Zohaib et al. [6] In this paper they have applied histogram and obtained an equalized histograms on the grayscale X-Ray images. So, they have shown that histo - gram equalization gives a very simple way to enhance any image and images can be made more visible and sufficient for the examination process.

Ramkumar et al. [16] In this paper it is explored that the different types of image enhancement approaches and their comparative study is done. In this paper Cumulative Distributive Function (CDF) is used as a form of Histogram Equalization. They have also shown that Histogram Equalization is considered better for image contrasts as compared to the other method.

3 Introduction to Various Enhancement Techniques

Unlike other histograms, which show only frequency, image histogram shows the frequency of pixel intensity values where the x-coordinate stands for the gray level intensity and the y-coordinate correspond to the frequency of gray level intensity.

Some of the histogram equalization techniques discuss here are

- 3.1 Histogram Equalization (HE).
- 3.2 Brightness Preserving Bi-Histogram Equalization (BBHE).
- 3.3 Minimum Mean Brightness Error Bi-Histogram Equalization in Contrast Enhancement (MMBEBHE).
- 3.4 Brightness Preserving Dynamic Histogram Equalization (BPDHE).
- 3.5 Adaptive Histogram Equalization (AHE).
- 3.6 Contrast-Limited Adaptive Histogram Equalization (CLAHE).
- 3.7 Contrast Enhancement.

3.1 Histogram Equalization (HE)

Histogram Equalization distributes the pixels uniformly and computes the intensity value to obtain an enhanced image as output [6]. Therefore, the dynamic range of the pixels is increased in HE technique to get a better image (Fig. 1).

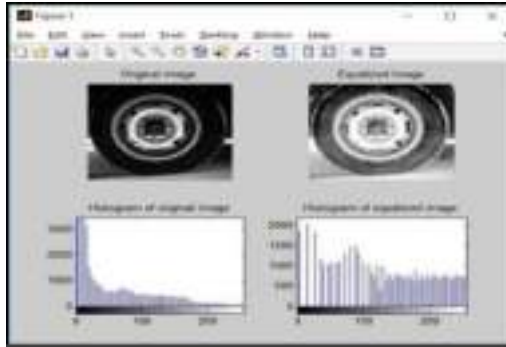


Fig. 1. Original and equalized gray image with their respective histograms

3.2 Brightness Preserving Bi-Histogram Preservation Equalization (BBHE)

This approach is an extension of the conventional HE technique where the mean intensities of the output image and the input image is made almost equal. Therefore, the mean brightness of the image can be maintained by BBHE [7] and hence, overcomes the restraint of HE. This method is enhanced to the Dynamic HE.

3.3 Minimum Mean Brightness Error Bi-Histogram Equalization in Contrast Enhancement (MMBEBHE)

MMBEBHE is an enhanced version of BBHE. This method returns minimum absolute mean brightness error as separation in MMBEBHE [17] is based on the threshold level. Three steps described by the following

For every threshold level, it calculates an Absolute Mean Brightness Error (AMBE). To yield minimum Mean Brightness Error (MBE), it finds a minimum threshold level. Lastly, it separates the input histogram. It is separated based on the threshold found in step (ii) and HE is extending to every divided histograms as in BBHE.

3.4 Brightness Preserving Dynamic Histogram Equalization (BPDHE)

This method is an augmentation to the Histogram Equalization method which processes the mean intensity of the output image almost equal to the input image mean intensity, therefore, the mean brightness of the picture can be preserved. The BPDHE has five steps which are as follows

- (i) Histogram smoothness can be maintained through a one- dimensional Gaussian Filter.
- (ii) With the help of the smoothed histograms, the position of the local maximums can be detected.
- (iii) Every partition must be allocated to a new dynamic range.

- (iv) Every partition must be independently histogram equalized.
- (v) Mean Brightness of the image is normalized

BPDHE will produce better enhancement and better in preserving the mean brightness.

3.5 Adaptive Histogram Equalization (AHE)

There are many ways in which AHE can be defined. In one way, around each pixel, the gray levels (GL's) [8] histogram in a window is generated. The input pixel gray levels to output GL's can be map by the histogram progressive summation or by the cumulative distribution of GL's. The gray outcome obtained can be 50% if the median gray level pixel value is within its window and the outcome obtained can be black in maximum if the value is less than the neighboring windows of all the other pixels.

The contrast of a region of an image will not be sufficiently enhanced by Histogram Equalization. AHE improves the contrast of a region of an image by converting each pixel with a transformation function derived from a surrounding region. By AHE, some drawback of global linear min-max windowing method can be overcome [8]. Therefore, it can revamp the contrast of grayscale color images and noise in regions of the image is also reduced (Fig. 2).

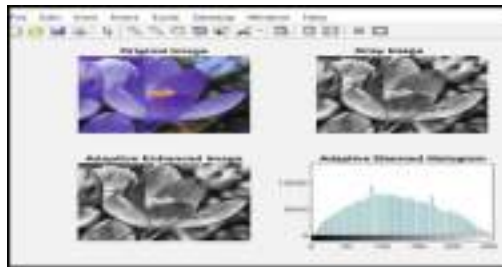


Fig. 2. Original, gray and adaptive enhanced image with its histogram

3.6 Contrast Limited Adaptive Enhancement (CLAHE)

In Adaptive Histogram Equalization, the regions with relatively small intensity are more enhanced. AHE can also cause some kind of artifacts to appear in those regions. An improvement of limiting the slope of the Cumulative Distribution Function, the contrast enhancement can be limited because the slope of the Cumulative Distribution Function is directly proportional [12] to the slope of the amount of contrast enhancement for some intensity. The height of the histogram for some bin is used to calculate the slope of the Cumulative Distribution Function at a bin location. In order to restrict the Cumulative Distribution Function slope and the contrast enhancement amount, we first have to restrict the height of the histogram up to some extent. So, if we limit the histogram height to a certain level, the slope of the CDF and hence the amount of contrast enhancement can be limited.

The dissimilarity between AHE and CLAHE is that before the computation of its CDF there is one more step for histogram clipping as the mapping function is performed [12]. AHE which is known as CLAHE can be made to limit such artifacts and noise.

3.7 Contrast Enhancement

Contrast Enhancement automatically brightens images that seem to be dark or unclear. To deliver improved quality and clarity apply appropriate tone correction. As the visual quality of the image is of utmost importance in the diagnosis of diseases that's why contrast enhancement has wide medical applications. X-Ray [13] especially useful for check bone fracture, used to record the internal functioning of the human physique. Due to the excessive presence of water in the human body, the X-Ray technology gives low contrast images. Magnifying an image is a foremost task in many applications while to enlarge the size of the image, pixels are inserted [15] (Fig. 3).

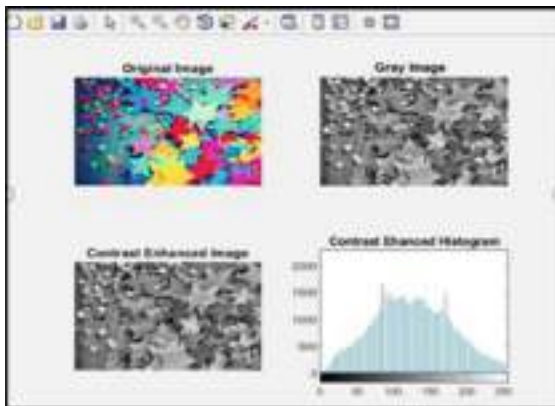


Fig. 3. Original, gray and contrast enhanced image with its histogram

4 Image Parameters

Some static and dynamic parameters are calculated for measuring image performance in different aspects.

4.1 Statistical Parameters

Mean

Mean is a fundamental static parameter. Mean are generally used in geometry and analysis. With respect to image processing, the filtering technique (using mean) which is used for noise reduction is categorized as spatial filtering.

Median

The intensity level of a pixel is measured using the median as the median separates the pixels of high-intensity value from lower intensity value pixels [5]. The mid-value of the pixel is selected from an ordered set of values. Therefore, it can also be represented as a kind of order-statistic filter and is also widely accepted, effective of the rank filters. If 's t' is an even number the computation of the average of the two values which are near to the mid-value of the ordered set is done. It can be expressed as,

$$f(a, b) = \text{median}\{d(r, c) | (r, c) \text{ belongs to } X\} \quad (2)$$

where $f(a, b)$ is represented as the restored image 'r' and 'c' are the coordinates of rows and column respectively The computation occurs on the window 'W' having a size of 'sxt'. 'd' is represented as a noisy image

Mode

In mode [4], each object is placed in a certain category or class. In a contest of statistics, the mode is the value that has frequent occurrence. Mathematically,

$$\text{Mode} = \text{Mean} - 3(\text{Mean} - \text{Median}) \quad (3)$$

Standard Deviation

In a contest of image processing, shows the extent of "disparity" or "dispersion" that occurs from the average (mean or expected) value The high value of the standard deviation represents that there is a wide range of data points whereas the value of the data points is nearer to the mean if it's having the lower value for the standard deviation. It can also be used as a measure of variability in terms of statistics.

4.2 Dynamic Parameters

Mean Square Error (MSE) and the Peak Signal to Noise Ratio (PSNR).

The estimation of the compression of images in terms of its characteristics is done mainly by the two of mostly used error-metrics parameters known as PSNR and MSE [2]. To depict the cumulative squared error for the compressed and the original image MSE is used.

On the other hand, for the calculation of the quality of reconstruction of lossy compression for image compression PSNR is taken into consideration.

Here, in this context, the original data is the signal and the generated compression error is noise.

While measuring the compression codecs, PSNR is an estimation to the human judgment of quality restoration.

In the Table 1, the various image enhancement approaches like Histogram Equalization, Brightness Preserving Bi-Histogram Equalization, Adaptive Histogram Equalization, Contrast Limited Adaptive Histogram Equalization and Contrast Enhancement are compared along with their advantages and disadvantages.

Table 1. Comparative study of different image enhancement approaches

Enhancement techniques	Advantages	Disadvantages
HE	The brightness of the background can be maintained	It does not give satisfactory results for the color images
BBHE	The mean brightness of the image can be conserved	It requires more time for computation
BPDHE	In the BPDHE, the intensity range of both the input as well as the output images are made equal	Transparency in the contrast of the images cannot be obtained
AHE	In the images with dark regions, the contrast is very low	The edges get blurred
CLAHE	Avoids amplifying noise that might present an image	More operations
Contrast enhancement	It works better with the X-Ray images and gives a clear contrast	Complexity is high

5 Computation of Various Parameters in Different Types of Equalization Techniques Using Various Images of Many Datasets and Comparing Them

The different image parameters such as mean, median, mode, standard deviation, PSNR, MSE are calculated as given in the following Tables 2, 3, 4, 5 and 6 and these parameters are compared for different types of histogram equalization techniques on various types of images which are taken from the various datasets as shown in the Figs. 4, 5, 6, 7 and 8. The images along with their parameters are as follows:

The images used for measuring image quality are taken from various datasets



Fig. 4. Image of a flower to calculate various parameters by applying image enhancement techniques

Table 2. Parameters calculation on a flower image

Parameters	Gray	B&W	Equalized	Adaptive	Contrast
Mean	94.37	0.448	127.51	121.88	120.589
Median	82	–	130	121	119
Mode	27	–	45	116	103
Standard deviation	56.56	0.2785	74.65	62.968	51.22
PSNR	5.81	0.053	4.67	6.13	7.88
MSE	17185.8	64742	22359.1	15983.4	10685.4

**Fig. 5.** Image of a face to calculate various parameters by applying image enhancement techniques**Table 3.** Parameters calculation of face image

Parameters	Gray	B&W	Equalized	Adaptive	Contrast
Mean	137.16	0.497	127.53	145.63	131.59
Median	147	–	125	161	136
Mode	209	–	69	207	161
Standard deviation	69.24	0.558	74.73	66.66	51.53
PSNR	5.25	0.072	4.67	5.36	7.87
MSE	19551.8	64457.4	22337.7	19087.8	10688.4

**Fig. 6.** Image of a face of a dog to calculate various parameters by applying image enhancement techniques

Table 4. Parameters calculation on a dog image

Parameters	Gray	B&W	Equalized	Adaptive	Contrast
Mean	169.49	0.446	127.51	171.118	151.01
Median	194	–	125	194	163
Mode	211	–	170	224	196
Standard deviation	55.69	0.726	74.79	59.46	48.00
PSNR	5.27	0.083	4.67	4.79	7.58
MSE	19463.9	64287.1	22379.3	21754.7	11428.5



Fig. 7. Underwater image to calculate various parameters by applying image enhancement techniques

Table 5. Parameters calculation of the given fruits image

Parameters	Gray	B&W	Equalized	Adaptive	Contrast
Mean	117.08	0.493	127.41	123.92	120.39
Median	110	–	125	119	114
Mode	48	–	40	40	88
Standard deviation	58.56	0.418	74.85	71.17	56.29
PSNR	6.67	0.062	4.66	5.09	7.06
MSE	14151.2	64600.4	22413.3	20310.2	12879.6

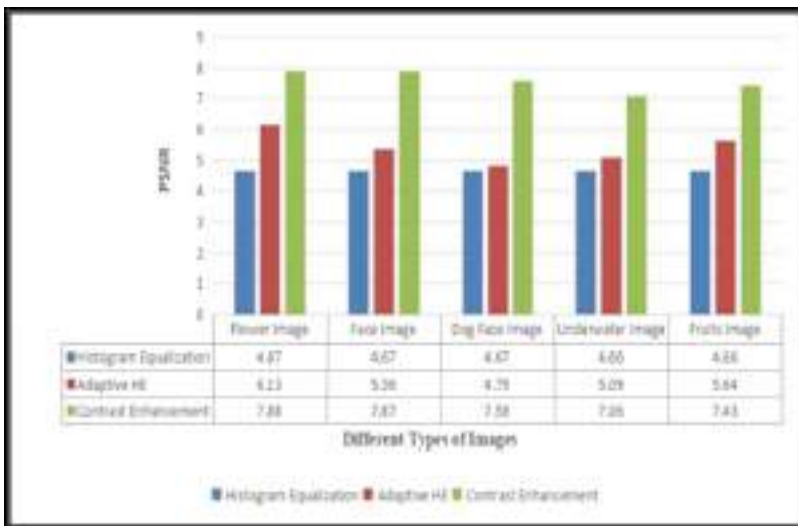


Fig. 8. Image of a mixed fruit image to calculate various parameters by applying image enhancement techniques

Table 6. Parameters calculation of a mixed fruit image

Parameters	Gray	B&W	Equalized	Adaptive	Contrast
Mean	98.03	0.479	127.55	122.53	119.77
Median	93	–	125	122	117
Mode	7	–	8	10	104
Standard deviation	57.25	0.355	74.83	66.67	53.87
PSNR	5.97	0.058	4.66	5.64	7.43
MSE	16581.9	64663.8	22399	17883	11847.7

The graph shown in Fig. 9 represents the PSNR comparison of the different histogram equalization techniques. The PSNR value of HE, AHE and contrast Enhancement is calculated as show in the graph below in Fig. 9.

**Fig. 9.** PSNR calculation of different types of images by using various HE techniques

The graph shown in Fig. 10 represents the MSE comparison of the different histogram equalization techniques. The MSE value of HE, AHE and Contrast Enhancement is calculated as show in the graph below in Fig. 10.

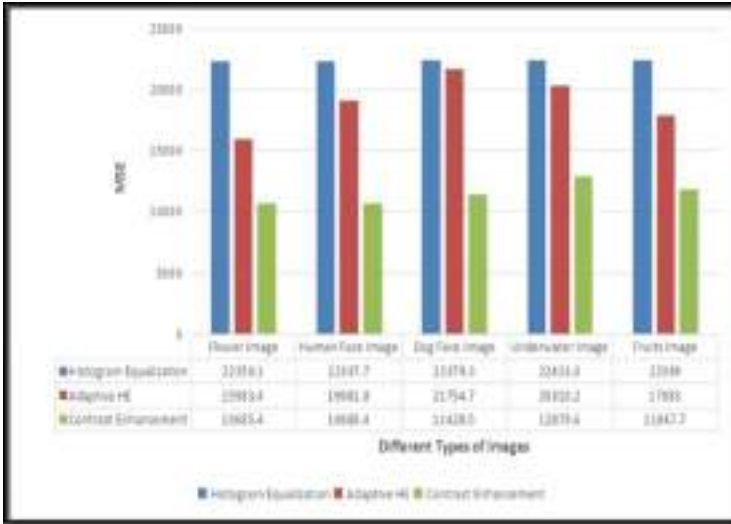


Fig. 10. MSE calculation of different types of images by using various HE techniques

6 Conclusion

In this survey paper, a review of the different types of histogram based image enhancement techniques is done along with the computation of static and dynamic parameters of different images on various datasets. These histogram based image enhancement techniques are also compared based on their advantages, disadvantages, and the calculated parameters. The computation of the parameters and the implementation of the techniques have been done in the MATLAB 2018a environment.

In future work, these techniques can be applied to 3D images and the improvement and modification in these approaches can be done to obtain a more accurate result based on their enhanced image quality and parameter calculated.





References

1. Ackar, H., Abd Almisreb, A., Saleh, M.A.: A review on image enhancement. *Southeast Eur. J. Soft Comput.* **8**(1), 42–48 (2019)
2. Sara, U., Akter, M., Uddin, M.S.: Image quality assessment through FSIM, SSIM, MSE and PSNR—a comparative study. *J. Comput. Commun.* **7**, 8–18 (2019)
3. Mallikeswari, B., Sripriya, P.: A review of image enhancement algorithms for low-contrast, infra-red and night image. *IJCRT* **6**(1) (2018). ISSN 2320-2882
4. Liu, Y.F., Guo, J.M., Yu, J.C.: Contrast enhancement using stratified parametric-oriented histogram equalization. *IEEE Trans. Circuits Syst. Video Technol.* **6**(1) (2018)
5. Oktavianta, B., Purboyo, T.W.: A study of histogram equalization techniques for image enhancement. *Int. J. Appl. Eng. Res.* **13**(2), 1165–1170 (2018). ISSN 0973-4562
6. Aziz, M.N., Purboyo, T.W., Prasasti, A.L.: A survey on the implementation of image enhancement. *Int. J. Appl. Eng. Res.* **12**(21), 11451–11459 (2017). ISSN 0973-4562

7. Hanspal, R.K., Sahoo, K.: A survey of image enhancement techniques. *Int. J. Sci. Res. (IJSR)* (2017). ISSN (Online) 2319-7064
8. Garg, P., Jain, T.: A comparative study on histogram equalization and cumulative histogram equalization. *Int. J. New Technol. Res. (IJNTR)* **3**(9), 41–43 (2017). ISSN 2454-4116
9. Bhagat, A.K., Deshpande, S.P.: Various image enhancement methods a survey. *IOSR J. Comput. Eng. (IOSR-JCE)*, 63–66 (2017). e-ISSN 2278-0661, p-ISSN 2278-8727
10. Yadav, V., Verma, M., Kaushik, V.D.: Comparative analysis of contrast enhancement techniques of different image. In: 2016 Second International Conference on Computational Intelligence & Communication Technology (CICT) (2016)
11. Khan, M.A., Ali, M.N.: Contrast enhancement using histogram equalization. In: Proceedings of the 3rd International Conference on Engineering & Emerging Technologies (ICEET), 7–8 April 2016. Superior University, Lahore, Pakistan (2016)
12. Narnaware, S.K., Khedgaonkar, R.: A review on image enhancement using artificial neural network and fuzzy logic. (*IJCSIT*) *Int. J. Comput. Sci. Inf. Technol.* **6**(1), 133–136 (2015)
13. Joany, R.M., Rathish, J.: Image enhancement by histogram equalization (2015). ISSN Online 2395-701
14. Jasper, J., Shaheema, S., Shiny, B.: Natural image enhancement using a biogeography based optimization enhanced with blended migration operation. *Math. Probl. Eng.* **2014**, 11 (2014)
15. Mohanta, K., Khanaa, V.: An efficient contrast enhancement of medical X-ray images adaptive region growing approach. *Int. J. Eng. Comput. Sci.* (2013). ISSN 2319-7242
16. Ramkumar, M., Karthikeyan, B.: A survey on image enhancement methods. *Int. J. Eng. Technol. (IJET)* **5**(2), 960 (2013). ISSN 0975-4024
17. Suganya, P.: Survey on image enhancement techniques. *Int. J. Comput. Appl. Technol. Res.* **2**(5), 623–627 (2013). ISSN 2319-8656
18. Manvi, R.S.C., Singh, M.: Image contrast enhancement using histogram equalization. *Int. J. Comput. Bus. Res.* (2012). ISSN (Online) 2229-6166
19. Kumar, V.: Importance of statistical measures in digital image processing. *Int. J. Emerg. Technol. Adv. Eng.* **2**(8) (2012). www.ijetae.com, ISSN 2250-2459
20. Song, H., Shang, Y., Hou, X., Han, B.: Research on image enhancement algorithms based on Matlab. In: 4th International Congress on Image and Signal Processing (2011)
21. Gonzalez, R.C., Woods, R.E.: *Digital Image Processing*. Pearson Education, Inc.



Performance Evaluation of 30.5 kWp On-Grid Solar System Using PVsyst

Ramdeew Rawat^(✉) , Vishal Chaudhary , Hari Mohan Dubey ,
and Manjaree Pandit 

Department of Electrical Engineering, Madhav Institute of Technology
and Science, Gwalior, India
dewwrawat@gmail.com,
vishal.chaudhary30@mitsgwalior.in,
harimohandubeymits@gmail.com, drmanjareep@gmail.com

Abstract. Solar power is the most prominent and popular source of alternate energy. For India which has abundant solar radiation, important of solar power is quite significant. PVsyst software simulates the photovoltaic (PV) system for providing a complete analysis of the generation of solar energy. This paper provides the assessment and design evaluation of a 30.5 kWp On-Grid Rooftop solar system installed in Gwalior city which has an attractive amount of annual average solar radiation of 5.63 kWh/m² per day. This evaluation determines the feasibility of the proposed system based on the simulation carried out by PVsyst software. In the present work, the total installed capacity was 30.5 kWp which generates approximately 55.670 MWh/Year DC energy from the array. As a final outcome, the total actual AC energy transferred to the local Grid is found to be 54.575 MWh/Year. The present simulation study provides the overall performance ratio as 87% for the year.

Keywords: PVsyst · Solar irradiance · PV module array · Orientation and tilt angle

1 Introduction

The energy plays a very important role in the economic, political and social development of the human being. The per capita annual consumption of energy of a country depicts its GDP (Gross Domestic Product) and literacy rate [1]. In the present scenario, the fossil fuels are furnishing almost 80% need of worldwide energy requirement. Only 13.5% and 6.5% of the total energy needed is supplied by renewable and nuclear sources [2]. The energy sources belong to fossil fuels like oil, gas and coal are exhaustible and causes environmental pollution due to greenhouse gas emissions. Therefore, sustainable and clean energy sources are becoming popular. Solar energy is one of the most encouraging solutions to global energy dilemma [3]. India is enriched with an abundant potential of solar energy. As the location of India is in equatorial Sun Belt, hence about 5000 trillion kWh energy per year is an incident over the land of India. The geographical position of India has experienced about 250 to 300 days clear, sunny weather in the year. The annual global radiation received in India varies from

1600 to 2200 kWh/m² which is quite closed to tropical and sub-tropical regions [4]. In spite of this India is far behind in harnessing inexhaustible solar resources. The Government of India, the national solar mission has decided a target of 100 GW solar power by 2022. Out of this 40 GW has been targeted to be achieved by rooftop solar plants while 60 GW capacity through large and medium scale ground mount solar system [5, 6]. In this regard being enriched with huge solar potential, India is experiencing the greatest progress in the power generation from Photovoltaic cells. PVsyst is a design tool which provides a necessary working environment to develop a solar plant. This software is very effective for providing performance evaluation and pre-feasibility analysis of the proposed solar plant [7]. Presented as a complete design, analysis of 300MWp solar plant and its comparison with Quaid-e Azam Solar Park (QASP) situated in Pakistan [8]. A 60 kWp rooftop Grid-Tied PV plant was designed and analyzed for two geographical conditions in Nepal [9]. Performance evaluation and design, feasibility analysis of rooftop Grid-connected solar plants are described in references [10–12] using PVsyst environment. The above mentioned solar plants are designed to supply electricity to the Grid, while [13] presented a stand-alone 54 kW PV plant for an academic institute to fulfil its own energy needs. A comparative study on the basis of different load requirements for the laboratories and whole building, for fixed-tilt angle and various azimuth angles, has been presented. The performance of the solar plant hence maximum power production of the plant can be achieved by varying tilt and azimuth angles [14, 15]. By varying the orientation of the PV array the total global irradiance can be improved. The optimum tilt and azimuth angles have been obtained through the RBF (radial basis function) neural network [16] for installing a PV array.

This paper presents the performance evaluation of the proposed 30.5 kWp, On-Grid rooftop solar system. The solar system is proposed to be installed in an educational institute, Dr Bhimrao Ambedkar Polytechnic College in Gwalior. The present paper is organized in five sections as follows: Sect. 1 introduces the area of the research and contemporary work carried out by other researchers. Section 2 describes the proposed research methodology and simulation tool. Section 3 expresses the formulation of the present problem. Section 4 presents the results and a discussion of the work carried out in the paper and finally in Sect. 5 concluding remarks have been given.

2 Proposed Research and Simulation Methodology

The proposed schematic view of on-grid rooftop PV solar system is given in Fig. 1. The design of the PV array depends on the seasonal solar irradiance variation and ambient temperature. In PV array, the energy of photons which are incident as solar irradiance is converted into DC energy. A Power conditioning unit which comprises of DC to DC converter and inverters converts DC energy into AC energy. This final resultant AC energy is supplied to the Grid.



Fig. 1. A schematic view of the proposed simulation study

Effectiveness of the proposed design is achieved by adopting Monocrystalline Silicon cell technology, adjusting the tilt angle of an array and setting of albedo value according to climate. For accessing meteorological data, i.e. a series of irradiation and temperatures, Meteonorm 7.2 (in PVsyst) has been followed. This data has been collected from Gwalior having the geographical location of 26.23° N latitude and 78.18° E longitude. The systematic block diagram presenting the complete research methodology has been shown in Fig. 2. This figure shows the illustrative view of the required conversion of energy from solar irradiance to electrical AC energy followed by different channels of losses.

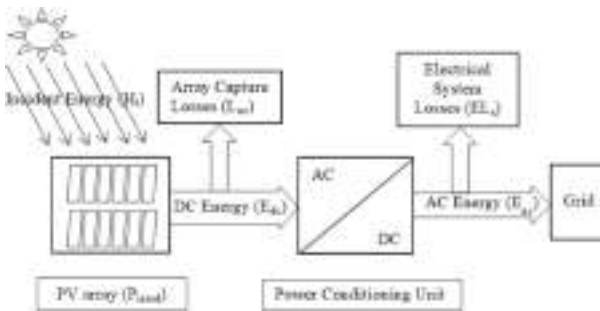


Fig. 2. Basic block diagram of the proposed research methodology.

2.1 Description of Proposed Configuration

The proposed rooftop PV array system is shown in Fig. 3. In the present work, a Siliconcrystalline PV module has been used to configure 30.5 kWp solar systems.

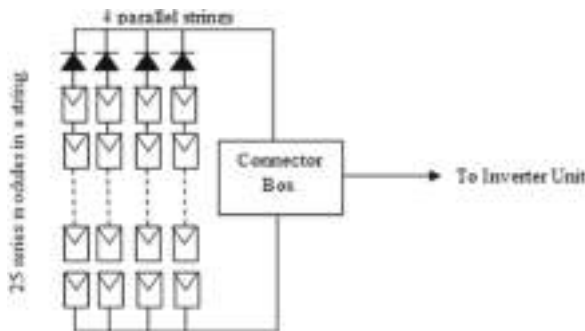


Fig. 3. The proposed rooftop PV array

Si-monocrystalline technology provides better cell efficiency and less module area [7]. The proposed PV array comprises of four strings and each string consists of 25 modules connected in series. This configuration has been decided as per the requirement of inverter's maximum power point tracking (MPPT) rating. The ratio of an inverter to array sizing has been estimated through a systematic approach and is found to be 1.14. The specification for the present PV module and inverter has been given in Table 1.

Table 1. Specifications of PV module and inverter.

PV module			Inverter		
S.no	Parameters	Specification	S.no	Parameters	Specification
1.	Type of module	Si-monocrystalline	1.	Model	SE25K-JP
2.	Model	LR6-60HPH 305 M	2.	Manufacturer	SolarEdge-2017
3.	P_{max}	305 W	3.	Phase, Efficiency	3-Phase, 50 Hz
4.	I_{sc} , V_{oc}	9.68 Amp, 40.5 V	4.	DC input voltage	750 V
5.	I_{mpp} , V_{mpp}	9.2 Amp, 32.2 V	5.	Max DC Voltage	900 V
6.	R_{se} , R_{sh}	0.28, 600 Ω	6.	Input DC current	38.0 Amp
7.	Fill factor	0.779	7.	Output AC current	37.5 Amp
8.	α	-0.36%/°C	8.	Rating	24.8 kW
9.	η_{cell}	20.79%	9.	Efficiency	98.16%
10.	η_m	18.07%	-	-	-

2.2 Orientation Transfiguration

The roof-mounted PV systems can be of two types viz building applied PV systems and building integrated PV systems [17]. The rooftop solar system, PV modules is directly attached to the building roof using additional mounting structures. The PV system arrays mounted on the rooftop is tilted with respect to the horizontal axis. This tilt angle is adjusted (using PVsyst) to acquire maximum solar radiation. By having several trials an optimum tilt angle of 28° has been achieved to get maximum solar radiation. The orientation angle has been set as 0° by arranging the PV array at south-facing.

3 Problem Formulation

In this section for evaluating the performance of a proposed solar system, with respect to solar resources, overall system losses and energy generation, various performance parameters are framed and defined. In this paper, various performance parameters have been used for analysis purpose, namely reference yield, array system yield, array capture losses, final system yields electrical system losses and performance ratio [7].

3.1 Reference Yield (Y_R)

Reference yield means the ratio of the total amount of in-plane solar irradiance (in kWh/m²) to the reference solar irradiance [15].

$$Y_R = H_t / G_o \quad (\text{Hours}) \quad (1)$$

Where H_t is Total amount of solar radiation in the plane over the installed PV array in the given period of time (kWh/m²) and G_o is the reference irradiance in standard testing condition (STC). The reference solar irradiance i.e. G_o is taken as 1000 W/m². Thus Y_R directly represents the solar radiations in kWh/m² per day or the number of peak sun hours ready for the radiation in a day. Its standard mathematical significant unit is kWh/m² per day or month or year [18]. Y_R is the primary resource of the PV system. It depends upon location, i.e. geographical conditions, the orientation transfiguration of the PV array and seasonal weather variations.

3.2 Array System Yield (Y_A)

The array system yield (Y_A) is the ratio of daily or monthly generated DC energy output of a PV array to the rated DC power output of the installed PV array i.e. nameplate rating of PV array at STC [15].

$$Y_A = E_{dc} / P_{rated} \quad (2)$$

Where

$$E_{dc} = V_{dc} \times I_{dc} \times t \quad (3)$$

E_{dc} is the generated DC energy output of the PV array in kWh, P_{rated} is the nameplate rating of PV array in kWp, V_{dc} is the terminal voltage of PV array in Volts, I_{dc} is the direct current output of array in Amp and t is a time in hours.

3.3 Array Captures Losses (L_{ac})

The array capture losses (L_{ac}) are the difference between the reference yield (Y_R) and array system yield (Y_A). This basically describes the losses, mainly occur in PV array due to various factors like the temperature rise of PV modules, dust accumulation, reflection or, climate-changing effects, i.e. heavy raining, snow falling, and cloudy sky etc. [18, 19].

$$L_{ac} = Y_R - Y_A \quad (\text{Hours}) \quad (4)$$

3.4 Final System Yield (Y_F)

The final system yield (Y_F) is the ratio of the net amount of AC energy produced by the PV array to the DC power output of the installed PV array i.e. nameplate rating of PV array at STC [19].

$$Y_F = E_{ac}/P_{rated} \quad (Hours) \quad (5)$$

E_{ac} is the net amount of AC energy produced by the PV array in kWh, and P_{rated} is the nameplate rating of PV array in kWp. In the present paper later unit has been adopted as it conveniently describes the quantities. Basically, Y_F standardizes the final energy produced with respect to system sizes.

3.5 Electric System Losses (EL_S)

The electrical system losses (EL_S) are represented by the difference between the array system yield and final system yield. This is a very important parameter which imparts the information for evaluating the electrical efficiency of the solar plant. It includes the losses in the inverter system and in the electrical components employed in Grid integration [18].

$$EL_S = Y_A - Y_F \quad (Hours) \quad (6)$$

Where Y_A is the array yield of the system in kWh/kWh per day or month or year and Y_F is the final yield of system array in kWh/kWp per day or month or year.

3.6 Performance Ratio (PR)

The performance ratio is the ratio of final system yield (Y_F) to the reference yield (Y_R) of the proposed PV array system [18, 19].

$$PR = Y_F/Y_R \quad (7)$$

It is a dimensionless quantity. The performance ratio basically quantifies the overall effect of these various losses on the final output. It is an important parameter to evaluate the overall efficiency of the plant as it bridges the net input in the form of solar irradiance to the final output in the form of energy injected into the Grid.

4 Results and Discussions

In the present paper installed capacity of the proposed on the rooftop Grid solar plant has been chosen to be 30.5 kWp using PVsyst working platform as per project specification and constraints [7]. The choice of the rooftop solar plant may be justified to take advantage of direct sunlight and maximum energy and to overcome the effect of shadows. For the proposed south-facing rooftop solar plant, the optimum value of global on collector irradiance was taken as 2063 kWh/m² which has been found by

having several trials for the present geographical location i.e. 26.23°N latitude and 78.18°E longitude. For arranging the PV array in a flawless position, the tilt angle is used to be taken as approximately equal to the latitude angle [20]. However, in this work, the tilt angle has been found to be 28° which is not equal to the latitude angle of the Gwalior city, but it is corresponding to optimum solar irradiance (to get the highest energy received according to PVsyst software) [7].

4.1 Input Solar Irradiance Data

To obtain input solar irradiance data, the meteorological study has been carried out on the Meteonorm7.2 PVsyst tool. As a result of this study, a series of solar irradiations and ambient temperature were acquired, which are given in Table 2. The total global horizontal irradiance (G_{hor}) energy was found to be 1875.2 kWh/m² for a year. The irradiance received from above by a surface horizontal to the ground. The total irradiation energy diffused into the environment (G_{diff}) was found to be 805.22 kWh/m² in the year under consideration. The actual incident irradiation (G_{inc}) collection on a plane, after getting all directional reflections was 2056.0 kWh/m² a year. This incident solar irradiance can be improved by properly following the sun through utilizing an appropriate sun tracking system. However, in the present work, a fixed tilted plane has been adopted in place of having any sun tracking system. Reason of this is that the location taken in this work experiences the clear sunny weather throughout the year. It has been experienced that after air mass losses and shadow losses, effective irradiation (G_{eff}) was found to be 2014.0 kWh/m² a year.

Table 2. Monthly solar irradiance data and energy generated by the plant

Month	G_{hor} kWh/m ²	G_{diff} kWh/m ²	T_{amb} °C	G_{inc} kWh/m ²	G_{eff} kWh/m ²	E_{array} MWh	E_{Grid} MWh
Jan.	111.0	46.10	14.61	150.1	147.6	4.274	4.190
Feb.	163.8	45.10	18.57	174.0	171.2	4.805	4.712
March	183.6	59.70	25.09	208.2	204.3	5.551	5.444
April	203.0	71.60	30.52	205.9	201.6	5.408	5.302
May	211.8	89.50	34.60	197.0	192.4	5.139	5.038
June	174.7	94.00	33.27	157.0	152.9	4.164	4.081
July	160.4	87.00	30.79	145.0	141.1	3.912	3.833
Aug.	152.5	86.50	29.56	147.7	144.1	3.992	3.911
Sept.	158.6	77.80	28.66	168.9	165.2	4.545	4.455
Oct.	150.1	59.00	26.21	180.2	176.9	4.863	4.768
Nov.	119.2	45.80	20.34	159.2	156.4	4.407	4.322
Dec.	113.5	40.00	15.87	162.8	160.2	4.608	4.519
Year	1875.20	802.10	25.71	2056.00	2014.00	55.670	54.575

4.2 Performance Parameters and Performance Ratio

The various parameters have been determined to evaluate the performance of the proposed 30.5 kWp solar plants. These parameters are indispensable for carrying out the complete pre-feasibility analysis of the plant. In the present work performance parameters to be considered are reference yield, array capture losses, array yield, electrical system losses, final yield and performance ratio. Table 3 shows the values of these performance parameters for the proposed plant month-wise for a year.

Reference yield (Y_R) is the total amount of solar irradiance with respect to reference irradiance. The reference yield is found to be 5.63 kWh/m² per day in a year. This means on an average, 5.63 h sun was available in fully shining mode. The maximum sun shining hours was obtained 6.86 in April month, however; this availability of the sun could not be converted into high energy output as the losses were also becoming higher due to high-temperature rise in that month i.e. 30.52 °C. In the present work, the solar system conversion ratio is found to be 18.40%.

Array capture losses (L_{ac}) indicate the time duration in which solar irradiation is lost in various activities like temperature rise, dust particles, reflection, etc. These losses also occur due to an around air temperature and seasonal weather changes, e.g. heavy rains, cloudy sky and snowfall etc. The value of array capture losses is found to be 0.632 kWh/kWp per day. This is an important parameter which imparts the knowledge of actual efficiency of the PV array. In the present work, the array system yield is found to be 5.00 kWh/kWp per day.

Table 3. Performance parameters of 30.5 kWp installed PV pant

Month	Y_R kWh/m ² /Day	L_{ac} kWh/kWp/Day	Y_A kWh/kWp/Day	EL_S kWh/kWp/Day	Y_F kWh/kWp/Day	PR
Jan.	4.84	0.322	4.52	0.088	4.43	91.50
Feb.	6.22	0.588	5.63	0.110	5.52	88.80
March	6.72	0.844	5.87	0.114	5.76	85.70
April	6.86	0.952	5.91	0.116	5.79	84.40
May	6.36	0.920	5.44	0.107	5.33	83.80
June	5.23	0.684	4.55	0.091	4.46	85.20
July	4.68	0.540	4.14	0.084	4.05	86.70
Aug.	4.76	0.542	4.22	0.086	4.14	86.80
Sept.	5.63	0.662	4.97	0.098	4.87	86.50
Oct.	5.81	0.671	5.14	0.100	5.04	86.70
Nov.	5.31	0.489	4.82	0.093	4.72	89.00
Dec.	5.25	0.376	4.87	0.094	4.78	91.00
Year	5.63	0.632	5.00	0.098	4.90	87.00

Electrical system losses (EL_S) are another important parameter to be evaluated. This parameter specifies the difference between array system yield and final system yield. The value of this parameter is found to be 0.098 kWh/kWp per day. Final system yield

represents the AC energy outcome of the plant for the DC power rating of the PV array. Its value is found to be 4.90 kWh/kWp per day. Which is shown in Table 3.

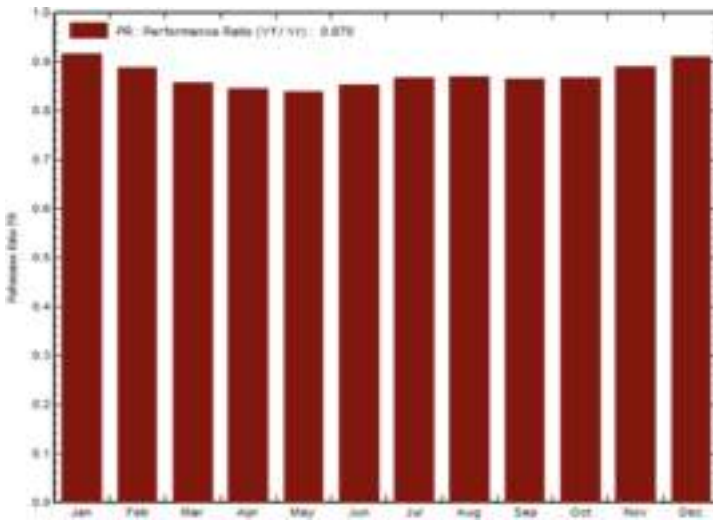


Fig. 4. Performance ratio variation of the proposed plant

The overall performance of the solar plant has been judged by evaluating the performance ratio. It furnishes the overall system losses and operational efficiency of the proposed solar plant which is found to be 87.00% for the year. Performance ratio depends upon the proper conversion of solar irradiations into electrical energy, including the effect of different losses. Table 3 shows, the highest value of performance ratio at 91.5% in January month and lowest value as 83.8% in May month. It shows that performance is found to be worst in May month because of occurrence of losses due to high temperature rise in this month i.e. 34.60 °C. On the other hand, the best performance in January is due to minimize losses as the least possible temperature rise was taken place in that month i.e. 14.61 °C. Hence the PR was found to be higher. The variation of the performance ratio of the proposed solar plant is shown in Fig. 4.

4.3 Simulation Results of 30.5 KWp Si-Mono PV System

Table 2 shows the final energy outcome of the proposed On-Grid rooftop solar plant. The journey of the energy which is transferred to the Grid is started in the form of photon energy. The designed PV array transforms the photon energy into DC energy which is denoted by E_{array} in Table 2. It denotes the DC energy output of the designed PV array. The DC output of the PV array was again converted into AC energy by the power conditioning unit system which contains inverter. This AC energy is finally

injected into the local Grid. The proposed PV system has generated 55.67 MWh in a year, whereas only 54.575 MWh energy could be transferred to the local Grid in a year. In the March month, highest energy was generated and injected into the Grid, which was 5.55 MWh and 5.444 MWh respectively. On the other hand, the lowest production of energy was taken place in July month, which was 3.912 MWh and 3.833 MWh respectively.

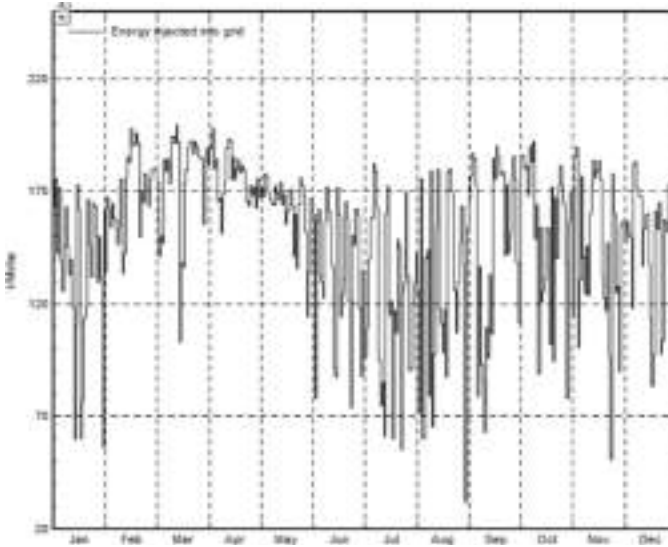


Fig. 5. The daily variation of energy injected into the Grid

The visual representation is more powerful than the data reading. Hence the variation of final injected energy into the Grid month-wise per day has been shown in Fig. 5. That PR was found to be higher in January month while energy production was highest in March month. This shows the proper conversion of input solar irradiance into energy output was taken place in January. Figure 6 shows the overall energy flow diagram in which input starts from G_{hor} i.e. Global horizontal irradiance to the final outcome of the plant energy i.e. injected into the Grid (E_{Grid}). This journey of energy has been accomplished by getting lost in several stages. Figure 6 shows all the losses occurred in between in the form of energy flow. The conversion efficiency of the designed PV array was found to be 18.4%. Total losses in between, installed a PV array to the final outcome of the power conditioning unit, were found to be 14.5% of the total installed capacity of the plant. Shown in Table 2.

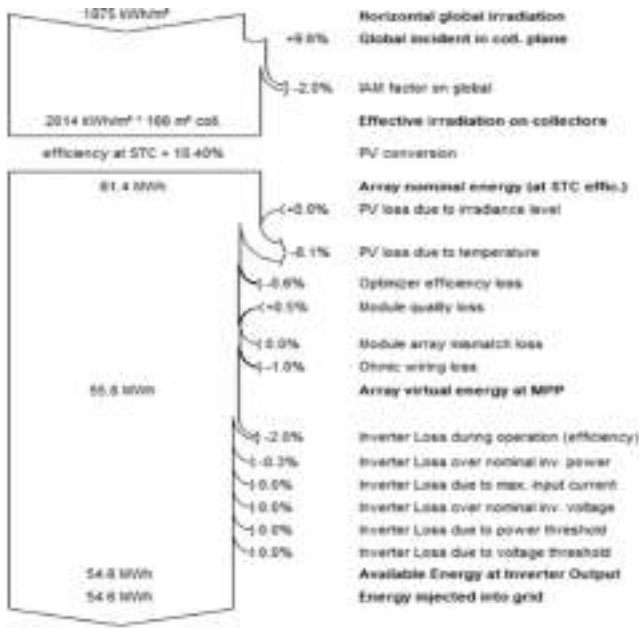


Fig. 6. Energy flow diagram for the proposed plant

5 Conclusions

The present paper presents the complete energy flow analysis of a 30.5 kWp photovoltaic rooftop system connected to the local grid, using PVsyst tool. The various components of the proposed plants like PV panels, inverters, etc. have been chosen in such a way to get reduced losses, better performance ratio and enhanced energy injected into the Grid. This paper evaluates the performance of the PV plant configured for Gwalior city. The total global irradiance obtained for this geographical location in terms of average time in a day was 5.63 h, which indicates the time of continuous availability of the shining sun. That to get the highest energy outcome. In the present work, the solar-system conversion ratio is found to be 18.40%. It can be concluded from the results obtained in the present work, that the total annual gross AC energy injected into the Grid was 54.6 MWh while annual energy generated by the PV array was 55.67 MWh which is supposed to be a good outcome. The maximum energy injected into the Grid was 5.44 MWh occurred in March month, while maximum performance ratio of the plant was found to occur in January month. This discloses the fact that the performance of the plant depends upon the conversion efficiency, which was better in January than March. Where area or space occupation is concerned, the solar plant occupies the most optimized area as compared to any other conventional power plant and provides pollution less green energy. It has also been observed that the area occupied by the present solar plant was 166 m².

Further by employing different PV cell technology, some other better technique for getting optimum orientation angles and different installation methods, a new case study can be carried out in future. In future, performance comparison for different PV modules can be discussed.

Acknowledgements. The authors sincerely acknowledge the support from Director, Madhav Institute of Technology & Science, Gwalior (M.P.) India to provide facilities to carry out this research work.

Nomenclature

E_{ac} : Array produced an AC Energy in kWh/m²

E_{array} : DC Energy of Array in kWh

E_{dc} : Inverter input DC Energy in kWh/m²

E_{Grid} : Grid Injected energy in (kWh)

EL_S : Electrical system losses

G_{diff} : Diffuse irradiation energy in kWh/m² per day

G_{eff} : Effective irradiation of the array in kWh/m² per day

G_{hor} : Total global horizontal irradiation in kWh/m² per day

G_{inc} : Global incident irradiation collects on a surface plane in kWh/m² per day

H_t : Amount of solar radiation in kWh/m²

L_{ac} : Array capture losses in hours

P_{rated} : Rated power of the PV array in kWp

R_{se} : Series Resistance of a module in ohms

R_{sh} : Shunt Resistance of a module in ohms

T_{amb} : Ambient Temperature in °C

V_{mpp} : Maximum power point Voltage

Y_A : Array system Yield in hours

Y_F : Final system Yield in hours

Y_R : Reference Yield in hours

η_{cell} : Cell efficiency

η_m : Module efficiency

α : Temperature coefficient in/°C

References

1. Erdinc, O., Uzunoglu, M.: Optimum design of hybrid renewable energy systems: Overview of different approaches. *Renew. Sustain. Energy Rev.* **16**(3), 1412–1425 (2012)
2. Asif, M., Munner, T.: Energy supply, its demand and security issues in developed and emerging economies. *Renew. Sustain. Energy Rev.* **11**(7), 1388–1413 (2007)
3. Yadav, P., Kumar, N., Chandel, S.S.: Simulation and performance analysis of a 1kWp photovoltaic system using PVsyst. In: International Conference on Computation of Power, Energy, Information and Communication (ICCPEIC), Chennai, pp. 0358–0363 (2015)
4. Central Electricity Regulatory Commission Report.: Performance of solar power plants in India (2011). <http://www.cercind.gov.in>
5. Gov. of India, Jawaharlal Nehru National Solar Mission: Towards Building solar India (2009). <http://www.mnre.gov.in>
6. National Solar Mission.: Report (2015). <https://www.mnre.gov.in>
7. PVsyst User Manual. <http://www.pvsyst.com>
8. Akram, I., Awais, M., Bashir, B., Khan, R.A.J., Iqbal, J.: Design and analysis of 300 MW solar configuration and its comparison with quaid-e-azam solar park. In: IEEE, International conference on engineering and Emerging Technology, ICEET (2018)
9. Karki, P., Adhikary, B., Sherpa, K.: Comparative study of grid-tied photovoltaic (PV) system in Kathmandu and Berlin using PVsyst. In: IEEE, Third International Conference on Sustainable Energy Technology (ICSET), pp. 196–199 (2012)
10. Kumar, B.S., Sudhakar, K.: Performance evaluation of 10 MW grid-connected solar photovoltaic power plant in India. *Energy Rep.* **1**, 184–192 (2015)
11. Sharma, R., Goel, S.: Performance analysis of an 11.2 kWp Rooftop grid-connected PV system in Eastern India. *Energy Rep.* **3**, 76–84 (2017)
12. Ahsan, S., Javed, K., Rana, A.S.: Design and cost analysis of 1 kW photovoltaic System based on actual performance in the Indian scenario. *Perspect. Sci.* **8**, 642–644 (2016)
13. Sharma, S., Kurian, C.P., Paragond, L.S.: Solar PV system design using PVsyst: a case study of an academic institute. In: International Conference on Control, Power, Communication and Technologies, ICCPCCT (2018)
14. Meriem, C., Boumdienne, B., Asma, C., Mohamed, B.M., Aicha, S.: Study of a photovoltaic system connected to the network and simulated by the code PVsyst. In: North African Workshop on Dielectric Materials for Photovoltaic Systems (NAWDMPV) (2014)
15. Mehleri, E.D., Zervas, P.L., Sarimveis, H., Palyvos, J.A., Markatos, N.C.: Determination of the optimal tilt angle and orientation for solar photovoltaic arrays. *Renew. Energy* **35**, 2468–2475 (2010)
16. Singh, H., Sirisamphanwong, C., Rekha, S.M.S.: Effect of tilt and azimuth angle on the performance of PV rooftop system. *Appl. Mech. Mater.* **839**, 159–164 (2016). ISSN: 1662-7482
17. Kumar, N.M., Gupta, R.P., Mathew, M.: Performance, energy loss, and degradation prediction of a roof-integrated crystalline solar PV system installed in Northern India. *Case Stud. Therm. Eng.* **13**, 100409 (2019)
18. Kumar, N.M., Kumar, M.R., Rejoice, P.R., Mathew, M.: Performance analysis of 100 kWp grid-connected Si-poly photovoltaic system using a PVsyst simulation tool. In: 1st International Conference on Power Engineering, Computing CONTROL, PECCON, Chennai, vol. 117, pp. 180–189 (2017)
19. Sharma, V., Chandel, S.S.: Performance analysis of a 190 kWp grid interactive solar photovoltaic power plant in India. *Energy* **55**, 476–485 (2013)
20. Garg, H.P., Garg, S.N.: Modal evaluation and optimum collector slope for a tropical country. *Energy Convers. Manag.* **21**, 299–312 (1981)



Wiener System Identification Using Iterative Instrumental Variable Method

Vikram Saini¹✉  and Lillie Dewan² 

¹ MITS, Gwalior 474005, Madhya Pradesh, India
ivikramsaini@gmail.com

² NIT Kurukshetra, Kurukshetra 136119, Haryana, India
l_dewan@nitkkr.ac.in

Abstract. This paper discusses instrumental variable method for Wiener system identification by using bilinear parameterized formulation. This particular method decomposes the model form and assumes the invertibility of the non-linearity involved in the modeling of Wiener model. In addition, the output of the linear block is corrupted with noise signal resulting in a model with correlated noise disturbance. The consistent estimates are obtained by combining Instrumental Variable method wherein the instruments are constructed by means of data filtering of observed and auxiliary variables. To support the speculation, the paper presents performance analysis using simulation results.

Keywords: Instrumental variable · Parameter estimation · Least square · Wiener models · Data filtering

1 Introduction

If the nonlinear distortions are too large and a model is required to capture the nonlinear behavior in a much large operating region, it is reasonable to characterize the behavior using nonlinear models which is useful to improve the identification performance. One way is to describe the behavior using the block-oriented models. Wiener model is one of the simplest block-oriented model with linear dynamic system and static output nonlinearity. Data identification using wiener models constitute an important research area, this particular structure can effectively model various dynamical systems. Wiener models have been earlier utilized to model many industrial processes such as distillation column control, linear dynamic systems connected with nonlinear sensors, and Solar Photovoltaic module [1–4].

System identification methods provides specialized way to identify a particular model based on the requirement of application. It also requires a high dimensional data set in the form of input-output, if the process exhibits nonlinear characteristics. It was shown that with the help of system identification technique, linear dynamic models can be used to model solar PV module with very good accuracy [3]. Also, in weather forecasting control nonlinear model can be used for the energy utilization, since the present control design rely on the predicted solar insolation [4].

In the context of estimation methods employed for the Wiener models, the identification approaches can be classified into four groups [5]. Iterative methods using the

linear and nonlinear optimization cover the vast literature on the identification of Wiener models [6–11]. In some cases, the inverse of static nonlinearity is expressed using the finite number of nonlinear basis functions with the assumption that nonlinearity is invertible. This particular formulation provides estimate using the iterative nonlinear least square method [6, 9]. The invertibility approach was considered for the non-linear distortion's compensator design [12].

This paper discusses the iterative estimation method for Wiener model consists of invertible nonlinearity and rational linear part. The model is expressed using the assumption on the coefficient of first basis function involved in the expansion of static nonlinearity resulting a bilinear parameterized form. The Wiener model with output correlated noise is estimated using the instrumental variable method to address the inconsistency involved in the LS procedure. An extended dimension IV method is derived using the iterative updates of the estimate, by using the filtering of observed and auxiliary variables. Thus, the filtering approach provides an iterative method, where the variables are iteratively filtered to compute the model. The proposed IV method provide estimates with better convergence properties towards true parameters.

This paper is organized as follows. Section 2 describes the Wiener model description and associated identification problem formulation. The IV method using the data filtering approach is presented in Sect. 3 along with the consistency conditions to obtain the unbiased estimates. Section 4 presents numerical simulation through Monte-Carlo study. Finally, the last section describes some conclusions and direction for future research.

2 Wiener Model Description

The Wiener model is composed of a linear dynamic block in series with a static nonlinearity block. The linear rational transfer function can be described as an ARMAX model

$$x(k) = \sum_{i=1}^{n_a} a_i x(k-i) + \sum_{j=1}^{n_b} b_j u(k-j) + e(k) \quad (1)$$

where

$$e(k) = C(q^{-1})\epsilon(k) = \epsilon(k) + \sum_{i=1}^{n_c} c_i \epsilon(k-i) \quad (2)$$

and $x(k)$ represents output of linear system. Denote the nonlinear block as a function f . Let Ω be a compact subset of \mathbb{R} . The function f is defined by, $f : \Omega \rightarrow \mathbb{R}$ and the output can be expressed using

$$y(k) = f(x(k)) = \sum_{i=1}^{n_p} p_i x^i(k) \quad (3)$$

It is assumed that f is continuous, one-one on Ω , and inverse of f namely $g : f(\Omega) \rightarrow \Omega$ is polynomial. Thus, linear combination of polynomials is used to model the function

Therefore, $x(k)$ can be written as

$$x(k) = g(y(k)) = \sum_{i=1}^{n_q} q_i y^i(k) \tag{4}$$

Without loss of generality and for unique parameterization, the parameter q_1 is assumed to be 1. For the simplicity, rewrite the Eq. (4) as

$$x(k) = g(y(k)) = y(k) + \sum_{i=2}^{n_q} q_i y^i(k) \tag{5}$$

From Eqs. (1) and (5), it follows that

$$y(k) = - \sum_{m=2}^{n_q} q_m g_m(y(k)) - \sum_{i=1}^{n_a} a_i \sum_{m=1}^{n_q} q_m g_m(y(k-i)) + \sum_{j=1}^{n_b} b_j u(k-j) + e(k) \tag{6}$$

with $q_1 = 1$. Using (6), the following linear regression form is obtained

$$y(k) = \psi(k)\theta + e(k) \tag{7}$$

Define $\beta = [1 \quad q_2 \quad \dots \quad q_{n_q}]$, then the parameter vector $\theta \in \mathbb{R}^{n_q + n_a n_q + n_b - 1}$ is defined as

$$\theta = [q_2 \quad q_3 \quad \dots \quad q_{n_q} \quad a_1 \beta^T \quad a_2 \beta^T \quad \dots \quad a_{n_a} \beta^T \quad b_1 \quad b_2 \quad \dots \quad b_{n_b}] \tag{8}$$

and $\psi(k)$ is defined as

$$\begin{aligned} \psi(k) = & [-g_2(y(k)) \quad -g_3(y(k)) \quad \dots \quad g_{n_q}(y(k)) \\ & -g_1(y(k-1)) \quad -g_2(y(k-1)) \quad \dots \quad -g_{n_q}(y(k-1)) \\ & -g_1(y(k-2)) \quad -g_2(y(k-2)) \quad \dots \quad -g_{n_q}(y(k-2)) \quad \dots \dots \\ & -g_1(y(k-n_a)) \quad -g_2(y(k-n_a)) \quad \dots \quad -g_{n_q}(y(k-n_a)) \\ & \qquad \qquad \qquad u(k-1) \quad u(k-2) \quad \dots \quad u(k-n_b)] \end{aligned} \tag{9}$$

then, the unconstrained Least Square estimates can be obtained by

$$\hat{\theta} = \min_{\theta} \|Y - \psi\theta\|_2^2 \tag{10}$$

Given input-output data set $(u(k), y(k))$, the objective is to determine the consistent Wiener model.

3 Identification of Wiener Model

This section presents the extended IV method for the over-parameterized model with invertible nonlinearity.

3.1 Extended Instrumental Variable Method

The best possible way to construct IV vector is to use the auxiliary model outputs and filtering of the elements of the regressor matrix $\psi(k)$, resulting filtered instrumental variables. The instrumental vector can be obtained as

$$\begin{aligned} \xi^T(k) = & \left[-\hat{g}_2(y(k)) \quad -\hat{g}_3(y(k)) \quad \cdots \quad \hat{g}_{n_{q'}}(y(k)) \right. \\ & -\hat{g}_1(\hat{y}(k-1)) \quad -\hat{g}_2(\hat{y}(k-1)) \quad \cdots \quad -\hat{g}_{n_{q'}}(\hat{y}(k-1)) \\ & -\hat{g}_1(\hat{y}(k-2)) \quad -\hat{g}_2(\hat{y}(k-2)) \quad \cdots \quad -\hat{g}_{n_{q'}}(\hat{y}(k-2)) \quad \dots\dots \\ & -\hat{g}_1(\hat{y}(k-n_a)) \quad -\hat{g}_2(\hat{y}(k-n_a)) \quad \cdots \quad -\hat{g}_{n_{q'}}(\hat{y}(k-n_a)) \\ & \left. u(k-1) \quad u(k-2) \quad \cdots \quad u(k-n_b) \right] \end{aligned} \tag{11}$$

where $n_a \leq n_{a'}$, $n_b \leq n_{b'}$ and $n_q \leq n_{q'}$. In Eq. (6), the model output $y(k)$ depends on the functions of present value $y(k)$. The predicted output $\hat{x}(k)$ of linear system given by

$$\hat{x}(k) = - \sum_{i=1}^{n_a} \hat{a}_i x(k-i) + \sum_{j=1}^{n_b} \hat{b}_j u(k-j) \tag{12}$$

The estimated signal $\hat{y}(k)$ is computed using the model output defined as

$$\hat{y}(k) = - \sum_{i=2}^{n_q} \hat{q}_i g_i(y(k)) - \sum_{i=m}^{n_a} \hat{a}_m \hat{x}(k-m) + \sum_{j=1}^{n_b} \hat{b}_j u(k-j) \tag{13}$$

where

$$\hat{g}_l(\hat{y}(k-j)) = \frac{1}{\hat{C}(q^{-1})} g_l(\hat{y}(k-j)), \quad j = 1, 2, \dots, n_{a'} \text{ and } l = 1, 2, \dots, n_{q'} \tag{14}$$

$$\hat{g}_i(y(k)) = \frac{1}{\hat{C}(q^{-1})} g_i(y(k)), \quad i = 1, 2, \dots, n_{q'} \tag{15}$$

Here $\hat{C}(q^{-1})$ is the estimate of $C(q^{-1})$ and can be estimated from a preliminary stage using the least square method. Define the following

$$\widehat{\mathbf{R}}_{\xi\psi}(N) = \frac{1}{N} \sum_{k=1}^N \xi(k)\psi^T(k) \tag{16}$$

$$\widehat{\mathbf{r}}_{\xi y}(N) = \frac{1}{N} \sum_{k=1}^N \xi(k)y(k) \tag{17}$$

Now for any $\mathbf{W} \succ 0$ and consistency conditions are satisfied (discussed in the next paragraph) with

$$\text{rank}\left(\widehat{\mathbf{R}}_{\xi\psi}^T \mathbf{W} \widehat{\mathbf{R}}_{\xi\psi}\right) = \mathbb{R}^{n_q + n_a n_q + n_b - 1} \tag{18}$$

then, an extended IV estimates of θ can be computed using the following expression

$$\widehat{\theta}^{IV} = \left(\widehat{\mathbf{R}}_{\xi\psi}^T \mathbf{W} \widehat{\mathbf{R}}_{\xi\psi}\right)^{-1} \widehat{\mathbf{R}}_{\xi\psi}^T \mathbf{W} \widehat{\mathbf{r}}_{\xi y} \tag{19}$$

Here $\widehat{\theta}^{IV}$ represents the IV estimate.

To ensure the consistency of instruments, the following assumptions are made

A_1 The signals $u(k)$ and $\epsilon(k)$ are stationary, ergodic and have zero mean so that ensemble average may be replaced by time average over one sample function.

A_2 The signals $u(k)$ and $\epsilon(k)$ are statistically independent with each other.

3.2 Nonlinear IV Method

For N number of measurements, an estimator of θ can be obtained as the solution of

$$\frac{1}{N} \sum_{i=1}^N \xi(k)\rho(k) = 0 \tag{20}$$

where $\rho(k) = \widetilde{y}(k) - \widetilde{\psi}(k)\widehat{\theta}^{IV}$ is the residual vector with $\widetilde{y}(k)$ and $\widetilde{\psi}(k)$ represents the filtered output and information matrix respectively. For the iterative estimates of the parameters, the objective function for the IV estimation is defined as

$$\text{arg} \underbrace{\min}_{\theta} J(\theta), J(\theta) = \left(\widehat{\mathbf{r}}_{\xi y} - \widehat{\mathbf{R}}_{\xi\psi}\theta\right)^T \mathbf{W} \left(\widehat{\mathbf{r}}_{\xi y} - \widehat{\mathbf{R}}_{\xi\psi}\theta\right) \tag{21}$$

which after solving provides extended IV estimates (Eq. 19). The matrix $\mathbf{W} \succ 0$ provides weighted solution which may sometimes give more consistent estimates. Alternatively using the iterative nonlinear estimation method, Eq. (19) can be represented as (l is used as iteration variable and μ is a converging constant)

$$\widehat{\theta}^{IV}(l) = \widehat{\theta}^{IV}(l-1) + \mu \left(\widehat{\mathbf{R}}_{\xi\psi}^T \mathbf{W} \widehat{\mathbf{R}}_{\xi\psi} \right)^{-1} \widehat{\mathbf{R}}_{\xi\psi}^T \mathbf{W} \widehat{\mathbf{r}}_{\xi\rho} \tag{22}$$

A variable sequence can be used which provides sufficient decrease such that $J(\widehat{\theta}^{IV}(l)) - J(\widehat{\theta}^{IV}(l-1)) \leq 0$. The sufficient decrease condition for the objective function is equivalent to find the smallest positive integer $\kappa : \kappa \geq 0$ such that

$$J(\widehat{\theta}^{IV}(l+1)) \leq J(\widehat{\theta}^{IV}(l)) - \eta \mu^\kappa \nabla J(\widehat{\theta}^{IV}(l)) \Delta \widehat{\theta} \tag{23}$$

Also, a reasonable small value of μ which can provide sufficient decrease in objective function can be employed such that the matrix $\widehat{\mathbf{R}}_{\xi\psi}^T \mathbf{W} \widehat{\mathbf{R}}_{\xi\psi}$ is nonsingular in each iteration.

3.3 Consistency of the Estimates

The consistency of the estimates can be shown by the following conditions [13]

$$\mathbb{E}[\xi(k)e(k)] = 0 \tag{24}$$

$$\text{rank} \left(\widehat{\mathbf{R}}_{\xi\psi}^T \mathbf{W} \widehat{\mathbf{R}}_{\xi\psi} \right) = \mathbb{R}^{n_q + n_a n_q + n_b - 1} \tag{25}$$

The vector of instrumental variables satisfies the consistency conditions given by equations. Let the basis functions satisfy

$$|y^i(k)| \leq \mu_{max}, i = 1, 2, \dots, n_q \text{ for some } \mu_{max} > 0 \tag{26}$$

This condition implies that the basis functions are bounded within the experimental range of output with the assumption that the output is bounded. The independence assumption A_1 of $u(k)$ and $\epsilon(k)$ implies that the functions $(\varphi(u(k))$ and $\phi(e(k)))$ are independent (page 49 [14]). Now for ϕ being as identity function, $\varphi(u(k))$ and $e(k)$ are independent, and the instrumental variables vector in Eq. (11) and $e(k)$ is independent.

The common choice to ensure that the matrix \mathbf{W} is positive definite is to choose it as an identity matrix. But this choice provides poor asymptotic efficiency of the estimates. In the presented IV method, in addition to this choice the weight matrix is taken as $\mathbf{W} = \widehat{\mathbf{R}}_{\xi\xi}$ which improves the asymptotic efficiency of estimates and also ensures the consistency of estimates.

The steps of the EIV method are as follows:

- Step 1: Obtain LS estimates $\widehat{\theta}^{LS}$ and compute the residuals.
- Step 2: Estimate $C(q^{-1})$ using the computed residual vector. Compute the predicted outputs $x(k)$ and $y(k)$ using Eqs. (12) and (13) respectively.
- Step 3: Make an instrumental variables vector using Eq. (11) and compute the IV estimates using Eq. (19). Compute the residuals using the IV estimate $\widehat{\theta}^{IV}$.
- Step 4: Repeat the steps 2 and 3 until some criterion is fulfilled.

4 Simulation Study

This section presents numerical example to compare the performance of the EIV method. Monte-Carlo simulation with 300 runs are used to investigate the stochastic properties. Two noise levels with different amplitudes have been investigated in the presented example. The convergence analysis is shown using the evaluation of performance criterions. The first criterion is taken as statistically estimation error (SEE) which is defined as

$$SEE = \sqrt{\frac{\|m(\hat{\theta}_s) - \theta_s^\circ\|_2}{\|\theta_s^\circ\|_2}} \tag{27}$$

where $m(\hat{\theta}_s)$ represents the sample mean of 300 simulation runs. Also, the average coefficient of variation (ACV) is computed using the following

$$ACV = \frac{1}{n_s} \sum_{i=1}^{n_s} \frac{\sigma(\hat{\theta}_s(i))}{|m(\hat{\theta}_s(i))|} \tag{28}$$

where $n_s = n_a + n_b + n_p - 1$, ($\hat{\theta}_s(i)$ represents i th component) and $\sigma(\blacksquare)$ represents the standard deviation. The data filtering-based LS method is implemented using the steps described [15, 16]. The EIV method is implemented using the instrumental variable vector defined in Eq. (11).

Example: In this example, the linear block of Wiener system with invertible non-linearity is expressed by the following

$$x(k) = \frac{0.4238q^{-1} - 1.1227q^{-2}}{1 - 0.25q^{-1} + 0.45q^{-2}} u(k) + \frac{1 - 1.0q^{-1} - 0.20q^{-2}}{1 - 0.25q^{-1} + 0.45q^{-2}} \epsilon(k) \tag{29}$$

The nonlinearity is expressed as

$$y(k) = f(x(k)) = \left(5\sqrt{0.6x(k)} - 1 + 5\right) \tag{30}$$

and the inverse of the nonlinearity is expressed using basis functions as

$$x(k) = g(y(k)) = y(k) - 0.2y^2(k) + 0.0133y^3(k) \tag{31}$$

Two noise levels with SNR = 13.91 dB and 05.84 dB are investigated. The order of numerator polynomial of noise model is taken as $n_c = 2$ for DFLS method. In this example, EIV estimates are computed using the ARMAX model with $n_c = 2$. The choice of $n_{a'}$, $n_{b'}$ and $n_{q'}$ (number of instruments) effects the consistency as well as efficiency of the estimator. Therefore, simulations are carried out using different combinations of $n_{a'}$ and $n_{b'}$ ranges between 2 (order n_a and n_b) to 5 (arbitrary chosen).

The order for the basis functions of the invertible nonlinearity in the instrumental variable vector is taken as 3 i.e. $n_q = 3$. The estimates obtained using three combinations are shown in the table. Note that the different combinations which provided the minimum SEE are selected.

Table 1. Monte-Carlo simulation results for example with SNR = 13.36 dB.

Parameters		a_1	a_2	b_1	b_2	p_2	p_3	SEE	ACV
LS	Mean	-0.2171	0.4293	0.4125	1.0810	-0.1999	0.0130	0.2097	0.0145
	Std	0.0053	0.0060	0.0064	0.0069	0.0020	0.0002		
DFLS	Mean	-0.2558	0.4417	0.4180	-1.1076	-0.2003	0.0132	0.1203	0.0110
	Std	0.0052	0.0045	0.0042	0.0055	0.0015	0.0002		
EIV $n_{a'} = 3$ $n_{b'} = 2$	$W = I$ Mean	-0.2488	0.4436	0.4208	-1.1122	-0.2037	0.0136	0.1002	0.0452
	$W = I$ Std	0.0302	0.0144	0.0082	0.0166	0.0062	0.0007		
	$W = \widehat{R}_{\xi\xi}$ Mean	-0.2512	0.4453	0.4191	-1.1111	-0.2023	0.0135	0.1017	0.0257
	$W = \widehat{R}_{\xi\xi}$ Std	0.0118	0.0080	0.0044	0.0066	0.0054	0.0006		
EIV $n_{a'} = 5$ $n_{b'} = 2$	$W = I$ Mean	-0.2432	0.4441	0.4214	-1.1149	-0.2041	0.0137	0.0987	0.1380
	$W = I$ Std	0.0642	0.0415	0.0428	0.0502	0.0244	0.0028		
	$W = \widehat{R}_{\xi\xi}$ Mean	-0.2516	0.4451	0.4190	-1.1106	-0.2024	0.0135	0.1037	0.0250
	$W = \widehat{R}_{\xi\xi}$ Std	0.0115	0.0075	0.0044	0.0065	0.0052	0.0006		
EIV $n_{a'} = 5$ $n_{b'} = 5$	$W = I$ Mean	-0.2424	0.4436	0.4210	-1.1147	-0.2043	0.0137	0.1019	0.1402
	$W = I$ Std	0.0661	0.0419	0.0413	0.0490	0.0250	0.0029		
	$W = \widehat{R}_{\xi\xi}$ Mean	-0.2569	0.4470	0.4183	-1.1080	-0.2024	0.0135	0.1152	0.0240
	$W = \widehat{R}_{\xi\xi}$ Std	0.0104	0.0069	0.0044	0.0061	0.0053	0.0006		
True value		-0.25	0.45	0.4238	-1.1227	-0.2	0.0133		

Table 2. Monte-Carlo simulation results for example with SNR = 05.41 dB.

Parameters		a_1	a_2	b_1	b_2	p_2	p_3	SEE	ACV
LS	Mean	-0.1018	0.3536	0.3683	-0.9226	-0.1950	0.0115	0.4544	0.0454
	Std	0.0128	0.0133	0.0147	0.0167	0.0035	0.0004		
DFLS	Mean	-0.2871	0.4043	0.3916	-1.0387	-0.1997	0.0125	0.2853	0.0241
	Std	0.0117	0.0105	0.0108	0.0129	0.0028	0.0003		
EIV $n_{a'} = 3$ $n_{b'} = 2$	$W = I$ Mean	-0.2645	0.4216	0.4001	-1.0547	-0.2095	0.2451	0.2451	0.1032
	$W = I$ Std	0.0733	0.0399	0.0198	0.0397	0.0121	0.0014		
	$W = \widehat{R}_{\xi\xi}$ Mean	-0.2660	0.4222	0.3956	-1.0502	-0.2073	0.2529	0.2529	0.0537
	$W = \widehat{R}_{\xi\xi}$ Std	0.0291	0.0197	0.0110	0.0162	0.0092	0.0011		
EIV $n_{a'} = 5$ $n_{b'} = 2$	$W = I$ Mean	-0.2369	0.4123	0.3719	-1.0436	-0.2126	0.2798	0.2798	0.4466
	$W = I$ Std	0.1323	0.0874	0.4488	0.2143	0.0384	0.0044		
	$W = \widehat{R}_{\xi\xi}$ Mean	-0.2692	0.4209	0.3949	-1.0476	-0.2072	0.2581	0.2581	0.0502
	$W = \widehat{R}_{\xi\xi}$ Std	0.0264	0.0180	0.0110	0.0160	0.0088	0.0010		
EIV $n_{a'} = 5$ $n_{b'} = 5$	$W = I$ Mean	-0.2344	0.4140	0.4062	-1.0601	-0.2128	0.2415	0.2415	0.3242
	$W = I$ Std	0.1450	0.0879	0.1636	0.1871	0.0414	0.0048		
	$W = \widehat{R}_{\xi\xi}$ Mean	-0.2870	0.4301	0.3937	-1.0424	-0.2100	0.2697	0.2697	0.0571
	$W = \widehat{R}_{\xi\xi}$ Std	0.0286	0.0189	0.0115	0.0177	0.0116	0.0013		
True value		-0.25	0.45	0.4238	-1.1227	-0.2	0.0133		

The SEE, ACV and estimates with two noise levels are shown in Tables 1 and 2 respectively. In this case, two different weight matrices $\mathbf{W} = \mathbf{I}$ and $\mathbf{W} = \widehat{\mathbf{R}}_{\xi\xi}$ are considered for the EIV method.

It is observed that, DFLS method provide better asymptotic efficiency as compared to the LS method. The proposed EIV method provide consistent estimates with lower SEE than the DFLS method for both SNR cases. However, the ACV is higher than obtained using the DFLS method. The effect of choice of weight matrix is also visible on the obtained ACV i.e. with $\mathbf{W} = \widehat{\mathbf{R}}_{\xi\xi}$, asymptotic efficiency improves as compared to $\mathbf{W} = \mathbf{I}$.

5 Conclusions and Directions for Future Research

In this paper, iterative method using the introduction of instrumental variables has been presented for the identification of Wiener model. The IV methodology using extended instrumental variable vector consists of the filtered instruments have been suggested. As a result, the estimates with lower SEE and better bias-variance trade-off have been obtained as compared to the DFLS method which is validated using a simulation example with two different cases of noise level through Monte-Carlo simulation study.

The identification method presented in this paper can be used for the modeling of Solar Photovoltaic module either in the form of Wiener model or linearized model. The sensor to record the output for data driven identification can be modeled as nonlinear system corrupted with noise, which leads to a simple photovoltaic linear model with nonlinear noise in sensor. The resulting model shows Wiener model characteristics and can help to design an improved controller which will improve the economic benefits.

Acknowledgement. The authors gratefully acknowledge to Ministry of Human Resource Development (MHRD), New Delhi for providing the financial support under TEQIP (TEQIP-II & TEQIP-III).

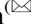



References

1. Kalafatis, A.D., Wang, L., Cluett, W.R.: Identification of Wiener-type non-linear systems in a noisy environment. *Int. J. Control* **66**, 923–941 (1997)
2. Kalafatis, A.D., Wang, L., Cluett, W.R.: Identification of time-varying pH processes using sinusoidal signals. *Automatica* **41**, 685–691 (2005)
3. Kulkarni, R.S., Talange, D.B., Mate, N.V.: Output estimation of solar photovoltaic (PV) system. In: 2018 International Symposium on Advanced Electrical and Communication Technologies (ISAECT), pp. 1–6 (2018)
4. Malvoni, M., De Giorgi, M.G., Congedo, P.M.: Data on photo voltaic power forecasting models for Mediterranean climate. *Data Brief* **7**, 1639–1642 (2016)
5. Janczak, A.: Identification of nonlinear systems using neural networks and polynomial models. In: Ser. Lecture Notes in Control and Information Sciences, vol. 310. Springer, Berlin (2005)
6. Bruls, J., Chou, C., Haverkamp, B., Verhaegen, M.: Linear and non-linear system identification using seperable least-squares. *Eur. J. Control* **5**(1), 116–128 (1999)

7. Voros, J.: Modeling and identification of Wiener systems with two-segment nonlinearities. *IEEE Trans. Control Syst. Technol.* **11**(2), 253–257 (2003)
8. Vikram, L.D.: Constrained least square based identification for Wiener systems. In: 2015 Annual IEEE India Conference (INDICON), New Delhi, India (2015)
9. Celka, P., Bershad, N.J., Vesin, J.M.: Stochastic gradient identification of polynomial Wiener systems: analysis and applications. *IEEE Trans. Signal Process.* **49**(2), 301–313 (2001)
10. Saini, V., Dewan, L.: Regularized least square based identification for Wiener systems. In: 2016 11th International Conference on Industrial and Information Systems (ICIIS), Roorkee, India (2016)
11. Saini, V., Dewan, L.: Identification of Wiener system using iterative prefiltering-based algorithm. In: 2017 International Conference on Innovations in Electrical, Electronics, Instrumentation and Media Technology (ICEEIMT), Coimbatore, India (2017)
12. Kang, H.W., Cho, Y.S., Youn, D.H.: Adaptive precompensation of Wiener systems. *IEEE Trans. Signal Process.* **46**(10), 2825–2829 (1998)
13. Stoica, P., Soderstrom, T.: Optimal instrumental variable estimation and approximate implemetations. *IEEE Trans. Autom. Control* **28**(7), 757–772 (1983)
14. Grimmett, G., Stirzaker, D.: *Probability and Random Processes*. Oxford University Press, Oxford (2001)
15. Wang, D., Ding, F.: Parameter estimation algorithms for multivariable Hammerstein CARMA systems. *Inf. Sci.* **355–356**, 237–248 (2016)
16. Wang, Y., Ding, F.: Iterative estimation for a nonlinear IIR filter with moving average noise by means of the data filtering technique. *IMA J. Math. Control Inf.* **34**(3), 745–764 (2015)



Role of Computational Fluid Dynamics in Sustainable Urban Built Environment: A Review

Rishika Shah  , R. K. Pandit , and M. K. Gaur 

Madhav Institute of Technology and Science, Gwalior 474005, India
shahrishika24@gmail.com, drpanditrk@gmail.com,
gmanojkumar@rediffmail.com

Abstract. The global built environment is under development at unprecedented scale and has brought with it global challenges like climate change and global warming. About 50% of energy demand is from the built environment sector, which also responsible for contributing 40% of carbon emissions and continues to add estimated 1% every year according to reports by UN Environment. To address these issues researchers are investigating solutions for built environment. In the last decade, tools like Computational Fluid Dynamics (CFD) have risen as aid to these researches with respect to energy conservation. Therefore, this work aims to present a short review of the studies establishing the role of CFD in built environment solutions of the past decade i.e. from 2008 to 2018. The studies on complex built environment have been considered against studies on generic built environment shapes and further classified under analysis with validation and analysis without validation. These studies are then analyzed based upon their location, built environment setting, numerical and turbulence models, focus parameters category. It is found that 38% of studies had urban block as their built environment setting, 98% of the studies used RANS numerical equation and standard $k-\epsilon$ model, 45% of studies were without validation and 55% with validation out of these 58% of the studies focus on assessing thermal environment.

Keywords: CFD · Urban built environment · Sustainable development

1 Introduction

Climate change is the direct consequence of the rapid urbanization the world is facing. It is estimated that by the year 2060, the 230 billion square meters of building floor area will be added to the already existing [1]. Alarming statistical figures like these have brought in light the increasing stress on urban built environment thereby triggering the need to study urban built environment with respect to the global challenges and striving for relative solutions. Earlier, urban built environment was studied through field measurements, surveys etc. these techniques known as an observational method were complex, time-consuming and produced approximate results. With the advent of computational methods, simulation techniques have become increasingly popular, paving way for more accurate and fruitful investigations. Computational Fluid

Dynamics (CFD) gained popularity as a technique for urban microclimate research through simulation method.

For research in the theme built environment and climate change, CFD proves to be advantageous in terms of performing simulations in the explicit assessment of wind flow or urban ventilation, temperature, pollutant dispersion and humidity. It also enables the researcher to study detailed models at smaller spatial scales like building or indoor level. Knowledge of boundary conditions for the flow parameters and appropriate simulation software is required for CFD application. In the existing literature, CFD application to assess built the environment is classified in two on the basis of built form: generic urban forms (consisting of simple shapes) and real urban forms (consisting complex shapes).

This study reviews research published on CFD analysis of the complex urban built environment. The scope of this short review encompasses published research in the past ten years (2008–2018) in referred SCI journals of English language. This paper limits itself in representing studies based on the vegetation and the built environment. The subsequent sections cover the role of CFD in the built environment in the second section, the third section showcases a summarized review of the CFD studies based on validation theory, followed by a brief introduction to the numerical equation and turbulence models used in the studied investigations in the fourth section. The fifth section presents the results analyzed from these studies.

2 CFD and Built Environment

Computational Fluid Dynamics can be applied to evaluate the built environment on multiple spatial scales. These scales range from mesoscale to microscale followed by building scale and the indoor level of spatial configuration. Application of CFD at mesoscale covers a horizontal distance up to a hundred kilometres, assessing atmospheric occurrences. At the microscale, CFD assists in analyzing horizontal distance of about two kilometres covering buildings and streets in an urban block or a larger urban area. It offers the possibility of analyzing the parameters considered with respect to the buildings and streets in an urban area through numerical modelling. Usually, the key objectives while evaluating a certain urban area or block at microscale level is to investigate the urban ventilation, pedestrian comfort, CO₂ emissions, pollutant dispersion etc. At building scale i.e. the buildings constructed within the horizontal range of fewer than 100 m distance, CFD allows the analysis of building energy demands, thermal comfort etc. through Building Energy Simulation for the study of indoor environment and studies based on Convective Heat Transfer Coefficients for outdoor thermal environment and ventilation. The recent trends in the field of CFD and built environment show inclination towards the application of CFD and BES models together for more detailed and accurate results. The last and smallest scale is the study of the indoor environment where horizontal distance is up to 10 m.

According to Soe and Khaing, “For a typical simulation, the user has to select the target variables, the computational geometry, the computational domain, the computational grid, the turbulence model, the boundary conditions, the near-wall treatment, the discretization schemes, the convergence criteria, etc.” [2]. The simulation results

can be analyzed and compared to solve the problem and if the results are not satisfactory the process is repeated until the desired solution is acquired, thus concluding the process of Computational Fluid Dynamics.

Earlier researchers investigating the built environment using CFD did not opt for validation i.e. in their studies not even one parameter in relation to temperature or velocity were compared with the analytical data; thus rendering their study to be known as “CFD analysis without validation” and the studies where at least one parameter was compared with the analytical data are known as “CFD analysis with validation” [3]. These studies falling under these two domains are explained in following sections.

3 CFD Analysis with and Without Validation

Based on the validation classification, the CFD studies can be classified as CFD analysis with validation and CFD analysis without validation. As explained in the above section comparing the parameters with solutions the study is deemed as validated. For real urban built environment, validation of CFD studies are typically performed with data from observational methods. CFD analysis of the complex built environment, conducted without validation are usually studies showing comparative analysis, where two or more built environment settings, focus parameters, within a particular urban neighborhoods are extrapolated. The typical aim of these analyses is to optimize the focus parameters like thermal environment, urban ventilation etc. out of 46 studies taken into consideration for review, 21 studies are without validation and 25 studies are carried out with validation. These studies are showcased in Tables 1 and 2 respectively. These tables exhibit spatial scale, location type for which the study is conducted, governing equations and turbulence models used in the study and focus parameter category taken into consideration to be optimized.

Table 1. Summary of CFD analysis in real urban built environment without validation

Authors	Spatial scale	Location type	Equation/TM	Focus parameter category	Ref.
Huang et al. (2008)	Micro	Urban block	RANS/STKE	Pollutant dispersion/CO ₂ emissions	[4]
Chen et al. (2009)	Micro	Urban block	RANS/STKE	Thermal environment	[5]
Al-Sallal and Al-Rais (2011)	Micro	Urban block; street Canyon	RANS/STKE	Wind flow/Urban ventilation	[6]
Ashie and Kono (2011)	Meso	Urban area (23 wards, Tokyo)	RANS/STKE	Wind flow/Urban ventilation	[7]
Kaoru et al. (2011)	Micro	Urban block	RANS/STKE	Thermal environment	[8]
Fahmy and Sharples (2011)	Micro	Urban block	RANS/YMEE	Pollutant dispersion/CO ₂ emissions	[9]

(continued)

Table 1. (continued)

Authors	Spatial scale	Location type	Equation/TM	Focus parameter category	Ref.
Synnefa et al. (2011)	Building		RANS/STKE	Thermal environment; energy load	[10]
Tominaga (2012)	Micro	Urban block	RANS/DKE	Wind flow/Urban ventilation	[11]
Maragkogiannis et al. (2013)	Micro	Public square	RANS/CKEKE	Thermal environment	[12]
Taleb and Hijleh (2013)	Micro	Urban area	RANS/YMEE	Wind flow/Urban ventilation	[13]
Radhi et al. (2013)	Meso	District	RANS/RNGKE	Thermal environment	[14]
Miao et al. (2013)	Micro	Urban area	RANS/STKE	Pollutant dispersion/CO ₂ emissions	[15]
Frohlich and Matzarakis (2013)	Building		RANS/YMEE	Thermal environment	[16]
Gros et al. (2014)	Micro	Urban Block	RANS/STKE	Thermal environment	[17]
Yi and Peng (2014)	Indoor	Building	RANS/YMEE	Indoor thermal performance	[18]
Peng and Elwan (2014)	Micro	Urban block	RANS/YMEE	Environmental performance	[19]
Ciaramella et al. (2014)	Meso	District	RANS/YMEE	Environmental performance	[20]
Taleghani et al. (2014)	Building	University Campus	RANS/YMEE	Thermal environment	[21]
Peng et al. (2015)	Meso	District	RANS/RKE	Thermal environment	[22]
Cao et al. (2015)	Micro	Urban block	–	Thermal environment	[23]
Girgis et al. (2016)	Micro	Street Canyon	RANS/YMEE; STKE	Thermal environment	[24]
Allegrini and Carmeliet (2017)	Micro	Urban block	RANS/RKE	Thermal environment	[25]
Du and Mak (2018)	Micro	Street Canyons	RANS/STKE	Wind flow	[26]

Table 2. Summary of CFD analysis in real urban built environment with validation

Authors	Spatial scale	Location type	Equation/MM	Focus parameter category	Ref.
Priyadarsini et al. (2008)	Meso	Singapore	RANS/STKE	Thermal environment/Wind flow/Urban ventilation	[27]
Dimitrova et al. (2009)	Micro	Urban block	RANS/TEKE; STKE	Thermal environment	[28]
Kakon et al. (2009)	Micro	Street Canyon	RANS/YMEE	Thermal environment/Wind flow/Urban ventilation	[29]
Kakon et al. (2010)	Micro	Urban block	RANS/YMEE	Thermal environment	
Krüger et al. (2011)	Micro	Street Canyon	RANS/YMEE	Thermal environment; Wind flow/Urban ventilation	[30]
Zhang et al. (2012)	Building		RANS/RNGKE	Thermal environment; Wind Flow/Urban ventilation	[31]
Liu et al. (2012)	Micro	Urban area	LES/SLSGS	Pollutant dispersion/CO2 emissions	[32]
Ma et al. (2012)	Micro	Urban area	RANS/DKE	Thermal environment	[33]
Yang et al. (2013)	Micro	Buildings	RANS/YMEE	Thermal environment	[34]
Carnielo and Zinzi (2013)	Building		RANS/YMEE	Energy load; Thermal environment	[35]
Goldberg et al. (2013)	Meso	District	RANS/YMEE	Thermal environment; Wind flow/Urban ventilation	[36]
Hedquist and Brazel (2014)	Micro	Street Canyons	RANS/YMEE	Thermal environment	[37]
Maggiotto et al. (2014)	Meso	City	RANS/YMEE	Thermal environment	[38]
Zoras et al. (2014)	Micro	Urban block	–	Thermal environment	[39]
Du et al. (2014)	Building		RANS/STKE	Thermal environment	[40]
Dimoudi et al. (2014)	Micro	Urban Block	RANS/STKE	Thermal environment	[41]
Acero and Herranz-Pascual	Meso	City	RANS/YMEE	Thermal environment	[42]
Tominaga et al. (2015)	Micro	Urban block	RANS/RNGKE	Thermal environment	[43]
Gracik et al. (2015)	Micro	Urban block	RANS/RNGKE, RKE	Energy load; Thermal environment	[44]
Liu et al. (2015)	Building		RANS/MDKE	Wind flow/Urban ventilation	[45]

(continued)

Table 2. (continued)

Authors	Spatial scale	Location type	Equation/MM	Focus parameter category	Ref.
Elnabawi et al. (2015)	Micro	Street Canyon	RANS/YMEE	Thermal environment	[46]
Toparlar et al. (2015)	Meso	City	RANS/RKE	Thermal environment; Wind flow/Urban ventilation	[47]
Yang et al. (2015)	Micro	Street Canyon	RANS/YMEE	Thermal environment	[48]
Zoras (2015)	Micro	Street Canyon	RANS/SSTKW	Thermal environment; Wind flow/Urban ventilation	[49]
Bijad et al. (2016)	Micro	Urban block	RANS/RKE	Pollutant dispersion	[50]
Calautit et al. (2017)	Meso	City	RANS/STKE	Wind flow/Urban ventilation	[51]
Fouad et al. (2018)	Building		LES/RNGKE	Wind flow	[52]

4 Mathematical Formulations Used for CFD Analysis

CFD is based on the concepts of Fluid Mechanics, where numerical equations can be used to express the state of parameters like ventilation, solar radiation, rate of heat transfer etc. for evaluating the efficiency of built environment analytically. These primary mathematical equations are known as the governing equations based on the concept of conservation of mass and Second Law of Newton. There are two most popular approaches researchers have opted for their investigations as governing equations – Reynolds Averaged Navier Stokes commonly known as RANS and Large Eddy Simulation is commonly known as LES; as is evident in mentioned studies.

Although LES provides accurate results for CFD simulation the technique, RANS is most widely used due to low complex simulations and low computational costs, despite the affirmations that RANS would become outmoded in this practice of building simulation. From the viewpoint of building simulation, governing equations applied in CFD refers to the conservation equations. The solution parameters in these governing equations are referred to as Reynolds decomposition which is the sum of a mean and a variable component:

$$\theta = \bar{\theta} + \theta'; u_i = \bar{u}_i + u'_i; c = \bar{c} + c'; p = \bar{p} + p' \tag{1}$$

Where $\bar{\theta}, \bar{u}_i, \bar{c}, \bar{p}$ are the mean and θ', u'_i, c', p' are the variable component with respect to the mean. And the Navier Stokes equation for a three dimensional confined flow in Cartesian coordinates and in partial differential form are [53]:

$$\frac{\partial u_i}{\partial x_i} = 0 \quad (2)$$

$$\frac{\partial u_i}{\partial t} + \frac{\partial}{\partial x_j} (u_i u_j) = -\frac{1}{\rho} \frac{\partial p}{\partial x_i} + \frac{\partial}{\partial x_j} (2\nu s_{ij}) \quad (3)$$

Assuming, the specific heat of fluid to be constant, con equations for the temperature can be represented as [53]:

$$\frac{\partial \theta}{\partial t} + \frac{\partial}{\partial x_j} (\theta u_j) = \frac{\partial}{\partial x_j} + \left(\frac{k}{\rho c_p} \frac{\partial}{\partial x_j} \right) \quad (4)$$

And the equation for vapor and pollutants is as follows [53]:

$$\frac{\partial c}{\partial t} + \frac{\partial}{\partial x_j} (c u_j) = \frac{\partial}{\partial x_j} + \left(D \frac{\partial c}{\partial x_j} \right) \quad (5)$$

Where u_i is the instantaneous velocity, x_i is the position, c is the instantaneous concentration, θ is the instantaneous temperature, p is the instantaneous pressure, ρ is the density, t is the time, ν is the molecular viscosity, s_{ij} is strain rate tensor, c_p is the specific heat, D is the molecular diffusion coefficient, k is the thermal conductivity.

When the Eqs. 2–5 are substituted by the Reynolds decomposition (Eq. 1), the equation for Reynolds Averaged Navier Stokes (RANS) in its resultant form is [53]:

$$\frac{\partial \overline{u_i}}{\partial x_i} = 0 \quad (6)$$

$$\frac{\partial \overline{u_i}}{\partial t} + \frac{\partial}{\partial x_j} (\overline{u_i u_j}) = -\frac{1}{\rho} \frac{\partial \overline{p}}{\partial x_i} + \frac{\partial}{\partial x_j} (2\nu s_{ij}) - \frac{\partial}{\partial x_j} (\overline{u'_i - u'_j}) \quad (7)$$

$$\frac{\partial \overline{\theta}}{\partial t} + \frac{\partial}{\partial x_j} (\overline{\theta u_j}) = \frac{\partial}{\partial x_j} + \left(\frac{k}{\rho c_p} \frac{\partial \overline{\theta}}{\partial x_j} \right) - \frac{\partial}{\partial x_j} (\overline{\theta' - u'_j}) \quad (8)$$

$$\frac{\partial \overline{c}}{\partial t} + \frac{\partial}{\partial x_j} (\overline{c u_j}) = \frac{\partial}{\partial x_j} + \left(D \frac{\partial \overline{c}}{\partial x_j} \right) - \left(\overline{c' - u'_j} \right) \quad (9)$$

In LES, large eddies are influenced by the geometry of the problem. The solution variables for LES can be represented as [53]:

$$\theta = \tilde{\theta} + \theta'; u_i = \tilde{u}_i + u'_i; c = \tilde{c} + c'; p = \tilde{p} + p' \quad (10)$$

Where $\tilde{\theta}$, \tilde{u}_i , \tilde{c} , \tilde{p} are the parts which can be resolved and θ' , u'_i , c' , p' are the parts which are not resolved. Substituting Eq. 10 in Eqs. 2–5, the resultant equations will be for momentum, temperature and concentration and can be expressed as [53]:

$$\frac{\partial \tilde{u}_i}{\partial t} + \frac{\partial}{\partial x_j} (\tilde{u}_i \tilde{u}_j) = -\frac{1}{\rho} \frac{\partial \tilde{p}}{\partial x_i} + \frac{\partial}{\partial x_j} (2\nu \tilde{s}_{ij}) - \frac{\partial \tau_{ij}}{\partial x_j} \quad (11)$$

$$\frac{\partial \tilde{\theta}}{\partial t} + \frac{\partial}{\partial x_j} (\tilde{\theta} \tilde{u}_j) = \frac{\partial}{\partial x_j} \left(\frac{k}{\rho c_p} \frac{\partial \tilde{\theta}}{\partial x_j} \right) + \frac{\partial q_{t,ij}}{\partial x_j} \quad (12)$$

$$\frac{\partial \tilde{c}}{\partial t} + \frac{\partial}{\partial x_j} (\tilde{c} \tilde{u}_j) = \frac{\partial}{\partial x_j} \left(D \frac{\partial \tilde{c}}{\partial x_j} \right) - \frac{\partial q_{c,ij}}{\partial x_j} \quad (13)$$

With the use of RANS equations only mean flow is estimated and in LES equations, the small scale of eddies remains unresolved. In both cases, turbulence models are used to resolve the scales. Some that are widely used in building simulation are the standard k- ϵ model (STKE) [4–8, 10, 15, 17, 26–28, 40, 41, 51] and the one-equation Spalart-Allmaras model. The modified versions of the standard k- ϵ model are the Renormalization Group k- ϵ model (RNGE) [14, 31, 43, 44, 52] and the realizable k- ϵ model (RKE) [22, 25, 44, 47, 50], the standard k- ω model [49] and the Yamada and Mellor E- ϵ model (YMEE) [9, 13, 16, 18–21, 24, 29, 30, 34–38, 42, 46, 48].

5 Results

According to this review, in the past ten years, the studies on CFD and built environment are mostly conducted at mid-latitude urban locations and the most studied urban setting is Urban Block (38%), followed by Street Canyons (20%) and Buildings (20%) (Fig. 1). Out of the 51 studies, 23 studies were found to be without validation and 28 were conducted with validation. The rise in studies with validation can be observed since 2014, before that studies without validation were on rise in the year 2011 (Fig. 2). As is evident from Tables 1 and 2, RANS is the most popular numerical equation (98%) and YMEE turbulence model (58%) is most commonly used followed by the standard k- ϵ model (28%) in the above reviewed studies irrespective of the studies classified under without validation or with validation (Fig. 3). Thermal Environment is the focus parameter category of 58% of the reviewed studies, followed by Wind Flow/ Urban Ventilation (25%).

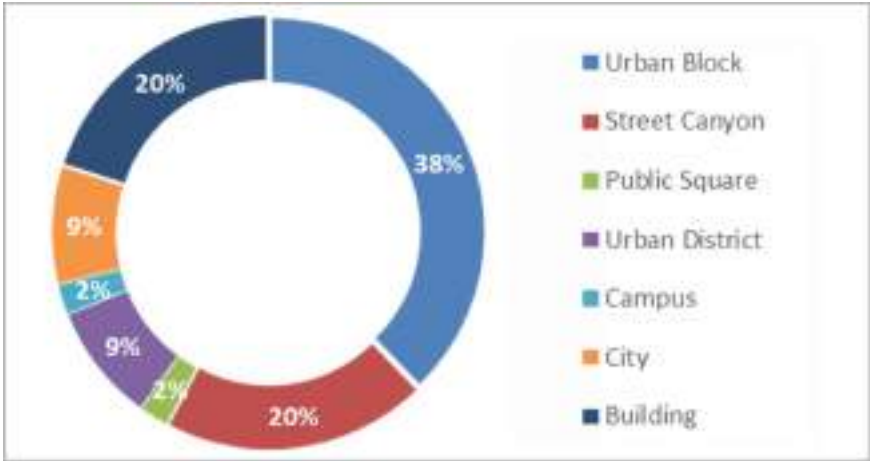


Fig. 1. Percentage share of CFD studies for complex built environment in past ten years on the basis of selected built environment setting.



Fig. 2. Graph showing CFD studies with and without validation for complex built environment for past ten years.

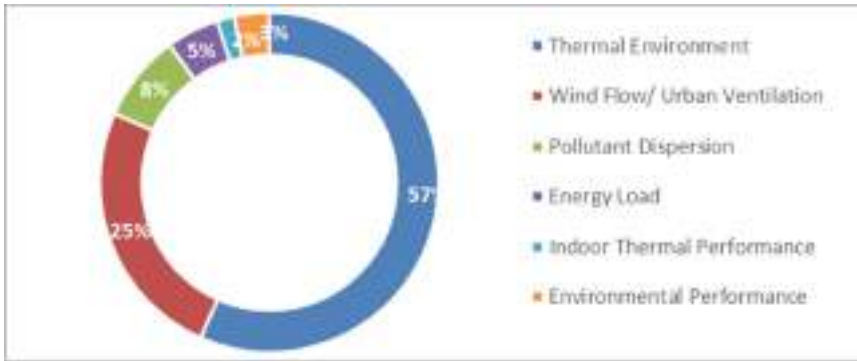


Fig. 3. Percentage share of parameters in CFD analysis of complex built environment for past ten years.

6 Conclusion

It is evident from the studies taken into consideration that the reviewed studies lack representation from arctic and subtropical regions. Future studies from these regions will be potentially beneficial in contributing to evaluating climate change issues and solutions. Since the study is more time consuming and complex in the case of city or region level and indoor level as compared to other spatial scales; the most studied built environment setting is found to be an urban block (38%). Thus, more studies are required in the case of cities (7%) and indoor level study (2%). Although the ratio of studies without validation and with validation is almost 1:1, among the investigated 46 studies, only 45 studies used RANS equation (98%), 1 study used only LES equations (2%); 34 studies had Thermal Environment as their focus parameter category, 15 studies investigated wind flow/ urban ventilation, only 5 studies were on pollutant dispersion making indoor thermal performance least studied focus parameter (1 study) after energy load (3 studies) and environmental performance (2 studies). There is high contrast in the number of studies on urban setting, focus parameters and the equations used. To bring diversified content and balanced addition to the existing knowledge, more studies of the city an indoor level, diverse focus parameters and use of LES for accurate results appears to be a way forward

References

1. United Nations, Global status report 2017 (2017)
2. Mon Soe, T., Yu Khaing, S.: Comparison of turbulence models for computational fluid dynamics simulation of wind flow on cluster of buildings in mandalay. *Int. J. Sci. Res. Publ.* 7(8), 337–350 (2017)
3. Toparlak, Y., Blocken, B., Maiheu, B., van Heijst, G.J.F.: A review on the CFD analysis of urban microclimate. *Renew. Sustain. Energy Rev.* 80, 1613–1640 (2017)





4. Huang, H., Ooka, R., Chen, H., Kato, S., Takahashi, T., Watanabe, T.: CFD analysis on traffic-induced air pollutant dispersion under non-isothermal condition in a complex urban area in winter. *J. Wind Eng. Ind. Aerodyn.* **96**(10–11), 1774–1788 (2008)
5. Chen, H., Ooka, R., Huang, H., Tsuchiya, T.: Study on mitigation measures for outdoor thermal environment on present urban blocks in Tokyo using coupled simulation. *Build. Environ.* **44**(11), 2290–2299 (2009)
6. Al-Sallal, K.A., Al-Rais, L.: Outdoor airflow analysis and potential for passive cooling in the modern urban context of Dubai. *Renew. Energy* **38**(1), 40–49 (2012)
7. Ashie, Y., Kono, T.: Urban-scale CFD analysis in support of a climate-sensitive design for the Tokyo Bay area. *Int. J. Climatol.* **31**(2), 174–188 (2011)
8. Kaoru, I., Akira, K., Akikazu, K.: The 24-h unsteady analysis of air flow and temperature in a real city by high-speed radiation calculation method. *Build. Environ.* **46**(8), 1632–1638 (2011)
9. Fahmy, M., Sharples, S.: Urban form, thermal comfort and building CO₂ emissions - a numerical analysis in Cairo. *Build. Serv. Eng. Res. Technol.* **32**(1), 73–84 (2011)
10. Synnefa, A., Karlessi, T., Gaitani, N., Santamouris, M., Assimakopoulos, D.N., Papakatsikas, C.: Experimental testing of cool colored thin layer asphalt and estimation of its potential to improve the urban microclimate. *Build. Environ.* **46**(1), 38–44 (2011)
11. Tominaga, Y.: Visualization of city breathability based on CFD technique: case study for urban blocks in Niigata City. *J. Vis.* **15**(3), 269–276 (2012)
12. Maragkogiannis, K., Kolokotsa, D., Maravelakis, E., Konstantaras, A.: Combining terrestrial laser scanning and computational fluid dynamics for the study of the urban thermal environment. *Sustain. Cities Soc.* **13**, 207–216 (2014)
13. Taleb, D., Abu-Hijleh, B.: Urban heat islands: Potential effect of organic and structured urban configurations on temperature variations in Dubai. *UAE. Renew. Energy* **50**, 747–762 (2013)
14. Radhi, H., Fikry, F., Sharples, S.: Impacts of urbanisation on the thermal behaviour of new built up environments: a scoping study of the urban heat island in Bahrain. *Landsc. Urban Plann.* **113**, 47–61 (2013)
15. Yucong, M., Shuhua, L., Bicheng, C., Bihui, Z., Shu, W., Shuyan, L.: Simulating urban flow and dispersion in Beijing by coupling a CFD model with the WRF model. *Adv. Atmos. Sci.* **30**(6), 1663–1678 (2013)
16. Fröhlich, D., Matzarakis, A.: Modeling of changes in thermal bioclimate: examples based on urban spaces in Freiburg. Germany. *Theor. Appl. Climatol.* **111**(3–4), 547–558 (2013)
17. Gros, A., Bozonnet, E., Inard, C.: Cool materials impact at district scale - coupling building energy and microclimate models. *Sustain. Cities Soc.* **13**, 254–266 (2014)
18. Yi, C.Y., Peng, C.: Microclimate change outdoor and indoor coupled simulation for passive building adaptation design. *Procedia Comput. Sci.* **32**, 691–698 (2014)
19. Peng, C., Elwan, A.: An outdoor-indoor coupled simulation framework for climate change-conscious urban neighborhood design. *Simulation* **90**(8), 874–891 (2014)
20. Ciaramella, A., Puglisi, V., Truppi, T.: Environmental performance assessment for urban districts. *J. Place Manag. Dev.* **7**(1), 74–89 (2014)
21. Taleghani, M., Sailor, D.J., Tenpierik, M., van den Dobbelsteen, A.: Thermal assessment of heat mitigation strategies: the case of Portland State University, Oregon. USA. *Build. Environ.* **73**, 138–150 (2014)
22. Peng, C., Ming, T., Gui, J., Tao, Y., Peng, Z.: Numerical analysis on the thermal environment of an old city district during urban renewal. *Energy Build.* **89**, 18–31 (2015)
23. Cao, A., Li, Q., Meng, Q.: Effects of orientation of urban roads on the local thermal environment in Guangzhou city. *Procedia Eng.* **121**, 2075–2082 (2015)

24. Girgis, N., Elariane, S., Elrazik, M.A.: Evaluation of heat exhausts impacts on pedestrian thermal comfort. *Sustain. Cities Soc.* **27**, 152–159 (2016)
25. Allegrini, J., Carmeliet, J.: Coupled CFD and building energy simulations for studying the impacts of building height topology and buoyancy on local urban microclimates. *Urban Clim.* **21**, 278–305 (2017)
26. Du, Y., Mak, C.M.: Improving pedestrian level low wind velocity environment in high-density cities: a general framework and case study. *Sustain. Cities Soc.* **42**, 314–324 (2018)
27. Priyadarsini, R., Hien, W.N., David, C.K.W.: Microclimatic modeling of the urban thermal environment of Singapore to mitigate urban heat island. *Sol. Energy* **82**(8), 727–745 (2008)
28. Dimitrova, R., et al.: Influence of thermal effects on the wind field within the urban environment. *Bound.-Layer Meteorol.* **131**(2), 223–243 (2009)
29. Kakon, A.N., Mishima, N., Kojima, S.: Simulation of the urban thermal comfort in a high density tropical city: analysis of the proposed urban construction rules for Dhaka. Bangladesh. *Build. Simul.* **2**(4), 291–305 (2009)
30. Krüger, E.L., Minella, F.O., Rasia, F.: Impact of urban geometry on outdoor thermal comfort and air quality from field measurements in Curitiba. *Brazil. Build. Environ.* **46**(3), 621–634 (2011)
31. Zhang, W., Mak, C.M., Ai, Z.T., Siu, W.M.: A study of the ventilation and thermal comfort of the environment surrounding a new university building under construction. *Indoor Built Environ.* **21**(4), 568–582 (2012)
32. Liu, Y.S., Miao, S.G., Zhang, C.L., Cui, G.X., Zhang, Z.S.: Study on micro-atmospheric environment by coupling large eddy simulation with mesoscale model. *J. Wind Eng. Ind. Aerodyn.* **107–108**, 106–117 (2012)
33. Ma, J., Li, X., Zhu, Y.: A simplified method to predict the outdoor thermal environment in residential district. *Build. Simul.* **5**(2), 157–167 (2012)
34. Yang, X., Zhao, L., Bruse, M., Meng, Q.: Evaluation of a microclimate model for predicting the thermal behavior of different ground surfaces. *Build. Environ.* **60**, 93–104 (2013)
35. Carnielo, E., Zinzi, M.: Optical and thermal characterisation of cool asphalts to mitigate urban temperatures and building cooling demand. *Build. Environ.* **60**, 56–65 (2013)
36. Goldberg, V., Kurbjuhn, C., Bernhofer, C.: How relevant is urban planning for the thermal comfort of pedestrians? Numerical case studies in two districts of the city of Dresden (Saxony/Germany). *Meteorol. Zeitschrift* **22**(6), 739–751 (2013)
37. Hedquist, B.C., Brazel, A.J.: Seasonal variability of temperatures and outdoor human comfort in phoenix, Arizona, USA. *Build. Environ.* **72**, 377–388 (2014)
38. Maggiotto, G., Buccolieri, R., Santo, M.A., Leo, L.S., Di Sabatino, S.: Validation of temperature-perturbation and CFD-based modelling for the prediction of the thermal urban environment: the Lecce (IT) case study. *Environ. Model Softw.* **60**, 69–83 (2014)
39. Zoras, S., Tsermentselis, A., Kosmopoulos, P., Dimoudi, A.: Evaluation of the application of cool materials in urban spaces: a case study in the center of Florina. *Sustain. Cities Soc.* **13**, 223–229 (2014)
40. Du, X., Bokel, R., van den Dobbels, A.: Building microclimate and summer thermal comfort in free-running buildings with diverse spaces: a Chinese vernacular house case. *Build. Environ.* **82**, 215–227 (2014)
41. Dimoudi, A., Zoras, S., Kantzioura, A., Stogiannou, X., Kosmopoulos, P., Pallas, C.: Use of cool materials and other bioclimatic interventions in outdoor places in order to mitigate the urban heat island in a medium size city in Greece. *Sustain. Cities Soc.* **13**, 89–96 (2014)
42. Acero, J.A., Herranz-Pascual, K.: A comparison of thermal comfort conditions in four urban spaces by means of measurements and modelling techniques. *Build. Environ.* **93**(P2), 245–257 (2015)

43. Tominaga, Y., Sato, Y., Sadohara, S.: CFD simulations of the effect of evaporative cooling from water bodies in a micro-scale urban environment: validation and application studies. *Sustain. Cities Soc.* **19**, 259–270 (2015)
44. Gracik, S., Heidarinejad, M., Liu, J., Srebric, J.: Effect of urban neighborhoods on the performance of building cooling systems. *Build. Environ.* **90**, 15–29 (2015)
45. Liu, J., Heidarinejad, M., Gracik, S., Srebric, J., Yu, N.: An indirect validation of convective heat transfer coefficients (CHTCs) for external building surfaces in an actual urban environment. *Build. Simul.* **8**(3), 337–352 (2015)
46. Elnabawi, M.H., Hamza, N., Dudek, S.: Numerical modelling evaluation for the microclimate of an outdoor urban form in Cairo. Egypt. *HBRC J.* **11**(2), 246–251 (2015)
47. Toparlar, Y., et al.: CFD simulation and validation of urban microclimate: a case study for Bergpolder Zuid. Rotterdam. *Build. Environ.* **83**, 79–90 (2015)
48. Yang, W., Wong, N.H., Lin, Y.: Thermal comfort in high-rise urban environments in Singapore. *Procedia Eng.* **121**, 2125–2131 (2015)
49. Zoras, S.: Urban environment thermal improvement by the bioclimatic simulation of a populated open urban space in Greece. *Int. J. Ambient Energy* **36**(4), 156–169 (2015)
50. Bijad, E., Delavar, M.A., Sedighi, K.: CFD simulation of effects of dimension changes of buildings on pollution dispersion in the built environment. *Alexandria Eng. J.* **55**, 3135–3144 (2016)
51. Calautit, J.K., Hughes, B.R., Nasir, D.S.: Climatic analysis of a passive cooling technology for the built environment in hot countries. *Appl. Energy* **186**, 321–335 (2017)
52. Fouad, N.S., Mahmoud, G.H., Nasr, N.E.: Comparative study of international codes wind loads and CFD results for low rise buildings. *Alexandria Eng. J.* **57**, 3623–3639 (2018)
53. Blocken, B.: LES over RANS in building simulation for outdoor and indoor applications: a foregone conclusion? *Build. Simul.* **11**(5), 821–870 (2018)



A Smart Grid Technique for Dynamic Load Prediction in Nigerian Power Distribution Network

E. Ndidi Osegi¹ , O. Egerton Taylor² ,
B. Alexander Wokoma² , and A. Ogacheko Idachaba² 

¹ National Open University of Nigeria, Lagos, Nigeria

² Rivers State University, Port Harcourt, Rivers, Nigeria

Abstract. The current situation of power system in Nigeria is faced with the obvious challenge of circumventing faulty transmission lines and assuring optimum power distribution and utilization. In the context of smart grids, this warrants the need for intelligent solutions powered by digital signal processing engines. In this paper, a recently proposed technique inspired by intelligent processing in mammalian auditory cortex is applied to load forecasting in the Nigerian power distribution network, Port-Harcourt, Diobu Zone. The auditory inspired algorithm is designed in such a way as to intelligently estimate in advance the received energy loading at a particular bus in a power distribution network. Simulations are conducted in the MATLAB environment in order to validate the proposed system.

Keywords: Distribution · Machine intelligence · Predictions · Power system distribution network · Smart grid

1 Introduction

The need to improve existing power infrastructures coupled with the emergent requirements of modernization has led to the renewed interest in smart solutions for power networks in the country. One direction in this regard is the development of smart grids which are basically enhancements of conventional power grids using digital computation and communication technologies for improved services to both the power operators and consumers [1]. Smart grid solutions improve the overall performance of the goods and services in a society. It can save the government of any nation the ever increasing costs of funding new power plants, save large corporations from incessant maintenance operations, and provide useful feedback and control for end users. Some reviews of related smart grid applications that have been developed in the literature can be found in [2–4].

In a power distribution network, energy management is a primary issue faced by the power system regulators. For instance, in a residential household in Nigeria, a typical problem that may occur is the inability of the end users to turn off appliances when not at home. This may lead to energy wastage and increased cost of utility bills. In another instance, where a renewable resource is used as back-up energy supply, the users may

abuse the power circuitry by connecting equipment loads with large capacities to distribution network.

Since prediction capable smart grids are important for timely power failure interventions, it will be advantageous to develop algorithms that can be integrated in smart grid systems.

In this paper, a technique that uses machine intelligence concept inspired by changes observed in the auditory cortex of mammals is presented. The primary object of the technique is to automatically estimate in advance the amount of power loading at a receiving bus in a power distribution smart grid system which in turn can be used to compute the energy shortfall and hence the required amount of alternate energy integration that may be needed in the particular load bus under study.

2 Methodology

2.1 Systems Model Formulation

The proposed smart grid distribution system follows a modular approach where the smart grid is modeled as a system of interconnecting modules with separate or related functions. The system model includes the following basic modules:

- (1) Power Source Module
- (2) Transmission Module
- (3) Intelligent Processor Module
- (4) Feedback/Control Module

The Power Source Module (PSM) serves as input to the entire system which basically includes the standard generation and optional alternate renewable energy sources.

The Transmission Module (TM) ensures the proper transfer of power to the various load buses in the power network; where the load buses serve the immediate residential homes, a renewable resource is supplied otherwise it is disabled.

The Intelligent Processor Module (IPM) functions as a smart prediction unit and ensures that power system trends are quickly identified for proper energy management; this module specifically features a machine intelligent algorithm for electrical energy demand forecasting.

The Feedback/Control Module (FCM) is an optional feature that can serve the purpose of automatic adjustment of load demand schedules during an energy management phase. Thus, it is tightly integrated with the IPM.

2.2 Auditory Machine Intelligence Technique

Auditory Machine Intelligence (AMI) is basically a deterministic machine intelligence neural technique that was introduced in [5] under the name “Deviant Learning Algorithm for time series prediction. This technique was further developed in [6] to overcome the limitations in the temporal learning phase of the existing Hierarchical Temporal Memory (HTM) neural techniques developed in [7, 8].

AMI exploits the idea and findings about the mismatch negativity effect (MMN) and intelligent processing in mammalian auditory cortex to build an algorithm that can give more precise predictions in a timely and more reliable manner. The MMN is a differential neuronal response to a repetition of stimulus presentations and an oddball or deviant stimulus signal [9]. MMN has been shown to exhibit very important high level cognitive processes [10].

Recent experiments on macaque monkeys using electro-corticography in the context of the roving odd-ball has shown the MMA (corresponding MMN effect in animals) to exhibit Specific-Stimulus Adaptation (SSA) properties including cortical response to deviant stimulus (odd-balls) over a wide area of cortical regions [9]. In [11], it has also been shown via neuronal simulations that functional reorganization of the receptive fields in mature primary auditory cortex, A1, will occur when subjected to appropriate frequency fine-tuning and exposure of the cortical front (ON/OFF) receptive fields to sound waves. Thus, in a developing auditory cortex, the ON/OFF receptive fields sensitivity to sensory signals (frequency modulated tone sweeps) can be explained by using a simple universally accepted Hebbian rule. A visual concept of this frequency tuned learning for functional reorganization is as shown in Fig. 1; in the visual, the large white blob represent a neuron, excitatory and inhibitory ON synaptic weight inputs are indicated as green, open and filled blobs while excitatory and inhibitory OFF inputs are indicated as red, open and filled blobs. As can be seen from Fig. 1, after hebbian learning, there is a divergence in the synaptic weight inputs (indicated by the thick dark connected arrows) to the processed or simulated neuron (now grey).

In subsequent paragraphs, we describe the principle of AMI and discuss its relevance in a smart grid system.

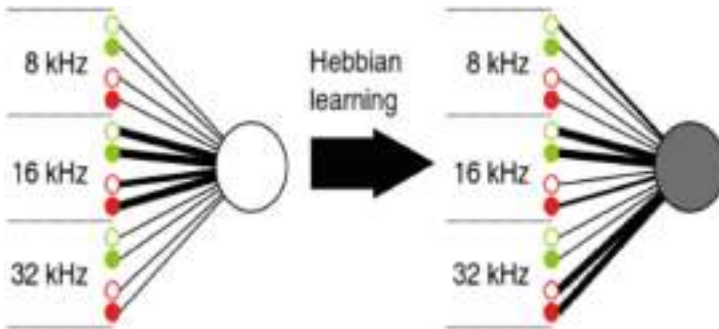


Fig. 1. A visual of a frequency-tuned hebbian learning concept in A1 [11].

AMI Principle. The AMI principle is based on the MMN theory [9, 10, 12–14] and the theory of functional reorganization in mammalian auditory cortex [11]. In the context of MMN, the change detection theory features more prominently. Furthermore, the concept of functional reorganization is exhibited by a frequency-tuned hebbian-like learning mechanism.

The AMI algorithm is as described in Algorithm 1. It basically occurs in two-phases [15]:

- A Phase-1 or low-level prediction for making a prediction in the current time step given a history of sparse data points in the previous time step. These sparse data points correspond to the evoked potentials originally observed in [12] as the “odd-ball”.
- A Phase-2 or high-level prediction that performs look-ahead predictions several time steps ahead.

In the proposed smart grid system, a Phase-1 prediction is used to perform single or one-step-ahead forecasts of streaming power loads. The AMI performs this operation using the computation of a single learning formula and no specific random fine-tuning is needed to learn on the data. In phase-1 predictions, the AMI learns a sequence of data points (values) automatically/temporally in an adaptive manner such that a mean deviant point is computed as in (1):

$$S_{dev(mean)} = \frac{\left(\left(\frac{\sum [S_{dev}]}{(n-1)} \right) + S_{deviant} \right) - 2}{n + 1} \tag{1}$$

where,

- n = number of data points in a temporal sequence
- $S_{deviant}$ = the $(n - 1)$ th value of the temporal sequence
- S_{dev} = the difference between $S_{deviant}$ and S_{stars}
- S_{stars} = the $(n - 2)$ th values of the temporal sequence
- S^* = sparse set of input sequences

In order to make a prediction with the AMI, the formula in (2) is used as:

$$S_{pred} = S_{deviant} + S_{dev(mean)} \tag{2}$$

where,

$$S_{deviant} = S_n^* - 1 \tag{3}$$

$$S_{stars} = S_n^* - 2 \tag{4}$$

Algorithm 1. AMI Processing Algorithm

- 1: Initialize S_{pred} , as prediction parameter, S_{stars} , as input sequences (standards) $S_{dev(mean)}$ as deviant mean, j as iteration counter.
- 2: for all $s \in s.S_{stars}$, && $j > 1$, do
- 3: Compute $S_{deviant}$ and S_{stars} using equations (3) and (4)
- 4: $S_{dev} \leftarrow \|S_{deviant} - S_{stars}\|$ // deviations from standards
- 5: Compute $S_{dev(mean)}$ using equations (1)
- 6: Compute S_{pred} using equations (1) and (3)
- 7: Update $S_{dev(mean)}$ using Algorithm 2
- 8: end for

Learning Rule. The AMI algorithm uses a Hebbian learning rule as follows:

If the current prediction error of the AMI neuron is greater than or lower than zero, we reinforce its prediction by decreasing or increasing its deviant weight value by the absolute prediction error difference at the current time step; otherwise we perform zero or negligible positive reinforcement by adding a very small value (deviant-Laplacian correction). In the case where exact matches occur, a small Laplacian correction value (typically in small fractions of about a hundredth), is used for deviant weight updates. The learning rule is described succinctly in Algorithm 2.

Algorithm 2. AMI Learning Algorithm

- 1: Initialize S_{pred} , as prediction parameter, S_{stars} , as input sequences (standards) State, $S_{dev(mean)}$ as deviant mean, $S_{diff(1)}$ as difference between S_{pred} , $S_{deviant+1}$ and $S_{diff(2)}$ as difference between $S_{dev(mean)}$ and $|S_{diff(1)}|$, I_p as correction factor or bias.
- 2: for all $s \in s.S_{stars}$ do
- 3: if $S_{diff(2)} > 0$
- 4: $S_{dev(mean)} \leftarrow S_{dev(mean)} - |S_{diff(1)}|$ // Weaken deviant mean by a factor, $|S_{diff(1)}|$
- 5: elseif $S_{diff(2)} < 0$
- 6: $S_{dev(mean)} \leftarrow S_{dev(mean)} + |S_{diff(1)}|$ // Reinforce deviant mean by a factor, $|S_{diff(1)}|$
- 7: else
- 8: $S_{dev(mean)} \leftarrow S_{dev(mean)} + I_p$
- 9: end if
- 10: end for

Application of AMI to Smart Grids. One of the primary systems (or sub-systems) of a smart grid, the Advanced Distribution Operation System (ADOS), represents a key improvement in the operations of distribution power systems by providing specialized functions such as automated distribution, control and protection, distributed energy management etc. [16]. In a machine intelligent smart grid, the AMI leverages on the energy management functions by making energy (electrical load) demand forecasts in advance. This is important in two aspects:

First, using the principle of continual temporal re-sequencing based on a unique temporal-differencing algorithm, the AMI can aid in the online detection of important trends that may exist in the power distribution network demand data. Thus, proper power budgets can be made based on well informed system operations.

Secondly, the AMI technique facilitates the automation procedures that will be implemented in real time systems. By enabling a predictive algorithm in real power distribution, it is possible to perform secure and timely adaptive control of distribution power system supply which in turn enables better power delivery to prospective consumers.

3 Experiments and Results

3.1 Systems Description

Experiments have been performed in the MATLAB-SIMULINK environment. The experiments are based on a section of the Nigerian power distribution network, Port-Harcourt (PH) Diobu Zone and the data for simulations are obtained from the Port-Harcourt Electricity distribution (PHED) company of Nigeria.

PHED forms part of 11 distribution companies (DISCOS) all of which are responsible for managing the wiring, sales, billing and customer support functions within their area of operation. Presently, PHED company serves Bayelsa, Cross-Rivers, Akwa-Ibom and a number of locations in Delta State all in Nigeria. This DISCO comprises six districts (Calabar, Diobu, Ikom/Ogoja, Borokiri, Uyo and Yenegoa). This DISCO (PHED) also operates 33 kV circuits (22 in number) and 11 kV circuits (64 in number). Further details about the Nigerian power distribution can be found in [17]. This study investigates the Diobu district of the PHED network.

A cross-section of PHED network Diobu Zone is as shown in Fig. 2. It is a 4-bus power system network that includes a power grid (Afam Power Transmission Station – AFAM T/S), Transmission/Distribution lines, Step-Down Transformers, Isolators and lumped loads representing the feeder loads UST FDR, Rumuolemeni FDR and Silverbird FDR at bus sites 2, 3 and 4 respectively.

The accompanying power systems model in the SIMULINK environment is also shown in Fig. 3 which includes a smart prediction module defined as an Embedded MATLAB function block. This model enables the Diobu PHED network to be emulated as a smart grid in software.

The bus considered for analysis in the experimental simulations is Bus2 (UST Feeder).

Bus 1 (PHTown) is a PV bus and serves as a main feeder source to the load buses: buses B2, B3 and B4; it may also be used as a Slack bus. Bus 1 (B1) sources its power from the Afam Power Station located in Rivers State Nigeria. The system is designed to operate at 0.8 lagging power factor and at a frequency of 50 Hz. The MVA ratings of the grid and the associated feeder buses are as indicated in Fig. 2.

The bus nomenclature including operational load ratings of the considered distribution system are also given in Table 1.

The power systems simulation model network (see Fig. 3) consists of the following key modules:

Prediction Module. This is used for estimating in advance the probable power received at a particular bus. This module is based on the auditory machine intelligence (AMI) technique described in the previous section (Subsect. 2.2). This module is especially coded using the Embedded MATLAB function block in MATLAB-SIMULINK.

Dynamic Load Bus. This is used for emulating the variable nature of load in a power distribution network. It captures the random states inherent in a typical power distribution network load bus and is modeled as a random source block in MATLAB-SIMULINK. The load (feeder) buses include B2, B3 and B4 and their system ratings are provided in Table 1. The bus under analysis, Bus module B2, is specifically connected to the prediction module via the Embedded MATLAB function block. All feeder buses have been implemented as a sub-system in SIMULINK.

Line Blocks. These blocks model the short lines used in the Diobu zone PHED power network. The lines are L12, L13, and L14 denoting the interconnection between the PV bus (Bus 1) and the other power system (load) buses; their respective ratings are also given in Table 2.

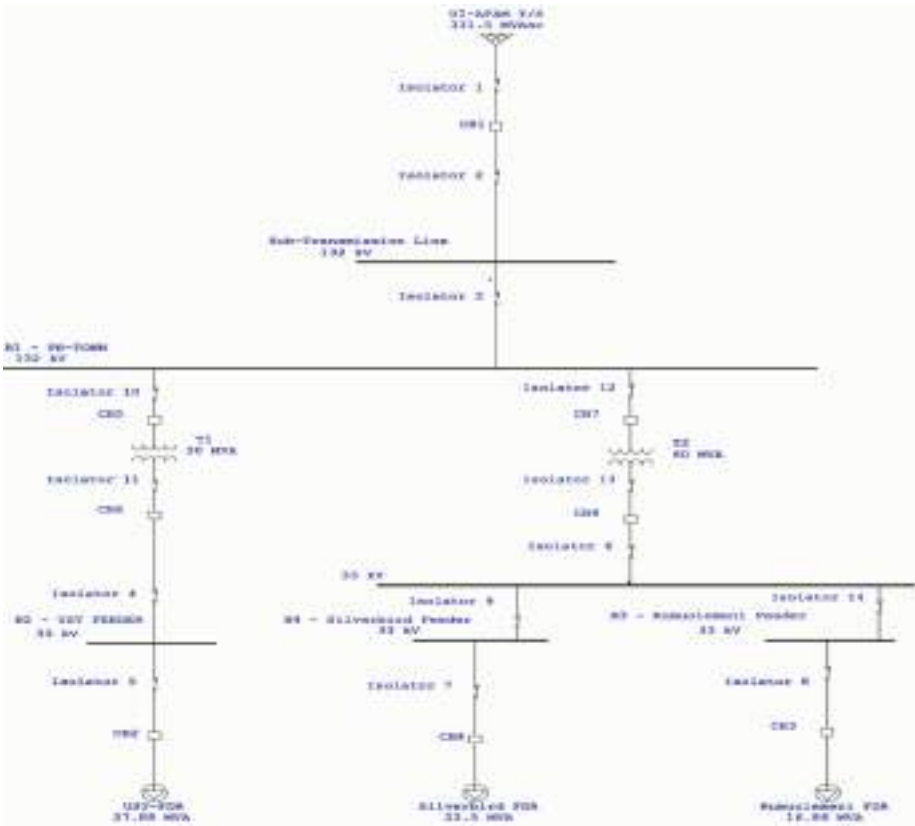


Fig. 2. Generalized single line diagram of a section of PH power distribution network, Diobu Zone

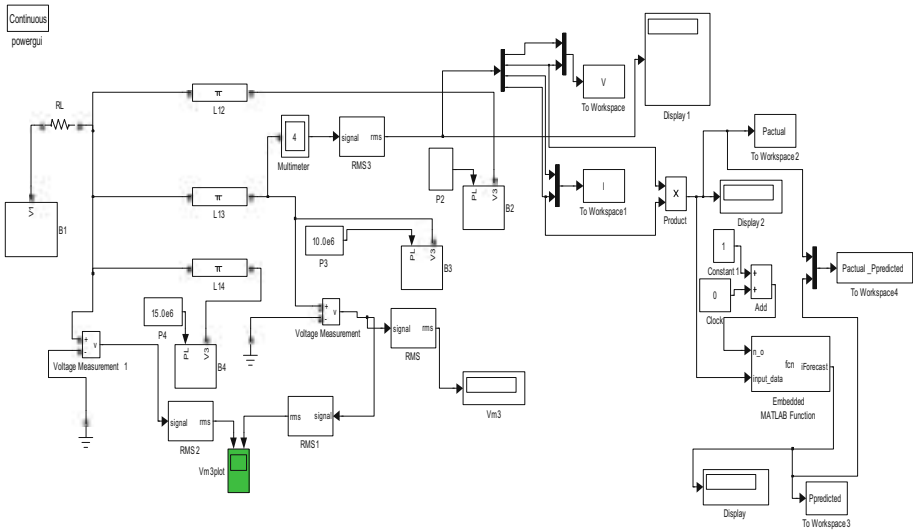


Fig. 3. Scheme of a section of PHED power network (Diobu Zone) in MATLAB SIMULINK

3.2 Load Variation Experiments

The prediction results obtained by varying the loading at bus 2 using the power demand range provided in Table 1 are as shown in Figs. 4, 5 and 6. The results are compared with the expected (actual) load demand values generated in pseudo-real time using the system model in Fig. 3. In Fig. 4, the simulation acquisition steps are defined for 100 data points with 20 data points used as initial sequence set for the AMI algorithm. In Fig. 5 the simulation acquisition steps are defined for 100 data points in the AMI algorithm. The results indicate that the system will predict an increase in power loading at bus 2 for the first 50 data points after which it predicts a decrease for the remaining data points.

In particular, increasing the number of training points in the AMI algorithm leads to improvements in predictions. This is validated by increasing the number of training data points from 100 to 500 (see Fig. 6).

Table 1. Bus nomenclature for system model (see Fig. 1).

Bus label	Bus name	Bus designation	Load range (MW)
B1	PH-TOWN	PV bus	45.0–95.0
B2	UST Feeder	Load bus	20.8–22.3
B3	Rumuolemeni Feeder	Load bus	10.0–13.5
B4	Silverbird Feeder	Load bus	15.0–18.0

Table 2. Line block parameters (see Fig. 1).

Line block	Line resistance (Ohms/km)	Line length (km)
L12	2.21	15.50
L13	3.21	22.78
L14	0.44	3.06

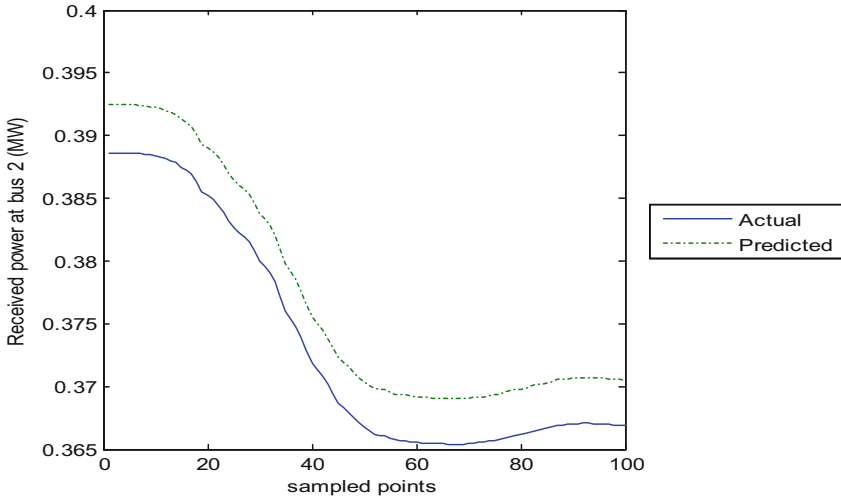


Fig. 4. Simulated load prediction response and actual values; simulation data points set to 100 and AMI training data points set to 20.

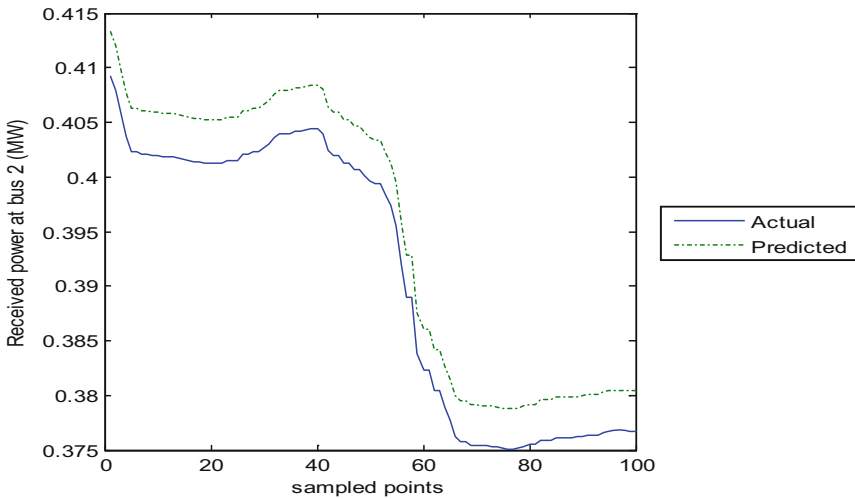


Fig. 5. Simulated load prediction response and actual values; simulation data points and AMI training data points set to 100.

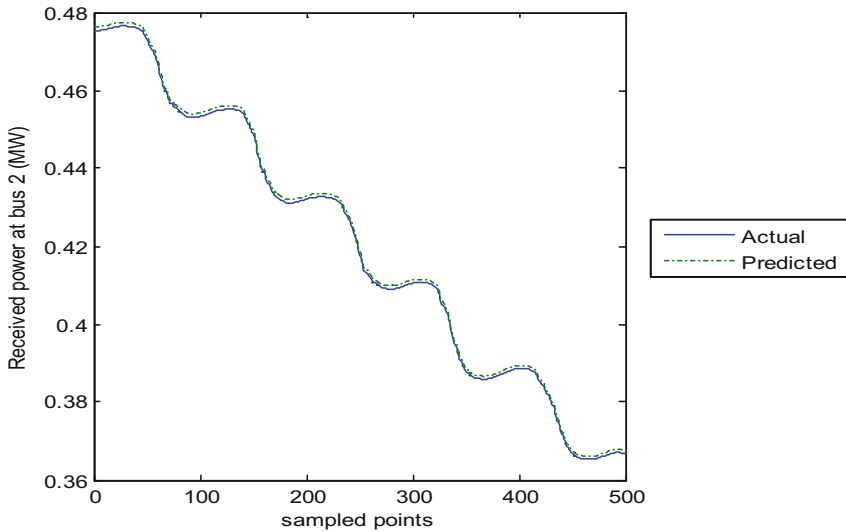


Fig. 6. Simulated load prediction response and actual values; simulation data points and AMI training data points set to 500.

4 Discussions and Conclusions

In this paper, a predictive approach based on Auditory Machine Intelligence (AMI) algorithm for load management that can support smart grid applications is proposed. The AMI uses an online learning program to dynamically predict in advance the load demand at a feeder bus; this approach eliminates the use of training and testing dataset as is common with most traditional neural network approaches. Through simulation experiments, it has been shown how this new machine intelligence algorithm can be used to continually (in pseudo-real time) predict in advance the power received in a section of the Nigerian power distribution network.

The results of prediction show the importance of training points on the prediction capability of the proposed AMI technique and in turn on the smart grid prediction performance. For instance, when the AMI training points is less than the data training points, the AMI prediction and actual (training) data plots do not meet at all (see Fig. 4). When the training points for both the AMI and training data are made equal and set to about 100 data points, there is a noticeable improvement in their respective plots between the 45th to 60th data points with a reduced gap between the plots (see Fig. 5). Also, when the AMI and training data points are both increased to a value of 500, there is significant improvement as the AMI predictions now closely match the training data as indicated in Fig. 6.

The AMI prediction results also indicate that there will be a power increase so the need to integrate additional power support such as renewable resources may be necessary. An interesting observation is that the AMI algorithm can emulate the shape of the input load pattern; this is very important for pattern following systems and can be a

useful indicator of anomaly or outliers present in power system data due to unusual changes in load demand.

This research study is to the best of our knowledge, the first application using auditory-inspired machine intelligence for forecasting energy loads in a power distribution network.

Future work should focus on a real time embedded system implementations of the proposed model in real power distribution networks with renewable energy penetration; this can be useful in the event of an imminent energy rise where the predictions of the Auditory Machine Intelligence (AMI) algorithm in conjunction with a consensus mining algorithm can be used for resetting the power distribution network to appropriate levels as the energy demand varies.

More interactive and user friendly automated smart grid load management designs including renewable energy integration is also anticipated with a view to enhancing end-user experiences as well as the operators of the distribution power systems.

References

1. Reka, S.S., Dragicevic, T.: Future effectual role of energy delivery: a comprehensive review of Internet of Things and smart grid. *Renew. Sustain. Energy Rev.* **91**, 90–108 (2018). <https://doi.org/10.1016/j.rser.2018.03.089>
2. Ismagilova, E., Hughes, L., Dwivedi, Y.K., Raman, K.R.: Smart cities: advances in research—an information systems perspective. *Int. J. Inf. Manage.* **47**, 88–100 (2019). <https://doi.org/10.1016/j.ijinfomgt.2019.01.004>
3. Michalec, A., Hayes, E., Longhurst, J., Tudgey, D.: Enhancing the communication potential of smart metering for energy and water. *Util. Policy.* **56**, 33–40 (2019). <https://doi.org/10.1016/j.jup.2018.11.002>
4. Zafar, R., Mahmood, A., Razzaq, S., Ali, W., Naeem, U., Shehzad, K.: Prosumer based energy management and sharing in smart grid. *Renew. Sustain. Energy Rev.* **82**, 1675–1684 (2018). <https://doi.org/10.1016/j.rser.2017.07.018>
5. Osegi, E.N., Anireh, V.I.E.: Deviant Learning Algorithm: Learning Sparse Mismatch Representations through Time and Space. *arXiv preprint arXiv:1609.01459* (2016)
6. Osegi, E.N., Anireh, V.I.E.: AMI: An Auditory Machine Intelligence Algorithm for Predicting Sensory-Like Data (2019, in press)
7. Cui, Y., Ahmad, S., Hawkins, J.: The HTM spatial pooler—a neocortical algorithm for online sparse distributed coding. *Front. Comput. Neurosci.* **11**, 111 (2017). <https://doi.org/10.3389/fncom.2017.00111>
8. Osegi, E.N.: Using the hierarchical temporal memory spatial pooler for short-term forecasting of electrical load time series (2018). <https://doi.org/10.1016/j.aci.2018.09.002>
9. Takaura, K., Fujii, N.: Facilitative effect of repetitive presentation of one stimulus on cortical responses to other stimuli in macaque monkeys - a possible neural mechanism for mismatch negativity. *Eur. J. Neurosci.* **43**(4), 516–528 (2016). <https://doi.org/10.1111/ejn.13136>
10. Näätänen, R., Paavilainen, P., Rinne, T., Alho, K.: The mismatch negativity (MMN) in basic research of central auditory processing: a review. *Clin. Neurophysiol.* **118**(12), 2544–2590 (2007). <https://doi.org/10.1016/j.clinph.2007.04.026>
11. Sollini, J., Chapuis, G.A., Clopath, C., Chadderton, P.: ON-OFF receptive fields in auditory cortex diverge during development and contribute to directional sweep selectivity. *Nat. Commun.* **9**(1), 2084 (2018). <https://doi.org/10.1038/s41467-018-04548-3>

12. Näätänen, R., Gaillard, A.W.K., Mäntysalo, S.: Early selective-attention effect on evoked potential reinterpreted. *Acta Psychol. (Amst)*. **42**(4), 313–329 (1978)
13. Lieder, F., Daunizeau, J., Garrido, M.I., Friston, K.J., Stephan, K.E.: Modelling trial-by-trial changes in the mismatch negativity. *PLoS Comput. Biol.* **9**(2), e1002911 (2013). <https://doi.org/10.1371/journal.pcbi.1002911>
14. Lieder, F., Stephan, K.E., Daunizeau, J., Garrido, M.I., Friston, K.J.: A neurocomputational model of the mismatch negativity. *PLoS Comput. Biol.* **9**(11), e1003288 (2013). <https://doi.org/10.1371/journal.pcbi.1003288>
15. Osegi, E.N., Anireh, V.I., Onukwugha, C.G.: pCWoT-MOBILE: a collaborative web based platform for real time control in the smart space. In: 11th *iSTEAMs* Conference. vol. 3, no. 13, pp. 237–250 (2018)
16. Yang, T.: ICT technologies standards and protocols for active distribution network. In: *Smart Power Distribution Systems*, pp. 205–230. Academic Press (2019). <https://doi.org/10.1016/b978-0-12-812154-2.00010-9>
17. Abanihi, V.K., Ikheloa, S.O., Okodede, F.: Overview of the Nigerian power sector V. *Am. J. Eng. Res.* **7**(5), 2320–2847 (2018)



Modeling and Control of Wind Energy System with PMSG Using Maximum Power Tracking

Hitesh Joshi[✉]  and A. K. Swami 

G.B. Pant University of Agriculture and Technology, Pantnagar, India
haitijoshi@gmail.com, anuragkswami@yahoo.com

Abstract. In this paper, a modelling of wind energy system with permanent magnet synchronous generator (PMSG) is presented. The system been modeled in MATLAB/Simulink environment contains several models including wind turbine along with a permanent synchronous generator, bridge diode rectifier, dc to dc boost converter circuit with a inverter (VSI). The MPPT controller based on Perturb & Observe (P&O) algorithm is developed which in terms provide the ideal duty ratio by adjusting the rotor speed of generator to the dc to dc converter. The inverter circuit is controlled using a proposed control scheme employing a PI controller which gives the controlled PWM pulses for output load voltages.

Keywords: PMSG · MPPT · Dc to dc converter · P&O · PI controller · VSI

1 Introduction

In the past few decades, non-conventional energy sources for the generation of electric power has experienced a tremendous growth in view of the worldwide concerns that are being related to the conventional (fossil fuels, etc.) generation and encouraging shortages in global energy demands. In this perspective, a larger interest has been experienced by the wind energy systems for fulfilling the energy distribution demands as desired towards the rapid market expansion. Recent development suggests a trend towards using high power ratings and larger wind turbines in wind energy conversion systems (WECS). In view of operation wise, the wind energy systems having variable speeds have numerous benefits such as improving the power quality and efficiency, providing output with maximum power, producing very less level of mechanical stress as when compared with fixed speed wind energy systems [1, 2]. Wind energy systems driving the permanent magnet synchronous generator (PMSG), thus overall improves the reliability for the turbines having variable speeds. Among all other different kinds of generator configurations employed in the wind energy systems, the PMSG has numerous advantages as its ability to operate in low speeds, has a very simple structure, has high power factor in the sense that it is self- excited and it yields high efficiency [3]. A gearbox is primarily not required for the low speed operation of PMSG, which means in low speed operation it is prone to several faults and unreliability of the system is caused due to regular maintenance [4, 5]. A system configuration of such a system with WT connected to a load using PMSG and machine and grid side converters is shown in Fig. 1.

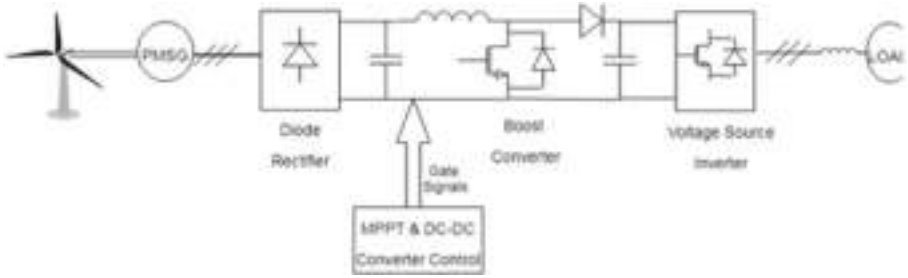


Fig. 1. The configuration of the wind energy system with the MPPT and converter controllers

This paper proposes a study in which the wind turbine is modelled in a way that the power which is available from the wind is being transformed to the generator rotor shaft mechanical power, then this available mechanically generated power in the generator rotor is been converted to electric power that involves a PMSG for this overall conversion process. The generated voltage through the permanent synchronous generator is connected to the 3-phase bridge rectifier circuit that in turn rectifies this voltage, and which simultaneously transforms the generated alternating voltage produced with the help of synchronous generator to the required DC generated voltage. The primary composition of the circuit consists of a turbine [8, 9], a generator and boost converter circuit, etc. is converted to the required equivalent circuit for the theoretical analysis of this wind governed generator system. The other characteristics primarily the output power generated and the output voltage of DC converter are properly represented as the relative functions in terms of the boost converter’s duty ratio and of the synchronous machine with the achieved rotating speed. PMSG generated electric power has the similar characteristics as of the load conditions which are available with the peak power point. Therefore, the theoretical deduction of the maximum power was obtained by overall differentiation of the equations of generated power output by the boost converter duty ratio and with the significance of taking the optimum duty ratio [6].

2 Modeling of Wind Energy Generation System

2.1 Modeling the Wind Turbine System

The actual modeling of the wind turbine based on the aerodynamic non-linear power characteristics is denoted as P_m and is basically written in the equation form [7, 11] as:

$$P_m = 0.5\rho A v^3 C_p(\lambda, \beta) \tag{1}$$

where A , represents the swept area (in metres) of rotor of the turbine blades and, ρ is defined as the density of air (in kg/m^3), v is the wind velocity (in m/sec), C_p denotes the coefficient of performance, β denotes the angular position of the pitch of the blades and λ is described with a ratio between the tip of the rotor blade divided by the velocity of

the wind, which is typically represented as the tip speed ratio (λ) of the turbine, as such given by:

$$\lambda = \frac{\omega_m * R}{v} \tag{2}$$

The coefficient of performance of the wind turbine blades reflects the relationship among the tip speed ratio, λ [3] and the power coefficient, C_p of the wind turbine system and is depicted in Fig. 2. The mathematical relation involving C_p is given by:

$$C_p(\lambda, \beta) = [0.22 \left(\frac{116}{\lambda_i} - 0.4\beta - 5 \right) \exp\left(\frac{-12.5}{\lambda_i}\right)] \tag{3}$$

where λ_i is given as:

$$\lambda_i = \left[\frac{1}{(\lambda + 0.089)} - \frac{0.035}{(\beta^3 + 1)} \right]^{-1} \tag{4}$$

When the value of the pitch blade is $\beta = 0^\circ$ then the value of tip speed ratio is simultaneously taken as, $\lambda = 6.325$, then under these conditions C_p has its maximum value which occurs at $C_{pmax} = 0.4382$ [4]. So this is the value of C_p at which the maximum energy from wind is being captured and through this we can easily get the optimal point of operation of λ_{opt} .

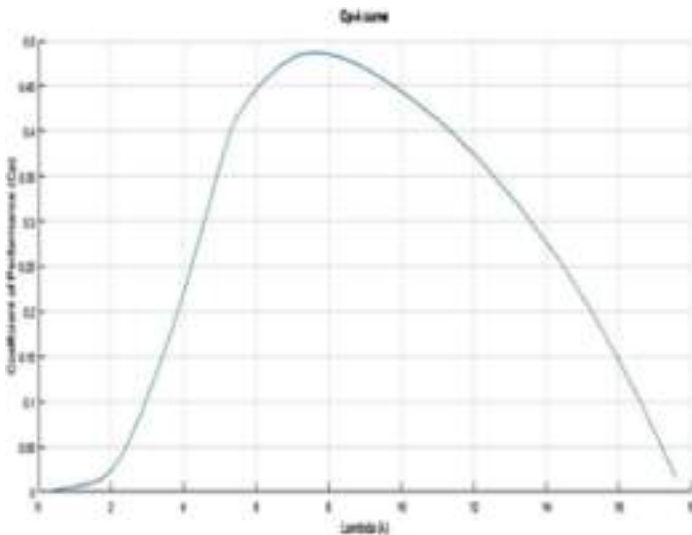


Fig. 2. Curve of wind turbine power coefficient

The aerodynamic or mechanical torque T_m (N-m) can therefore be expressed in terms of the ratio of power as captured directly from the wind system P_m (in watts) with the speed of a rotor of wind turbine, denoted as ω_m (rad/s), hence this ratio could be expressed as [5] (Fig. 3):

$$T_m = \frac{P_m}{\omega_m} \tag{5}$$

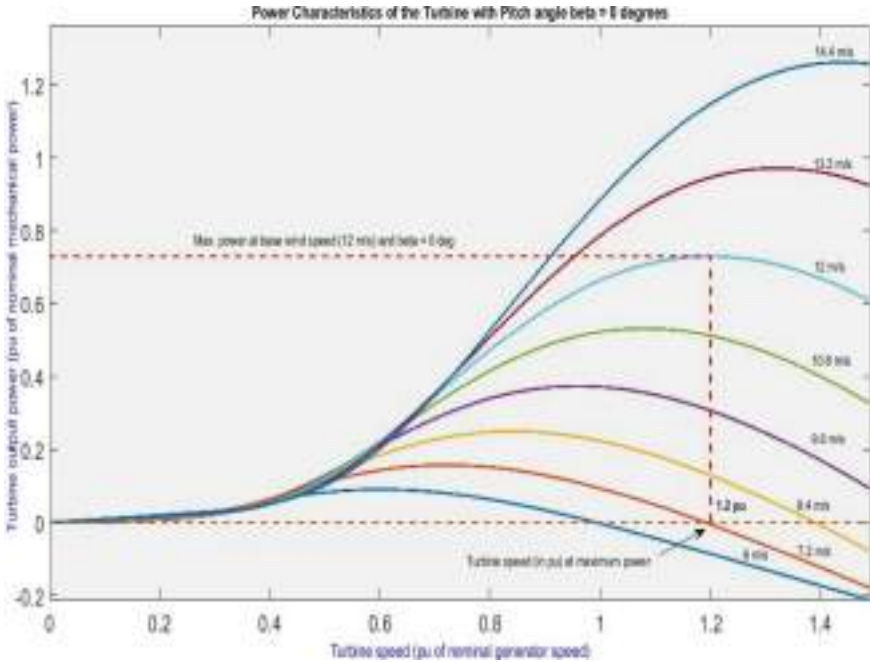


Fig. 3. Typical turbine power versus rotor speed characteristics of a wind turbine

2.2 Drive Train

The problem regarding the wear and tear in the gearbox can simply be avoided by using directly driven wind turbine without any gearbox, the other advantages includes that this also reduce cost of maintenance and successively reliability of the wind turbine operation can be equally ensured. So a relation can be developed in terms of the generator shaft rotating speed of the electrical machine ω_e to the rotor mechanical speed ω_g [4] as:

$$\omega_e = \omega_g P_n \tag{6}$$

where P_n denotes the number of poles in the stator shaft of the synchronous generator using permanent magnet rotor.

The modelling of the drive train circuit in the wind turbine [8] can be expressed by the equation as follows:

$$\frac{d\omega_g}{dt} = \frac{T_e - T_w - B_f * \omega_g}{J_{eq}} \quad (7)$$

where T_e is the electromagnetically generated torque of the electric machine, and B_f is the coefficient of viscous friction.

3 Model of Permanent Magnet Synchronous Generator

The model which is mainly used to define the dynamic behaviour of the PMSG in reference d-q frame could then be demonstrated [8–10] considering the equations below:

$$V_{ds} = -R_s i_{ds} + \frac{d}{dt} \phi_{ds} - \omega \phi_{qs} \quad (8)$$

$$V_{qs} = -R_s i_{qs} + \frac{d}{dt} \phi_{qs} - \omega \phi_{ds} \quad (9)$$

The equations involving the flux linkage are described as:

$$\phi_{ds} = -L_{ds} * i_{ds} + \phi_f \quad (10)$$

$$\phi_{qs} = L_{qs} * i_{qs} \quad (11)$$

The equation that derives the synchronous generator mechanically [13] can be evaluated as:

$$J \frac{d}{dt} (\Omega) = T_w - T_e - B * \Omega \quad (12)$$

for the above equation, the electromagnetic torque been represented in d-q [14] reference frame as:

$$T_e = P (\phi_{ds} * i_{qs} - \phi_{qs} * i_{ds}) \quad (13)$$

in which:

$$\Omega = \frac{d}{dt} \theta, \omega = \frac{d}{dt} \theta_e = p\Omega, \theta_e = p\theta \quad (14)$$

where R_s denotes the resistance in the stator, L_{ds} and L_{qs} are the direct-axis and quadrature-axis inductances in the stator, ϕ_{ds} and ϕ_{qs} are the direct-axis and quadrature-axis fluxes, respectively. ϕ_f is the flux in the field circuit, T_w is the torque available from the wind and been applied to the PMSG rotor shaft, T_e is used to represent the electromagnetically induced torque, p is used to express the no. of poles

in pairs, B is the co-efficient of damping, J [15] is the inertia constant (kg/m^2), ω represents the generator angular rotor speed expressed in electrical degrees, Ω is the angular speed in mechanical radians, θ is the position of mechanical rotor, and θ_e is the position of the electrical rotor.

4 Maximum Power Tracking Algorithm (MPPT)

The main objective of the MPP algorithm is to calculate the optimum duty ratio as required for tracking the maximum power output. For this purpose our boost converter voltage as well as current should be at maximum levels. The MPPT based on Perturb and Observe algorithm generates pulses for the converter by maintaining the desired optimum value of the duty and hence the voltage value of the dc/dc converter is boosted as required by the load (Fig. 5).

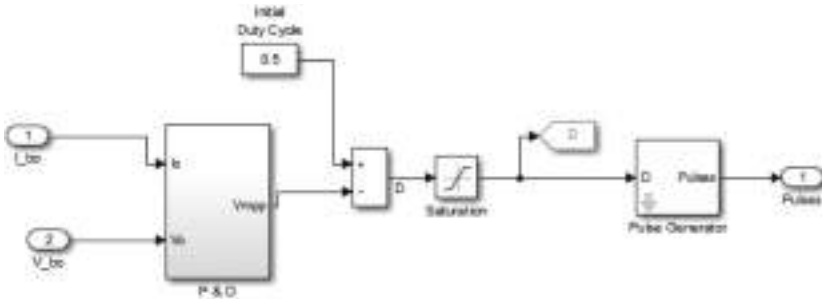


Fig. 4. The Simulink model of the MPPT controller

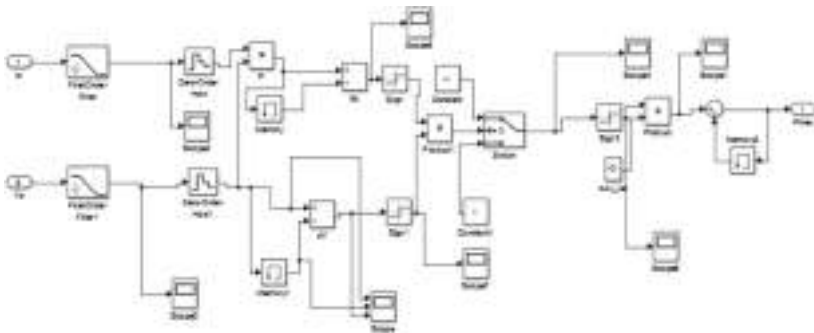


Fig. 5. P & O algorithm simulation diagram

5 Simulation Results

In Fig. 4 the complete model of the WECS is simulated so as to consider and derive the parameters using the developed control strategy. Figures 6 and 7 represents the torque generated by the PMSG & rotor speed of the permanent generator as coupled into a

turbine shaft. The simulation model is driven for a variable speed which is between 5–12 m/s. The result of Fig. 8 shows the voltage of uncontrolled bridge rectifier circuit, this voltage is boosted by the control pulses provided using the MPPT technique to the boost converter, which is as shown in Fig. 9. Figure 10 demonstrate the voltage for the inverter circuit and it shows that during the conversion from ac to dc the voltage remains constant as per the parameters taken into consideration. In Fig. 11, a load voltage waveform is depicted showing that this system is capable of handling any type of loads upto its design capacity. The Fig. 12 shows the three-phase voltages of the controller circuit which was designed to provide controlled pulses to the inverter circuit (Figs. 13, 14 and 15).

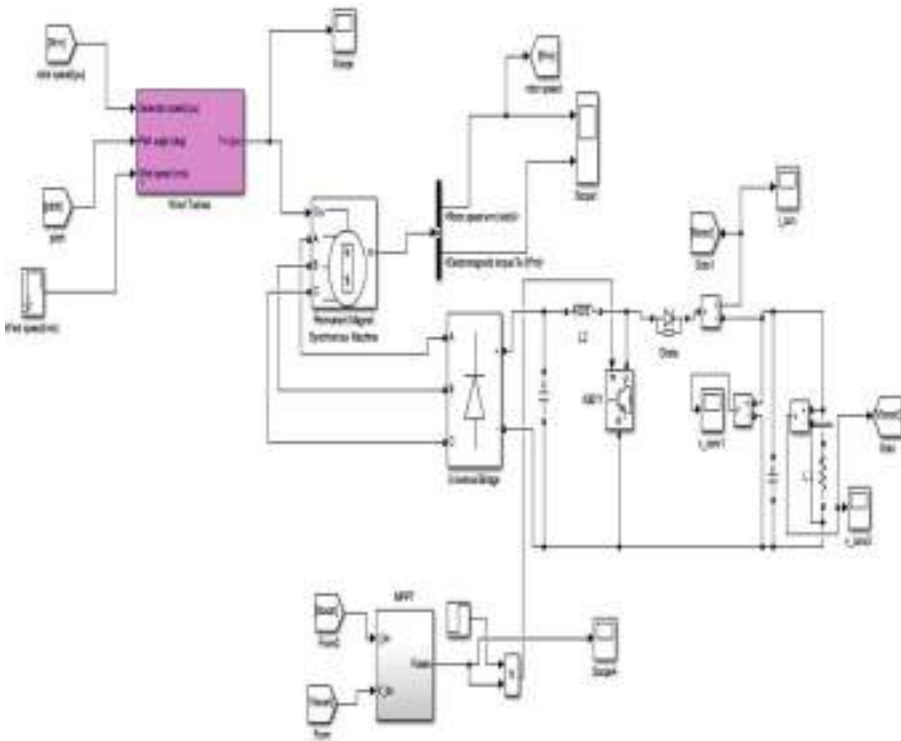


Fig. 6. The WT with PMSG detailed diagram modelled in MATLAB Simulink

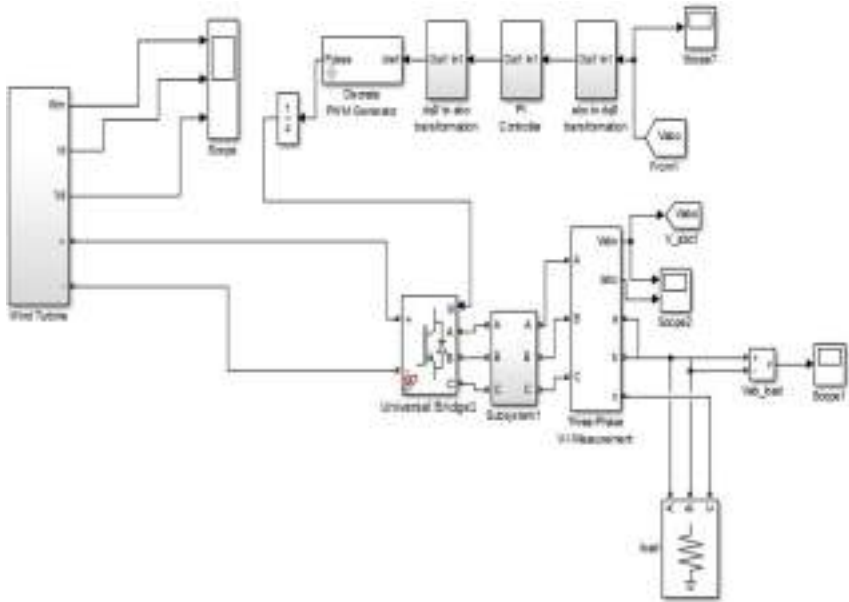


Fig. 7. The overall system diagram connected with load

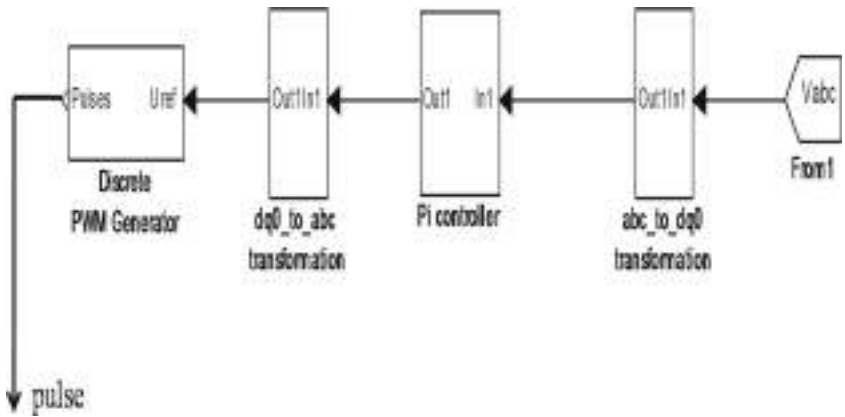


Fig. 8. The controller for the inverter circuit

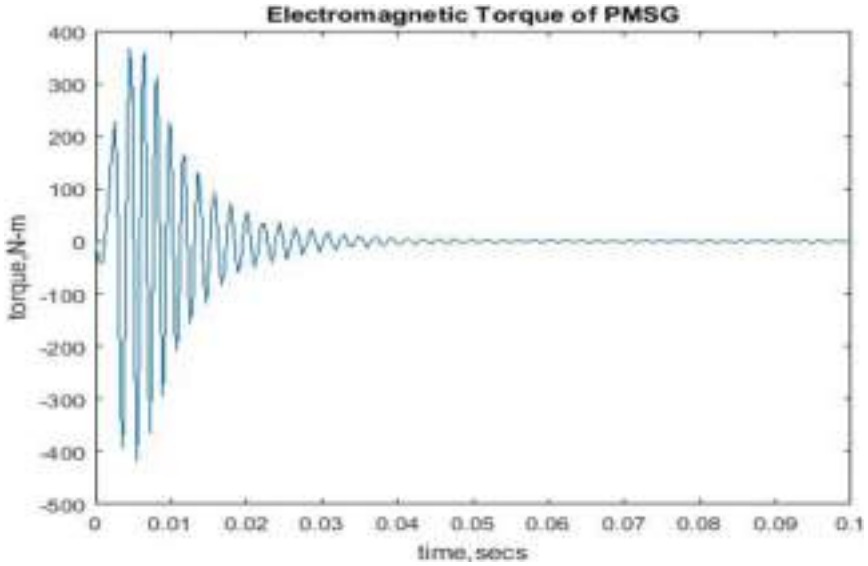


Fig. 9. Torque of PMSG

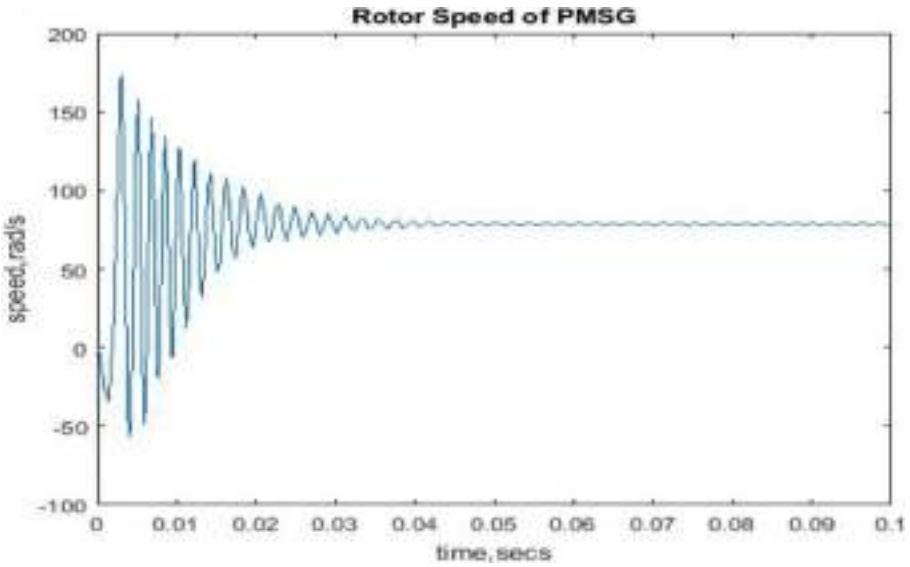


Fig. 10. Rotor speed of PMSG

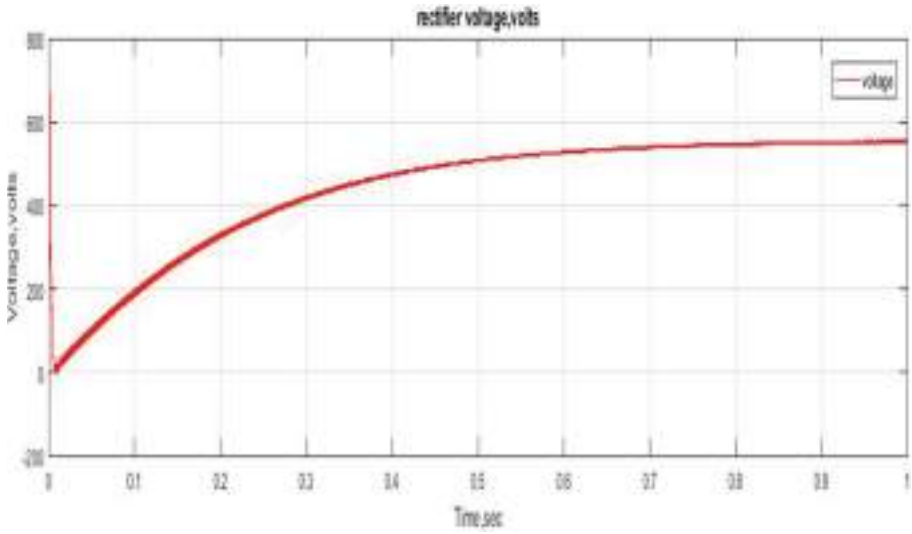


Fig. 11. AC to DC converter voltage

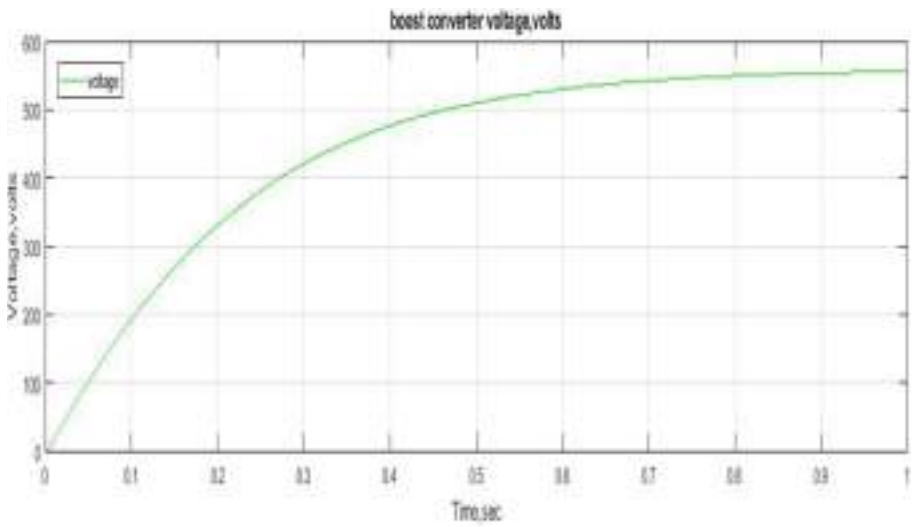


Fig. 12. DC to DC boost converter voltage

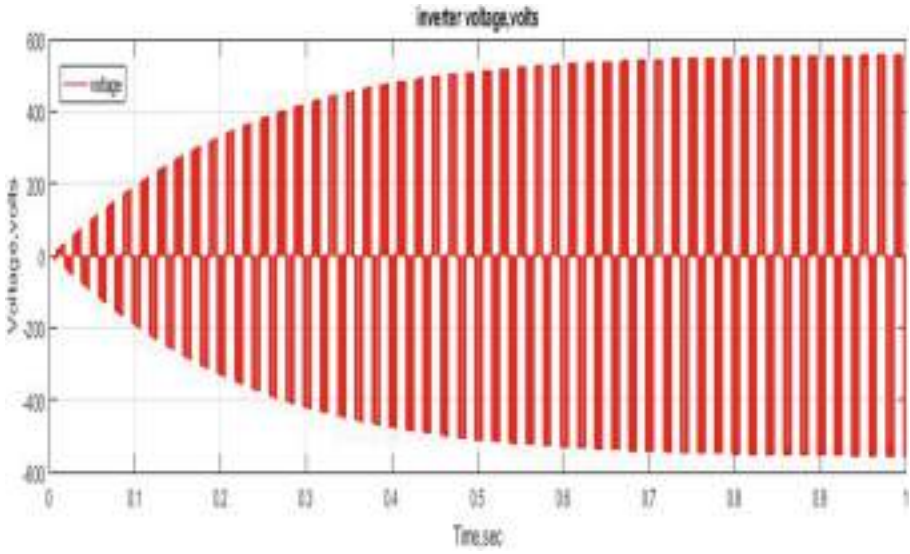


Fig. 13. Inverter voltage

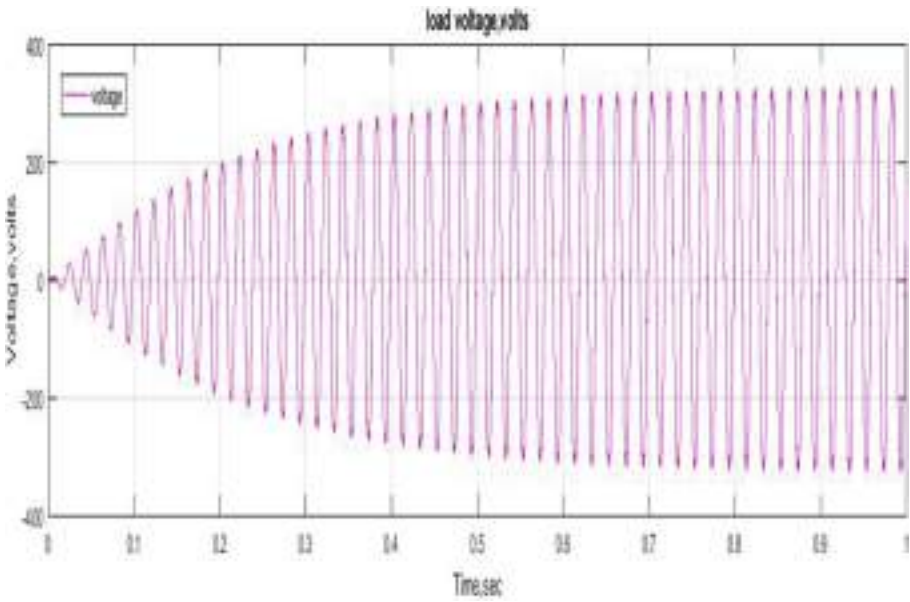


Fig. 14. Load voltage

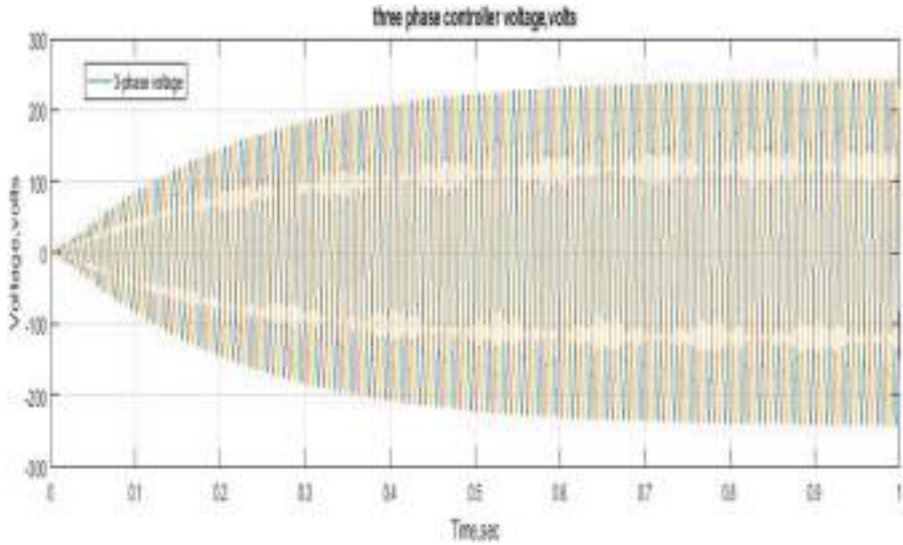


Fig. 15. Controlled three-phase voltage of the inverter controller

6 Conclusion

In this paper, an overall design, modelling and simulation of PMSG driven wind energy conversion system is carried out. The MPPT controller which is developed by the consideration P & O algorithm has been simulated and designed which gives controlled pulses for uniform operation of the dc/dc converter circuit. In terms of variable wind speeds also, this model works accurately for the non-linear characteristic behaviour of the system involving wind energy. The results from the simulation study shows that there is the possibility of extracting maximum available power from the simulink model of the wind turbine rotor by adjusting and simultaneously regulating the turbine's generator speed and the required speed of the driven machine. The work that has been proposed could be further extended in future with the help of more MPPT control algorithms and also other control schemes can be developed with the inclusion of several robust controllers.


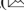

References

1. Tripathi, S.M., Tiwari, A.N., Deependra, S.: Grid-integrated permanent magnet synchronous generator based wind energy conversion systems: a technology review. *Renew. Sustain. Energy Rev.* **51**, 1288–1305 (2015)
2. Bakhda, J.S., Patel, T.V., Deshpande, A.: Simulation and modelling of VSC based HVDC transmission line. *Int. J. Res. Electron. Commun. Technol.* (2014)
3. Nandana, J., Murthy, P.K., Durga, S.: VSC-HVDC transmission system analysis using neural networks. *Int. J. Eng. Sci. Innov. Technol.* (2013)

4. Bakhda, J.S., Patel, T.V., Deshpande, A.: Simulation and modelling of VSC based HVDC transmission line. *Int. J. Res. Electron. Commun. Technol.* **1**, 41–45 (2014)
5. Arnaltes, S., Rodriguez-Amenedo, J.L., Montilla-DJesus, M.E.: Control of variable speed wind turbines with doubly fed asynchronous generators for stand-alone applications. *Energies* **11**, 26 (2018)
6. Patil, A., Chavan, D.S., Yadav, S.V.: Output voltage control scheme for standalone wind energy system. In: *International Conference on Computation of Power, Energy Information and Communication*, pp. 534–541 (2016)
7. Chavero-Navarrete, E., Trejo-Perea, M., Jáuregui-Correa, J.C., Carrillo-Serrano, R.V., Ríos-Moreno, J.G.: Expert control systems for maximum power point tracking in a wind turbine with PMSG: state of the art. *J. Appl. Sci.* **9**, 2469 (2019)
8. Elbeji, O., Ben, H.M., Sbita, L.: PMSG wind energy conversion system: modeling and control. *Int. J. Mod. Nonlinear Theory Appl.* **03**(03), 88–97 (2014)
9. Lertnuwat, C., Oonsivilai, A.: Stability for wind turbine using observer method with permanent magnet synchronous generator (PMSG). *Energy Procedia* **138**, 122–127 (2017)
10. Rahimi, M.: Mathematical modeling, dynamic response analysis, and control of PMSG-based wind turbines operating with an alternative control structure in power control mode. *Int. Trans. Electr. Energy Syst.* **27**(12), 1–18 (2017)
11. Rezaei, N., Mehran, K., Cossar, C.: A practical model and an optimal controller for variable speed wind turbine permanent magnet synchronous generator. In: *Proceedings of the 2017 9th International Conference on Modelling, Identification and Control, ICMIC 2017*, vol. 2018-March, pp. 1008–1013 (2018)
12. Saihi, L., Boutera, A.: Robust control of a variable-speed wind turbine with variable pitch control and strategy MPPT control based on a PMSG, no. 1, pp. 24–30 (2016)
13. Abedi, M.R., Lee, K.Y.: Modeling, operation and control of wind turbine with direct drive PMSG connected to power grid. In: *IEEE Power Energy Society General Meeting*, vol. 2014-October, no. October (2014)
14. Samanvorakij, S., Kumkratug, P.: Modeling and simulation PMSG based on wind energy conversion system in MATLAB/SIMULINK. *Adv. Electron. Electr. Eng.* **2**(1), 978–981 (2013)
15. Rolak, M., Kot, R., Malinowski, M., Goryca, Z., Szuster, J.T.: Design of small wind turbine with maximum power point tracking algorithm. In: *2011 IEEE International Symposium on Industrial Electronics*, no. 1, pp. 1023–1028 (2011)



Retail Market in India and Its Best Practices: A Review on Initiatives and Challenges

Tripta Thakur  and Tushar Kumar  

Maulana Azad National Institute of Technology, Bhopal 462003, India
tusharkumar1729@gmail.com

Abstract. As an intermediary body, the retailer is at the helm of supplying electricity to consumers in trade for certain remittance. A place where the end-user chooses its electricity provider among competing retailers is the retail market of electricity. This paper tries to give an assessment of the international experiences and study the best practices entailed to instigate the retail electricity market in India. The report also aspires to emphasize various matters related to retail competition and recommendations for Indian market.

Keywords: Cross-subsidy · Retail competition · Regulatory framework

1 Introduction

At the end of the 19th century, with the opening up of the generation sector for independent power producer (IPP) and also supply is available to third parties, retailing began. The basic principle of supply still remains the same. The customer is charged for the amount of energy used, measured through an advanced smart electric meter. This also gives freedom first time to the consumer to choose its suppliers.

In 1990 there was a significant development in electricity market all over the world with different objectives for developed and developing nations. Market mechanism open up the competition in the electricity sector and thus retail electricity market was introduced. Consumers now have the choice to choose their supplier which is termed as “energy choice”.

Although market structures vary from country to country, there are some common functions for all, which retailer should have capability to perform in order to compete effectively such as billing, credit control, customer management, spot market purchase agreement.

The retail competition is going to influence stakeholders in three ways;

- (i) Less price for consumers,
- (ii) Due to best practices reduction of Aggregate technical and commercial losses (AT&C), and
- (iii) Consumers have freedom to choose service provider.

India is one of the fastest developing economies of the world and would like to take advantages of the market mechanism in distribution sector in the form of retail market.

The implementation has several challenges which are discussed ahead and lessons are drawn from the developed nations who have already implemented retail electricity market.

2 International Experience

Electricity sector reforms were introduced in developed countries around 1990, and UK reforms were considered as most successful reforms. Other developed nations like Norway, Australia, Canada and USA have fully open electricity retail market. Table 1 shows details of developed countries retail market. The experience of other nations shows that it is important to first create proper awareness and strong policy framework. The retail market was therefore introduced in phased manner everywhere.

Table 1. Full retail market opening in different countries in phase manner with End User coverage.

Country	1997	1999	2000	2003	2005	2007
Austria	0%	33%	100%	100%	100%	100%
Norway	100%	100%	100%	100%	100%	100%
Finland	40%	100%	100%	100%	100%	100%
Germany	0%	100%	100%	100%	100%	100%
UK	50%	100%	100%	100%	100%	100%
Sweden	40%	100%	100%	100%	100%	100%
Australia	30%	50%	75%	100%	100%	100%
Hungry	N/A	N/A	N/A	40%	67%	100%
Poland	N/A	N/A	N/A	N/A	80%	100%
Spain	0%	54%	54%	100%	100%	100%
Czech Republic	N/A	N/A	N/A	N/A	74%	100%
Luxembourg	0%	30%	N/A	57%	84%	100%
Estonia	N/A	N/A	N/A	N/A	12%	N/A
Latvia	N/A	N/A	N/A	N/A	76%	100%
Slovakia	N/A	N/A	N/A	N/A	79%	100%

Source: Compiled by Author by different sources

3 Indian Distribution Sector

The weakest link in the electricity value chain of India is ‘distribution sector’, which suffered due to huge aggregate technical and commercial (AT&C) losses, unsystematic growth, unclear policy and ageing infrastructure [1]. Government of India (GoI) is trying best to improve the sector by introducing electricity amendment act 2014 and imposing many financial schemes to improve infrastructure of distribution utilities like accelerated power development reform program (APDRP) and the restructured accelerated power development reform program (R-APDRP). Distribution franchisee (DF) is a new approach suggested by Shinglu committee [2] is being introduced and Bhiwandi

in Maharashtra is the first city in India working on franchisee model. Torrent Power took the charge of Bhiwandi and it is important to note that before the takeover, the prevailing AT&C loss was 58% and at the end of 2008-09 it was 24%, clearly a marked reduction in a span of two years [4].

The success story of Bhiwandi has encouraged many cities in India to opt DF model like Agra, Sagar etc., and clearly spells the need in power supply/distribution business for a private player intervention. In the Retail market mechanism as a first step distribution sector is separated in two business models. One is network business and other one is supply business. The network will be taken care by the 'distribution licensee' and they will serve consumers as a service provider whereas 'supply licensees' will supply electricity through the same network and tariff would be determined based on the demand-supply balance. As renewable energy generation is encouraged at the end of individual consumers also through rooftop solar PV, they are also encouraged to feed back their excess generation through grid by using smart meters. The first basic requirement for the retail market mechanism is mature, transparent wholesale electricity market [4]. The basic aim for this is to ensure many players in the market with the objective that no one has a dominant position, enough to manipulate the market. This step requires unbundling and resolving big generation companies into smaller one. An efficient wholesale market mechanism ensures low cost and reasonable quality of bulk power purchase.

The provision for multiple licenses in distribution sector is given in section 14 of the electricity act, 2003. Mumbai distribution is one of the examples where multiple private licenses are giving services like Tata Power, Reliance, BEST etc., the section 14 distribution franchisee is also permitted.

4 Challenges for the Introduction of Retail Competition

The following are the challenges for implementing retail market in India.

4.1 Lack of Basic Infrastructure

India still needs proper distribution infrastructure, which in its current state is not only ageing but has grown without scientific approach, thus prone to systemic errors and breakdowns. The lack of upgraded infrastructure creates congestion issues and could make introduction of smart grid facilities very difficult.

4.2 Lacking of Understanding for Open Access

Open access was the concept introduced by The Electricity Act, 2003 through which network lines of transmission and distribution can be used by any utility to transfer its power. The Electricity (Amendment) Bill 2014 also supports the open access along with retail supply competition. However very few utilities and consumers have taken advantage of this scheme due to lack of awareness. Another issue hampering the open access is cross subsidy. A high amount of cross subsidy surcharge is charged from consumers, who wish to change distribution operator which acts as a deterrent for change.

4.3 Irrational Tariff Structure

Current tariff scheme in place is known as Availability Based Tariff (ABT), which is indigenously designed for the Indian market. This is basically three part frequency sensitive tariff mechanism with improved grid discipline [5].

For retail competition, cost of power procurement, wheeling and transmission charges, distribution charges, charges which account transmission and distribution losses, and cost of supply services would be taken care as important component [6]. This should also include supply services cost like; meter reading, billing, revenue collection, and consumer services. The cost of supply services can be reduced by implementation of prepaid metering mechanism.

4.4 Distribution Monopoly and Cross-Subsidy

The retail choice to large commercial consumers may significantly impact load served by distribution utilities if they wish to switch service provider. As the subsidizing consumers have higher purchasing power, new market participants would prefer to serve them at a cheaper cost than the incumbent supplier [7]. The subsidized and subsidizing consumers would not be served equally thus destroying the competition.

4.5 Privacy and Security

Due to extensive use of modern metering infrastructure, which is not fully mature, chances are very high for cyber-attacks. This is major concern for security and privacy for utilities and consumers. It is essential to track cyber-attacks because it exposes consumer points as well as the data collection points and updating the firmware capable to resist such cyber-attacks is paramount. Proper care is needed in terms of awareness from consumer before transaction of any data [8].

4.6 Integration of Renewable Energy Resources

Environmental and energy security concerns have been the prime agenda of Government of India which has driven renewable energy penetration. India also made commitment in Paris Climate summit to add 170 GW by 2022 in the installed capacity. In retail competition model, synchronizing renewable energy source to power grid without incurring any power loss is a challenge [8]. Net metering is the only way to connect individual consumer to the grid. Grid integration is a very complex and challenging issue and many issue need to be addressed like Anti-islanding, storage and other technical issues.

5 Recommendations for Indian Retail Market

Based on the overview of some of the world's finest market and also recently established Indian Energy Exchange (IEX), which is the first online electricity trading platform of India following are the recommendation for Indian retail market.

- Enhanced infrastructure and proper planning for implementation of retail market in phased manner. This will allow the market under the control of a regulator, to evolve towards a competition-based price setting market.
- Mature trading pool formation that should be monitored, assessed and routinely modified through several review mechanisms to ensure proper functioning of trading arrangements in the country.
- Breaking of distribution business components into two segments namely network and retail supply. This will not only eliminate conflict of interest, but provide transparency.
- The tariff design on scientific principle like The Maximum Uniform Tariff (MUT) regime implemented by Victoria. This may ensure tariff reduction to end consumers.
- Retail should reach the end domestic consumers like in case of Argentina. Common consumers should have the options for switching their distribution providers if they could access better services by doing so. Deterrents to switching would hamper retail adoption in electricity sector.
- In India 'cost of supply' still does not match 'cost of production' and cross subsidies still prevails in tariff set by regulators. These cross subsidies must be phased out soon. In this regard, India can learn from Philippines power industry, where universal charges are put on all electricity users in order to phase our cross subsidies.
- To become successful in implementing retail competition a strong independent regulator is required, who can work autonomously and design effective regulatory framework. In India since Electricity Regulatory Act (ERC) 1998, central electricity regulatory commission (CERC) and state regulatory commission (SERC) are formed and doing their task.

6 Conclusions

This paper discusses forthcoming reforms with the electricity amendment act 2014 in the distribution sector in the form of retail electricity market. Case studies of various developed countries and what lesson India can learn to follow best practices is also discussed. The ultimate reforms in the form of retail market needs ground preparations. This paper highlights the challenges India is going to face during implementation of reforms in retail sector in view of the ground realities of the Indian power sector. An international experience shows that the opening up of retail business to competition has been cause of disagreement and sometimes failure if not properly planned and executed. The Indian reform in electricity sector was introduced since 1990 and experience so far suggests that we should not copy the reform schemes from other countries. This gives us motivation and guidelines in case of retail market reforms by suggesting indigenously designed policies based on ground realities to make retail reform successful. The paper also discussed challenges for implementing retail reforms and suggests steps to be taken for addressing these challenges.

Success of reforms requires strong political will and support from Government and proper management of risks and expectations. Above all, sustainable reform requires



locally acceptable solutions. Although the retail market reforms are little slow due to many reasons such as, political constraints or lack of trust on market outcomes, but there is positive ray of hope with the Mumbai success story in retail market.

References

1. Thakur, T., Deshmukh, S., Kaushik, S., Kulshrestha, M.: Impact assessment of the Electricity Act 2003 on the Indian power sector. *Energy Policy* **33**, 1187–1198 (2005)
2. Shunglu, V.: High Level Panel on Financial Position of Distribution Utilities. Planning Commission, Government of India (2014)
3. Thakur, T., Bag, B., Prakash, S.: A critical review of the franchisee model in the electricity distribution sector in India. *Electr. J.* **30**, 15–21 (2017)
4. IDFC, The Bhiwandi Electricity Distribution Franchisee Model: A Resolute Step in Distribution Reforms, Policy Group Quarterly, 1–4 June 2009
5. Verma, Y., Kumar, A.: Economic-emission load dispatch in renewable integrated system under availability based tariff (ABT) environment. *Sustain. Energy Technol. Assess.* **4**, 78–88 (2013)
6. Singh, A.: Towards a competitive market for electricity and consumer choice in the Indian power sector. *Energy Policy* **38**, 4196–4208 (2010)
7. Harris, C.: Problems with Cross Subsidy and Redistribution of Wealth, *Electricity Markets*. Wiley, Hoboken (2013)
8. Eurelectric, Customer-Centric Retail Markets: A Future-Proof Market Design, *Eurelectric Policy Paper* (2011)
9. Anees, A.: Grid integration of renewable energy sources: Challenges, issues and possible solutions. In: *IEEE 5th India International Conference on Power Electronics (IICPE)*. IEEE (2019)



Laminar Airflow Computational Modelling in the Human Nasal Cavity

Punjan Dohare^{1,2,3}  and Amol P. Bhonekar^{2,3} 

¹ Electrical Engineering Department, Madhav Institute of Technology and Science, Gwalior, India

punjan.nitk@gmail.com

² CSIR-Central Scientific Instruments Organisation, Chandigarh, India

³ Academy of Scientific and Innovative Research, New Delhi, India

Abstract. In the human nose, air travels from an external environment in the upper segment of the human nose and this phenomenon can be clearly understood by using the nasal airflow dynamics, which is also responsible for proper functioning of human nose. In the present work, MIMICS (Materialise, USA) software is used to reconstruct an anatomical 3-dimensional of a human nose structure cavity using Computed Tomography (CT) scan. Numerical simulations were carried out using finite volume techniques for flow velocity of 7.5, 10 and 15 L/min. Results show that changes in nasal airflow in the nasal valve and olfactory region alter the distribution of airflow. Separate nasal airflow patterns were noted at different flow rates at coronal cross-sections. Maximum airflow was noticed in the nasal valve portion and the posterior end of the turbinate region.

Keywords: Nose physiology · Laminar flow · Nasal cavity · Computational fluid dynamics

1 Introduction

A human nose's physiological function starts with the transfer of ambient air to the respiratory tract, filtering, warming, humidifying the air inhaled. These parameters depend on the aerodynamics behaviour in the nasal cavity that impacts the smell [1–5]. Detailed research of aerodynamics in nasal cavity, however, was not feasible without the growth of computational fluid modelling owing to the complexity of the nasal structure. Computational fluid dynamic modelling has now appeared as a main technique for achieving a deeper understanding of biological flows and their parameters.

Airflow dynamics based study has been conducted in vitro and by using CFD models by many researchers [6–10] to understand and analyse the airflow dynamics in the human nose with distinct flow rates. A three-dimensional right human nose computational model was reconstructed [8]. Simulations were performed for the two different rates of flow of 125 and 200 ml/s to investigate the various anatomical deformities. Further, the total flux and flow of odorant particles behaviour on the olfactory mucosa was investigated by Keyhani et al. [9]. Later, both sides of the nose were reconstructed [11]. At 7.5 and 15 L/min, numerical simulation was conducted to determine the

physiology of the nose as there are inter-subject differences in nasal anatomy. In the model of the left and right human nose, there was a shift in flow patterns and flow characteristics. Both the sections of nasal cavity were compared with the available literature results with respect to flow patterns in the human nose [10].

In clinical research, rhinomanometry and acoustic rhinometry are employed to analyse the flow resistance and area of cross-section [12, 13]. Nevertheless, it was challenging to visualize the airflow pattern at different points. Numerical modelling of nasal airflow dynamics has proven successful in predicting the clinical outcomes [14–16]. Septal deviation, turbinate hypertrophy, allergy, or inflammation affects the airflow pattern in the human nose that can cause nasal obstruction. Inferior turbinate reduction [1, 17] and middle turbinate removal [16] technique were used to improve the nasal patency and many results suggest that any change in turbinate structure would seriously impair its air-conditioning performance. CFD based pre-surgical analysis is quite helpful to analyse the airflow pattern in the clinical field.

Olfaction based study has been conducted in humans, rodents, canine and many other animals for many decades [2, 4, 9, 11, 15, 18–21], however, the sense of smell is least understood in a physiological sense. Nasal aerodynamics in the nasal cavity is responsible for transferring air from the atmospheric environment to the sensory region [19]. Zhao et al. [3] performed simulation for the flow rates between 300 and 1000 ml/s in human and rat nasal cavity. The simulation disclosed that the odorant uptake flux to the olfactory mucosa may increase in the human nasal cavity airflow frequency during sniffing, but cumulative complete uptake in the olfactory region reduces when the amount inspired air is fixed.

The aim of this research is to explore the impact and significance of flow velocity on flow behaviour. In order to study the nasal airflow parameters such as velocity and pressure and various airflow profiles, numerical simulation was conducted for the 7.5, 10 and 15 L/min. Furthermore, on both sides of the cavities, the impacts of distinct airflow were researched in the nasal valve and turbinate portion. The flow distribution and streamlines were provided for the left and right nasal cavity and the findings were contrasted through the literature available.

2 Methodology

CT scan pictures are used to reconstruct an anatomical accuracy of a three-dimensional structure of the upper nasal section of the human. The CT images are in the form of DICOM (Digital Imaging and Medicine Communication). On <http://www.osirix-viewer.com/resources/dicom-image-library>, DICOM file human head dataset is accessible as an open-source. Each axial scan has a slice thickness of 1.5 mm with 512×512 pixels. These pictures are processed via MIMICS (Materialise, USA) software to model a three-dimensional structure that involves both the left and right cavity and, the nasopharynx. The resulting file format of the nose passageway for stereolithography (STL) is demonstrated in Fig. 1.

Using the ICEM-CFD 14.5 software (Ansys Inc., Canonsburg, PA, USA), a computational model of the human nose was discretised into an unstructured mesh. The final mesh shown in Fig. 2 includes 13,02,582 tetrahedral elements. Simulations for the flow rates of 7.5, 10 and 15 L/min have been analysed. The rate of flow between 7.5 to 15 L/min was considered as laminar airflow [22, 23], while the rate of flow beyond 15 L/min was taken as turbulent airflow.

Because of the complicated nasal structure, the airflow behaviour was predicted using ANSYS FLUENT 14.5 (ANSYS Inc., USA). Newtonian and incompressible was assumed to be the air. In this study, the conservation equation of mass (the equation of continuity) and the equation of Navier-Stokes were used to model laminar flow. The conservation equation of mass and Navier-Stokes equation are expressed as

$$\frac{\partial \rho}{\partial t} = 0 \quad (1)$$

Navier-Stokes equation expressed as

$$\rho \frac{DV}{Dt} = -\nabla P + \mu \nabla^2 V + \rho g \quad (2)$$

where V is the velocity, P is pressure, ρ is the mass density of air and μ is the dynamic viscosity coefficient. The momentum equation was solved through second-order upwind scheme. A SIMPLE (Semi-Implicit Method for Pressure-Linked Equation) algorithm was applied to realize the pressure and velocity coupling. SIMPLE algorithm

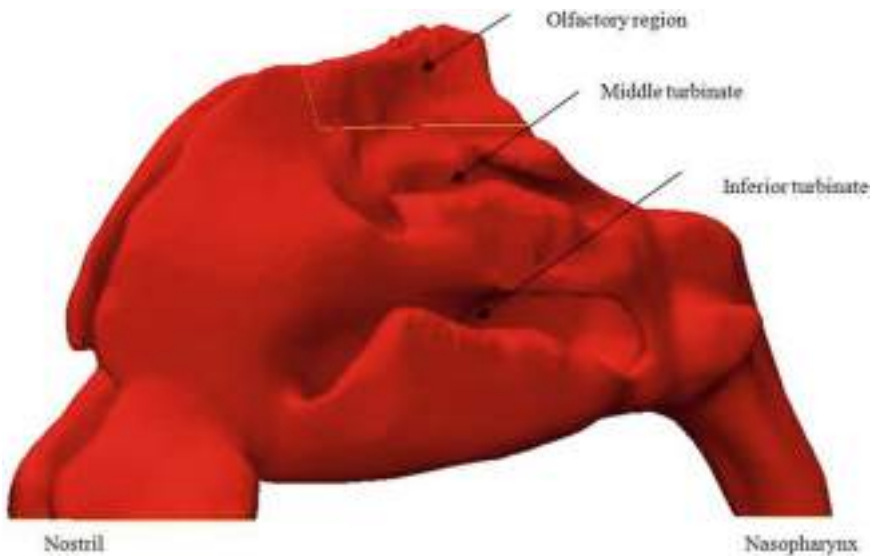


Fig. 1. Computational model of a human nose structure



Fig. 2. Computational mesh model of nasal upper airways

is deployed on finite-volume discretization methods of the Navier-Stokes equations. This method was introduced by Patankar and Spalding [24]. The discretized form of momentum equation and pressure correction equation are interpreted implicitly, where the velocity correction is solved explicitly. The boundary conditions were (i) the nasal walls were supposed to be rigid; (ii) no-slip boundary condition was defined at the nasal walls; (iii) zero pressure value was taken at the nostrils and the outlet was placed at the nasopharynx. Density and dynamic viscosity of the air was 1.225 kg/m^3 and $1.7894 \times 10^{-5} \text{ kg/m-s}$ respectively. The convergence of solution for residual values of governing equations was set to 0.001.

3 Results and Discussion

3.1 Structure Comparison and Pressure Drop in the Human Nose

The area of cross-section versus axial distance from the frontal region of the human nose is compared with available literature [11, 25] as shown in Fig. 3. The posterior section of the nasal structure ($x > 6 \text{ cm}$) has a lesser area of cross-section than other nasal cavities. The frontal region ($x > 1 \text{ cm}$) and the middle part ($x < 6 \text{ cm}$) have a larger cross-sectional area than the available data. The variations found in the geometry of human nose occur due to the changes in inter-subjects and intra-subjects' variations.

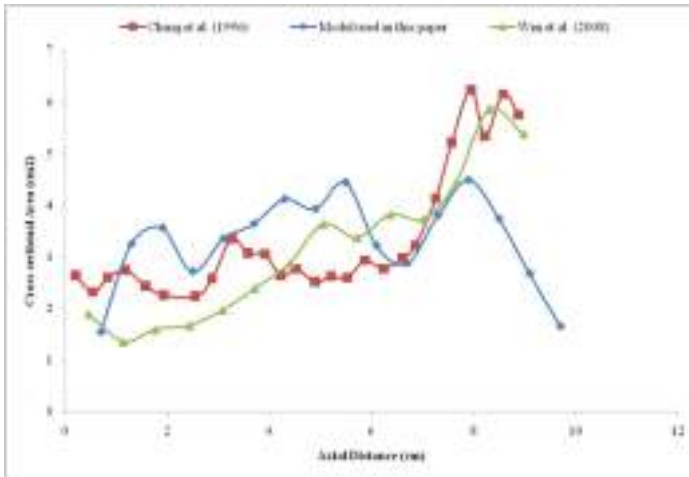


Fig. 3. Relation between area of cross-section versus axial distance from the frontal region of the nose

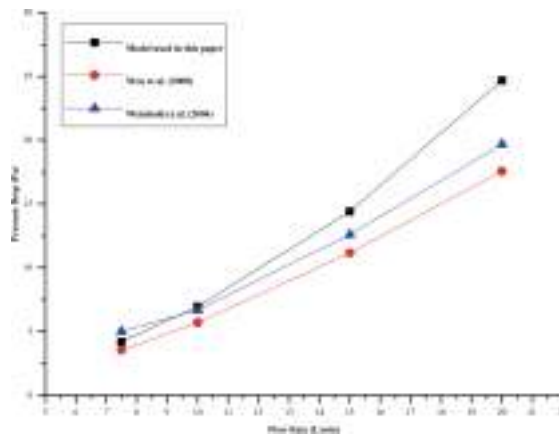


Fig. 4. Pressure drop versus flow rate with different flow rates

For various inspiratory rates of flow of 7.5, 10 and 15 L/min, the pressure drops across inlets and outlets is shown in Fig. 4. Similar outcomes are shown in the published literature [11, 15] in Fig. 4 at 7.5 and 10 L/min for pressure drop, but there is a slight divergence at a flow velocity of 15 L/min that may be ascribed to modifications in the human nasal structure.

3.2 Airflow Pattern and Velocity Distribution

The velocity profile distribution and streamlines with different flow rates are presented in this paper. Four coronal sections are selected named as ‘a’, ‘b’, ‘c’, and ‘d’ for the better understanding of olfaction. The velocity contour plots with streamlines are presented for different flow rates. The cross-section is a front view and a left nasal cavity is represented on the right side and the green contours show main flow field (Figs. 5, 6 and 7).

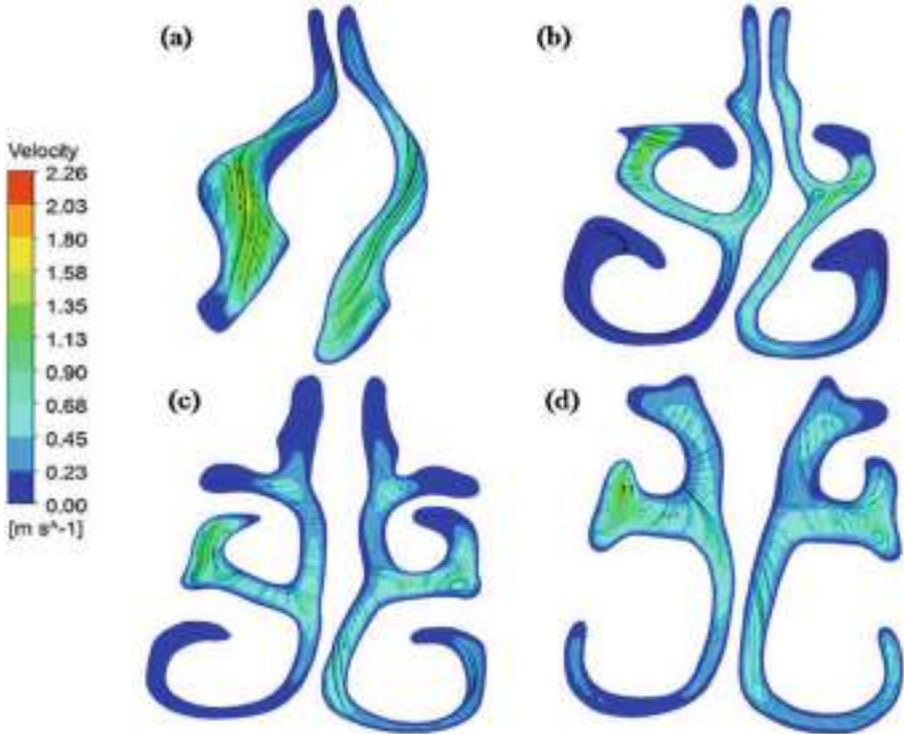


Fig. 5. Contour plots with streamlines in coronal cross-section for different sections (a–d) at a flow velocity of 7.5 L/min

Figure 5 shows the velocity field in dissimilar coronal segments for the flow rate of 7.5 L/min. At section ‘a’, one vortex is found on the right nasal cavity and some recirculation occurs. Air enters from the nostrils with the upward direction. As move towards the frontal tip of the nose, the structure gets wider and direction of flow field transforms from upward to horizontal direction. At section ‘c’, one vortex is noticed in the left cavity. As the air travels after the frontal tip of the nose, one vortex is noticed in the central segment of the left cavity at sections ‘d’.

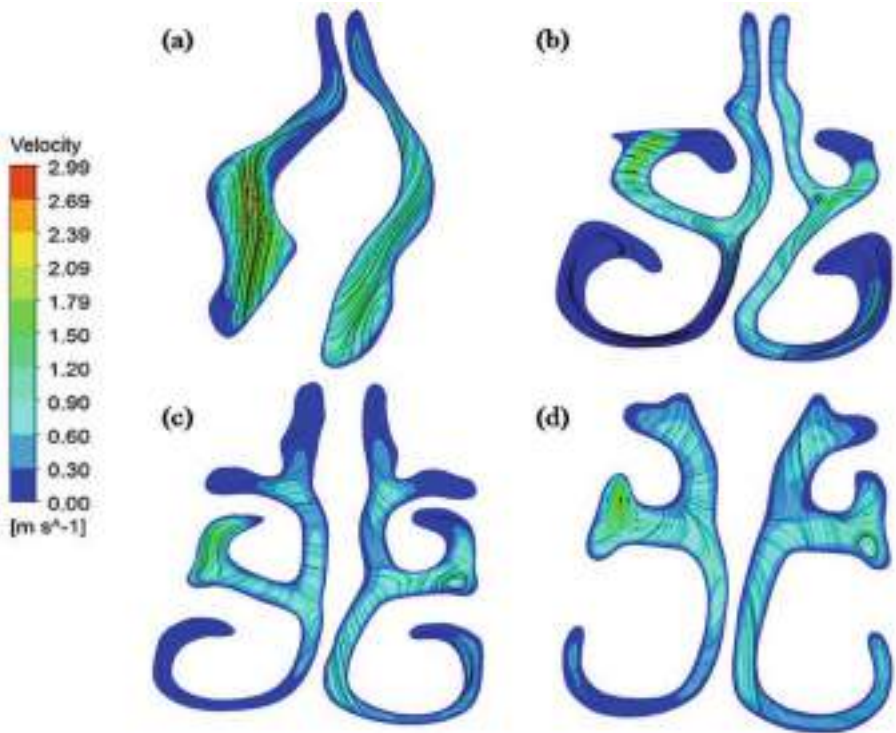


Fig. 6. Contour plots with streamlines in coronal cross-section for different sections (a–d) for the flow rate of 10 L/min

Figure 6 demonstrates the velocity field for the flow rates of 10 L/min. Maximum flow is formed in the nasal valve part at section a. At section 'b', some weak recirculation is noticed in the left nasal structure. One vortex is noticed in the middle segment of the left cavity at section 'c', and 'd'. However, no vortex is found in the right cavity.

Velocity distribution with streamlines at a rate of flow of 15 L/min is shown in Fig. 7. At coronal cross-section section 'a', one vortex is found in the right nasal cavity and some recirculation exists. As the distance increases in an axial direction, two vortices are found in the left cavity, i.e. one is in the middle part and another at the inferior portion of the cavity in section 'b' and 'c'. At section 'd', one vortex is originated in the intermediate section of the left cavity and some recirculation occurs in the superior section.

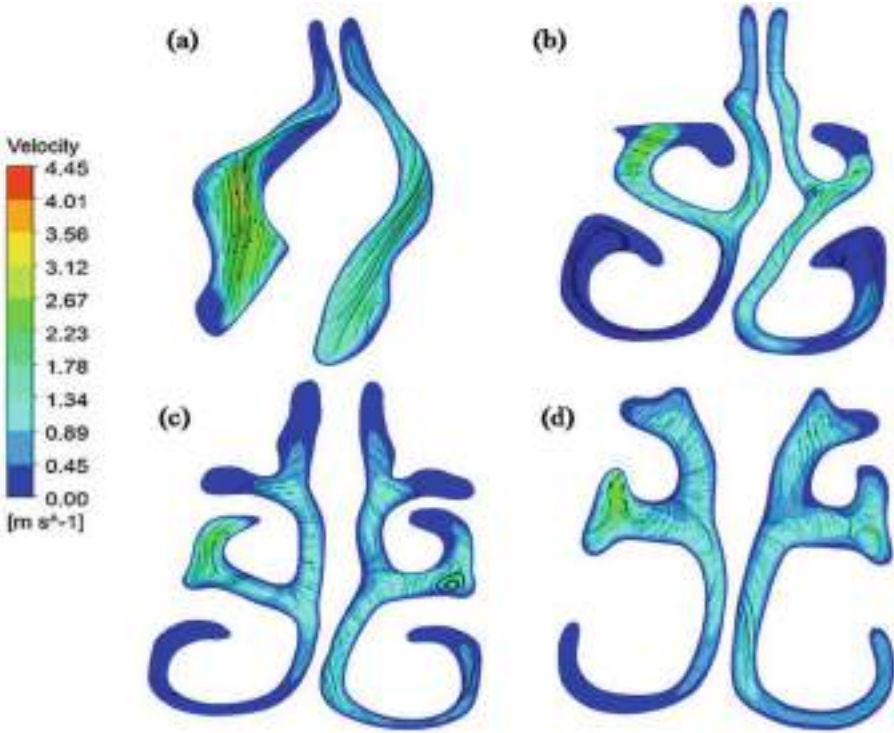


Fig. 7. Contour plots with streamlines in coronal cross-section for different sections (a–d) at a flow velocity of 15 L/min

3.3 Path Streamlines

Plots of laminar and turbulent flow streamlines with distinct flow rates are shown in Fig. 8. In order to accomplish the flow pattern in the nasal cavity, pathlines travelled from the right and left nostrils. The smooth flow pattern for the flow rates of 7.5 and 10 L/min in Fig. 8 is noted in the left cavity. Due to constriction in the nasal valve section, vortices are discovered in the right nasal cavity and secondary flows are noticed in the posterior part for the rates of flow of 7.5 and 10 L/min. Most of the flow is concentrated in the right cavity through the central part and little flow reached the upper portion of the nasal cavity. But in comparison with literature Keyhani et al. [9] was found the recirculation zone in the middle turbinate. Recirculating flow lines were found in the vestibule section of the nose and swirls in the nasopharynx [26]. At the flow velocity of 7.5 L/min in left cavity, vortex was noticed in nasal valve region and no recirculation was observed in the right cavity [11].

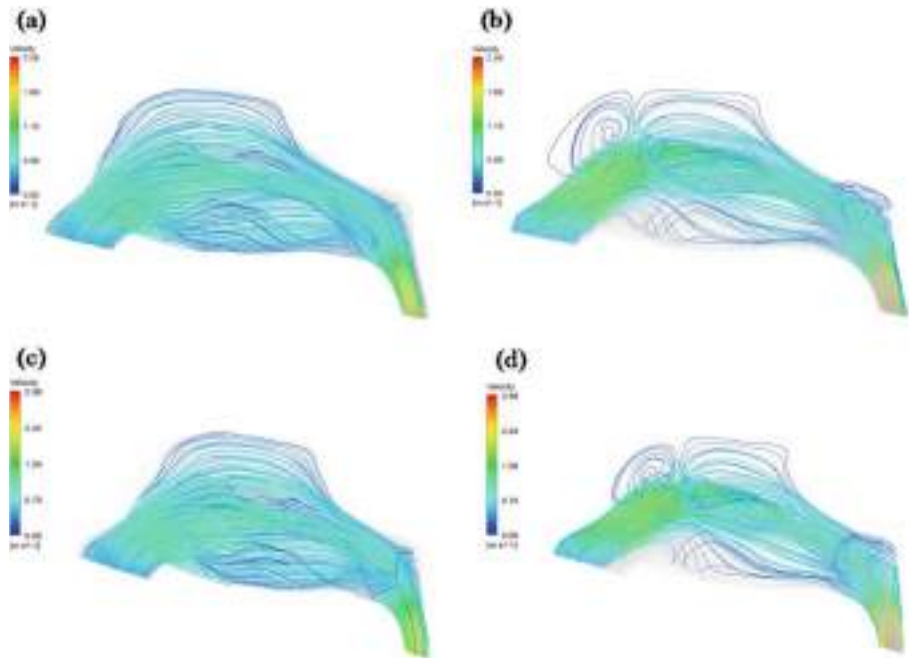


Fig. 8. Pathlines for left and right cavity (a) left nasal cavity at 7.5 L/min; (b) right cavity at 7.5 L/min; (c) left nasal cavity at 10 L/min; (d) right nasal cavity at 10 L/min.

4 Conclusion

We created a human nose's anatomical structure using CT scanning pictures. In order to analyse the airflow distribution and flow behaviour for distinct flow rates, Laminar inspiratory flow model was simulated. This paper's primary aim is to understand and calculate the airflow behaviour and its features. The relationship between the cross-section region and axial distance from the human nasal cavity's frontal tip indicates that geometry differences happen as a result of changes in human nasal structure in inter-subjects and intra-subjects.

The distribution of velocity and streamlines is depicted. Maximum flow is noted due to a lower cross-section area in the part of the nasal valve. As the distance from the frontal tip of the nose rises, some vortices with distinct flow rates are discovered in the central part of the left and right nasal structure. These vortices are responsible for mixing the air.

Results of numerical simulation have shown that modifications in inspiratory airflow may result in modifications in airflow distribution, particularly in the nasal valve and the olfactory region. The airflow reaches the frontal tip of the nose that travels to the nasal cavity's olfactory region and then reaches the nasopharynx. Simulation results clearly implicate that only a little amount of flow reaches to the upper part of the human nose. Maximum airflow is originated in the nasal valve section and the posterior end of the turbinate region.




References

1. Chen, X.B., et al.: Impact of inferior turbinate hypertrophy on the aerodynamic pattern and physiological functions of the turbulent airflow - a CFD simulation model. *Rhinology* **48**(2), 163–168 (2010)
2. Zhao, K., et al.: Numerical modeling of turbulent and laminar airflow and odorant transport during sniffing in the human and rat nose. *Chem. Senses* **31**(2), 107–118 (2006)
3. Zhao, K., et al.: Numerical modeling of nasal obstruction and endoscopic surgical intervention: outcome to airflow and olfaction. *Am. J. Rhinol.* **20**(3), 308–316 (2006)
4. Zhao, K., et al.: Effect of anatomy on human nasal air flow and odorant transport patterns: implications for olfaction. *Chem. Senses* **29**(5), 365–379 (2004)
5. De Yun Wang, H.P., Gordon, B.R.: Impacts of fluid dynamics simulation in study of nasal airflow physiology and pathophysiology in realistic human three-dimensional nose models. *Clin. Exp. Otorhinolaryngol.* **5**(4), 181–187 (2012)
6. Brucker, C., Park, K.-L.: Experimental study of velocity fields in a model of human nasal cavity by DPIV. In: TSFP Digital Library Online. Begel House Inc. (1999)
7. Kelly, J., Prasad, A., Wexler, A.: Detailed flow patterns in the nasal cavity. *J. Appl. Physiol.* **89**(1), 323–337 (2000)
8. Keyhani, K., Scherer, P., Mozell, M.: Numerical simulation of airflow in the human nasal cavity. *J. Biomech. Eng.* **117**(4), 429–441 (1995)
9. Keyhani, K., Scherer, P.W., Mozell, M.M.: A numerical model of nasal odorant transport for the analysis of human olfaction. *J. Theor. Biol.* **186**(3), 279–301 (1997)
10. Riazuddin, V.N., et al.: Numerical study of inspiratory and expiratory flow in a human nasal cavity. *J. Med. Biol. Eng.* **31**(3), 201–206 (2011)
11. Wen, J., et al.: Numerical simulations for detailed airflow dynamics in a human nasal cavity. *Respir. Physiol. Neurobiol.* **161**(2), 125–135 (2008)
12. Chan, K.-O., Huang, Z.-L., Wang, D.-Y.: Acoustic rhinometric assessment of nasal obstruction after treatment with fluticasone propionate in patients with perennial rhinitis. *Auris Nasus Larynx* **30**(4), 379–383 (2003)
13. Hilberg, O., et al.: Acoustic rhinometry: evaluation of nasal cavity geometry by acoustic reflection. *J. Appl. Physiol.* **66**(1), 295–303 (1989)
14. Kimbell, J.S., et al.: Computed nasal resistance compared with patient-reported symptoms in surgically treated nasal airway passages: a preliminary report. *Am. J. Rhinol. Allergy* **26**(3), e94–e98 (2012)
15. Weinhold, I., Mlynski, G.: Numerical simulation of airflow in the human nose. *Eur. Arch. Otorhinolaryngol.* **261**(8), 452–455 (2004)
16. Zuber, M., et al.: Computational fluid dynamics study of middle turbinectomy. In: 2012 International Conference on Biomedical Engineering (ICoBE). IEEE (2012)
17. Lee, T.S., et al.: Computational fluid dynamics to evaluate the effectiveness of inferior turbinate reduction techniques to improve nasal airflow. *JAMA Facial Plast. Surg.* **20**(4), 263–270 (2018)
18. Yang, G.C., et al.: Numerical modeling of odorant uptake in the rat nasal cavity. *Chem. Senses* **32**(3), 273–284 (2007)
19. Lawson, M., et al.: A computational study of odorant transport and deposition in the canine nasal cavity: implications for olfaction. *Chem. Senses* **37**(6), 553–566 (2012)
20. Craven, B.A., Paterson, E.G., Settles, G.S.: The fluid dynamics of canine olfaction: unique nasal airflow patterns as an explanation of macrosmia. *J. R. Soc. Interface* **7**(47), 933–943 (2010)

21. Samarat, K., et al.: Application of computational fluid dynamics to simulate a steady airflow in all regions of Chimpanzee's nasal cavity. *Procedia Eng.* **61**, 264–269 (2013)
22. Swift, D.L., Proctor, D.F.: Access of air to the respiratory tract. *Respir. Def. Mech.* **5**(1), 63–93 (1977)
23. Hahn, I., Scherer, P.W., Mozell, M.M.: Velocity profiles measured for airflow through a large-scale model of the human nasal cavity. *J. Appl. Physiol.* **75**(5), 2273–2287 (1993)
24. Patankar, S.V., Spalding, D.B.: A calculation procedure for heat, mass and momentum transfer in three-dimensional parabolic flows. In: *Numerical Prediction of Flow, Heat Transfer, Turbulence and Combustion*, pp. 54–73. Elsevier (1983)
25. Cheng, Y., et al.: Nasal deposition of ultrafine particles in human volunteers and its relationship to airway geometry. *Aerosol. Sci. Technol.* **25**(3), 274–291 (1996)
26. Subramaniam, R.P., et al.: Computational fluid dynamics simulations of inspiratory airflow in the human nose and nasopharynx. *Inhalation Toxicol.* **10**(2), 91–120 (1998)



Non-invasive Estimation of HRV Performance for Diabetes Mellitus with Cardiac Disorder on the Basis of Time-Frequency and Poincare Plot Analysis

Monika Saraswat^(✉) , A. K. Wadhvani ,
and Sulochana Wadhvani 

Department of Electrical Engineering,
Madhav Institute of Technology and Science, Gwalior, India
monikasaraswat20@gmail.com,
wadhvani_arun@rediffmail.com,
sulochana_wadhvani@mitsgwalior.in

Abstract. Diabetes is a malfunctioning disease which increases the risk of cardiac autonomic neuropathy. People with Diabetes mellitus are over two times as probable to ensure a heart stroke as compared to those people who don't have diabetes. This research work is to examine heart rate changeability in type-2 diabetes mellitus patients (T2DM) versus non-diabetic patients. The linear and Poincare plot analytical techniques are applied on ECG signals to determine the pathological and physiological status, like sympathetic variation and parasympathetic variation in the heart. At the initial stages of the analysis, the removal of various noises from the corrupted ECG signal by different types of filters such as Savitzky-Golay least square polynomial filter, Butterworth filter and Wavelet technique are employed. The electrocardiogram signal is performed for efficient detection of all peaks by QRS segment, P-wave, Q-wave, T-wave and ON-set, OFF-set on each beats. In the Next phase of the analysis RR interval, QT-interval, QT-dispersion, ST-depressions are computed from the filtered ECG signal for identification of Diabetes. The comparison is carried out on the basis of Signal to Noise Ratio among filter techniques for their better results.

Keywords: ECG · Heart rate variability · Cardiac disorder · Poincare plot analysis · Diabetes mellitus

1 Introduction

According to the International Diabetes federation, in current scenario 415 million people are surviving with diabetes and their ratio will increases in upcoming years to approximately 640 million by 2040 [1]. Type II diabetes mellitus (T2DM) is life threatening diseases which can have direct effects on function of internal organs. If this disease is not controlled, the patient have chances and higher risk of complication such as cardiac vascular disease, kidney failure, liver damage, poor healing of wounds and gangrene. ECG is an electrocardiogram device which represents the electrical contractile

variation of the heart in waveform. Cardiologist can easily find out the abnormalities of the heart, when looking at their waveform printout [2]. Heart rate variability is an investigative tool; it works to investigate the medicative stages in the human body which is based on Physical Evaluation and Clinical Evaluation of Patient. The performance of heart is only visible in hrv test at a commencement stage wherever no clinical signs are observable [3]. Heart rate variability test stands measure the variations of time series of RR interval from ECG which are defined between the successive heart beats. Uddin et al. [4] has used Kubios software for analysis of hrv and classification by linear discriminant analysis. Gospodinov et al. [5] suggested non-linear technique to determine the variation of standard descriptor in normal and abnormal cases and perform statistical analysis by using SPSS tool. Lu and Pan et al. [6] suggested QRS complex detection with improved adaptive threshold algorithm and RR-Lorenz plot for monitoring the variation in the heart. Our proposed work is to remove the artifacts noise from the corrupted signals by different filter techniques such as Butterworth filter, Savitzky-Golay least square polynomial filter technique and wavelet technique which is widely used for analysis of non-stationary signals. Now, noisy data is transferred from a filter and we find their Signal to Noise Ratio (SNR). The next phase of the analysis is to extract the peaks of ECG signals like ON-set and OFF-set of QRS-complex, amplitudes-durations, T-wave and features which are estimates related to diabetes like, QT-dispersion (QTd), ST-depression (STd), QT-corrected (QTc), P-wave dispersion and heart rate variability in type-II diabetic patients.

2 Data Collection

ECG database were collected from (Physikalisch-Technische Bundesanstalt) PTB-Diagnostic for the analysis of 25 non-diabetic patients and 30 diseased patients having diseases such as myocardial infarction, cardiomyopathy, bundle-branch block and myocardial hypertrophy with additional diagnosis diabetes mellitus. PTB-Diagnostic is an online database which is available on physionet.org site. Each ECG lead have 10000 samples and their amplitude range is ± 16.384 mV with sampling frequency 1000 Hz [7]. In this study 55 cases were analyzed and results of 20 cases are shown here. ECG database MATLAB R2018b software were used for analysis.

3 Pre-processing by Different Filter Techniques

Since, the Raw ECG signal/database contains various types of noises such as motion artifacts, power-line interference, and baseline correction. Therefore, pre-processing of the signal is necessary to obtain a clean signal. The preprocessing is done by different filter techniques are as following.

3.1 Butterworth Filter

The property of Butterworth filter shows flat frequency response in both frequency band such as pass band and stop band. Butterworth low pass filter is used to eliminate

the noises in the signal as compared to high pass filter because the high pass filter have contain more distortion in the signal. The low pass filter is implemented at cutoff frequency 15 Hz and order of filter is 8. This filter is designed by using

$$[c, d] = butter(N, \omega n) \tag{1}$$

Where, N = order of the filter

c is represent the (denominator) and d is (numerator)

ωn = cutoff frequency and it is varies in between 0 and 1.

3.2 Savitzky-Golay Least-Squares Polynomial Filter

Savitzky-Golay least-squares polynomial filter works to smoothen the data minimize the least square error and increase the Signal-Noise-Ratio (SNR) without disturbing the structure and Peak shape of the waves [8].

The working of Savitzky-Golay least-squares polynomial filter can be more clearly described as a symmetrical window, $[Y_n]$ of $2m + 1$ at $n = 0$, $(-m \leq n \leq m)$ where m denotes equally spaced data points that are to be smoothed. A sequence of optimal polynomial signal $y[n]$ replaced by $[K_n]$ of its own neighboring value

$$K_n = \sum_{n=-m}^m a_n y_n \tag{2}$$

Where,
$$a_n = \frac{1}{2m + 1} \tag{3}$$

The idea of S-G least-squares polynomial filter is to approximate or smooth the data under consideration with the specified range by a polynomial but not by a polynomial.

$$Z_n = \sum_{c=0}^N f_c n^c \tag{4}$$

$$\varepsilon = \sum_{n=-m}^m -m(z_n - y_n)^2 \tag{5}$$

$$\varepsilon = \sum_{n=-m}^m (\sum_{c=0}^N f_c n^c - y_n)^2 \tag{6}$$

The polynomial is fit to $2m + 1$ and then K_n is set to the value that polynomial at position 'n'. Now, the smooth output samples values can be obtained by discrete convolution of the form.

$$x_n = \sum_{M=-m}^m g[M]y[n - M] \tag{7}$$

$$x_n = \sum_{M=n-m}^{n+m} g[n - M]y[M] \tag{8}$$

Where $g[M]$ is fixed weighting coefficient. The least square polynomial fitting process is performed by inversion and multiplication of linear relationship between coefficient of the polynomial and original samples. To better understand Eqs. 6 and 7 are expressed in matrix form. The matrix β is designed for the polynomial fitting problem [9].

$$\beta = \{\beta_{nc}\} = n^c \tag{9}$$

$$\text{Where, } g = 0, 1, \dots N \ \& \ (-M \leq n \leq M) \tag{10}$$

Their matrix representation is:

$$\beta_a = A^T A_a = A^T x \tag{11}$$

The solution of the polynomial coefficient written as

$$a = (A^T A)^{-1} A^T x = Jx \tag{12}$$

The main observation is that matrix ‘J’ depends on the values of ‘N’ and the value of ‘m’ is independent of the Input data. So, the least square smoothing reduces the noise and smoothen the signal with maintained amplitude and height of the waveform peaks. The Raw ECG signal are shown in Fig. 1 and Signal noise extraction by different filters techniques are shown in Fig. 2.

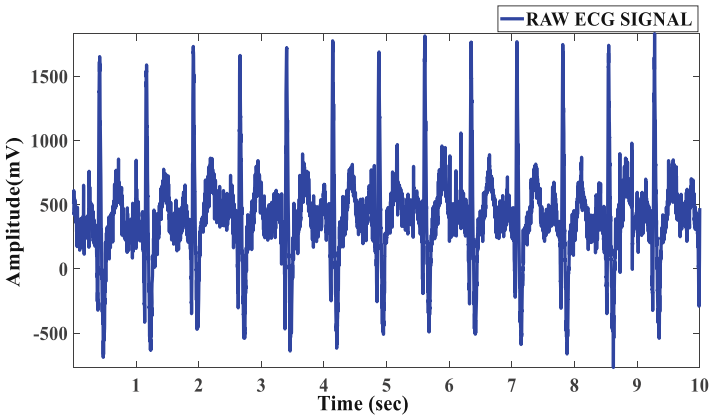


Fig. 1. Raw ECG signal.

3.3 Wavelet Technique

Wavelet technique is works on various applications such as in the field of biomedical signal and image processing. This technique is used for the analysis of non-arbitrary signal and is accurate to determine the multisolution. Wavelet represents the function

that have continuous, non-continuous and sharp peak. The wavelet is scaled by factor ‘x’ and shifted towards a factor ‘y’.

$$\Psi_{xy}(t) = m_1/\text{sqrt}(x)\Psi(t - y/x) \tag{13}$$

The strategy of wavelet analysis is a decomposition of raw signal using filters. The corrupted data is transferred from a filter and to extract their remaining output as detailed coefficient (D) and approximation coefficient (A). Daubechies wavelet family is similar in structure to the ECG, QRS-complex. The signal is usually stated as from the bandwidth 0.05 to 100 Hz [10, 11]. QRS-complex of all peaks and find out their on-sets and off-sets on each and every beats of ECG signal as shown in Fig. 3.

4 ECG Feature Extractions in Patient Affected by Diabetes

After obtaining the clean signal, the following clinically important parameters were obtained. These clinical important parameters give the reflection of physiological as shown in Tables 1 and 2 shows the comparison of diabetes in Male and Female Patients.

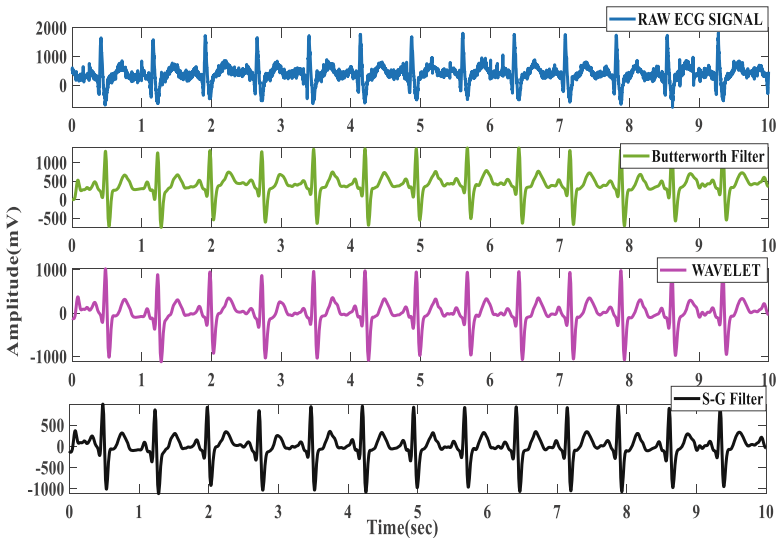


Fig. 2. ECG signal noise extraction by different filter techniques.

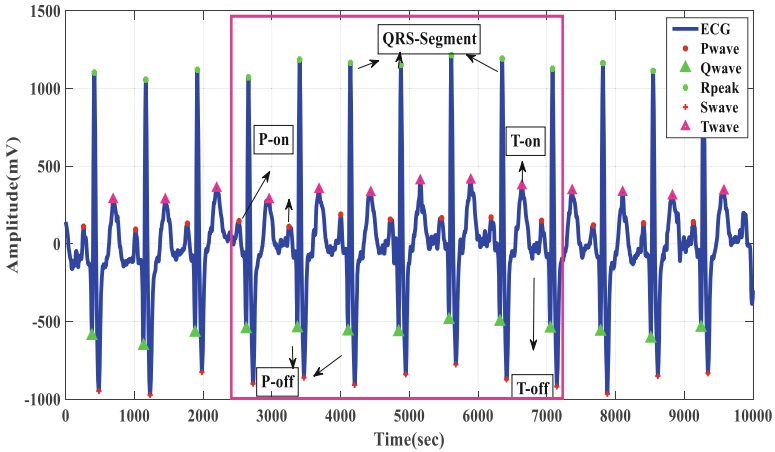


Fig. 3. PQRST-peak identification of ECG signal

Table 1. ECG feature extraction in patient affected by diabetes

Clinically important features	Physiological reflection	Range
1. Corrected QT-interval (QTc)	1. It can be prolonged secondary to metabolic disorder or drug effect 2. Best indicator for the study of ventricular depolarization and repolarization $QTc = QT_{int} / \sqrt{RR_{int}}$	For males- value of QTc below 0.40 s If QTc > 0.40 s is consider as Diabetes For females- value of QTc below 0.44 s If QTc > 0.44 s is consider as Diabetes
2. QT dispersion (QTd)	1. QTd is increases in peripheral vascular disease, cardiomyopathy, diabetes 2. In autonomic neuropathy disorder the QTc is prolonged and increase in QTd dispersion is higher in Diabetic patients as compared to non-diabetic patients 3. It gives the information of recovery time of repolarization $QTd = QT_{max} - QT_{min}$	If QTd > 60 s is considered as abnormal
3. ST Depression (STd)	ST Depression measures the Abnormality in repolarization	STd > 50 μ V for both male and female patients
4. P-wave Dispersion (PD)	It measures the heterogeneity of atrial refractoriness $PD = P_{max} - P_{min}$	It depends on prolongation of diabetes for both male and female patients

5 Heart Rate Variability Analysis (HRV)

This is a non-invasive method to find out the activities of the heart [4]. The Heart Rate Variability parameters are summarized in Table 3. It involves in two sections, Statistical and Frequency Domain Analysis of Non- Diabetic and Diabetic Patients which are shown in Table 4. Time domain parameters are Mean, Standard deviation and Root mean square.

SDNN - we determine the deviation of first beat to last beat- interval of cardiac disorder in diabetic patients. When heart is in impaired condition, their basal heart rate is high and heart is not in relaxed condition, that means SDNN becomes lower but in healthy state, it responds as per the rise in heart rate according to demands of the human body and it has higher SDNN.

RMSSD - RMSSD stands for the RMS difference of RR-interval cardiac disorder in diabetic patients. The patients with diabetes have significantly lower value of heart rate variability parameters which maintain the activity of vagus.

Frequency domain parameters are Low frequency, High frequency and ration between LF/HF.

LF (Low Frequency) - It measures the Sympathetic activity of the human body.

HF (High Frequency) - it measures the Para-Sympathovagal activity of the human body.

LF/HF - If the Heart is in impaired condition then LF and HF powers are imbalanced The Heart is in healthy condition or under relaxed condition so, their parasympathetic power is high. If, their condition is stressful and suffering from overloaded physical work so, their Sympathetic power is high.

Table 2. Comparison of diabetes in male and female patients

Data	Age/sex	QTc	QTd	STd	PD
P_001	41/F	446	75	28	50
P_002	40/F	432	71	26	35
P_003	57/M	418	94	28	41
P_004	60/F	598	80	31	32
P_005	56/M	420	75	23	48
P_006	54/M	421	72	09	12
P_007	77/M	329	74	13	30
P_008	33/F	384	44	10	19
P_009	47/F	425	59	08	12
P_010	55/M	395	67	14	48
P_011	37/F	430	49	18	15
P_012	45/F	445	67	22	28
P_013	67/M	323	44	20	13
P_014	50/F	512	69	25	37
P_015	66/M	423	61	38	28
P_016	44/M	220	24	12	14
P_017	67/M	236	46	18	19
P_018	63/F	542	78	34	28
P_019	37/F	522	64	27	26
P_020	75/M	434	77	40	30

Table 3. Heart rate variability parameters

Time domain	Mean HRV	SDNN	RMSSD
	$mRR = \frac{1}{M} \sum RR(i)$	$\sqrt{\frac{1}{M} \sum (RR(i) - (mRR))^2}$	$\sqrt{\frac{1}{M} \sum (RR(i+1) - (RR(i))^2}$
Frequency domain	LF	HF	LF/HF
	Its power spectrum range 0.04 to 0.15 Hz	Power Spectrum range 0.18 to 0.4 Hz at 0.25 Hz	It indicates Sympathetic to Parasympathetic autonomic balance on HRV

These all bands in frequency domain determine the information about the Physiological terms and it is used in clinical application for the prediction of whether the person has diabetes or not.

6 Poincare Plot Analysis

Poincare-Plot analysis determines the non-linearity of Electrocardiogram signal (ECG). This technique is more accurate than other technique. It is a pictorial software tool and uses the proportion between the standard descriptors for shortest term correlation (SD1) and elongated term correlation (SD2) between RR-Intervals that indicates the condition of the heart and provides beat to beat information on the behavior of heart [5].

SD1 shows the width and SD2 shows the length of the ellipse, with the use of this method we determine the elliptical and non-elliptical pattern of disease and non-disease and provides the revealing information of first beat to last beat interval as shown in Table 5 and in Figs. 4 and 5.

In RR-intervals, each interval-term $RR(k + 1)$ is plotted and designed as a purpose and Function of successive interval-term $RR(k)$, the resultant design of plot is called as Poincare Plot analysis.

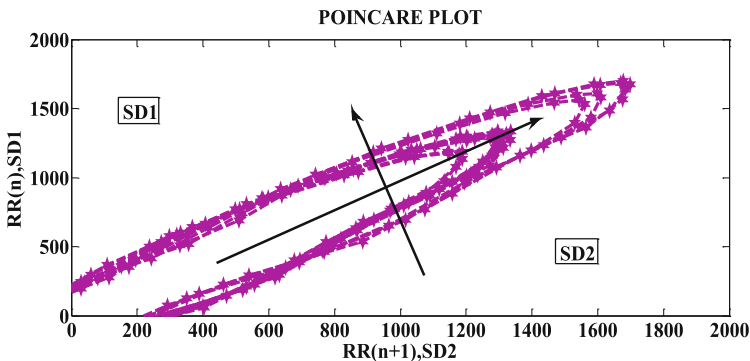


Fig. 4. Poincare plot of non-diabetic (Patient_010)

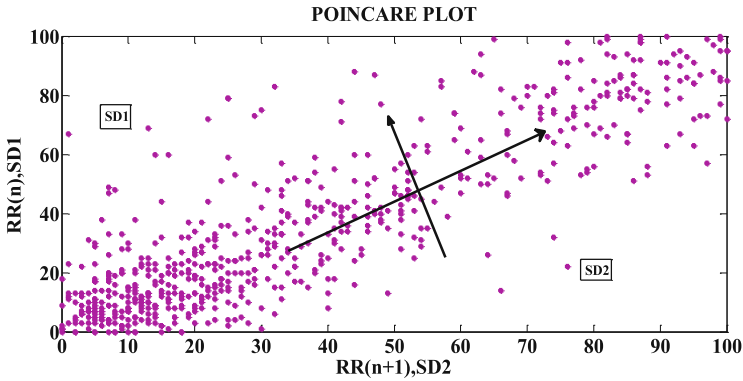


Fig. 5. Poincare plot of diabetic (Patient_004)

7 Result and Discussions

This paper is aimed to establish an algorithm for the detection of diabetes at an early stage. In this study out of 55 cases, the results of 20 cases are shown here.

Table 4. Statistical and frequency domain analysis of non-diabetic and diabetic patients.

P* ID	Mean HRV	SDNN	RMSSD	LF	HF	LF/HF	DI
P_001	380.0	12.79	11.57	25.62	74.37	0.34	DM
P_002	342.3	5.34	2.32	12.17	90.82	0.13	DM
P_003	268.2	18.98	1.43	16.23	89.33	0.18	DM
P_004	249.5	11.23	10.54	10.18	80.77	0.12	DM
P_005	248.6	16.9	2.45	24.11	85.89	0.28	DM
P_006	429.1	30.3	33.54	92.86	11.23	8.26	ND
P_007	521.3	22.90	50.1	79.63	10.36	7.68	ND
P_008	454.6	43.4	34.54	87.23	7.89	11.05	ND
P_009	463.3	33.03	48.67	72.45	12.34	5.87	ND
P_010	425.7	25.5	21.07	63.60	20.55	3.09	ND
P_011	536.3	19.03	31.23	89.33	13.34	6.69	ND
P_012	248.1	6.0	7.69	36.39	79.56	0.45	DM
P_013	672.3	39.2	34.34	74.1	11.56	6.41	ND
P_014	235.8	10.6	8.09	19.51	77.18	0.25	DM
P_015	239.8	7.56	2.05	20.36	74.18	0.27	DM
P_016	864.6	28.7	42.08	76.23	11.98	6.36	ND
P_017	629.8	27.33	39.12	74.86	15.13	4.94	ND
P_018	280.7	8.09	13.02	10.33	81.39	0.12	DM
P_019	133.6	6.76	13.05	14.55	91.02	0.15	DM
P_020	296.02	4.60	3.2	11.24	89.21	0.12	DM

P*: Patient DI: Disease Identification, DM: Diabetes Mellitus and ND: Non-Diabetes

Diabetes-related ECG features are then estimated for all the acquired data. Out of 20 cases, 11 cases were found Diabetic and 09 cases were found Non-diabetic. Out of 10 male patients, 03 patients have $QTc > 400$ ms, 06 patients have $QTd > 60$ ms, 02 patients have $STd > 50$ μ V.

Out of 10 female patients, 04 patients have $QTc > 440$ ms, 07 patients have $QTd > 60$ ms, 03 patients have $STd > 50$ μ V.

10 male patients have separately analyzed the effect of Diabetes. 06 patients who had heart disease are reported that they have higher values of QTc , QTd and STd and the remaining 04 are without any problem have experience non-diabetic.

In the case of 10 female patients, 07 patients who had heart disease is reported that they have higher values of QTc , QTd and STd and the remaining 03 are without any problem have experience non-diabetic. In HRV analysis Out of 20 patients, 11 patients were found lower Mean HRV, SDNN, RMSSD, LF, the ratio of LF/HF and higher HF respectively for diabetes mellitus and remaining 09 patients were found higher HRV.

In Poincare plot analysis out of 20 cases, 11 patients have a ratio of Standard Descriptor $SD1/SD2 < 20$ were found for a diabetic. Figure 6(a) shows Heart Rate Variability in male Diabetic and Non-diabetic Subject, Fig. 6b shows Heart Rate Variability in female Diabetic and Non-diabetic Subject. Figure 7 shows the Estimation of features in Diabetic Male and Female Patients. The females who suffered from diabetes mellitus have more chances to build cardiac disorders as compared to males.

All these parameters show the tremendous variation in cardiac disorder in diabetic patients easily find out the performance of the person whether he/she is healthy or unhealthy. In the Comparison of signal to noise ratio, of different noise removing techniques, the noise ratio of Savitzky-Golay least-squares polynomial filter is better.

Signal to noise ratio was compared and shown in Table 6. Comparison of Signal Noise Ratio (SNR) of Noise Removing Techniques are shown in Fig. 8.

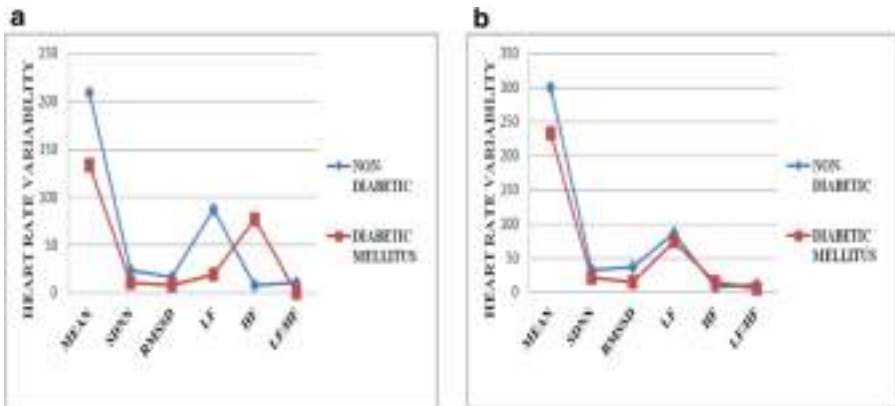


Fig. 6. (a) Heart rate variability in male diabetic and non-diabetic subject. (b) Heart rate variability in female diabetic and non-diabetic subject.

Table 5. Poincare plot analysis of non-diabetic and diabetic patients.

P* ID	SD1	SD2	T = SD2/SD1	DI
P_001	13.04	224.53	13.20	DM
P_002	10.28	194.53	15.92	DM
P_003	16.13	120.19	19.85	DM
P_004	17.8	152.52	18.01	DM
P_005	12.54	215.97	17.22	DM
P_006	31.78	787.81	44.78	ND
P_007	12.54	688.45	54.90	ND
P_008	47.03	563.00	33.04	ND
P_009	21.22	769.54	36.26	ND
P_010	36.04	460.16	38.68	ND
P_011	25.77	595.56	42.10	ND
P_012	10.54	159.55	15.13	DM
P_013	21.29	671.12	31.2	ND
P_014	10.65	132.12	12.40	DM
P_015	11.20	187.11	16.70	DM
P_016	39.81	915.17	41.14	ND
P_017	32.41	980.23	30.24	ND
P_018	12.20	142.43	11.67	DM
P_019	11.52	129.63	11.29	DM
P_020	19.10	198.43	10.38	DM

SD1: Short-Term Correlation, SD2: Long-Term Correlation

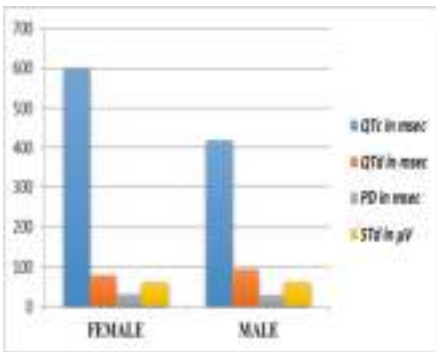


Fig. 7. Estimation of features in diabetic male and female patients.

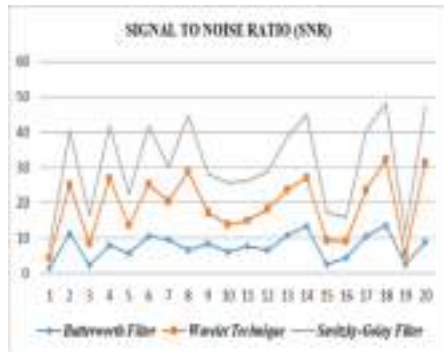


Fig. 8. Comparison of signal noise ratio of different noise removing techniques.

Table 6. Evaluation and comparison of SNR of noise removing techniques

P* ID	SNR (BW)	SNR (Wavelet)	SNR S-G Filter
P_001	1.714	2.613	2.986
P_002	11.281	13.712	15.411
P_003	2.209	6.072	7.981
P_004	7.871	18.998	14.762
P_005	5.675	7.871	8.790
P_006	10.561	14.568	16.675
P_007	9.538	10.655	9.665
P_008	6.453	22.567	15.761
P_009	8.321	8.907	10.892
P_010	6.098	7.675	11.776
P_011	7.600	7.409	10.991
P_012	6.500	11.564	10.765
P_013	10.654	12.876	14.872
P_014	13.239	13.765	17.898
P_015	2.543	6.694	7.897
P_016	4.500	4.543	6.720
P_017	10.540	12.965	16.800
P_018	13.450	18.769	15.781
P_019	2.539	2.900	5.792
P_020	8.759	22.540	15.788

SNR: Signal to noise ratio, BW: Butterworth filter, S-G: Savitzky golay filter

8 Conclusions

The identification of diabetes and their physiological effects on human's heart are determined by the HRV analysis and ECG features such as QT interval, QT Dispersion, ST Depression (STd) and P-wave Dispersion (PD).

Out of 55 cases (29 patients are male and remaining 26 are female patients), 31 cases were found Diabetic and 24 cases were found Non-diabetic.

In all cases (including male and female) it is found that the range of any one of the parameter QTc, QTd and STd becomes higher from 400 ms for male & 440 ms for female, 60 ms for both, and 50 μ V for both respectively then he/she is diabetic. The duration of P-wave dispersion is increasing with the increase in the period of diabetes in patient. The Patient with diabetes is below 5 years their value of P-wave dispersion is 26 ms. Patient with diabetes for around 10 years the value of PD dispersion of around 28 ms and Patient with diabetes for around 20–30 years the value of PD dispersion of around 30 ms. The value of PD is exceed 30 ms it shows that the period of diabetes is above 30 years.

In HRV analysis, it is also found that the range of time domain parameters Mean HRV, SDNN and RMSSD were below 400 ms, 20 ms and 20 ms respectively for diabetic cases. The Power range of frequency domain parameters LF were above


40 ms², the range of HF and ratio of LFHF were below 20 ms² and 1(unity) respectively for diabetic cases. In Poincare Plot analysis, the ratio of standard descriptors SD1/SD2 must be lower than 20 and it shows the graph in non-elliptical pattern for diabetic Patients. It conclude that the final finding are, the Patients with diabetes had increased value of QTc, QTd, PD and STd, lower value of HRV and lower value of ratio of standard descriptors (SD1/SD2). The sympathetic and parasympathetic changes in the human are identified from HRV analysis, which is used here in identification of diabetes and heart disease at the premature stage. These methods are used and easily helpful to cardiologists to determine the pathological and physiological variations in the Patients.

References

1. International Diabetes Federation: IDF Diabetes Atlas, 1st edn, pp. 362–367. International Diabetes Federation, Brussels (2017)
2. Khandoker, A.H., Al-Angari, H.M., Khalaf, K., et al.: Association of diabetes related complications with heart rate variability among a diabetic population in the UAE. *PLoS One* **12**, 1–16 (2017)
3. Shaffer, F., McCraty, R., Zerr, C.L.: A healthy heart is not a metronome: an integrative review of the heart's anatomy and heart rate variability. *Front. Psychol.* **5**, 1–19 (2014)
4. Uddin, Md.S.A., Rahman, Md.A.: Myocardial infarction classification by HRV analysis using single lead ECG. *AIUB J. Sci. Eng.* **16**(3), 1608–3679 (2017)
5. Gospodinov, M., Gospodinova, E., Domuschiev, I., et al.: Nonlinear analysis of heart rate variability in Type 2 diabetic patients. *Fractal Geom. Nonlinear Anal. Med. Biol.* **2**(1), 134–139 (2016)
6. Lu, X., Pan, M., et al.: QRS detection based on improved adaptive threshold. *J. Healthc. Eng.* **2018**, 1–8 (2018)
7. <https://physionet.org/physiobank/database/ptbdb/>
8. Hargittai, S.: Savitzky-Golay least square polynomial filters in ECG signal processing. *Comput. Cardiol.* **32**, 763–766 (2005)
9. Schafer, R.W.: What is a Savitzky-Golay filter? *IEEE Sig. Process. Mag.* **28**, 111–117 (2011)
10. Banerjee, S., Mitra, M.: Application of cross wavelet transform for ECG pattern analysis and classification. *IEEE Trans. Instrum. Meas.* **63**, 326–333 (2014)
11. Lin, C.C., Yang, C.M.: Heartbeat classification using normalized RR intervals and morphological features. *Math. Probl. Eng.* **12**, 1–11 (2014)



Analysis of Dispersion Characteristics of Helical Metal Clad and Graphene Clad Circular Core Step Index Fiber

Raghvi Gupta, Archana Tripathi, and Amritanshu Pandey^(✉) 

Department of Electronics Engineering,
Indian Institute of Technology (BHU) Varanasi, Varanasi, India
apandey.ece@iitbhu.ac.in

Abstract. In this paper, we have reported the study of the optical signal propagation characteristics in a nontraditional optical fiber having circular core (made of dielectric) and helical winding clad (metallic and graphene). Study has been done at different pitch angles. This analysis also includes the absorption characteristic of waveguide by including imaginary part of refractive index. Normal and helical boundary conditions have been applied to derive the model characteristic equation. Dispersion curves and model cut-off conditions have been obtained on the basis of characteristic equation derived theoretically. The dispersion curves are derived by varying the pitch angles of the winding. The results obtained for different pitch angles have been analyzed; and the changes in dispersion curve have been explained. The results obtained show a standard shape of dispersion curve and the numbers of guided modes are estimated on the basis of standard parameters of fiber such as core radius, reflective indices of core and cladding and operation wavelength. The difference in the results obtained for metal clad and graphene clad fiber is also presented.

Keywords: Helical clad optical fiber · Dispersion curve · Pitch angle · Graphene

1 Introduction

Optical fiber based waveguides have emerged a attractive technology having applications not only limited to communications but in diverse areas of all type of digital data transmissions, medical imaging, intersatellite communications and very recent fiber-to-home application etc. [1–6]. Researchers have investigated optical waveguides from different perspectives such as different shapes of it, use of different types of materials including dielectrics, metals, organic materials, polymers, photonic crystals, quasi crystals, nano-materials etc. [7–13]. One of the most vastly explored fiber is a helical clad waveguide in which the shape of cladding is inspired from electromagnetic devices using the traveling wave technology (TWT). Most of the helical clad fibers studied have resulted in improvement of performance in comparison to standard fibers and therefore, multiple applications have emerged employing helical waveguides in various ranges [14–22]. The first investigation of helically cladded circular waveguides was done by Bunch *et al.* [13]. A lot of progress has been done in the field of cladding

design including a report by Singh et al. [16] proposing a conducting helical cladding on the circular waveguide. They reported that the number of modes is reduced in comparison to standard optical fibers. Kumar et al. [19] had given an idea about helically cladded elliptical waveguides. Annular waveguides under helical boundaries have been discussed along with their propagation characteristics by some researchers. Different geometrical designs have been explored to get excellent optical properties. Different sizes and shapes (square, elliptical, circular), materials and designs including photonic crystal structures are continuously being explored in different sensing applications.

The present paper introduces a helical optical waveguide whose cladding is made of sheath helix of different metal/graphene. Optical fibers with helical winding are known as complex optical waveguides. The sheath helix, as discussed in [19], is a circular cylindrical surface conducting only in the helical direction. It can be thought of as the windings of thin wire around a cylindrical surface with close spacing such that the gap between the adjacent windings is negligible. The characteristic equation, describing the nature of fields in this idealized structure, has been obtained theoretically based on unified approach. This analysis results that the number of propagating modes depends on the helix pitch angle (varied between 0 to $\pi/2$) therefore, helical winding at interface are the controlling parameter of characteristics. The analysis therefore is of the sheath helix cladded cylindrical surface core with high conductivity. It is assumed that the waveguide core has real constant refractive index (n_1). And the cladding has imaginary refractive index ($j n_2$), such that $n_1 > |n_2|$ as shown in Fig. 1.

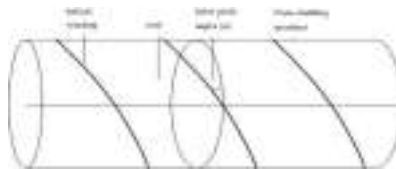


Fig. 1. Proposed fiber with a sheath helix around the dielectric core.

2 Theoretical Analysis

In a waveguide, the propagating light rays, or electromagnetic fields assume certain patterns whose theoretical analysis is important in order to obtain the various experimental observables. Unlike electrical circuits Ohm's law cannot be used to obtain current in waveguides. In optical waveguide theory generally three different approaches are used namely ray theory, wave theory and electromagnetic theory [22].

The mode theory [3–5] analysis is preferred as it is able to explain the propagation of modes in side the optical fiber. The mode theory treats light as electromagnetic wave and its propagation behavior is analyzed using Maxwell's equations governing the propagation of electromagnetic fields under the imposed boundary conditions. Under this theory, the guided electromagnetic waves are called the modes. Mode characteristics depend on many parameters including the wavelength of the propagation and

hence, a change in wavelength may cease the mode from propagating in a particular optical fiber along it. Every optical fiber has one lowest order mode named as fundamental mode which do exists under all conditions i.e. this mode has no cut-off. In the present analysis of helical optical waveguide whose cladding is made of sheath helix, it is assumed that spacing between the nearby two isolated windings is very small with a constant helix pitch angle (ψ).

Maxwell's equations applied in the dielectric medium lead to the wave equation of electric (magnetic) fields. The field component E_z and H_z satisfy the scalar wave equation. Using cylindrical coordinate system, taking z direction as direction of propagation of wave, the general field expression is given by

Let β is propagation constant and $n_2 k < \beta < n_1 k$ and k is free space number. The expressions for E_z and H_z inside the core i.e. $r < a$, may be written as,

$$E_{z1} = AJ_v(ua)e^{iv\Phi - j\beta z + j\omega t} \tag{1}$$

$$H_{z1} = BJ_v(ua)e^{iv\Phi - j\beta z + j\omega t} \tag{2}$$

Where $u^2 = \omega^2\mu_0\epsilon_1 - \beta^2$

Further, the fields E_z and H_z outside the core and inside the cladding i.e. $r > a$ may be expressed as

$$E_{z2} = CK_v(wa)e^{iv\Phi - j\beta z + j\omega t} \tag{3}$$

$$H_{z2} = DK_v(wa)e^{iv\Phi - j\beta z + j\omega t} \tag{4}$$

Where $w^2 = \beta^2 - \omega^2\mu_0\epsilon_2$

Using Maxwell's equations for the transverse field components (E_ϕ and H_ϕ) may be written.

The expressions for E_ϕ and H_ϕ inside the core are

$$E_{\phi1} = -\frac{j}{u^2} \left[j\frac{\beta v}{a}AJ_v(ua) - \mu\omega uBJ'_v(ua) \right] e^{iv\Phi - j\beta z + j\omega t} \tag{5}$$

$$H_{\phi1} = -\frac{j}{u^2} \left[j\frac{\beta v}{a}BJ_v(ua) + \omega\epsilon_1uAJ'_v(ua) \right] e^{iv\Phi - j\beta z + j\omega t} \tag{6}$$

The expressions for E_ϕ and H_ϕ outside the core are

$$E_{\phi2} = -\frac{j}{w^2} \left[j\frac{\beta v}{a}CK_v(wa) - \mu\omega wDK'_v(wa) \right] e^{iv\Phi - j\beta z + j\omega t} \tag{7}$$

$$H_{\phi2} = -\frac{j}{w^2} \left[j\frac{\beta v}{a}DK_v(wa) + \omega\epsilon_2wDK'_v(wa) \right] e^{iv\Phi - j\beta z + j\omega t} \tag{8}$$

The boundary conditions are applied at the core-cladding interface at $r = a$, this corresponds to the metal-dielectric helix boundary. It is observed that at the

dielectric-metal interface, the electric field along the direction of pitch angle will vanish. The resultant expressions at the boundary therefore, are

$$E_{z1} \sin \psi + E_{\Phi 1} \cos \psi = 0 \tag{9}$$

$$E_{z2} \sin \psi + E_{\Phi 2} \cos \psi = 0 \tag{10}$$

Next, the electric field components normal to the direction of ψ are also continuous due to absence of any fixed charges. Hence,

$$(E_{z1} - E_{z2}) \cos \psi + (E_{\Phi} - E_{\Phi 2}) \sin \psi = 0 \tag{11}$$

Again tangential magnetic field components, similarly, along ψ are also continuous. So

$$(H_{z1} - H_{z2}) \sin \psi + (H_{\Phi 1} - H_{\Phi 2}) \cos \psi = 0 \tag{12}$$

With the help of these boundary conditions, a set of four equations having four arbitrary constants are found. By using elimination technique, the following characteristic equation of propagation constant β is found [6].

$$u \frac{J_v(ua)}{J'_v(ua)} \left(\sin \psi + \frac{\beta v}{u^2 a} \cos \psi \right)^2 + \frac{k_1^2 J'_1(ua)}{u J_v(ua)} \cos^2 \psi - w \frac{k_v(wa)}{k'_v(wa)} \left(\sin \psi + \frac{\beta v}{u^2 a} \cos \psi \right)^2 + \frac{k_2^2 k'_v(wa)}{w k_v(wa)} \cos^2 \psi = 0 \tag{13}$$

This characteristic equation is used to determining propagation characteristic of the fiber under investigation.

3 Result and Discussion

The characteristic equation presents the model properties of unconventional waveguide having helical clad. For doing so, the normalized propagation constant vs. normalized frequency graph (core radius a) is drawn to obtain dispersion curve of fiber, using MATLAB. Normalized frequency (V) and normalized propagation constant (b) can be calculated by using the following equations

$$V = a \sqrt{(u^2 + w^2)} = \frac{2\pi a}{\lambda} \sqrt{(n_1^2 - n_2^2)}$$

and

$$b = \left(\frac{aw}{V} \right)^2 = \left(\frac{(\beta/k)^2 - n_1^2}{n_1^2 - n_2^2} \right)$$

(a) **Copper (metal) as cladding material**

At lower frequency electromagnetic waves metals act as perfect conductor because at lower frequencies conductivity $\sigma \gg \omega\epsilon$ but at higher frequencies σ becomes comparable to $\omega\epsilon$ so metals do not remain good conductors. As $\sigma \neq 0$ and σ is comparable to $\omega\epsilon$ so metals behave as lossy dielectrics [26]. This turns out in complex dielectric constant ϵ . Drude's theory also states the same that at higher frequencies metals behave as a dielectric material. As, refractive index $n = \sqrt{\epsilon}$, and dielectric constant is complex number so that n will be also a complex number which is function of frequency.

For the calculations, the core refractive index n_1 and the metal cladding refractive index are assumed as 1.50 and $1.03 + 0.98i$, respectively at $\lambda = 1.55 \mu\text{m}$. Further, $\nu = 1$ is assumed for simplicity, but the results are valid for any integer value of ν , in general. The pitch angle values of ψ as $0^\circ, 30^\circ, 60^\circ$ and 90° are analyzed on a constant difference of 30° (Figs. 2, 3, 4 and 5).

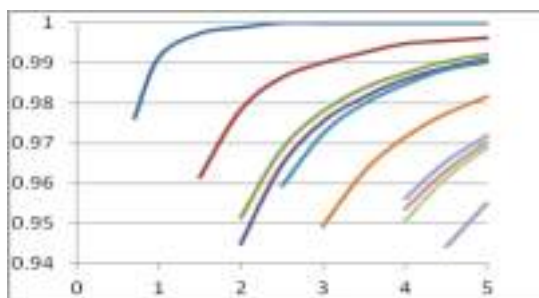


Fig. 2. b vs. V plot for $\psi = 0^\circ$ for copper as cladding material

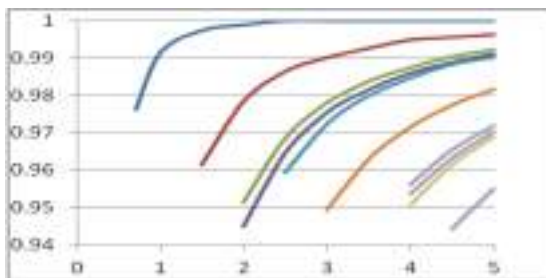


Fig. 3. b vs. V plot for $\psi = 30^\circ$ for copper as cladding material

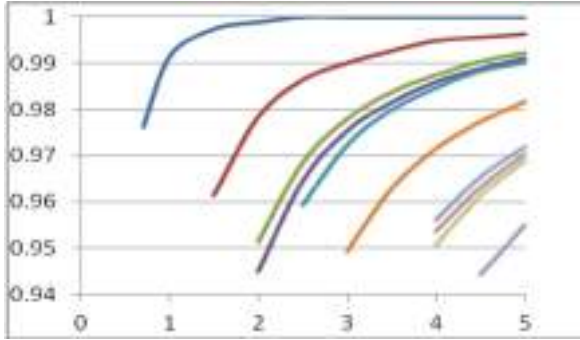


Fig. 4. b vs. V plot for $\psi = 60^0$ for copper as cladding material

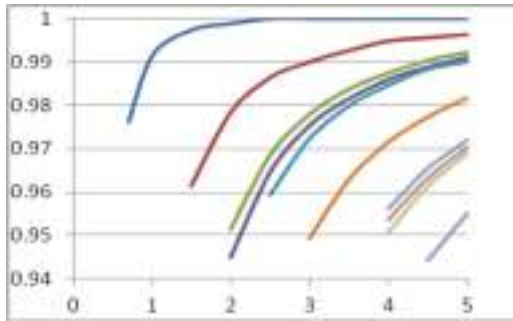


Fig. 5. b vs. V plot for $\psi = 90^0$ for copper as cladding material

(b) Graphene as cladding Material

Graphene belongs to a class of two dimensional materials having a single layer of carbon atoms arranged in a honeycomb form. It has wonderful properties of conductor, semiconductor and insulator depending upon the number of graphene layers. The absorption co-efficient of Graphene is very low hence, it is almost transparent at optical frequencies. Single layer Graphene is zero-gap semiconductor. Therefore, some of its electrical properties are similar to metals however some optical properties differ. It also has complex refractive index which depends on operating wave length. For wave length $\lambda = 1.55 \mu m$ refractive index of graphene is equal to $n = 2.66 + 2.84i$. For the calculation let the core material is gallium arsenide and $n_1 = 3.93$. Remaining parameters are similar as in previous case (Figs. 6, 7, 8 and 9).

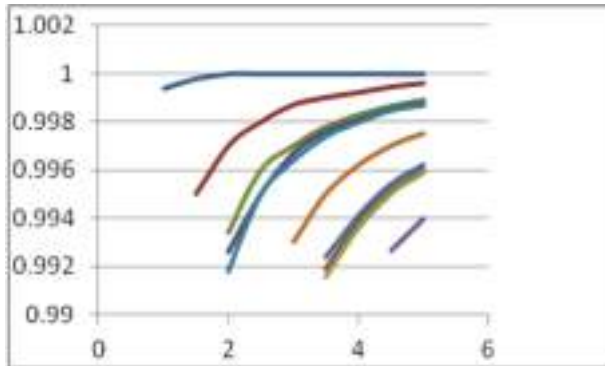


Fig. 6. b vs. V plot for $\psi = 0^\circ$ for graphene as cladding material

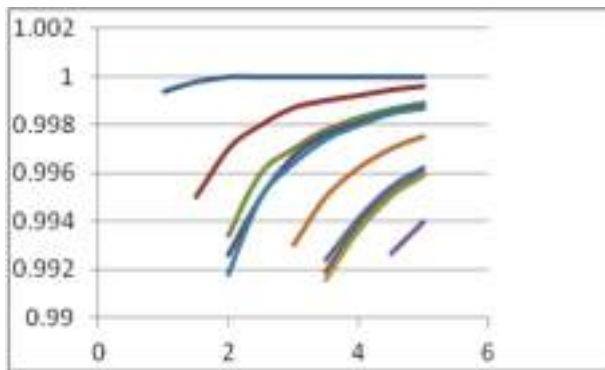


Fig. 7. b vs. V plot for $\psi = 30^\circ$ for graphene as cladding material

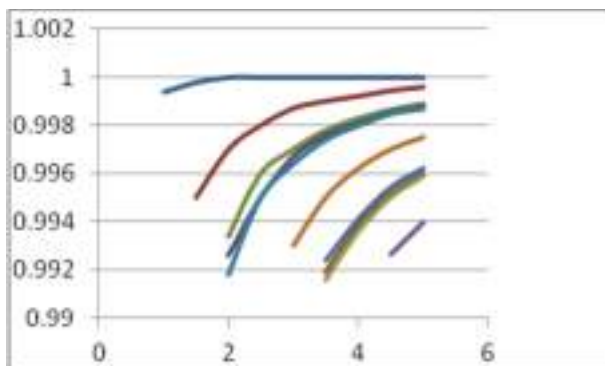


Fig. 8. b vs. V plot for $\psi = 60^\circ$ for graphene as cladding material

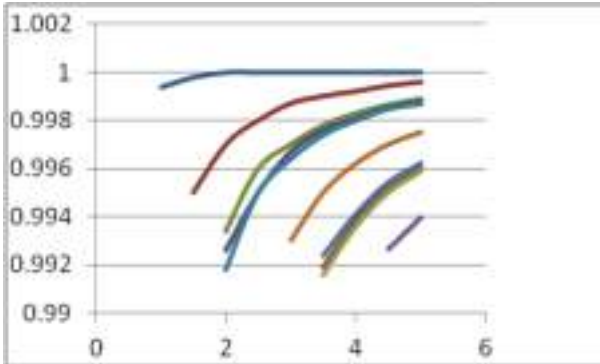


Fig. 9. b vs. V plot for $\psi = 90^\circ$ for graphene as cladding material

4 Conclusion

The novel designed fibers show that all the modes have b starting from more than 0.90 in contrast to the standard dielectric clad waveguides which have b starting from zero. For first few modes b is not having any values less than 0.94. This anomalous effect may suggest that cutoff condition do not exist. The relative propagation constant b increases with core radius in all cases. The pitch angles are not having any effect on dispersion curve, at least for few lowest order modes analyzed. This structure may permit Single mode and Double mode operation of the fiber, because second mode is not grouped with other modes. This is very different from standard dielectric clad waveguides. However, the higher order modes are coupled as usual the operation of the modes for b less than 0.90. When graphene was used as cladding material all modes have b starting from more than 0.99 and this effect may suggest that cutoff condition do not permit same as in metal clad case. Pitch angle also has similar no effect for few lowest order modes analyzed. Number of modes is equal in both cases however their existence occurs at different V . This type of novel optical fibers has applications in new generation optical communication systems.

References

1. Ballato, J., Hawkins, T., Foy, P., Morris, S., Hon, N.K., Jalali, B., Rice, R.: Silica-clad crystalline germanium core optical fibers. *Opt. Lett.* **36**, 687–688 (2011)
2. Kumar, N., Srivastava, S.K., Ojha, S.P.: A theoretical analysis of the propagation characteristics of an annular circular waveguide with a helical winding as the inner cladding. *Microw. Opt. Technol. Lett.* **37**, 69–74 (2003)
3. Kapany, N.S.: *Fiber Optics Principles and Applications*. Academic Press, New York (1967)
4. Ghatak, A.K., Thyagarajan, K.: *Introduction to Fiber Optics*. Cambridge University Press, Cambridge (1999)
5. Kieser, G.: *Optical Fiber Communications*. McGraw-Hill, New York (1991)
6. Yeh, C.: Elliptical dielectric waveguide. *J. Appl. Phys.* **33**, 3235–3242 (1962)

7. Chiang, K.S.: Effective index method for the analysis of optical waveguides couplers and arrays: an asymptotic theory. *J. Lightwave Technol.* **9**, 62–72 (1991)
8. William Hayt, J.A.: Buck, “Engineering Electromagnetics”. McGraw-Hill, New York (1991)
9. Yoin, W.Y., Liand, P., Wang, W.B.: Guided electromagnetic waves in a parallel-plate gyroelectronic biaxial chirowaveguide. *J. Mod. Opt.*, **412**, 59–65 (1994)
10. Rao, M.P.S., Singh, V., Prasad, B., Ojha, S.P.: An analytical study of the dispersion curves of an annular waveguide made by liquid crystal. *Photon Optoelectron* **5**, 73–78 (1998)
11. Kumar, N., Srivastava, S.K., Ojha, S.P.: A comparative study of modal dispersion characteristics of different types of concave lens shaped dielectric waveguides. *Microwave Opt. Technol. Lett.* **35**, 337–342 (2002)
12. Bertone, J.F., Jiang, P., Hwang, K.S., Mitllaman, D.M.: Thickness dependence of the optical properties of silica-air and air-polymer photonic crystals. *Phys. Rev.* **83**, 300–303 (1999)
13. Bunch, K.J., Grow, R.W.: The helically wrapped circular waveguide. *IEEE Trans. Electron Devices ED* **34**, 1873–1885 (1987)
14. Jones, E.M.T.: A negative dispersion helix structure. Elec Res Lab, Stanford University, Technical Report, vol. 27 (1950)
15. Ahn, S., Ganguly, A.K.: Analysis of helical waveguide. *IEEE Trans. Electron Devices ED* **33**, 1348–1355 (1986)
16. Singh, U.N., Singh II, O.N., Khastgir, P., Dey, K.K.: Dispersion characteristics of helically clad step-index fiber: an analytical study. *J. Opt. Soc. Am. B* **12**, 1273–1278 (1995)
17. Chaube, V.K., Dey, K.K., Ojha, S.P., Khastgir, P.: Modal characteristics of a doubly clad step-index fiber: a general analytical approach. *Can. J. Phys.* **61**, 796 (1998)
18. D’Agostino, S., Emma, F., Paoloni, C.: Accurate analysis of the helix slow wave structure. *IEEE Trans. Electron Devices* **45**, 1605 (1998)
19. Kumar, D.: Propagation characteristics of helically clad elliptical step-index fiber. Ph.D. Thesis, Applied Physics, IT, BHU, India (1999)
20. Srivastava, S.K., Pandey, P.C., Singh, U.N., Ojha, S.P.: Effect of pitch angle on modal propagation characteristics of an annular circular dielectric waveguide having helical windings on the inner and outer boundaries as the claddings. *Microwave Opt. Technol. Lett.* **33**, 338–344 (2002)
21. Ming-Liu, J.: *Photonic Devices*. Cambridge University Press, Cambridge (2005)
22. Sadiku, M.N.O.: *Element of Electromagnetics*. Oxford University Press, Oxford (2007)



T-Type Multilevel Inverter Topology with Reduced Switch Count Using Different PWM Techniques

Monika Agrawal, Vijay Bhuria^(✉), and Shishir Dixit^(✉)

MITS, Gwalior, MP, India

monikaagrawal67@gmail.com,

vijay.bhuria@mitsgwalior.in, shishir.dixil@gmail.com

Abstract. The basic idea of a multi-level medium and high power inverter is to use a series of power switches with several low voltage dc sources to transform energy by synthesizing the stepped voltage waveform. Multilevel inverter is capable of increasing output voltage and efficiency with small switching losses and total harmonic distortion as the level improves the harmonic itself. This paper proposes a 1-phase 9-level T-style inverter with various SPWM strategies having less number of devices which posses high and low power region as compared to conventional inverter. Generally, it is used for low power appliances having maximum efficiency. A 1-phase 9-level T-style inverter was implemented and to generate 9-level voltage advanced multicarrier PWM control techniques are used. Finally, multi-level inverter topology simulation outcomes are performed using MATLAB/SIMULINK R2013a with different SPWM approaches such as PD, POD, APOD, HRPWM, VFISW, PS and SFO modulation techniques and its switching on/off pattern of IGBT's.

Keywords: Multi-level inverter (MLI) · T-style inverter and SPWM techniques

1 Introduction

In the current electronic power converter situation, semiconductor devices extend their range of applications because they provide less consumption, enhanced effectiveness, enhanced performance, enhanced maintenance and many more. It is best to link one power semiconductor switches directly in a medium voltage grid [1–4]. A multi-level inverter circuit with distinct options in cases of extremely high and medium voltage. It offers cost-effective solution for multi-level inverter alternatives that not only achieve large power ratings, but also uses low power rating applications in sources of renewable energy such as photo voltaics [3], Wind energy that can simply be attached to the high-powered multi-level inverter scheme. Multilevel inverter primary region has traction [5] in both locomotives and static converters on the track side [6, 7].

Multilevel inverter offers many benefits over two-level (2-level) inverters, near sinusoidal output voltage waveform, low magnitude of Electromagnetic Interference and (less dv/dt) across switches, lower frequency switches and low power rating devices, Inverter can operate in low and high switching frequencies. Each switch

requires a individual driver circuit, thus improving the circuit complexity and reduces the size of circuit. In Fig. 1, the conventional two-level (2-L) inverters are used to produce an alternating current voltage waveform from the supply of DC voltage. Only two reverse polarity output voltages can be created for the load by the two-level inverter, $V_{dc}/2$ or $-V_{dc}/2$. These voltages are generally switched with PWM to create an AC output voltage. But it produces very high harmonic contents in output voltage, high (EMI) and high stress across switches (as compared to MLI).

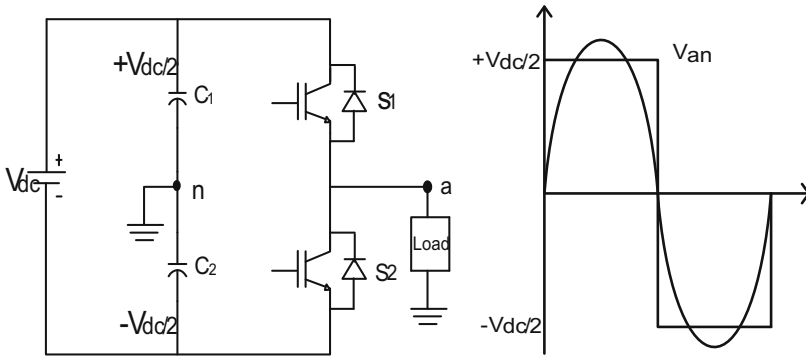


Fig. 1. Two-level single-phase inverter and two-level output voltage waveform circuit

Several conventional & advanced topologies of multilevel inverter and their PWM methods have been explored as a replacement of old conventional topologies as described above. The inverter output voltage n levels produced from several sources of DC voltage. As the amount of voltage level increases, the effectiveness of the voltage is fine that greatly reduced the size of the filter. Figure 2 shows the basic topologies of conventional MLI. The First suggested in 1975 was the cascade multilevel inverter [4]. The cascaded multilevel inverter comprises of distinct DC-sourced connections that have been projected for full-bridge cells [2, 9, 10] in sequence to synthesize a staircase AC output voltage so it is easy. Multi-level inverter is basically began from the converter of three voltage levels [6]. For very low power and voltage circuits, these three-level inverter topologies are therefore not appropriate. The Nine-level T-style inverter (9L-TI) was suggested for high effectiveness and performance is good in terms of THD as compared to other topologies.

This paper discussed a single phase T-style 9-level topology that requires fewer switches and gate driver circuits than standard multilevel inverters. The T-style topology suggested earlier here is applied with distinct PWM methods in a single phase. The pulse-width control (PWM) is the most efficient way to regulate the inverter output voltage [4, 5]. The most widely used method to generate the PWM is the carrier-based schemes intersected with a reference sinusoidal waveform. This paper attempts to demonstrate that 9L-TI in terms of component amount and THD is better than standard multilevel inverters. Although the 3LTI is generally implemented and studied for use in low-voltage installations, the use of low-voltage and low-power domestic appliances is hard because the enhanced effectiveness is not adequate owing to its complexity and cost issue [1].

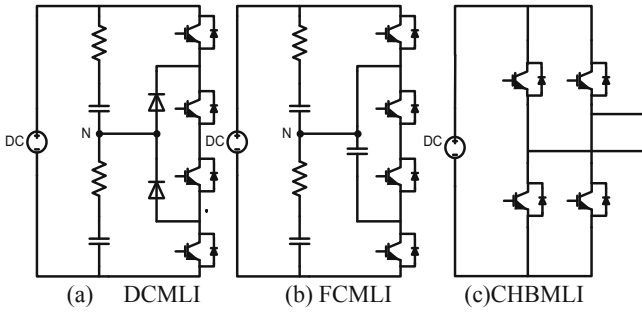


Fig. 2. Conventional multi-level inverter topologies

2 T-Style Multilevel Inverter

The basic generalized circuit of the 3L-TI is shown in Fig. 3 [3] With an active bidirectional switch, this topology able to flow current in both the directions. For small-voltage applications, switches would normally employed with IGBTs with feedback diodes to block the full DC link voltage at load.

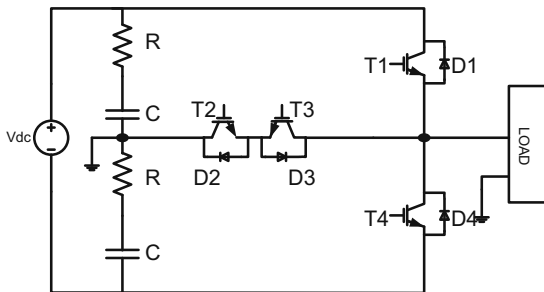


Fig. 3. Single phase 3-level inverter (T-style)

It is being observed from the literature that conventional MLI topologies such as DCMLI, FCMLI and CHBMLI are widely used in different applications but they are very complex, requires large gate drive and level shifter circuits which may increase its cost and also require a distinct DC sources for each level that becomes creates a problem for high level operation.

In keeping with this view of this new approach, this paper satisfies the 9L-TI topology that requires fewer switches and gate driver circuits than standard multilevel inverters. The Reversing Voltage method is discussed in [3] that implemented in a single phase system using separate PWM techniques and it is observed that control of the inverter with distinct PWM is the most efficient way to regulate the inverters. The carrier-based PWM schemes to generate firing pulses for MLI are the convenient method in which the modulating signal is intersected with a high frequency (nearly about 2–5 kHz) carrier waveform (triangular). The paper reported the simulation results

of 9 level T-style inverter and also shows that the proposed inverter have used lesser number of power switches and THD is better than old topologies of Multilevel inverter.

Indeed, use of multidirectional switch used the half of the dc link is blocked. IGBTs, with antiparallel feedback diodes are used as shown in Fig. 3 with devices with a decreased voltage rating. The bidirectional switch shows less switching (frequency) losses and low conductive losses owing to low risk of high blocking voltage, although two units are connected in series. There is no direct (series). Connection of Devices that can able to block dc-link voltage in three-level. NPC topology and other topology. For topology of NPC, transitions straight from the positive (P) to the adverse (N) DC link voltage phase which can produce a double blocking voltage across the switch. This effect is not appear in T-style (Table 1).

Table 1. Shows the 3-level combination of T-style inverter

Generation of level	Switching devices				Output voltage
	T1	T2	T3	T4	
$+V_{dc}/2$	1	0	1	0	+1 v
0	0	1	1	0	0 v
$-V_{dc}/2$	0	1	0	1	-1 v

3 Modes and Operation of 9-Level T-Style Topology

Using single-phase 9-level MLI with four input DC source, the generalized circuit of the suggested topology is provided shown in Fig. 4.

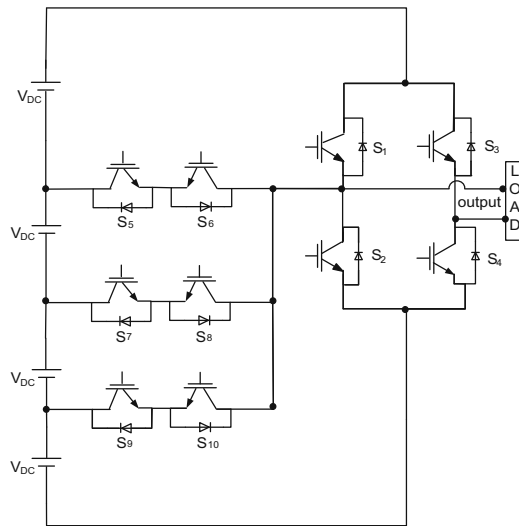


Fig. 4. 9-level T-style inverter

Using single-phase 9-level MLI with four input DC source, as depicted in Fig. 4, the working principle of the suggested topology is discussed. It has ten power switches in which six are connected with a distinct DC source in sandwich form. Figure 5 shows the working modes and is summarized in Table 2. The following switching combinations are available with the assistance of working modes as shown in Fig. 5.

- (a) voltage level is zero when S_2 & S_3 is turned on.
- (b) If S_3 & S_4 is turned on, V_{dc} will be the output voltage level.
- (c) voltage is $2V_{dc}$ if S_3 & S_8 are turned on
- (d) voltage is $3V_{dc}$ if S_2 & S_3 is switched on
- (e) If S_1, S_2, S_3, S_4, S_5 and S_8 are on the output voltage level is $4 V_{dc}$
- (f) voltage is $-V_{dc}$ if S_4 & S_9 are turned on
- (g) voltage is $-2V_{dc}$ if S_4 & S_7 are turned on
- (h) voltage is $-3 V_{dc}$ if S_4 & S_5 are switched on
- (i) voltage is $-4V_{dc}$ if switches S_1 & S_4 are turned on.

Switches S_2 & S_3 are used for an additional pair. Positive(+) half-cycle to generate the positive levels when both S_1 and S_4 are ON and adverse negative cycle to generate the negative cycles can be produced.

Table 2. Single phase 9-Level T-style MLI switching table

Generation of level	Different states										Output voltage (Van)
	S_1	S_2	S_3	S_4	S_5	S_6	S_7	S_8	S_9	S_{10}	
4	0	1	1	0	0	0	0	0	0	0	4 V
3	0	1	0	0	0	0	0	0	0	1	3 V
2	0	1	0	0	0	0	0	1	0	0	2 V
1	0	0	1	0	0	1	0	0	0	0	1 V
0	1	0	1	0	0	0	0	0	0	0	0 V
-1	0	0	0	1	0	0	0	0	1	0	-1 V
-2	0	0	0	1	0	0	1	0	0	0	-2 V
-3	0	0	0	1	1	0	0	0	0	0	-3 V
-4	1	0	0	1	0	0	0	0	0	0	-4 V

3.1 Modes of Operation

To generate the 9-level output the different switching combinations is shown in Fig. 5.

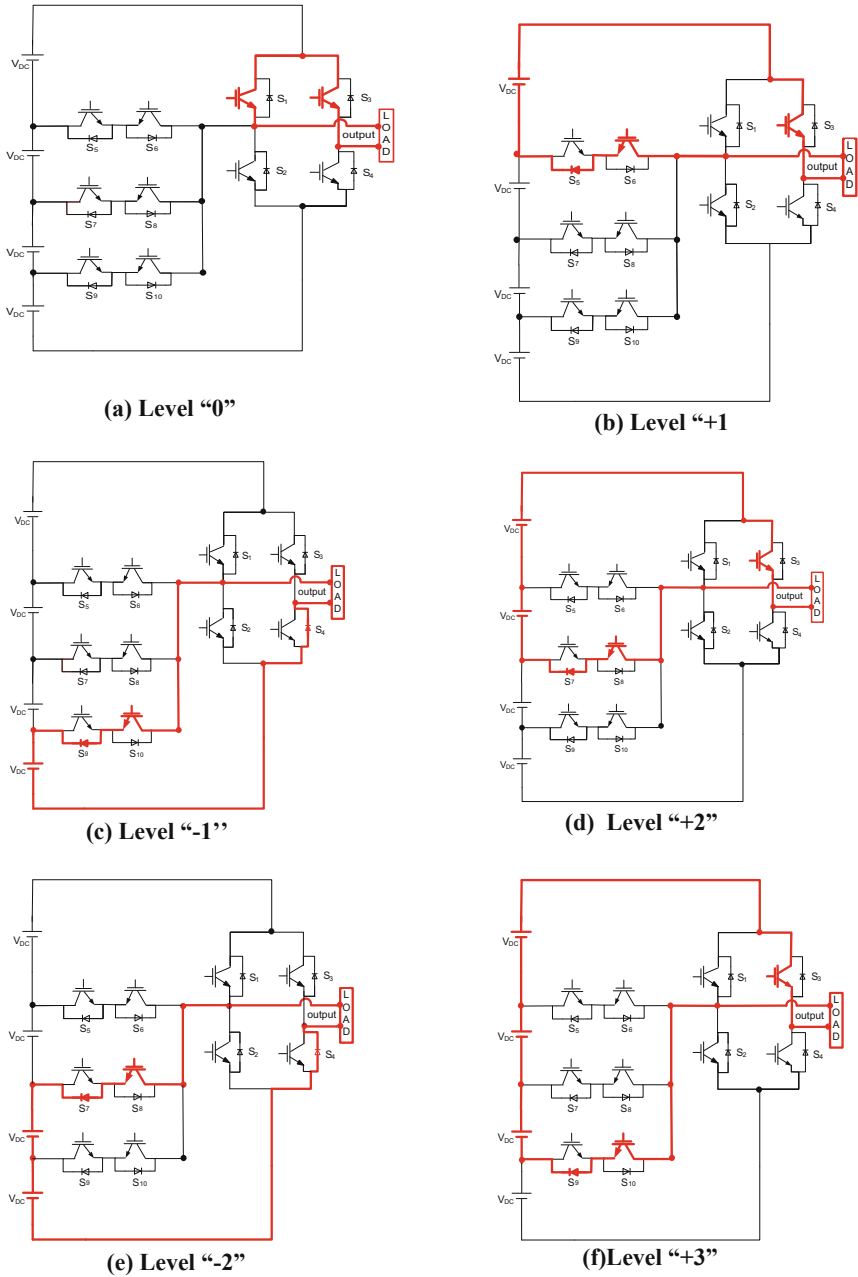


Fig. 5. (a-i) Different switching states of 9 level T-style inverter

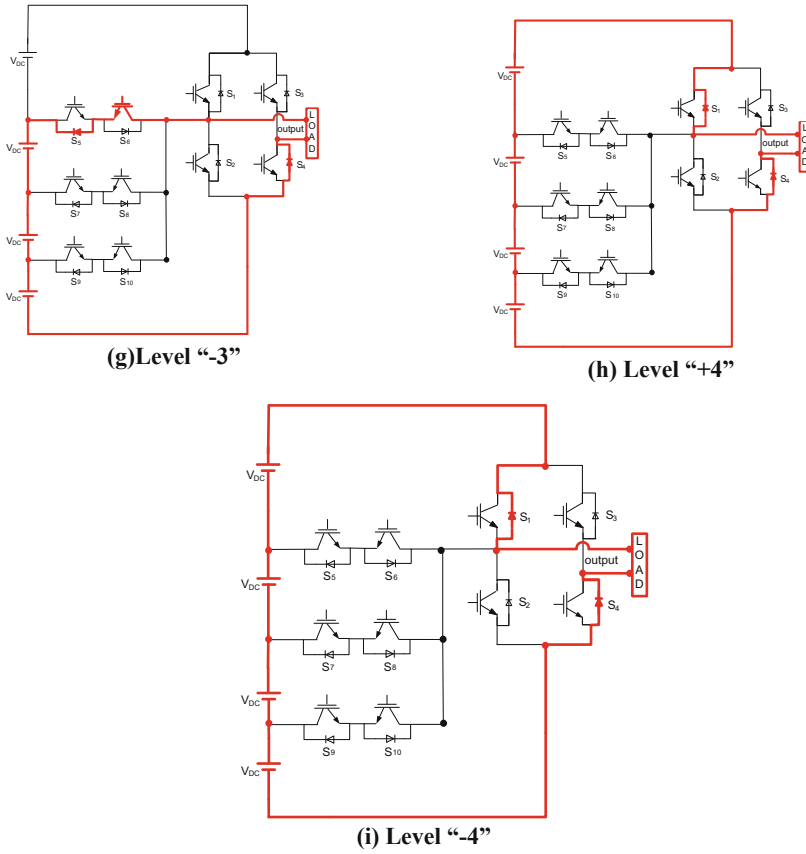


Fig. 5. (continued)

4 Modulation Techniques

There are different pulse width modulation strategies with different phase relationships as follows [6–8] (Fig. 6):

- a. Phase disposition PWM technique (PD-PWM): In this modulation techniques all carrier wave (eight in case of 9 level) are in same phase.

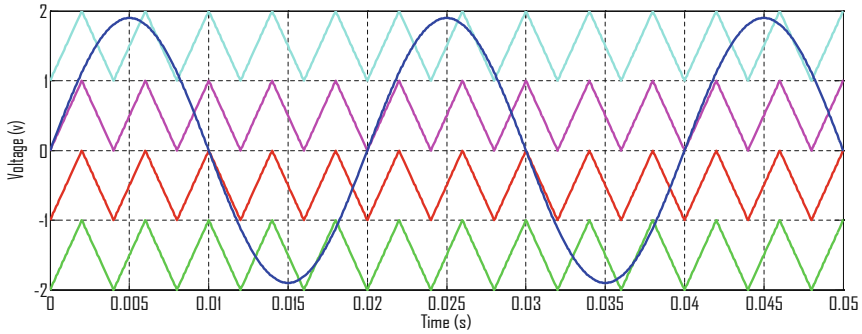


Fig. 6. Carrier scheme of PDPWM ($M_a = 0.8$ & $M_f = 22$)

- b. **Phase opposition disposition PWM technique (POD-PWM):** In this scheme all Carrier above and below zero reference are opposite as shown in Fig. 7.

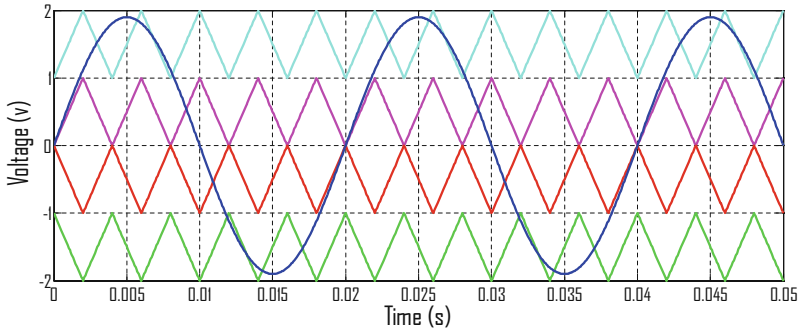


Fig. 7. Carrier scheme of PODPWM ($M_a = 0.8$ and $M_f = 22$)

- c. **Alternate phase opposition disposition PWM Scheme (APOD-PWM):** In this scheme all carrier are alternatively 180° out of phase with each other as shown in Fig. 8.

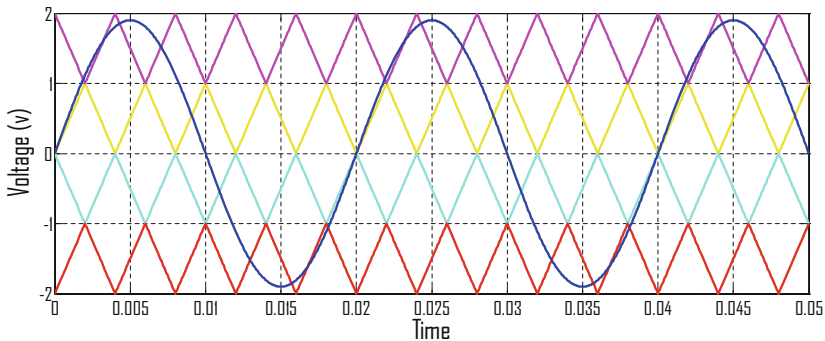


Fig. 8. Carrier scheme of APODPWM ($M_a = 0.8$ and $M_f = 22$)

- d. **Sine inverted Carrier scheme (ISWCPWM):** In this scheme all carrier inverter sine signals above and below are in same phase as shown in Fig. 9.

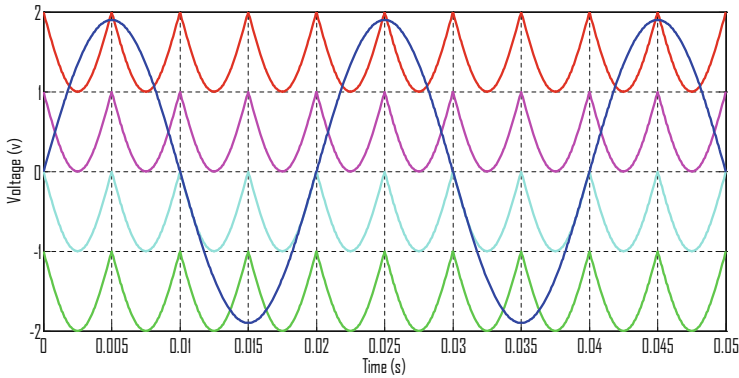


Fig. 9. Carrier scheme for ISWCPWM ($Ma = 0.8$ and $Mf = 22$)

- e. **Harmonic Reduction pulse width modulation (HRPWM):** In this scheme harmonic wave is compared with triangular wave as shown in Fig. 10.

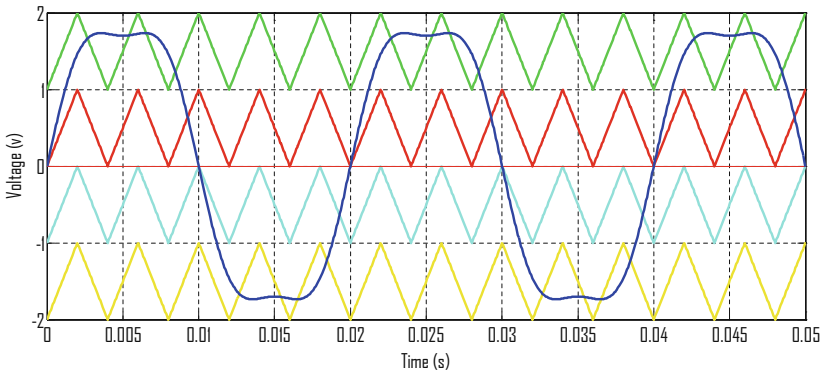


Fig. 10. Carrier scheme of HRPWM ($Ma = 0.98$ and $Mf = 22$)

5 Simulation Results and Discussion

The output voltage of 9-level MLI is shown in Fig. 11. Table 3 demonstrated the THD at various indices of modulation. It is also noted that the voltage and present waveforms produce very few notches. For 9-level MLI, the respective (percent) THD PD = 14.46, POD = 14.66, APOD = 14.46, PS = 14.46, HRPWM = 15.79 and are shown in Figs. 12, 13, 14, 15 and 16 in the modulation index (Ma) = 0.9 and $Mf = 20$.

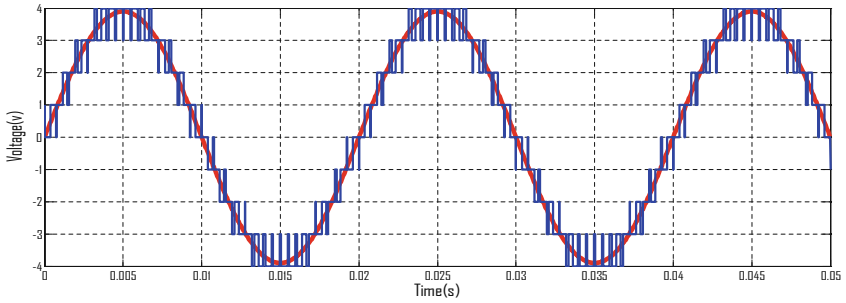


Fig. 11. Voltage of 9-Level MLI for R-L load

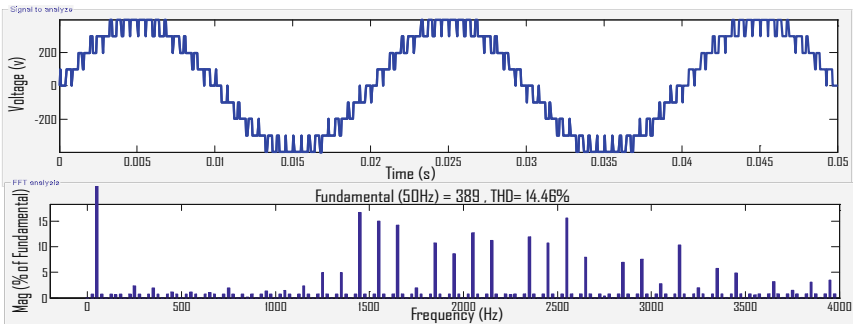


Fig. 12. Voltage of PDPWM for R-L load ($M_a = 0.9$, $M_f = 20$)

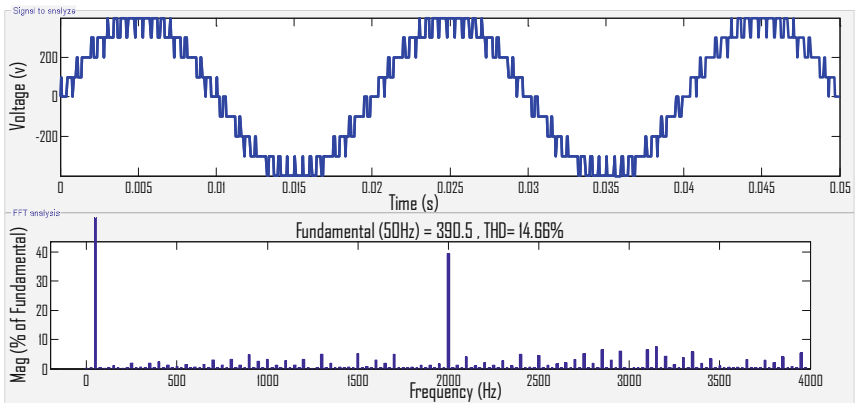


Fig. 13. Output voltage by PODPWM for R-L load ($M_a = 0.9$, $M_f = 20$)

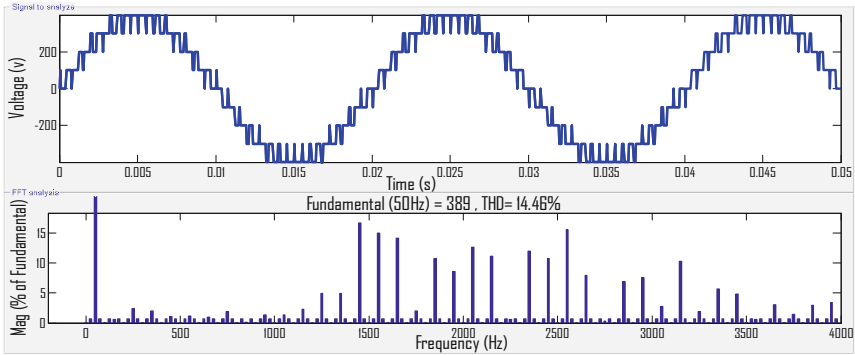


Fig. 14. Voltage of APODPWM for R-L load ($M_a = 0.9$, $M_f = 20$)

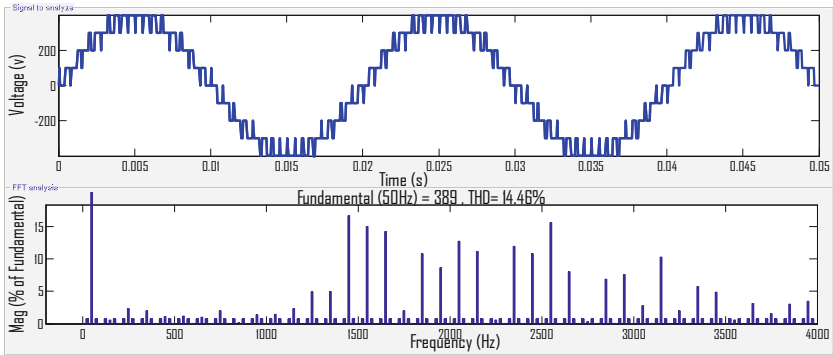


Fig. 15. Voltage of PSPWM for R-L load ($M_a = 0.9$, $M_f = 20$)

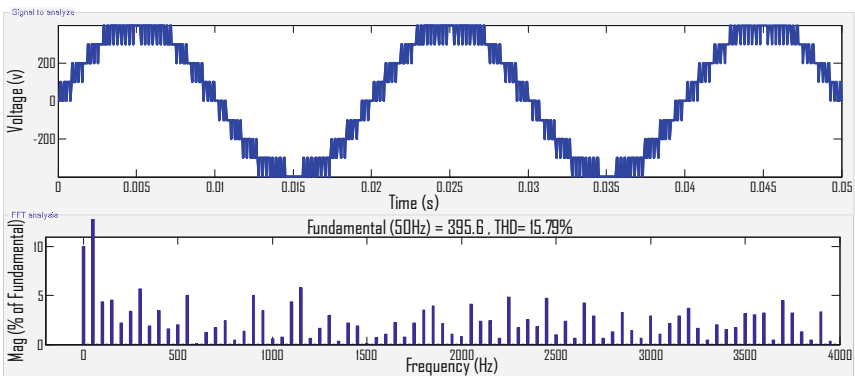


Fig. 16. Output voltage by HRPWM for R-L load ($M_a = 0.9$, $M_f = 20$)

Table 3. Comparative THD of different PWM techniques for 9-Level MLI

Index Ma	PD	POD	APOD	PS	HR
1	14.11	13.74	13.67	13.87	15.79
0.9	14.66	14.46	14.50	14.46	16.64
0.8	16.22	15.91	16.17	15.91	16.65
0.7	16.40	16.10	16.66	16.10	17.13
0.6	16.98	17.03	16.82	17.03	17.13

6 Conclusion





This paper uses a recommended topology with superior characteristics in terms of the necessary energy switches and isolated dc supplies, control requirements, cost and reliability compared to standard topologies. This topology is used in power application such as FACTS, HVDC, and PV systems. Using MATLAB/Simulink, this topology for 9-level T-style MLI is being implemented. For 9-level modulation index 1 for PD PWM scheme, the smallest percentage of THD is 14.11%. It is therefore evident that the THD of the output Voltage Waveform decreases as the amount of levels rises.

References

- Rodriguez, J., Lai, J.S., Peng, F.: Multilevel inverters: a survey of topologies, controls, and applications. *IEEE Trans. Ind. Electron.* **49**(4), 724–738 (2002)
- Daher, S., Schmid, J., Antunes, F.L.M.: Multilevel inverter topologies for stand-alone PV systems. *IEEE Trans. Ind. Electron.* **55**(7), 2703–2712 (2008)
- Sheir, A., Youssef, M.Z., Orabi, M.: A novel bidirectional T-Type multilevel inverter for electric vehicle applications. *IEEE Trans. Power Electron.* **34**(7), 6648–6658 (2019). <https://doi.org/10.1109/TPEL.2018.2871624>
- Joshi, H., Tekwani, P.N., Kolorrol, A.H.: Multilevel inverter for induction motor drives using RV topology. *IEEE Trans. Ind.* (2010)
- Silva, C.A., Cordova, L.A., Lezana, P., Empringham, L.: Implementation and control of a hybrid multilevel converter with floating DC links for current waveform improvement. *IEEE Trans. Ind. Electron.* **58**, 2304–2312 (2010)
- Nabae, A., Takahashi, I., Akagi, H.: A new neutral-point clamped PWM inverter. *IEEE Trans. Ind. Appl.* **IA-17**, 518–523 (1981)
- Peng, F.Z., Lai, J.S.: Multilevel cascade voltage-source inverter with separate DC source. U. S. Patent 5 642 275, June 24 1997
- Choi, N.S., Cho, J.G., Cho, G.H.: A general circuit topology of multilevel inverter. In: *Proceedings of IEEE PESC 1991*, pp. 96–103 (1991)
- Hosseinzadeh, M.A., Sarbanzadeh, M., Sarbanzadeh, E., Rivera, M., Babaei, E., Muoz, J.: Cascaded multilevel inverter based on new submodule inverter with reduced number of switching devices. In: *2017 IEEE Southern Power Electronics Conference (SPEC)*, Puerto Varas, pp. 1–6 (2017)
- Jiaguag, G., Suan, C.: A cascaded multilevel DC-link inverter. *Proc. IEEE Trans. Ind. Appl.* **41**(3), 848–854 (2005)
- Abdelhakim, A., Mattavelli, P., Spiazzi, G.: A very high resolution stacked multilevel inverter topology for adjustable speed drives. *IEEE Trans. Ind. Electron.* **65**(3), 2049–2056 (2018)



A Comprehensive Study on AC Microgrid Control Strategies at Primary Control Level

Bhavna Rathore^(✉) , Laxmi Srivastava , Nipun Gupta ,
Shailendra Pratap Singh, and Rahul Sagwal 

Department of Electrical Engineering,
Madhav Institute of Technology and Science, Gwalior, India
{rathore.puja, srivastava.l, nipun.gupta2212,
rahul.sagwal190}@mitsgwalior.in, shlile9drl@gmail.com

Abstract. Due to increasing demand of electricity and environmental pollution concern, the integration of distributed energy resource is the most promising concept for the future power system to provide reliable and clean energy. Typically, a microgrid comprises of distributed energy sources, energy storage systems and loads that can operate in a grid-connected mode or stand-alone mode. In both operating modes, microgrid should have voltage and frequency regulation capabilities to ensure system stability. This work provides a comprehensive study of the recent key issues of existing control strategies of microgrid operation. Various primary control strategies of microgrid are compared, and their respective advantages and disadvantages are highlighted in tabular form. This comprehensive study emphasizes the prospective research areas and significant findings that could improve future microgrid facilities.

Keywords: Microgrid · Distributed energy resource · Primary control · Synchronous generator

1 Introduction

The globe faces a significant shift from its existing centralized system of synchro generator-based generation to a future with distributed renewable energy generation. Researchers around the globe are already studying impact of renewable energy sources, like wind and hydro, integration on existing power system [51, 52]. With low emission of CO₂ and recent development in power electronics technology, Renewable energy sources (RES) based microgrid is seen as a promising concept to decrease dependency on depleting fossil fuel reserves [1–8]. A microgrid is a collection of DERs, storage units and local loads that deliver several advantages to the current power system in terms of consistent power supplies and potential to integrate renewables with non-renewable based energy resources [5–8].

There are various technical issues associated with microgrid:

- Coordinated control and operation of a large number of DER
- The precision of power sharing is impacted by the output impedance of the line

- Inverter-interfaced inertia less distributed sources which have zero kinetic energy dominate microgrids.
- They provide bad transient load sharing in standalone mode when inverter based sources are coupled with alternator working under voltage control mode.
- Storage elements are required to prevent unstable operation during faults and different network disturbances, which raises overall system costs.
- During moving from grid connected to islanded mode of operation, a big discrepancy between generation and load happens, posing a serious issue of frequency and voltage control.

Therefore, distribution network requires a novel smart grid concept [6]. In this regard, a flexible and reliable microgrid is required, having the capability of operating smartly in both grid-connected and island modes [6]. An adequate microgrid control is needed to ensure a reliable, effective and economical operation [2–8]. To solve above mentioned technical issues, a hierarchical control structure is needed [10, 11]. The hierarchical structure of a microgrid is shown in Fig. 1. The primary control maintains the voltage and frequency in case of large and sudden disturbances. In the existence of both linear and non-linear load, primary control also guarantees proper active and reactive power sharing between the DER units. The secondary level control compensates the difference between rated and actual voltage/frequency caused by primary level control. Power flow in between the main grid and the microgrid is regulated by the tertiary control and thus provides an economically optimal operation.

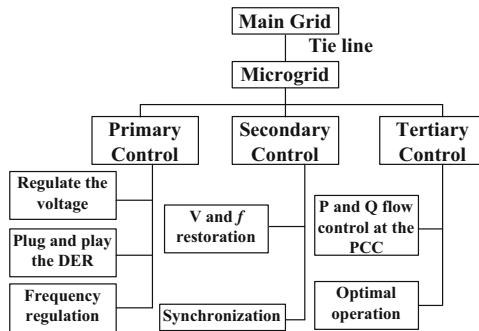


Fig. 1. Hierarchical control structure of microgrid

At primary control level, both centralized and decentralized control schemes are adopted to supply the load demand by regulating the output voltage of voltage source converter [1–5, 7–17]. The centralized control is communication-based method utilized in the parallel operation of the converters [15]. Center limit control, master-slave control, circular chain control method, and distributed control come in the category of centralized control techniques. In centre limit control, by getting a same current set

point, an equal amount of load is shared by each source [16]. In the case of master-slave control, one converter acted as a master and generated the reference signal for other slave converters [15]. Here master converter operates in voltage controlled mode, while slave controller acts as a current source. In the distributed control, the reference current signal for each DER unit is average current [17]. The reference signal for each unit is given by its preceding converter in case of circular chain control, and all the converters are connected to each other through communication link [18]. If a fault in any communication link or malfunctioning of any DER unit occurs in this control, it can cause the system in halt condition and the system reliability entirely depends on centralized controller. Decentralized control methods have been suggested to overcome these disadvantages [1–5]. Droop control is a decentralized control method, uses conventional voltage and frequency droop characteristics of synchronous generator to regulate the output voltage of inverter [1–3]. By adjusting P and Q separately on the inverter, frequency and size of the PCC voltage is controlled. Various modifications to droop characteristics have been suggested by the researchers to overcome the problems in power sharing due to different line impedance between sources, harmonic current distribution, and resistive line impedance [5, 20–25]. In a case of highly resistive line impedance, inverse droop may be used [3]. A virtual frequency-voltage frame technique is suggested to fix the issue of inaccurate power sharing owing to different R/X ratios [27]. In LV network the conventional active power-frequency (P-f) along with reactive power-voltage (Q-V) droop can be adopted by emulating virtual inductive impedance at the output terminal of inverter [5, 20–22]. Angle droop control is adopted instead of frequency droop [30, 31], as the selection of a high value of frequency droop coefficient may cause instability. In order to improve the stability under large load changes a supplementary droop control loop method is suggested in [32].

The primary issues of microgrid operation are frequency control and system stability. This is due to reduced inertia of inverter based distributed energy resources (DERs) having very less kinetic energy [34–37]. If inverter-based generators coupled with alternator function in voltage control mode under stand-alone operation, poor load sharing during transient condition is observed [34]. During large load changes, these DERs based on inverter, having poor load sharing impacts your system frequency profile. In frequency droop an active power derivative is proposed in [34] so as to prevent conflict between sources having inertia and no-inertia while sharing load demand. In [35], a droop characteristic is modified to provide as a function of frequency change rate to improve transient stability of the system and to limit unwanted source triggering during abrupt shift of load. Improving the system's transient response in a stand-alone microgrid can also be achieved through the use of energy storage devices to provide virtual kinetic energy, but this may lead to heavy battery discharge current and impact their life. Different methods have been suggested such as virtual synchronous machines (VSMs), virtual synchronous generators (VSGs) and adaptive virtual inertia control to improve microgrid transient performance when both inertial and non-inertial sources are operated [36–50].

The significant technical difficulties in the primary control, attracts publishers to work in this control level. This paper is providing a comprehensive study of the microgrid control strategy at the primary level for the practicing engineers and researchers to work in this field. Various primary control strategies of microgrid are compared and their respective advantages and disadvantages are highlighted in tabular form. In conclusion, the study emphasizes the remarkable finding and potential research in the control strategies that could enrich the future microgrid.

2 Primary Level Control

In this control the reference signals for the frequency and voltage loops of DER unit are provided. Generally, primary control used either PQ control mode or voltage control mode. In case of PQ control mode, the active and reactive power of DER units are regulated using pre-determined reference signals. Reference frequency is set by main grid itself in case of grid-connected mode, whereas in islanded mode of operation, the DER unit maintains the frequency. The PQ control is realized based on current-controlled voltage source, as shown in Fig. 2.

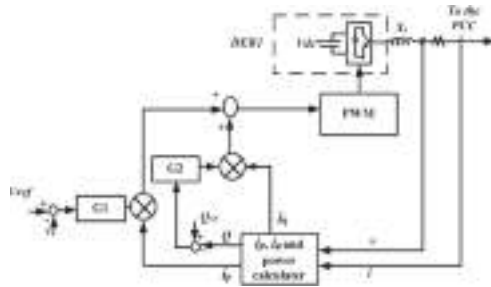


Fig. 2. PQ control of DER [4].

The dc - link voltage error is regulated by G1 by modifying the value of active current output of DER unit, caused by power mismatches in a microgrid. Similarly, the output reactive power is regulated by the G2 controller by modifying the value of the inverter reactive current output.

DER unit operates as voltage-controlled voltage-source in case of voltage control mode and the reference signal of voltage is obtained through centralized control (Master slave control) or decentralized control (droop control) [1–5]. The frequency and size of the PCC voltage is controlled in droop control by individually adjusting P and Q of the inverter. The suggested control strategies expressed in literature are mainly classified in two categories, which are briefly described in below sections.

2.1 Centralized Control

The main objective of the centralized control is to generate reference signals for each DER unit based on the information received from DER units placed and this can be subdivided into;

1. Master Slave Control
2. Central Limit Control
3. Distributed Control

2.1.1 Master Slave Control

In this control, one DER unit acts as “Master” and maintains the voltage and frequency of the grid in islanded mode [15], while other units adopt the voltage and frequency from Master, and in grid connected mode all DERs follow the grid frequency and voltage and operate in current control mode as shown in Fig. 3.

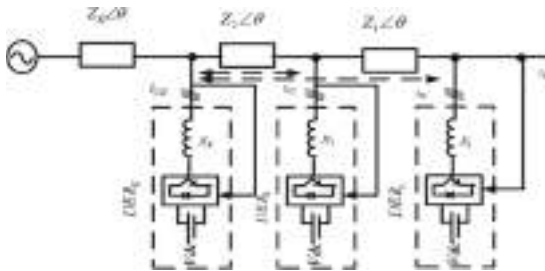


Fig. 3. Single line diagram for master slave control

The DER unit with highest rating is often favorable to act as “Master”. Reference current signal for K^{th} DER unit is given by Eq. (1).

$$i_{CK} = i_{Ld} \left(\frac{M_K P_K}{P_L} \right) \text{ (where } k = 1, 2, 3, \dots, n) \tag{1}$$

where P_K and M_K are the active power rating and weight of K^{th} DER unit. P_L Total rated active power capacity of DER units can be calculated as;

$$P_L = M_1 P_1 + M_2 P_2 + M_3 P_3 + \dots + M_n P_n \tag{2}$$

and i_{Ld} is the total load current active component.

2.1.2 Central Limit Control

A central controller measures the total amount of active and reactive component of load and then assigns a specific amount of component to each DER unit to compensate the

load demand [18]. Generally, SRF based control strategy has been used for extraction of d-q component from the load phase current. Figure 4 shows the central limit control of DER units.

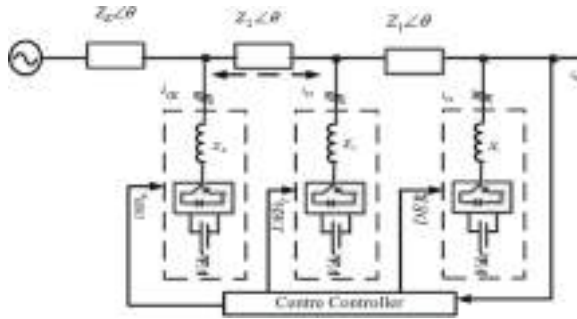


Fig. 4. Single line diagram for central limit control

The main disadvantage is this control strategy is that if central unit fails the whole system will shut down.

2.1.3 Distributed Control

An equal amount of reference signal is generating for each unit by dividing the load current by total number of DER units [17, 18]. If there are N modules of same ratings are operating then the current reference of each module will be,

$$I_{ldqN} = \frac{I_{ldq}}{N} \tag{3}$$

The single line diagram of distributed control is shown in Fig. 5.

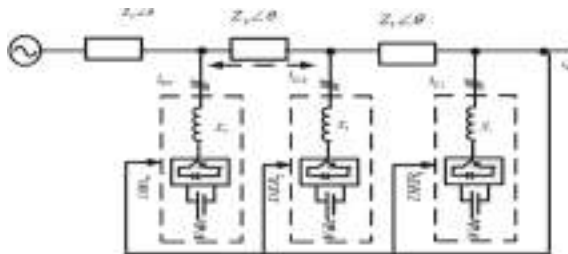


Fig. 5. Single line diagram for distributed control

This method is easy to install and maintain. Similar to master slave and center limit control, in this control all the units are interconnected. Hence malfunctioning of any unit or a fault in any communication link can cause the system halt.

2.2 Decentralized Control

In this control, each unit only uses the information of its point of common coupling. There is no communication between the DER units and has been refereed as the autonomous, independent, and wireless or droop control.

2.2.1 Droop Control

The basic principle of this method can be understood by using an equivalent circuit as shown in Fig. 6. Here, a DER unit is connected to main grid through line impedance.

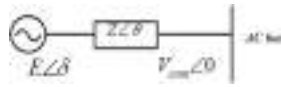


Fig. 6. Single line diagram of a DER unit connected to AC bus.

For purely inductive line, $\theta = 90^\circ$, then active and reactive power from the DER unit to grid is given by

$$P = \frac{V_{com}E}{Z} \sin \delta \tag{4}$$

$$Q = \frac{V_{com}E \cos \delta - V_{com}^2}{Z} \tag{5}$$

Where, V_{com} is the common bus voltage and E is the output voltage of DER unit. Z and δ are the impedance of connecting lines and voltage difference between the DER unit and common bus, respectively.

If the phase difference between common bus and the DER unit is considered small, then $\sin \delta \approx \delta$ and $\cos \delta \approx 1$. Considering these assumptions, one can use the frequency and voltage droop to regulate the frequency and output voltage of DER unit and given as

$$(\omega_{ref} - \omega_g) = k_p (P_{in} - P_{ref}) \tag{6}$$

$$(v_{ref} - v) = k_q (Q - Q_{ref}) \tag{7}$$

Where ω_{ref} and v_{ref} are the rated frequency and rated voltage of the system respectively. P_{ref} and Q_{ref} are the set points for real and reactive of the inverter

respectively. k_p is the active power droop coefficient and k_q is the reactive power droop coefficient, given by [1–4].

$$k_p = \frac{\Delta\omega}{P_{max}} \quad k_q = \frac{\Delta V}{Q_{max}}$$

where P_{max} and Q_{max} are the rated active and reactive power of the inverter, and $\Delta\omega$ and ΔV are the allowable variation ranges in frequency and voltage magnitude respectively. The reference signal generation through droop control is shown in Fig. 7.

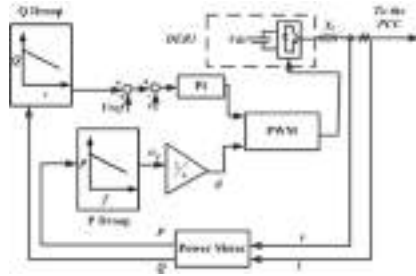


Fig. 7. Droop control of DER [4].

In a microgrid, if N DER units are operating in parallel, then they should satisfy following criteria;

$$k_{p1}P_{max1} = k_{p2}P_{max2} = \dots = k_{pN}P_{maxN} = \Delta\omega \tag{8}$$

$$k_{q1}Q_{max1} = k_{q2}Q_{max2} = \dots = k_{qN}Q_{maxN} = \Delta V$$

In grid-connected mode, the main grid dominates the system dynamics due to high inertia and maintains the rated voltage and rated frequency of the DER unit.

2.2.2 VSG or VSM Control

Stand-alone mode offers poor transient load sharing if inverter-based sources are combined with a synchronous generator functioning in the voltage control mode. Inverter-based devices react quicker and share the bulk of the load demand as the output of the synchronous generator gradually rises until they achieve their steady state energy sharing due to the droop characteristics. This poor load sharing with limited size of the inverter based DERs affects the system frequency profile during large load change. Improvement of the transient response of the system in a stand-alone microgrid can be done by providing virtual kinetic energy using energy storage devices, but this may lead to high discharge current from the batteries, and affect their lives. Various

methods like VSG, VSM, and modified VSG have been reviewed in the literature to overcome these problems [35–49].

In the VSG control, according to the swing equation of synchronous generator, virtual inertia is embedded into the control of inverter based DER to emulate the inertial nature of the synchronous generator [18]. The active power-frequency control of VSG is expressed as,

$$2H_v \frac{d\omega}{dt} = (P_{in} - P_{out}) - K_{d,v}(\omega - \omega_{ref}) \quad (9)$$

For the simplification, Eq. (9) can be rewritten as,

$$a = (b - c)$$

where,

$$a = 2H_v \frac{d\omega}{dt}, \quad b = (P_{in} - P_{out}) \quad \text{and} \quad c = K_{d,v}(\omega - \omega_{ref})$$

Here, H_v is the virtual inertia constant. P_{in} is the virtual input power to the shaft, P_{out} is the measured output active power of DER, ω is the virtual rotor angular frequency, and $K_{d,v}$ is the virtual damping factor constant. The basic block diagram of a VSG control is shown in Fig. 8. The droop characteristic is introduced into the active power-frequency control block to maintain the frequency.

$$(P_{in} - P_{ref}) = \frac{1}{k_p} (\omega_{ref} - \omega_g) \quad (10)$$

From (9) and (10), the virtual governor model is obtained, and the virtual angular frequency of the output voltage in VSG control can be obtained by taking integration of Eq. (11).

$$\left[\frac{1}{k_p} (\omega_{ref} - \omega_g) + (P_{ref} - P_{out}) - K_{d,v}(\omega - \omega_g) \right] \frac{1}{2H_v} = \frac{d\omega}{dt} \quad (11)$$

Let $H_v = 0$, $K_{d,v} = 0$, Eq. (11) is equivalent to Eq. (6), and indicates that droop control is a special case of VSG control, where both the damping factor and the inertia time constant are set to zero [48]. In [35–41], the calculation of the complete model of the equivalent SG is necessary, which increases the system algorithm complexity and requires high processing capacity and speed. In [41–50], only the parameters of swing equation are considered to calculate the virtual rotor angle frequency and hence processing speed increases with simple calculations.

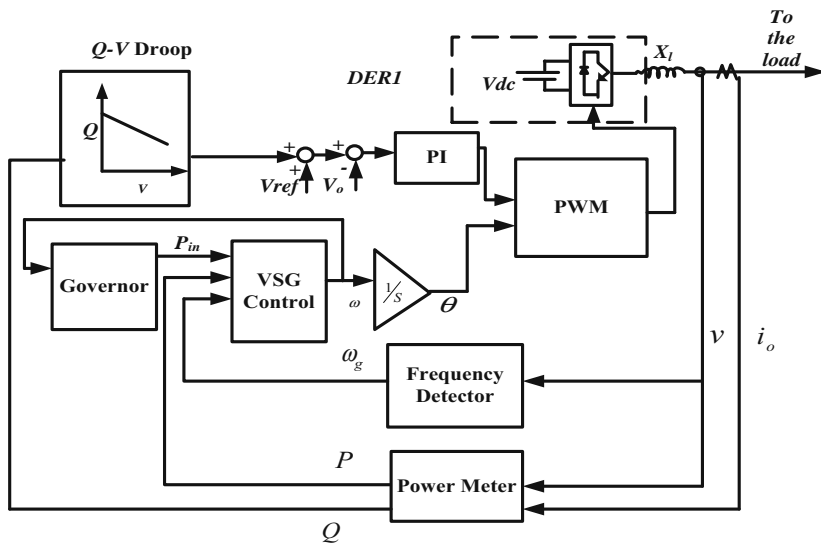


Fig. 8. VSG control of inverter

The advantages and disadvantages of the various control techniques are highlighted in Table 1 and the following points can be concluded:

- Prior knowledge of system parameters is needed in virtual frame transformation technique.
- Virtual impedance method ensures the proper load sharing in the presence of both linear and non-linear loads.
- Angle droop control ensures proper load sharing even in weak grid condition.
- All the modified frequency and angle droop control do not ensure voltage regulation except supplementary control.
- VSG and modified VSG control improves transient response of the microgrid, by enhancing the system inertia.

Table 1. Advantages and disadvantages of various primary level control techniques

		Advantages	Disadvantages
Centralized control	Master slave control	<ul style="list-style-type: none"> • It provides accurate current sharing with high power quality 	<ul style="list-style-type: none"> • The usage of sensors is higher because of interconnection between the inverters • Not fully autonomous • Malfunctioning of any unit and even a small fault in any communication can cause the system halt
	Center limit control	<ul style="list-style-type: none"> • It ensures the proper load sharing as high bandwidth communication channel is used 	<ul style="list-style-type: none"> • Reliability depends upon centralized controller • Not share accurate power if any link removes from the DER units
	Distributed control	<ul style="list-style-type: none"> • Easy maintenance and installation 	<ul style="list-style-type: none"> • Malfunctioning of any unit and even a small fault in any communication can cause the system halt

(continued)

Table 1. (continued)

		Advantages	Disadvantages
Decentralized control	Droop control	<ul style="list-style-type: none"> • Facility of expandability and redundancy • No interconnection between inverters therefore system manufacturing cost is less • No supervisory control • More reliable 	<ul style="list-style-type: none"> • Power sharing speed is slow • Inaccurate power sharing by the DER units due to inherent trade-off between output voltage/frequency regulation and active/reactive power • Large circulating current between the units due to unequal line impedance at the output • Performance of convention droop control is affected for different R/X ratio of interconnecting lines • Provides distorted output voltage with high THD in case of non-linear load • Provides poor transient response when both inertial and non-inertial sources operated in parallel
	Reverse droop control	<ul style="list-style-type: none"> • Easy to implement • Provides accurate power sharing in LV microgrid 	<ul style="list-style-type: none"> • Performance of the controller is affected by the system parameters • works for resistive dominant line • Does not ensure proper load sharing in case of non-linear load
	Modified droop with virtual frame transformation	<ul style="list-style-type: none"> • Simple Implementation • Ensures proper load sharing 	<ul style="list-style-type: none"> • Does not ensure proper load sharing in case of non-linear load • Prior information of line parameters is required
	Modified droop with virtual output impedance	<ul style="list-style-type: none"> • Line parameters do not affect the power sharing accuracy • Maintains the rated frequency and voltage for both linear and non-linear loads • Provide low THD output voltage during non-linear load 	<ul style="list-style-type: none"> • It does not guarantee voltage regulation • Complicated implementation
	Angle droop	<ul style="list-style-type: none"> • Easy to implement • Ensures proper load sharing during frequent load change • Provides better frequency regulation 	<ul style="list-style-type: none"> • Higher value of angle droop gain affects the overall system stability • It does not guarantee voltage regulation
	Supplementary control	<ul style="list-style-type: none"> • Ensure accurate load sharing even if high value of angle droop is used • It guarantees better frequency and voltage regulation 	<ul style="list-style-type: none"> • Affects the transient stability during sudden and large disturbances, when both inertial and non-inertial sources are connected in parallel to share the load demand
	Modified droop to mimic nature of SG	<ul style="list-style-type: none"> • Improves transient response • guarantees better frequency regulation • Easy to implement • Improves system damping 	<ul style="list-style-type: none"> • It does not guarantee voltage regulation
	Modified droop as a function of rate of change of frequency	<ul style="list-style-type: none"> • Improves transient response in post-islanding conditions • Reduces the unwanted triggering of sources out of synchronism • Reduces unwanted load shedding in an islanded microgrid 	<ul style="list-style-type: none"> • It does not guarantee voltage regulation • Complicated implementation • Does not ensure proper load sharing in case of non-linear load
	VSG control	<ul style="list-style-type: none"> • Enhances frequency response of microgrid • Reduces unwanted triggering of sources 	<ul style="list-style-type: none"> • It does not guarantee voltage regulation • Complicated implementation • Slow down the system response

3 Conclusion

With recent devolvement in power electronics technology, Renewable energy sources (RES) based microgrid is seen as a promising concept to provide economical, environment friendly, and efficient power delivery. The primary level control techniques such as centralized, decentralized, and distributed control are reviewed in this paper. Different type of modified droop control techniques has been discussed in this paper, which ensure accurate power sharing in grid as well as islanded mode in the presence of linear and non-linear load. VSG and modified VSG methods have been briefly reviewed to enhance frequency response during transient condition, when both inertial and non-inertial sources are operated in parallel. And finally the potential advantages and disadvantages are highlighted in tabular form.

Acknowledgment. Authors are thankful to NPIU (TEQIP –III) and AICTE for providing financial support through CRS project: Application id-1-5729547592 under Collaborative Research Scheme.

References

1. Majumder, R.: Some aspects of stability. *IEEE Trans. Power Syst.* **28**(3), 3243–3252 (2013)
2. Chandorkar, M.C., Divan, D.M., Adapa, R.: Control of parallel connected inverters in standalone ac supply systems. *IEEE Trans. Ind. Appl.* **29**(1), 136–143 (1993)
3. Engler, A., Soultanis, N.: Droop control in LV-grids. In: *Proceedings of International Conference on Future Power System*, pp. 1–6 (2006)
4. Vandoom, T.L., Renders, B., Degroote, L., Meersman, B., Vandevelde, L.: Active load control in islanded microgrids based on the grid voltage. *IEEE Trans. Smart Grid* **2**, 139–151 (2011)
5. Guerrero, J.M., Matas, J., Vicuna, L.G.D., Castilla, M., Miret, J.: Decentralized control for parallel operation of distributed generation inverters using resistive output impedance. *IEEE Trans. Ind. Electron.* **54**, 994–1004 (2007)
6. The smart grid: an introduction United States Department of Energy, Office of Electricity Delivery and Energy Reliability, Washington, DC (2008). <http://www.oe.energy.gov/1165.htm>
7. Debrabandere, K., Bolsens, B., Van den Keybus, J., Woyte, A., Driesen, J., Belmans, R.: A voltage and frequency droop control method for parallel inverters. *IEEE Trans. Power Electron.* **22**(4), 1107–1115 (2007)
8. Majumder, R., Ghosh, A., Ledwich, G., Zare, F.: Load sharing and power quality enhance operation of a distributed microgrid. *IET Renew. Power Gener.* **2**(3), 109–119 (2009)
9. Majumder, R., Ghosh, A., Ledwich, G., Zare, F.: Load frequency control of rural distributed generation. *Electr. Power Compon. Syst.* **38**(6), 637–656 (2010)
10. Guerrero, J.M., Vásquez, J.C., Matas, J., Castilla, M., Vicuña, L.G.D., Castilla, M.: Hierarchical control of droop-controlled AC and DC microgrids—A general approach toward standardization. *IEEE Trans. Ind. Electron.* **58**, 158–172 (2011)
11. Mohamed, Y.A.R.I., Radwan, A.A.: Hierarchical control system for robust microgrid operation and seamless mode transfer in active distribution systems. *IEEE Trans. Smart Grid.* **2**, 352–362 (2011)




12. Karimi, H., Nikkhajoei, H., Iravani, M.R.: Control of an electronically-coupled distributed resource unit subsequent to an islanding event. *IEEE Trans. Power Deliv.* **23**, 493–501 (2008)
13. Li, Y.W., Vilathgamuwa, D.M., Loh, P.C.: A grid-interfacing power quality compensator for three-phase three-wire microgrid applications. *IEEE Trans. Power Electron.* **21**, 1021–1031 (2006)
14. Guerrero, J.M., Hang, L., Uceda, J.: Control of distributed uninterruptible power supply systems. *IEEE Trans. Ind. Electron.* **55**, 2845–2859 (2008)
15. Cheng, Y.J., Sng, E.K.K.: A novel communication strategy for decentralized control of paralleled multi-inverter systems. *IEEE Trans. Power Electron.* **21**, 148–156 (2006)
16. Iwade, T., Komiya, S., Tanimura Y.: A novel small-scale UPS using a parallel redundant operation system. In: *Proceedings of International Telecommunications Energy Conference*, pp. 480–483 (2003)
17. Sun, X., Lee, Y.S., Xu, D.: Modeling, analysis, and implementation of parallel multi-converter system with instantaneous average-current sharing method. *IEEE Trans. Power Electron.* **18**, 844–856 (2003)
18. Wu, T.F., Chen, U.K., Huang, Y.H.: 3C strategy for inverters in parallel operation achieving an equal current distribution. *IEEE Trans. Ind. Electron.* **47**, 273–281 (2000)
19. Guerrero, J.M., Matas, J., Vicuna, L.G.D., Castilla, M., Miret, J.: Control strategy for flexible microgrid based on parallel line-interactive UPS systems. *IEEE Trans. Ind. Electron.* **56**, 726–736 (2009)
20. Guerrero, J.M., Matas, J., Vicuna, L.G.D., Castilla, M., Miret, J.: Wireless-control strategy for parallel operation of distributed generation inverters. *IEEE Trans. Ind. Electron.* **53**, 1461–1470 (2006)
21. Pogaku, N., Prodanovic, M., Green, T.C., Kling, W.L., Van Der Sluis, L.: Modeling, analysis and testing of autonomous operation of an inverter-based microgrid. *IEEE Trans. Power Electron.* **22**(2), 613–625 (2007)
22. Guerrero, J.M., Matas, J., Vicuna, L.G.D., Castilla, M., Miret, J.: Output impedance design of parallel-connected UPS inverters with wireless load-sharing control. *IEEE Trans. Ind. Electron.* **52**(4), 1126–1135 (2005)
23. Borup, U., Blaabjerg, F., Enjeti, P.N.: Sharing of nonlinear load in parallel-connected three-phase converters. *IEEE Trans. Ind. Appl.* **37**, 1817–1823 (2001)
24. Salamah, A.M., Finney, S.J., Williams, B.W.: Autonomous controller for improved dynamic performance of AC grid, parallel-connected, single-phase inverters. *IET Gener. Trans. Distrib.* **2**(2), 209–218 (2008)
25. Lee, T.L., Cheng, P.T.: Design of a new cooperative harmonic filtering strategy for distributed generation interface converters in an islanding network. *IEEE Trans. Power Electron.* **22**, 1919–1927 (2007)
26. Li, Y., Li, Y.W.: Virtual frequency-voltage frame control of inverter based low voltage microgrid. In: *Proceedings of IEEE Electrical Power & Energy Conference*, pp. 1–6 (2009)
27. Li, Y., Li, Y.W.: Decoupled power control for an inverter based low voltage microgrid in autonomous operation. In: *Proceedings of IEEE 6th International Power Electronics and Motion Control Conference*, pp. 2490–2496 (2009)
28. Li, Y., Li, Y.W.: Power management of inverter interfaced autonomous microgrid based on virtual frequency-voltage frame. *IEEE Trans. Smart Grid* **2**, 30–40 (2011)
29. Yao, W., Chen, M., Matas, J., Guerrero, J.M., Qian, Z.: Design and analysis of the droop control method for parallel inverters considering the impact of the complex impedance on the power sharing. *IEEE Trans. Ind. Electron.* **58**, 576–588 (2011)

30. Majumder, R., Ghosh, A., Ledwich, G., Zare, F.: Angle droop versus frequency droop in a voltage source converter based autonomous microgrid. In: IEEE Power Engineering Society General Meeting (2009)
31. Majumder, R., Chaudhuri, B., Ghosh, A.: Improvement of stability and load sharing in an autonomous microgrid using supplementary droop control. *IEEE Trans. Power Syst.* **25**(2), 796–808 (2010)
32. Majumder, R., Shahnia F., Ghosh, A., Ledwich, G., Wishart M., Zare, F.: Operation and control of a microgrid containing inertial and non-inertial micro sources. In: IEEE TENCON, Singapore, (2009)
33. Majumder, R., Ghosh, A., Ledwich, G., Zare, F.: Power sharing and stability enhancement of an autonomous microgrid with inertial and non-inertial DGs with DSTATCOM. In: Third International Conference on Power Systems, pp. 1–6 (2009)
34. Soni, N., Doolla, S.: Improvement of transient response in microgrids using virtual inertia. *IEEE Trans. Power Deliv.* **28**(3), 1830–1838 (2013)
35. Xiang-Zhen, Y., Jian-Hui, S., Ming, D., Jin-Wei, L., Yan, D.: Control strategy for virtual synchronous generator in microgrid. In: Proceedings of 4th International Conference Electric Utility Deregulation and Restructuring and Power Technologies, pp. 1633–1637 (2011)
36. Zhong, Q.C., Weiss, G.: Synchronverters: inverters that mimic synchronous generators. *IEEE Trans. Ind. Electron.* **58**(4), 1259–1267 (2011)
37. Zhong, Q.C., Nguyen, P.L., Ma, Z., Sheng, W.: Self-synchronized synchronverters: inverters without a dedicated synchronization unit. *IEEE Trans. Power Electron.* **29**(2), 617–630 (2014)
38. Driesen, J., Visscher, K.: Virtual synchronous generators. In: IEEE Power and Energy Society General Meeting - Conversion and Delivery of Electrical Energy in the 21st Century, pp. 1–3 (2008)
39. Beck, H.P., Hesse, R.: Virtual synchronous machine. In: Proceedings of IEEE EPQU Conference, pp. 1–6 (2007)
40. Van Wesenbeeck, M.P.N., De Haan, S.W.H., Varela, P., Visscher, K.: Grid tied converter with virtual kinetic storage. In: Proceedings IEEE Powertech Conference, pp. 1–7 (2009)
41. Meng, J., Shi, X., Wang Y., Chao, F.: A virtual synchronous generator control strategy for distributed generation. In: China International Conference on Electricity Distribution (CICED), pp. 495–498, September 2014
42. Liu, J., Miura, Y., Ise, T.: Dynamic characteristics and stability comparisons between virtual synchronous generator and droop control in inverter-based distributed generators. In: Proceedings of International Power Electronics Conference (IPEC-Hiroshima), pp. 1536–1543 (2014)
43. Torres, M., Lopes, L.A.C.: Virtual synchronous generator control in autonomous wind-diesel power systems. In: Proceedings of IEEE Electrical Power Energy Conference (EPEC), Montreal, QC, Canada, pp. 1–6 (2009)
44. Rathore, B., Chakrabarti, S., Anand, S.: Frequency response improvement in microgrid using optimized VSG control. In: 2016 National Power Systems Conference (NPSC) Bhubaneswar, pp. 1–6, 19–21 December 2016
45. Karapanos, V., de Haan, S., Zwetsloot, K.: Real time simulation of a power system with VSG hardware in the loop. In: Proceedings 37th Annual Conference IEEE Industrial Electronics Society, pp. 3748–3754 (2011)
46. Shintai, T., Miura, Y., Ise, T.: Oscillation damping of a distributed generator using a virtual synchronous generator. *IEEE Trans. Power Deliv.* **29**(2), 668–676 (2014)
47. Hesse, R., Turschner, D., Beck, H.P.: Micro grid stabilization using the virtual synchronous machine. In: Proceedings of International Conference on Renewable Energies Power Quality (ICREPQ), vol. 472, pp. 1–6, April 2009

48. Yan, D., Guerrero, J.M., Chang, L., Su J., Mao, M.: Modelling, analysis, and design of a frequency - droop based virtual synchronous generator for microgrid application. In: ECCE Asia Downunder (ECCE Asia), pp. 643–649 (2013)
49. Alipoor, J., Miura, Y., Ise, T.: Distributed generation grid integration using virtual synchronous generator with adoptive virtual inertia. In: Proceedings of IEEE Energy Conversion Congress Exposition (ECCE), pp. 4546–4552 (2013)
50. Alipoor, J., Miura, Y., Ise, T.: Power system stabilization using virtual synchronous generator with alternating moment of inertia. *IEEE J. Emerg. Sel. Topics Power Electron.* **3**, 451–458 (2015)
51. Sagwal, R., Kumar, A.: Congestion management solution for hybrid system considering voltage stability margin. *Procedia Technol.* **25**, 726–734 (2016)
52. Sagwal, R., Kumar, A.: Voltage stability margin based congestion management for hybrid system considering secure bilateral trading: MINLP approach. In: IEEE 6th International Conference on Power Systems (ICPS), New Delhi, pp. 1–6 (2016)



Collaborative Filtering Techniques for Trust Prediction in Online Social Network

Rajeev Goyal¹ , Arvind Kumar Upadhyay¹ ,
and Sanjiv Sharma² 

¹ Department of Computer Science and Engineering,
Amity School of Engineering and Technology,
Amity University Madhya Pradesh, Maharajpura Dang,
Gwalior, MP, India

goyal.rajeev@gmail.com

² Department of Computer Science and Engineering,
Madhav Institute of Technology and Science, Gwalior, MP, India

Abstract. Collaborative filtering is one of the rapidly grown techniques in Machine learning for the recommendation. Several algorithms based on Collaborative filtering are developed and analysis by researchers in e-commerce and other areas of the business. As data is becoming the next economy of the world, the online social network is now playing a crucial role in various regions of the humankind and organization. It is uttermost important to have a secure and trustworthy Online Social Network. To achieve the goal, the techniques required to predict trustworthy users. Collaborative filtering can be one of the technique to predict the trusted users in the online social network. The study will provide different Collaborative filtering techniques, classify the collaborative filtering techniques, analysis the issue with the techniques, also discuss the use of collaborative filtering in perspective with OSN and compare these algorithms with the real-life dataset.

Keywords: Collaborative filtering · Trust prediction · OSN

1 Introduction

The use of social media has exploded along with the rapid growth of the internet and smart gadget. It makes communication and interaction between people are becoming easier and faster. More than a billion individuals around the world are connected and networked together to create, collaborate, and contribute their knowledge and wisdom. With more than 560 million internet users India ranked second in the world. China is the only country above India in terms of online users. The biggest online shopping company of India is Flipkart having a net worth of \$2500 million. In the organization, social media give enormous implications for their internal use, such as knowledge management. As a vast amount of data generated by OSN that is virtually impossible to analyze. Data in the OSN can be unstructured, unreliable, unusable, and irrelevant. User and organization required more trusted users, suggestion, items, and opinion in OSN.

Trust provides a more reliable and superior and relevant view in OSN [1]. Trust can also help to prevent cyber-attacks and spams.

Trust defined as social capital for the OSN. Rapid emerging demand for trustworthy OSN leads the researcher to analyze and develop the trust aware Online Social Network. [2] Survey the trust calculation, dissemination, and prediction in the social network. Trust and reputation system in an online social network is analyzed and reviewed by Josang et al. [4]. A lot's of the survey done on trust analysis in Online social network, but few of them emphasis on machine learning techniques on trust prediction for OSN. [3] Provides a comprehensive survey on machine learning techniques for pair-wise trust prediction on the social network, Machine Learning methods classification for the pair-wise trust and analysis of the currently available dataset. Researchers rarely investigate collaborative filtering to predict trust in an online social network.

Use of Collaborative filtering for trust prediction in OSN has a lot's of benefits. In recent time Collaborative filtering is used more commonly for recommender systems [4]. Even in Netflix competition, collaborative filtering used as the base for the recommendation system. Collaborative filtering methods recommend user-item; user - user. The recommendation in a particular context, temporal prediction, etc. The first part of the paper analysis the trust in Online social Network, The second section of the paper study the collaborative filtering techniques. The third part discusses the different type of collaborative methods. In the fourth section, compare these techniques with real-world dataset. The last section concludes the analysis of the collaborative filtering techniques and the future guidelines for the researchers.

2 Trust Prediction in OSN

Trust between two users in the Online Social Network can be denoted as a directed graph $G(V, E)$. Here V denoted the Online social user and E meant the trust relationship or strength between the given users. In this author, define each edge between the users as a trust rating [5]. The objective of the problem is to predict the trust rating between the given user in a given dataset. To predict the trust first calculate the trust with the several factors [6]. Identify the factor for trust is the most critical part of the Trust prediction model. Following are the properties to measure the trust in Online social network [3].

2.1 Trust is Subjective

Trust is subjective in nature means trust is personal phenomena. Personal preference of the truster is inherent in the users. It shows that the trust can be evaluated on personal factors and measurement only objective factors can be incomplete and not possible for any trust prediction model [7].

2.2 Trust is Dynamic

Trust is highly dynamic in nature. A person most trustworthy to a person can be highly trustworthy after a particular time. Trust rating can change over a period of time as new

activity and behavioral changes in term of social context. The previous rating of trust have an impact on the new rating, but trust also degraded over time. Recent activity in OSN has a high impact on trust rating [8].

2.3 Trust is Contextual

Trust can vary in a different context. A person x has high trust in person y for driving a car cannot have the same trust for flying a plane. Trust can be disseminated in a similar context such a person x trust a person y for C++ training can also the same person for teaching Java on some extent. Due to the context has some similarity [9].

2.4 Trust is Propagative

Trust is proliferated. If user X trusts Y, and Y trust Z, then X will trust to Z to some extent. Hence users create a chain in the context of trust propagation. Here the important thing is that trust is propagative in nature not transmit within the users. In the above trust between X and Y will not transfer to Trust in Y and Z [10].

2.5 Trust is Asymmetric

Trust is not symmetric in nature. If a user X trust on User Y, it does not mean that Y can trust on X. It also shows that trust between users represented with a directed graph, and trust can be different in between two users for each other.

2.6 Trust is Tenuous

As per the study of sociology, trust is very delicate. It is sensitive to adverse rating or interaction. One harmful activity damaging the trust so bad that a positive rating. Improve the trust between users may take much time, but it takes a fraction of time to break the trust.

3 Recommender System

Recommender System is the way to find the relation between users, items based on the relation suggestion or prediction done. Several enterprises require techniques for predicting customer behavior based on the previous dataset. Business houses also want to predict the future trend, customer behavior, and activity for their organizational growth. In an online social network, the recommender system is used to predict the behavior of users more commonly. So the recommender system is the software that predicts or suggest the product or users to the customer. Figure 1 displays the different Types of the recommender system (Table 1).

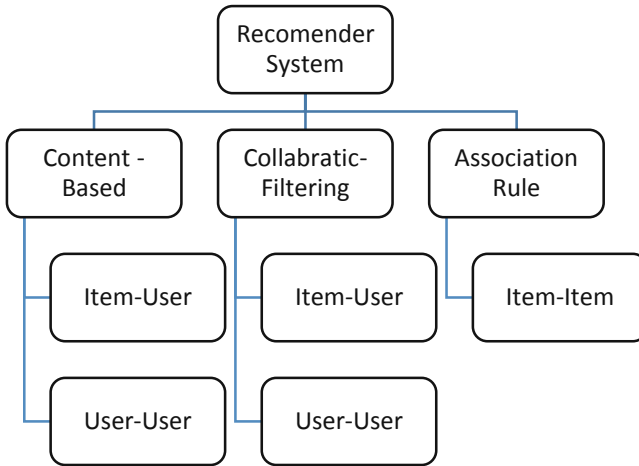


Fig. 1. Recommender system

Table 1. Approach for the recommender system

S. no.	Model name	Approach
1	Content-based	Find the item of similar attributes
2	Collaborative-filtering	A similar type of user can have a similar liking
3	Association rules	Find complementary products

3.1 Content-Based

Content-based recommender systems implement based on similar type of products or items. In content-based recommender System, experts are required to rank the product. Based on the ranking, the same kind of product recommended. The user who has already purchased or liked a similar type of product will notify these products as content-based RS required an expert who ranked all the products. In the organization having dynamic nature for products, users, and customers such as Online Social Network use of the content-based method are quite tedious and less accurate.

3.2 Association Rules

Association rule is used to find the relationship between the products like if the user purchases the mobile, it may be possible he will buy headphones with the cellular phone. Association Rules are a different type of Recommender system. It finds the relationship between items. So in trust prediction for users in Online social Network can't use this technique. Association rule used for finding purchase behavior and use them for product display in a big mart. Content-based and association rule is out of the scope of this paper.

3.3 Collaborative Filtering

Collaborative filtering recommended the item, product, or users based on the activity and behavior of the user. Collaborative filtering uses the latent factor. A similar type of user can have the same liking. The similarity between users can identify by the user's activity and behavior which can be measured by the owner of the social network. Collaborating filtering doesn't require experts to rank the item or user. In collaborative filtering, two types of input feedback used. Implicit and explicit feedback explicit. Feedback is given by the user explicitly on the contrary, and implicit feedback can calculate by user activity such as Purchased history, and browsing history.

There are two types of collaborative filtering methods,

- (i) Neighborhood.
- (ii) Latent Factor Approach.

In the neighborhood, the approach finds a relationship between item-item and user-user. Neighborhood approaches used for recommendation system such as K-Nearest Neighbor. In this approach, researchers measure the distance between items or users and calculate the K no of nearest neighbor, which displays the top K rank for the product or items.

In latent factor approach, a matrix created for both item and user in the same matrix space. Latent factor measures the rating based on different factors of the users or item. Then use this rating for the recommendation. Latent factor approach is more accurate than the neighborhood approach. Let analysis these approaches in the context of finding trust prediction between Online Social Networks [11].

4 Matrix Factorization Model

Matrix factorization is the most commonly used collaborative filtering technique. Matrix factorization uses latent-factor to define the relationship. Here in matrix factorization techniques, two low-rank matrices are used, one is for Truster for the user who Trust and other is for the trustee that has to be trusted. As trust has not rated all the trustee, Recommendation can be given by multiply these two matrices and find a matrix that has all the ratings for truster to the trustee. As sown in Eq. 1.

$$R = X_i Y_j \quad (1)$$

Here R is the matrix having a rating between truster and trusty. X is the strength of the truster and Y is the matrix having factors of trusty. Equation 2 Used To find the prediction of trust between user i and trusty j as follows

$$r_{ij} = X_i Y_j = \sum_{k=1}^f x_{ik} y_{kj} \quad (2)$$

Here x_i and y_j are the Truster and Trustee and r_{ij} is the predicted rating for user x_i and y_j .

4.1 Singular Value Decomposition (SVD)

In contrast to trust between user’s matrix factorization map the truster and trusty in joint space of latent factor, due to this truster - trustee are modeled as a product in common space. This space classifies truster and trustee on the features that are given by users [4].

As each trustee is from the vector $Y_j \in R^f Y$ and each trustee x is associated with a vector $X_i \in R^f$ for a given trustee j am the element y_j measures the rating of the trustee having positive or negative. For the truster, the value x_i measures the rating that the truster has. The rating is predicted by the following Eq. 3.

$$r_{xy} = C + b_y + b_x + x_i y_j^T \tag{3}$$

Generally, CF data is biased due to human habits and behavior. There may be a case were user x gives a higher rating then others similarly a critical user may provide rating lass than the normal users. Predicting the trust based on such a biased data recommendation to improve accuracy for the model it is advisable to minimize this tendency. In Eq. 3 b_x and b_y are the deviation of trusters and trustees. To overcome overfitting author minimized the regularize the square error as shown in Eq. 4.

$$\min_{b^*, q^*, p^*} \sum_{(i,j)}^n (r_{xy} - C - b_y - b_x - X_i Y_j^T) + C_2 (b_y^2 + b_x^2 + \|x_i\|^2 + \|Y_j\|^2) \tag{4}$$

Here C_2 is the constant determined by cross-validation.

4.2 SVD++

SVD uses explicit feedbacks. Accuracy of the recommendation can improve if the method will use both explicit as well as implicit feedback. Implicit feedback provides an additional Indication of the truster and trustee preferences. Most of the user are hesitated to provide explicit feedback. Significant relation can identify by the uses activity instead of the explicit rating. SVD++ uses explicit as well as an implicit rating which gives higher accuracy than SVD.

In trust prediction for OSN new features of Trustee is added, the relate the implicit feature in a vector $a_j \in R^n$ of the trustee. Factors added used to measure rating for trustee rated by truster. The following is the Eq. 5 for the approach.

$$r_{ij} = C + b_y + b_x + y_j^T \left(x_i + |R(x)|^{\frac{-1}{2}} \sum_{j \in R(x)} a_j \right) \tag{5}$$

Here the set $R(x)$ has the trustee rating given by truster x . In this equation x_i is the explicit feedback and $|R(x)|^{\frac{-1}{2}} \sum_{j \in R(x)} a_j$ is the implicit feedback. Several implicit

feedback can be added in the model such as if truster have some tendency to a certain type of the trustee then we can measure this and add this in SVD++ and improve the accuracy further.

4.3 Time-Based Matrix Factorization

Trust can change according to time. Two main factors that are highly sensitive to the time, First that the trust rating value is altered as time passes next that new user added and the based on their activity trust rating is changed [12]. Time is an essential factor that can improve the accuracy of the trust prediction. Matrix factorization allows to analyze the time factor separately, such as truster biases $b_x(t)$, trustee biases $b_y(t)$ and the truster rating $x_i(t)$ also the trustee characteristics $y_j(t)$. To measure truster tendency over time. The estimation of time span for measuring the changes in trust rating factors is essential. Shorter the time span required the more values of factors in the time span. Higher the time span less the accuracy. The model uses a monthly time span, so the values are between 1 to 12. The truster tendency is as shown in Eq. 6

$$b_x(t) = b_x + b_{x,span(t)} \tag{6}$$

Here we can capture the factors that change over time and the model was denoted as time SVD++ As shown in Eq. 7.

$$\begin{aligned} \min_{b^*, q^*, p^*} \sum_{(i,j)}^n & \left(r_{xy} - C - b_y(t) - b_x(t) - X_i Y_j^T \right) \\ & + C_2 \left(b_y^2(t) + b_x^2(t) + \|x_i\|^2 + \|Y_j\|^2 \right) \end{aligned} \tag{7}$$

5 Experiments

To evaluate the accuracy of these model implement these model with the underlying predictors of the online social network. It is applying these model to predict trust of two online social network user that has not previously communicated. The constant C2 is 0.04. Many datasets are available for the analysis of Online Social Network like ciao, Epinions, Avacado, and so forth. epinionion.com is one of the commonly used datasets for trust analysis in Online Social Network [13]. For improve the performance, the dataset is optimized. Ant colony algorithm has extracted the dataset. Epinionion.com is one of the datasets that have distrust information. Some of the datasets have distrust information, but they do not have user interactions. Epinionion.com also have rating time. Epinionion.com have three standard dataset epinionion_tang shown in Table 2, extended epinionion.com and Epinionion_Massa. Paper used epinionion_tang for the experiment.

Structure of the dataset is as follows.

Table 2. epionion_tang Dataset

File name	Product rating	Trust
No. of records	922,267	300528
Fields	Userid, Productid, Catogoryid, rating, Helpfulness, Timestamps	UserId1, UserId2, Timestamps

By using the epionion_tang Dataset following is the trust predicting results through different collaborative filtering techniques.

Table 3. Comparison of the MF techniques on RSME and MAE matrices

Training	Metrics	Normal MF	SVD	SVD++	Time-based MF
80%	MAE	0.2948	0.1917	0.1715	0.1628
	RSME	0.4583	0.3435	0.2256	0.2078
60%	MAE	0.2998	0.1987	0.1885	0.1728
	RSME	0.4886	0.3534	0.2556	0.2187

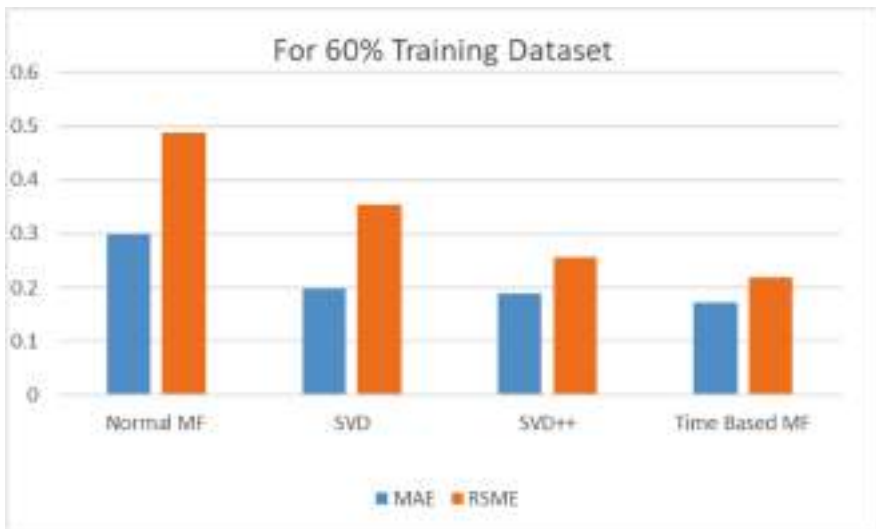


Fig. 2. RSME and MAE metrics for the Different MF Techniques for 60% training dataset

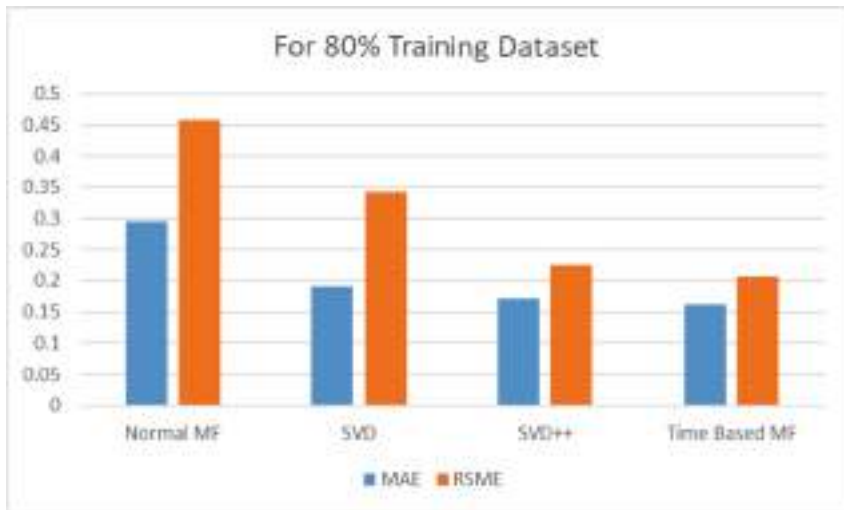


Fig. 3. RSME and MAE metrics for the Different MF Techniques for 60% training dataset

Table 3 displays a comparison of all the techniques of matrix factorization approaches. Figures 2 and 3 also represent the variation when to used different size of the training dataset. First is the standard matrix factorization method second is the SVD method which improves the accuracy from the standard Matrix factorization method due to baseline and regularization. The third is the SVD++ technique that promotes the accuracy over SVD due to implicit feedback, and last is the time SVD++ improve the efficiency over SVD++ as it adds the time factor in the technique but in the time SVD++ it is required to add extra parameters to clear presentation of each truster factor.

6 Conclusion





Matrix factorization in collaborative literacy is one of the most common techniques traditional matrix factorization technique classifies both truster and trustee by vector of features, finds the pattern of trustee rating. The matrix factorization gives better accuracy as compared to other cf techniques. Matrix factorization also provides optimum use of memory which can easily be trained. Due to this, SVD is the apparent choice for Netflix competition. These techniques can overcome and handle several critical aspects of the dataset. First, they integrate the different types of truster feedback also predict the trust by analyzing other activities by the same truster. The SVD++ model has the advantage to use explicitly as well as implicit feedback. One of the other very important features that affect trust is time. Time SVD++ uses this feature to predict trust more accurately. The use of time as a factor improve the accuracy dynamically.

References

1. Goyal, R., Upadhyay, A.K., Sharma, S., Mishra, P.K.: Trust factor organization for trust prediction in online social network. *Int. J. Innov. Technol. Explor. Eng.* **8**(7), 296–300 (2019)
2. Sherchan, W., Paris, C.: A survey of trust in social networks. *ACM Comput. Surv.* **45**(4), 1–33 (2013)
3. Liu, S., Zhang, L., Yan, Z.: Predict pairwise trust based on machine learning in online social networks: a survey. *IEEE Access* **6**, 51297–51318 (2018)
4. Mehta, M.R.: A review on matrix factorization techniques in recommender systems, pp. 269–274 (2017)
5. Wang, Y., Wang, X., Tang, J., Zuo, W., Cai, G.: Modeling status theory in trust prediction, pp. 1875–1881 (2013)
6. Goyal, R., Sharma, S., Mishra, P.K.: *ScienceDirect Analysis of Predicting Trust in Complex Online Social Networks* (2018)
7. Liu, G.: *Trust Management in Online Social Networks* (2013)
8. Fong, S., Zhuang, Y., Yu, M., Ma, I.: Quantitative analysis of trust factors on social network using data mining approach, pp. 70–75 (2012)
9. Zheng, X., Wang, Y., Orgun, M.A., Liu, G.: Social context-aware trust prediction in social networks, pp. 527–534 (2014)
10. Ureña, R., Kou, G., Dong, Y., Chiclana, F., Herrera-viedma, E.: A review on trust propagation and opinion dynamics in social networks and group decision making frameworks. *Inf. Sci.* **478**, 461–475 (2019)
11. Ricci, F., Rokach, L., Shapira, B., Kantor, P.B., Ricci, F.: *Recommender Systems Handbook* 123
12. Munasinghe, L.: *Time-aware methods for Link Prediction in Social Networks* (2013)
13. Goyal, R., Sharma, S., Upadhyay, A.K.: Pair-wise trust prediction employing matrix factorization for online social network. (5), 2686–2690 (2019)



Improved Multi-verse Optimizer for Numerical Optimization

Dilip Kumar Mishra¹ , Vikas Shinde² , Kamal Wadhwa³ ,
and Sanjay Chaudhary¹ 

¹ Government Narmada PG College Hoshangabad, Hoshangabad 461001, India
mishradilip3826@gmail.com, drsanjay0702@gmail.com

² Madhav Institute of Technology and Science, Gwalior 474005, India
v_p_shinde@rediffmail.com

³ Government PG College, Pipariya 461001, India
wadhwakama168@gmail.com

Abstract. In this paper an improved version of multi-verse optimizer proposed and tested on numerical optimization problems. Multi-verse optimizer (MVO) is novel optimization approach inspired from the concepts of cosmology, which are named as white hole, black hole, and wormhole. To carry out exploitation, exploration and local search mathematical modeling of these concepts has been performed. Improvisation in MVO has been made by introducing concept of dynamic variation in population size (universe). Improved multi-verse optimizer (IMVO) was tested on 13 benchmark functions having distinct complexity. Finally statistical comparisons of results were made with other methods, which show that IMVO performs better than other algorithms given in the literature.

Keywords: Optimization · Particle swarm optimization · Genetic algorithm · Benchmark functions

1 Introduction

Optimization techniques generally population-based techniques have one major inspiration i.e. nature. Detail classification of algorithm on the basis collective behavior can be found in Ref. [1]. Some of the algorithms which are inspired from the nature and carry out optimization as: Genetic algorithm (GA) [2], which mimics the biological evolution such as mutation, selection and crossover to carry out the optimization. Particle swarm optimization (PSO) [3], which is inspired by the social behavior of birds, insects and fish. Artificial bee colony (ABC) optimization [4], which mimics the foraging behavior of honey bees. Gravitational search algorithm (GSA) [5], uses Newtonian laws for the optimization. Cuckoo search algorithm (CSA) [6], follows the brood parasitism of cuckoo birds for the optimization. Flower pollination algorithm (FPA) [7], gets inspiration from the pollination of flowering plants. Grey wolf optimization (GWO) [8], which mimics the hunting behavior of grey wolves for the optimization. To start any optimization process generally a set of random outcome is created, then these outcomes are mixed over the course of iterations, this is the basic

framework for most of the population-based algorithms. Only the method of evolution or combination makes the difference between the algorithms.

Another concept which is common between population-based algorithms is the process of exploration and exploitation. Researchers always try to discover search space globally, the thing which take the solution towards the best global optimum is proper balance between inflation and exploitation.

In this paper, a nature-inspired population based algorithm known as improved multi-verse optimizer (IMVO) is proposed. Its name itself suggests that it get inspiration from the multi-verse theory in physics. To develop the IMVO algorithm, three concepts of multi-verse theory has been mathematically modeled like that white hole, black hole, and wormhole.

The remaining part of the paper is organized is as follows: Sect. 2 deals with the proposed algorithm (MVO) and its improvisation, results and discussion are shown in Sect. 3 and conclusion is given in Sect. 4.

2 Multi-verse Optimization

The existence of this world depends upon a theory which is known as big bang theory [9]. This theory is considered as the source of everything happening in the world. Now there is another theory known as multi-verse theory [10], which says that one big bang produces one universe and there are more than one big bang. There is a cosmos in which we are existing now, but according this theory, more than one universe exists in this world, these universes may have interaction, collisions and different laws of physics.

MVO algorithm mainly works on three concepts, which are chosen from the multi-verse theory and these concepts are: white holes, black holes and wormholes. Cyclic model of multi-verse theory [11], says that creation of white holes is done by the collision of parallel universes. Black holes are in contrast with white holes. They try to lure everything also shaft of light with a very high attraction force [12]. Wormholes are meant to join all other parts of universes with each other. As it connects other parts of universe, therefore it is used as a tunnel by the objects to travel from one place to another place in the universe [13]. Also it provides path for the objects to travel from one cosmos to another cosmos. Models of these three constituent are show in Fig. 1.

Every cosmos possesses an expansion rate which is accountable for the inflation of cosmos in terms of space. Inflation rate is a very important factor for every universe because formation of stars, asteroids, planets, suitability for life, physical laws, white, black and wormholes depends upon inflation rate. White, black and wormholes are way for all universes to interact with each other to acquire a stable situation this idea provides the inspiration of MVO algorithm.



Fig. 1. White hole, black hole, wormhole

2.1 MVO Algorithm

As we now that, exploration and exploitation are considered as search processes in case of population-based techniques. But here in MVO algorithm white holes and black holes are used for the expansion of search space, and for the exploitation of search space wormholes are used.

For the optimization some assumptions has been made such that each outcome obtained is like to cosmos and each variable in that outcome is liked object in the cosmos. Additionally, we also provide inflation rate to every solution which is directly proportional to fitness function value of outcome. Also, here we have considered time in place of iteration because this term is common in cosmology and multi-verse theory.

Some rules are framed to cosmos for optimization using MVO algorithm which are as follows [14]:

- a. Expansion rate is directly proportional to the probability of having white holes.
- b. Expansion rate is inversely proportional to the probability of having black holes.
- c. Cosmos having greater expansion rate try to remit entity via white holes.
- d. Cosmos having smaller expansion rate try to accept entities via black holes.
- e. Entities of all cosmos transfer randomly towards best cosmos through wormholes without considering the expansion rate.

Roulette wheel selection is used for the selection of white or black holes and exchange of cosmos's entities. Every time, universes based upon their rate of inflation are sorted and then one out of them gets selected Applying roulette wheel selection to possess a white hole. Step by step method of MVO is described as below:

Nomenclature

X_q	q th parameter of the best cosmos
WEP	Wormhole existence probability
r_2, r_3, r_4	random number
m	number of universes
x_p^q	q th parameter of p th universe,
lb_q, ub_q	lower and upper bound of q th variable
TDR	travelling distance rate
n	number of objects

Suppose that,

$$u = \begin{bmatrix} x_1^1 & x_1^2 & \cdots & x_1^n \\ \vdots & \vdots & \ddots & \vdots \\ x_m^1 & x_m^2 & \cdots & x_m^n \end{bmatrix} \tag{1}$$

Where, ‘ n ’ is the no. of variables (parameters) and ‘ m ’ is the no. of solutions (universes) [14].

$$x_p^q = \begin{cases} x_s^q & r_1 < NI(u_p) \\ x_p^q & r_1 \geq NI(u_p) \end{cases} \tag{2}$$

Where, x_p^q indicates the q th parameter of p th cosmos, u_p denotes the p th cosmos, $NI(u_p)$ is normalized rate of inflation of p th universe, r_1 is a random no. lies in $[0,1]$, and x_s^q denotes the q th parameter of s th universe selected by a roulette wheel mechanism.

According to Eq. (1), roulette wheel is used to select and determine white holes, which depends upon normalized rate of inflation. For lower rate of inflation probability to transfer entities via white or black hole tunnels will be more. This mechanism provides surety for the exploration, because for the exploration cosmoses are required to interchange entities and undergo sudden change in search space. In sequence carry out exploitation, we suppose that every cosmos has wormholes to transfer objects via leeway haphazardly.

To update the position in optimal universe following calculation need to be performed:

$$x_p^q = \begin{cases} \begin{cases} X_q + TDR * ((ub_q - lb_q) * r_4 + lb_q) & r_3 < 0.5 \\ X_q - TDR * ((ub_q - lb_q) * r_4 + lb_q) & r_3 \geq 0.5 \end{cases} & r_2 < WEP \\ x_p^q & r_2 \geq WEP \end{cases} \tag{3}$$

Where, X_q denotes the q th parameter of best cosmos found so far, TDR is co-efficient, WEP is one more multiplier lb_q denotes lower bound of q th variable, ub_q denotes upper bound of q th variable, x_p^q denotes the q th parameter of p th cosmos, and r_2, r_3, r_4 are random numbers lie in $[0,1]$.

Wormhole existence probability (WEP) and travelling distance rate (TDR) are co-efficient. They are supposed to increase over the course of repetitions to accentuate the exploitation. These co-efficient can be formulated as follows:

$$WEP = min + i * \left(\frac{max - min}{I} \right) \tag{4}$$

Where, min is minimum (0.2), max is maximum (1), i denotes current iteration and I denotes maximum iteration.

$$TDR = 1 - \frac{i^1/k}{I^1/k} \quad (5)$$

Where, $k = 6$, defining accuracy of exploitation over the course of repetitions.

In MVO algorithm, process of optimization starts by producing a set of random cosmos. In every repetition entities, objects lying in the universe having high rate of exploration try to transfer towards the cosmos having low rate of inflation through white or black holes. Meanwhile, every cosmos undergoes abrupt teleportation in its entities via wormholes towards best cosmos. This process continues till the required criterion is reached. The computational complexity of MVO algorithm is given as:

$$O(IMVO) = O(I(O(\text{quick sort}) + m * n * (O(\text{roulette wheel})))) \quad (6)$$

$$O(IMVO) = O(I(m^2 + m * n * \log m)) \quad (7)$$

Where, m is the no. of cosmoses, I is the max. no. of repetitions, n is the number of entities (Fig. 2).

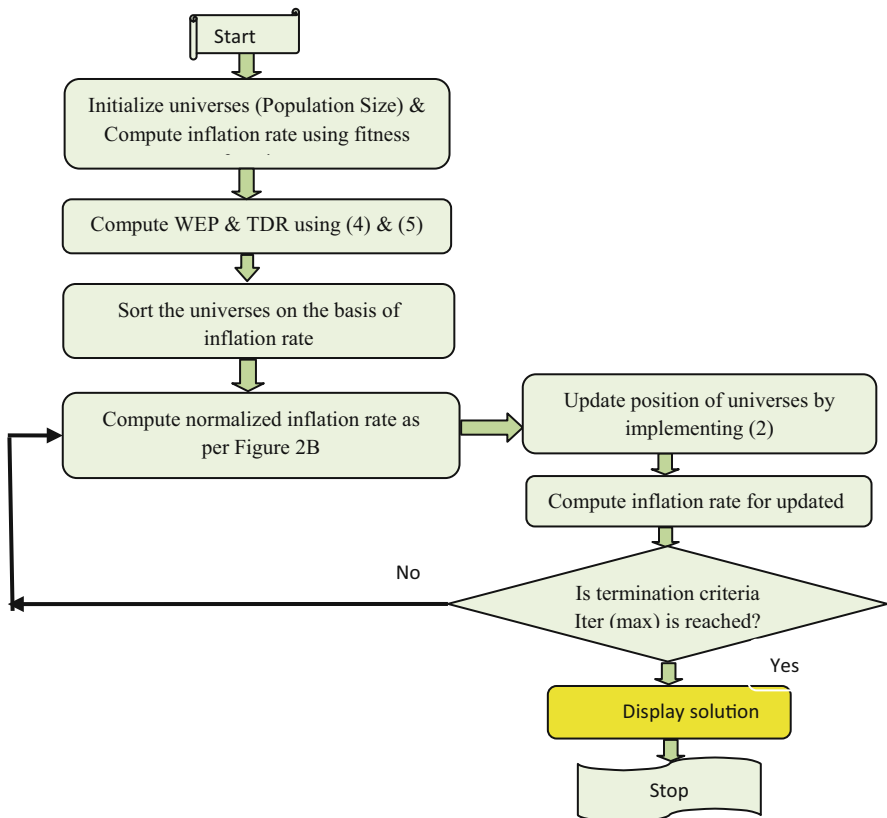


Fig. 2. Flow chart for multi-verse optimization

2.2 Improved MVO Algorithm

Improvisation in MVO is made to in two ways:

- (a) Here universe numbers are varied iteratively and
- (b) By introducing more randomness in algorithm that helps to minimize stagnation of standard MVO. These steps are depicted in Fig. 3A and B as below.

```
x=Iter/Iter_max;
  if (x<=0.5)
    Universes_no=100
  end
  if (x>0.5)
    Universes_no=50
  end
```

(A)

```
for each Universe i
  for each Universe j
    if r2<WEP
      r2∈random(0,1)
      r3∈random(0,1)
      if r3<0.7
        Universes(i,j)=Best_universe(1,j)+TDR*((ub-lb)*rand+lb);
      end
      if r3>0.7
        Universes(i,j)=Best_universe(1,j)-TDR*((ub-lb)*rand+lb);
      end
    end
  end
end
end
```

(B)

Fig. 3. (A, B) Pseudo code of improvisation phase of MVO

3 Numerical Benchmarks and Simulation Results

In this paper, 13 benchmark functions are selected, dimension of these test functions is considered as 50 and these test functions are given in Tables 1 and 2. The employed benchmark functions are classified in to two groups: unimodal benchmark functions and multi-modal benchmark functions. In unimodal benchmark functions there is only one global optimum, therefore, it is useful to test the exploitation of algorithms. Whereas, multi-modal benchmark functions having only one global optimum and multiple local optima.

Table 1. Unimodal benchmark functions

Function	Dimension	Range	Fmin
$\phi_1(x) = \sum_{i=1}^n x_i^2$	50	[-100, 100]	0
$\phi_2(x) = \sum_{i=1}^n x_i + \prod_{i=1}^n x_i $	50	[-10, 10]	0
$\phi_3(x) = \sum_{i=1}^n \left(\sum_{j=1}^i x_j\right)^2$	50	[-100, 100]	0
$\phi_4(x) = \max_i\{ x_i , 1 \leq n \leq i\}$	50	[-100, 100]	0
$\phi_5(x) = \sum_{i=1}^{n-1} \left[100(x_{i+1} - x_i^2)^2 + (x_i - 1)^2\right]$	50	[-30, 30]	0
$\phi_6(x) = \sum_{i=1}^n (x_i + 0.5)^2$	50	[-100, 100]	0
$\phi_7(x) = \sum_{i=1}^n ix_i^4 + \text{random}(0, 1)$	50	[-1.28, 1.28]	0

Table 2. Multi-modal benchmark functions

Function	Dimension	Range	Fmin
$\phi_8(x) = \sum_{i=1}^n -x_i \sin(\sqrt{ x_i })$	50	[-500, 500]	0
$\phi_9(x) = \sum_{i=1}^n [x_i^2 - 10 \cos(2\pi x_i) + 10]$	50	[-5.12, 5.12]	0
$\phi_{10}(x) = -20 \exp\left(-0.2 \sqrt{\frac{1}{n} \sum_{i=1}^n x_i^2}\right) - \exp\left(\frac{1}{n} \sum_{i=1}^n \cos(2\pi x_i)\right) + 20 + e$	50	[-32, 32]	0
$\phi_{11}(x) = \frac{1}{4000} \sum_{i=1}^n x_i^2 - \prod_{i=1}^n \cos\left(\frac{x_i}{\sqrt{i}}\right) + 1$	50	[-600, 600]	0
$\phi_{12}(x) = \frac{\pi}{n} \left\{ 10 \sin(\pi y_1) + \sum_{i=1}^{n-1} (y_i - 1)^2 [1 + 10(\sin(\pi y_{i+1}))^2] + (y_n - 1)^2 \right\} + \sum_{i=1}^n u(x_i, 10, 100, 4)$ $y_i = \left(1 + \frac{x_i + 1}{4}\right)$ $u(x_i, a, k, m) = \begin{cases} k(x_i - a)^m & x_i > a \\ 0 & -a < x_i < a \\ k(-x_i - a)^m & x_i < -a \end{cases}$	50	[-50, 50]	0
$\phi_{13}(x) = 0.1 \left\{ \sin^2(3\pi x_1) + \sum_{i=1}^n (x_i - 1)^2 [1 + \sin^2(3\pi x_i + 1) + (x_n - 1)^2 [1 + \sin^2(2\pi x_n)]] + \sum_{i=1}^n u(x_i, 5, 100, 4) \right\}$	50	[-50, 50]	0

For the simulation analysis the number of universes is considered as 100 for have of maximum iteration and 50 for the remaining iteration. The maximum number of iteration which is nothing but the stopping criterion considered as 100.

The benchmark functions were tested by performing consecutive 30 runs and the obtained statistical results of test functions are tabulated in Tables 3 and 4. The obtained outcomes are also compared with other methods as MVO [14] and PSO [14]. Form the tabulated results it is clearly observed that IMVO performs better in sequence of average value and the standard deviation (SD) while comparison to other reported methods.

The comparison of convergence curves of all the tested functions were plotted and presented in Fig. 4. Here it is clearly observed that convergence characteristics of IMVO are found to be better than MVO.

Table 3. Results of unimodal benchmark functions

Function	IMVO		MVO [14]		PSO [14]	
	Mean	SD	Mean	SD	Mean	SD
F ₁	0.5122	0.1107	2.08583	0.648651	3.552364	2.853733
F ₂	6.6960	12.9725	15.92479	44.7459	8.716272	4.929157
F ₃	348.0897	70.3062	453.2002	177.0973	2380.963	1183.351
F ₄	2.6214	0.9809	3.123005	1.582907	21.5169	6.71628
F ₅	320.9255	497.0913	1272.13	1479.477	1132.486	1357.967
F ₆	0.5059	0.0764	2.29495	0.630813	86.62074	147.3067
F ₇	0.0323	0.0111	0.051991	0.029606	0.577434	0.318544

Table 4. Results of multimodal benchmark functions

Function	IMVO		MVO [14]		PSO [14]	
	Mean	SD	Mean	SD	Mean	SD
F ₈	-12,426.023	935.0651	-11,720.2	937.1975	-6727.59	1352.882
F ₉	236.4299	41.9270	118.046	39.34364	99.83202	24.62872
F ₁₀	1.6191	0.5845	4.074904	5.501546	4.295044	1.308386
F ₁₁	0.5905	0.0782	0.938733	0.059535	624.3092	105.3874
F ₁₂	2.0517	1.0229	2.459953	0.791886	13.38384	8.969122
F ₁₃	0.1254	0.0848	0.222672	0.086407	21.11298	12.83179

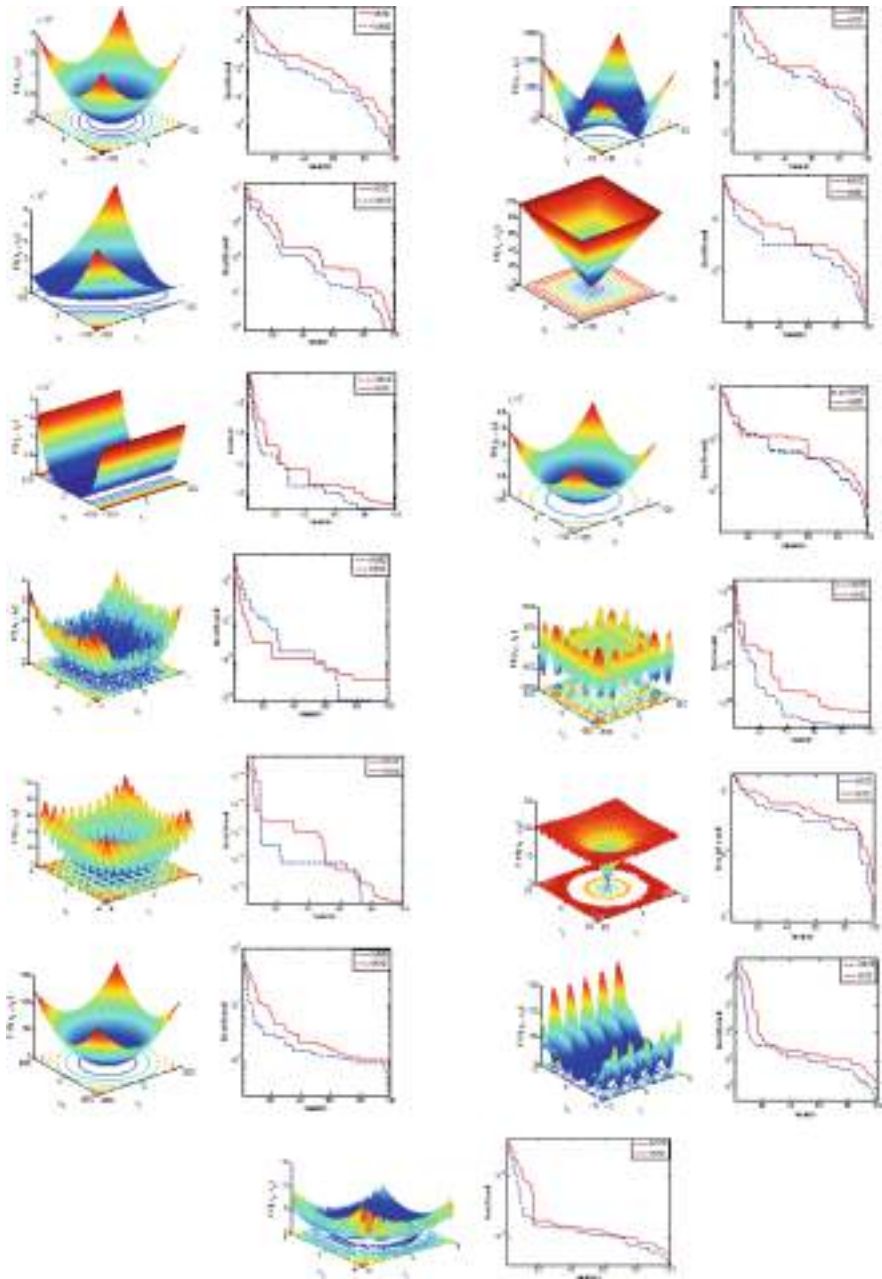


Fig. 4. Plot of benchmark function and their convergence curve

4 Conclusion

In this paper, an improved version of optimization algorithm inspired from the concepts of cosmology and multi-verse theory in physics is proposed. IMVO is depended on the three views i.e. white, black and wormholes. To study IMVO 13 benchmark functions have been considered, these test functions provides the information related to exploitation, exploration and convergence of IMVO.

In cosmos having high rate of inflation, white holes might be produced so that white holes can transfer entities to other cosmoses and support them to enhance their rate of exploration. In universes having low rate of inflation, black holes might be produced so that they can accept entities from other universes which in turn improves their inflation rate. White or black hole tunnels are used for the transferring of entities from cosmoses having high rate of inflation to low rate of inflation, such that overall rate of inflation of all cosmoses can be enhanced over the course of repetition. Wormholes have the tendency to seem haphazardly in any cosmos without considering the rate of inflation, which maintains the diversity of universes over the course of repetition. White or black hole tunnels has the requirement of abrupt changes in universe, which causes exploration of search space. Sudden changes in universes leads to the resolution of problem of stagnation of local optima. Wormholes re-span variables of universes around obtained best solution in a random manner, which improves exploitation. The convergence of IMVO has been improved by accentuating local search proportional to the no. of repetitions.





References

1. Dubey, H.M., Pandit, M., Panigrahi, B.K.: An overview and comparative analysis of recent bio-inspired optimization techniques for wind integrated multi-objective power dispatch. *Swarm Evol. Comput.* **38**, 12–34 (2018)
2. David, E.: Goldberg, Genetic Algorithms in Search, Optimization, and Machine Learning. Addison-Wesley, Reading (1989)
3. Kennedy, J., Eberhart, R.: Particle swarm optimization. In: Proceedings of IEEE International Conference on Neural Networks, vol. IV, pp. 1942–1948 (1995)
4. Karaboga, D.: An idea based on honeybee swarm for numerical optimization (Technical report TR06), Erciyes University, Engineering Faculty, Computer Engineering Department (2005)
5. Rashedi, E., Nezamabadi-pour, H., Saryazdi, S.: GSA: a gravitational search algorithm. *Inf. Sci.* **179**(13), 2232–2248 (2009)
6. Yang, X.S., Deb, S.: Cuckoo search via Lévy flights. In: Proceedings of the World Congress on Nature & Biologically Inspired Computing, pp. 210–214 (2009)
7. Yang, X.S.: Flower pollination algorithm for global optimization. In: Unconventional Computation and Natural Computation 2012. LNCS, vol. 7445, pp. 240–249 (2012)
8. Mirjalili, S., Mirjalili, S.M., Lewis, A.: Grey wolf optimizer. *Adv. Eng. Softw.* **69**, 46–61 (2014)
9. Khoury, J., Ovrut, B.A., Seiberg, N., Paul, J.S., Turok, N.: From big crunch to big bang. *Phys. Rev. D* **65**, 086007 (2002)

10. Tegmark, M.: Parallel universes. In: Barrow, J.D., Davies, P.C.W., Harper Jr., C.L. (eds.) *Science and Ultimate Reality: Quantum Theory, Cosmology, and Complexity*, pp. 459–491. Cambridge University Press (2004)
11. Paul, J.S., Neil, T.: A cyclic model of the universe. *Science* **296**, 1436–1439 (2002)
12. Michael, S.M., Kip, S.T.: Wormholes in space time and their use for interstellar travel: a tool for teaching general relativity. *Am. J. Phys.* **56**, 395–412 (1988)
13. Alan, H.G.: Eternal inflation and its implications. *J. Phys. A Math. Theory* **40**, 6811 (2007)
14. Mirjalili, S., Mirjalili, S.M., Hatamlou, A.: Multi-verse optimizer: a nature-inspired algorithm for global optimization. *Neural Comput. Appl.* **27**(2), 495–513 (2016)



Smart Grid Communication: A Survey of State-of-the-Art

Vimal Tiwari[✉] , Salil Madhav Dubey , Hari Mohan Dubey ,
and Manjaree Pandit 

Madhav Institute of Technology and Science, Gwalior, India
vimaltiwari01@gmail.com, salil.dubey3107@gmail.com,
harimohandubeymits@gmail.com, manjaree_p@hotmail.com

Abstract. The existing power grid has undergone drastic changes within a decade, in order to deal with the increase in energy demand. With the integration of different distributed energy resources (DERs) for a group of interconnected loads within a defined electrical boundary, microgrid came into existence. However, with the increased use of effective communication, automation and monitoring skills the microgrids are technologically advanced with fast response and are referred to as ‘Smart Grids’. In smart grid, efficient and reliable communication is incorporated to improve the efficiency, sustainability, and stability of the whole system. This paper presents a review on the different types of available communication methods and protocols which are used for data communication within and outside a smart grid based power supply system.

Keywords: Smart grid · Communication methods · Communication protocols · Microgrid

1 Introduction

A Microgrid (MG) can be defined as a small-scale, self-sustaining electric network which consists of distributed energy resources (DERs), such as wind, solar, and fuel cells, with storage devices and controllable loads. MG is designed to provide uninterrupted power supply to a balanced load demand for various diverse and changing customer demands. In MG, energy is supplied by one or more DERs of same or different types. It can reduce feeder loss, improve the reliability of the local power distribution system and increase energy efficiency. Depending on the coupling of different elements, MG can be divided into AC MG, DC MG, and hybrid MG structures which include AC and DC both elements. MGs can be connected to the main network or operated separately. Depending on these operations, MGs are operated in two modes namely Island mode and Grid-connected mode. In island mode MG can operate standalone i.e. the DERs can supply power to load only. In grid-connected mode, MG can exchange power with the power grid i.e. it can feed extra power to the power grid or consume the power of grid when needed.

MG can be disconnected from the power grid at the time of occurrence of fault or when the grid has no power. Also, it can be reconnected to the power grid when the fault is cleared provided that this transition does not cause any negative effects on the

power grid, DERs and critical loads connected to it. MG should always be synchronized with the power grid for smooth reconnection. The term synchronization means a connection of MG with the power grid. Synchronization of the generator with a grid is easier by using traditional synchronizers. However, synchronization of an MG with the power grid is very difficult, due to the fact that MG operates with multiple DERs that simultaneously produce electric power for the significant loads that cannot be controlled by conventional synchronizers. To overcome this problem, it is must achieve synchronized MG for controlling multiple generators and balancing energy storage systems in an efficient way. The difference between SG and MG is explained in Sect. 2. The importance of communication in SG is described in Sect. 3. Sections 4 and 5 describe the different communication standards and popular communication methods used in SG respectively.

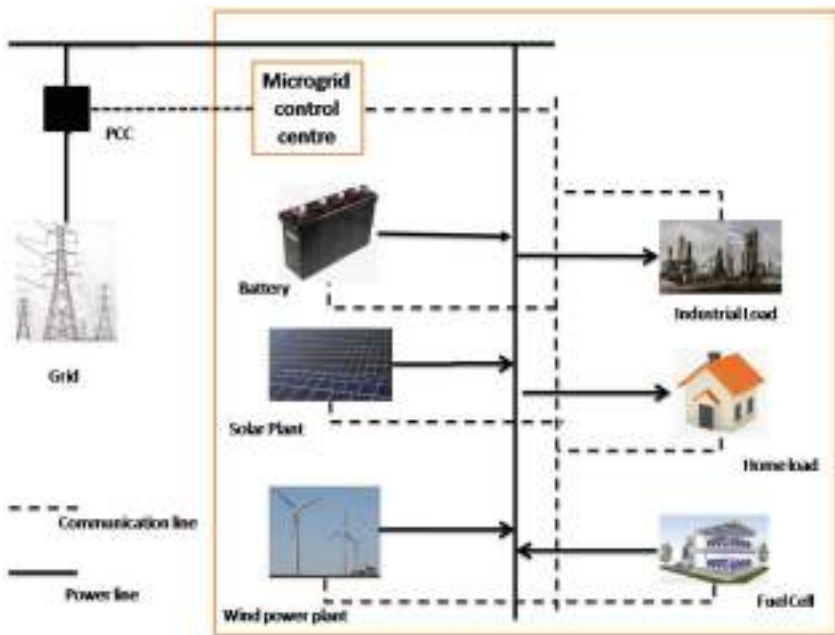


Fig. 1. Architecture of MG

2 Difference Between a Micro-grid and Smart Grid

MG and SG have a conceptual difference which is explained in this section. MG was introduced to overcome the irregular behaviour and the increased penetration of the distribution generation (DG) in power production. However, around 2007, a new term 'Smart Grid' (SG) was introduced in the USA [1]. SG and MG both terms appear to be same but they have a distinct basic difference. "The United States Department of Energy Microgrid Exchange Group" defines MG as a group of interconnected loads

and DERs within clearly defined electrical boundaries that operate as a single controllable entity with respect to the grid [2]. On the other hand, *International Electrotechnical Commission (IEC)* defines SG is a developing network of transmission lines, equipment, controls and new technologies that are working together to quickly respond to our electricity demand in the 21st century [1].

The MG is aimed to give power supply for small area. It is like providing power for remote area where supply cannot be given from national grid-like mountains areas, remote village in the forests, islands etc. whereas SG is an intelligent system which employs information and communication technologies as an add on to the existing electrical equipment like advanced metering infrastructure and significantly improves the power quality of national grid. The Smart Grid has two types of flows: two-way information flows and two-way energy flows. The two-way information flow means that the utilities have access to real-time information as well as customers control the continuous flow of energy and collect various parameters related to electricity. Information flow transport information (data) for monitoring the status, collecting various parameters and information in the SG and controlling the dynamic energy flows, whereas the energy flow transports electrical energy to meet customer energy demand. SG monitors the entire power system, that is, the working of transmission and distribution systems from generation plants to consumers [3].

3 Role of Communication in Smart Grid

The grid is called “smart” when it completely supports the two-way flow of information (communication) and two-way flow of energy [4]. For success of SG effective and reliable information exchange is needed. Here advanced and improved communication system is used as compared to the traditional one. The communication network helps in collecting, routing and monitoring nodes, finally acting on the received data [5]. Communication systems in SG have mainly two roles: (i) to provide continuous two-way communication between customers and utilities with low latency and (ii) to perform real-time monitoring and controlling of vast network of power grid. In the existing power grid, communication network is one-way in which little information is exchanged.

4 Types of Standards Followed in Grid Communication

There are several applications, methods and technical solutions for the SG system that have been developed or are still in the developing phase. SG standardization aims to achieve seamless interoperability, robust protection of information, increased safety of new products and systems and compact the set of protocols and information exchange. Summary of different communication standards used in SG are given in Table 1.

Table 1. Summary of different communication standards used in SG

S No.	Applications	Standards	Description	Standard organization
1.	DERs	IEEE 1547.3 [2]	Provides guidance to monitor, control and exchange of information between DERs Interconnected and Electric Power Systems	IEEE
		IEC 61850-7-420 [6]	Defines the control interfaces of communication for all DERs devices with various system IEDs	IEC
		IEC 61400-25	Describe communication protocols to monitor and control wind power plants	
2.	Revenue metering information model	IEC62056 [7]	Set of standards used to exchange the data of smart electric meter	IEC
3.	Building automation	IEEE 802.15.4 [8]	Defines the standard for physical layer (PHY) and medium access control (MAC) sub-layer specifications for personal area network (PAN) which support simple wireless devices consuming low power and operating in a short communication range	IEEE
4.	Substation Automation	IEEE 1646 [9]	Defines protocols for internal and external communications in an electrical substation	
		IEEE std. 1379 [9]	Discuss data communication between remote terminal units (RTUs) and intelligent electronic devices (IEDs)	
5.	Power line networking	G3-PLC [7]	Provides interoperability, cyber security, and robustness with high speed communication across existing power lines	ERDF

(continued)

Table 1. (continued)

S No.	Applications	Standards	Description	Standard organization
6.	Energy management system	IEC 61970 [10]	Work in transmission domain and provides common information model	IEC
		IEC 61968 [10]	Work in distribution domain and provides common information model	IEEE
7.	Home area network	IEEE P1901 [7]	High speed power line communication	
8.	Inter-control and interoperability centre communication	IEEE P2030 [11]	Standard for SG Interoperability of information technology operation and energy technology with power system, load, and end-use applications	
		ITU-T G.9955/G.9956 [10]	Contain data link layer specification and physical layer specification	ITU
		ITU-T G.9960 [12]	Providing regulations for distribution of audio, video, and data on home networks	
9.	Cyber security	IEC 62351 [8]	Guide to deal with the issue of cyber security of smart grid	IEC
10.	Electric vehicles	SAE J2293 [13]	Standard for electrical energy transfer from electric utility to electric vehicles (EVs)	SAE
		SAE J2836 [13]	Supporting use cases for DC Charging communications in plug-in electric vehicles (PEVs)	
		SAE J2847 [13]	Supporting use case requirements into the signals and messages to communicate between PEVs and utility grid	

5 Popular Methods of Communication

5.1 ZigBee Technology

ZigBee (ZB) is a low cost wireless technology which uses relatively low power with low data transfer rate and less complexity [14]. It is utilized in SG for various

application like automatic meter reading (AMI), home automation, smart lighting, energy monitoring system and MG, etc. ZB Alliance is one of the most recent technologies enabling Wireless Personal Area Networks (WPAN) [15].

ZB is a wireless mesh network which combines different nodes that are organized in a mesh topology. It is working as a self-sufficient router where each node can work independently. In case a node of the network is omitted, the self-healing property will help to find a route via active nodes to the communication signal. The wireless mesh network is generally distributed in nature, which enables one node to exchange information to others [10]. For small business operations and communication in remote areas, wireless mesh networks are found to be economical. It is found to be a better technology for home area network (HAN) communication, due to low power consumption, flexibility and short wake-up time [16]. It has 16 channels which operates on 2.4 GHz bandwidth. Here every channel has bandwidth of 5 MHz with maximum output power of 0 dBm (1 mW) [10]. Maximum transmission range is between 1 m to 100 m with the data transfer rate is about 250 Kb/s and uses OQPSK modulation.

ZigBee is best suited for high-level communications protocols with IEEE 802.15.4 Standard but low-power digital radios signals, small memory size, low processing capabilities, small delay requirements are also its limitation of practical implementation [11].

5.2 Cellular Network Communication

Cellular networks (CN) are used for exchange of information between distant nodes for utility purpose. CN are generally utilized to create a specified path for data exchange and implementation of smart meters in a wide area. These are highly tested and well-established networks that allow high data rates of up to 100 Mbps. Different cellular network technologies such as GSM, GPRS, 2G, 2.5G, 3G, 4G, and LTE are used for various applications of SG with some modifications. In addition, 4G can provide wider bandwidth, make it possible to allow more numbers of channels with the increasing needs of SGs [17]. The advantage is easy to deploy with high security and high data transfer rate because the network already exists. The disadvantage of cellular networks is that it is human-centric and difficult to use for machine-to-machine (M2M) communication [18].

5.3 Power Line Communication

PLC is a wired communication method that can operate in a ultra-narrow band, narrowband and broadband. In PLC, power feeder line is used as communication medium, therefore, provide a direct route between controllers and other subsystems to ensure low latency. These systems typically operate by transmitting a modulated carrier signal over the wiring system. Electric wire circuits have limited capability to carry high frequencies because the main objective of wiring is to deliver alternating current (AC) [15]. There are many power line standards in the market today but all of them are based on only two type of basic modulation schemes namely Orthogonal Frequency-Division Multiplexing (OFDM) and frequency-shift keying (FSK) [19].

For long ranges of the transmission lines, the data rate are low while, data rates are higher for different short transmission lines. Thus different sections of the power lines may be used for PLC at different frequency bands. With the development of SGs, the PLC on the power distribution and transmission networks has become one of the important technologies to exchange information between the utilities and the end-users. PLC is used for NAN (neighborhood area network) to exchange information between the smart meters and the local data concentrators. The main use of PLC in SGs is related to power distribution and exchange information between consumers and utilities. Some examples of these applications are EV charging systems, Smart Cities, Tele-control applications, AMI systems, and DERs systems. NB-PLC and BPL technologies are used in SG for above applications [20, 21].

5.4 Wireless Local Area Network (WLAN)

WLAN uses orthogonal frequency division multiplexing (OFDM) or spread-spectrum to make two or more devices to communicate and connect to a comprehensive Internet access point. WLAN is a wireless distribution method and its modems are standardized to follow IEEE 802.11 standard and its bandwidth range varies from 2.4 GHz to 3.5 GHz. WLANs have become very popular at home and in commercial complexes as they offer ease of installation and wireless access to their customers. This network is suitable to be deployed in an SG application as it is easy to deploy and low cost. However, the downside is that due to the bandwidth with which it operates, the WLAN has high interference susceptibility [18].

5.5 Fibre-Optic Communication

Fibre optic communication has been used by large power companies to connect their network control facilities with their generating system. An optical light has the ability to travel with the speed of 126,000 miles per second. Single-mode fibre and multi-mode fibre are two types of cables that are used in fibre optic communication. A single-mode fibre carries large amount of data in one direction, but it does not provide a return path while a multi-mode fibre can transmit and receive data from many directions. It has very less prone to failure and resistance against electromagnetic and radio interference which makes fibre optic communication suitable for high voltage operating condition. Its bandwidth capacity and immunity characteristics are high. Though the installation cost of optical fibers may be expensive, it provides a secure, reliable high-speed communication network which is the backbone of the futures SG [5].

5.6 Satellite Communication

While the primary commercial use of satellite communications in the past was only for one-way communication in media services, nowadays customers are provided IP services using two-way communication systems. Communication systems such as M2M

are very common and are growing rapidly. In addition, these technologies have steadily advanced, become more efficient and less expensive. In the past, data rates of some kbps were thought of state-of-the-art satellite technology for the availability of IP services. Today, data rates up to a few Mbps with compact devices are also possible. Given the needs and recent trends in satellite communications for M2M applications, the role of this communications technology in the rapidly evolving landscape of SGs needs to be discussed by identifying specific domain requirements, key features, and complexities. It gives analytical tools to measure the practicability of satellite systems with various trajectory configurations in M2M applications. It offers an overview of how satellite communications can support remote communication in SGs, environmental monitoring, and emergency management applications. The practicability of IP data services on the satellite was explored to support active network management solutions in distribution networks [22, 23].

5.7 The 5G Network

According to the 5G Public-Private Partnership (PPP) Network Working Group, the goal of 5G network is to fulfil the requirements of three groups. (i) Massive Broadband: It transfers gigabytes of bandwidth on demand, (ii) Massive Machine-Type Communications: It connects billions of terminals and (iii) Critical Machine-Type Communications: It provides high reliability and allows immediate response with competence. i.e. remote control over robots and autonomous driving system.

The challenge facing 5G technologies is to provide a structure that will help in simple detection of automated device in real-time so that network auto-configuration can be achieved automatically. Even though 5G networks have great potential to be used as the communication technology in SGs, these systems have not been fully adopted in practice.

The main challenge an SG network faces is the unpredictably large number of small generation stations and the fluctuating energy consumption at the end-user level. Moreover, the demand side and the supply side of the conventional grid are mutually exclusive. With respect to SGs, the end-user becomes the producer as well. The communication technique involved in SGs should be able to control up to the end-user level. The main challenge in introducing any new technology is standardization. The 5G network is expected to be standardized by 2020. New technology must have the interoperability and backward compatibility with existing technologies. The existing infrastructure should be affordably utilized, and modifications must be made in order to make it compatible with 5G standards [24].

The different applications of SG require different bandwidth, data rate and range. Therefore details of different communication technologies with their bandwidth, data rate, range, cost, and application are presented in the Table 2.

Table 2. Summary of different communication technologies used in SG

Communication technology	Bandwidth	Data rate	Range	Capital cost	Applications
ZigBee [10, 25]	2.4 GHz	250 Kbps	1 m to 100 m	Low	HAN
Cellular network communication [10, 25]	470–2600 MHz	Up to 1 Gbps	Hundreds of km	High	HAN, AMI, Demand response, DA
Power line communication [25]	1–30 MHz	2 to 3 Mbps	1–3 km	Low	AMI, fraud detection, DAU, PEV
Wireless local area network (WLAN) [10, 25]	2.4 GHz to 3.5 GHz	Up to 75 Mbps	Up to 1 km	Low	HAN, NAN, AMI, DAU, Distribution Automation (DA)
Fiber optic communication [25]	100 MHz to 20 GHz	Up to 10 Gbps	Up to 20 km	High	DAU, Asset monitoring, SCADA, DA
Satellite communication [25]	7 GHz to 8 GHz	Up to 1 Mbps	100 to 6000 km	High	SCADA, DA, WAN
5G [25]	600 MHz to 6 GHz	Up to 10 Gbps	Hundreds of km	High	DA, WAN

6 Conclusion

The SG is a fundamental technology that offers substantial changes to the current power grid, traditional energy resources, quality of power distribution and consumer life. The new power grid is basically different from the existing system in monitoring, controlling and energy management. The communication systems will play a significant role in the SG for effective energy management and real-time monitoring and controlling of system. The success of SG directly depends on a secure, reliable and robust communication system with high data rate transfer capability.

The integration of different SG technologies into the current power grid has been accelerated with the help of different generic standards and protocols endorsed by various organizations and government regulations. In this paper, various communication technologies and different communication standards for SGs are discussed and reviewed.

Acknowledgement. The financial support provided by AICTE-RPS project File No. 8-36/RIFD/RPS/POLICY-1/2016-17 dated 2.9.2017 and TEQIP III is sincerely acknowledged. Thanks are also due to the Director and management of M.I.T.S. Gwalior, India, for providing facilities and support.

References

1. Dileep, G.: A survey on smart grid technologies and applications. *Renew. Energy* **46**, 2589–2625 (2019)
2. Sood, V.K., Fischer, D., Eklund, J.M., Brown, T.: Developing a communication infrastructure for the smart grid. In: *IEEE Electrical Power and Energy Conference (EPEC)*, Montreal, QC, vol. 4, pp. 1–7 (2009)
3. Rehmani, M.H., Reisslein, M., Rachedi, A., Erol-kantarci, M., Radenkovic, M.: Integrating renewable energy resources into the smart grid: recent developments in information and communication technologies. *IEEE Trans. Ind. Inform.* **14**(7), 2814–2825 (2018)
4. Parhizi, S., Lotfi, H., Khodaei, A., Bahramirad, S.: State of the art in research on microgrids: a review. *IEEE Access* **3**, 890–925 (2015)
5. Daoud, M., Fernando, X.: On the communication requirements for the smart grid. *Energy Power Eng.* **03**(01), 53–60 (2011)
6. Yan, Y., Qian, Y., Sharif, H., Tipper, D.: A survey on smart grid communication infrastructures: motivations, requirements and challenges. *IEEE Commun. Surv. Tutor.* **15**(1), 5–20 (2013)
7. Baimel, D., Tapuchi, S., Baimel, N.: Smart grid communication technologies - overview, research challenges and opportunities. In: *2016 International Symposium on Power Electronics, Electrical Drives, Automation and Motion (SPEEDAM)*, Anacapri, pp. 116–120 (2016)
8. Chang, K.-H., Mason, B.: The IEEE 802.15.4g standard for smart metering utility networks. In: *IEEE Third International Conference on Smart Grid Communications (SmartGridComm)*, Tainan, pp. 476–480 (2012)
9. Wang, W., Xu, Y., Khanna, M.: A survey on the communication architectures in smart grid. *Comput. Netw.* **55**(15), 3604–3629 (2011)
10. Gungor, V.C., Sahin, D., Kocak, T., Ergut, S., Buccella, C., Cecati, C., Hancke, G.P.: Smart grid technologies: communication technologies and standards. *IEEE Trans. Ind. Inform.* **7**(4), 529–539 (2011)
11. Fouda, M.M., Fadlullah, Z.M., Kato, N., Lu, R., Shen, X.S.: A lightweight message authentication scheme for smart grid communications. *IEEE Trans. Smart Grid* **2**(4), 675–685 (2011)
12. Yigit, M., Gungor, V.C., Tuna, G., Rangoussi, M., Fadel, E.: Power line communication technologies for smart grid applications: a review of advances and challenges. *Comput. Netw.* **70**, 366–383 (2014)
13. Gungor, V.C., Sahin, D., Kocak, T., Ergut, S., Buccella, C., Cecati, C., Hancke, G.P.: A survey on smart grid potential applications and communication requirements. *IEEE Trans. Ind. Inform.* **9**(1), 28–42 (2013)
14. Bilgin, B.E., Gungor, V.C.: Performance evaluations of ZigBee in different smart grid environments. *Comput. Netw.* **56**(8), 2196–2205 (2012)
15. Devidas, A.R., Ramesh, M.V., Rangan, V.P.: High performance communication architecture for smart distribution power grid in developing nations. *Wirel. Netw.* **24**, 1621 (2018)
16. Ma, R., Chen, H., Huang, Y., Meng, W.: Smart grid communication: its challenges and opportunities. *IEEE Trans. Smart Grid* **4**(1), 36–46 (2013)
17. Gao, J., Xiao, Y., Liu, J., Liang, W., Chen, C.L.P.: A survey of communication/networking in Smart Grids. *Future Gen. Comput. Syst.* **28**(2), 391–404 (2012)
18. Kuyumani, M., Joseph, M.K., Hassan, S.: Communication technologies for efficient energy management in smart grid. In: *2018 International Conference on Advances in Big Data, Computing and Data Communication Systems (icABCD)*, Durban, pp. 1–8 (2018)

19. Naamane, A., Msirdi, N.K.: Towards a smart grid communication. *Energy Procedia* **83**, 428–433 (2015)
20. Lopez, G., Matanza, J., De La Vega, D., Castro, M., Arrinda, A., Moreno, J.I., Sendin, A.: The role of power line communications in the smart grid revisited: applications, challenges, and research initiatives. *IEEE Access* **7**, 117346–117368 (2019)
21. Yousaf, A., Khan, F., Hameed, Z., Ali, H.: Deployment of smart grid on narrowband power line communication using OFDMA. In: 9th International Renewable Energy Congress (IREC), Hammamet, pp. 1–6 (2018)
22. Kabalci, Y.: A survey on smart metering and smart grid communication. *Renew. Sustain. Energy Rev.* **57**, 302–318 (2016). *Global System for Mobile Communications*
23. Meloni, A., Atzori, L.: The role of satellite communications in the smart grid. *IEEE Wirel. Commun.* **24**(2), 50–56 (2017)
24. Leligou, H.C., Zahariadis, T., Sarakis, L., Tsampasis, E., Voulkidis, A., Velivasaki, T.E.: Smart grid: a demanding use case for 5G technologies. In: *Workshop on Pervasive Sensing for Sustainable Smart Cities and Smart Buildings*, pp. 215–220 (2018)
25. Emmanuel, M., Rayudu, R.: Communication technologies for smart grid applications: a survey. *J. Netw. Comput. Appl.* **74**, 133–148 (2016)



A Study on Adsorptive Removal of Malachite Green Dye from Model Liquid Phase onto Activated Pongamia Pinnata Pod Powder: An Eco-Friendly Bioadsorbent

Anjula Gaur^(✉) , Swati Goyal , and Preeti Gupta 

Madhav Institute of Technology and Science,
Gwalior 474005, Madhya Pradesh, India
anjulagaur@gmail.com, swatipc2011@gmail.com,
preeti.gupta605@gmail.com

Abstract. The present investigation has been aimed to produce a cheap adsorption process for the removal of contaminants from aqueous solution using an eco-friendly bioadsorbent. Activated pongamia pinnata pod powder (AP4) was used as an adsorbent which is extracted from ground shells of pongamia pinnata pods (Karanj tree). Systematic batch adsorption studies of Malachite Green (MG) on activated pongamia pinnata pod powder (AP4) were carried using various parameters which affect the adsorption procedure. The adsorptive behaviour of MG onto AP4 was studied by Langmuir adsorption isotherm model. Thermodynamic analysis was also done to evaluate the nature of following procedure. The estimated value of Gibbs free energy ΔG° (-11.22×10^3) reveals spontaneous nature of the process which involves pseudo first order kinetics controlled by particle diffusion process and the value of entropy ΔS° (29.478) confirms the randomness of the adsorption procedure. Results showed that developed ecofriendly, cost efficient adsorbent activated pongamia pinnata pod powder (AP4) can be successfully used for adsorptive removal of Malachite Green (MG) from aqueous solution because it have very high adsorption potential over MG.

Keywords: Adsorption · Malachite Green (MG) · Activated pongamia pinnata pod powder (AP4) · Isotherms · Equilibrium study

1 Introduction

The insertion of waste products into the environment has become a universal problem in recent time. Wastewater is a liquid waste which is discharged by different sources like commercial properties, industries, domestic residences, agriculture areas etc. [1]. On the basis of these origins wastewater can be classed as commercial waste, sanitary waste, agricultural waste, industrial waste or surface runoff. The sources of industrial wastewater includes pharmaceutical industries, food industries, cement industries, pulp paper industries, textile industries, rubber industries, leather industries, organic compost, cosmetics industries, plastic industries and other industries [2, 3]. A number of variety of chemical and dyes are being used in these types of industries therefore the

wastes generated by these industries can produce public health threat [4]. These industries released the remaining dye waste in water stream which is aesthetically detrimental and can produce serious environmental impacts.

Number of studies has been done to measure the harmful impacts of these types of materials on the environment and it was found that they can cause several troubles in water bodies in many ways:

- (i) Dyes can produce intense or continual effects on the creatures which depend on the absorption of dye and on the contact time.
- (ii) Dyes have an affinity to sequester metal ions which can produce toxicity in aquatic biota.
- (iii) Dyes have naturally extremely visible characteristics therefore their minor release of bilge water may cause unusual coloration of outer layers of water.
- (iv) When dyes enter in wastewater, they can absorb dissolved oxygen from the water surface and can also do some chemical and biological changes in water bodies; consequently it can destroy the aquatic life.
- (v) The dyes have ability to absorb or reflect the sunlight entering into the water so it can affects the bacterial growth and can prohibit their biological activity.
- (vi) Every dye has diverse and complex molecular structures therefore it is not easy to deal these types of waste with simple municipal waste treatment operations hence it required an innovative technique.

Due to these reasons it is necessary to develop a technique which can treat these types of contaminants from waste water. A number of techniques have been discovered for this reason such as reverse oxidation [5], osmosis [6], biological treatment [7], photocatalysis [8] and adsorption [9] etc. Adsorption is most promising method and has wide applications in wastewater treatment. Adsorption is a mass transfer process in which accretion of substances at the boundary of two phases occurs and the phases can be liquid–liquid, liquid–solid, gas–liquid or gas–solid. Adsorption is economically cost effective, sludge free and simple method which is efficiently able to treat these types of contaminants even in more concerted form [10, 11]. Therefore it has superiority over other removal techniques. Our Co-workers have also been contributed in this field [12]. A number of studies have been done on adsorptive and photocatalytic exclusion of organic and inorganic pollutants from aqueous solutions [13, 14]. One of author of this research work has also done study on the adsorptive [15, 16] and photocatalytic [17–19] removal of pharmaceuticals from waste water. The present study is also a contribution in the field of adsorptive removal of dyes from water bodies. An environmental friendly bioadsorbent has been developed from *Pongamia pinnata* seed shell and the removal efficiency of the developed adsorbent was studied over the adsorbate Malachite Green (MG). A batch adsorption kinetic study has been done over the different concentration range of adsorbate and adsorbent to assess the effect of parameters viz., dye (MG) concentration, bioadsorbent (AP4) dosages, equilibrium time, pH of the medium to present adsorption dynamics. After that Adsorption isotherm models has also been evaluated to find the adsorptive behaviour and removal efficiency of the adsorbent. Thermodynamic studies have also been investigated to find out the Gibbs free energy of adsorption (ΔG°), entropy (ΔS°) and enthalpy (ΔH°) by assessing the experimental data.

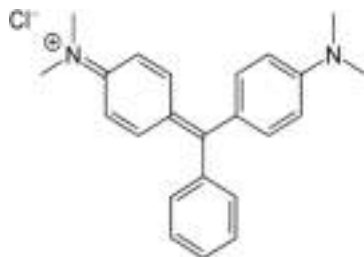
2 Experimental

2.1 Development of Eco-Friendly Bioadsorbent

For the present study the adsorbent (AP4) was developed by the seed shells of pongamia pinnata (Karanj). For this purpose the pongamia pinnata pods were collected from the institute campus, Madhav Institute of Technology and Science (MITS), Gwalior, India. The pod's shells were compacted in fine particles and sieved to a particular mesh size. Then it was soaked in the solution of hydrogen peroxide (H_2O_2) (30%) for 24 h at 60 °C to oxidize the organic impurities. After that it was rinsed with doubly distilled water and kept in hot air oven at 150 °C for heating. Now it was sodden overnight in the solution of $NaHCO_3$ (1%) to take away any acid. Thus developed material was cleaned with milli-Q water and dehydrated in oven at same temperature (150 °C). Finally, developed bioadsorbent was kept safely in air tight box till further use of it.

2.2 Preparation of Adsorbate (MG)

Malachite Green (MG) (Scheme 1) (Table 1) was purchased from E. Merck, India and was used with no additional distillation. The stock solution of MG (1 mg/mL) was prepared by dissolving 1 g of MG in 1 L of doubly distilled water. After that stock solution was diluted to desired concentrations by double distilled water for further experiments.



Scheme 1. Structure of Malachite Green (MG)

Table 1. Main properties of the Malachite Green.

Property	Malachite Green (MG)
Chemical formula	$C_{23}H_{25}N_2$
Molecular mass	$364.911 \text{ g mol}^{-1}$
Solubility	Water & alcohol
Water solubility	0.00138 mg/mL
Melting point	$158\text{--}160 \text{ }^\circ\text{C}$
Appearance	Green color powder
Density	1 g mL^{-1}
λ_{max}	617 nm

2.3 Instrumentation

Digital pH meter (DB 1011 India) fixed with glass electrode was used to analyze the pH of the solutions. Adsorption measurement has been done on a spectrophotometer (Sytonic model S-922) with a 1.0 cm light path quartz cells at λ_{\max} 617 nm. A Sartorius CP224S (Gottingen, Germany) weighing balance was used to weigh the dye and chemicals.

2.4 Adsorption Studies

Batch adsorption kinetic studies have been done at 30, 40 and 50 °C temperatures. A preset amount of the bioadsorbent (AP4) (10 mg) was added to the flask containing 30 mL of MG solution of varying concentrations from 1×10^{-5} to 8×10^{-5} M. The flasks were stirred continuously at stable temperature in a water bath shaker. After a definite time (determined initially) the samples were withdrawn and the solution was extracted using Whatman filter paper no. 42. The absorbance of filtrate was measured at λ_{\max} 617 nm using a spectrophotometer.

After that when equilibrium has been achieved, the adsorption capacity q_e (mg g^{-1}) of the adsorbent was determined using the following mass balance relationship equation:

$$q_e = (C_0 - C_e) * (V/W) \quad (1)$$

Where, C_0 and C_e is the preliminary concentration & concentration of MG at any time respectively. Both of the concentrations are in mg L^{-1} . W is the weight of adsorbent (AP4) and V is the Volume of adsorbate (MG).

2.5 Quality Assurance/Quality Control

Accurateness and precision are always necessary in a research therefore all the experiments were performed twice to set up the accuracy, dependability, and reproducibility of the data. All the glasswares which were used in this study were soaked in HNO_3 (5%) solution for 3 days then washed with distilled water and oven dried.

3 Results and Discussions

3.1 Bioadsorbent Characterization

Scanning electronic microscopy (SEM) study is one the most important, popular and broadly used characterization technique which is used to the study morphology and surface properties of any synthesized material. It can reveal about the porosity and texture of material. The morphological structure of bioadsorbent activated *Pongamia pinnata* pod powder (AP4) was observed under SEM (Zeiss EVO 50 instrument) and the micrograph is shown in Fig. 1 which indicates it has small cavities on the surface or quite rough surface and there are asymmetrical shaped pores present. It has a porous surface that may supply bulky surface to the dye molecules to get adsorbed over it.

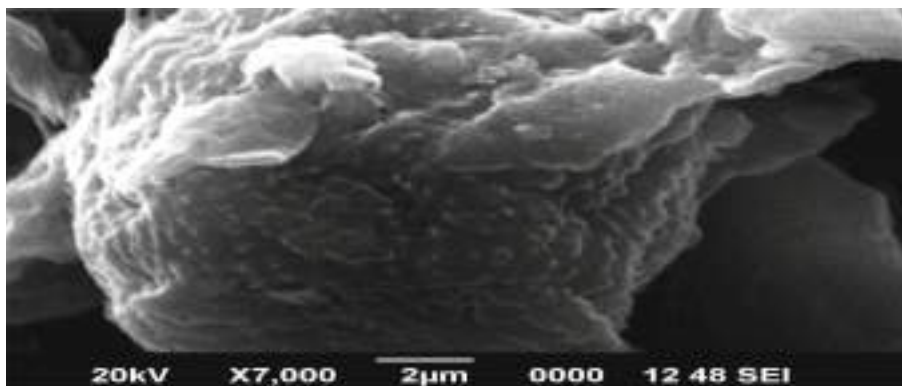


Fig. 1. SEM image of Bioadsorbent (AP4).

3.2 Bioadsorbent (AP4) Dosage Effect

It is a significant parameter to study the adsorptive behaviour of any adsorbent. In the present study, this factor was studied by increasing the dose of bioadsorbent from 0.066 to 0.53 g L⁻¹ and the other parameters (pH, initial concentration, and contact time) was kept constant. When we increase the adsorbent dose the rate of adsorption is increased to 0.33 g L⁻¹ and on auxiliary increase in dose a sudden decreased in adsorption rate of MG occurred. Hence 0.33 g L⁻¹ was taken as optimum amount of adsorbent dose for evaluation of other parameters. The results are shown by Fig. 2 which concludes that on increasing the adsorbent dosage uptake capacity decreases.

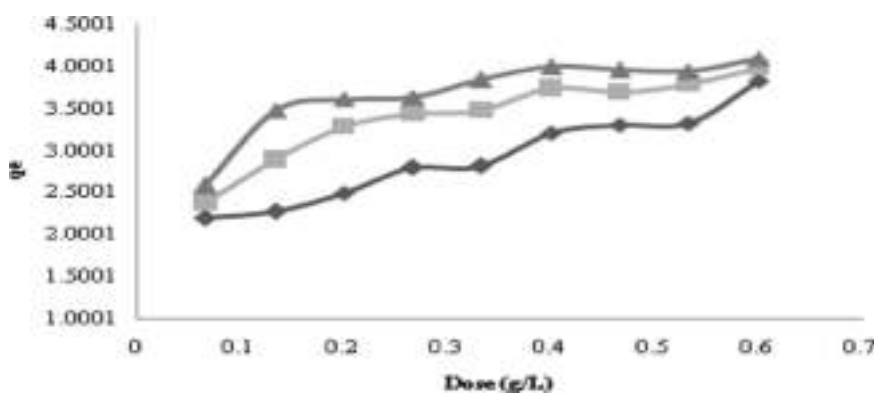


Fig. 2. Effect of AP4 dose onto Malachite Green at 4×10^{-5} M MG Concentration, pH 9.2 and different temperatures

3.3 Effect of Temperature

This is also an important parameter because it changes the equilibrium capability of the adsorbent over the adsorbate. In this study it was found that removal efficiency of MG was directly proportional to temperature. So when the temperature was amplified from 30 °C to 50 °C, the maximum efficiency was found at 50 °C which indicates that the nature of present reaction is endothermic.

3.4 Effect of pH

When the charges present on the surface of adsorbent and adsorbate cooperate with each other then the reaction occurred [20]. Some parameters such as surface charges, adsorption capacity and active sites which are present on adsorbent might be attributed to the adsorption behaviour of the adsorbent at different pHs. Therefore the experiments were performed at pH range from 2.48 to 12.3 and it was found that the percent removal of MG was different at every pH range. When the pH range was enlarged from above reported value in increasing order, the removal percentage also increased from 42% to 90% till pH 9.2 and on further increasing it almost get constant therefore 9.2 was taken as optimum pH value for further study (Fig. 3).

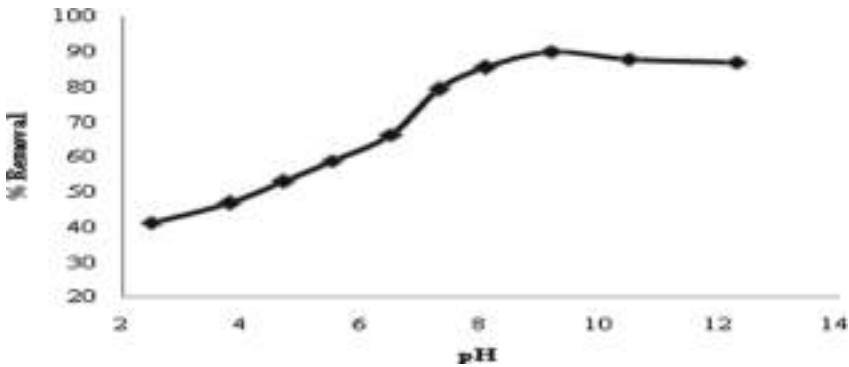


Fig. 3. pH effect on adsorption of Malachite Green at 4×10^{-5} M and 0.33 g/L dose of adsorbent.

4 Adsorption Isotherm Model

The isotherms define the distribution of adsorption molecules between the two phases i.e. liquid and the solid at equilibrium [21]. Adsorption isotherms also play an important role in studying the adsorptive behavior of solid-liquid adsorption systems. In the present investigation Langmuir isotherm model has been studied.

4.1 Langmuir Adsorption Model

Langmuir adsorption isotherm model was given by Irving Langmuir in 1916 [22]. This model states that the adsorption of a homogeneous monolayer occurs at a surface having partial number of adsorption sites and identical qualities with no transmigration of adsorbate [23]. The mathematical expression of this model is as following:

$$1/q_e = 1/Q^\circ + 1/bQ^\circ C_e \tag{2}$$

Where C_e is the concentration of the adsorbate (mol L^{-1}) at equilibrium and q_e is the quantity of adsorbent adsorbed (mol g^{-1}). b and Q° are the constants of langmuir related to energy adsorption and maximum adsorption capacity, respectively. To study this model a graph was plotted between $1/q_e$ and $1/C_e$ and a straight line with slope $1/bQ^\circ$ was obtained. From this it was found that the adsorption of MG over AP4 fitted well in this isotherm model (Fig. 4) model. The constants of Langmuir were calculated at 30, 40, and 50 °C and reported in Table 2.

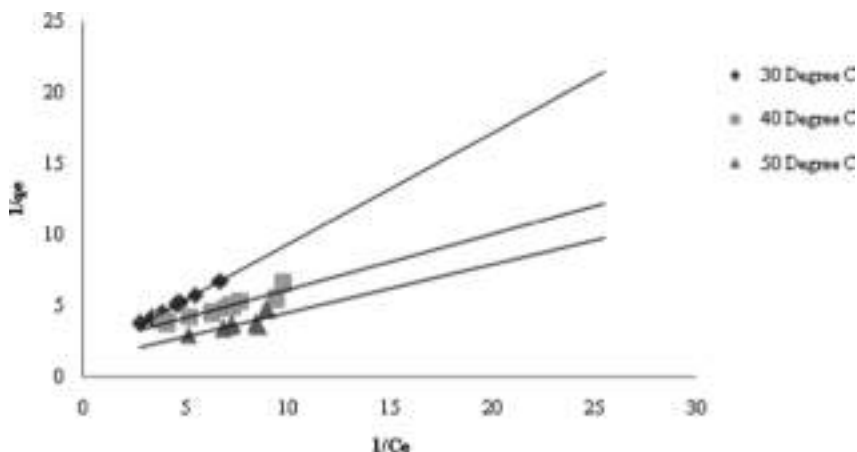


Fig. 4. Langmuir isotherm model for adsorption of Malachite Green at different temperatures.

Table 2. Langmuir constants for MG over bioadsorbent at different temperatures.

Temp. (°C)	b (mol g ⁻¹)	Q° (mol L ⁻¹)	bQ°	R ²	%RSD [#]
30	1.628	118.12	2.016	0.998	0.983
40	1.416	84.32	3.621	0.932	0.901
50	1.388	69.30	3.434	0.915	0.898

5 Adsorption Kinetics Studies

The kinetic study in adsorptive procedure is important factor to understand the adsorption dynamics in terms of order of the rate constant and it provides useful information regarding the efficiency of the adsorption of solid/liquid systems. It can be determined by many mathematical calculations but Lagergren's rate equation plays major role in it. Lagergren and Svenska [24] suggested the kinetic model to study the efficiency of adsorption of any system. In the present work the kinetics study of MG adsorption was studied using the following equation first-order kinetics [25]:

$$\text{Log}(q_e - q_t) = \log q_e - k_{ad} \times t/2.303 \quad (3)$$

Where q_e and q_t are the amount of the AP4 adsorbed at equilibrium condition and at time t , respectively. Lagergren plot was found when we plot a graph between $\log(q_e - q_t)$ and time (t) which exhibits straight lines at different temperatures and constant pH 9.2 and that confirms the first order kinetics of the adsorption procedure.

6 Thermodynamics Study

Thermodynamic constants [26] are the key features of any adsorption procedure. These are studied to find out the feasibility and nature of the procedure. Different types of thermodynamic constants such as Gibbs free energy (G°), change in enthalpy (ΔH°) and change in entropy (ΔS°) were evaluated in the present investigation using the following thermodynamic relations [27].

$$\Delta G^\circ = -RT \ln b \quad (4)$$

$$\Delta H^\circ = -R(T_2 * T_1)/(T_2 - T_1)\ln(b_2/b_1) \quad (5)$$

$$\Delta S^\circ = (\Delta H^\circ - \Delta G^\circ)/T \quad (6)$$

Here b , b_1 and b_2 are constants of equilibrium which can be calculated from the graph of Langmuir adsorption isotherm. These values were calculated from Fig. 4 and given in Table 3. The negative values of ΔG° confirm that the process is spontaneous in nature. The value of ΔH° (3.153×10^3) shows that the reaction is of endothermic nature while value of ΔS° states that randomness was increasing at the solid/solution interface during the MG adsorption onto AP4.

Table 3. Thermodynamic parameters of MG over bioadsorbent

ΔG° (kJ mol ⁻¹)			ΔH° (kJ mol ⁻¹)	ΔS° (JK ⁻¹ mol ⁻¹)
30 °C	40 °C	50 °C	30 °C	30 °C
-11.22×10^3	-14.19×10^3	-15.09×10^3	3.153×10^3	29.478

7 Conclusion

Adsorption of Malachite Green onto developed bioadsorbent was studied experimentally in a batch adsorber. The investigation reveals that activated *Pongamia pinnata* pod powder (AP4) can be an excellent, inexpensive and environment friendly bioadsorbent to remove out the dye contaminants from aqueous system. The different parameters such as pH of MG solution, dose of AP4 and temperature determined in the present study, were effective in determining the efficiency of MG onto the AP4. Langmuir isotherm fitted very well in the data. It was also found that the reaction followed the pseudo first-order kinetic model with dynamical behavior for the adsorption of MG onto AP4. The values of thermodynamic parameters ΔG° was negative and ΔH° was positive which confirm the spontaneous and endothermic nature of the reported procedure, respectively. Thus it was found that developed activated *pongamia pinnata* pod powder (AP4) adsorbent has higher adsorption capacity to remove MG from liquid phase. Hence it can be concluded that developed activated *pongamia pinnata* pod powder (AP4) is a cost efficient, highly proficient, and environmental friendly bioadsorbent that can be used to remove the different types of pollutants from water bodies.

Acknowledgement. Authors are thankful to Director Madhav Institute of Technology and Science Gwalior and TEQIP III for providing facilities in the institute.


References

1. Ormad, M.P., Miguel, N., Claver, A., Matesanz, J.M., Ovelleiro, J.L.: Pesticides removal in the process of drinking water production. *Chemosphere* **71**(1), 97–106 (2008)
2. Muff, J., Andersen, C., Erichsen, R., Soegaard, E.G.: Electrochemical treatment of drainage water from toxic dump of pesticides and degradation products. *Electrochim. Acta* **54**(7), 2062–2068 (2009)
3. Zahrim, A.Y., Hilal, N.: Treatment of highly concentrated dye solution by coagulation/flocculation–sand filtration and nanofiltration. *Water Resour. Ind.* **3**(5), 23–34 (2003)
4. Allen, S.J., Koumanova, B.: Decolourisation of water/wastewater using adsorption. *J. Univ. Chem. Technol. Metall.* **40**(3), 175–192 (2005)
5. Sharma, Y.C., Upadhyay, U.S.N., Gode, F.: Adsorptive removal of a basic dye from water and wastewater by activated carbon. *J. Appl. Sci. Environ. Sanit.* **4**(1), 21–28 (2009)
6. Vogelpohl, A., Kim, S.M.: Advanced oxidation processes (AOPs) in wastewater treatment. *J. Ind. Eng. Chem.* **10**(1), 33–40 (2004)
7. Malik, P.K., Saha, S.K.: Oxidation of direct dyes with hydrogen peroxide using ferrous ion as catalyst. *Sep. Purif. Technol.* **31**(3), 241–250 (2003)
8. Goyal, S.: Photocatalytic degradation of an antiparkinson drug entacapone in an aqueous suspension of titanium dioxide. *J. Indian Chem. Soc.* **92**(7), 1155–1160 (2015)
9. Bilal, A.: Adsorption of Congo red from aqueous solution onto calcium-rich fly ash. *J. Colloid Interface Sci.* **274**(2), 371–379 (2004)
10. Asfaram, A., Ghaedi, M., Dashtian, K., Ghezalbash, G.R.: Preparation and characterization of $\text{MnO}_4\text{ZnO}_6\text{Fe}_2\text{O}_4$ nanoparticles supported on dead cells of *yarrowia lipolytica* as a novel and efficient adsorbent. *ACS Sustain. Chem. Eng.* **6**(4), 4549–4563 (2018)

11. Asfaram, A., Ghaedi, M., Abidi, H., Javadian, H., Zoladl, M., Sadeghfar, F.: Synthesis of $\text{Fe}_3\text{O}_4@\text{CuS}@\text{Ni}_2\text{P}$ -CNTs magnetic nanocomposite for sonochemical-assisted sorption and pre-concentration of trace Allura Red from aqueous samples prior to HPLC-UV. *Ultrason. Sonochem.* **44**, 240–250 (2018)
12. Goyal, S., Patidar, D., Gaur, A.: Adsorptive removal of dyes from aqueous solution onto cost effective and non-conventional adsorbents: a review. *Int. J. Res. Anal. Rev.* **6**(2), 750–765 (2019)
13. Jain, R., Sikarwar, S.: Photocatalytic and adsorption studies on the removal of dye Congo red from wastewater. *Int. J. Environ. Sci. Technol.* **27**(1–3), 158–178 (2006)
14. Jain, R., Sikarwar, S.: Removal of hazardous dye Congo red from waste material. *J. Hazard. Mater.* **152**(3), 942–948 (2008)
15. Jain, R., Sikarwar, S., Goyal, S.: Kinetics and isotherm studies on the adsorption of an antiparkinsonism drug Entacapone from aqueous solutions using unsaturated polyester resin (UPR). *Desalin. Water Treat.* **54**(11), 3169–3176 (2015)
16. Jain, R., Sikarwar, S., Goyal, S.: Adsorption study of tetracycline onto an unsaturated polyester resin. *Desalin. Water Treat.* **57**(15), 6875–6883 (2016)
17. Kadam, S., Goyal, S., Sikarwar, S., Jain, R.: Photocatalytic degradation kinetics of anti-inflammatory drug Balsalazide using semiconductor TiO_2 under UV irradiation. *J. Indian Chem. Soc.* **93**(3), 327–332 (2016)
18. Jain, R., Sikarwar, S., Goyal, S.: Semiconductor sensitized photodegradation of antibiotic tetracycline in water using heterogeneous nanoparticles. *J. Sci. Ind. Res.* **75**(06), 355–358 (2016)
19. Jain, R., Goyal, S., Kadam, S.: Photocatalytic removal of antacid histamine H₂-receptor antagonist Ranitidine. *J. Indian Chem. Soc.* **94**(6), 623–630 (2017)
20. Maurya, N.S., Mittal, A.K., Cornel, P., Rother, E.: Biosorption of dyes using dead macro fungi: effect of dye structure, ionic strength and pH. *Biores. Technol.* **97**(3), 512–521 (2006)
21. Hu, Z., Chen, H., Yuan, S.: Removal of Congo red from aqueous solution by cat tail root. *J. Hazard. Mater.* **173**(1–3), 292–297 (2010)
22. Langmuir, I.: The constitution and fundamental properties of solids and liquids. Part I. Solids. *J. Am. Chem. Soc.* **38**(11), 2221–2295 (1916)
23. Uddin, M., Islam, M., Chakrabarti, M.H., Sakinul, M.: Adsorptive removal of methylene blue from aqueous solutions by means of HCl treated water hyacinth isotherms and performance studies. *J. Purity Utility React. Environ.* **2**(3), 63–84 (2013)
24. Lagergren, S.: About the theory of so-called adsorption of soluble substances, Zur theorie der sogenannten adsorption gelster stoffe. *Kungliga Svenska Vetenskapsakademiens Handlingar* **24**(4), 1–39 (1898)
25. Vasanth Kumar, K., Ramamurthy, V., Sivanesan, S.: Modeling the mechanism involved during the sorption of methylene blue onto fly ash. *J. Colloid Interface Sci.* **284**(1), 14–21 (2005)
26. Khattri, S.D., Singh, M.K.: Colour removal from synthetic dye wastewater using a bioadsorbent. *Water Air Soil Pollut.* **120**(3), 283–294 (2000)
27. Yavus, O., Altunkaynak, Y., Guzel, F.: Removal of copper, nickel and manganese from aqueous solution by kaolinite. *Water Res.* **37**(4), 948–952 (2003)



Comparative Analysis of Wideband Integrated Circular Slot and Dual Band Integrated Elliptical Slot Microstrip Patch Antennae for RF Energy Harvesting

Himanshi Sharma  and Laxmi Shrivastava ^(✉) 

Department of Electronics Engineering, Madhav Institute of Technology and Science, Gwalior, Madhya Pradesh, India
himanshisharma251194@gmail.com, lselex@mitsgwalior.in

Abstract. This paper presents the comparison of wideband microstrip patch antenna with integrated circular slot to the dual band integrated elliptical slot microstrip patch antenna for Radio Frequency Energy Harvesting (RFEH). These both proposed antennae are designed on FR4 lossy substrate with thickness of 1.6 mm. The wideband integrated circular slot antenna covers 2650 MHz frequency band and dual band integrated elliptical slot covers the frequency range from 2300 to 2400 MHz and 2450 to 2550 MHz. Circular slot is integrated inside a square patch which helps to increase the bandwidth of the antenna whereas the elliptical circular slot and stubs are integrated on the radiating patch which is used for increasing the resonating band of the dualband Microstrip patch antenna. Energy harvesting is used to replace the batteries, saves energy and it is portable which is helpful for the applications of healthcare, medicinal services and detecting systems, RFID etc.

Keywords: Circular and elliptical slot · Radio Frequency Energy Harvesting (RFEH) system · Stubs-slots · Microstrip patch antenna

1 Introduction

RF strength is primarily based on extracting the electricity from the environment particularly from RF spectrum and this comes from the signals which are present in the environment, the sources are totally wireless [1]. For the maximization of RF strength antenna must be design in this way so that it can acquire signals from all the committed sources i.e. from all the directions [2, 3]. Energy extracting from the environment is a challenging task to design the circuit and also for the research purpose because of its complex circuitry as it contains rectifier and antenna [4]. Radio transceiver like cell phones, television, broadcast stations are radio frequency energy sources. Energy which is harvested from the environment can be reused [5, 6]. The RFEH includes an antenna, a matching circuit and a rectifier. In harvesting system antenna is implemented at receiver end and it takes electromagnetic waves as its input, a rectifier circuit [7]. The RF energy is available towards any path and arbitrary polarization. In the surrounding scenario, the polarization of EM waves is either vertical or roundabout or

direct polarized. Different antenna is fabricated and designed at various resonating band and designed for direct or roundabout polarization utilizing various method in the literature [8–12].

For wideband microstrip patch antenna, Wi-max is application which is used at 2.65 GHz and it is a service of wireless broadband communication [13]. Wi-max is for the WAN (wide area network) and is much faster, WAN connects several LANS (local area network). The RF signal range from 3 kHz to 300 GHz be the source or medium to any radio frequency harvesting system. RFEH have found their applications in forms like wireless charging system, wireless sensor network etc. [13–16].

For dual band microstrip patch antenna, it consists side stubs, slots and elliptical circle which are integrated inside the patch and coaxial feed. The designing method of dual band antenna is discussed in Sect. 2, by integrating stubs and circle in the microstrip patch make the antenna to operate at 2.35 GHz and 2.52 GHz. The proposed antennae have been designed and analyzed using the Computer Simulation Technology-Microwave Studio [17], it is a software which is useful for electromagnetic analysis and design in the high frequency range.

2 Antenna Design

In this paper, a wideband microstrip patch antenna integrated circular slot and a dual band integrated elliptical slot microstrip patch antenna have been designed, with the circular and elliptical slots with different stubs respectively integrated on the patch. The cross sectional view with coaxial feed of wideband and dual band microstrip patch antenna is shown in Fig. 1. Microstrip patch is placed in the x-y plane, the size of both the microstrip patch are 46 mm × 46 mm and 31 mm × 44 mm.

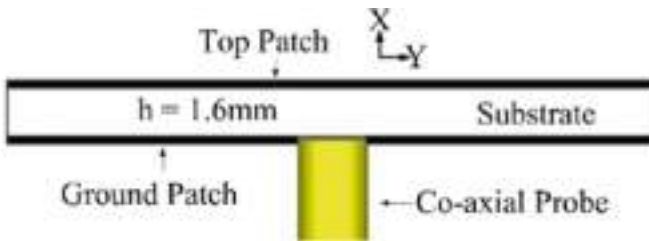


Fig. 1. Cross sectional view

Wideband Microstrip Patch Antenna Integrated Circular Slot

Four symmetric length stubs are introduced and integrated with square patch with symmetric gaps as shown in Fig. 2 whereas Fig. 3 shows the symmetric length stubs along with integrated circular slot. The length of stubs are $S1 \neq S2 = S3 \neq S4$. Along the negative y-axis of square patch a feeding stub is integrated with width F_w and length F_l . Parameter inside the square patch of circular slots are $S5L$, $S5W$, R . All designing dimensions parameter of antenna is shown in Table 1.

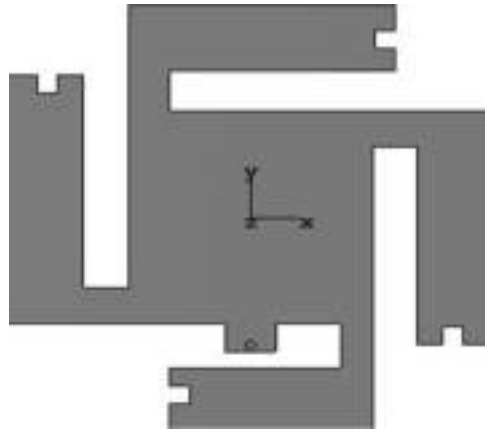


Fig. 2. Wideband microstrip patch antenna without slots

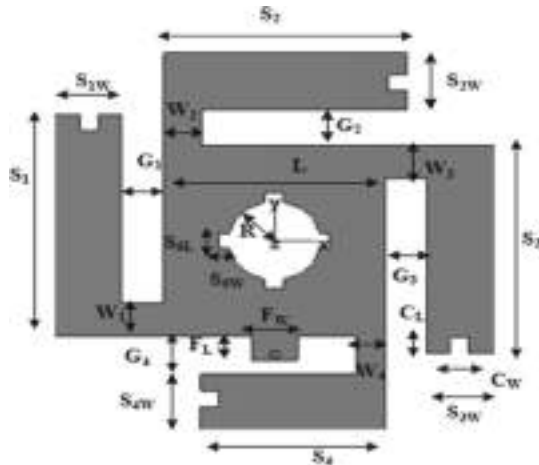


Fig. 3. Wideband radiator

Dual Band Integrated Elliptical Slot Microstrip patch Antenna

The length of vertical stubs $S_{1L} = S_{2L}$ and width $S_{1W} = S_{2W}$, whereas length of horizontal stubs are $S_{3L} = S_{4L} = S_{5L} = S_{6L}$ and width $S_{3W} = S_{4W} = S_{5W} = S_{6W}$ is shown in Figs. 4 whereas Fig. 5 consists vertical and horizontal stubs along with integrated elliptical slot. The gap between the stubs is $G_1 = G_4$ and $G_2 = G_3$. Along the negative y-axis of patch a feeding stub is integrated with width F_w and length F_L . All designing dimension parameters is shown in Table 2.

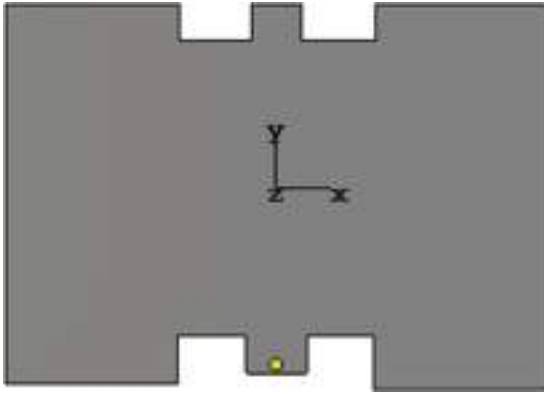


Fig. 4. Dual band microstrip patch antenna without slots, stubs and circle

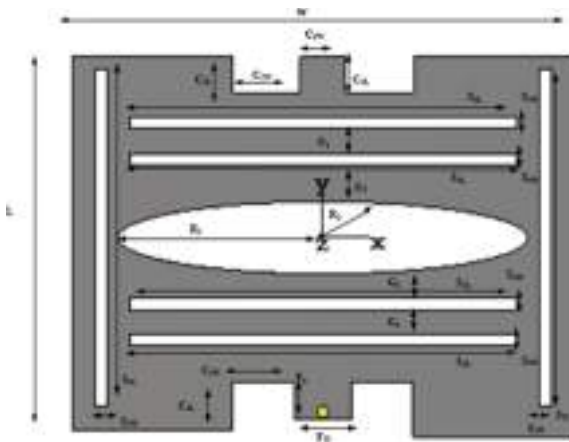


Fig. 5. Dual band radiator

Table 1. Wideband antenna design dimensions

Parameters	Dimensions (mm)	Parameters	Dimensions (mm)
S ₁	28	C _w	2
S ₂	26.3	C _L	2
S ₃	26.3	L	12
S ₄	20	R	5
S _{1W}	7.3	S _{5L}	2
S _{2W}	7.3	S _{5W}	4
S _{3W}	7.3	W ₁	4.1
S _{4W}	6.9	W ₂	4.1
G ₁	4.9	W ₃	4.1
G ₂	4.9	W ₄	3.1
G ₃	4.9	F _L	3.1
G ₄	4.9	F _w	5

Table 2. Dual Band antenna design dimension

Parameters	Dimensions (mm)	Parameters	Dimensions (mm)
L	31	C _{1L}	3
W	44	C _{1W}	4
S _{1L}	28	C _{2L}	3
S _{1W}	1	C _{2W}	6
S _{2L}	28	C _{3L}	4
S _{2W}	1	C _{3W}	5.5
S _{3L}	1	R ₁	9
S _{3W}	34	R ₂	1.5
S _{4L}	1	F _L	3.1
S _{4W}	34	F _W	5
S _{5L}	1	G ₁	2
S _{5W}	34	G ₂	4.5
S _{6L}	1	G ₃	3.5
S _{6W}	34	G ₄	2

3 Fabricated Design of Wideband and Dual Band Antennae

The designed antennae is manufactured and experimentally tested to verify the simulations results, the picture of fabricated wideband and dual band antennae is given in Figs. 6 and 7. It is printed on a low cost commercially obtainable FR-4 lossy substrate.

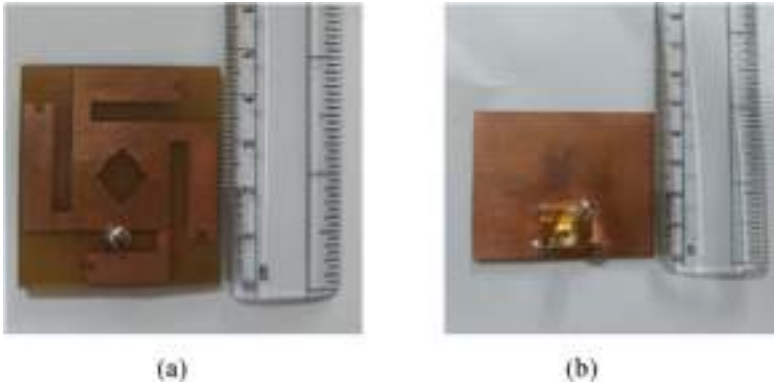


Fig. 6. (a) Front view of wideband antenna. (b) Back view of wideband antenna



Fig. 7. (a) Front view of dual band antenna. (b) Back view of dual band antenna

4 Results and Discussion

From the Figs. 2 and 4, the wideband antenna without using circular slot the antenna is not able to achieve the proper results as its return loss is less than -10 dB and it does not have the proper bandwidth, whereas in dual band antenna without using elliptical slots and stubs is also not able to achieve the proper results as its return loss is less than the proposed antenna, with single resonating band. Comparison graph of both the antenna without using slot, stubs and circle is shown in Fig. 8.

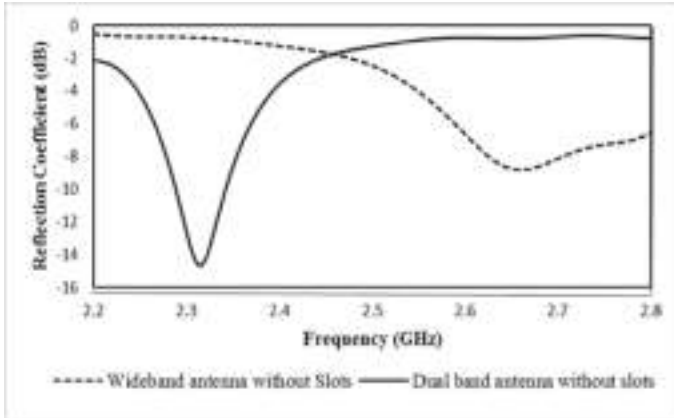


Fig. 8. Reflection coefficients of wideband and dual band antenna without using slots and stubs

Figure 9 shows the simulated reflection coefficients of both the proposed antennae (wideband and dual band antenna), In wideband antenna, the presence of slots gives better bandwidth of 200 MHz and return loss is also more than -10 dB with the frequency band of 2.65 GHz, hence return loss has been reduced, whereas in dual band antenna, the presence of stubs, slots and elliptical circle gives better result in resonating band with better return loss for the frequency band of 2.35 GHz and 2.52 GHz.

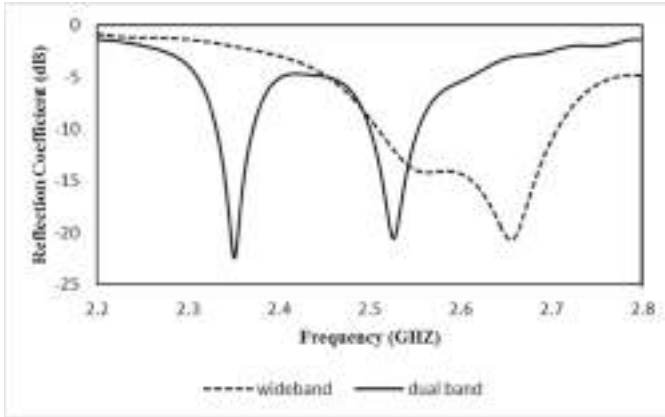


Fig. 9. Simulated reflection coefficients of wideband and dual band with slots

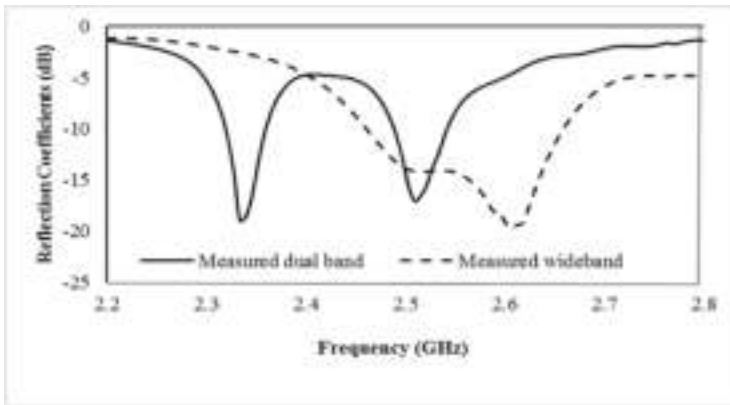


Fig. 10. Measured reflection coefficients of wideband and dual band with slots

Figure 10 shows the measured result of proposed (wideband and dual band with slots) antenna, the performance of proposed antenna was measured on FS315 spectrum analyzer, it is clearly observed that there is small discontinuity between simulated and measured result, this is because of cable losses and environmental effects.

5 Rectifier Circuit for Energy Harvesting

The rectifier circuit plays a vital role for the conversion of RF Energy into DC. RF Energy contains electromagnetic waves (in the form of Voltage and current). From the Fig. 11 the main components of the rectifier circuit are diodes D_1 , D_2 , D_3 , D_4 , Capacitor and LED (load) are selected to convert the RF to DC. The diode has a low

turn on voltage and is capable of working in the RF frequency range also diode is work in low power requirements. Comparison of efficiency for both the proposed antenna at different points is discussed in Table 3. Equation (1) is used for the calculation of efficiency of rectifier.

$$\eta = \frac{P_{DC}}{P_{RF}} * 100 \tag{1}$$

The maximum converted RF to DC power of proposed work (wideband and dual band) is 42% and 46% respectively as shown in Fig. 12.

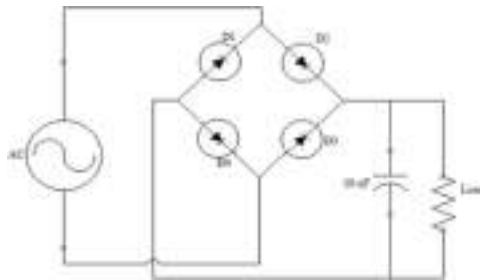


Fig. 11. Circuit diagram of rectifier

Table 3. Comparison of wideband and dual band efficiency

RF power (dBm)	Efficiency % (wideband)	Efficiency % (dual band)
-20	22	26
-15	35	39
-10	42	46
-5	20	24

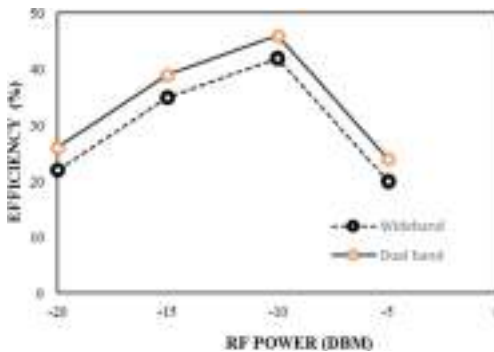


Fig. 12. RF-DC conversion

6 Conclusion

A Wideband microstrip patch antenna with integrated circular slot and Dual band integrated elliptical slot microstrip patch antenna are designed on FR-4 lossy substrate for RFEH, bandwidth enhancement and increasing resonating band applications. From the results it is observed that introduction of integrated circular slot in patch increases bandwidth and reduces the return loss of the antenna hence it is wideband antenna and introduction of integrated elliptical slot in patch, antenna gives dual band performance. The proposed work (wideband and dual band) covers the resonating band of 2650 MHz and from 2300–2400 MHz to 2450–2550 MHz, design includes circular and elliptical slots, stubs which is useful for the compact size of both the patch antenna. For further research in proposed work (both) the increment in number of bands and bandwidth for same structure is required, which provides appropriate properties for the use in energy harvesting applications like Health care, RFID, Wireless sensors and detecting systems etc.

References

1. Khaliq, H.S., Awais, M., Ahmad, W., Khan, W.T.: A high gain six band frequency independent dual CP planar log periodic antenna for ambient RF energy harvesting. In: 2017 Progress in Electromagnetics Research Symposium - Fall (PIERS - FALL) (2017)
2. Elsheakh, D.M.: Planar antenna for RF energy harvesting applications. In: 2017 IEEE International Symposium on Antennas and Propagation & USNC/URSI National Radio Science Meeting (2017)
3. Arrawatia, M., Baghini, M., Kumar, G.: Broadband bent triangular omnidirectional antenna for RF energy harvesting. *IEEE Antennas Wirel. Propag. Lett.* **15**, 1 (2015)
4. Saini, G., Sarkar, S., Arrawatia, M., Baghini, M.S.: Efficient power management circuit for RF energy harvesting with 74.27% efficiency at 623nW available power. In: 2016 14th IEEE International New Circuits and Systems Conference (NEWCAS) (2016)
5. Song, C., Huang, Y., Carter, P., Zhou, J., Yuan, S., Xu, Q., Kod, M.: A novel six-band dual CP rectenna using improved impedance matching technique for ambient RF energy harvesting. *IEEE Trans. Antennas Propag.* **64**(7), 3160–3171 (2016)
6. Palazzi, V., Hester, J., Bito, J., Alimenti, F., Kalialakis, C., Collado, A., Mezzanotte, P., Geogiadis, A., Roselli, L., Tentzeris, M.M.: A novel ultra-lightweight multiband rectenna on paper for RF energy harvesting in the next generation LTE bands. *IEEE Trans. Microw. Theory Tech.* **66**(1), 366–379 (2018)
7. Pham, B.L., Pham, A.-V.: Triple bands antenna and high efficiency rectifier design for RF energy harvesting at 900, 1900 and 2400 MHz. In: 2013 IEEE MTT-S International Microwave Symposium Digest (MTT), June 2013
8. Arrawatia, M., Baghini, M.S., Kumar, G.: Differential microstrip antenna for RF energy harvesting. *IEEE Trans. Antennas Propag.* **63**(4), 1581–1588 (2015)
9. Gonçalves, R., Carvalho, N.B., Pinho, P.: Small antenna design for very compact devices and wearables. *IET Microw. Antennas Propag.* **11**(6), 874–879 (2017)
10. Inbaraj, D., Kailasam, M., Sankararajan, R.: Statistical analysis on ambient RF energy harvesting for low-power wireless applications. *Int. J. Commun. Syst.* **31**(8), e3538 (2018)
11. Singh, M., Agrawal, S., Parihar, M.S.: Design of a rectenna system for GSM-900 band using novel broadside 2×1 array antenna. *J. Eng.* **2017**(6), 232–236 (2017)

12. Kim, S., Vyas, R., Bito, J., Niotaki, K., Collado, A., Georgiadis, A., Tentzeris, M.M.: Ambient RF energy-harvesting technologies for self-sustainable standalone wireless sensor platforms. *Proc. IEEE* **102**(11), 1649–1666 (2014)
13. Shen, S., Chiu, C.-Y., Murch, R.D.: A dual-port triple-band L-probe microstrip patch rectenna for ambient RF energy harvesting. *IEEE Antennas Wirel. Prop. Lett.* **16**, 3071–3074 (2017)
14. Khemar, A., Kacha, H., Takhedmit, H., Abib, G.: Design and experiments of a dual-band rectenna for ambient RF energy harvesting in urban environments. *IET Microw. Antennas Propag.* **12**(1), 49–55 (2018)
15. Aboualalaa, M., Abdel-Rahman, A.B., Allam, A., Elsadek, H., Pokharel, R.K.: Design of a dual-band microstrip antenna with enhanced gain for energy harvesting applications. *IEEE Antennas Wirel. Propag. Lett.* **16**, 1622–1626 (2017)
16. Fantuzzi, M., Masotti, D., Costanzo, A.: A novel integrated UWB–UHF one-port antenna for localization and energy harvesting. *IEEE Trans. Antennas Propag.* **63**(9), 3839–3848 (2015)
17. CST Microwave Studio © 2018



Identification of Urban and Water Areas from Polarimetric SAR Images Using Thresholding Algorithm

Tanvi Agarwal  and Laxmi Shrivastava  

Department of Electronics Engineering, Madhav Institute of Technology and Science, Gwalior 474005, Madhya Pradesh, India
tanviagarwal83@gmail.com, lselex@yahoo.com

Abstract. Synthetic Aperture Radar is an active remote sensing technique provides high – resolution image independent of atmospheric conditions. In this paper, the effect of decomposition technique on classification of region has been analyzed. For the classification, quad polarized SAR data has been used. The classified image obtained by thresholding algorithm is compared with reference data to obtain the accuracy. The decomposition methods are helpful in mapping the earth’s surface according to scattering behavior. The thresholding algorithm has great significance in applications such as target identification, edge detection, extraction and classification of remote sensing images, in detecting landslides and monitoring their activity which is of great importance for disaster prevention, preparedness and mitigation in hilly areas.

Keywords: Remote sensing · Polarization · Polarimetric decomposition

1 Introduction

Remote sensing means detecting earth’s surface from space by making use of properties of electromagnetic waves emitted, reflected or diffracted by sensed objects. Active remote sensing is one in which interaction of radiation of specific wavelength can be studied by sensing the scattered radiance from the target. Microwaves are used for remote sensing for their penetration capacity. The polarization is defined as when electric and magnetic field are perpendicular to each other as well as perpendicular to direction of propagation of wave. The satellite data can be single polarized like H/V, dual polarized like HH/HV or VV/VH and quad polarized data like HH + HV + VH + VV. The term ‘HH’ denotes transmit H and receive H, ‘HV’ denotes transmit H and receive V, ‘VH’ denotes transmit V and receive H and ‘VV’ denote transmit V and receive V. In this work, we are using quad polarized data i.e. Radarsat-2 [1]. On this data, we are performing different decomposition techniques to determine its scattering behavior [2]. As a result, we obtained decomposed images. This work is carried out using Sentinel Application Platform tool. The thresholding algorithm is carried out on decomposed images using different libraries of python programming language to classify into urban and water features [3]. The accuracy of classification is checked with respect to reference data (created using ArcMap) using in-built functions of python language [4].

Section 2 describes Polarimetric decomposition methods such as Van-Zyl decomposition, Cloude decomposition and H-alpha Quad Pol decomposition [6]. These decomposition techniques are applied on satellite images using Sentinel Application Platform tool, as a result, we get three bands, that is, volume scattering, surface scattering and double bounce scattering. These scattering bands determine the surface nature of the target.

The histogram plot of these decomposed images is a graph that shows the number of pixels in an image at each different intensity value found in that image. As our aim is to classify an image into urban and water areas, so to achieve this classification we need a threshold value with which we can compare each pixel value of an image. The threshold value is selected from the histogram of an image. This value is different for each decomposition technique. This thresholding algorithm is explained in Sect. 3.

Richmond area and quad polarized data i.e. Radarsat-2 data for this work is selected. So, Sect. 4 describes the study area and data used.

Section 5 describes the methodology employed to achieve the objective of this work. The results of classified images are compared on the basis of performance evaluation metrics such as accuracy and kappa coefficient which is discussed in Sect. 6. The results of each decomposition technique is described in Sect. 7.

2 Polarimetric Decomposition

As the data available was fully polarimetric, so following decomposition methods were applied like, Van-Zyl, Cloude and H-alpha. The decomposition methods were applied so that the original satellite image can be decomposed into three bands and with the help of their histogram thresholding conditions can be applied to them. On the basis of threshold value, classification can be done into urban and water area respectively. Brief introduction about decomposition methods are as follows:

2.1 Van-Zyl Decomposition

Van-Zyl disintegration demonstrates that the initial two eigenvectors speak to equivalent dispersing grids that can be translated as far as odd and significantly number of reflections [9]. The double bounce gives great detachment between man-made structure and vegetation yet less distinctness in regular vegetation.

2.2 Cloude Decomposition

Cloude proposed an eigenvector disintegration model, utilizing dissipate edge and entropy H to express arbitrary spellbound character [9]. Eigenvector analysis is targeted for coherent matrix, as formula follows:

$$\langle T \rangle = \lambda_1 e_1 * e_1^H + \lambda_2 e_2 * e_2^H + \lambda_3 e_3 * e_3^H \quad (1)$$

e_i is for eigenvalue and λ_i is for eigenvector, e_i is defined as:

$$e_i = \cos \alpha_i \sin \alpha_i \cos \beta_i e^{j\delta_i} \sin \alpha_i \sin \beta_i e^{j\eta_i} \quad (2)$$

Entropy is defined as:

$$H = - \sum_{i=1}^3 P_i \log_3 P_i \quad P_i = \frac{\lambda_i}{\sum_{i=1}^3 \lambda_j} \quad (3)$$

Angle α is defined as:

$$\alpha = \sum_{i=1}^3 P_i \alpha_i \quad (4)$$

2.3 H-Alpha Quad Pol Decomposition

The H-alpha polarimetric decay hypothesis depends on the eigenvalue – eigenvector based examination of a coherency matrix [11]. It gives a premise invariant portrayal of the scatterer. Eigenvector investigation gives data about various kinds of dissipating forms, while eigenvalue examination gives data about their relative sizes.

3 Thresholding Algorithm

Thresholding is simplest method of image classification. In this algorithm, pixels are assigned to classes according to range of values in which pixel lies [3]. Since, in this work only two classes are considered i.e. urban area and water area. So, in this case the output of algorithm is binary image. Mathematically, it can be stated as:

$$g(x, y) = \begin{cases} 1 & \text{if } f(x, y) < T \\ 0 & \text{if } f(x, y) \geq T \end{cases} \quad (5)$$

Where, T is as threshold value.

4 Study Area and Datasets

The study area for this work is Richmond, capital of U.S. state of Virginia as shown in Fig. 1. It is in the Piedmont district of Virginia, at the James River's most noteworthy navi-peak point. The region is described by moderately low, moving slopes, and lies between the low, level tidewater locale and Blue Ridge Mountains. RADARSAT – 2 C-Band fully polarimetric single look complex data has been used in this study [10]. RADARSAT is a propelled Earth perception satellite task created by Canada to screen natural change and to help asset supportability. This utilizes Synthetic Aperture Radar (SAR) a functioning microwave sensor, permitting 24 h information gathering

autonomous of climate conditions and illumination. The Radarsat-2 data for this area is downloaded from mdacorporation. The description of dataset is provided in Table 1.

Table 1. Description of the dataset

Description of the dataset	
Sensor	Radarsat-2
Date	09-04-2008
Polarization	HH + HV + VH + VV
Mode	Ascending
Orbit number	1665



Fig. 1. Richmond as study area

5 Methodology

The following section describes the details of methodology employed to meet the objective of this work. The overview of the methodology adopted for this work has been shown in Fig. 2. In this work, the methodology is to carry out classification of decomposed satellite images into urban and water body features [5].

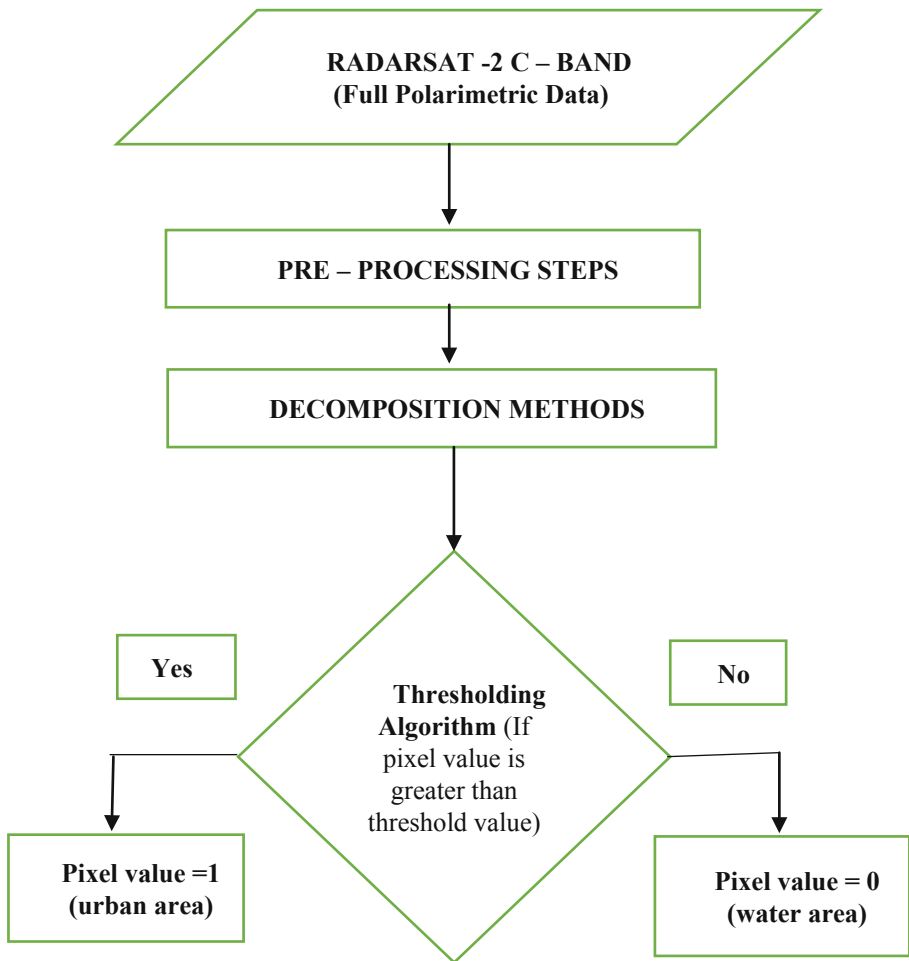


Fig. 2. Methodology flow diagram

Explanation of Flowchart:

Step 1: As the dataset was available in single look complex format, therefore, pre – processing steps were carried out using Sentinel Application Platform tool (SNAP).

Step 2: The second step involved applying polarimetric decomposition technique on data using SNAP (Sentinel Application Platform) tool [7].

Step 3: The third step involves analyzing the histogram plot of decomposed images using Sentinel Application Platform (SNAP) tool and deciding the threshold value. This value is used in implementing thresholding algorithm.

Step 4: In the fourth step, thresholding algorithm is applied on decomposed image where threshold value is compared with each pixel values of an image using python programming language in Jupyter notebook. This is done to classify an image into urban and water area.

Step 5: Thereafter, classified images were displayed on Google Earth to make sure classification is done properly.

Step 6: This step includes creating reference data using ArcMap.

Step 7: Lastly, the accuracy of classification process with respect to reference data is checked by calculating confusion matrix, overall accuracy and kappa coefficient [8] using python language.

In this paper, Van-Zyl, Cloude and H-alpha quad pol decomposition methods are considered [9].

6 Performance Evaluation Metrics

The parameters under which the performance of classification is obtained are as follows:

6.1 Accuracy Score

The accuracy_score capacity registers the exactness, either the fraction (default) or the count (normalize = False) of right forecasts [8]. In the event that the whole arrangement of anticipated marks for an example carefully coordinate with the genuine arrangement of names, at that point the subset precision is 1.0; else it is 0.0. If \hat{y}_i is the anticipated value of the i-th sample and y_i is the genuine value, then the fraction of correct predictions over $n_{samples}$ is defined as

$$accuracy(y, \hat{y}) = \frac{1}{n_{samples}} \sum_{i=0}^{n_{samples}-1} 1(\hat{y}_i = y_i) \quad (6)$$

Where $1(x)$ is the indicator function.

6.2 Kappa Score

Cohen's kappa is a measurement that measures between annotator understanding [8]. This capacity processes Cohen's kappa, a score that communicates the degree of understanding between two annotators on an order issue. It is defined as:

$$k = (p_o - p_e) / (1 - p_e) \quad (7)$$

where p_o is the observational likelihood of agreement on the label assigned to any sample (the observed agreement ratio), and p_e is the anticipated understanding when both annotators assign labels randomly.

7 Results and Discussions

This section describes the result of decomposition methods followed by classification results. Thereafter, results were compared on the basis of accuracy and kappa score.

The raster input for polarimetric decomposition method is shown in Fig. 3. The raster size for this input is 543×761 .



Fig. 3. Raster input

Now, different decomposition methods and terrain corrections are applied on this raster input. The results of which are depicted in following section.

7.1 Van-Zyl Decomposition

Figure 4 shows the result of Van Zyl decomposition on an input image. The size of decomposed image is 783×485 . Figure 5 shows the histogram of volume scattering band of decomposed image.

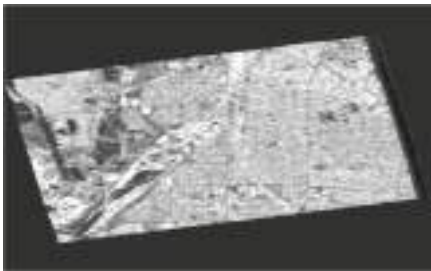


Fig. 4. Decomposed image

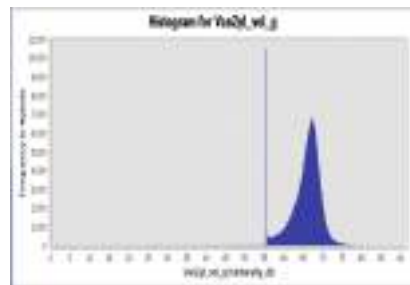
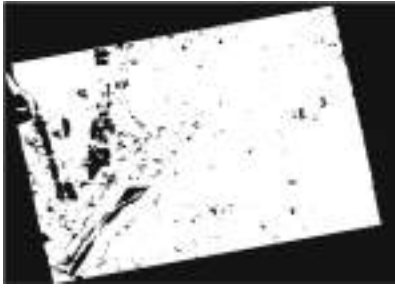


Fig. 5. Histogram plot

The threshold value ‘60’ is selected from the histogram plot. Now, thresholding algorithm is applied on decomposed image to classify pixels into two classes. Figure 6 shows the result of classification into urban and water area. Figure 7 shows the classified urban area on Google Earth.



■ Water Area
□ Urban Area

Fig. 6. Classified image



Fig. 7. Displaying urban area on Google Earth

7.2 H-Alpha Quad Pol Decomposition

Figure 8 shows the result of H – Alpha Quad Pol decomposition on an input image. The size of decomposed image is 783×485 . Figure 9 shows the histogram of alpha scattering band of decomposed image.

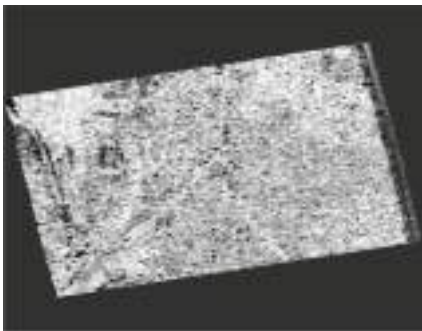


Fig. 8. Decomposed image

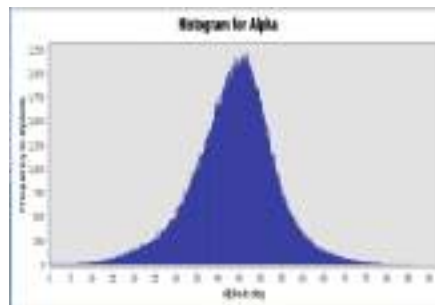


Fig. 9. Histogram plot

The threshold value ‘25’ is selected from the histogram plot. Now, thresholding algorithm is applied on decomposed image to classify pixels into two classes. Figure 10 shows the result of classification into urban and water area. Figure 11 shows the classified water area on Google Earth.

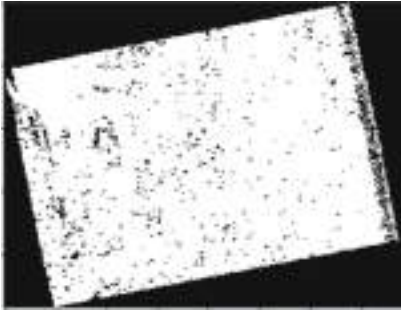


Fig. 10. Classified image



Fig. 11. Displaying water area

7.3 Clouds Decomposition

Figure 12 shows the result of Clouds decomposition on an input image. The size of decomposed image is 783×485 . Figure 13 shows the histogram of double bounce scattering band of decomposed image.

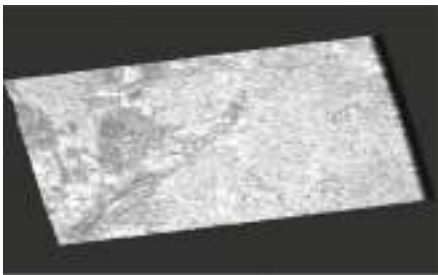


Fig. 12. Decomposed image

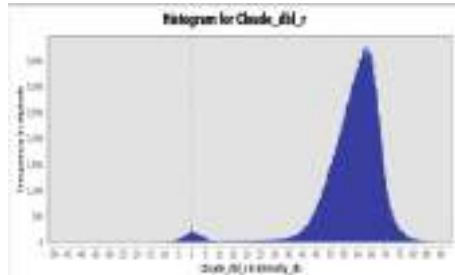


Fig. 13. Histogram plot

The threshold value '35' is selected from the histogram plot. Now, thresholding algorithm is applied on decomposed image to classify pixels into two classes.

Figure 14 shows the result of classification into urban and water area. Figure 15 shows the classified urban area on Google Earth.



Fig. 14. Classified image



Fig. 15. Displaying water area

7.4 Accuracy Assessment

The Accuracy Assessment of classified images are done on the basis of overall accuracy and kappa coefficient [3]. For computing the accuracy, reference data is essential. So, reference data for classification assessment is created using QGIS – 2.18.4. This reference data is composed of three different vector layer classes – urban area, water area and unclassified area. These vector layer classes were merged into one vector layer which is then converted into raster. This process is known as digitization.

The reference data is shown in Fig. 16.

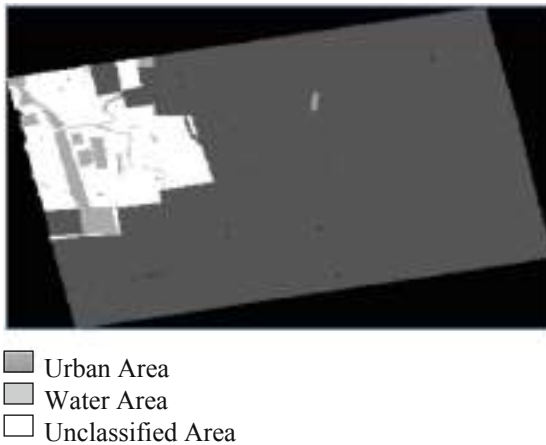


Fig. 16. Reference data

The comparative analysis on the basis of overall accuracy and kappa coefficient for all the decomposition methods are shown in Table 2.

Table 2. Accuracy assessment comparison

Decomposition method	Accuracy	Kappa coefficient
Van Zyl decomposition	59.98%	0.238
H Alpha Quad decomposition	62.1%	0.26006
Cloude decomposition	61.39%	0.253

8 Conclusion

Classification has an important role in microwave remote sensing. The goal of this work is to classify the decomposed satellite images into urban and water area. Different decomposition methods were applied on raster image resulting in decomposed images. Classification was done on the basis of thresholding algorithm. Thresholding

technique is an important algorithm of classification technique. From the observations, it can be concluded that H Alpha Quad Pol decomposition method has highest accuracy i.e. 62.1%. Van Zyl decomposition method has least accuracy compared to other methods i.e. 59.98%. The thresholding algorithm find its application in detecting landslides and monitoring their activity which is of great importance for disaster prevention, preparedness and mitigation in hilly areas.

References

1. Luo, S., Tong, L., Chen, Y., Tan, L.: Landslides identification based on polarimetric decomposition techniques using Radarsat-2 polarimetric images. *Int. J. Remote Sens.* **37**, 2831–2843 (2016)
2. Dave, B., Mohan, S.: Study of polarimetric decomposition techniques for monitoring temporal growth of major kharif crops and surrounding landuse in India. In: *IEEE International Geoscience and Remote Sensing Symposium*, pp. 4627–4630 (2018)
3. Goh, T.Y., Basah, S.N., Yazid, H., Safar, M.J.A., Saad, F.S.A.: Performance analysis of image thresholding: Otsu technique. *J. Meas.* **114**, 298–307 (2017)
4. Mahdavi, S., Salehi, B., Granger, J., Amani, M., Brisco, B., Huang, W.: Remote sensing for wetland classification: a comprehensive review. *Geosci. Remote Sens.* **55**, 623–658 (2017)
5. Varghese, A.O., Suryavanshi, A., Joshi, A.K.: Analysis of different polarimetric target decomposition methods in forest density classification using C band SAR data. *Int. J. Remote Sens.* **37**(3), 694–709 (2016)
6. Han, Y., Shao, Y.: Full polarimetric SAR classification based on Yamaguchi decomposition model and scattering parameters. In: *IEEE International Conference on Progress in Informatics and Computing*, pp. 1104–1108 (2010)
7. Varghese, A.O., Joshi, A.K.: Polarimetric classification of C-band SAR data for forest density characterization. *Curr. Sci.* **108**(1), 100–106 (2015)
8. Salmon, B.P., Kleynhans, W., Schwegmann, C.P., Olivier, J.C.: Proper comparison among methods using a confusion matrix. In: *IEEE International Geoscience and Remote Sensing Symposium (IGARSS)*, pp. 3057–3060 (2015)
9. Ustuner, M., Balik Sanli, F.: Polarimetric target decompositions and light gradient boosting machine for crop classification: a comparative evaluation. *Int. J. Geoinf.* **8**, 97 (2019)
10. Wang, X., Zhang, L., Zhu, S.: A four component decomposition model for polarimetric SAR image based on adaptive volume scattering model. In: *IEEE International Geoscience and Remote Sensing*, pp. 4563–4566 (2018)
11. Haldar, D., Rana, P., Hooda, R.S.: Biophysical parameter assessment of winter crops using polarimetric variables-entropy (H), anisotropy (A) and alpha (α). *Arab. J. Geosci.* **12**(12), 375 (2019)

Author Index

A

Afridi, Juhi, 123
Agarwal, Anshul, 261
Agarwal, Tanvi, 555
Agrawal, Bulbul, 163
Agrawal, Monika, 476
Agrawal, Ruchin, 97
Ali, Nazim, 307
Alim, Abdul, 237

B

Batham, Deepak, 88
Bharadwaj, Manish, 292
Bhattacharya, Shourabh, 12
Bhondekar, Amol P., 443
Bhuria, Vijay, 476
Bhutia, Pema Rinzing, 132
Byjubai, T. P., 271

C

Chakraborty, Amit, 146
Chaudhary, Sanjay, 513
Chaudhary, Vishal, 376

D

Dabariya, Chandrika, 249
Das, Piyali, 132
Das, Priyanath, 146
Dewan, Lillie, 389
Dey, Diptanu, 146
Dixit, Manish, 163, 363
Dixit, Shishir, 476
Dohare, Punjan, 443
Dubey, Hari Mohan, 376, 524
Dubey, Rahul, 1

Dubey, Salil Madhav, 524
Dubey, Shradha, 363

G

Gaur, Anjula, 535
Gaur, M. K., 18, 28, 399
Gautam, Divya, 176
Goyal, Rajeev, 503
Goyal, Swati, 535
Gupta, Ashish, 66
Gupta, Awadhesh, 123
Gupta, Nipun, 488
Gupta, Preeti, 535
Gupta, R. K., 219
Gupta, Raghvi, 467
Gupta, Rekha, 66

I

Idachaba, A. Ogacheko, 412

J

Jain, Ravi, 320
Jaiswal, Abhishek Kumar, 111
Jarial, Raj Kumar, 209
Johari, Punit Kumar, 219
Joshi, Hitesh, 424

K

Kaur, Perminder Jit, 340
Khandegar, Vinita, 340, 346
Kosti, Siddhartha, 39, 330
Kumar, Arinjay, 346
Kumar, Jitendra, 185
Kumar, Praveen, 52
Kumar, Tushar, 437

M

Mahor, Vikas, 230
 Malvi, Chandra S., 39
 Mandal, Monisha Mridha, 307
 Markam, Karuna, 1
 Mehta, Ram Krishna, 132
 Mishra, Aastha, 300
 Mishra, Dilip Kumar, 513

N

Nain, Garima, 66
 Nigam, Anjani Kumar, 97

O

Osegi, E. Ndid, 412

P

Pandey, Amritanshu, 467
 Pandit, Manjaree, 376, 524
 Pandit, R. K., 399
 Parmar, Poonam, 1
 Pathak, Anupam, 346
 Pawar, Rahul B., 351

R

Rathore, Bhavna, 488
 Rawat, Ramdew, 376
 Roshan, Rajesh, 209
 Roy, Om Prakash, 132

S

Sagar, M. K., 28
 Sagwal, Rahul, 488
 Saini, Vikram, 389
 Saraswat, Monika, 454
 Shah, Rishika, 399
 Sharma, Garima, 52
 Sharma, Himanshi, 545
 Sharma, Manisha, 209
 Sharma, Ravinder, 77
 Sharma, Sanjiv, 503
 Sharma, Satya Prakash, 77
 Sheikh, Mohd. Yunus, 320
 Shinde, Vikas, 185, 292, 513
 Shrivastava, Laxmi, 52, 545, 555

Shrivastava, Shikha, 123
 Shukla, Diwakar, 237
 Shukla, Vikas, 282
 Singh, Anurendra, 146
 Singh, Dharmendra, 320
 Singh, Madhav, 230
 Singh, Preetvanti, 300
 Singh, Pushpendra, 18
 Singh, Rajeev Kumar, 249
 Singh, Shailendra Pratap, 488
 Singhal, P. K., 261
 Sneha, K., 271
 Srivastava, Amitabh Kumar, 97
 Srivastava, Laxmi, 488
 Swami, A. K., 424

T

Taylor, O. Egerton, 412
 Thakare, V. V., 261
 Thakre, Vandana Vikas, 123
 Thakur, Tripta, 437
 Thakur, Vikas Kumar, 28
 Tiwari, Vimal, 524
 Tokekar, Vrinda, 176
 Tomar, Chavi, 340
 Tripathi, Archana, 467
 Tripathi, Manoj, 320
 Trivedi, Manoj Kumar, 282, 292, 111

U

Upadhyay, Arvind Kumar, 503

V

Venkata Rao, R., 351

W

Wadhwa, Kamal, 513
 Wadhvani, A. K., 454
 Wadhvani, Sulochana, 454
 Wokoma, B. Alexander, 412

Y

Yadav, Amit, 300
 Yadav, Dharmendra Singh, 88